CHARACTERISTICS OF GAS-LIQUID COUNTERFLOW IN INCLINED DUCTS WITH PARTICULAR REFERENCE TO REFLUX CONDENSERS

Albert Zapke

Dissertation presented for the degree of Doctor of Philosophy (Mechanical Engineering) at the University of Stellenbosch

Promoter: Prof. D.G. Kröger

External examiners:

1. Prof. Dr.-Ing. Dr.-Ing. E.h. F. Mayinger, Technische Universität München

2. Prof. J. S. Chang, McMaster University, Hamilton, Ontario

Internal examiner: Prof. T.W. von Backström

Department of Mechanical Engineering

University of Stellenbosch

Stellenbosch, South Africa

September 1997

DECLARATION

I, Albert Zapke, the undersigned, hereby declare that the work contained in this dissertation is my own original work and has not previously, in its entirety or in part, been submitted at any university for a degree.

A. Zapke

.....

Signature of candidate

10th day of September 1997

OPSOMMING

Die teenvloei van gas en vloeistof in reghoekige skuins buise is eksperimenteel ondersoek. Die drukverlies oor die skerp gasinlaat en die drukval in die buis is gemeet vir verskillende kombinasies van water, propanol, metanol, lug, argon, helium en waterstof. Buishoogtes en breedtes van 50 mm tot 150 mm en 10 mm tot 20 mm respektiewelik is getoets. Die klem van die ondersoek is op lae vloeistofvloeitempos soos teenwoordig tydens kondensasie van stoom in lugverkoelde teenvloeikondensors.

Vir lae tot matige gasvloeitempos is die drukval afhanklik van die gas Reynolds-getal terwyl die densimetriese gas Froude-getal die heersende parameter word soos die gasvloei toeneem. Die hidrouliese diameter verteenwoordig die dimensie in die Reynolds-getal maar die buishoogte word die karakteristieke dimensie in die Froude-getal gebied.

Vloedingskurwes is vir 'n reeks van buishoeke gegenereer. Die vloedingdata korreleer in terme van die Froude-getal en 'n dimensielose parameter bestaande uit die hidrouliese diameter, oppervlakspanning, vloeistofdigtheid en die vloeistofviskositeit. Die vloeidingsnelheid is primêr van die buishoogte, vloeierdigthede en die buishoek afhanklik. Die vloeistofviskositeit-effek is sterker as dié van die oppervlakspanning. Beide dié eienskappe speel egter 'n sekondêre rol. Die gas Reynolds-getal beïnvloed nie die vloeidingsproses nie.

Die fundamentele bevindinge van die teenvloeiondersoek is toegepas om die werkverigting van 'n lugverkoelde teenvloeikondenser teoreties te modelleer. Werkverigtingstoetse is uitgevoer op 'n volskaal teenvloeikondenser. Die toetsresultate word vergelyk met die teoretiese voorspelling. Die teenvloeikondensor behaal slegs sowat 60% van die voorspelde warmteoordrag omdat van die gevinde buise gedeeltelik by omgewingstemperatuur is. Hierdie verskynsel heet koue of dooie sones. Dit blyk dat die kondensaat in die onderste spruitstuk nie vrylik kan dreineer nie en in die vorm van druppels deur die stoom opgesleur word. Gevolglik versamel kondensaat binne die buise en sodoende kan nie-kondenseerbare gasse nie effektief uit die teenvloeikondensor verwyder word nie. Soos die gasse versamel word koue sones gevorm. Dit blyk dat vloeding soos waargeneem in enkelbuise nie tot die vorming van koue sones bydra nie.

Trefwoorde: Gas-vloeistof-vloei, Teenvloei, Skuins buise, Drukval, Vloeiding, Teenvloeikondensasie, Deflegmator, Dooie sones.

ABSTRACT

An experimental investigation on gas-liquid counterflow in inclined rectangular ducts is conducted. The pressure drop across the sharp-edged gas inlet and the pressure gradient inside the duct are measured. Combinations of water, methanol, propanol, air, argon, helium and hydrogen are tested. The duct height and width are varied from 50 mm to 150 mm and 10 mm to 20 mm respectively. The emphasis is on high void fraction flow, i.e. low liquid flow rates as encountered in air-cooled reflux condensers.

At low to moderate gas flow rates the pressure gradient is gas Reynolds number related while it becomes dependent on the superficial densimetric gas Froude number as the gas flow is increased. According to experiment the hydraulic diameter is the required length dimension in the gas Reynolds number while the duct height becomes the characteristic dimension in the Froude number regime.

Flooding curves are generated for duct inclinations from close to the horizontal to the vertical. The data correlate in terms of the phase Froude numbers and a dimensionless liquid property parameter containing the hydraulic diameter, density, surface tension and the viscosity. The flooding gas velocity is found to be strongly dependent on the duct height, the phase densities and the duct inclination. The liquid viscosity has a stronger effect than the surface tension. Both these properties however play a secondary role. Flooding is not related to the gas Reynolds number.

A theoretical model, based on the phenomenological findings of the adiabatic counterflow investigation, is derived to evaluate the performance of an air-cooled reflux condenser. Field tests are conducted on a full scale reflux condenser and the measured performance is compared to the model prediction. The reflux condenser is found to achieve only ≈60% of the predicted heat rejection rate due to the existence of so-called cold or dead zones. Indications are that excessive entraiment in the bottom header and the subsequent accumulation of condensate in the finned tubes causes a maldistribution of the steamside flow. In the process noncondensable gases accumulate and form dead zones, causing ineffective performance. Flooding as found in single-ducts does not appear to contribute to the formation of the dead zones.

***Keywords*:** Gas-liquid flow; Countercurrent flow; Inclined ducts; Pressure drop; Flooding; Reflux condensation; Dephlegmator; De-aerator; Dead zones.

ACKNOWLEDGEMENTS

Firstly, I would like to express my gratitude for Prof. Kröger for his guidance and motivating influence throughout my postgraduate studies.

I further would like to thank my family for their support.

Kobus Zietsman and my fellow students who assisted me in the laboratory and during the investigation of the full scale condenser deserve a special word of thanks. Your help meant a lot and is very much appreciated.

I dedicate this dissertation to my wife and wonderful companion, Liezel.

TABLE OF CONTENTS

DECLARATION i
OPSOMMING ii
ABSTRACT iii
ACKNOWLEDGEMENTS iv
TABLE OF CONTENTS v
NOMENCLATURE xi
Symbols xi
Greek symbols xii
Subscripts xii
Superscripts xiv
Dimensionless groups xiv

PART A: ADIABATIC COUNTERFLOW INVESTIGATION

CHAPTER 1 INTRODUCTION 1.1
1.1 Gas-liquid counterflow in reflux condensers employed in the power industries 1.1
1.2 Scope of the present investigation 1.2
1.2.1 Part A: Adiabatic countercurrent flow and flooding investigation 1.3
1.2.2 Part B: Full scale dephlegmator tests and analysis 1.4
1.3 Past investigations on gas-liquid countercurrent flow 1.4
CHAPTER 2 LITERATURE SURVEY ON EXPERIMENTAL FLOODING, PRESSURE DROP AND ENTRAINMENT STUDIES FOR COUNTERCURRENT FLOW 2.1
2.1 Introduction 2.1
2.2 Flow patterns 2.1
2.2.1 Vertical cocurrent upflow 2.1
2.2.2 Vertical countercurrent flow 2.5

2.2.3 Horizontal cocurrent flow 2.6
2.2.4 Flow patterns during inclined upward flow 2.8
2.3 Flooding during adiabatic flow inside vertical tubes and ducts 2.9
2.3.1 The flooding definition 2.9
2.3.2 Gas-liquid interactions during counterflow and the effect of the liquid outlet/gas inlet configuration on the flooding process 2.11
2.3.3 Discussion of the observations on the behaviour of the gas-liquid interface and flooding 2.22
2.4 The effect of the test section geometry on flooding during adiabatic flow 2.26
2.4.1 The tube length effect 2.26
2.4.2 The influence of the cross-sectional duct geometry on counterflow 2.27
2.4.3 Flooding inside inclined ducts and tubes 2.31
2.5 The role of the fluid properties during flooding 2.33
2.5.1 Previous investigations 2.33
2.5.2 Discussion 2.43
2.6 Limiting conditions during reflux condensation 2.47
2.7 Pressure gradient during countercurrent gas-liquid flow 2.52
2.8 Liquid entrainment encountered in countercurrent flow 2.55
2.9 Conclusions and aim of the present adiabatic counterflow investigation 2.57
CHAPTER 3 EXPERIMENTAL EQUIPMENT AND DATA ACQUISITION 3.1
3.1 Introduction 3.1
3.2 Liquid supply 3.1
3.3 Gas supply 3.6
3.4 Test section configurations 3.7
3.4.1 Long configuration 3.7
3.4.2 Short configuration 3.11
3.4.3 Entrainment measurements 3.13
3.5 Instrumentation 3.13
3.5.1 Pressure measurements 3.13
3.5.2 Data acquisition system 3.16
3.6 A typical experimental run 3.19

3.7 Accuracy of the system.....3.20

CHAPTER 4 EXPERIMENTAL RESULTS: FLOW PATTERNS AND PRESSURE DROP.....4.1

4.1 Presentation of data.....4.1

4.1.1 Frictional pressure drop.....4.1

4.1.2 Entrance pressure drop.....4.3

4.2 Flow patterns observed at a duct inclination of 60° to the horizontal.....4.4

4.2.1 Air-propanol flow inside the 50 mm duct (W_t = 10 mm).....4.4

4.2.2 Air-propanol flow inside the 100 mm duct.....4.13

4.2.3 Air-water flow inside the 100 mm duct.....4.18

4.3 Pressure drop characteristics at an inclination of 60° to the horizontal.....4.23

4.3.1 The effect of the duct height.....4.23

4.3.2 The effect of the gas properties.....4.23

4.3.3 The effect of the liquid properties and wetting on the pressure drop characteristics.....4.28

4.3.4 The effect of the liquid flow rate wetting on the pressure drop characteristics.....4.32

4.4 Flow patterns observed at a duct inclination of 5° to the horizontal.....4.34

4.4.1 Air-propanol flow inside the 50 mm duct (W_t = 10 mm).....4.34

4.4.2 Air-propanol flow inside the 100 mm duct.....4.38

4.5 Flow patterns observed during vertical flow of air-propanol in the 50 mm duct (W_t = 10 mm).....4.41

4.6 The effect of the duct inclination on the flow patterns and the pressure drop.....4.53

4.7 The transient nature of gas-liquid counterflow at intermediate angles.....4.59

4.8 Summary of the results.....4.64

CHAPTER 5 EXPERIMENTAL RESULTS: FLOODING AND ENTRAINMENT.....5.1

5.1 The flooding definition for counterflow in vertical and inclined ducts.....5.1

5.2 The role of the duct dimensions during flooding.....5.4

5.3 The effect of the fluid properties on flooding inside inclined ducts.....5.14

5.3.1 The effect of the gas properties.....5.14

5.3.2 The effect of the liquid properties 5.14
5.4 The effect of the duct inclination on flooding 5.23
5.5 Correlation for flooding inside inclined rectangular ducts 5.29
5.6 The effect of the liquid properties on flooding inside vertical rectangular ducts 5.32
5.7 Entrainment during counterflow in the 150 mm duct inclined 60° 5.36
5.8 Discussion of the flooding results 5.39
CHAPTER 6 EVALUATION OF THE VALIDITY OF THE FROUDE-*Zk* NUMBER COMBINATION AND CONCLUSIONS 6.1
6.1 Flooding data of other investigations 6.1
6.1.1 Clift *et al.* [66CL1] 6.1
6.1.2 Suzuki and Ueda [77SU1] 6.2
6.1.3 Chung *et al.* [79CH1,80CH1] 6.2
6.1.4 Zapke and Kröger [96ZA1] 6.7
6.2 General remarks and conclusions 6.10

PART B: PERFORMANCE MODELLING AND INVESTIGATION OF A FULL SCALE AIR-COOLED CONDENSER

CHAPTER 7 BACKGROUND ON THE CONDENSER-DEPHLEGMATOR SYSTEM 7.1
CHAPTER 8 DESCRPTION OF THE FULL SCALE TEST PROCEDURE 8.1
8.1 Airside measurements and instrumentation 8.1
8.2 Steamside measurements and instrumentation 8.4
8.3 Data acquisition and test procedure 8.5
CHAPTER 9 ANALYSIS OF A DIRECT DRY-COOLED FORCED DRAFT CONDENSER 9.1
9.1 Introduction 9.1
9.2 Steamside flow analysis 9.2
9.2.1 Condenser unit 9.2

9.2.2 Dephlegmator unit 9.9
9.3 Airside flow 9.15
9.4 Ejector characteristics 9.18
9.5 Turbine characteristics 9.21
9.6 System solution 9.22
CHAPTER 10 COMPARISON BETWEEN FIELD TEST RESULTS AND THEORY 10.1
10.1 Performance evaluation of a single condenser unit 10.1
10.1.1 Air inlet temperature for equation (8.1) 10.1
10.1.2 Input data for simulation model 10.2
10.1.3 Airside prediction according to theory 10.3
10.1.4 Heat transfer and steamside flow prediction according to theory 10.5
10.1.5 Comparison of the predicted and measured performance 10.6
10.2 Performance evaluation of a single dephlegmator unit 10.8
10.2.1 Infra-red images of the dephlegmator bundles 10.9
10.2.2 Comparison of the predicted and measured dephlegmator performance 10.18
10.2.3 Discussion of the dephlegmator performance 10.22
10.3 Reduction in turbine output due to ineffective dephlegmator performance 10.28
10.4 Closing remarks 10.30
CHAPTER 11 SUMMARY 11.1
REFERENCES R.1

APPENDIX A DETAIL DRAWINGS OF FULL SCALE AIR-COOLED CONDENSER A.1
APPENDIX B ORIFICE PLATE DESIGN AND FLOW RATE CALCULATION B.1
APPENDIX C PROPERTIES OF FLUIDS C.1
APPENDIX D PRESSURE DROP DATA FOR THE LONG CONFIGURATION INCLINED AT 60° TO THE HORIZONTAL D.1
APPENDIX E PRESSURE DROP DATA FOR THE SHORT CONFIGURATION E.1

APPENDIX F FLOODING DATA.....F.1

APPENDIX G DRAFT EQUATION FOR FORCED DRAFT INCLINED HEAT EXCHANGERS.....G.1

APPENDIX G FIELD TEST DATA AND SAMPLE CALCILATION G.1

APPENDIX I PRESSURE DROP AND FLOODING DURING REFLUX CONDENSATION IN AN INCLINED AIR-COOLED FINNED TUBE.....I.1

APPENDIX J PERFORMANCE CHARACTERISTICS OF FINNED TUBE BUNDLES J.1

NOMENCLATURE

Symbols

A - Area, m^2

a - Velocity of sound, m/s, or coefficient, dimensionless

C - Discharge coefficient, dimensionless

c_p - Specific heat at constant pressure, J/kg K

c_v - Specific heat at constant volume, J/kg K

D - Diameter, m

D_e - Hydraulic diameter, m

d - Diameter, m

E - Energy, J, or velocity of approach factor, dimensionless

e - Energy per unit mass, J/kg, or heat exchanger effectiveness, dimensionless

F - Force, kg m/s^2, or orifice correction factor, dimensionless

f - Friction factor, dimensionless

g - Gravitational acceleration, m/s^2

H - Duct height, m, or elevation, m

h - Heat transfer coefficient, $W/m^2 K$

i - Enthalpy, J/kg

i_{lg} - Latent heat, J/kg

K - Coefficient, dimensionless

k - Conductivity, W/m K

L - Length, m

M - Mass, kg

m - Mass flow rate, kg/s

N - Revolutions per second, s^{-1}

Ny - Characteristic heat transfer parameter, m^{-1}

n - Exponent or number of, dimensionless

P - Work rate or power, W, or pitch, m

p - Pressure, N/m^2

Q - Heat transfer rate, W

R - Universal gas constant, J/kg K, or thermal resistance, m^2 K/W

Ry - Characteristic flow parameter, m^{-1}

s - Tip clearance, m

T - Temperature, °C, or K

t - Time, s

U - Overall heat transfer coefficient, $W/m^2 K$

u - Internal energy, J/kg

V - Volume flow rate, m^3/s

v - Velocity, m/s

W - Width, m, or work, J

x - Distance, m

y - Co-ordinate,

z - Co-ordinate, or elevation, m

Greek Symbols

α - Correction factor, dimensionless, or fan blade angle, °

β - Diameter ratio or condensation friction factor coefficient, dimensionless

Δ - Differential

δ - Film thickness, m

η - Efficiency, dimensionless

μ - Viscosity, kg/m s

θ - Angle, °

ρ - Density, kg/m^3

σ - Surface tension, N/m, or area ratio, dimensionless

Ω - Heat, J

Subscripts

Ar - Argon

a - Air

amb - Ambient

b - Bundle, or backflow, or beam

C.V. - Control volume

c - Condensate, or condensation, or contraction, or casing

D - Drag

do - Downstream

e - Equivalent, or expansion, or effective

F - Fan

Fb - Fan bays

Fr - Fan rows

f - Frictional, or fin

fr - Frontal

g - Gas phase, or gravitational

He - Helium

he - Heat exchanger

Hy - Hydrogen

h - Hub

i - Inlet, or interfacial, or $i = l, g$

l - Liquid phase

m - Momentum, or mean

o - Outlet

p - Constant pressure, or passes

r - Root

s - Superficial, or static, or screen

sp - Single-phase

t - Tube or duct, or turbine, or total

tb - Tubes per bundle

tc - Tube or duct cross-section

ti - Inside of tube or duct

tp - Two-phase

tr - Tube rows

ts - Tower support

up - Upstream

v - Vapour, or constant volume

w - Water, or walkway

(1) - Row (1)

(2) - Row (2)

θ - Inclined

Superscripts

* - Dimensionless

Dimensionless groups

Single-phase flow

f	-	Darcy friction factor	$\frac{\Delta p}{1/2\,\rho v^2}\frac{D_e}{L}$
M	-	Mach number	$\frac{v}{a}$
Nu	-	Nusselt number	$\frac{h D_e}{k}$
Pr	-	Prandtl number	$\frac{\mu c_p}{k}$
Re	-	Reynolds number	$\frac{\rho v D_e}{\mu}$
γ	-	Ratio of specific heats	$\frac{c_p}{c_v}$

Two-phase flow

Bo	-	Bond number	$D\left[\frac{g\left(\rho_l-\rho_g\right)}{\sigma}\right]^{1/2}$
Fr_{Dsl}	-	Densimetric liquid Froude number based on the hydraulic diameter	$\frac{\rho_l v_{sl}^2}{g D_e\left(\rho_l-\rho_g\right)}$
Fr_{Hsl}	-	Densimetric liquid Froude number based on the duct height	$\frac{\rho_l v_{sl}^2}{g H_t\left(\rho_l-\rho_g\right)}$

Fr_{Dsg} - Densimetric gas Froude number based on the hydraulic diameter

$$\frac{\rho_g v_{sg}^2}{g D_e \left(\rho_l - \rho_g\right)}$$

Fr_{Hsg} - Densimetric gas Froude number based on the duct height

$$\frac{\rho_g v_{sg}^2}{g H_t \left(\rho_l - \rho_g\right)}$$

f_i - Interfacial friction factor (annular flow)

$$\frac{\Delta p}{1/2\, \rho_g v_g^2} \frac{\left(D - 2\delta\right)}{L}$$

f_{sg} - Friction factor based on gas superficial velocity

$$\frac{\Delta p}{1/2\, \rho_g v_{sg}^2} \frac{D_d}{L}$$

Ku_{sl} - Liquid Kutateladze number

$$\frac{\rho_l^{1/2} v_{sl}}{\left[g\sigma\left(\rho_l - \rho_g\right)\right]^{1/4}}$$

Ku_{sl} - Gas Kutateladze number

$$\frac{\rho_g^{1/2} v_{sg}}{\left[g\sigma\left(\rho_l - \rho_g\right)\right]^{1/4}}$$

Re_l - Liquid film Reynolds number

$$\frac{\rho_l v_l \delta}{\mu_l}$$

Re_{sl} - Superficial liquid Reynolds number

$$\frac{\rho_l v_{sl} D_e}{\mu_l}$$

Re_g - Gas Reynolds number (annular flow)

$$\frac{\rho_g v_g \left(D - 2\delta\right)}{\mu_l}$$

Re_{sg} - Superficial gas Reynolds number

$$\frac{\rho_g v_{sg} D_e}{\mu_g}$$

Zk_D - Zk number

$$\frac{\left(\rho_l D_e \sigma\right)^{0.5}}{\mu_l}$$

CHAPTER 1

INTRODUCTION

1.1 Gas-liquid counterflow in reflux condensers employed in the power industries

In a power generating cycle high pressure steam expands as it drives a turbine. The exhaust steam is condensed at sub-atmospheric pressures before it is returned to the boiler. Such a cycle is illustrated in figure 1.1. Forced draft direct air-cooled condensers are often employed in arid areas as an alternative to wet-cooling systems to achieve the desired cooling. Such a direct air-cooled condenser or dry-cooling system consists of inclined bundles of finned tubes in which the steam and condensate flow cocurrently downwards, followed by a secondary condenser in which the flow is countercurrent. The secondary condenser which acts as a de-aerator operates in a reflux mode and is also referred to as a dephlegmator.

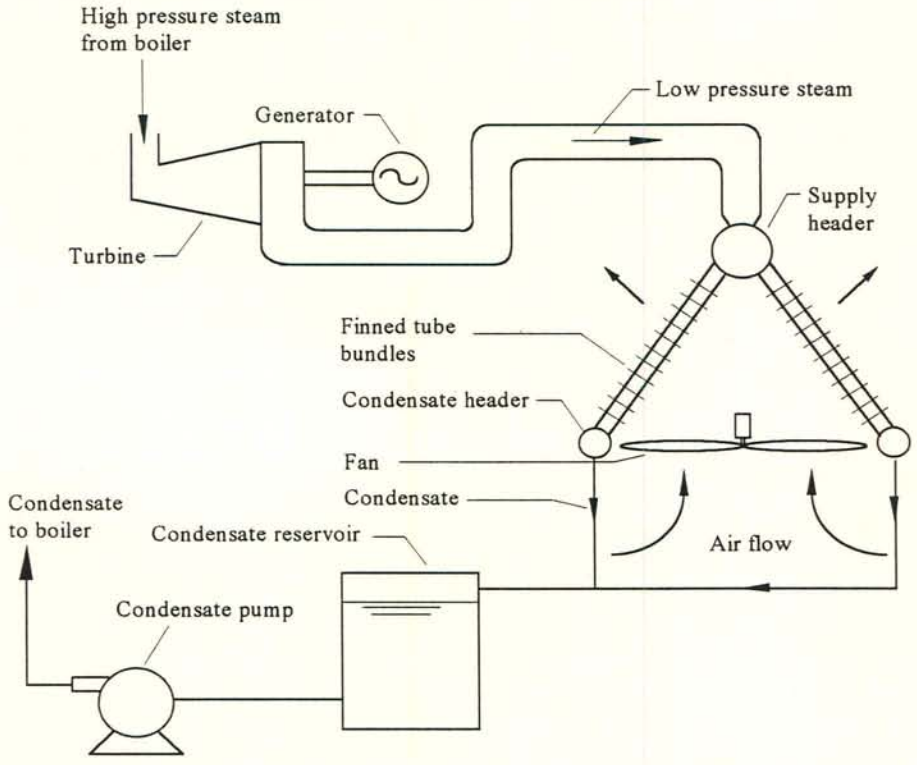

Figure 1.1: Schematic of a power generating cycle employing a direct air-cooled condenser system.

The purpose of a secondary condenser or dephlegmator is to facilitate a net outflow of steam at the bottom of the main condenser. This prevents noncondensable gases, such as air leaked into the system, from accumulating inside the main condenser and the subsequent formation of stagnant pockets. Naturally the noncondensable gases will flow with the steam, but are trapped and subsequently accumulate in zones where there is no or little steam flow. The regions occupied by the noncondensables become unavailable for condensation. By adding a dephlegmator to the condensing system, one aims to draw the non-condensable gases out of the primary condenser and concentrate them at a predetermined location inside the secondary condenser, from where they can be removed by a suction pump such as steam driven ejector. More detail regarding the condenser-dephlegmator system is presented in chapter 7.

Under such desirable or ideal conditions the temperature distribution of the finned tube bundles will be uniform due to the essentially isothermal condensation process. Cold zones were, however, observed on an existing dephlegmator. Infrared measurements showed that at times approximately 40% of the dephlegmator frontal area was close to the ambient temperature. The dephlegmator frontal area forms 14.4% of the entire cooling system under consideration and thus the net loss in heat rejection capability due to the presence of cold or dead zones amounts to approximately 6%. This presents a significant reduction in performance.

The dephlegmator under consideration operates in a countercurrent mode, i.e. vapour enters the finned tubes at the bottom and is condensed as it flows upwards while the condensate drains downwards under the action of gravity. During countercurrent flow there is no or little gas-liquid interaction at low fluid flow rates. As the flow rates are increased, liquid droplets may be entrained into the gas core. Eventually the film becomes unstable and liquid is propelled upwards causing flooding. Flooding and countercurrent flow limitation can impose an upper limit on the heat rejection capability of a condenser operating in a reflux mode and may perhaps lead to the formation of cold zones.

1.2 Scope of the present investigation

The aim of the dissertation is to identify the cause of the ineffective dephlegmator operation. It was approached by i) conducting adiabatic gas-liquid countercurrent flow experiments and ii) by carrying out extensive measurements on the existing dephlegmator. The dissertation is presented in two parts. Part A deals with the countercurrent flow laboratory experiments. The results presented in part A are applied in part B to analyse the dephlegmator under investigation. The dephlegmator analysis forms part of a performance evaluation model for a forced draft air-cooled system which is derived in part B.

1.2.1 Part A: Adiabatic countercurrent flow and flooding investigation

In chapter 2 a literature survey on adiabatic countercurrent flow, flooding and reflux condensation is presented. The heat transferred by an air-cooled condenser is primarily governed by the airside convection heat transfer because the steamside condensation heat transfer coefficient is orders of magnitude higher than the airside heat transfer coefficient. Condensation heat transfer is therefore not that critical to the performance modelling of a dephlegmator and is beyond the scope of the present investigation. The prevailing flow patterns encountered during reflux condensation and the corresponding pressure drop are , however, fundamental to the understanding of the steamside flow and are addressed in the literature survey. The survey concentrates on gas-liquid interactions during counterflow and associated instabilities.

The existing dephlegmator under investigation is constructed of flattened tubes inclined at 62° to the horizontal with sharp-edged vapour inlets. An apparatus designed and built for adiabatic countercurrent flow experiments in such a geometrical configuration is described in chapter 3. The emphasis of the experimental study is on pressure drop and flooding. The majority of the experiments were conducted for rectangular ducts inclined at 60°. Although, inclinations from near horizontal to vertical were also tested to gain a better understanding of the flooding phenomenon.

Chapter 4 contains discussions of the flow patterns observed during counterflow and the corresponding pressure drop characteristics. The flooding and entrainment results are presented in chapter 5. Conclusions on the counterflow experiments are presented in chapter 6 together with a comparison between the present flooding results and previous findings by other researchers.

1.2.2 Part B: Full scale dephlegmator tests and analysis

The role of a dephlegmator is explained in chapter 7, followed by a detailed description of the present condenser-dephlegmator system under investigation. The specifications of the entire air-cooled system are given in Appendix A.

The measurement procedure employed during the full scale field tests is described in chapter 8. A performance model for the entire direct air-cooled condenser and dephlegmator system is derived in chapter 9. In chapter 10 the results of the full scale investigation are compared to the performance model. Possible reasons for the observed inefficient dephlegmator performance are discussed. A summary of the dissertation is presented in chapter 11.

1.3 Past investigations on gas-liquid countercurrent flow

Countercurrent gas-liquid flow and flooding have been the subject of numerous investigations in the past five decades. Research was initially conducted for applications in the chemical industries where packed and plate columns are used for gas-liquid contacting during absorption operations. A typical packed column is shown in figure 1.2. It consists of a cylindrical shell containing a support plate for the packing material. Liquid enters the top of the column through a distributor and is drained at the bottom. Vapour is introduced at the bottom and flows upwards countercurrent to the liquid. At sufficiently high vapour flow rates the liquid hold-up increases and flooding may occur. The flow rates just below flooding represent the maximum fluid rates at which a packed or plate column can operate efficiently in a counterflow mode.

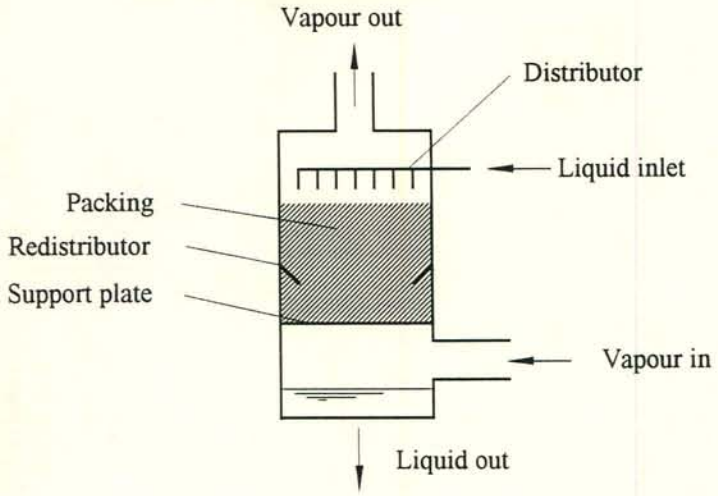

Figure 1.2: Schematic of a packed column used in the chemical industries.

More recently nuclear reactor design has been a major driving force behind two-phase flow and flooding research. Countercurrent flow and flooding play an important role in the safety analysis of a *Pressurised Water Reactor*. A schematic of such a nuclear power plant is illustrated in figure 1.3. Primary coolant water (pressurised water) is heated inside the core and passes through an inverted U-tube steam generator, where heat is transferred to the secondary coolant to generate steam. Under normal operating conditions the fuel is well cooled but the cooling may deteriorate in the case of a loss of forced circulation. During certain postulated accidents the primary heat transport may loose some coolant and is partially filled with steam. Emergency coolant is then injected at the top of the fuel rods. Upflowing steam may prevent emergency and primary coolant from reaching the core if flooding occurs. Also, part of the steam generated inside the core may escape from the reactor vessel and flow to the steam generators where it is condensed by the relatively cold water on the secondary side. Under such conditions the inverted U-tube generators may become the major heat sink where reflux condensation can be the primary heat transfer mechanism. Here, flooding may cause liquid hold-up inside the steam generators and the condensate becomes unavailable for reactor core cooling.

Countercurrent flow hydrodynamics also form an integral part of thermosyphon or heat pipe analysis. Thermosyphons make use of phase change heat transfer and are used as heat transport devices.

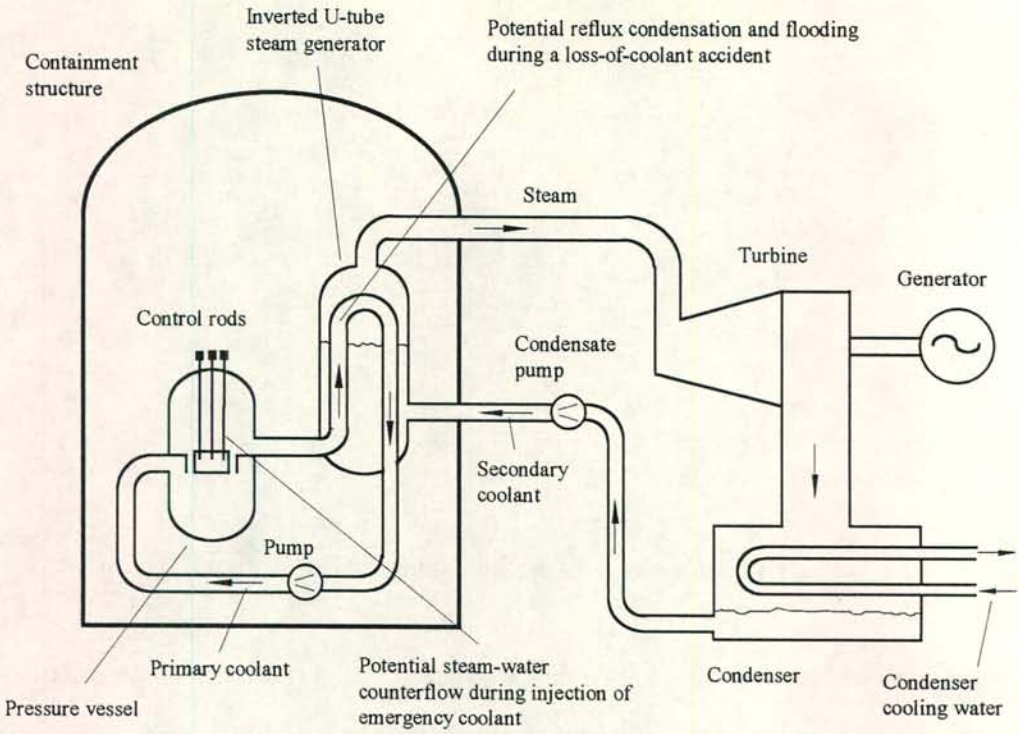

Figure 1.3: General view of a *Pressurised Water Reactor* power plant.

CHAPTER 2

LITERATURE SURVEY ON EXPERIMENTAL FLOODING, PRESSURE DROP AND ENTRAINMENT STUDIES FOR COUNTERCURRENT FLOW

2.1 Introduction

The literature survey aims at discussing information on gas-liquid flow which is relevant to the modelling of an air-cooled reflux condenser. Flooding may pose an upper limit on the heat rejection capability of a reflux condenser and is therefore addressed in detail. Extensive research on flooding during adiabatic flow and reflux condensation has been conducted in the past. There is still a lack of agreement on the flooding mechanism and some aspects of flooding appear to be contradictory. For this reason detailed summaries of selected flooding investigations are presented, followed by a critical discussion on the nature of flooding to address the apparent existing disagreement. Other important issues such as the influence of the duct geometry and the fluid properties are discussed.

A detailed description of reflux condensation phenomena is presented. Here the emphasis is on the vapour-condensate interactions encountered and associated instabilities. Finally existing literature on pressure drop characteristics and entrainment during adiabatic gas-liquid counterflow is discussed.

2.2 Flow patterns

Flow patterns form an integral part of two-phase flow studies and are briefly discussed in this section.

2.2.1 Vertical cocurrent upflow

Discussions of flow patterns encountered during cocurrent flow have been presented by Wallis [1969], Hewitt and Taylor [70HE1], Oshinowo and Charles [74OS1], Taitel *et al.* [80TA1], McQuillan and Whalley [85MC3] and Hewitt *et al.* [94HE1]. According to Wallis [69WA1] four basic flow patterns exist, namely bubbly, slug, annular and drop

flow. He suggests that a combination of some of these basic flows usually represents a transition from one pattern to another and can be denoted by hyphenated expressions such as slug-annular flow. Some investigators argue that the slug-annular transition can be regarded as a distinct flow pattern itself, the so-called churn flow region or pattern. The five aforementioned patterns are illustrated in figure 2.1.

a) *Bubbly flow:* At low gas flows and low to moderate liquid flow the gas phase is distributed in the form of discrete bubbles in a continuous liquid phase. When the bubbles are so large and almost span the entire cross-section of the duct, the flow is called *slug flow*. During bubbly flow the bubbles are usually distorted spheres. The bubbles increase in size, number and speed as the gas flow rate is increased. The bubble velocity may differ substantially from the liquid velocity. At high liquid flow rates the bubbles tend to break down into smaller closely packed bubbles. This is defined as *dispersed bubble flow*. The bubbles rise uniformly and steadily in bubbly flow while during slug flow large bubbles fill the tube and flow in each other's wake. During this transition the flow becomes agitated and unsteady. Zuber and Findlay [65ZU1] called this regime *churn-turbulent flow*.

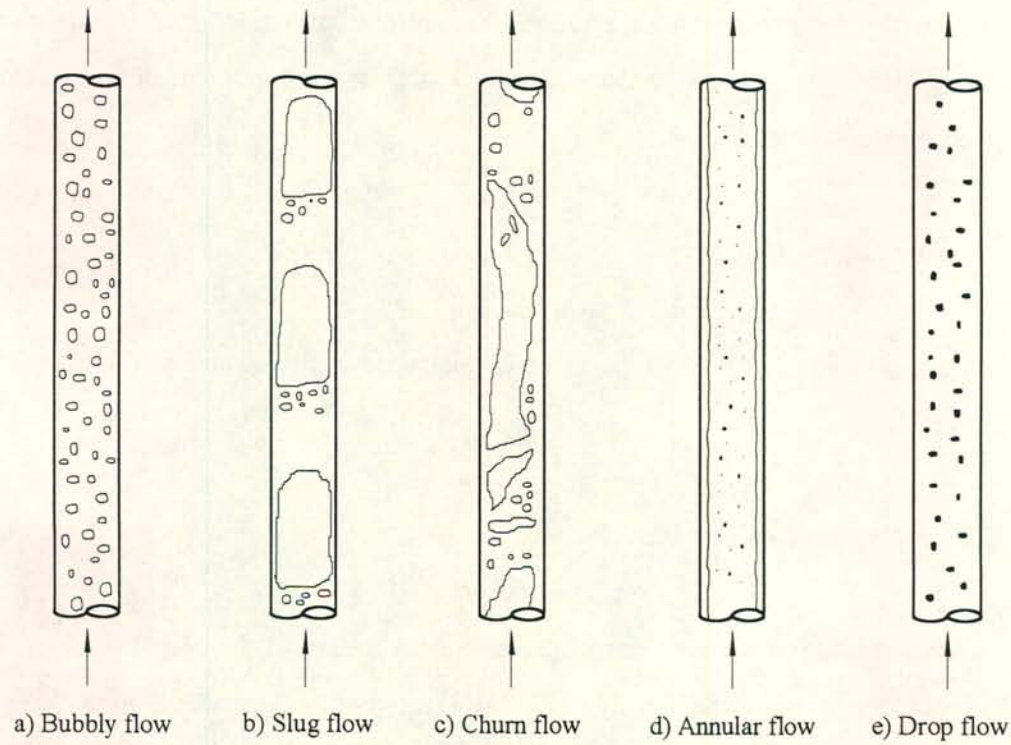

Figure 2.1: Gas-liquid flow patterns in vertical tubes during cocurrent upflow.

b) *Slug flow:* Here the gas phase flows upwards in large bullet-shaped bubbles which are sometimes designated as "Taylor bubbles". The shape of some of the bubbles approaches the cross-section of the tube. The bullet-shaped bubbles are separated by slugs of liquid which bridge the tube and may contain smaller dispersed gas bubbles. A thin liquid film exists between the Taylor bubbles and the pipe wall. This flow pattern is also called *plug* or *piston* flow at low flow rates where the gas-liquid boundaries are well defined [80TA1].

c) *Churn flow:* As the velocity of the two-phase slug flow mixture is increased, the flow structure becomes unstable. According to Taitel *et al.* [80TA1] the Taylor bubbles become distorted and the liquid slugs are repeatedly destroyed by the gas. The slugs fall, liquid accumulates, bridges the duct and is again propelled upwards by the gas. Eventually the instability results in a complete destruction of the liquid slugs [70HE1] and the flow becomes very oscillatory. This type of flow can be regarded as a transition from slug to annular flow. Hewitt [70HE1] argued that this transition is so distinct, to be given a separate identity and name, i.e. "churn flow". According to Jayanti and Hewitt [92JA1] churn flow is a highly disturbed flow of gas and liquid in which the liquid motion is oscillatory but not in a periodic manner. The net flow of liquid is generally in the direction of the gas flow, although it may be zero or negative, i.e. downwards. They further mentioned that at very high liquid flow rates a direct transition may occur from either slug flow or bubbly flow to annular. Churn flow is difficult to predict because the transition mechanism is not fully understood and/or more than one mechanism, depending on the flow conditions, may govern the transition to churn flow. Jayanti and Hewitt tested four different transition mechanisms and found that only a flooding mechanism was capable of predicting the transition from slug to churn flow.

Wall shear stress and void fraction measurements by Mao and Dukler [93MA1] in the slug flow regime and in the regime which is commonly referred to as churn flow, did not show a significant difference. According to their experimental evidence "the flow pattern which has been designated as vertical churn flow may not exist." In response to this Hewitt and Jayanti [93HE1] illustrated that at least three uses of the term "churn" exists. The first is in the context of churn-turbulent flow by Zuber and Findlay [65ZU1]. The second use, what they refer to as churn flow of the second category, describes the "churn

flow" regime presented by Taitel *et al.* [80TA1], which can be regarded as a developing slug flow [93HE1]. Churn flow of the third kind is the intermediate region between slug flow and annular flow. According to the authors [93HE1], churn flow of the third category has the following unique characteristics:

1) The regime is entered from the slug flow region by the formation of flooding-type waves and they persist throughout the regime. The flooding-type waves are not found in slug flow or annular flow.
2) Between successive flooding waves the liquid inside the film near the wall reverses direction to downflow and is eventually entrained by the next upward moving wave.

Hewitt and Jayanti concluded that the phenomenological models required for churn flow of the third kind differ from those for annular flow and that the existence of churn flow of the third kind as a distinct flow regime is justified. They also argued that some confusion might have been caused by the fact that the measurements conducted by Mao and Dukler [93MA1] were in the churn flow region of the second kind. It seems to be clearer to describe churn flow of the second kind as "churn-slug" flow and churn flow of the third kind as "churn-annular" flow [93HE1].

Further investigation by Jayanti *et al.* [93JA1] with the aid of high-speed video photography showed that flooding waves appear on the falling film between the Taylor bubbles and the tube wall in the slug flow region. They concluded that flooding waves are created in the Taylor bubbles as the transition to churn flow of the third kind is approached.

Some investigators refer to *froth flow* when, at higher liquid and gas flow rates, churn flow appears more finely dispersed [80TA1].

d) *Annular flow:* During annular flow the gas phase flows along the centre of the duct and the liquid phase flows up the wall in a thin film. The gas core may contain entrained droplets and gas bubbles may be present inside the liquid film. The pattern is called *wispy-annular flow* when the entrained liquid appears in the form of large lumps or

wisps, formed around the tube axis. This type of flow is found in fossil-fuelled boilers and probably results from the breakdown of liquid slugs at high mass flow rates [70HE1].

e) *Droplet flow:* Drop flow is analogous to bubbly flow. The liquid drops are carried upwards by the gas phase. While in bubbly flow the drag forces on the bubbles are large in comparison with their momentum, the opposite is true for drop flow. When the gas flow rate is increased during annular flow and complete dispersion of the liquid in the gas is reached, it is referred to as *mist flow*. Mist flow never occurs in adiabatic systems [70HE1].

2.2.2 Vertical countercurrent flow

Countercurrent flow cannot exist at certain combinations of gas and liquid flow rates. Taitel and Barnea [83TA1] modelled countercurrent flow pattern transition and pressured drop and considered three possible flow patterns: Annular flow, bubbly flow and slug flow. The flow pattern formed during countercurrent flow depends on the gas and liquid flow rates, pipe diameter, entrance and exit conditions and the fluid properties. The flow patterns are illustrated in figure 2.2.

a) *Annular flow:* When the liquid is free to exit the lower end of the tube, it flows in a falling film down the tube wall. The gas flows upwards in the centre of the tube and, depending on the gas flow rate, entrainment of liquid droplets may occur. At higher gas flow rates the liquid film is not smooth any longer and becomes disturbed.

b) *Bubbly flow:* If the liquid outflow is restricted at the bottom a sufficient head must develop to allow the liquid to exit the tube. Such conditions favour bubbly flow. Similar to cocurrent flow, the gas phase is dispersed as bubbles in the continuous liquid medium.

c) *Slug flow:* The bubbly flow can develop into slug flow where the gas phase flows upwards in the form of Taylor-type bubbles separated by slugs of liquid.

According to Taitel and Barnea [83TA1] there is a region in which all the three above-listed flow patterns can exist at the same combination of the fluid flow rates. From there, a region is entered where slug and annular flow may exist. Upon a further increase in the fluid flow rates a zone is reached where annular flow is the only possible pattern. Eventually flooding is reached and liquid is carried upwards. The gas-liquid interactions just before and at flooding are complex and usually form an integral part of flooding investigations.

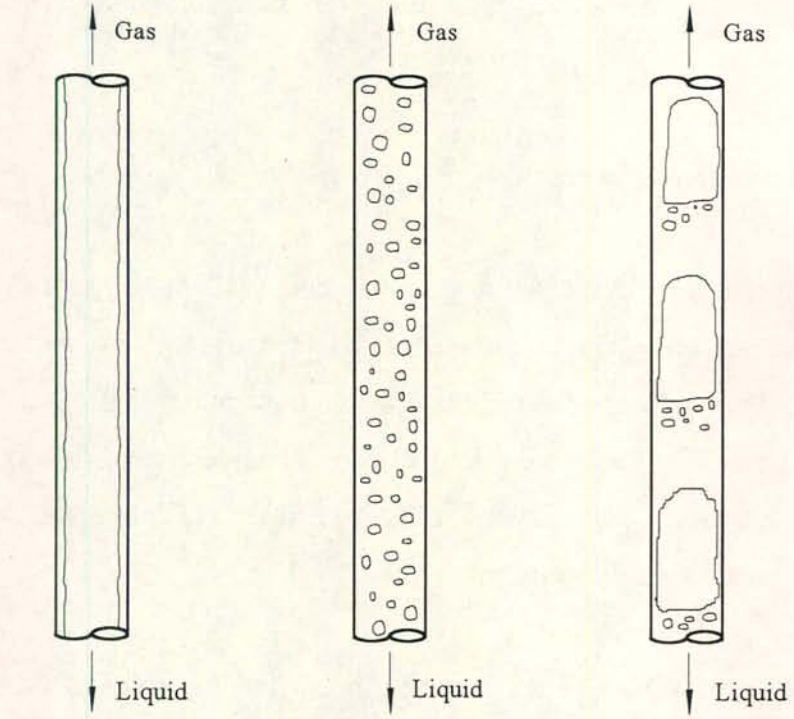

Figure 2.2: Vertical countercurrent flow patterns according to [83TA1].

2.2.3 Horizontal cocurrent flow

Descriptions and illustrations of flow patterns in horizontal pipes have been presented by Hewitt [82HE1], Dukler and Taitel [86DU1] and Hewitt *et al.* [94HE1]. Taitel and Dukler [76TA1] developed a semi-theoretical model for flow regime transitions in horizontal and near horizontal gas-liquid flow. Their method is recommended by Hewitt [82HE1], rather than making use of empirical prediction models. The discussion below follows the description of Hewitt [82HE1]. The flow patterns are illustrated in figure 2.3.

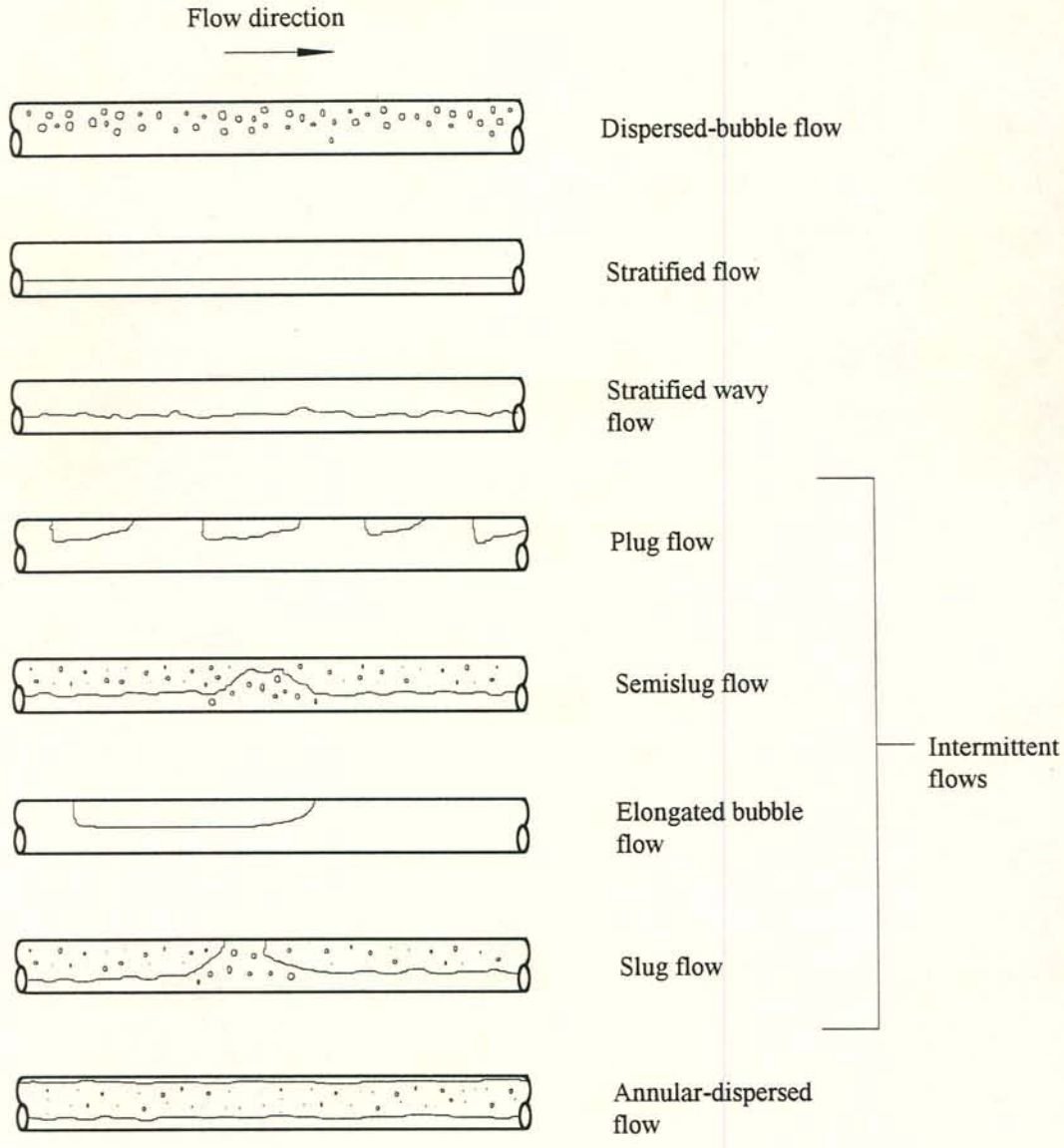

Figure 2.3: Flow patterns in horizontal gas-liquid flow.

a) *Stratified flow:* The liquid flows at the bottom of the pipe in a continuous phase and the gas flows at the top. The gas-liquid interface is smooth.

b) *Stratified wavy flow:* Waves are formed on the interface as the gas flow rate is increased. The two phases are still flowing in separated continuous layers.

c) *Dispersed bubble flow:* The gas flows in the form of dispersed bubbles in a continuous liquid phase. The bubbles tend to congregate in the top part of the tube.

d) *Annular-dispersed flow:* At higher gas flow rates the liquid is driven up the tube wall and flows along the wall in a film similar to that observed in vertical flow. The film is not uniform. It is thicker at the bottom of the tube. Liquid is entrained in the gas core, which is the rule, rather than the exception.

Intermittent flows: A variety of complex intermittent flows exist. The intermittent flow region can be subdivided into *plug flow*, *slug flow* and *semislug flow*.

e) *Plug flow*: The gas phase flows in the from of bullet-shaped bubbles. The bubbles tend to move along in a position closer to the top of the tube.

f) *Slug flow:* "Slugs" move along the tube. The liquid phase inside the slugs is continuous and it contains entrained bubbles. According to Hewitt [82HE1] it is, in practice, difficult to distinguish between the plug and slug flow regimes. The slug flow regime is sometimes subdivided into *elongated bubble flow* and slug flow. The liquid slug is free of entrained gas bubbles in the elongated bubble flow regime [86DU1].

g) *Semislug flow:* The above-mentioned slugs flow on a stratified layer and do not touch the top of the tube.

2.2.4 Flow patterns during inclined upward flow

When a tube is inclined, one component of the gravity force acts in the direction of the tube axis and the other component exerts a force on the fluid perpendicular to the flow. Thus, churn- and stratified-type flows or combinations thereof may exist in inclined flow. It can be expected that the flow patterns present during upward inclined flow are: *Stratified flow, stratified wavy flow, dispersed bubble flow, slug flow, churn flow, annular flow* and *drop/mist flow*. Mukherjee and Brill [85MU1] investigated cocurrent up- and downflow in inclined tubes, including horizontal and vertical flow. They preferred to present their flow pattern results in terms of the four basic flow patterns: Bubbly flow, slug flow, stratified flow and annular-mist flow and not to make use of any further subdivisions. Pipe inclination angles tested for cocurrent upflow were 0°, 30°, 45°, 70° and 90°. Curves were fitted to the transition boundaries. The correlating

equations contain the fluid flow rates, pipe inclination angle, liquid and gas density, liquid viscosity and surface tension and the gravitational acceleration.

Extensive experimental research on flow pattern transitions during inclined flow was conducted by Barnea *et al.* [80BA1, 85BA1]. At small angles the stratified-to-intermittent transition was found to be very sensitive to the pipe inclination. The flow patterns observed during cocurrent upflow were: Stratified wavy, elongated bubble, slug, churn, annular (and annular-dispersed), wavy annular and dispersed-bubble flow. The following inclination angles were tested: 0°,0.25°, 2°, 10°, 20°, 50°, 70° and 90° [85BA1]. Barnea [87BA1] analysed the flow pattern-transitions and presented a unified model for the whole range of pipe inclinations. More information on flow patterns in inclined flow can be found in [80SP1, 82HE1, 86ST1].

2.3 Flooding during adiabatic flow inside vertical tubes and ducts

2.3.1 The flooding definition

A systematic approach is essential when conducting flooding experiments because flooding is governed by so many variables such as the system geometry, flow rates and fluid properties. When generating flooding data under such a wide variety of conditions it is important to work according to a consistent point of reference. In the present investigation the definition by Hewitt and Taylor [70HE1] is employed. It is illustrated in figure 2.4.

Liquid is injected into the tube at a constant rate and is extracted smoothly at the bottom, so that the only influences on the film are due to the gas flow and gravity. At low gas flow rates a falling film exists (figure 2.4a) and as the gas flow rate is gradually increased, a point is reached where waves are formed on the liquid film and are carried upwards (figure 2.4b). Liquid is now transported above the injection point and a region has been entered in which both climbing and falling film flow are occurring simultaneously (figure 2.4c,d). The transition (figure 2.4b) to the region of simultaneous liquid up- and downflow is called *flooding*. The conditions depicted in figures 2.4c and d are referred to as a state of *partial liquid delivery*. With a further increase in the gas flow

rate, the liquid flow below the injection point changes to a climbing film flow (figure 2.4e) and eventually all the liquid is carried upwards. The gas velocity is now reduced and a point is reached where some of the liquid starts to creep down the wall below the injection point (figure 2.4h). This is defined as *flow reversal*. As the gas flow rate is further decreased, a state of simultaneous liquid up- and downflow is reached (figure 2.4i) and eventually the flow returns to a stable countercurrent mode (figure 2.4j). The transition from figure 2.4(i) to 2.4(j) has been termed *deflooding* by Clift *et al.* [66CL1].

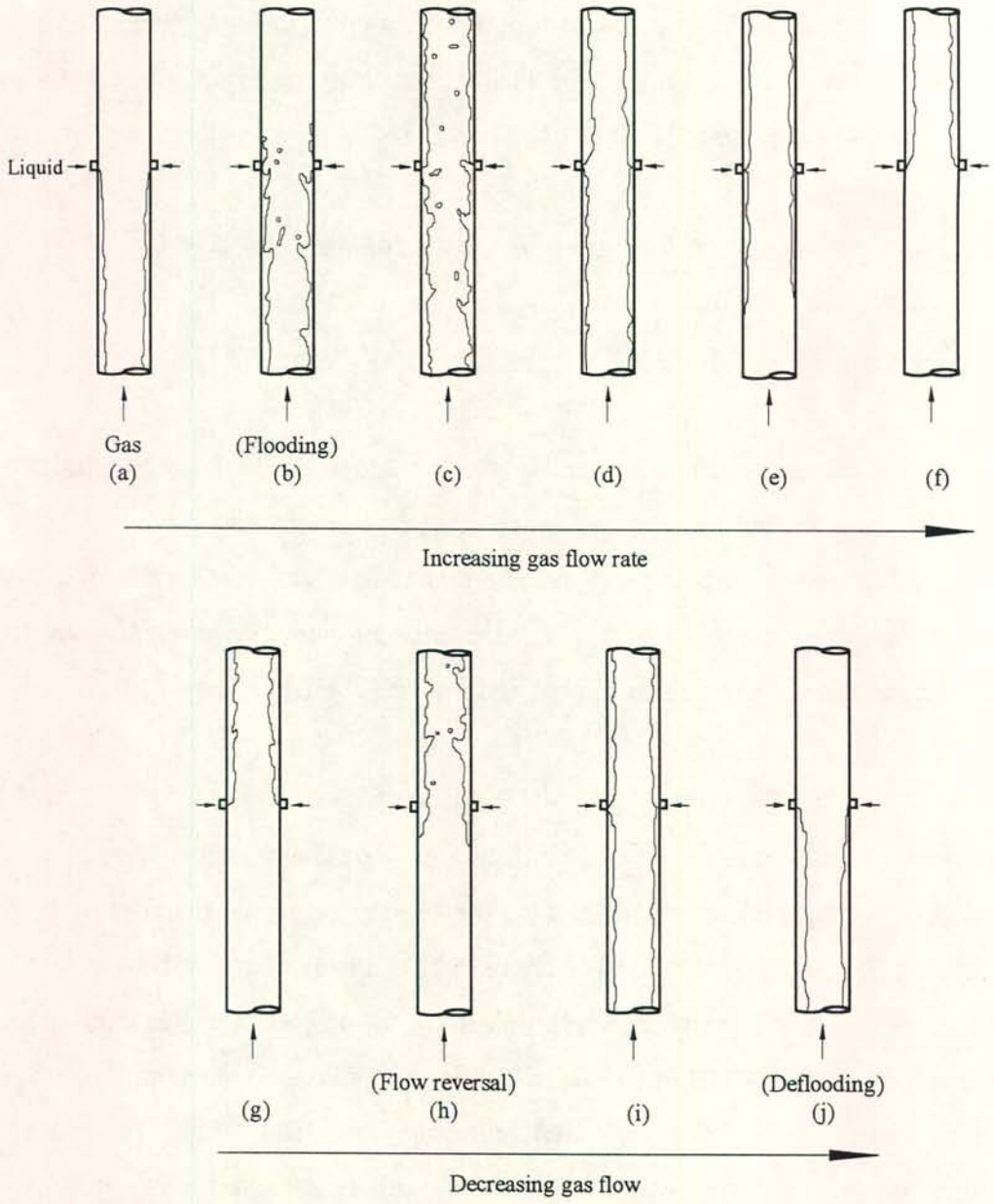

Figure 2.4: Flow transitions from countercurrent flow to cocurrent upflow inside vertical tubes.

2.3.2 Gas-liquid interactions during counterflow and the effect of the liquid outlet/gas inlet configuration on the flooding process

The flooding description presented in section 2.3.1 may not be valid for any flow system. The behaviour of systems with complex geometrical configurations and operating conditions will differ from figure 2.4. The basic bottom tube end configurations tested in the past are shown in figure 2.5. Following below are brief summaries of selected investigations to illustrate the different ways in which the transition from countercurrent to cocurrent upflow can take place.

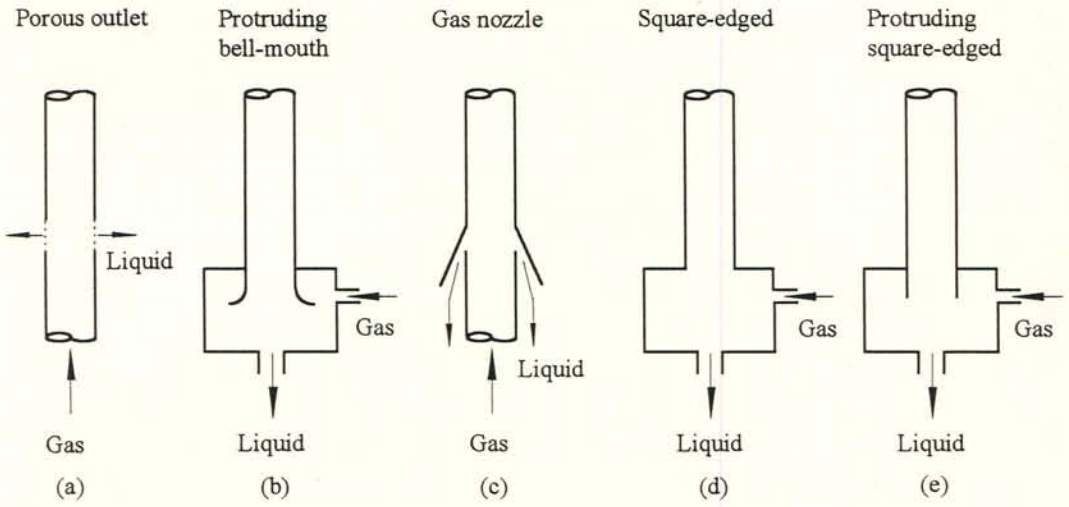

Figure 2.5: Basic types of liquid outlet geometry used in flooding studies according to Govan *et al.* [91GO1].

Clift *et al.* [66CL1] investigated flooding and the conditions beyond flooding. Their study concentrated on the effect of the liquid viscosity. The test section consisted of two 1.83 m lengths of acrylic plastic tube, interspaced by a ≈76 mm sintered bronze section for liquid injection. Air entered the test section via a bottom plenum and a bell-shaped inlet. Flooding was defined as the fluid flow rates at which the countercurrent flow becomes unstable and part of the liquid passes cocurrent with the gas. Flooding and deflooding were approached by increasing and decreasing the gas flow rate respectively, while maintaining a constant liquid flow into the test section. Just before flooding was reached the pressure drop across the column began to increase and waves on the film

grew so large to form thin bridges or slugs across the tube. These bridges were broken up by the air flow and droplets were entrained and carried upwards. With a further increase in either liquid or gas flow increased bridging occurred and a point was reached at which the liquid slugs were no longer immediately dispersed. The flow pattern became chaotic and liquid was carried above the inlet sinter resulting in a state of partial liquid delivery, i.e. part of the liquid flowed above the point of liquid injection in a cocurrent upflow mode. The flow below the sinter was now less chaotic and slugs were formed much less frequently. The gas flow was further increased causing dry-out in the lower tube.

Downflow measurements showed a marked decrease at flooding. The downflow remained constant upon further increases in the liquid input. After deflooding the downflow was again equal to the input. It was observed and concluded that:

1) The deflooding gas flow rate is lower than the flooding gas flow rate.
2) At flooding there is a discontinuity in the pressure drop curve, in other words the pressure drop experiences a sudden increase.
3) The downflow is independent of the total liquid input and it is equal to the deflooding curve.
4) A gas velocity exists at which the downflow becomes zero. It is independent of the liquid viscosity.
5) When flooding occurs inside a tube the rate at which liquid flows downwards immediately decreases. Suzuki and Ueda [77SU1] observed the same.

Imura *et al.* [77IM1] generated flooding data by setting the mass flow rate of the liquid at a fixed rate and gradually increasing the gas flow rate. A gas flow rate was reached at which the falling film became unstable and a sudden increase in pressure drop across the test section occurred. This gas flow was taken as the flooding gas velocity. The tests were conducted with 1 m long vertical tubes. The liquid entered the top end of the tube via a plenum and a bell-mouth inlet. The gas inlet was not clearly defined. According to the schematic describing their experimental apparatus it was rounded and/or tapered. It was concluded that flooding is not the result of shear forces acting on the falling film and the subsequent change in flow direction by the liquid from downflow to upflow.

According to the authors flooding is caused by waves which suddenly experience an increase in amplitude and subsequently bridge the tube.

Flooding, flow reversal and deflooding curves, as well as data on the transition to climbing film flow were presented by Suzuki and Ueda [77SU1]. Air was introduced through a bell-shaped section into a vertical transparent acrylic resin test tube. The liquid was injected through a porous section. The flooding gas flow rate was determined by increasing the gas flow rate by small increments at a constant liquid feed rate into the test section. The transition from countercurrent flow to climbing film flow (cocurrent upflow) and back to pure countercurrent flow was described as follows:

1) The waves on the liquid film grow in size as the gas flow rate is increased.
2) A gas flow rate is reached at which a large amplitude wave is formed on the liquid film *somewhere* in the tube and is immediately carried upwards by the gas phase.
3) When the wave reaches the inlet sinter, the falling film becomes disturbed and liquid begins to flow upwards above the porous section. For example, when the liquid feed rate into the test section was 2 *l*/min, flooding occurred at an air velocity of 5.7 m/s which resulted in a liquid upflow rate of 1.3 *l*/min and a downflow of 0.7 *l*/min.
4) As the gas flow rate is increased beyond the flooding rate, the upward flow above the sinter becomes less oscillating. The disturbance of the film below the sinter decays because the liquid downflow is reduced.
5) Eventually the transition to complete upflow is reached.
6) When the gas flow rate is decreased, a rate is reached at which some of the liquid starts to creep downwards, i.e. flow reversal is reached. The gas flow rate at flow reversal is well below the rate at the transition to climbing film flow.
7) Upon a further decrease in the gas flow rate, deflooding occurs and all the liquid drains downwards. The deflooding gas velocity is below the flooding velocity.

A high speed camera was used to observe the film behaviour. Waves with small amplitudes were formed on the falling film while there was no gas flow. At flooding a

large-amplitude wave occupied the most of the cross-section and liquid bridging occurred. This wave and entrained liquid droplets were then carried upwards.

Whalley and McQuillan [85WH1] investigated the hypothesis that flooding is caused by the growth of liquid waves on the surface of the falling film. Flooding was defined as the transition illustrated in figure 2.4(b). The emphasis was placed on the conditions at which the liquid begins to move upwards from the point of injection as a film along the wall of the tube. In some cases droplets were carried upwards past the liquid inlet prior to the point where a film was observed above the liquid inlet. This was not regarded as flooding. Air and water were used as working fluids. The water was injected through a porous sinter into a 32 mm i.d. acrylic plastic tube and removed via the same type of sinter lower down. The effect of artificial waves on the stability of countercurrent flow and flooding was investigated by injecting small amounts of water with a syringe through a porous sinter into the test section. This created a disturbance on the liquid film in the form of a wave. The sequence of events leading to flooding were as follows:

1) As the air flow rate is increased from zero, a rate is reached at which an instability on the liquid film occurs which leads to the rapid growth of waves on the film.
2) The waves travel downwards at velocities below that of the film. The wave velocity decreases as the gas flow is increased.
3) The growth rate of the waves is dependent on the gas velocity.
4) A gas velocity is reached at which a wave, initiated at the liquid inlet, grows sufficiently large as it reaches liquid outlet and causes a highly disturbed region of the film.
5) The disturbance contains water which could be provided from the wave by entrainment or by the upwards motion of part of the film as a result of the increased *interfacial shear* caused by the acceleration of the gas as it flows over the wave.
6) The disturbed region of the flow propagates upwards to carry water above the liquid inlet sinter and causes flooding.

The wave injection experiments revealed that flooding could be initiated at lower air flow rates by the injection of a wave.

The wave mechanism was further investigated by McQuillan *et al.* [85MC1] with the aid of high-speed cine photography of air-water flow inside a vertical 32 mm i.d. tube. Flooding was induced and photographic images were recorded at 500 frames/s in an axial direction down the tube. Just below the flooding gas velocity a wavelike disturbance was suddenly formed in the lower region of the test section. Its amplitude varied from 5 to 10 mm. The disturbance moved upwards and entrainment increased. This flooding disturbance was the source of entrainment with droplets being ripped off the peak of the disturbance and then travelling along the tube ahead of the disturbance. According to the authors the observations confirmed the importance of wave growth which leads to flooding, as postulated by Whalley and McQuillan [85WH1].

A good insight regarding flooding and the associated phenomena *partial liquid delivery* and *deflooding* can be obtained from the work by Govan *et al.* [91GO1]. Flooding and the conditions beyond flooding as well as deflooding and downflow measurements were conducted with air-water at ambient conditions in a vertical pipe. Flooding was defined as the condition at which liquid begins to be carried upwards above the liquid injection point. One of the main aims of the study was to generate flooding curves for pipes with porous wall, square-edged and bell-mouth liquid outlets in the same apparatus for direct comparison. The liquid was injected through a porous section. The test section comprised a lower acrylic resin 32 mm i.d. tube, a porous liquid inlet and an upper section made of drawn copper tubing. The upper tube enabled investigation of the flow conditions beyond flooding. In the case of the porous liquid outlet, the water flow rate was set at a constant value and the gas flow rate was gradually increased from a rate well below flooding conditions, until flooding was observed. At liquid rates above $\approx$12 g/s flooding occurred due to the formation of a single wave near the outlet sinter, which rapidly travelled upwards beyond the liquid inlet. At the lowest liquid flow rates the transition was more gradual. Small waves appeared on the film but initially did not travel above the point of liquid injection. As the gas velocity was further increased splashing occurred above the inlet. The gas rate was increased still further and a state of partial liquid delivery was reached. The liquid downflow rate was measured at a number of gas

flow rates. Once the downflow measurements had been taken, the gas flow rate was decreased until all the liquid flowed downwards from the injection point, i.e. *deflooding* was reached. Some important observations were:

1) Beyond flooding, the downflow rate is independent of the liquid input rate. Any additional liquid is carried upwards.

2) The deflooding curve lies below the flooding curve. In other words, once a state of partial liquid delivery has been reached, the gas flow rate must be decreased below the flooding gas velocity for all the liquid fed into the test section to flow downwards.

3) Once the tube has flooded at high liquid flow rates (above ≈12 g/s), part of the liquid flows downwards while the remaining liquid flows upwards above the inlet sinter in a cocurrent churn flow mode. The downflow rate is therefore less than the liquid feed rate, or in other words the downflow curve lies below the flooding curve. At liquid rates below ≈12 g/s the downflow curve lies above the flooding curve. This can be explained in terms of the flooding definition. Flooding was defined as the flow rates at which liquid begins to travel above the injection point. This does not mean that the liquid proceeds to leave the test section. A zone with no net flow may exist above the sinter, i.e. the flow can have a oscillatory nature and downflow near the wall is balanced by upflow near the interface. Only upon a *further increase* in the gas flow, partial liquid delivery is created and the downflow limit is reached, causing the downflow curve to lie above the flooding curve

For the square and bell-mouth liquid outlets the flooding and downflow curves were found to be identical. In these experiments the fluid flow rates were set above the flooding rates and the downflow rate corresponding to a certain gas flow rate was measured to obtain the flooding curve. The observations for the bell-mouth outlet were similar to that for the porous outlet. It is illustrated in figure 2.6. In the case of the sharp-edged inlet a thick standing wave was formed at low gas flow rates. As the gas flow was increased, liquid was entrained from this wave and redeposited on the falling film. Upon a further increase, a gas flow was reached which partially prevented the liquid from draining at the bottom of the tube. The liquid downflow became less than the inflow and the tube was filled with a churn-type flow from the bottom, which eventually reached the

liquid inlet point. This is shown in figure 2.7. Note that prior to flooding liquid was entrained and carried upwards in the form of entrained drops. This was *not* regarded as flooding.

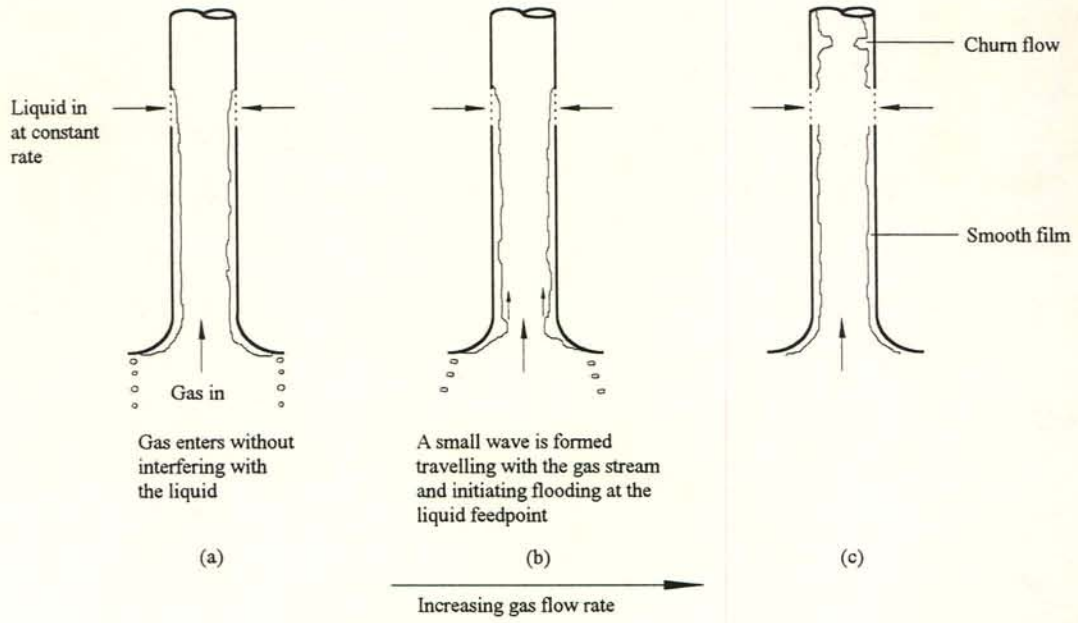

Figure 2.6: The flooding mechanism in a test section with a tapered liquid outlet according to Govan *et al.* [91GO1].

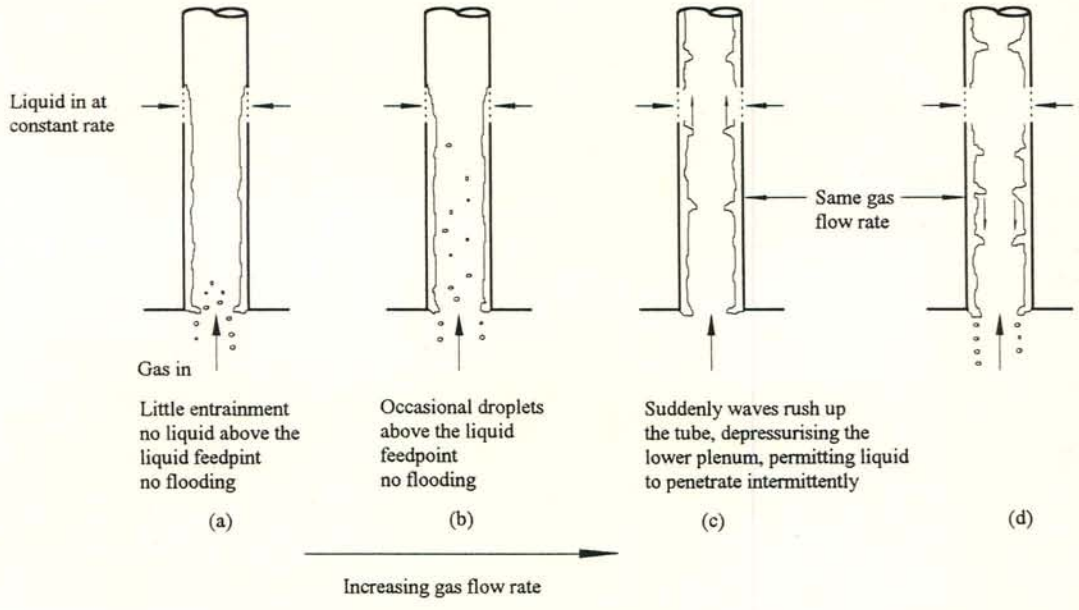

Figure 2.7: The flooding mechanism in a test section with a square-edged outlet according to Govan *et al.* [91GO1].

A thorough investigation of the effect of the tube end geometry on flooding during air-water flow in vertical tubes was conducted by Jeong and No [96JE1]. The experiments covered a wide range of water flow rates. The flow loop consisted of upper and lower plenums connected by a transparent 30 mm i.d. acrylic resin tube. Water was introduced via the upper plenum where it overflowed into the tube and drained downwards under the action of gravity. The top end of the tube could be fitted with rounded, protruding or square-edged inducer geometries. Similarly the bottom configuration could be rounded, protruding or square-edged. Air was supplied by a blower and entered the tube either through a bottom plenum or a 10 mm nozzle inserted in the tube and aligned with the tube axis. Flooding was approached by setting the liquid flow rate at a predetermined value and increasing the air flow rate. After each stepwise increase the flow was observed for about 10 minutes. The stepwise increase was repeated until the tube flooded.

Care was taken to observe whether flooding occurred by the formation of a highly disturbed region of the flow at the bottom of the tube, which then propagated upwards to expel liquid at the top, or by the loss of stability at the top of the tube where the liquid was introduced, while waves on the falling film down the tube appeared to be stable. The first-mentioned process was termed *exit flooding* and the latter *entrance flooding*. *Exit* refers to the liquid exit, i.e. the bottom of the tube and *entrance* refers to the liquid inlet point. In the case of the rounded liquid inlet the water entered the tube as a smooth film and waves were formed even if there was no gas flow. The wave amplitudes increased in size as the gas flow rate was increased. The waves grew as they travelled down the tube and reached their maximum amplitude around the exit. At a certain gas flow rate a wave would suddenly grow in size to cause a formation of highly disturbed flow along the entire length causing intensive entrainment.

In the case of the sharp and protruding exit configuration the chaotic flow did not propagate upwards. It remained inside a region close to the exit while smooth annular flow was maintained in the remaining upper region of the tube. This transition was termed *exit perturbation*. The inception of disturbed flow at the sharp-edged gas inlet was also the onset of entrainment. As the gas flow rate was further increased, the chaotic flow pattern region gradually propagated upwards in an oscillating nature. It was

concluded that entrainment does not precede flooding but that it is caused by flooding. Eventually the region of disturbed flow reached the tube entrance and water began to accumulate inside the upper plenum because it was partially prevented from entering the tube. A marked difference between the gas flow rate at flooding and at the exit perturbation transition was observed at low liquid flow rates. Above $Fr_{Dsl}^{*\,1/4} \approx 0.4$ flooding occurred at the gas flow rate at which the exit perturbation was formed. The flow transitions for the sharp-edged exit is illustrated in figures 2.8(a) to 2.8(d). Flooding for the rounded top and bottom ends is shown in figures 2.8(e) to 2.8(f). The flow illustrated inside a tube in the top row of figures and a tube directly below corresponds to equal fluid flow rates for comparison of the sharp and rounded exit flow modes. In the case of the rounded exit the chaotic flow pattern propagated to the top of the tube as soon as it was formed at the bottom, i.e. the gas velocities at the formation of the exit perturbation and at exit flooding were the same.

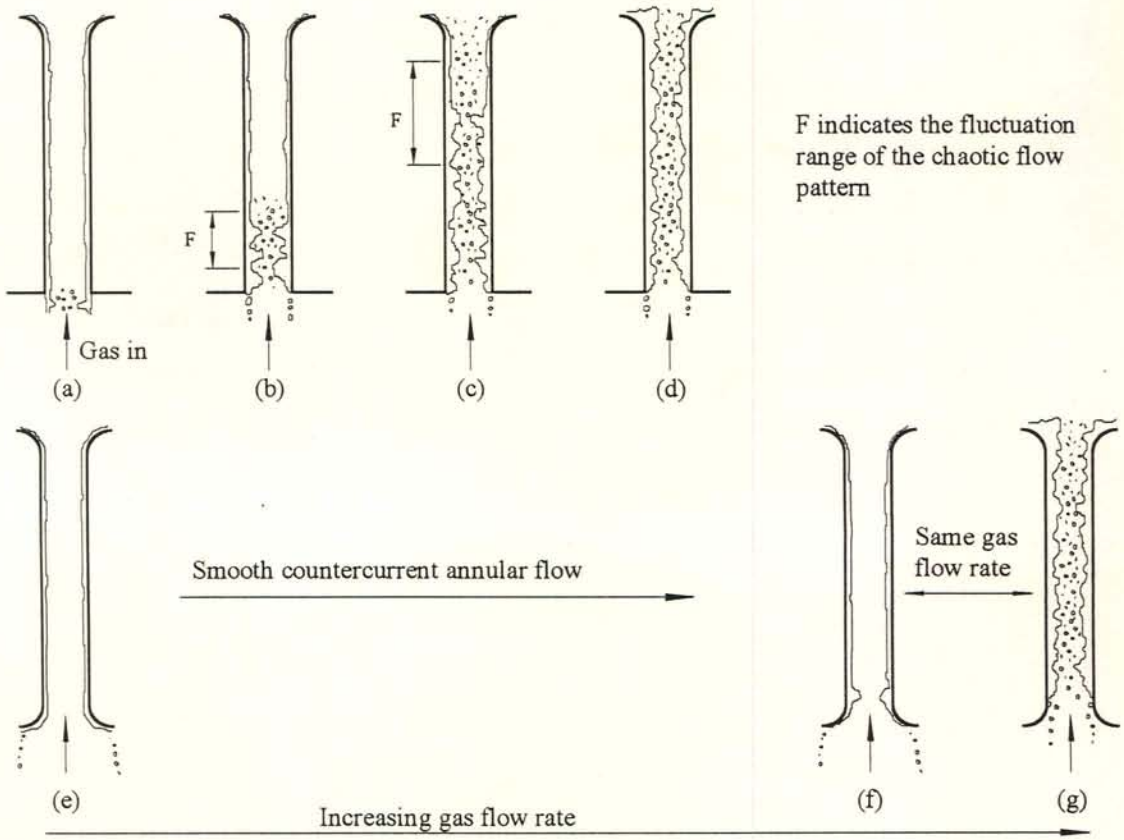

Figure 2.8: Flow modes and flooding inside vertical tubes with square and rounded bottom geometries according to Jeong and No [96JE1].

In the case of the sharp entrance the liquid flow experienced an abrupt change from horizontal flow to vertical down flow as it approached the tube from the plenum and drained downwards around the square edge. It caused a wave-like non-uniform flow at the tube entrance. This non-uniform flow could become unstable prior to the development of large waves in the region down the tube. Flooding could occur due to instabilities at the non-uniform flow at the top of the tube, which is *entrance flooding*. Experiments with protruding geometries at the top and bottom showed that exit flooding occurred at low liquid flow rates. In the intermediate region $0.25 < Fr_{Dsl}^{1/4} < 0.5$ entrance flooding was thought to compete with exit flooding. The mechanism, however, was entrance flooding because flooding occurred as a result of an instability at the top before chaotic flow initiated at the exit could reach the entrance. Above $Fr_{Dsl}^{1/4} \approx 0.5$ entrance flooding was the prevailing mechanism. According to photographic images of the entrance the liquid appeared to bridge the tube at the point of entrance flooding.

Detailed data of the pressure drop, film thickness, entrainment rate and downflow were presented by Dukler *et al.* [84DU1]. The investigation covered the conditions from stable countercurrent flow through flooding to a steady-state partial liquid delivery. Three different test section configurations consisting of 50.8 mm transparent tubes fitted with measuring flanges were used. The liquid feed consisted of a porous sinter. The top and bottom ends of the test section (similar to figure 2.5c) were constructed such that any disturbances of the liquid film were minimised at the point of injection. According to their downflow and upflow measurements a direct change from countercurrent flow to a state of partial liquid delivery took place once the tube had flooded. It was found that:

1) The gas rate at which flooding occurs is identical to the rate at which entrainment is detected first.

2) Flooding coincides with a step increase in the pressure gradient both below and above the liquid feed point.

3) Below the flooding point the mean liquid film thickness for the lower Reynolds numbers (Re_F = 310, 776, 1552) are in agreement with the Nusselt film thickness. In the case of the highest film Reynolds number (3155) it is equal to a prediction for turbulent films. The mean film thickness remains constant with an increase in the gas flow rate until just at flooding, where a step increase occurs. The maximum

film thickness increases, however, with an increase in the gas flow rate at conditions below flooding.

4) Under no conditions does liquid bridging occur, nor below the sinter as flooding is approached or at flooding, nor above the sinter during the formation of cocurrent upflow when steady-state partial liquid delivery is reached.

Zabaras and Dukler [88ZA1] conducted experiments similar to those of Dukler *et al.* [84DU1]. The investigation concentrated on the liquid film behaviour at two locations below the liquid feed, i.e. 0.15 m and 1.7 m respectively. As in the case of Dukler *et al.*, the flooding and downflow curve were found to be identical. In other words flooding is independent of the liquid feed rate. Similarly the maximum film thickness, wave amplitude and wall shear were found unaffected be the liquid feed rate during a state of partial liquid delivery. This, according to the Zabaras and Dukler, implied that the conditions at flooding are no different than the steady-state operation of the liquid film in countercurrent flow. It was found that the maximum film thickness never exceeded 20% of the tube radius, which did not support flooding models based on wave growth followed by liquid bridging of the pipe. At the measuring location immediately below the feed point the waves always travelled downwards and were never observed to move upwards, even along the flooding curve. These observations led the authors to speculate that flooding is controlled by the conditions at or close to the liquid feed. At or just below the feed some of the liquid flow experiences a change in direction due to interfacial shear and a *split* in flow occurs. Below this region of split flow pure countercurrent flow prevails which is not related to the flooding state (conditions at the liquid inlet).

Stephan and Mayinger [92ST1] studied flooding inside a vertical 20 mm x 68 mm rectangular duct. Saturated Refrigant 12 liquid and vapour were used as working fluids. The liquid was injected through a porous plate mounted flush with one of the larger walls. Flooding was approached by setting the vapour flow at a fixed rate and adjusting the liquid flow rate to obtain a state of partial liquid delivery. Once that had been obtained, the measured downflow of liquid and the corresponding pre-set vapour flow were taken as the flooding fluid flow rates. These flow rates, according to authors, represented the maximum flow rates possible under steady conditions. No liquid bridging

was observed and the flow pattern during countercurrent flow as well as during partial liquid delivery was annular-mist flow.

The film thickness along a porous liquid entry section and just below and above the porous section was measured by Lacey and Dukler [94LA1]. The investigation can be regarded as a continuation of the studies by Dukler *et al.* [84DU1] and Zabaras and Dukler [88ZA1] of the film behaviour during flooding. Before flooding all the liquid flowed downwards. As the gas flow was increased conditions were reached where part of the liquid flowed upwards (figure 2.5c). Time-varying thickness measurements were taken during these partial liquid delivery conditions. The apparatus used for the experiments was basically the system employed by Dukler *et al.* [84DU1]. Based on the film thickness results, the following was concluded:

1) The wave basis for explaining flooding is invalid.
2) Wave growth and/or blocking (bridging) of the tube does not occur at flooding.
3) Waves do not propagate from below to above the liquid feed to carry liquid upwards above the feed.
4) At flooding the liquid velocity distribution changes in the vicinity of the porous feed so that some of the liquid flows upwards.

2.3.3 Discussion of the observations on the behaviour of the gas-liquid interface and flooding

In section 2.3.1 the flooding gas velocity was defined as the velocity at *which liquid begins to flow upwards above the point of liquid injection* (figure 2.4b). In the context of flooding, this refers to liquid flowing upwards against the tube wall. Note that prior to flooding liquid entrainment may occur. The entrained droplets can be carried upwards by the gas stream and deposited on the tube wall above the liquid inlet. This is not regarded as flooding [85WH1, 91GO1]. There is no entrainment prior to flooding, or very limited entrainment, when the gas-liquid interactions are minimised at the bottom of the tube by using, for example, a tapered or a porous liquid outlet [84DU1, 91GO1]. Once flooding has occurred, the liquid above the inlet sinter does not necessarily proceed to leave the test section. In the case of low liquid flow rates it may form a hanging film above the

injector without a net upward flow [91GO1]. At higher liquid flow rates flooding causes a direct transition from countercurrent flow (figure 2.4a) to a steady state of simultaneous liquid up- and downflow (figure 2.4c) [66CL1, 77SU1, 91GO1]. The resulting cocurrent upflow above the liquid inlet was described as churn flow by Govan *et al.* [91GO1], while Suzuki and Ueda [77SU1] referred to it as semi-annular flow, which seems to imply churn flow. It can be concluded that the flow depicted in figure 2.4(b) can either be a steady state (in the case of low liquid flow rates) or a transient state during the almost instantaneous change from countercurrent flow (figure 2.4a) to a steady state of partial liquid delivery (figure 2.4c) in the case of higher liquid flow rates.

A marked decrease in the liquid downflow rate is experienced when a tube floods by direct transition from figure 2.4(a) to 2.4(b) [66CL1, 77SU1, 91GO1]. While it may be correct to refer to figure 2.4(c) as a flooded tube, the liquid downflow rate and the corresponding gas flow rate under such conditions of partial liquid delivery may not be called the flooding fluid flow rates, because of the decrease in downflow at flooding. The flow illustrated in figure 2.4(c) is not flooding, it is a result of flooding. Partial liquid delivery is a steady state during which the downflow rate is related to (or limited by) the gas flow rate [88ZA1]. The flow rates in this regime, however, are not necessarily equal to those which initiate flooding from conditions in which phase interactions do no limit the downflow rate [96WA1]. Yet some investigators are of the opinion that the downflow rate and the corresponding gas rate during steady-state partial liquid delivery are the maximum attainable flow rates for countercurrent flow [82TA1, 92ST1]. Stephan and Mayinger [92ST1] defined the conditions illustrated in figure 2.4(c) as "flooding" and plotted the fluid flow rates measured during such conditions as "flooding" curves on a v_{sl}-versus-v_{sg} plot. These "flooding" curves are in actual fact downflow curves, which can differ from the flooding curves [77SU1, 91GO1] and do not necessarily represent the maximum attainable flow rates for countercurrent flow.

Flooding has undoubtedly always been regarded as part of the breakdown of well-defined annular countercurrent flow which can lead to a simultaneous up- and downflow of liquid. But data recorded under such conditions of up- and downflow belong to a region beyond flooding and are not representative of flooding itself. Data obtained under steady-state conditions may not be used to describe flooding, because flooding is per

definition a transient process. Fluid flow rates measured under such steady-state conditions can, however, be representative of flooding rates if the downflow and flooding curves are identical for a particular experimental configuration [91GO1]. The research of the Dukler-group [82TA1, 84DU, 88ZA1, 94DU1, 94LA1] concentrated on countercurrent flow during steady simultaneous liquid up- and downflow. Their observations and results were claimed to substantiate the film flow mechanism. The present author is of the opinion that the results of the Dukler-group may not be used to describe the flooding event itself and that their use of the term *flooding* can be misleading.

Zabaras and Dukler [88ZA1] concluded that :"Consistent with many similar observations in the past, the experimental flooding curve is independent of the liquid feed rate." This is true for the downflow curve, which investigators have found to be de-coupled of the liquid feed rate and the churn flow region above the point of liquid injection. The flooding gas velocity (figure 2.4b) is, however, definitely a function of the liquid feed rate through the porous inlet. Also, according to Dukler *et al.* [84DU1], "... the downflow, or flooding curve, is independent of the feed rate ...". This statement implies that the Dukler-group does not seem to recognise the difference between the flooding and the downflow curve, which undoubtedly exists. In this regard the present author agrees with Jeong and No [96JE1] that " ... it is not thought to be good to adopt penetrating downflow rates to present flooding data."

Lacey and Dukler [94LA1] used the terminology "during flooding", "the flooding transition" and "steady-state flooding" in the same context. The first two phrases can however refer to the conditions illustrated in figure 2.4(b) while the latter can be used in the context of figure 2.4(c). Their film thickness data and "flooding" curve were recorded during steady-state partial liquid delivery or according to Lacey and Dukler, "after flooding". The authors claimed their data did not support the wave mechanism for flooding. Regardless of what the actual flooding mechanism is, it may not be explained in terms of such steady-state data which are recorded beyond flooding.

A number of researchers investigated and observed the effect of the bottom end configuration on flooding [63EN1, 69WA1, 80CH1, 91GO1, 96JE1, 96ZA1]. These

investigations showed that the flooding gas velocities for the bottom sinter outlet (figure 2.5a) were the highest. The lowest flooding gas rates were obtained with the square-edged (figure 2.5d) and the protruding square-edged (figure 2.5e) configurations. Intermediate flooding gas velocities were measured with the bell-mouth and tapered gas inlets (figures 2.5b and 2.5c). None such investigations and results were reported by the Dukler-group, which attributed flooding to the liquid flow distribution at the porous inlet (split flow mechanism) and consequently seemed to ignore the effect the bottom configuration may have. Zabaras and Dukler [88ZA1] commented on the effect of the bottom configuration and suggested that the above-mentioned trend is due to the turbulence induced in the gas phase at the liquid outlet/gas inlet. Different geometries were argued to cause different turbulence levels in the gas reaching the liquid entry, resulting in a range of flooding gas velocities. Considering the visual observations reported by other investigators [66CL1, 77SU1, 77IM1, 80CH1, 91GO1, 96JE1, 96ZA1] this explanation is unrealistic.

While some investigators reported chaotic flow behaviour and liquid bridging [66CL1, 77SU1, 77IM1, 80CH1, 91GO1, 96ZA1] others are adamant that the flow is annular during flooding [84DU1, 92ST1, 94LA1]. Once again care should be taken whether such statements refer to flooding or a steady-state of partial liquid delivery. According to Clift *et al.* [66CL1] and Suzuki and Ueda [77SU1] the flow below the liquid inlet becomes less chaotic once flooding has occurred and the liquid downflow is reduced. It is therefore certainly possible that liquid bridging may occur at flooding and but that the flow becomes annular once a state of partial liquid delivery is reached.

The terms *"flooding"*, *"flooding point"*, *"flooding range"*, *"onset of flooding"* and *"countercurrent flow limitation"* frequently appear in the literature. Their use is often inconsistent and it is not always clear whether they have the same meaning or whether different phenomena are referred to. The two conditions usually investigated are either the transition depicted in figure 2.4(b) or steady-state partial liquid delivery. According to Lee and Bankoff [83LE1] "the onset of flooding corresponds to the condition where the flow rates of neither the gas nor the liquid phase can be increased further without altering the flow pattern." This implies that the onset of flooding refers to the condition in figure 2.4(b). They further define "the *flooding range* as the range from 100 percent to

0 percent downward delivery of the entering liquid." Thus the flooding range describes the downflow conditions during steady-state partial liquid delivery. Similarly Osakabe and Kawasaki [89OS1] distinguish between the onset of flooding and partial liquid delivery. *"Countercurrent flow limitation"* is sometimes used for the onset of flooding, as described above, or for partial liquid delivery conditions. In the present investigation only the terms *"flooding"* and *"partial liquid delivery"* will be used in the case of adiabatic counterflow, where they refer to the conditions depicted in figures 2.4 (b) and (c) respectively.

2.4 The effect of the test section geometry on flooding during adiabatic flow

2.4.1 The tube length effect

A number of investigators observed and reported a tube length effect on the flooding fluid flow rates [77SU1, 79BH1, 85WH1, 91GO1, 96JE1]. In the case of rounded- and sinter-type liquid inlet geometries the flooding gas velocity was found to decrease as the tube length increases. This trend supports the wave growth flooding mechanism. A small wave initiated at the liquid inlet grows as it travels downwards. If the distance it travels is sufficiently long the wave amplitude will reach a size to either cause a formation of a liquid disturbance which propagates upwards, or result in liquid bridging and the subsequent upward motion of liquid slugs. The tube length is weaker at low liquid flow rates [85WH1, 96JE1]. Jeong and No [96JE1] conducted experiments on the tube length effect with a number of combinations of different inlet/exit geometries. In the case of sharp-edged pipe ends no influence of the tube length on the flooding gas velocity was found. Local liquid disturbances dominated the flooding process when sharp-edged top and bottom configurations were used.

Zabaras and Dukler [88ZA1] and Stephan and Mayinger [92ST1] did not observe any tube length effects during their experiments and concluded that flooding is independent of the falling film length. It must be kept in mind, however, that these authors presented downflow curves as "flooding" curves. Govan *et al.* [91GO1] measured the downflow rate beyond flooding for different tube lengths and did not observe a length effect on the

downflow rate. This is in agreement with the results of [88ZA1] and [92ST1] but it does not imply the flooding is independent of the tube length.

2.4.2 The influence of the cross-sectional duct geometry on counterflow

Suzuki and Ueda [77SU1] conducted flooding experiments inside vertical tubes of diameters 10, 18 and 28.8 mm. Water was introduced through a porous unit and air entered the 1.5 m long tubes at the bottom through a bell-shaped section. At a given flim thickness, the flooding gas velocity was found to be approximately proportional to the square root of the diameter. Kamei *et al.* [54KA1] and Imura *et al.* [77IM1], who studied flooding inside 18.1, 31.6, 41.8 and 49.1 mm and 11.2, 16.0, 21.0 and 24.2 mm tubes respectively, also found the flooding gas velocity to increase with an increase in tube diameter. Chung *et al.* [80CH1] investigated flooding in 15.9, 31.8, 46.0 and 69.9 mm tubes. The tubes were 0.914 m long and were tested in the vertical position. Water overflowed from inside an upper plenum into the test section and air entered at the bottom either via a lower plenum or directly through a nozzle aligned with the tube axis. The influence of the end geometry on the diameter effect was tested by making use of sharp-edged and 45° tapered tube end configurations. The flooding air velocity in general increased as the diameter was increased. In the case of the more ideal entry conditions (45° tapered ends and nozzle air supply) the diameter dependence was minimal. The diameter effect was stronger when flooding was the cause of a localised disturbance created at the sharp-edged tube ends.

Pushkina and Sorokin [69PU1] measured the gas velocity at flow reversal inside vertical tubes of diameters of 6.2, 8.8, 12.1 and 309 mm. Air and water was used as working fluids. The gas velocity at flow reversal ranged from 14 to 16 m/s. It was concluded that flow reversal is independent of the tube diameter and occurs at a Kutateladze number of ≈ 3.2. When solving for the gas flow at zero liquid penetration with the Wallis [69WA1] correlation for flooding, the resulting gas velocity is proportional to the square root of the diameter. This apparent contradiction was addressed by Wallis and Makkenchery [74WA1]. They suggested that both correlation methods are valid, each in a certain range of Bond numbers (dimensionless diameters). In large tubes the effect of the

hanging film on the gas flow becomes less, as illustrated in figure 2.9. The gas velocity at zero liquid penetration therefore becomes independent of the tube diameter. Richter [81RI1] analysed the effect of the interfacial shear on downward flowing liquid in tubes by employing the interfacial friction factor proposed by Wallis [69WA1]. His original model was unable to predict the results of Wallis and Makkenchery and the wave amplitude initially assumed had to be adjusted for better agreement. Richter's model provides an explanation for the contradicting Wallis- and Kutateladze-type predictions of the gas velocity at zero liquid penetration. In the case of small diameters the term containing the interfacial force due to waviness dominates, resulting in a relation for the gas velocity which contains the diameter. In the case of large diameters, the term originating from the interfacial force due to a smooth interface dominates and the resulting gas velocity at zero liquid penetration becomes independent of the tube diameter. The experimental results by Richter confirmed this. A similar trend resulted from the envelope theory for countercurrent flow by Bharathan and Wallis [83BH1].

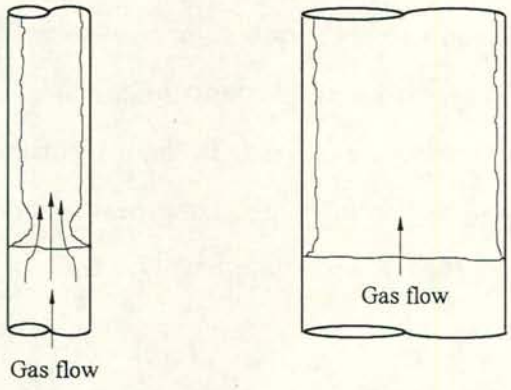

Figure 2.9: Shape of a hanging film in two tube sizes according to Wallis and Makkenchery [74WA1].

Jayanti *et al.* [96JA1] solved for the velocity distribution of a gas flowing over a standing wave, with a computational fluid dynamics code. It was found that the force exerted by the gas on the wave is mainly due to the pressure distribution around it, while shear effects are secondary. It further is strongly dependent on the channel dimensions and varies only weakly with the gas Reynolds number. The net pressure force was correlated in terms of the gas momentum flux and the ratio of the gas flow area at the wave crest and at the well upstream of the wave. The net pressure force decreases with an increase in this area ratio. These results were applied to countercurrent flow inside vertical tubes

and the resulting flooding gas velocity increased as the tube diameter increased. In large tubes, the reduction in gas flow area at the wave crest is relatively less compared to flow in small tubes. Waves in large tubes therefore require a higher gas velocity to be carried upwards. The velocity at which upward flowing gas balances the weight of a wave, i.e. the formation of a standing wave, was defined as the flooding gas velocity. For large diameters the gas flow required to carry waves upwards it was argued, may exceed the velocity at which droplets are entrained and carried upwards. Then flooding occurs due to entrainment close to the point of liquid injection and subsequent carryover. Based on existing equations, the diameter at which the transition of the flooding mechanism occurs, was tentatively suggested to be of the order of 50 mm.

Mishima and Nishihara [84MI1] measured the steady-state liquid downflow rate for air-water in vertical rectangular ducts. The duct height was 40 mm and the width 1.51, 2.4 and 5.0 mm respectively. Water was introduced via a plenum into the sharp-edged top end while air entered at the bottom through a tapered section. At the limiting conditions roll waves grew at the top end and spanned the entire duct height upon which the liquid bridge would brake up into droplets and the next roll wave started to form. In the test section below the formation of the roll waves the water concentrated on the narrow walls while the wider walls were almost dry. The effect of the duct width on the penetration rate was found to be fairly weak and no clear trend was observed with regard to the width effect.

Osakabe and Kawasaki [89OS1] conducted air-water countercurrent flow experiments with three rectangular channels of cross-sectional dimensions 10 x 100, 5 x 100 and 2 x 100 mm respectively. The test sections were 1.235 m long. Water overflowed from inside an upper plenum into the protruding duct while air entered at the bottom. This flow configuration simulated the partial liquid delivery as found in the annular downcomer in pressurised water reactors during a loss-of-coolant accident. The condition, where the steady downflow rate is limited by the upflowing gas, was referred to as *top flooding*. The air flow rate and the corresponding liquid downflow rate were plotted in terms of the Wallis [69WA1] dimensionless phase velocities. The data did not correlate when taking the gap size as the required length dimension, but were found to correlate by using the span (height) instead. It was concluded that the partial liquid

delivery rate is determined only by the height and is independent of the aspect ratio and the width, contrary to the envelope theory by Richter [81RI1] according to which the downflow limit is a function of the aspect ratio.

Sudo [89SU1, 91SU1] conducted air-water tests with rectangular and round geometries (vertical flow) to obtain the gas flow rate as a function of the liquid penetration during steady-state operation. The data for the rectangular ducts were presented in terms of the Wallis [69WA1] dimensionless phase velocities where the width (or channel gap) was taken as the representative length dimension. A Wallis-type correlation was proposed where the empirical constants were expressed as functions of the aspect ratio and a Bond number. The effect of the surface tension contained in the Bond number was not verified by experiment.

Lee and Bankoff [83LE1, 84LE1] investigated steam-water countercurrent flow inside an inclined rectangular test section. Two channel heights of 38 and 76 mm respectively were tested. The cross-sectional flow area was 0.38 m wide to obtain two-dimensional flow. The distance between the water inlet and outlet was 1.27 m. At conditions below flooding the flow was stratified. Flooding data were generated by increasing the steam flow rate at a given water flow rate. The flooding steam velocity increased with an increase in channel height. The flooding data were plotted in terms of modified Wallis [69WA1] dimensionless phase velocities with the hydraulic diameter (twice the channel height) chosen as the length dimension and a ($g \sin \theta$) term replacing g for vertical flow. At an inclination angle of $\approx 30°$ to the horizontal the data of this modified plot converged at low liquid flow rates but at higher liquid flow rates the dimensionless gas velocity for the 38 mm channel was higher than the 76 mm data. This lead to the conclusion that the effect of the channel height on flooding may not be expressed by a Wallis dimensionless velocity only.

Tests by Ueda and Susuki [78UE1] on annuli, three- and four-rod bundles showed that the flooding air velocity increases with an increase in the shroud-rod and rod-rod spacing. The data were correlated in terms of a characteristic length dimension

$$L = 4\, x\, flow\, area \Big/ \left[\pi \left(D_{shroud} + n_{rod} D_{rod}\right)\right]$$

where n_{rod} is the number of rods. A similar characteristic length was used by Shires and pickering [65SH1] to correlate steam-water data for rod bundles in the form of the Wallis [69WA1] equation for flooding.

Top flooding (partial liquid delivery) experiments by Osakabe and Funatso [96OS1] in a vertical annulus showed that the liquid distribution along the circumference consisted of "unit cells". One such a unit cell resembled the flow pattern encountered inside vertical rectangular ducts where the liquid concentrates at the two narrow walls. Based on this observation and the fact that the hydraulic diameter did not correlate the data, the authors suggested that the average circumference is the characteristic dimension of an annular channel. It was found that top flooding in high aspect ratio annuli can be correlated with an equation for rectangular ducts when taking 1/4 of the average circumference as the characteristic dimension. The behaviour of the unit cells changed continuously due to the coalescence of adjacent cells and separation.

Similar liquid penetration measurements during steady-state counterflow were carried out by Sudo [96SU1] for vertical tubes, rectangular ducts and annuli.

2.4.3 Flooding inside inclined ducts and tubes

Relatively little has been reported on flooding during inclined flow, compared to the extensive results available on vertical two-phase countercurrent flow and flooding. Lee and Bankoff [83LE1, 84LE1] presented flooding curves for inclination angles of 2.9, 4.5, 31, 33.5 and 87°. Their apparatus was described in the preceding section. The flooding steam velocities for 31 and 87° inclinations (channel height of 76 mm) were approximately equal while the 4.5° flooding velocities were lower. At nearly horizontal and moderately steep angles flooding occurred after well-developed roll waves were observed on the interface. In nearly vertical flow flooding was associated with a chaotic interface and strong droplet entrainment. No distinct roll waves appeared before flooding at this angle. The authors suggested that flooding may be caused by different modes, depending on the inclination angles: At smaller to moderate angles the film becomes very rough due to the formation of roll waves, resulting in an increased interfacial shear which

leads to flooding. Here, gravity has a stabilising effect. During near vertical flow flooding may be caused by unstable wave growth due to the diminishing stabilising effect of gravity. Droplets are, however, torn off the crests of unstable waves and redeposited onto the film and wave troughs, leading to a very chaotic flow pattern. The formation of liquid slugs and bridging was observed inside the 38 mm (height) test section at inclination angles of 4.5 and 33.5°. Prior to the slug formation at the liquid exit, roll waves developed on a rough thick liquid film. During the subsequent upward propagation of the slugs, the flow was oscillatory and entrainment occurred continuously.

Flooding experiments by Barnea *et al.* [86BA2] covered the entire range of inclinations from near horizontal to vertical flow. Air and water were used as working fluids. The test section was made of a 51 mm plexiglas pipe. The pipe ends were designed to minimise any entry effects. Two different liquid entry devices were used. One was a conventional porous section and the second type consisted of a 19 mm inner tube, located on the bottom of the plexiglas pipe. Experiments were conducted for inclination angles of 1, 10, 20, 30, 40, 70, 80 and 90° where flooding was defined as the condition when liquid was carried to the exit section above the point of liquid injection. Flooding was caused by a local disturbance generated at the liquid entrance or by disturbance waves somewhere along the tube, depending on the liquid entry device and the liquid flow rates. The flooding velocities increased with an increase in inclination from near horizontal, reached a maximum and decreased as vertical flow was approached. The highest flooding air velocities were measured at inclinations of 30, 50, and 70°. Similar trends were reported by Hewitt [77HE1] and Funnel [91FU1]. Barnea *et al.* [86BA2] listed three conflicting mechanisms which result in the complex effect of the angle on flooding:

1) An increase in angle from the horizontal results in higher liquid velocities which in turn cause lower liquid levels resulting in higher flooding gas velocities.

2) At steep angles (close to vertical) the film and wave structure becomes more unstable, thereby increasing the instability of the flow.

3) As the angle is increased from horizontal to vertical the liquid flow changes from stratified to annular flow resulting in an increased gas-liquid interface, enhancing flooding.

2.5 The role of the fluid properties during flooding

Five fluid properties, the phase densities and viscosities and the surface tension, may effect flooding. To establish a functional relationship between the flooding gas velocity and a fluid property, the property under consideration should ideally be varied while keeping the remaining properties constant in a series of experiments. This is, however, not always practically possible and thus care must be taken that the results of flooding experiments on the fluid property effect are correctly interpreted. Also, comparing the results of different investigators (different systems) to establish the role of the fluid properties can lead to wrong conclusions because flooding is so sensitive to the system geometry. For these reasons only selected investigations which were dedicated to quantify the effect of the fluid properties are discussed here.

2.5.1 Previous investigations

Kamei *at al.* [54KA1] used water, millet jelly, a soap solution and air as working fluids for their flooding experiments inside vertical tubes. The flooding air velocity decreased with an increase in surface tension while it increased with an increase in the liquid viscosity. The liquid viscosity had a weaker effect than the surface tension. The ratio of the gas and liquid mass fluxes at flooding were correlated in terms of five dimensionless groups:

$$\frac{\rho_g v_{sg}}{\rho_l v_{sg}} = 198\, Re_{sl}^{-1.225} \left(\frac{D^2 \rho_l g}{\sigma}\right)^{0.23} \left(\frac{\mu_g}{\mu_l}\right)^{0.71} \left(\frac{\rho_g}{\rho_l}\right)^{0.13} \left(\frac{D^3 \rho_l^2 g}{\mu_l^2}\right)^{0.231} \tag{2.1}$$

The experimental investigations by Feind [60FE1] and Clift *et al.* [66CL1] concentrated on the role of the liquid viscosity during countercurrent flow and flooding. Feind used water, water-diethylene glycol solutions and air while Clift *et al.* tested water and aquous glycerol solutions with air. Both investigators found the flooding air velocity to decrease

as the liquid viscosity was increased. According to Clift *et al.* the change in the flooding gas velocity is of the order of 20 percent for a 70 fold change in viscosity. Feind presented the following correlating equation:

$$Re_g = \frac{1.4\,x\,10^4}{a}\left(\frac{\rho_g}{\rho_l}\right)^{2/5}\left(\frac{\mu_l}{\mu_g}\right)^{3/4} Re_l^n\left[0.093\left(\frac{D}{2\delta_o}\right)^{5/4} - 1\right] \tag{2.2}$$

where $a = 58.2$ and $n = 1/3$ for $Re_l \le 400$

$a = 157.7$ and $n = 1/2$ for $Re_l > 400$

δ_o is the film thickness for vertical annular flow in the absence of a gas and was given by Feind as

$$\delta_o / D = 0.369\left(3\,\mu_l^2 / D^3 \rho_l^2 g\right)^{1/3} Re_l^{1/2} \tag{2.3}$$

Similar experiments were performed by Wallis [69WA1]. Air-water, air-ethylene glycol and air-glycerol solutions were used as working fluids. The flooding air velocity decreased with an increase in liquid viscosity. The data were correlated in terms of the familiar Wallis relation

$$Fr_{Dsg}^{1/4} + m\,Fr_{Dsl}^{1/4} = C \tag{2.4}$$

where m and C are functions of the dimensionless group

$$N_l = \left[g D^3 \rho_l\left(\rho_l - \rho_g\right)/\mu_l^2\right]^{1/2} \tag{2.5}$$

N_l was termed the *inverse viscosity parameter*. A similar group was used by Kamei *et al.* [54KA1] to correlate flooding data. The dimensionless group emerges form the *Nusselt* theory for the laminar film thickness during falling film flow under the action of gravity.

Suzuki and Ueda [77SU1] conducted extensive experiments to determine the effect of the liquid viscosity and surface tension on flooding. The authors plotted the flooding air velocity against the film thickness for various liquids tested. This plot led the authors to conclude that the flooding gas velocity increases with an increase in the liquid viscosity. According to some researchers, e.g. Tien and Liu [79TI1], this trend contradicts the

findings of other investigators [60FE1, 66CL1, 69WA1, 80CH1, 96ZA1]. The original plot by Suzuki and Ueda is shown in figure 2.10(a). The film thickness on the abscissa is related to the liquid viscosity. Thus, the plot does not give a true reflection of the effect of the liquid viscosity on flooding and may have led to the apparent contradiction. Figure 2.10(b) shows the same data in terms of the superficial velocities and illustrates that the flooding gas velocity decreases with an increase in viscosity. The conclusion by Suzuki and Ueda is only valid at a specific film thickness and their results do not contradict previous findings. Suzuki and Ueda further varied the surface tension from 0.037 to 0.068 N/m to establish the functional relationship between the flooding air velocity and the surface tension. At a surface tension of $\approx$ 0.05 N/m the flooding velocity reached a maximum. The data were correlated in terms of the four dimensionless groups

$$Fr = \left[\rho_g \left(v_g - v_l \right)^2 / \rho_l g \delta \right]^{1/2}, \tag{2.6}$$

Re_{sl} , $\rho_l g D^2 / \sigma'$ and μ_g / μ_l where

$$Fr = f \left[Re_{sl}^{-1/3} \left(\frac{\rho_l g D^2}{\sigma'} \right)^{1/4} \left(\frac{\mu_g}{\mu_l} \right)^{2/3} \right] \tag{2.7}$$

σ' is a modified surface tension

$$\sigma' = \sigma + 1.5 \left| \sigma - 0.05 \right| \tag{2.8}$$

which takes into account that the maximum flooding gas velocity occurs at σ = 0.05 N/m.

A similar investigation on the fluid properties was conducted by Chung *et al.* [80CH1]. The surface tension was found to have a stabilising effect on flooding, i.e. liquids with higher surface tensions require higher gas velocities to reach flooding. An increase in the liquid viscosity resulted in a decrease in the flooding gas velocity. The flooding air velocities for three oils with viscosities of 38.5 x 10^{-3}, 52.5 x 10^{-3} and 106 x 10^{-3} kg/ms respectively did not show a significant difference. They were, however, well below the flooding air velocities of water. Chung *et al.* therefore concluded that the viscosity

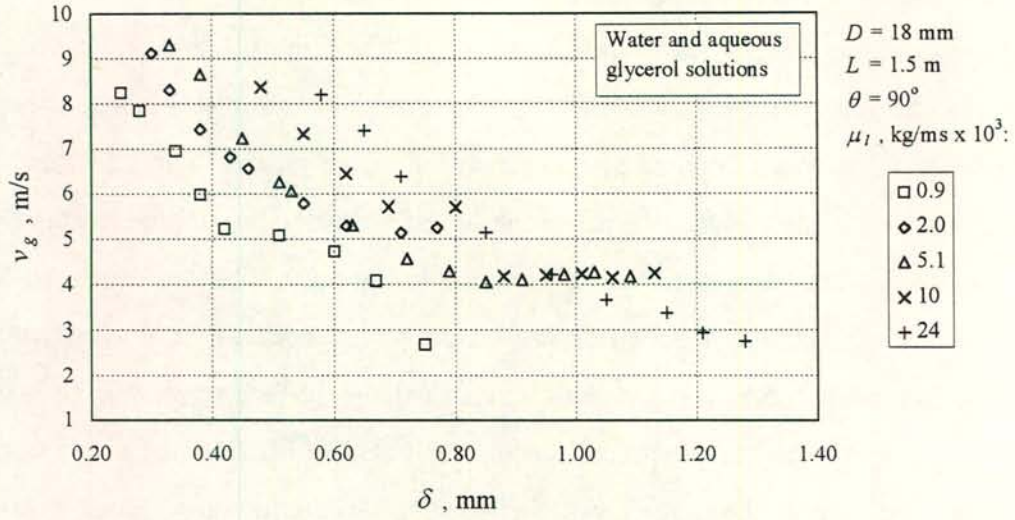

Figure 2.10 (a): Flooding data by Suzuki and Ueda [77SU1] to test the influence of the liquid viscosity.

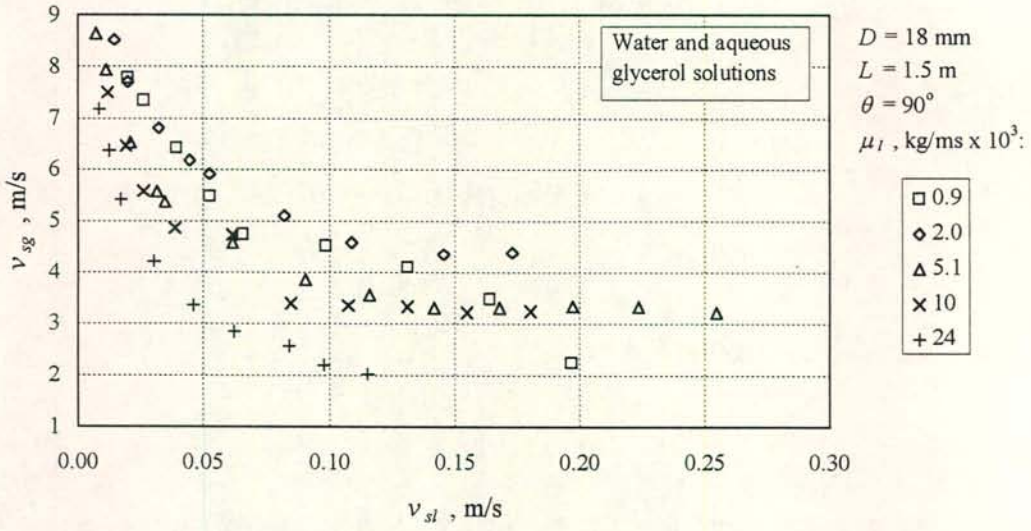

Figure 2.10 (b): The flooding of figure 2.10 (a) plotted in terms of the superficial phase velocities.

influence becomes important only when the change in viscosity is ten- to hundred-fold. No attempt was made to include the liquid viscosity as a parameter in a correlation. The authors argued that the surface tension has a stronger effect on flooding than the liquid viscosity. A correlation containing the Kutateladze numbers and the Bond number was proposed:

$$Ku_{sg}^{1/2} + m\,Ku_{sl}^{1/2} = a\,tanh\left[b\,(Bo)^{1/4}\right] \tag{2.9}$$

m, a and b depend on the tube end configuration and the liquid and gas supply method.

Countercurrent flow experiments were carried out by Stephan and Mayinger [92ST1] to determine the effect of the system pressure on the downflow rate during partial liquid delivery. Saturated Refrigerant 12 liquid and vapour were tested inside a vertical 20 mm x 68 mm rectangular channel. Three system pressures of 0.67, 1.0 and 1.3 MN/m^2 were tested with corresponding vapour densities of 38.0, 57.1 and 74.9 kg/m^3. The liquid downflow rate was measured and plotted against the corresponding vapour upflow rate. The vapour velocity increased with a decrease in vapour density at a constant liquid downflow rate.

More recently Zapke and Kröger [96ZA1] investigated the effect of the properties of both the gas and the liquid phase on flooding in vertical and inclined tubes. Their results were correlated in terms of the densimetric Froude numbers and a dimensionless group *Zk* which accounts for the liquid properties

$$Zk_D = \left(\rho_l \, D\sigma / \mu_l^2\right)^{1/2} \tag{2.10}$$

Zapke and Kröger recommended that flooding data should be correlated in the form

$$Fr_{Dsg}^{1/4} + m\, Fr_{Dsl}^{1/4} = K\left(Zk_D\right)^n \tag{2.11}$$

The values of m and K depend on the tube inclination angle and the bottom end geometry while the exponent n is determined by the tube inclination. A systematic approach was followed to arrive at equation (2.11). Counterflow and flooding data of three other investigators [66CL1, 80CH1, 92ST1] was successfully correlated by the method recommended. It is therefore considered worthwhile to briefly elaborate on the work by Zapke and Kröger [96ZA1].

Their flooding gas velocities for argon, air, hydrogen, helium and water measured inside a 30 mm vertical tube with a sharp-edged gas inlet and a porous liquid injection unit are shown in figure 2.11. A wide range of flooding gas velocities were measured due the variety of gas properties. Figure 2.12 is a plot of the same data in terms of the superficial gas Reynolds number. The Reynolds number at flooding varied from ≈4000 (helium) to ≈16000 (air). It was concluded that flooding is not related to the gas Reynolds number. The same data are plotted in figure 2.13 in terms of the gas momentum flux, based on the

superficial velocity. The plot illustrates that flooding occurred at a certain momentum flux, which in turn may be a function of other parameters such as the liquid flow rate.

The effect of the liquid properties was investigated by conducting tests with water, methanol, aqueous methanol solutions, propanol and air. The data are shown in figure 2.13 in terms of the densimetric Froude numbers. The gas Froude number at flooding decreased as the percentage methanol of the aqueous methanol solutions was increased but the pure methanol data were approximately equal (or slightly below) the pure water data. This trend suggests that Fr_{Dsg} decreases with an increase in the percentage methanol, reaches a minimum and increases subsequently so that the pure methanol and water data are equal. The authors found that the Zk number, defined by equation (2.10), exhibits such a trend. The number is plotted in figure 2.15 as a function of the percentage methanol (by volume) in an aqueous methanol solution. It was concluded that flooding data can be correlated by a Wallis-type [69WA1] relation, given by equation (2.4), where C is function of the Zk number, as illustrated by equation (2.11). Equation (2.11) can be rearranged as follows:

$$Fr_{Dsg}^{1/4} / Zk_D^n + m\, Fr_{Dsg}^{1/4} / Zk_D^n = K \qquad (2.12)$$

The data of figure 2.14 are shown in figure 2.16 in terms of the dimensionless groups $Fr_{Dsi}^{*\,1/4} / Zk_D^{\,n}$. A value of 0.05 for n correlates the measured trend. Figures 2.17 to 2.20 show the results by three other investigators [66CL1, 80CH1, 92ST1] in terms of the superficial velocities and in terms of the dimensionless groups of equation (2.12). The figures illustrate that also in the case of other investigations, the combination of the Froude and the Zk number successfully correlates the effect of the fluid properties on flooding or partial liquid delivery rates.

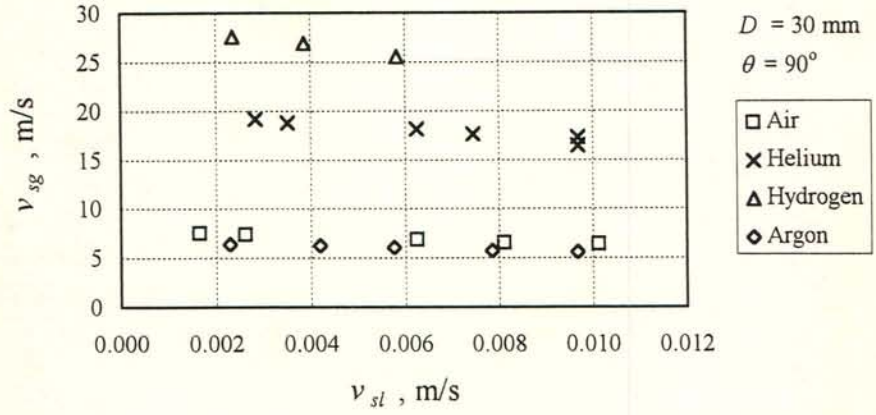

Figure 2.11: Flooding superficial velocities by Zapke and Kröger [96ZA1] measured with air, helium, hydrogen, argon and water inside a vertical tube with a sharp-edged gas inlet.

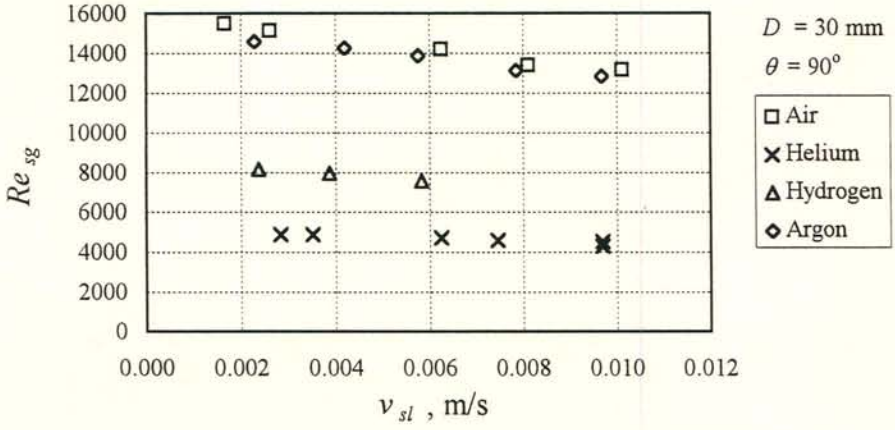

Figure 2.12: Flooding data by Zapke and Kröger [96ZA1] (figure 2.11) plotted in terms of the superficial gas Reynolds number.

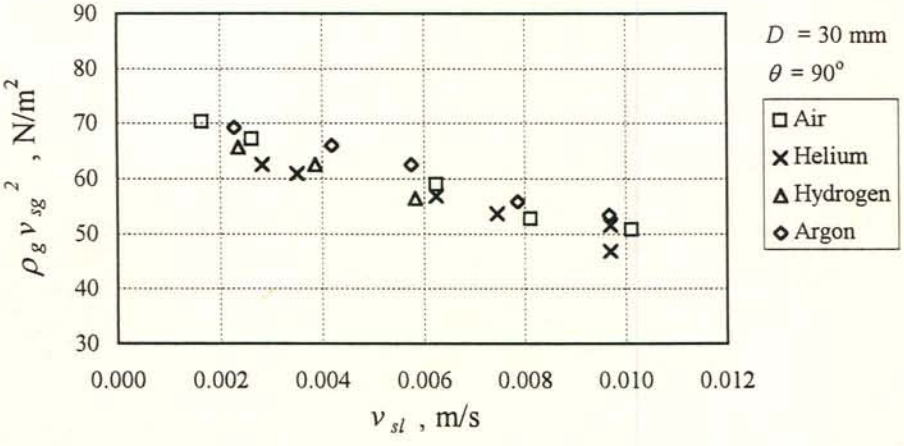

Figure 2.13: Flooding data by Zapke and Kröger [96ZA1] (figure 2.11) plotted in terms of the superficial gas momentum flux.

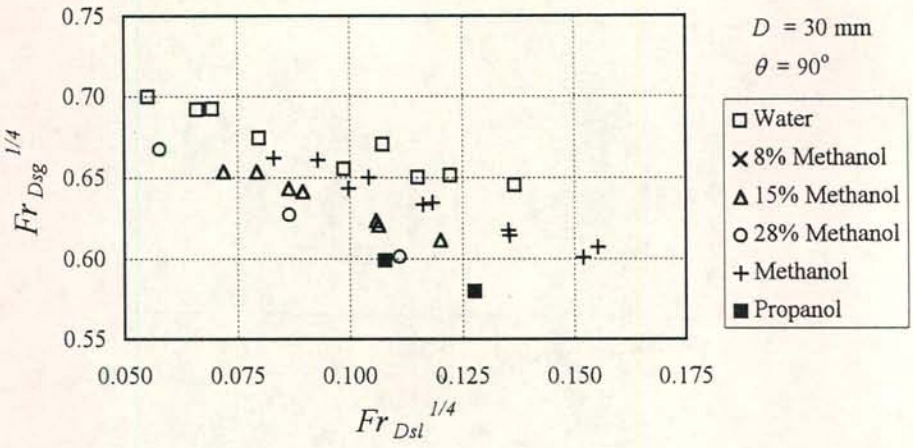

Figure 2.14: Phase Froude numbers at flooding by Zapke and Kröger [96ZA1], measured with various liquids and air inside a vertical tube with a sharp-edged gas inlet.

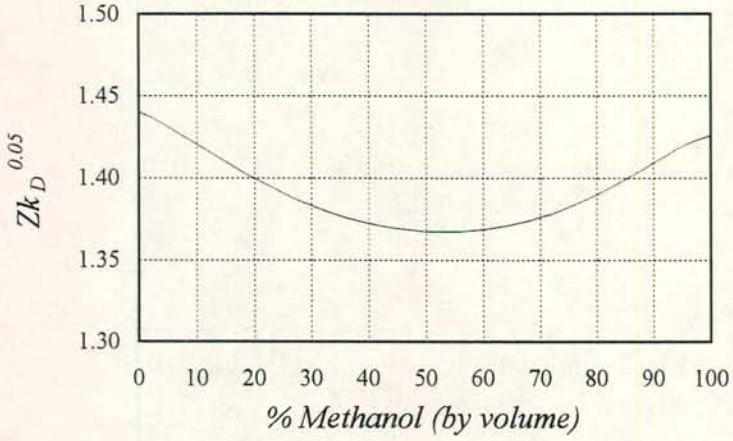

Figure 2.15: The Zk number (raised to the power of 0.05 to correlate the data of figure 2.14) for aqueous methanol solutions and D = 30 mm, plotted against the percentage methanol in the solution.

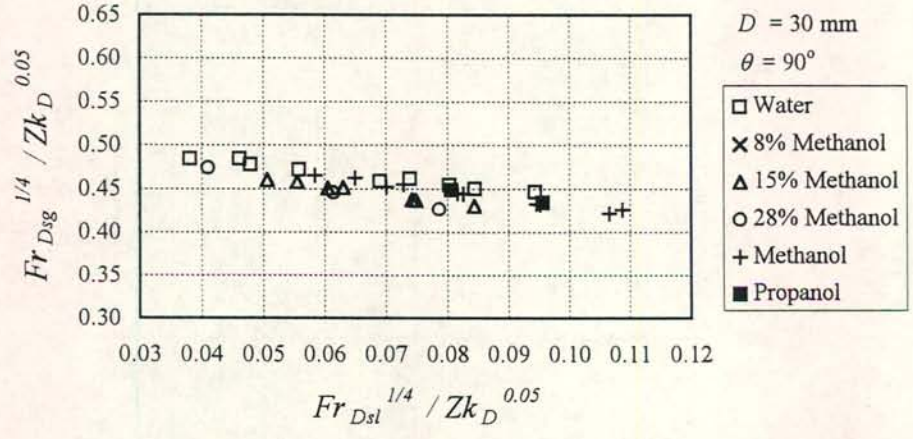

Figure 2.16 The data of figure 2.14 plotted in terms of the dimensionless form $Fr_{Dsi}^{1/4} / Zk_D^{n}$ of equation (2.12), as proposed by Zapke and Kröger [96ZA1]. A value of 0.05 for n correlates the data.

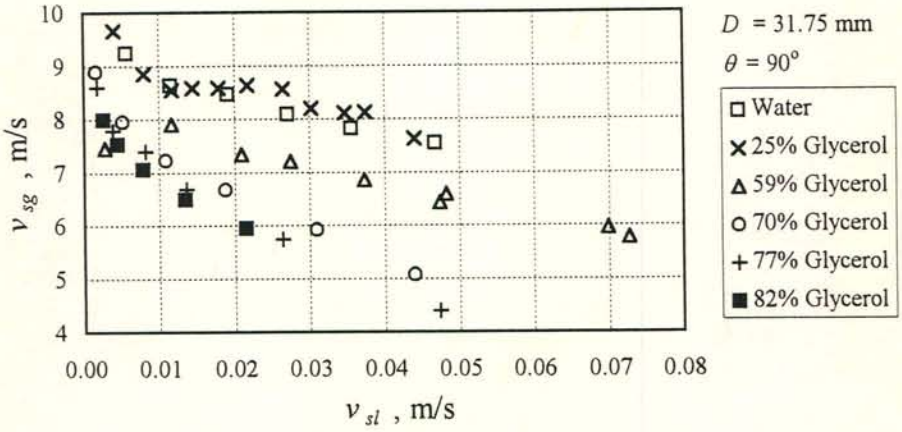

Figure 2.17 (a): Flooding superficial velocities of the aqueous glycerol solutions and air tested by Clift *et al.* [66CL1] inside a vertical tube with a bell-shaped gas inlet and a porous sintered liquid feed.

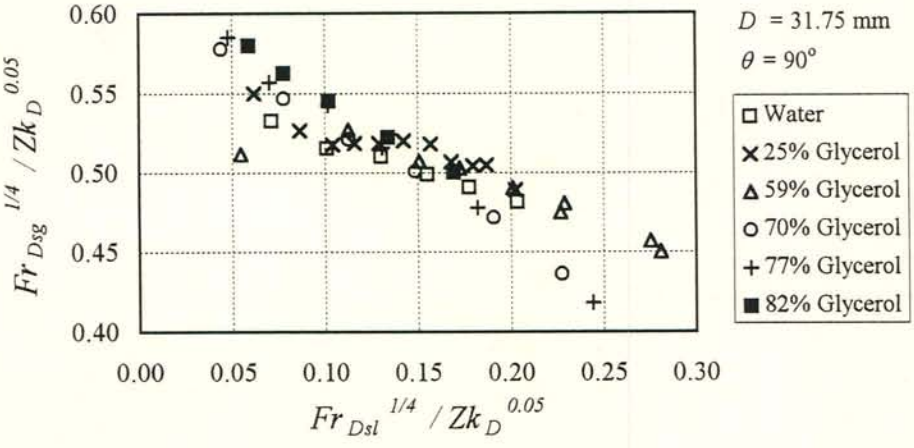

Figure 2.17 (b): The data of Clift *et al.* [66CL1] (figure 2.17a) plotted in terms of the dimensionless groups $Fr_{Dsi}^{1/4} / Zk_D^{0.05}$.

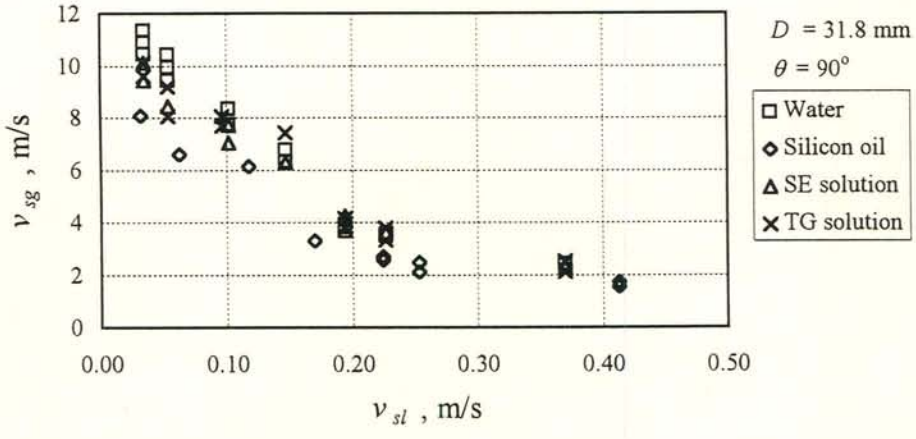

Figure 2.18 (a): Flooding superficial velocities of the liquids and air tested by Chung *et al.* [80CH1] inside a vertical tube with a sharp-edged gas inlet, to determine the surface tension effect on flooding.

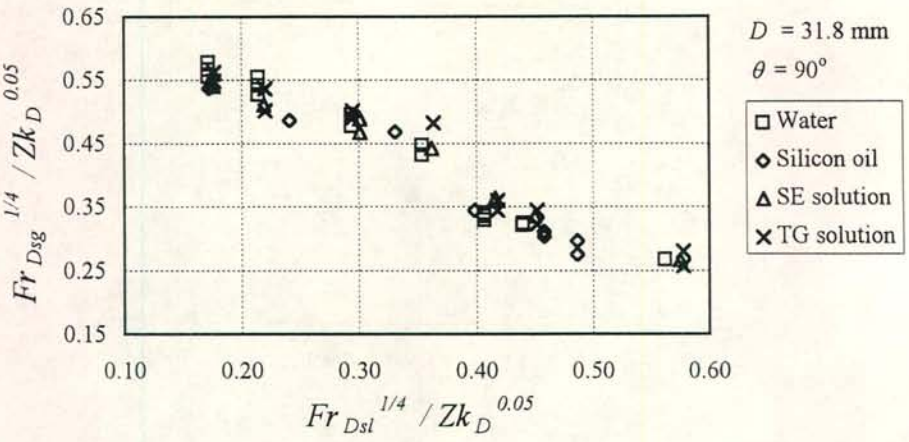

Figure 2.18 (b): The data of Chung *et al.* [80CH1] (figure 2.18a) plotted in terms of the dimensionless groups $Fr_{Dsi}^{1/4} / Zk_D^{0.05}$.

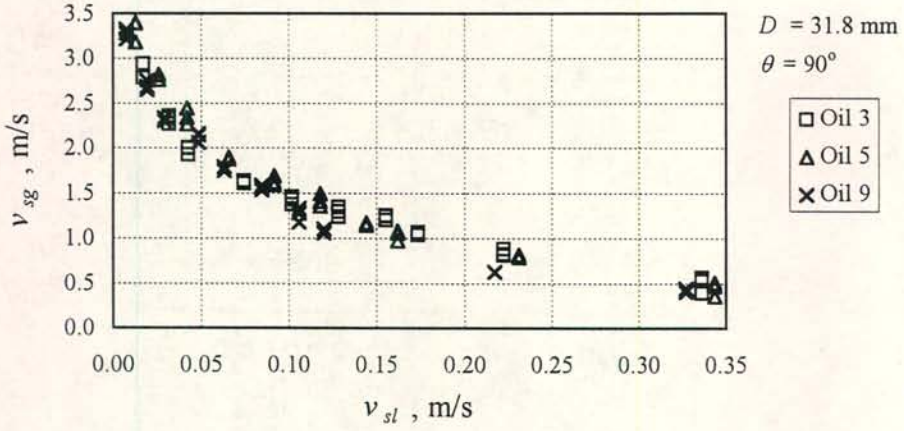

Figure 2.19 (a): Flooding superficial velocities of the liquids and air tested by Chung *et al.* [80CH1] inside a vertical tube with a sharp-edged gas inlet, to determine the liquid viscosity effect on flooding.

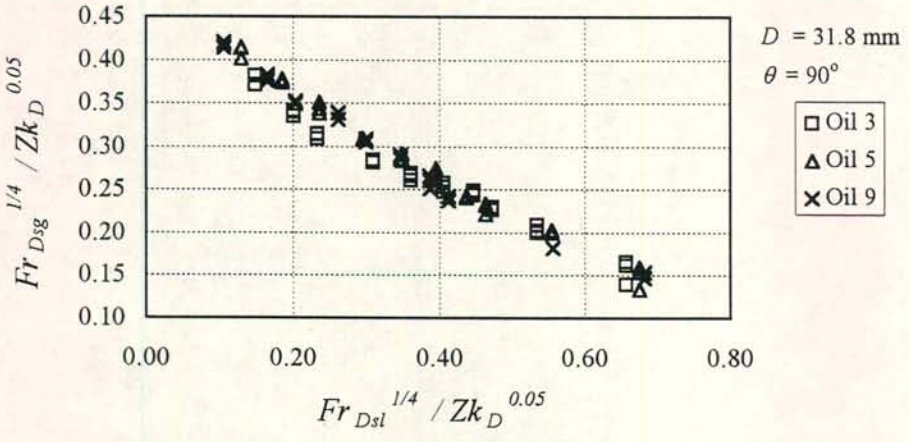

Figure 2.19 (b): The data of Chung *et al.* [80CH1] (figure 2.19a) plotted in terms of the dimensionless groups $Fr_{Dsi}^{1/4} / Zk_D^{0.05}$.

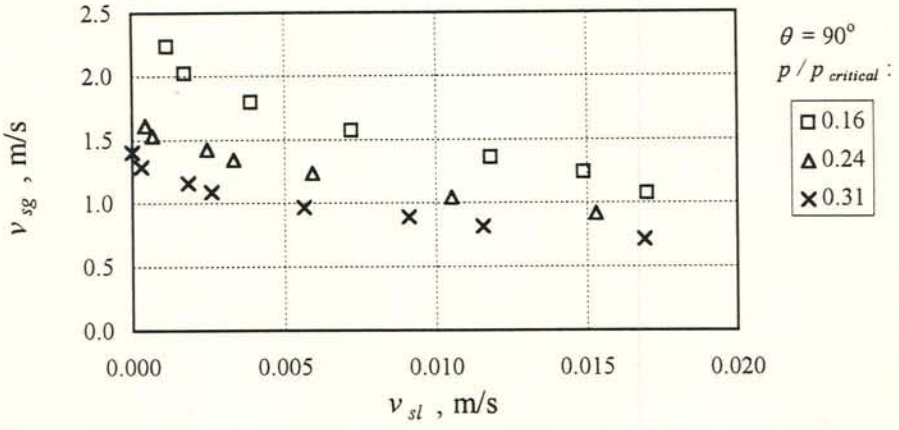

Figure 2.20 (a): The superficial phase velocities during partial liquid delivery by Stephan and Mayinger [92ST1], measured inside a vertical 20 mm x 68 mm rectangular duct at various system pressures.

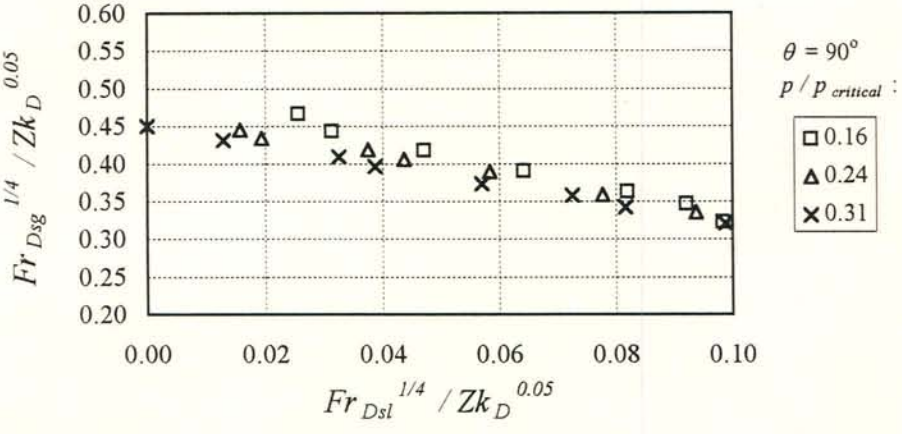

Figure 2.20 (b): The data of Stephan and Mayinger [92ST1] (figure 2.20a) plotted in terms of the dimensionless groups $Fr_{Dsi}^{1/4} / Zk_D^{0.05}$.

2.5.2 Discussion

Detailed information on experimental flooding correlations for adiabatic gas-liquid flow has been presented by McQuillan and Whalley [85WH1] and Bankoff and Lee [86BA1]. The basic dimensionless groups emerging from these surveys on flooding and the published literature are:

1) Gas Reynolds number	$\rho_g v_g L / \mu_g$
2) Liquid Reynolds number	$\rho_l v_l L / \mu_l$
3) Densimetric Froude-type numbers	$\rho_i v_i^2 / [g L (\rho_l - \rho_g)]$ or

	$\rho_i v_i^2 / [g L \rho_l]$
4) Kutateladze numbers	$\rho_i^{1/2} v_i / [g \sigma (\rho_l - \rho_g)]^{1/4}$
5) Bond-type numbers	$L [g (\rho_l - \rho_g) / \sigma]^{1/2}$ or
	$L^2 g \rho_l / \sigma$
6) Weber numbers	$\rho_i v_i^2 L / \sigma$
7) Dimensionless liquid volume flow rate (combination	
of the Kutateladze and the Bond number)	$Q_l [g (\rho_l - \rho_g)^3 / \sigma^3]^{1/4}$
8) Inverse viscosity parameters	$[g L^3 \rho_l (\rho_l - \rho_g) / \mu_l^2]^{1/2}$ or
	$g L^3 \rho_l^2 / \mu_l^2$
9) Mass flux ratio	$\rho_g v_{sg} / \rho_l v_{sl}$
10) Film thickness ratio	δ / L
11) Density ratio	ρ_l / ρ_g
12) Viscosity ratio	μ_l / μ_g
13) Reference viscosity ratio	$\mu_l / \mu_{reference}$
14) *Zk* number	$(\rho_l L \sigma / \mu_l^2)^{1/2}$

L represents a characteristic dimension in the above-listed groups. The experimental results by Zapke and Kröger [96ZA1] proved that flooding is not related to the gas Reynolds number. It was further shown that the gas parameters correlating flooding data appear in the form of the momentum flux and that the gas viscosity has no effect on the flooding fluid flow rates. The gas Reynolds number, the mass flux ratio and the viscosity ratio should therefore be excluded from the above-listed dimensionless groups for the purpose of correlating flooding data.

The data shown in figure 2.14 are plotted in figures 2.21 (a) and (b) in terms of the Kutateladze numbers and the Kutateladze-Bond number correlation proposed by Chung *et al.* [80CH1] respectively. According to figures 2.16, 2.18, 2.19 and 2.21 the method by Zapke and Kröger succeeds in correlating their own data and that of Chung *et al.*, but the Kutateladze-Bond number does not correlate the data of Zapke and Kröger. Thus for tube diameters of ≈30 mm the Froude-*Zk* correlation applies while the Kutateladze-Bond model is not valid. It further implies that the density ratio is not required because the phase densities are sufficiently accounted for by the Froude-*Zk* combination.

The dimensionless liquid volume flow rate can be excluded because it is a combination of the Kutateladze and the Bond number, which proved to be unsuccessful. The reference viscosity ratio should also be excluded as it is of no physical significance.

The remaining dimensionless groups are the film thickness ratio, the inverse viscosity-type parameters, the liquid Reynolds number and the Weber numbers. So far the Froude-*Zk* combination appears to be the most successful for the diameters of the order of 30 mm. Further research is required to establish if the remaining groups play a role in flooding and whether the *Zk* number accounts for a combined effect of some of these four groups.

It can finally be concluded that the flooding gas velocity decreases with an increase in the liquid viscosity. This trend has been observed by a number of investigators [60FE1, 63EN1, 69WA1, 77HE1, 80CH1, 96ZA1]. An opposites trend was reported by *Kamei et al.* [54KA1]. The author was unable to find an explanation for the observed trend.

A number of investigators [63EN, 69DI1, 77CH1, 80CH1, 96ZA1] found the flooding gas velocity to decrease with a decrease in the surface tension. Contrary to Chung *et al.* [80CH1], the results by Zapke and Kröger [96ZA1] showed that the effect of the liquid vicosity is stronger than the surface tension influence on flooding. The fact that the surface tension has such a little effect on flooding may explain the complex trend observed by Suzuki and Ueda [77SU1]. A small change in the liquid density and/or viscosity may have had a significant effect on the surface tension experiments by Suzuki and Ueda.

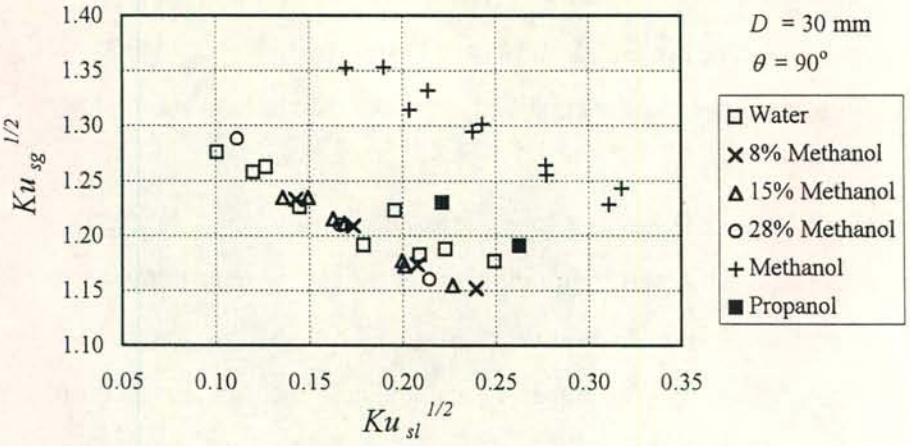

Figure 2.21 (a): The data of Zapke and Kröger [96ZA1] (figure 2.14) plotted in terms of the Kutateladze numbers.

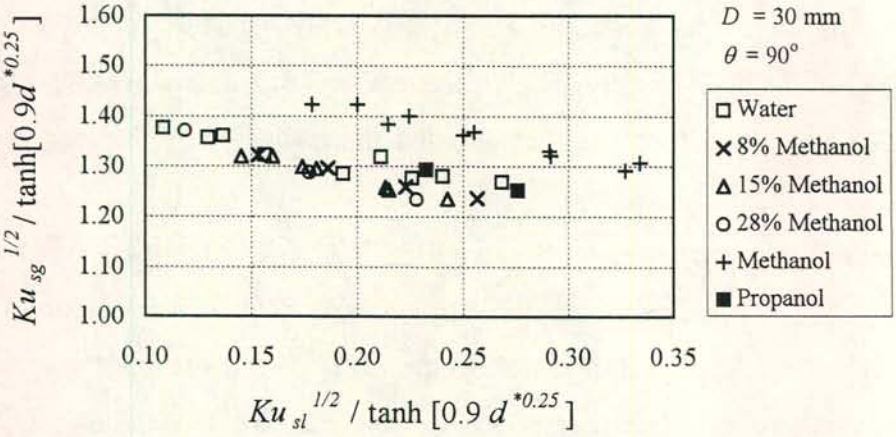

Figure 2.21 (b): The data of Zapke and Kröger [96ZA1] (figure 2.14) plotted in terms of the Kutateladze-Bond number model proposed by Chung *et al.* [80CH1].

2.6 Limiting conditions during reflux condensation

During reflux condensation inside vertical and inclined ducts or tubes, a vapour enters the duct at the bottom and is condensed as it flows upwards. The condensate drains down under the action of gravity. The heat transfer required for the condensation process can be achieved by bringing the vapour into contact with a sub-cooled liquid. A practical example of this type of reflux condensation is the emergency cooling water, injected at the top of a reactor core, flowing down against steam generated during a hypothetical-loss-of-coolant accident.

Heat transfer and the subsequent condensation of vapour can also be obtained by maintaining the duct wall temperature below the saturation temperature of the vapour. The vapour condenses in the presence of a liquid film (filmwise condensation), which is at a temperature just below the vapour saturation temperature. This type of condensation is found in air-cooled reflux condensers such as dephlegmators. One of the aims of the present investigation is to develop a correlation for potential limiting conditions encountered during reflux condensation inside dephlegmators or de-aerators as a result of flooding. Flooding caused by steam flowing countercurrent to sub-cooled water (reactor core conditions during loss-of-coolant accident) is however beyond the scope of this study and will not be addressed here. The reader may consult Tien and Liu [79TI1] and Bankoff and Lee [86BA1] for information on flooding affected by steam condensation in the presence of sub-cooled water.

Reflux condensation has been the subject of a number of studies [80RU1, 83BA1, 89FU1, 91BE1, 92GI1, 94OB1, 93GR1, 96RE1]. In these investigations steam was condensed inside a tube or duct by maintaining the wall temperature below the saturation temperature. While in some cases industrial-type air-cooled finned tubes were employed, other researchers made use of glass tubes placed inside acrylic plastic or glass cooling jackets. Water was pumped through the cooling jacket. The latter method enables visual observation of the flow patterns. Similar to the adiabatic case, the flow inside a reflux condenser tube changes from countercurrent, at low vapour flow rates (low heat transfer rates), to cocurrent upflow at higher vapour rates (higher heat transfer rates). The transition is, however, markedly different from that observed during adiabatic flow. It

has been observed that the transition from countercurrent to cocurrent upflow coincides with the formation of a single-phase region or plug of liquid if the tube length is sufficient. This plug formation imposes an upper limit on the heat transfer rate during reflux condensation. Banerjee *et at.* [83BA1] and Obinelo *et al.* [94OB1] presented, amongst others, detailed information on the conditions during plug formation.

Banerjee *et al.* studied single-tube reflux condensation of steam at atmospheric and above atmospheric pressure. The pressures at the top and bottom of the tube were controlled to maintain constant plenum pressures during an experimental run. The bottom plenum pressure was controlled by a pressure regulating valve, fed by steam at high pressures. The top plenum was either open to atmosphere, or pressurised once a liquid plug was formed. The condenser tube was jacketed and cooled with water. The pressure inside the lower plenum was increased by opening the regulating valve. At low bottom pressures (low steam flow rates) the steam was condensed in a two-phase region and no single-phase region was formed. As the bottom pressure was increased, the steam velocities at the inlet became sufficient to form a liquid plug above the two-phase condensing region. An important observation was that once the plug had been formed, the steam mass flow rate entering the tube remained fairly constant as the pressure drop was varied from ≈3000 to ≈30000 N/m^2. The inlet temperature of the cooling water was kept constant while increasing the bottom plenum pressure. Experiments where conducted with cooling water inlet temperatures of 9 and 20°. The cooling water temperature had no significant effect on the steam flow rate at which the single-phase region was formed.

As the pressure difference across the tube was increased, the single-phase region grew in length. The length of the two-phase region remained, however, unchanged while varying the pressure difference and keeping the secondary side temperature (cooling water temperature) constant. It decreased with a decrease in cooling water temperature. It can therefore be concluded that the length of the single-phase region is independent of the secondary side temperature, but directly related to the pressure difference across the tube, while the length of the two-phase region depends on the secondary side temperature.

The temperature inside the two-phase region was close to the saturation temperature but a sharp drop on temperature was observed as the single-phase region was entered. The liquid plug was significantly sub-cooled. Banerjee *et al.* [83BA1] concluded that flooding at the steam inlet of the tube controls the maximum steam rate during reflux condensation.

Obinelo *et al.* [94OB1] conducted similar experiments as Banerjee *et al.* [83BA1] and attempted to increase the reflux condensation capability by feeding pulsating steam flow into the condenser tube to destabilise the formation of the single-phase region. The flow patterns observed during steady inlet steam flow were similar to those described by Banerjee *et al.* The flow patterns are illustrated in figure 2.22. At very low vapour flow rates a wavy film was observed to flow downward countercurrent to the steam flow. All the steam entering the tube was condensed in a very short length of tube and the conditions were steady. Upon an increase in the steam flow rate, liquid droplets were entrained in the steam core and eventually a steam flow rate was reached at which a chaotic flow pattern was formed, with most of the condensate being carried up by the steam. The upward condensate flow led to the formation of a single-phase water column, oscillating above the two-phase condensing region. The bottom plenum pressure finally overcame the weight of the column an it was ejected at the top, followed by the reestablishment of the single-phase region. The cyclic period was typically 5 minutes long. This flow mode was categorised as cyclic carryover with a quasi-static water column because the conditions were transient and cyclic, but the oscillations of the liquid column were very small. It was referred to as the first carryover mode.

As the inlet steam flow rate was further increased, the liquid column became fully dynamic and oscillated at much faster frequencies than in the case of the first carryover mode. The unstable flow regime signalled a transition before the onset of steady upward two-phase flow and was referred to as the second carryover mode. During the second carryover mode the cycle periods were less than typically one minute. The flow pattern in the two-phase condensing region was churn-annular flow during both carryover modes. At steam flow rates beyond the second carryover mode, steady two-phase climbing flow prevailed and no condensate entered the inlet plenum, except for small amounts of condensate formed at the tube inlet and exit of the bottom plenum.

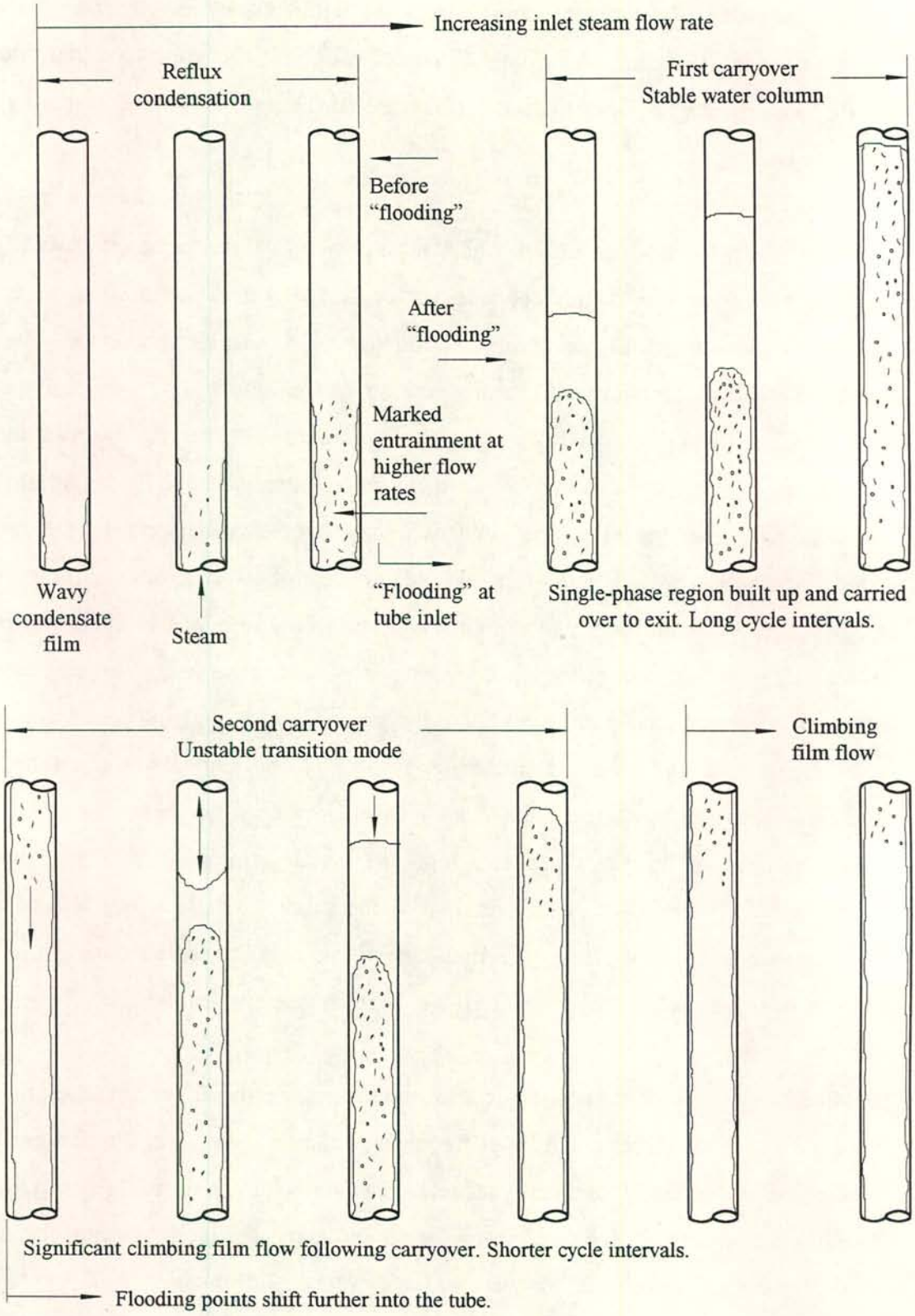

Figure 2.22: Flow patterns encountered during reflux condensation according to Obinelo *et al.* [94OB1].

The qualitative pressure drop characteristics of an inverted U-tube system, undergoing a transition from reflux condensation to cocurrent flow and subsequent natural circulation, is illustrated in figure 2.23 [83BA1]. In region AB reflux condensation occurs and no single-phase column is built up. At B "flooding" takes place at the tube inlet. It results in the formation of a single-phase region, which coincides with a sharp increase in pressure drop. The liquid build-up may be the result of controlled plenum pressures or sufficient heat transfer causing flooding velocities at the tube inlet [94RE1]. In region BC the pressure drop can be increased but the vapour mass flow rate at the inlet remains practically constant. At C liquid is ejected at the top. Region CD is an unstable region and the flow oscillates between refluxing and carryover. At point D the system becomes frictional pressure drop dominated. In region DE the steam and liquid flow cocurrently. If the system is pressure difference controlled, a continues increase in the steam mass flow rate takes place as point C is approached and from there it jumps to point E' on curve DE. Such a jump in the inlet steam flow rate has been observed by Banerjee *et al.* [83BA1]. On the other hand, if the inlet steam flow rate is heat transfer controlled, than the system experiences oscillating flow in region CD until the mass flow rate exceeds that at D. In the region of oscillatory flow pressure waves can have a shattering effect on the condenser tube [83BA1, 94RE1].

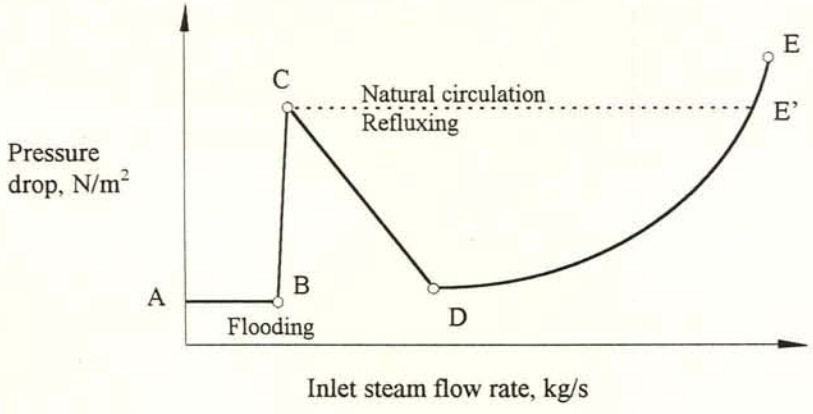

Figure 2.23: Pressure drop characteristics of a vertical inverted U-tube condenser according to Banerjee *et al.* [83BA1].

In section 2.3.1 flooding is defined for an adiabatic system with a porous liquid injection unit. This definition does not apply to reflux condensation because a condenser tube does not have a "point of liquid injection". Liquid is "injected" along the entire tube length. Liquid or condensate can, however, be ejected at the top of a reflux condenser tube. Condensate ejection can be regarded as equivalent to the conditions (fluid flow rates) at which liquid begins to flow upwards past the point of injection in an adiabatic system. This statement is based on the fact that in both cases liquid is transported upward, which can lead to cocurrent upflow of a two-phase mixture. Fürst [89FU1] for example, defined flooding in a reflux condenser tube as the fluid rates at which condensate is ejected at the top. According to the observation of Banerjee *et al.* [83BA1] the inlet steam flow rate at the onset of the formation of a single-phase region (point B) and that at the onset of ejection (point C) are practically equal. In other words, flooding in a reflux condenser can be defined as the steam flow rate at which a sudden rise in pressure drop occurs. In a concurrent study Reuter [94RE1] and Zapke [94ZA1] found that there is no significant difference in gas flow rates at which a sudden rise in pressure drop occurs (reflux condensation) and the gas flow rate at the transition depicted in figure 2.4(b). This was observed for vertical and inclined flow (60° to horizontal).

Fürst [89FU1] investigated the effect of the inclination angle on flooding inside a reflux condenser tube. The highest flooding vapour velocities were measured at an inclination angle of 60° to the horizontal. The flooding velocity at 15° exceeded that for vertical flow. An elliptical duct with the same internal circumference as that of a round tube was also tested for flooding. The round tube had a diameter of 25 mm and the aspect ratio of the elliptical duct was 3.5. The elliptical duct flooded at higher vapour velocities, but the flooding mass flow rate of the vapour was higher in the case of the round tube.

2.7 Pressure gradient during countercurrent gas-liquid flow

The frictional pressure drop experienced by the gas during annular countercurrent flow is usually expressed in terms of an interfacial friction factor

$$f_i = \left(dp/dz\right)_f \left(D_e - 2\delta\right) \Big/ \left(1/2\,\rho_g v_g^2\right) \tag{2.13}$$

Feind [60FE1] investigated the effect of the liquid flow and liquid properties on the pressure gradient for annular flow inside vertical tubes of diameters of 20 and 50 mm. The test section was constructed to minimise end effects where the phases enter the tubes and the measurements were taken during steady-state flow with all the injected liquid flowing downwards as illustrated in figure 2.4(a). Readings were taken from inside the laminar region (gas flow) up to flooding. The friction factor decreased with an increase in the gas Reynolds number similarly to single-phase flow. At flooding a sharp increase in pressure gradient was experienced. For higher liquid flow rates the transition from laminar to turbulent gas flow was continuous while at lower liquid flow rates the interfacial friction factor showed an increase in the transition zone. The interfacial friction factor was higher than for single-phase flow because of the presence of the wavy film and due to downward flow of gas at the interface. The latter had a stronger effect on f_i in the laminar region (gas) but the effect became weaker in the turbulent region. The data was correlated in terms of the dimensionless groups Re_g, Re_l, (μ_l/μ_g), (ρ_l/ρ_g) and $(2\delta_o/D)$, i.e.

$$G = c_1 \frac{Re_g}{Re_l^{c_2}} \left(\frac{\rho_l}{\rho_g}\right)^{2/5} \left(\frac{\mu_g}{\mu_l}\right)^{2/3} \left(\frac{2\delta_o}{D}\right)^{1/2} \tag{2.14}$$

where

$$f_i = 120/G^{5/3} + 0.14/G^{1/5} \tag{2.15}$$

The correlation is valid for gas flow in the presence of a wavy film and does not apply in the case of a smooth film or single-phase gas flow. It further does not account for the sudden increase in pressure drop at flooding and may only be applied for conditions below flooding where there is no accumulation of liquid inside the tube. It should be kept in mind that the correlation was developed from air data only and the effect of the gas properties, as correlated in equation (2.14), was not confirmed by experiment.

Bharathan and Wallis [83BH1] presented a correlation for f_i based on air-water counterflow experiments where the outflow of water was restricted at the bottom of the test section by the air flow. There is fundamental difference between these conditions and those of Feind [60FE1] where the liquid was allowed to drain freely and the downflow

was not limited by the upward flowing gas. According to Bharathan and Wallis the interfacial friction consists mainly of form drag over protruding waves and that it becomes independent of the tube diameter for large diameters. The interfacial friction factor was correlated in terms of the dimensionless film thickness and the Bond number.

$$f_i = 0.02 + 4c_1\delta^{*c_2} \tag{2.16}$$

where

$$log_{10}\, c_1 = -0.56 + 9.07/Bo \tag{2.17a}$$
$$c_2 = 1.63 + 4.74/Bo \tag{2.17b}$$

The correlation method implies that the waviness becomes stronger as the film thickness increases and weaker at higher values of surface tension. Only air-water data was used to obtain the correlation and the influence of the liquid properties on the interfacial friction was not verified be experiment. For large diameter tubes equation (2.16) reduces to

$$f_i = 0.02 + 210\delta^{*1.63} \tag{2.18}$$

f_i takes on a value of 0.02 when the film thickness is zero, which as an approximation for single-phase flow inside smooth tubes. Stephan and Mayinger [92ST1] presented a modified version of equation (2.16) where the value of 0.02 for single-phase flow was replaced by the Blasius relation

$$f_i = 0.316\,Re_g^{-0.25}\left(1 + 115\delta^{*c_1}\right) \tag{2.19}$$

where

$$c_1 = 3.95/\left(1.87 + 3.0/Bo\right) \tag{2.20}$$

Equation (2.19) is based on pressure gradient readings taken during steady-state partial liquid delivery. Under such conditions the liquid downflow is limited by the upward flowing gas similar to the experiments by Bharathan and Wallis [83BH1].

Equations (2.15), (2.16) and (2.19) are plotted in figure 2.24 for air-water flow at atmospheric conditions in a 50 mm tube. The difference between the Feind correlation for conditions below flooding and the other two correlations for limited liquid

penetration can clearly be seen. In the case of limited liquid outflow the film in the test section is thicker than for free outflow and thus a higher pressure drop is measured for limited outflow. The test section configuration influences the net outflow of liquid once flooding has occurred and thus also the pressure drop measured. The interfacial friction factor determined under conditions of limited outflow can therefore be affected by the test section configuration.

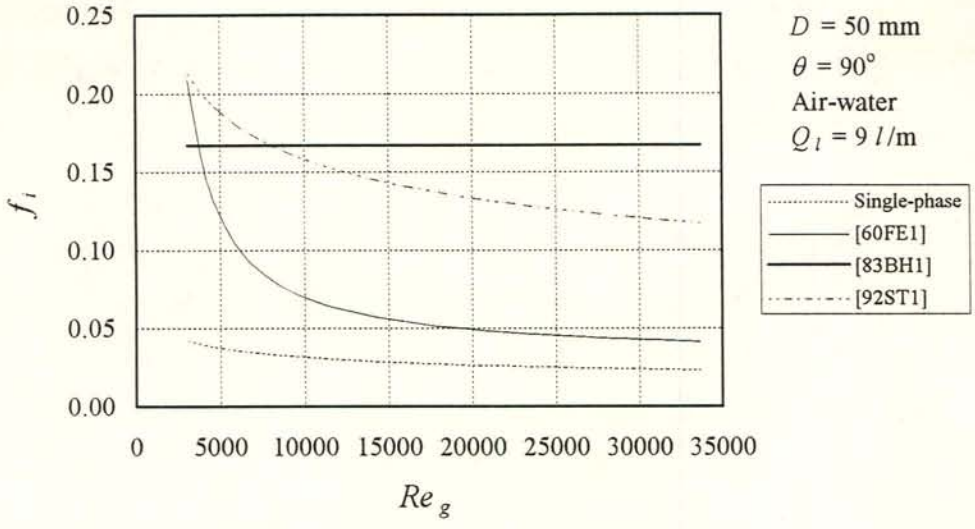

Figure 2.24 (a): Interfacial friction factor for annular countercurrent flow.

2.8 Liquid entrainment encountered in countercurrent flow

At low gas flow rates a draining liquid appears as a wavy film on the duct wall. As the gas velocity at the interface is increased liquid is entrained into the gas core in the form of droplets. Depending on the gas flow rate, the droplets are carried upwards or fall downwards and are redeposited on the film in the process. At sufficiently high gas velocities the droplets travel upwards to the top end of the duct.

Dukler *et al.* [84DU1] conducted air-water experiments and measured the entrainment rate during counterflow and the transition to a state of partial liquid delivery and beyond flooding. The water was fed through a porous sinter into the test section consisting of a vertical 50.8 mm i.d. tube. Air entered at the bottom through a bell-mouth. The entrained water was separated from the gas leaving the test section at the top to measure the rate

of entrainment. Inception of net entrainment was detected at flooding where part of the water started to flow upwards against the tube wall. Just beyond flooding the entrainment rate increased sharply as the gas flow was increased.

Liquid hold-up measurements by Stephan [90ST1] with the aid of optical sensors showed, however, that droplets can be entrained at gas velocities well below the flooding rate. But the net upward flow of entrained droplets was found to be insignificantly small. It was concluded that the droplet flow was characterised by a circulating nature of entrainment and redeposition and that the contribution by droplet flow to the upward transport at flooding was minimal.

Air-water experiments by Govan *et al.* [91GO1] for bell-shaped and square-edged gas inlets showed that the bottom geometry has an effect on the gas velocity at which entrainment occurs first. In the case of the rounded inlet no entrainment was observed at air flow rates below flooding. When testing with the square-edged gas inlet, a thick standing wave was formed at fairly low liquid flow rates. As the gas flow was increased part of the water was entrained from this wave but most of it redeposited on the falling film. Upon a further increase in the gas flow droplets would occasionally move above the liquid feed. At this stage flooding was not yet reached.

Similar findings were reported by Zapke [94ZA1] who conducted flooding tests in a vertical 30 mm i.d. tube with a porous feed and a square-edged inlet. Water, methanol, propanol and aqueous-methanol solutions together with air, argon, helium and hydrogen were used as working fluids. For the different gases with water flooding occurred in the range $0.24 > Fr_{Dsg} > 0.18$ (depending on the liquid flow rate) while the onset of entrainment at the corresponding liquid flow rate was observed at $0.06 < Fr_{Dsg} < 0.08$. The effect of the liquid properties on the onset of entrainment was tested with the different liquids and air. The liquid viscosity did not show a significant influence, while the surface tension had a stabilising effect, i.e. the onset of entrainment occurred at lower velocities for methanol and propanol.

2.9 Conclusions and aim of the present adiabatic counterflow investigation

The literature study has shown that flooding is strongly influenced by the tube end configuration. Consequently a wide variety of flow patterns are encountered during the transition from counterflow to a state of partial liquid delivery and cocurrent upflow, depending on the type of apparatus tested. A certain type of transition mechanism may therefore not be regarded as *correct* or *incorrect*. Each unique system may produce unique flow modes. Nevertheless researchers often attempted to detect and propagate the "correct" flooding mechanism, which does not appear to be objective.

Presently no detailed information exists on pressure drop characteristics and flooding in inclined rectangular ducts or flattened tubes with a sharp-edged gas inlet. The analysis of the steamside flow inside inclined reflux condensers requires such data on the entrance pressure drop at the bottom of the finned tubes, the frictional pressure drop experienced by the vapour flow in the presence of draining condensate and performance limitations due to flooding and/or entrainment. Because the duct geometry and inclination strongly effects the flow mode during counterflow, existing data for vertical tubes cannot be applied for the purpose of a dephlegmator analysis.

The aim of the present adiabatic experimental investigation is to generate the required data and to gain a better understanding of the fundamentals governing gas-liquid counterflow in inclined rectangular ducts. The emphasis is on high void fraction flow, i.e. low liquid flow rates commonly encountered in air-cooled condensers. According to existing literature on reflux condensation flooding is initiated at the bottom of the duct where the vapour and condensate velocities are the highest. Consequently the present adiabatic study focuses on the gas-liquid interaction at a sharp-edged gas inlet at the bottom of the test section. The liquid inlet unit at the top is constructed such that any gas-liquid interactions at the liquid feed are prevented or minimised, thereby eliminating any effects the liquid inlet configuration may have.

In an attempt to address the fundamental nature of gas-liquid counterflow four different rectangular ducts inclined at various angles are tested with three different liquids and four different gases. Attention is paid to the entire gas flow region from laminar flow up

to flooding. Although the existing dephlegmator layout was followed as a guide line to construct an apparatus for the experimental study, the test program covered a much wider range of the relevant parameters such as the duct dimensions and the fluid properties.

CHAPTER 3

EXPERIMENTAL EQUIPMENT AND DATA ACQUISITION

3.1 Introduction

Schematics of the duct profiles tested are shown in figure 3.1. Transparent acrylic plastic and glass was used for the construction of the test sections and plenums to enable flow visualisation. Conventional black and white photos were taken of the flow patterns during stable countercurrent flow and at the flooding point. Helium, hydrogen, argon, air, water, methanol and propanol were used as working fluids. The fluid properties at room temperature are given in table 3.1. The combinations of counterflow experiments performed are summarised in table 3.2.

The experimental system consists of a gas supply, a liquid supply, the test section and a data acquisition system. An aluminium and steel structure serves as a support for the plenums and the test section. A photo of the support and test section assembly is shown in figure 3.2 and a schematic illustration of the entire flow loop is given in figure 3.3.The total length of the support structure is 7 metres. It can be shortened to 5 m to fit into the laboratory when in its vertical position. The height of the laboratory roof is 7 m. The structure is supported at the bottom by a hinge and at the top by a suspending cable. The hinge is located 1 m above ground level. The entire assembly can be inclined at any angle from 0° to 60° to the horizontal when it is 7 m long. The shortened configuration can be inclined at any angle from horizontal to vertical.

3.2 Liquid supply

Liquid is supplied by a 200 *l* constant head reservoir. The maximum available head is 4 m. From the tank the liquid passes through a combination of three rotameters. Three ball valves are used to select the desired rotameter/rotameters. Their ranges are 0 - 0.13, 0 - 2.3 and 0 - 5 *l*/min respectively. The liquid enters the test section through porous plates made of sintered bronze. A copper-constantan thermocouple measures the liquid temperature at the porous inlet. Once inside the test section, the liquid drains downwards

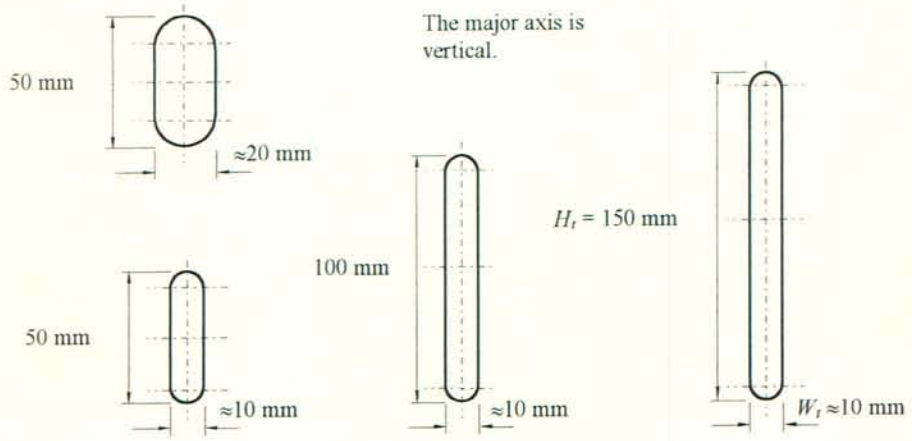

Figure 3.1: Cross-sectional view of the rectangular ducts.

Figure 3.2: Photo of the test section assembly in an inclined position.

Table 3.1: Fluid properties at ambient conditions (p = 101325 N/m^2 , T = 295 K).

Fluid	ρ, kg/m^3	μ x 10^6, kg/ms	σ x 10^3, N/m
Air	1.196	18.230	---
Argon	1.650	22.390	---
Helium	1.653 x 10^{-1}	20.040	---
Hydrogen	8.325 x 10^{-2}	8.863	---
Water	998	958	72
Methanol	791	575	22
Isopropanol	784	2362	22

Table 3.2: Summary of the flooding experiments.

Duct geometry	θ,° (to the horizontal)	Fluid combination
H_t = 50 mm $W_t \approx$ 10 mm	2, 10, 20, 40, 60, 70, 80, 90 2, 5, 10, 15, 20, 60, 80, 90 60, 90 60 60 60 60	Air-water Air-propanol Air-methanol Argon-water Helium-water Helium-methanol Hydrogen-methanol
H_t = 100 mm $W_t \approx$ 10 mm	2, 20, 40, 60, 70, 80, 90 2, 40, 60, 90 60, 90	Air-water Air-propanol Air-methanol
H_t = 150 mm $W_t \approx$ 10 mm	2, 20, 40, 60, 90 60, 90 60, 90	Air-water Air-propanol Air-methanol
H_t = 50 mm $W_t \approx$ 20 mm	2, 5, 10, 20, 40, 60, 70, 80, 90	Air-water

under the action of gravity into the gas inlet device, from where it flows to the circulation tank. It is then pumped back to the constant head reservoir. Another thermocouple measures the liquid temperature inside the circulation tank. The liquid temperature can decrease by a number of degrees due to evaporation inside the apparatus. For this reason the liquid properties are evaluated at the average of the temperature measured at the porous inlet and inside the circulation tank. A measuring-cylinder is mounted on top of the circulation tank to calibrate the rotameters, by determining the volume flow rate with the cylinder and a stop watch. The liquid inlet unit

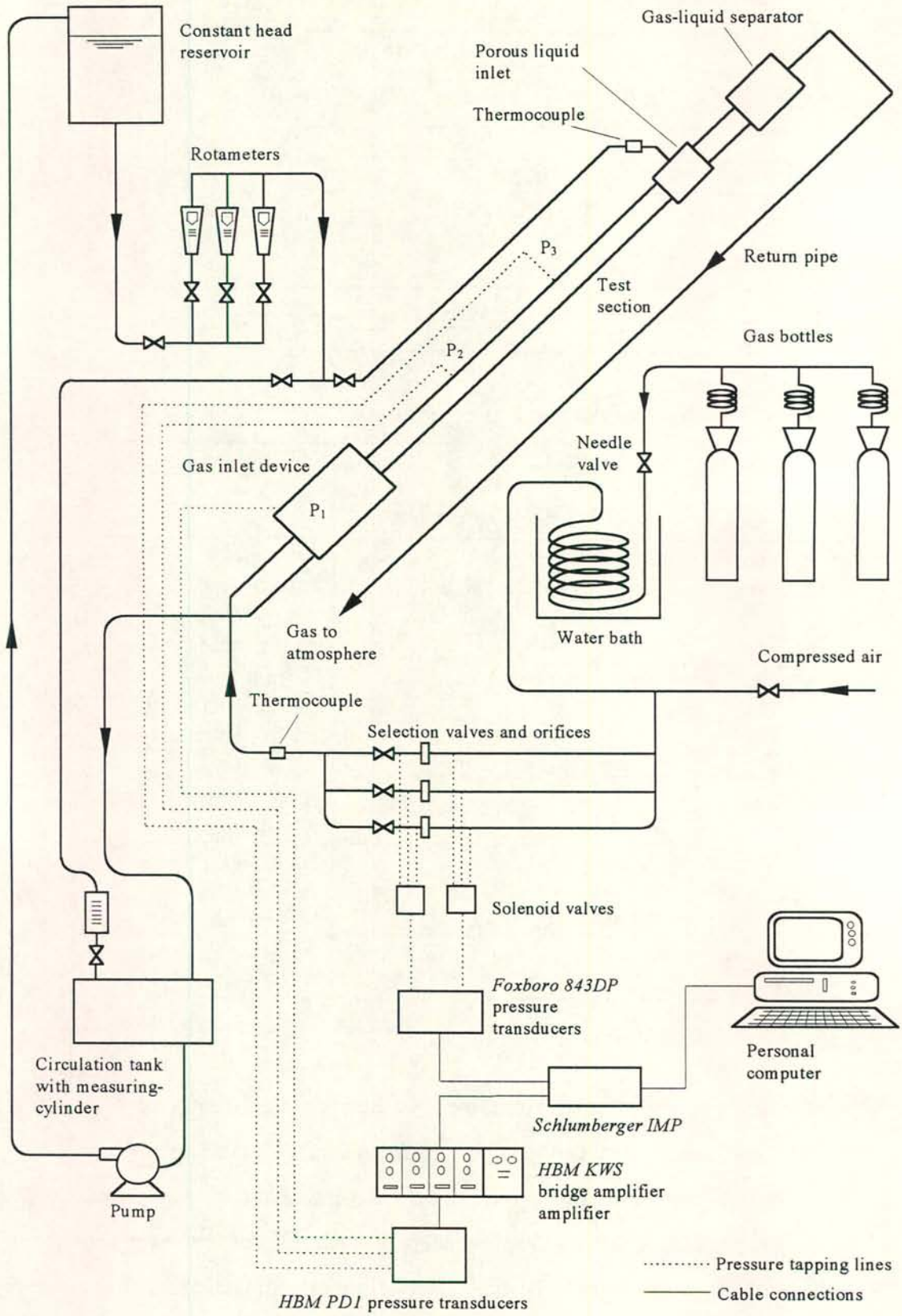

Figure 3.3: Schematic of the flow loop.

consists of a porous duct section, placed inside a glass cylinder. The unit is illustrated in figure 3.4. Liquid fills the chamber and passes through the porous plates into the test duct.

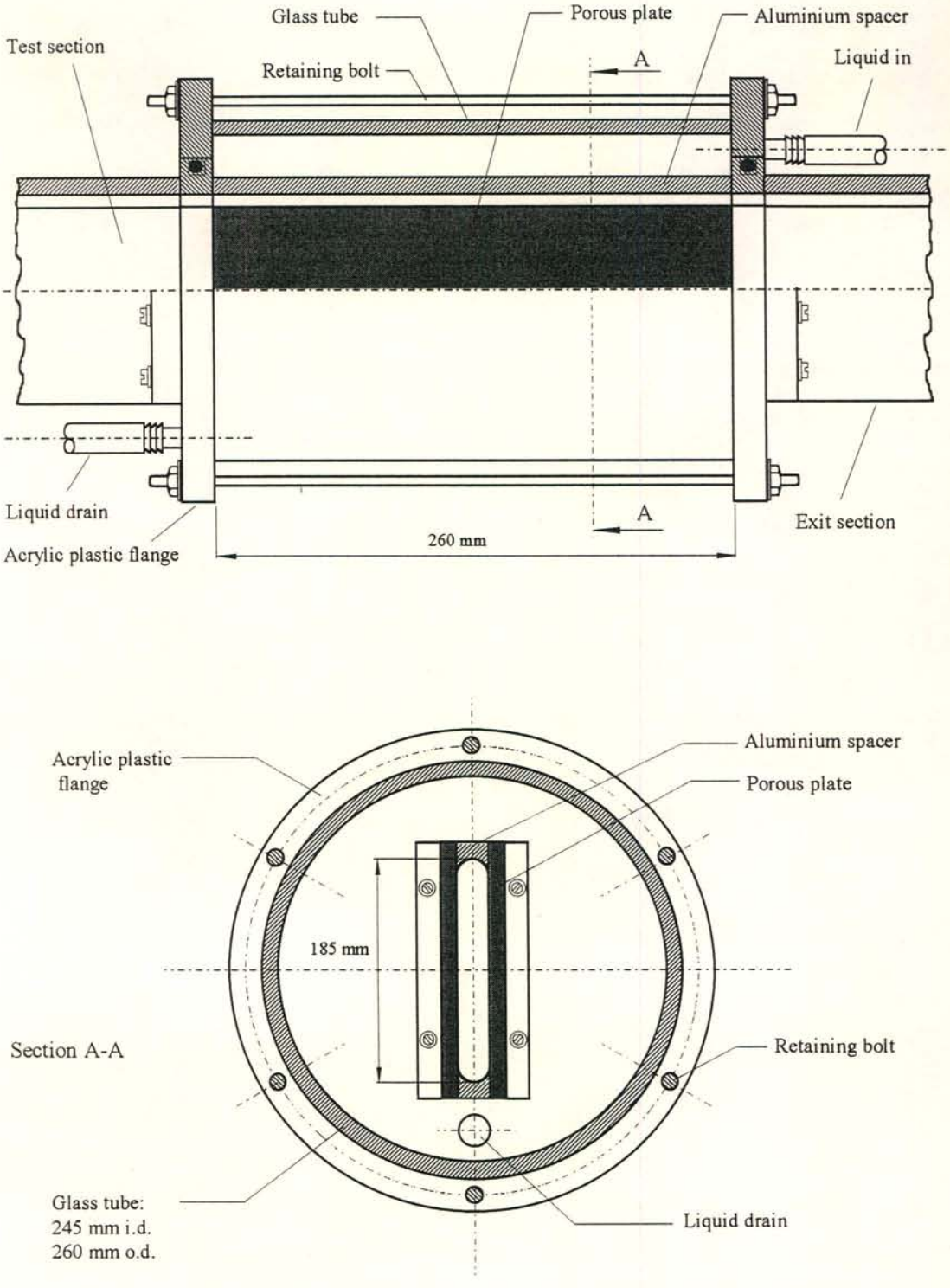

Figure 3.4: Schematic of the liquid inlet plenum.

3.3 Gas supply

Air is supplied by a 1.4 MN/m^2 reservoir. A pressure regulating valve controls the air flow rate. Argon, helium and hydrogen are supplied by 20 MN/m^2 pressurised bottles. Six bottles can be connected to a combining manifold at a time. The flow from the bottles is regulated manually by a needle valve. As the pressure inside the bottles decreases, the needle valve is gradually opened to maintain a constant flow rate through the test section. The gas temperature can drop well below zero during the expansion process at the valve. After the needle valve, the gas passes through a 3/4 inch coiled copper tube, which is submerged in a water bath to heat the gas to approximately ambient temperature. The pressure regulator (air supply) and the needle valve (hydrogen, helium and argon supply) are connected to a bank of three orifice plates. The orifice plates are designed according to the *British Standards* 1042 (sections 1.1 to 1.4) and are fitted with annular pressure tapping slots. Three ball valves are used to channel the gas flow through the desired orifice plate, by opening one and closing the remaining two valves of the orifice plates not to be used. The mass flow rate of the gas passing through an orifice plate is a function of the pressure drop across the plate (Δp_o) and the absolute pressure (p_o) and temperature at the upstream face of the orifice plate. The gas temperature is measured at an intermediate location, between the orifice bank and the gas inlet device. Both the test section and the upstream orifice gas thermophysical properties are evaluated at this temperature. Detailed drawings of the orifice plates are given in Appendix B. After having passed through an orifice plate, the gas enters the test section via the bottom plenum.

The bottom plenum or gas inlet device is shown in figure 3.5. The plenum serves two purposes: (i) It provides a uniform gas velocity profile at the duct inlet. A honeycomb sections straightens the gas flow once it has entered the gas inlet device and a fine mesh dampens out local high velocities, so that a uniform approach velocity is obtained at the sharp-edged inlet. (ii) It prevents the liquid from entering the gas feed pipe. The liquid is drained at the bottom of the plenum while the gas enters the plenum through a protruding pipe, which is shielded so that liquid cannot fall into the gas supply pipe. The gas is prevented from escaping through the liquid drain pipe into the circulation tank by a

valve in the drain line which is partially closed, so that liquid can accumulate at the bottom to act as a seal.

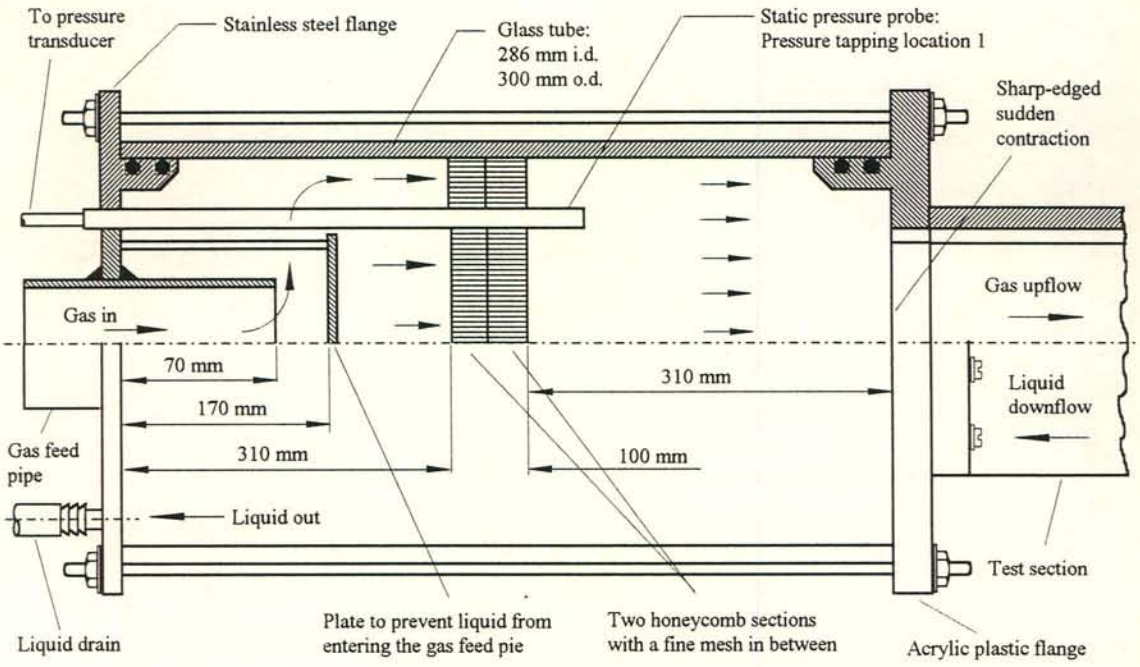

Figure 3.5: Schematic of the gas inlet plenum affixed to a rectangular test section.

3.4 Test section configurations

The experiments were conducted in two phases, the first comprising extensive tests at a duct inclination of 60° to the horizontal. The configuration constructed for this purpose, referred to as the long configuration, is shown in figure 3.6. After completion of the first phase the test section assembly was shortened to enable the performance of tests at inclinations above 60°. The shortened version is shown in figure 3.7 and will be referred to as the short configuration. It was employed to test the effect of the inclination angle on the pressure drop and flooding from inclinations close to the horizontal to vertical.

3.4.1 Long configuration

The long configuration consists of a 3.2 m test section of constant cross-sectional area followed by a 1 m long tapered duct which forms the transition from the test section

height (50, 100 or 150 mm) to the height of 185 mm inside the liquid inlet plenum. The width of the tapered duct is the same as that of the test section. It is straight at the bottom and tapered at the top, as illustrated in figure 3.6. The purpose of the tapered duct is to slow down the gas flow so that the gas velocity between the sintered plates is smaller than inside the test section, thus preventing the formation of liquid disturbances which could lead to flooding at the liquid inlet, while stable countercurrent flow prevails inside the test section. In the case of the 100 and 150 mm ducts this method proved to be insufficient and holes were drilled into the tapered section along the top, to allow part of the gas to escape before it reaches the liquid inlet plenum.

The test section is fitted with chambers to measure the pressure gradient inside the test section and the pressure change across the sudden contraction at the gas entrance. The pressure gradient and the pressure change across the entrance are measured over lengths of 1.6 and 0.81 m respectively. A cross-sectional view of a duct assembly is shown in figure 3.7 and figure 3.8 shows the assembly of the chambers at the pressure tapping holes. The two phases are separated inside the chambers so that the pressure lines connected to the transducers are filled with gas only. The complete dimensions of the ducts tested are given in table 3.3.

Table 3.3: Duct dimensions.

Duct	H_t m x 10^3	W_t m x 10^3	A_{tc} m^2 x 10^6	A_{ti} m^2/m x 10^3	D_e m x 10^3	L_{12} m x 10^3	L_{23} m x 10^3
1	150	9.824	1452.9	311.2	18.673	810	1600
2	100	9.738	953.4	211.1	18.064	810	1600
3	50	9.822	470.4	111.2	16.919	810	1600
4	50	20.000	914.1	122.8	29.767	810	1600

The cross-sectional areas of the ducts were determined very accurately by filling the duct with water while in a vertical position. A certain amount of water ($\approx$160 ml) was drained and the corresponding change in water level inside the duct recorded. The volume of the drained water was determined by weighing the water on a precision scale. The cross-sectional area was then calculated by dividing the volume by the change in water level.

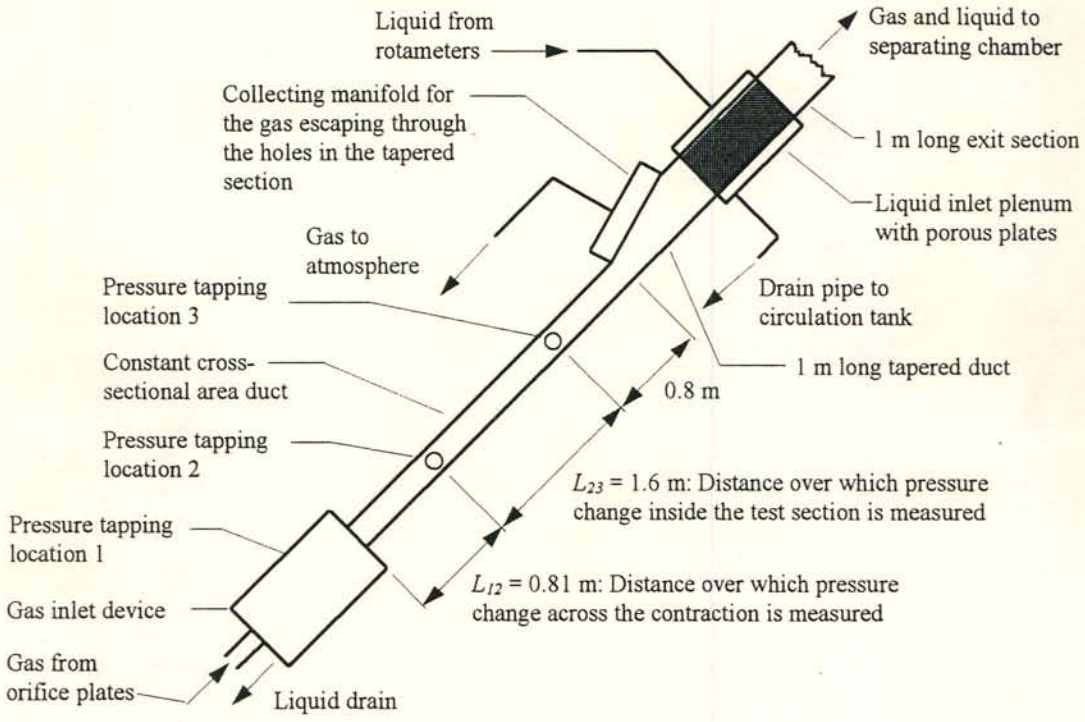

Figure 3.6: Schematic of the assembly for pressure gradient measurements and flooding during 60° inclined flow.

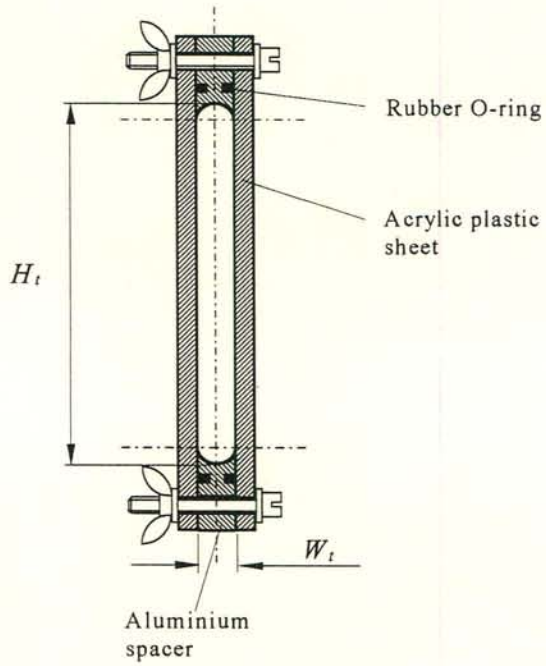

Figure 3.7: Cross-sectional view of the test section.

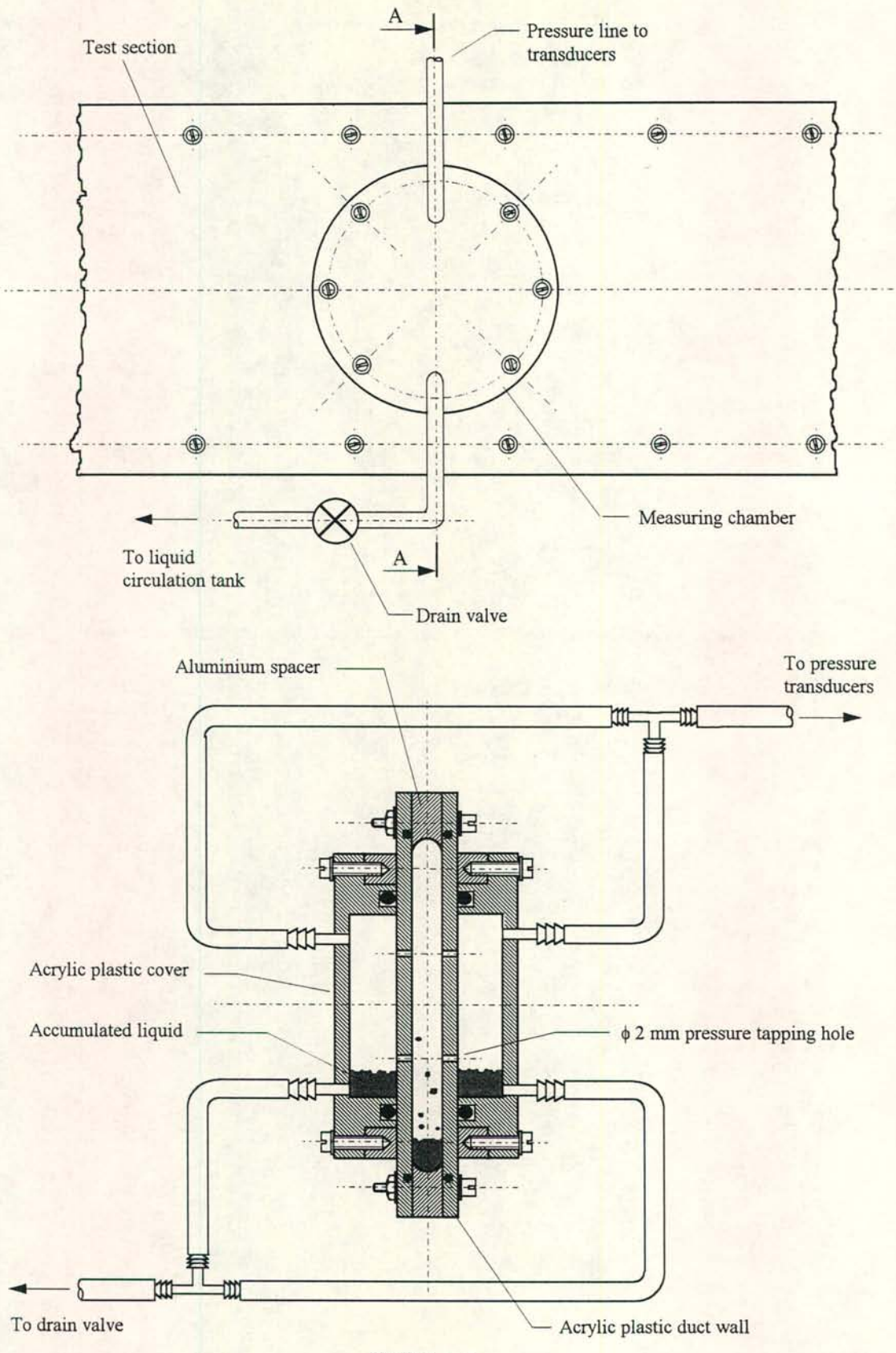

Figure 3.8: Schematic of the pressure measuring chambers fitted at P_1 and P_2 on the test section.

Once the gas has passed through the liquid inlet plenum, it flows through a 1 m long rectangular exit duct. The exit duct cross-section is the same as that of the porous section inside the liquid inlet plenum. The gas then enters a 201 mm i.d. and 200 mm long chamber where entrained liquid flowing up the exit section is separated from the gas and drained back to the circulation tank. The separating chamber is shown in figure 3.9. Finally the gas leaves the laboratory through a 50 mm i.d. P.V.C pipe which is connected to the outlet of the separating chamber and enters the atmosphere.

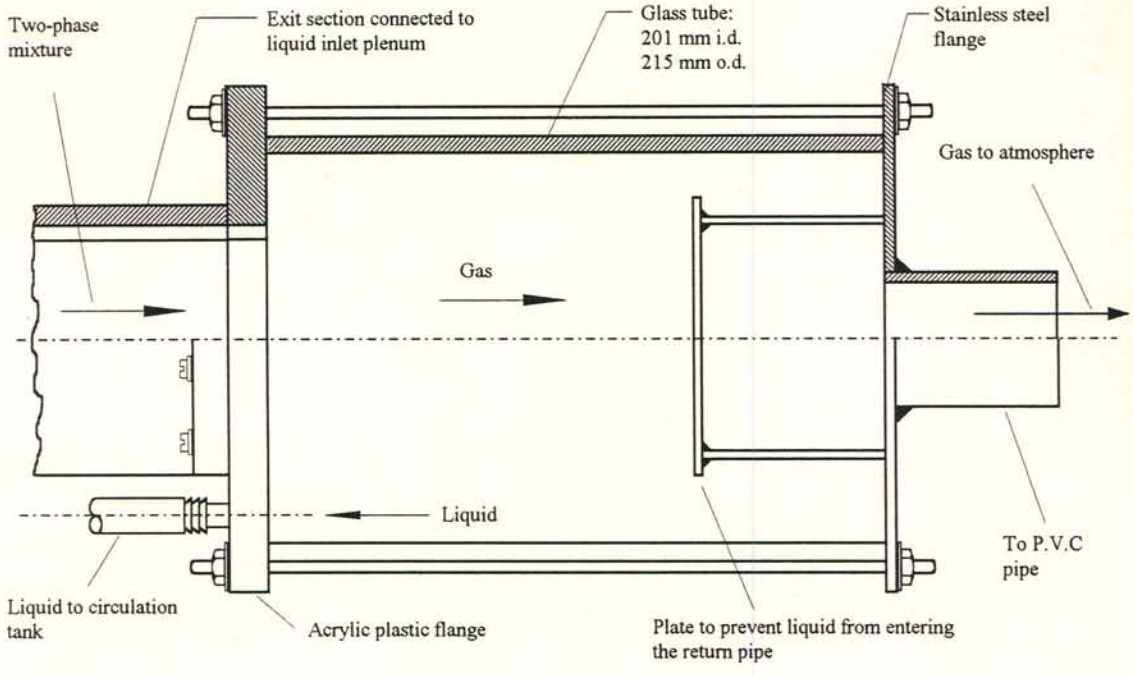

Figure 3.9: Gas-liquid separating chamber above the liquid inlet unit.

3.4.2 Short configuration

The short configuration used for experiments at duct inclinations from near horizontal to vertical is shown in figure 3.10. It is basically the same as the long configuration except that the tapered duct was removed and the 3.2 m constant cross-sectional test section was directly mounted onto the liquid inlet plenum. The inside height and width of the porous and the exit sections were the same as those of the test section. Holes were drilled into the acrylic plastic walls between the upper pressure measuring chamber and

the liquid inlet plenum along the top of the duct to allow part of the gas to escape before it reaches the porous plates in the case of inclined flow. The holes were covered by a manifold to channel the gas out of the laboratory. No gas bleed-off was employed during flooding experiments for vertical flow.

All the tests at 60° were carried out with the long configuration only, except for the air-water combination which was tested with both configurations. All the other angles were tested with the short configuration. Duct number 4 (Table 3.3) was constructed only in the short version.

When designing the long configuration for the first phase of experiments, emphasis was placed on accurate pressure gradient measurements and thus provision was made on either side of the pressure tapping points 2 and 3 for the flow to develop. In phase 2 the emphasis was on flooding and the test section assembly was shortened to enable inclinations above 60° to the horizontal. In the process the entrance length of 0.8 m for the liquid flow above point 3 (see figure 3.6) was effectively removed.

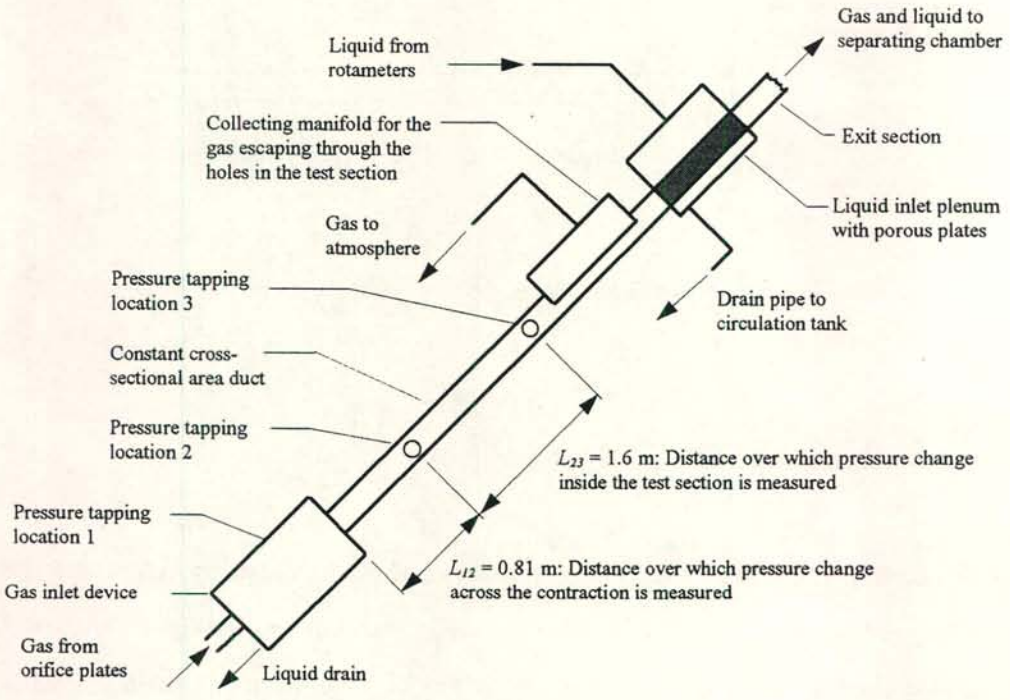

Figure 3.10: Schematic of the short test assembly used for flooding experiments at duct inclinations from near horizontal to vertical.

3.4.3 Entrainment measurements

The entrainment rate during air-water flow inside the 150 mm duct inclined at 60° to the horizontal was measured by making use if a cyclone separator. The separating chamber (shown in figure 3.9) was removed from the short configuration and replaced by the cyclone separator as shown in figure 3.11. The entrainment measurements did initially not form part of the investigation but were carried out at a later stage after intensive entrainment was observed at the sharp-edged gas inlet at high gas flow rates. The rate of entrainment was determined by measuring the rate at which water drained out of the cyclone separator with a measuring-flask and a stop watch.

Although part of the air was allowed to escape before reaching the porous plates, the amount of water carried out of the test section through the bleed-off holes was found to be insignificantly small. It was further found that at high gas flow rates the entrained droplets were carried over into the cyclone separator by their momentum through the region of lower gas flow inside the liquid inlet and the exit section. The entrainment measured provides a good indication of the gas velocity at which droplets start to reach the top end of the test section and the contribution by entrainment to upward liquid transport. The measured entrainment rates should however be regarded as being qualitative rather than quantitative because droplets could have been deposited behind the liquid inlet plenum before having reached the cyclone separator.

3.5 Instrumentation

3.5.1 Pressure measurements

a) Test section

Pressure lines were connected to the static probe inside the gas inlet device at P_1 and to the test section at P_2 and P_3 respectively, as shown in figure 3.3. Six inductive-type *Hottinger Baldwin Messtechnick PD1 (HBM PD1)* differential pressure transducers were arranged to measure the following pressure differentials during inclined flow:

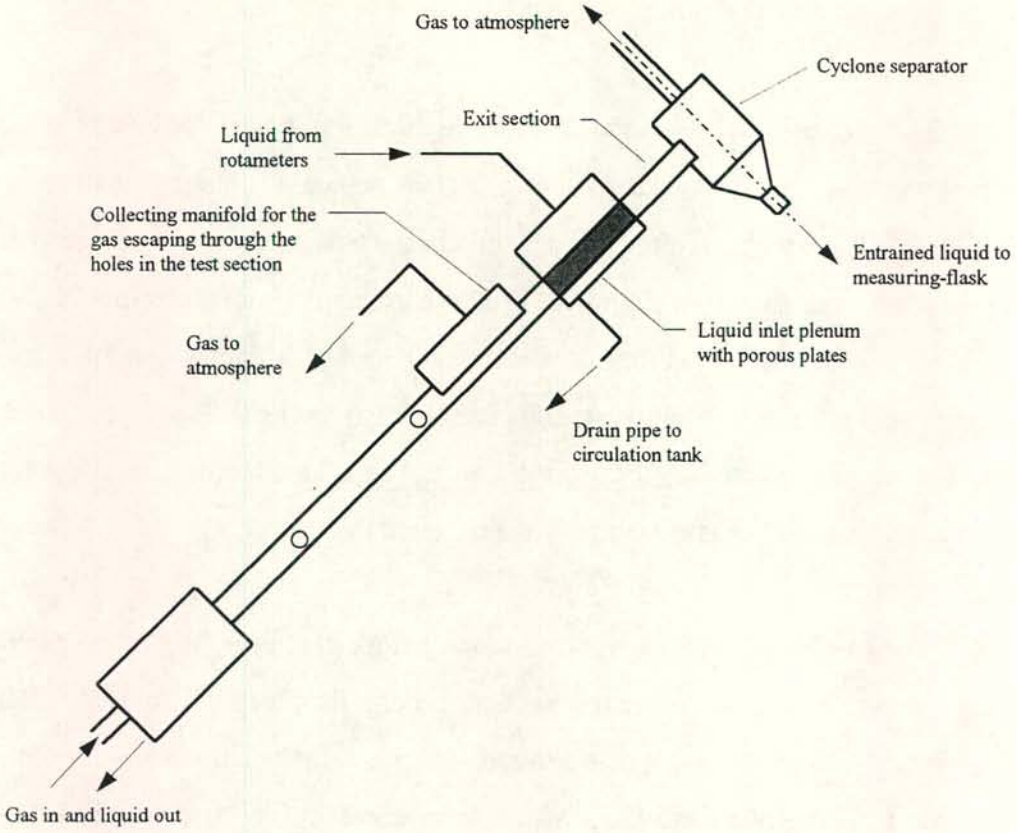

Figure 3.11: Schematic of the test assembly for entrainment measurements.

1) Δp_{12} inside the range 0 to 10 000 N/m^2.
2) Δp_{12} inside the range 0 to 1000 N/m^2.
3) Δp_{13} inside the range 0 to 10 000 N/m^2.
4) Δp_{23} inside the range 0 to 10 000 N/m^2.
5) Δp_{23} inside the range 0 to 1000 N/m^2.
6) $\Delta p_{2\text{-}amb}$: pressure at point 2 relative to the ambient pressure.

No pressure gradient and entrance pressure changes were measured for vertical flow. The bottom plenum pressure was, however, monitored during the flooding tests conducted for vertical flow.

A *KWS 3073 Hottinger Baldwin Messtechnick* bridge amplifier provides the energising voltages required by the transducers and amplifies the output to yield 0 to 10 V voltage signals. The transducers were calibrated to operate at full range, i.e. 0 to 10 V

corresponds to 0 to 10 000 N/m^2 in the case of the 10 000 N/m^2 transducers and to 0 to 1000 N/m^2 in the case of the 1000 N/m^2 transducers. The transducers are linear and therefore only two calibration readings were required. A *Betz* water manometer was used for the calibration. It has a 0 to 5000 N/m^2 range and scale increments of 2 N/m^2. The calibration signal provided by the bridge amplifier was not used because the *Betz* manometer method was considered to be more accurate.

b) Orifice bank

The gas flow rate was monitored by two *Foxboro 843DP* pressure transducers, one measuring the pressure change across an orifice plate and the other one measuring the orifice upstream pressure relative to the ambient pressure. The upstream and downstream pressure lines of the three orifice plates were connected to two manifolds via solenoid valves as shown figure 3.12. The pressure transducers were in turn connected to the manifolds. A set of two solenoid valves, one for an upstream and one for a downstream line, open the lines of the selected orifice to the manifolds when switched on.

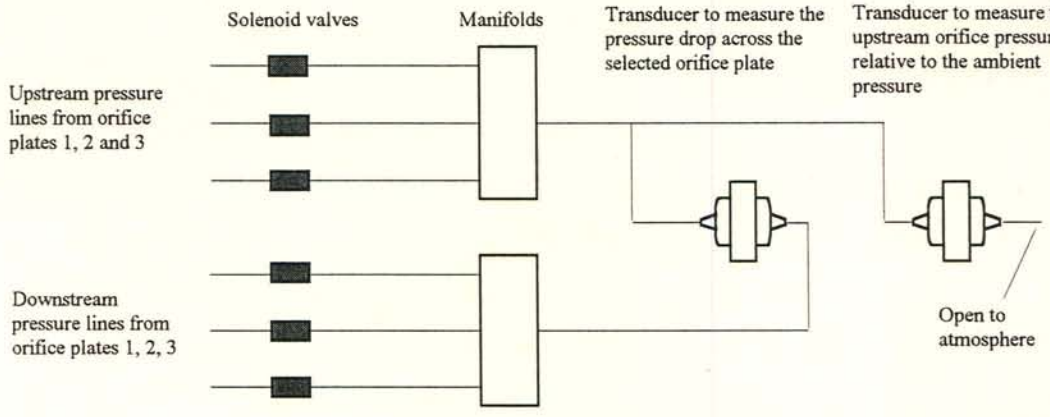

Figure 3.12: Pressure transducer arrangement to monitor the gas mass flow rate.

The Foxboro pressure transducers require a 24 V dc (direct current) supply and produce 4 to 20 mA dc output signal. Similarly to the *HBM* pressure transducers, two points were chosen for calibration. A 250 Ω resistor was built into the electronic circuitry of each *Foxboro* to produce a 1 to 5 V dc output signal across the resistor corresponding to

a 0 to 20 000 N/m^2 pressure differential. A few samples of the resistors were heated to establish possible temperature sensitivities. None were detected. A water manometer was used for calibration.

3.5.2 Data acquisition system

A *Schlumberger 3595C Isolated Measurement Pod (IMP)* controlled by an *IBM* compatible *Personal Computer (PC)* via a two-wire serial transmission network (*S-Net*) performed the data acquisition. The *IMP* measures thermocouple signals as well as voltage signals up to 12 V dc and returns readings to the *PC* interface every second. The output of the thermocouples, the *HBM* bridge amplifier and the *Foxboro* transducers was read by the *IMP*. The *IMP* contains 20 channels and facilitates simultaneous scanning of instrumentation. The analogue readings are digitised and then communicated to the controlling computer via the *S-Net*. A software program for communicating with the *IMP* and subsequent data processing was written in *Turbo Pascal* programming language. A flow diagram of the program is shown figure 3.13. The program performs four functions:

a) Scanning and calibration

When running this routine, the *IMP* scans the channels continuously and displays the measured temperatures and voltages on the monitor. The corresponding pressure differentials are displayed next to the voltage readings. While scanning the channels calibration can be performed by i) balancing the bridge circuitry of the transducers when the transducers are equalised and ii) adjusting the voltage input to the *IMP* with the range adjustment when the calibration pressure differential, monitored by the *Betz* manometer, is applied.

b) Input routine

The following information and data can be entered via the input routine:

1) The liquid volume and the corresponding time obtained with measuring cylinder and a stop watch, to determine the liquid flow rate.

2) The orifice plate selected to measure the gas flow rate.

3) The ambient pressure and the ambient temperature. The ambient pressure is measured with a *Thiers* mercury manometer which has a vernier scale with increments of 10 N/m^2. The instrument was calibrated by the manufacturer at 0 °C and the readings taken at room temperature while conducting the experiments were therefore corrected as prescribed by the user's manual.

4) The type of liquid and gas to be used during a test run.

c) Flow monitor routine

This routine calculates the superficial gas velocity and displays it on the monitor. When running this routine, the desired gas flow rate is set by adjusting the pressure regulating valve (air) or the needle valve (other gases). The routine enables real-time data sampling and processing and flow parameters like the superficial gas Reynolds number, the gas and liquid Froude numbers, the pressure gradient inside the test section and the pressure change across the sudden contraction are continuously displayed on the monitor. It also displays information like the type of fluids used and the orifice plate selected. A program unit containing the equations for the fluid properties (shown in Appendix C) uses the temperatures measured with the thermocouples to evaluate the fluid properties inside the test section and the gas properties at the upstream face of the orifice. The gas properties together with the measured pressure differentials at the orifice plate form the input to a subroutine for the calculation the gas mass flow rate, which is required for the evaluation of the above-mentioned parameters. A sample calculation for this subroutine is given in Appendix B.

d) Store averaged data on disk

Once the desired flow conditions are reached and the flow is steady, the values returned by the *IMP* can be averaged over a period specified by the user. Averaging occurs continuously by adding the measured values and dividing the sum by the number of scans at that time. The averaged data are stored in the form of a comma-delimited *ASCII* file

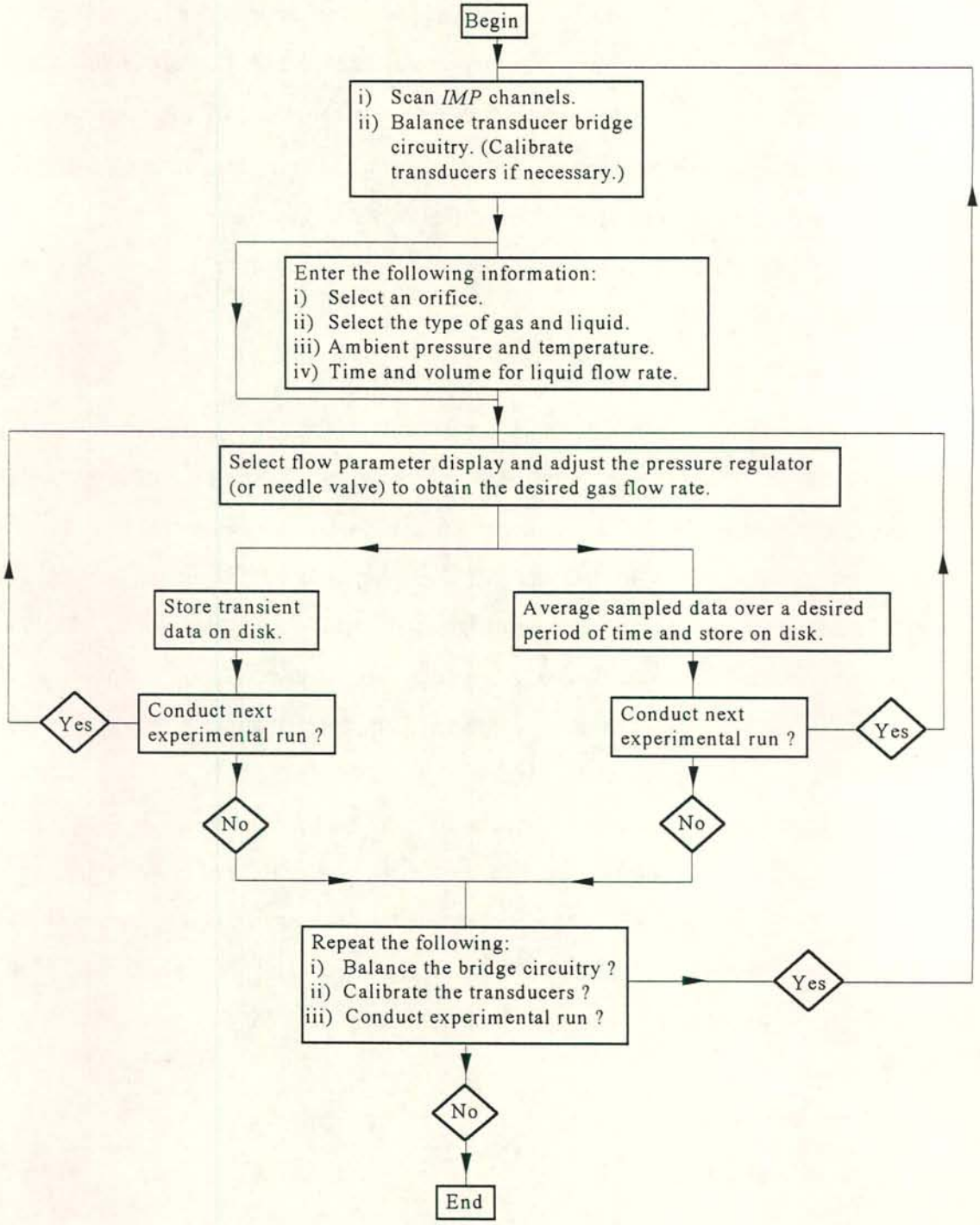

Figure 3.13: Flow diagram of the data acquisition program.

on the hard disk of the *PC* under a user defined filename. The file can be retrieved for further processing.

e) Store transient data on disk

The data returned by the *IMP* after each scan are stored continuously on the hard disk while maintaining the desired flow conditions. The sampling rate is approximately 1 s for a complete scan of all the channels connected.

3.6 A typical experimental run

Measure the ambient pressure and temperature and enter the readings into the data acquisition program.

Select routine (a) and balance the pressure transducer circuitry. The pressure transducers were calibrated for the first tests conducted and thereafter calibration was repeated every six months. The bridge circuitry was however always balanced before each experimental run because transducer drift can cause small bridge imbalances. The imbalance is negligible when working close to the full scale of the transducers but can induce significant errors when measuring pressures which are ≈10% of the full scale or less. When balancing the circuitry the gas and liquid flow was shut off and the pressure lines were equalised.

Set the liquid flow rate and measure the time it takes to fill the flask with a stop watch. Enter the volume and the time into the data acquisition program. Switch on the appropriate solenoid valves and open the ball valve of the orifice plate to be used. Adjust the pressure regulating valve to obtain the desired gas flow rate and store the data once the flow is steady. Begin at a low gas flow rate and increase the gas flow once the data has been stored. Repeat until the duct floods. Repeat the test with a different liquid flow rate. The lowest gas flow rates tested were typically close to $Re_{sg} = 500$. The gas flow rate was increased by increments in the range $500 < Re_{sg} < 2000$. Close to flooding the gas flow was increased by very small increments to enable accurate detection of the flooding gas velocity.

3.7 Accuracy of the system

The accuracy of the system was assessed by conducting a series of single-phase experiments with air. The measured pressure drop inside the ducts is presented in figure 3.14 in terms of the Darcy friction factor f against the Reynolds number Re together with the laminar and turbulent predictions for smooth parallel plates [91WH1]. Very good agreement was obtained for laminar and turbulent flow. Repeatable results within 1% of the predicted values were achieved. Small deviations were observed for the 50 mm duct in the laminar region. It must however be kept in mind that the laminar relation for parallel plates will tend to over-predict the measured data as the aspect ratio decreases. Another reason for the deviation may the very low gas flow rates present during laminar flow in the 50 mm duct (W_t = 10 mm) at which the orifice plates are used outside their prescribed range.

The good agreement with the predictions according to equation (4.4) and (4.5) indicates that the flow is developed between points 2 and 3 in the test section where the pressure gradient is measured.

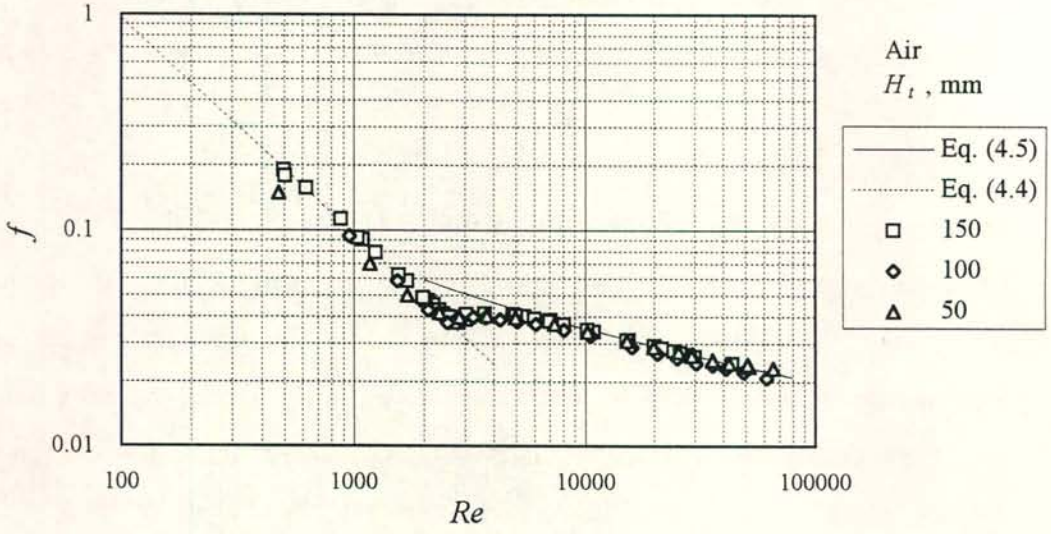

Figure 3.14: Single-phase friction factor for air. Broken line and solid line: Laminar and turbulent prediction for parallel plates. The width of the 50 mm duct is 10 mm.

CHAPTER 4

EXPERIMENTAL RESULTS: FLOW PATTERNS AND PRESSURE DROP

4.1 Presentation of data

The bulk of the pressure drop data is given in Appendix D and E for the long and the short test section configuration respectively. Only selected data are presented in this chapter for the purpose of describing the flow patterns and the corresponding pressure drop characteristics encountered. Following below in sections 4.1.1 and 4.1.2 are brief descriptions of the type of plots and dimensionless groups used for the presentation of the pressure drop data.

4.1.1 Frictional pressure gradient

For steady-state incompressible single-phase flow in a duct of constant cross-sectional area the resultant pressure drop consists of a frictional and a gravitational component. The frictional component is caused by shear forces exerted by the duct wall on the moving gas and can be regarded as an irreversible loss of mechanical energy. Similarly gas flowing in the presence of a liquid film experiences an irreversible loss. This irreversible loss consists of friction at the dry part of the duct walls and at the gas-liquid interface as well as form drag, where separation in the gas boundary layer occurs due to the wavy interface. An added drag effect is caused by droplets adhering to the duct walls and droplets carried in the gas core. In this chapter the term "frictional" refers to the total loss, i.e. losses due shear and drag.

The frictional pressure gradient typically experienced during counterflow in inclined ducts is shown figure 4.1(a) for air-water flow inside the 50 mm duct (W_t = 10 mm) inclined at 60° to the horizontal. The data are presented in terms of the Darcy friction factor, based on the superficial gas velocity, i.e.

$$f_{sg} = \left(\Delta p_{f23} / L_{23}\right) D_e \Big/ \left(1/2\, \rho_g v_{sg}^2\right) \tag{4.1}$$

where D_e is the hydraulic diameter

$$D_e = \frac{4 \, x \, cross - sectional \; flow \; area}{duct \; perimeter} \tag{4.2}$$

f_{sg} is plotted against the superficial gas Reynolds number

$$Re_{sg} = \rho_g v_{sg} D_e / \mu_g \tag{4.3}$$

The broken line in figure 4.1(a) represents the laminar friction factor for single-phase flow between parallel plates

$$f = 96/Re \tag{4.4}$$

The turbulent friction factor is represented by the solid line, i.e.

$$(1/f)^{1/2} = 2.0 \, log_{10}\left\{Re(f)^{1/2}\right\} - 1.19 \tag{4.5}$$

Equation (4.5) is valid for single-phase turbulent flow between parallel plates [91WH1].

In figure 4.1(b) the same data are plotted against the densimetric superficial gas Froude number

$$Fr_{Hsg} = \frac{\rho_g v_{sg}^2}{\left[g \, H_t (\rho_l - \rho_g)\right]} \tag{4.6}$$

At low to moderate gas flow rates the two-phase friction factor is equal to the corresponding single-phase friction factor. At a certain gas Froude number gas-liquid interaction causes the two-phase pressure gradient to rise above the single-phase pressure gradient and at flooding a sharp increase in pressure drop is experienced. The role of the gas Reynolds and Froude numbers are addressed in detail when the effect of the duct dimensions and the gas properties are discussed in sections 4.3.1 and 4.3.2.

The Reynolds number related frictional component can be removed from the two-phase pressure drop by subtraction of the single-phase gas-only pressure drop. The difference represents the added resistance due to the gas-liquid interaction experienced by the gas

flow. Dividing the added resistance by the gas-only frictional pressure gradient yields a dimensionless pressure gradient ratio denoted by (ϕ - 1), i.e.

$$(\phi - 1) = \frac{(dp/dz)_{ftp} - (dp/dz)_{fgo}}{(dp/dz)_{fgo}} \tag{4.7}$$

Figure 4.1(c) shows the data of figure 4.1(a) in terms of the pressure gradient ratio. At low Froude numbers where the two-phase frictional pressure drop is close to the corresponding single-phase pressure drop the pressure gradient ratio is approximately zero. It starts to rise as gas-liquid interactions develop on the interface.

4.1.2 Entrance pressure drop

In the case of single-phase incompressible flow, the change in static pressure across a sudden contraction in flow area is usually expressed in terms of a contraction loss coefficient K_{csp} where

$$\Delta p_c = p_1 - p_2 = \frac{1}{2}\rho v_2^2 \left[1 - \sigma_{21}^2 + K_{csp}\right] \tag{4.8}$$

σ_{21} is the area ratio A_2/A_1, A_2 being the smaller area. A similar expression can be derived for a gas entering the bottom of a duct in the presence of liquid draining into the plenum, i.e.

$$\Delta p_c = \frac{1}{2}\rho_g v_{sg2}^2 \left[\frac{1}{\alpha_2^2} - \sigma_{21}^2 + K_{ctp}\right] \tag{4.9}$$

where the void fraction inside the plenum α_1 is assumed to be unity and the two-phase contraction coefficient K_{ctp} is referred to the superficial gas velocity at section 2. α_2 can also be close to 1 in the case of high void fraction flow where the liquid phase drains continuously into the bottom header, but will deviate significantly from 1 if liquid accumulates inside the duct just above the sharp-edged gas inlet. The pressure drop across a sudden contraction in flow area during countercurrent gas-liquid flow can be expressed in terms of a two-phase loss coefficient K_{tp} defined by

$$\Delta p_c = \frac{1}{2}\rho_g v_{sg2}^2 \left[K_{tp} - \sigma_{21}^2\right] \tag{4.10}$$

where the sum of $1/\alpha_2^2$ and K_{ctp} in equation (4.9) has been replaced by K_{tp}. It suffices to correlate such data in a combined form of $1/\alpha_2^2$ and K_{ctp} because their actual separate values are difficult to measure and at the same time are not required for the prediction of Δp_c. Equation (4.10) can be rearranged to obtain an expression for K_{tp}, i.e.

$$K_{tp} = \left(\Delta p_{12} - L_{12}\left(dp/dz\right)_{f23}\right) \Big/ \left(1/2\,\rho_g v_{sg}^2\right) + \sigma_{21}^2 \tag{4.11}$$

Here the pressure drop inside the duct between the sharp-edged contraction and point 2 is subtracted from the change in static pressure Δp_{12} measured across points 1 and 2 to obtain the static pressure drop Δp_c across the sudden contraction. The contraction two-phase loss coefficient corresponding to the pressure gradient data of figure 4.1(a) is shown in figure 4.1(d).

4.2 Flow patterns observed at a duct inclination of 60° to the horizontal

4.2.1 Air-propanol flow inside the 50 mm duct (W_t = 10 mm)

Pressure drop data and the corresponding flow patterns are shown figures in 4.2 and 4.3 respectively. The solid symbols in figure 4.2 represent the air flow rates at which photos of the flow were taken. The top part of the gas inlet plenum and the bottom part of the test section can be seen in the photos. At the lowest gas flow rate (Re_{sg} = 614) no gas-liquid interaction can be observed and the propanol drains in the from of an undisturbed jet into the bottom plenum, as shown in figure 4.3(a). Inside the test section the propanol flows in the groove cut into the aluminium spacer and cannot be seen. The second photo, shown in figure 4.3(b), was taken at Re_{sg} = 7034. There is still no significant gas-liquid interaction. The jet inside the plenum experiences an upward deflection caused by the drag of the gas flow. Droplet entrainment occurs at the sharp-edged gas inlet. The drops are deposited on the duct walls just above the sharp-edged inlet. The gas-liquid interface is fairly smooth but small waves are present. Figure 4.3(c) illustrates the flow at Re_{sg} = 8969. The propanol jet is dispersed inside the gas inlet plenum. The duct walls just above the gas entrance are entirely wetted. The wetting film creeps slowly upwards.

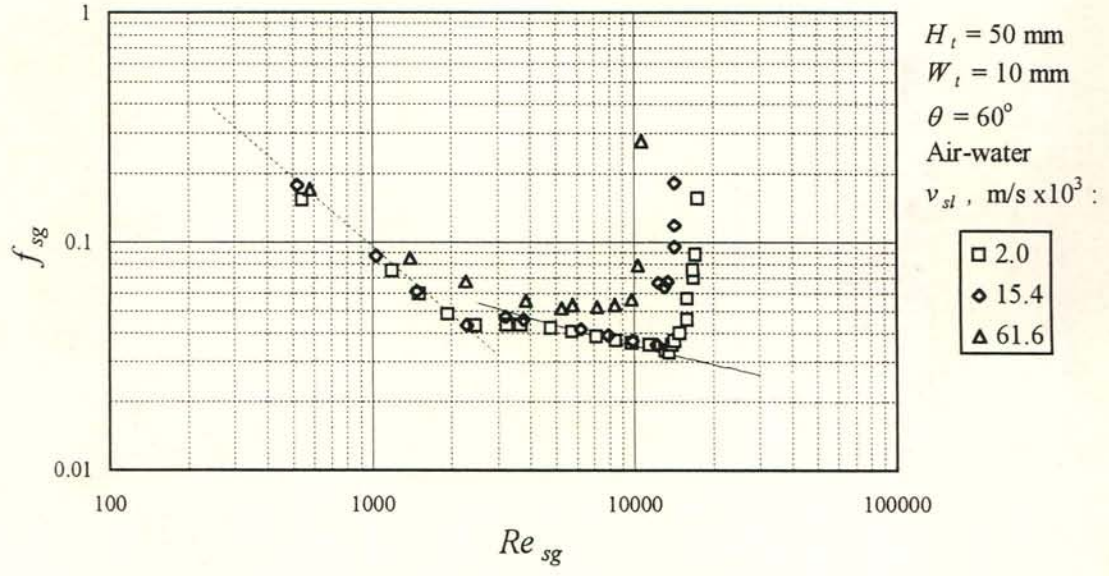

Figure 4.1(a): Two-phase friction factor for air-water flow plotted in terms of the superficial gas Reynolds number. Broken and solid line: Single-phase laminar and turbulent flow. Data: Long test section.

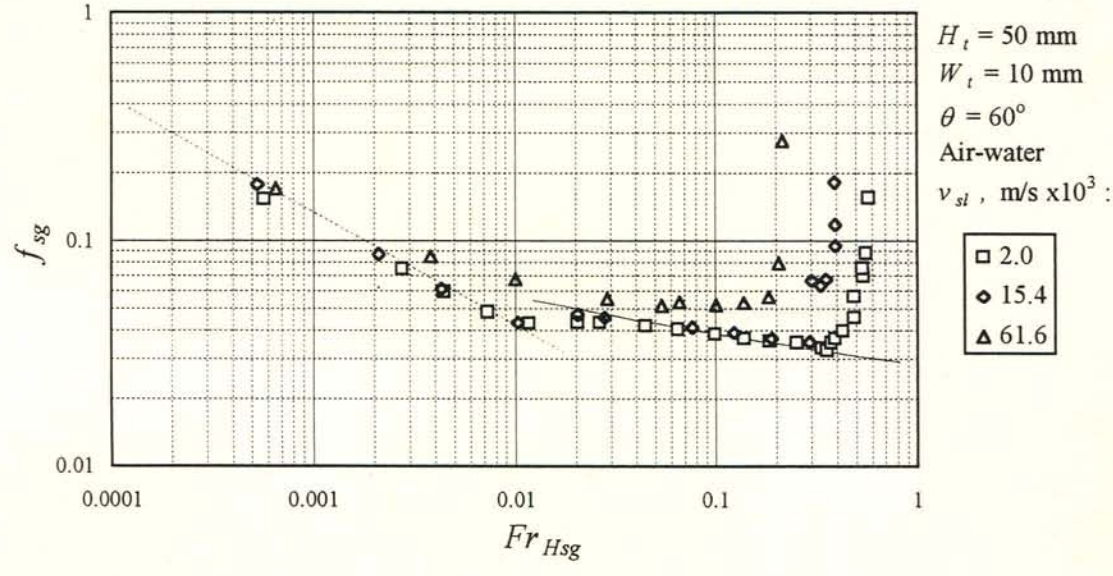

Figure 4.1(b): Two-phase friction factor for air-water flow plotted in terms of the densimetric superficial gas Froude number. Broken and solid line: Single-phase laminar and turbulent flow. Data: Long test section.

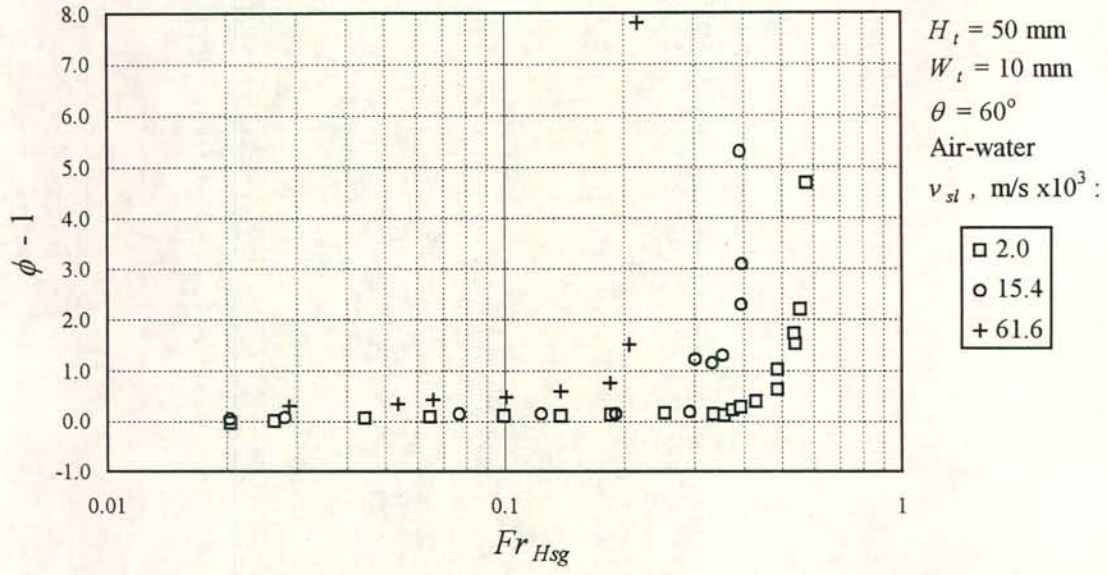

Figure 4.1(c): Pressure gradient ratio for air-water flow plotted in terms of the densimetric superficial gas Froude number. The gas flow is fully turbulent. Data: Long test section.

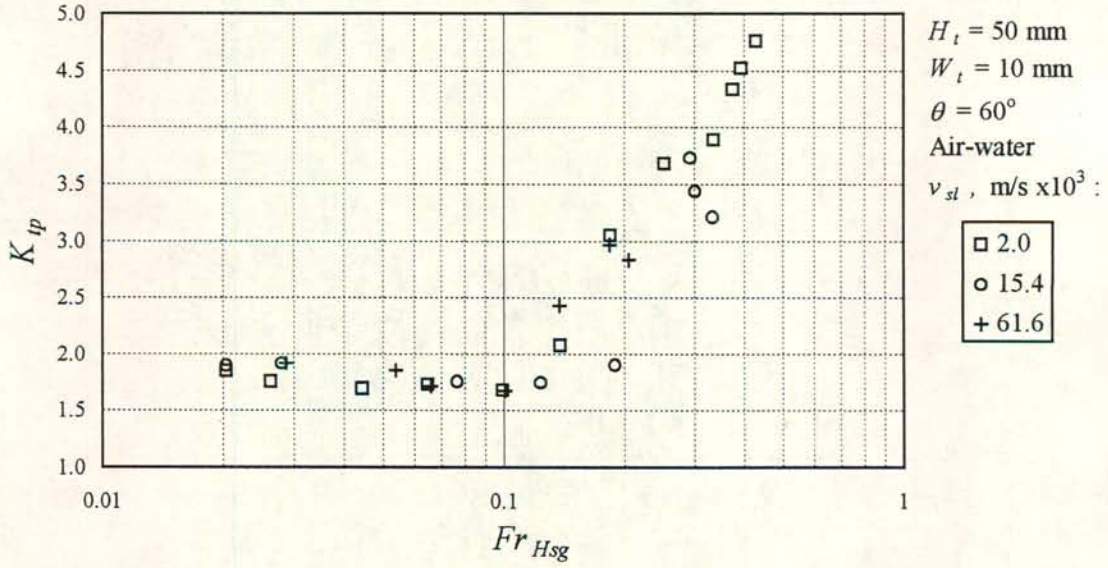

Figure 4.1(d): Two-phase entrance loss coefficient for air-water flow plotted in terms of the superficial densimetric gas Froude number. Data: Long test section.

Higher up the duct drops adhere to the walls.

In figure 4.3(d) the superficial gas Reynolds number is 10232. Entrainment and wetting are more intensive at the gas entrance. According to figure 4.2(a) the pressure gradient inside the duct is still equal to the air-only single-phase values. The dimensionless pressure drop across the entrance, shown in figure 4.2(b), has however started to rise due to the added resistance of the gas-liquid interaction just above the sharp-edged inlet. Upon a further increase in the air flow rate the liquid is sporadically sucked into the test section resulting in the formation of a rough liquid film, illustrated in figures 4.3(e) to (g). These photos were taken at Re_{sg} = 11218, 11482 and 11623 respectively.

The liquid flow is now becoming transient and oscillatory just above the gas entrance. Spurts of liquid enter the bottom plenum occasionally. A characteristic rotating flow pattern develops at the gas entrance. The rotating liquid flow or vortex-type flow is a result of simultaneous liquid up- and downflow: Liquid drains downwards at the bottom of the duct and is swept upwards by the gas when it reaches the gas entrance. Initially the rotational motion is confined to a small region above the gas entrance. Close to flooding the "diameter" of the vortex approaches the duct height and translates upwards. The formation of this characteristic vortex can be seen in figure 4.3 (h) where flooding is about to occur (Re_{sg} = 12029). Just below flooding the rotating gas-liquid mixture disintegrates after it has travelled approximately 1 m up the duct. At flooding, such a vortex formed at the bottom of the test section, reaches the tapered duct at the top. Then the pressure gradient inside the test section rises sharply but decreases immediately once the vortex collapses inside the tapered duct. Note the rise in pressure drop across the sharp-edged gas inlet in figure 4.2 (b) as a result of the vortex formation.

Small waves are present on the gas-liquid interface at zero gas flow rate. The waves grow as the gas flow rate is increased. The waves also grow while they are travelling downwards at constant fluid flow rates. At higher gas flow rates droplets are torn off the wave crests. Despite the presence of wave action and entrainment the two-phase frictional pressure gradient is equal to the single-phase pressure gradient inside the range $0 < Re_{sg} < 10000$ because the gas-liquid interface is very small relative to the dry part of the duct.

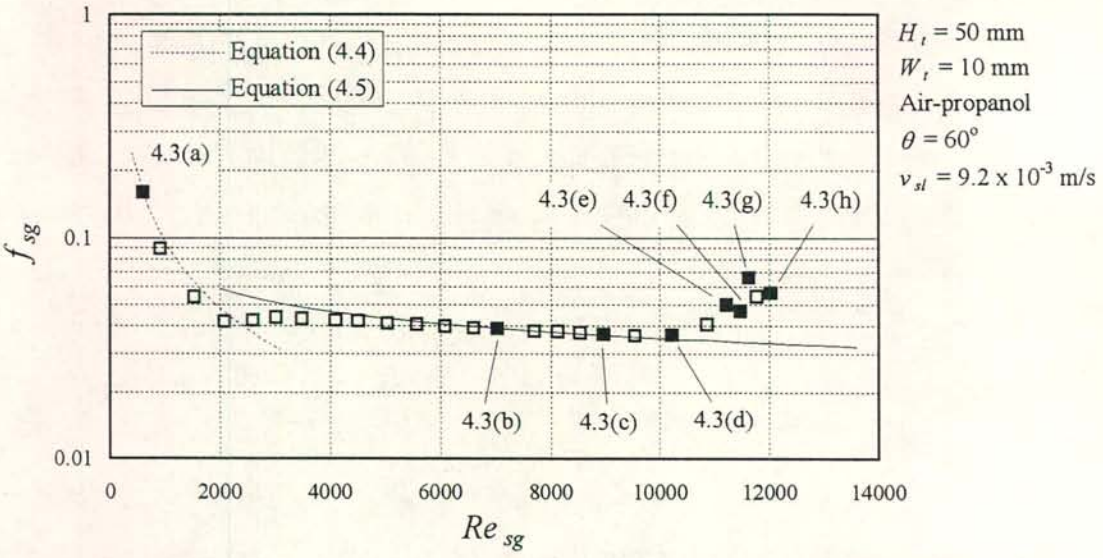

Figure 4.2(a): Two-phase friction factor for air-propanol flow. The solid symbols represent the gas flow rates at which photos, shown in figure 4.3, were taken.

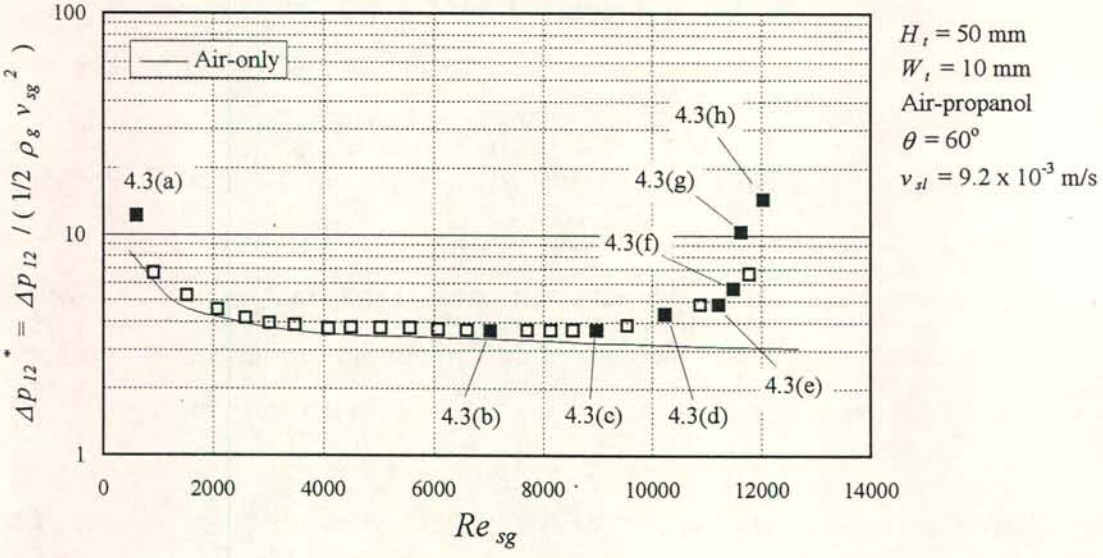

Figure 4.2(b): Dimensionless pressure drop measured across the sharp-edged gas entrance measured between points 1 and 2 for air-propanol flow. The solid symbols represent the gas flow rates at which photos, shown in figure 4.3, were taken.

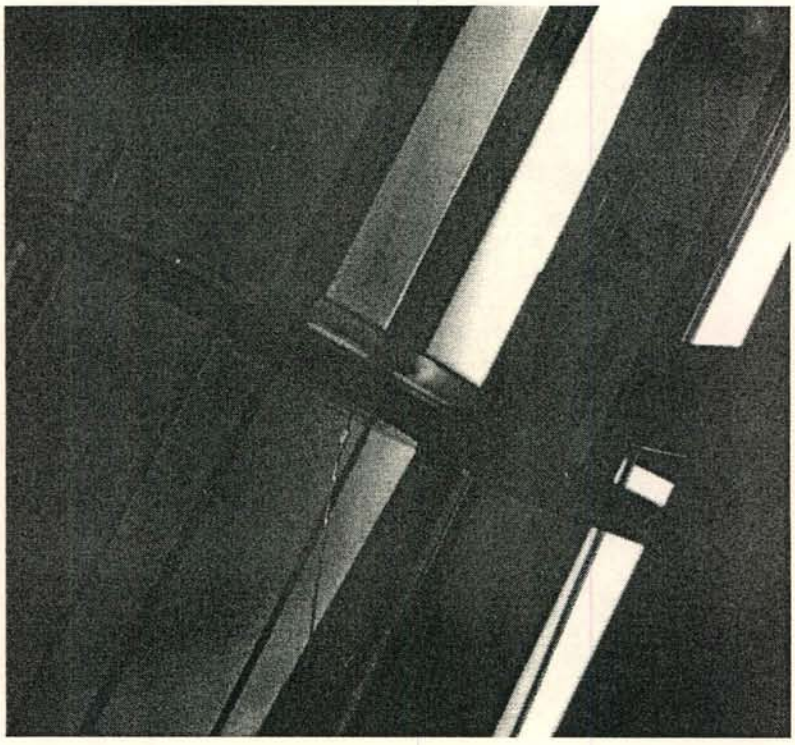

Figure 4.3(a): Air-propanol flow pattern inside the 50 mm (W_t = 10 mm) duct inclined at 60° to the horizontal. v_{sg} = 0.5 m/s, v_{sl} = 9.2 x 10^{-3} m/s, Re_{sg} = 614, Fr_{Hsg} = 0.001.

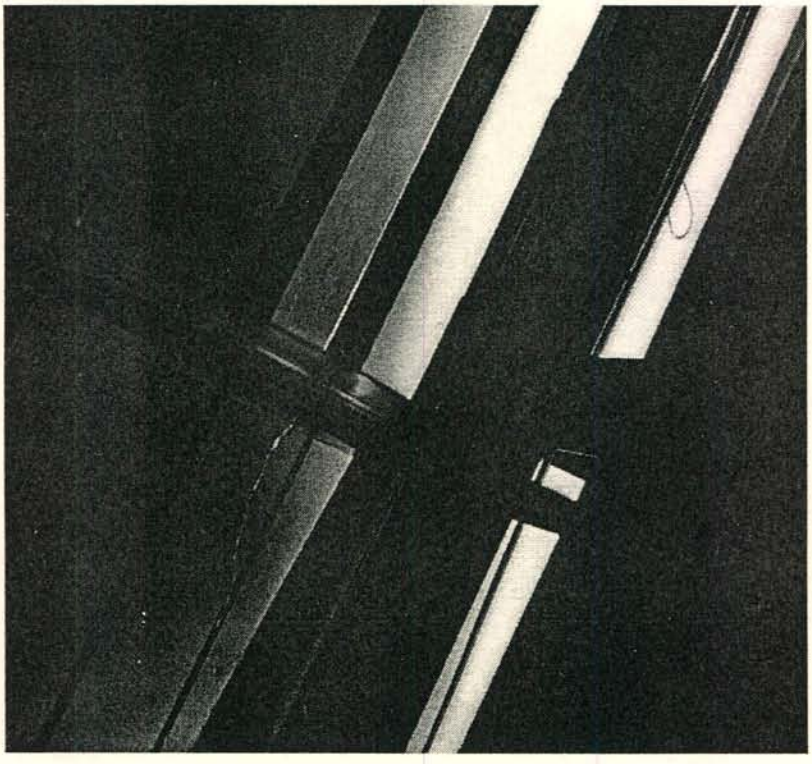

Figure 4.3(b): Air-propanol flow pattern inside the 50 mm duct (W_t = 10 mm) inclined at 60° to the horizontal. v_{sg} = 6.2 m/s, v_{sl} = 9.2 x 10^{-3} m/s, Re_{sg} = 7034, Fr_{Hsg} = 0.120.

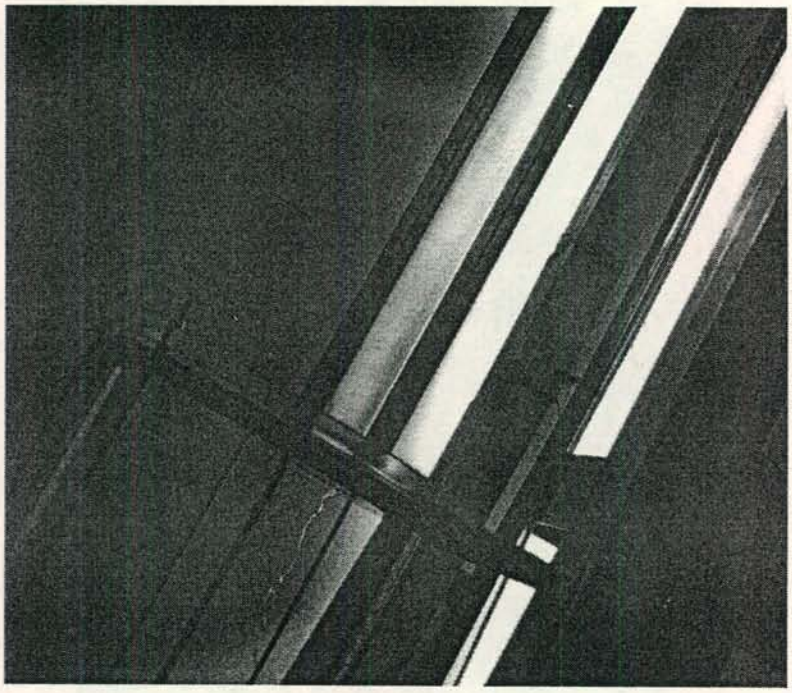

Figure 4.3(c) Air-propanol flow pattern inside the 50 mm (W_t = 10 mm) duct inclined at 60° to the horizontal. v_{sg} = 7.9 m/s, v_{sl} = 9.2 x 10^{-3} m/s, Re_{sg} = 8969, Fr_{Hsg} = 0.196.

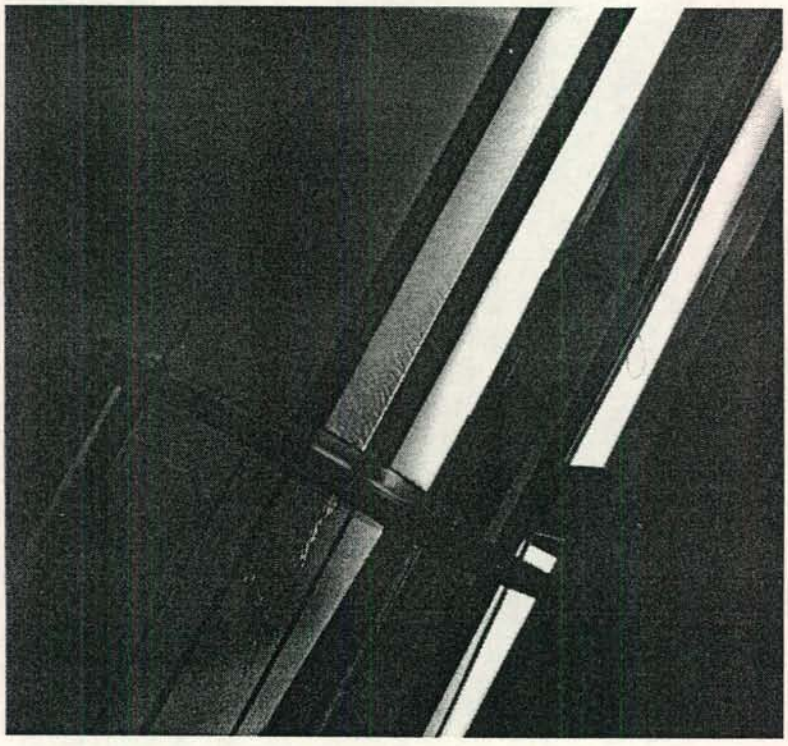

Figure 4.3(d): Air-propanol flow pattern inside the 50 mm (W_t = 10 mm) duct inclined at 60° to the horizontal. v_{sg} = 9.0 m/s, v_{sl} = 9.2 x 10^{-3} m/s, Re_{sg} = 10232, Fr_{Hsg} = 0.255.

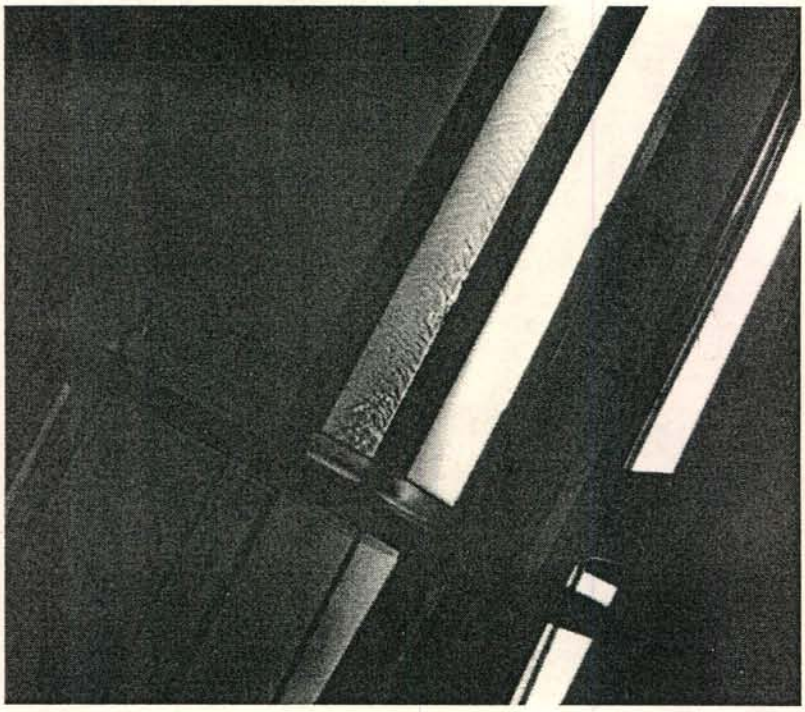

Figure 4.3(e): Air-propanol flow pattern inside the 50 mm (W_t = 10 mm) duct inclined at 60° to the horizontal. v_{sg} = 10.0 m/s, v_{sl} = 9.2 x 10^{-3} m/s, Re_{sg} = 11218, Fr_{Hsg} = 0.306.

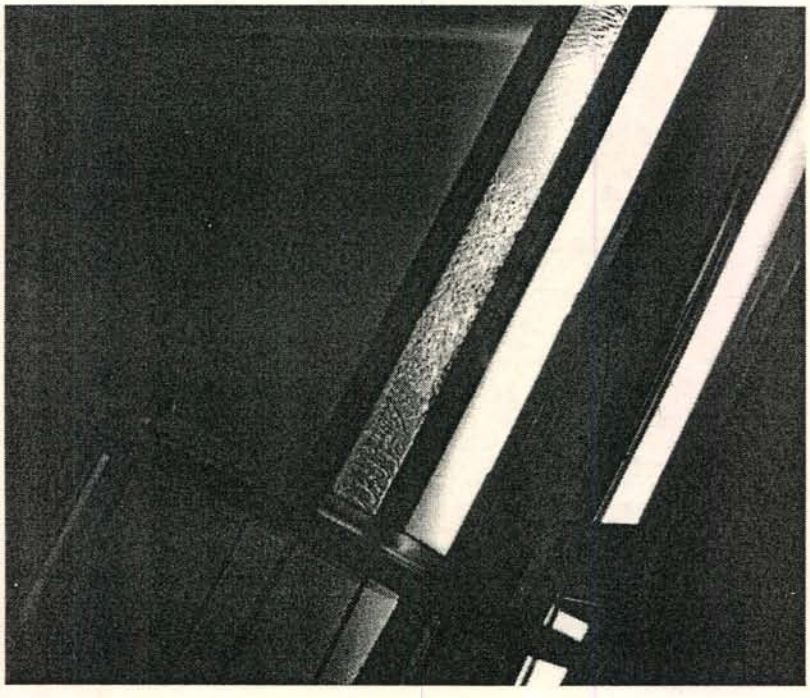

Figure 4.3 (f): Air-propanol flow pattern inside the 50 mm duct (W_t = 10 mm) inclined at 60° to the horizontal. v_{sg} = 10.1 m/s, v_{sl} = 9.2 x 10^{-3} m/s, Re_{sg} = 11483, Fr_{Hsg} = 0.320.

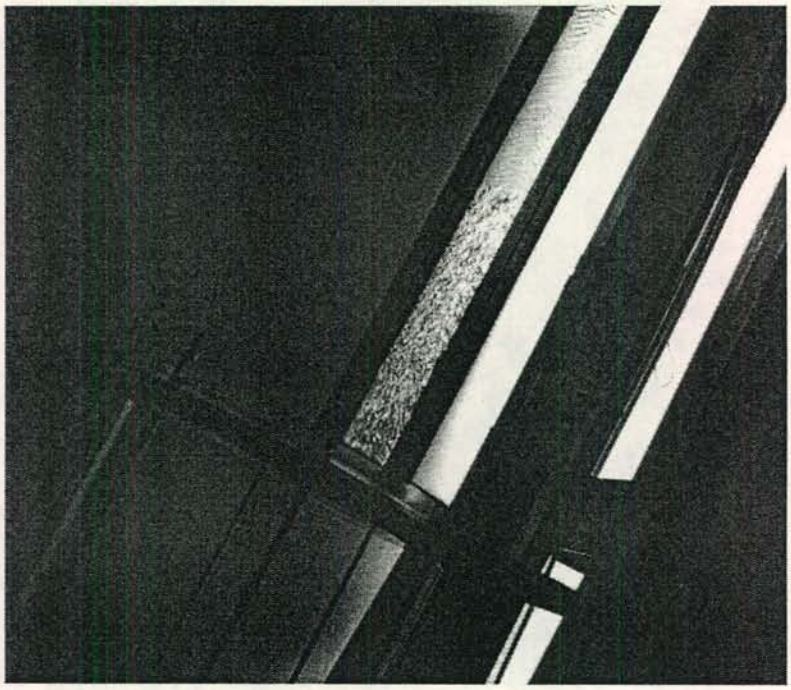

Figure 4.3(g): Air-propanol flow pattern inside the 50 mm (W_t = 10 mm) duct inclined at 60° to the horizontal. v_{sg} = 10.2 m/s, v_{sl} = 9.2 x 10^{-3} m/s, Re_{sg} = 11623, Fr_{Hsg} = 0.328.

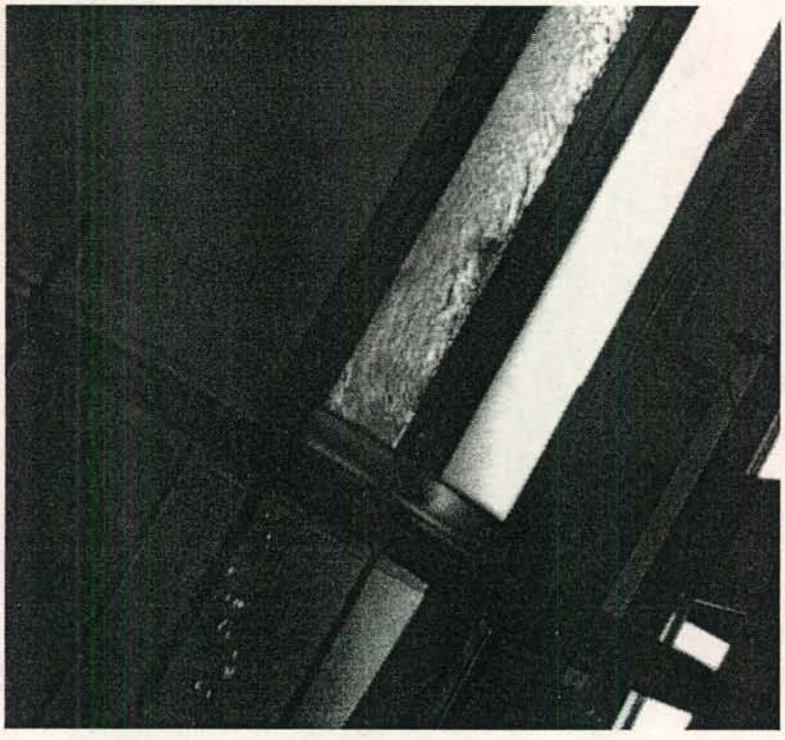

Figure 4.3 (h): Air-propanol flow pattern inside the 50 mm (W_t = 10 mm) duct inclined at 60° to the horizontal. v_{sg} = 10.6 m/s, v_{sl} = 9.2 x 10^{-3} m/s, Re_{sg} = 12029, Fr_{Hsg} = 0.351.

4.2.2 Air-propanol flow inside the 100 mm duct

A similar series of photos were taken of air-propanol flow in the 100 mm duct. The pressure drop characteristics and the corresponding flow patterns are shown figures 4.4 4.5 respectively.

In figure 4.5(a) the superficial gas Reynolds number is 12160. The pressure gradient inside the duct is still equal to the corresponding air-only single-phase value. The propanol jet is dispersed by the air flow as it drains into the bottom plenum and in the process droplet entrainment takes place at the gas inlet. Droplets are deposited on the lower part of the duct walls. The entrance pressure drop starts to rise slightly above that measured for air-only single-phase flow.

Upon an increase in the air flow rate to Re_{sg} = 15069 the entrainment rate increases and the duct walls are wetted by a propanol film, as shown in figure 4.5 (b). At the bottom part of the duct walls a rough film is beginning to form. Propanol, deposited above the rough film, drains in streaks against the acrylic plastic walls to the bottom spacer as it is driven upwards by the gas flow. Between points 2 and 3 the duct walls are still fairly dry and thus the pressure gradient is close to that for single-phase air flow.

In figure 4.5 (c) the air flow rate has been increased to Re_{sg} = 17050. The duct walls above the gas inlet are now completely wetted by a rough film. The entrance pressure drop has increased significantly. The strong gas-liquid interaction is still confined to the bottom ≈0.5 m of the test section. At the conditions shown figures in 4.5 (d) and (e) (Re_{sg} = 18254 and 18796 respectively) liquid accumulates just above the gas inlet and the characteristic rotating gas-liquid mixture or vortex is formed. A vortex can be seen in figure 4.5 (e). A sharp increase in the pressure gradient inside the duct is experienced while such a vortex travels upwards, as illustrated by figure 4.4.

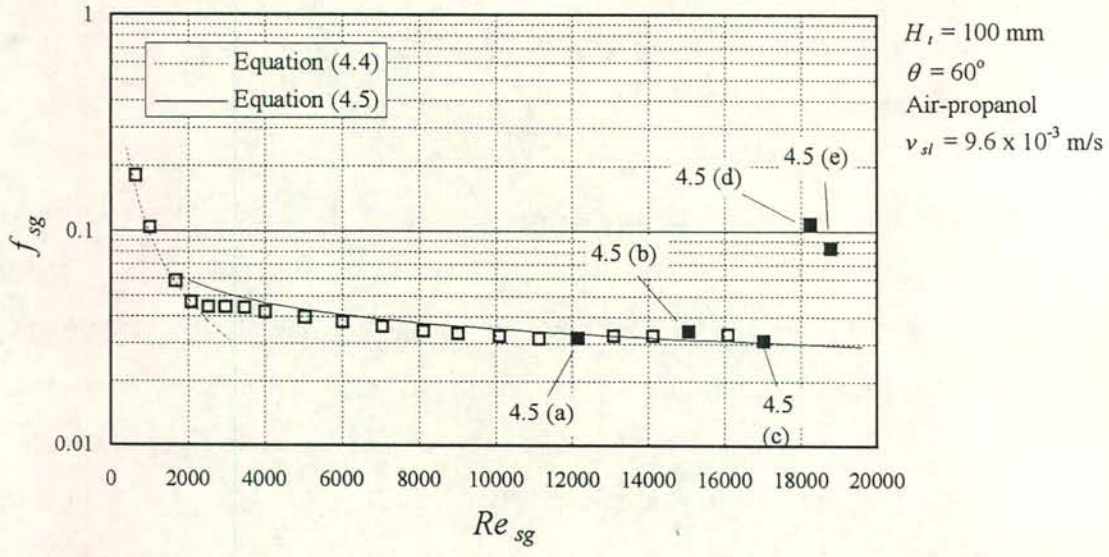

Figure 4.4(a): Two-phase friction factor for air-propanol flow. The solid symbols represent the gas flow rates at which photos, shown in figure 4.5, were taken.

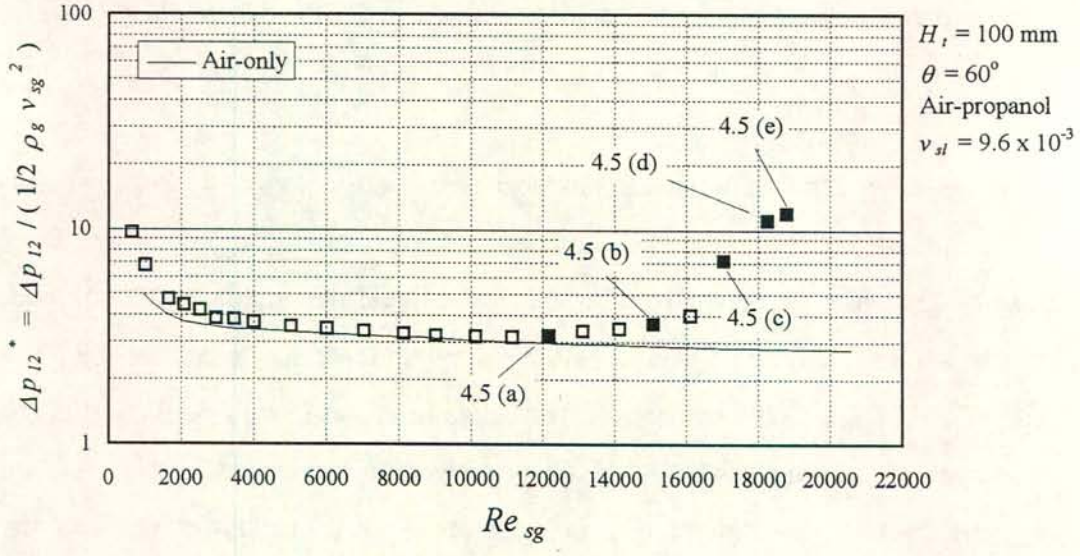

Figure 4.4(b): Dimensionless pressure drop measured across the sharp-edged gas entrance between points 1 and 2 for air-propanol flow. The solid symbols represent the gas flow rates at which photos, shown in figure 4.5, were taken.

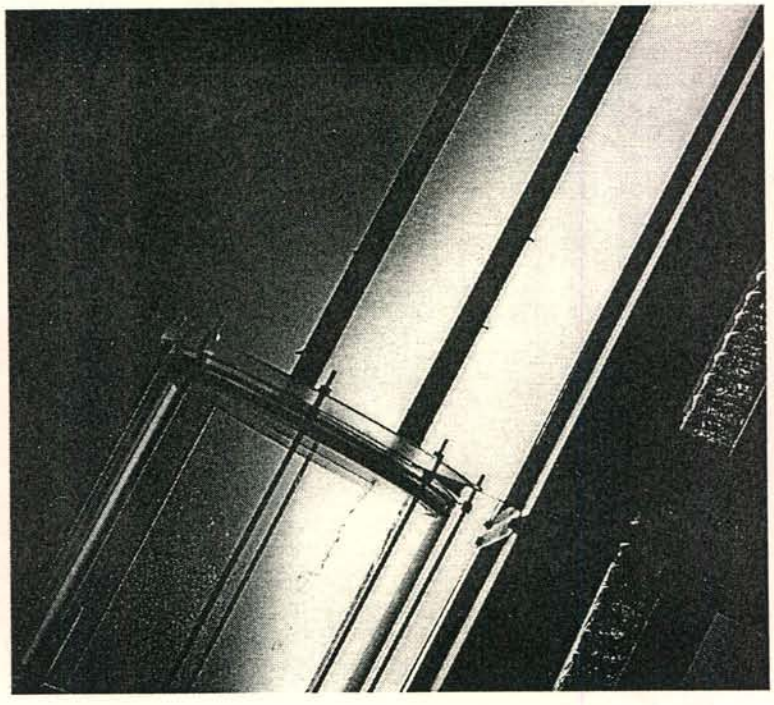

Figure 4.5(a): Air-propanol flow pattern inside the 100 mm duct inclined at 60° to the horizontal. v_{sg} = 10.2 m/s, v_{sl} = 9.6 x 10^{-3} m/s, Re_{sg} = 12160, Fr_{Hsg} = 0.161.

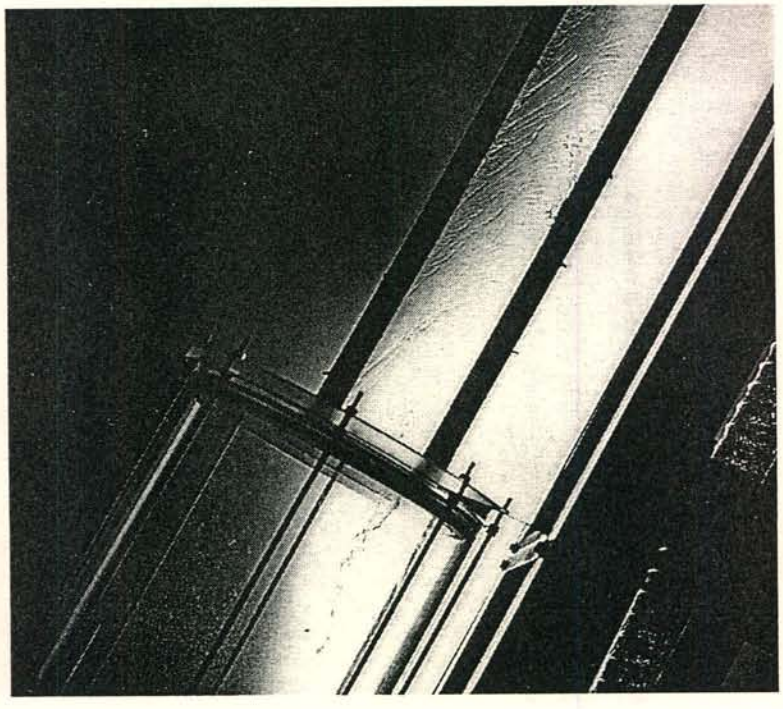

Figure 4.5(b): Air-propanol flow pattern inside the 100 mm duct inclined at 60° to the horizontal. v_{sg} = 12.6 m/s, v_{sl} = 9.6 x 10^{-3} m/s, Re_{sg} = 15069, Fr_{Hsg} = 0.246.

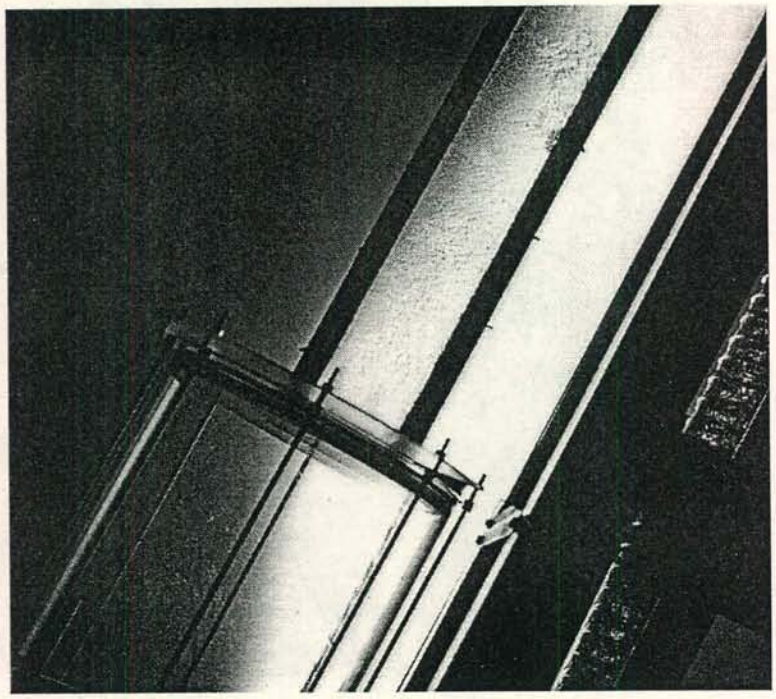

Figure 4.5(c): Air-propanol flow pattern inside the 100 mm duct inclined at 60° to the horizontal. v_{sg} = 14.2 m/s, v_{sl} = 9.6 x 10^{-3} m/s, Re_{sg} = 17040, Fr_{Hsg} = 0.313.

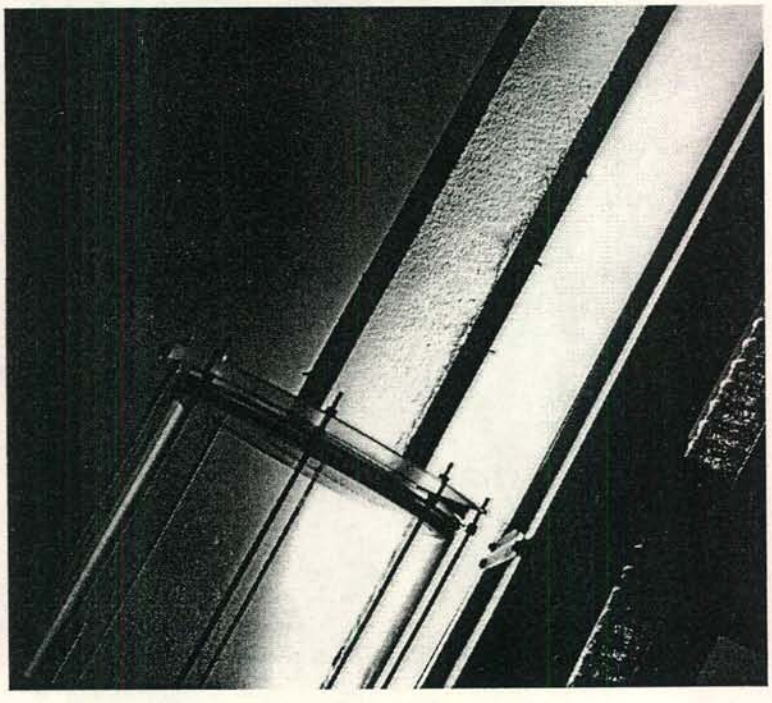

Figure 4.5 (d): Air-propanol flow pattern inside the 100 mm duct inclined at 60° to the horizontal. v_{sg} = 15.0 m/s, v_{sl} = 9.6 x 10^{-3} m/s, Re_{sg} = 18254, Fr_{Hsg} = 0.355.

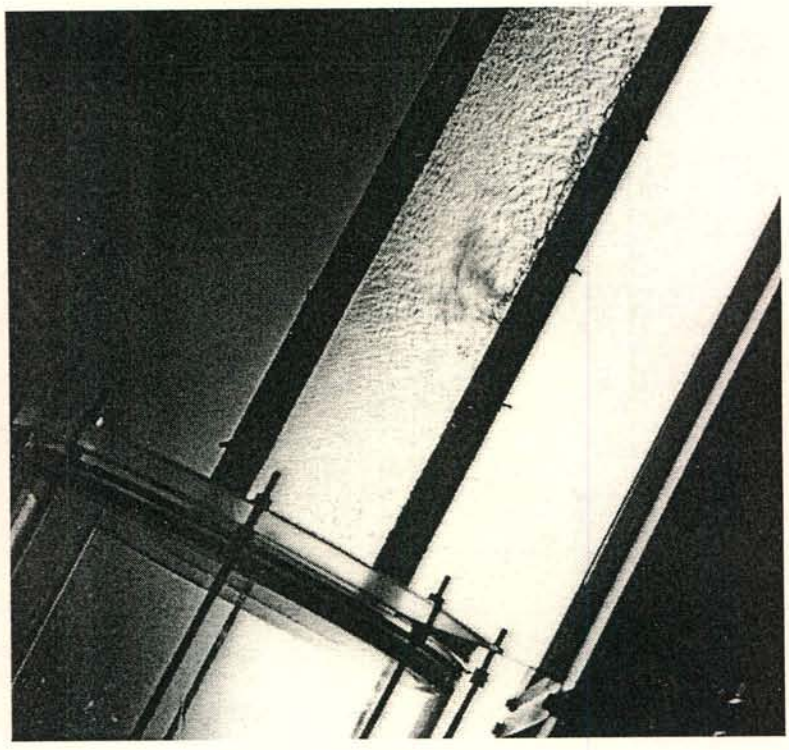

Figure 4.5(e): Air-propanol flow pattern inside the 100 mm duct inclined at 60° to the horizontal. v_{sg} = 15.5 m/s, v_{sl} = 9.6 x 10^{-3} m/s, Re_{sg} = 18796, Fr_{Hsg} = 0.378.

4.2.3 Air-water flow inside the 100 mm duct

Air-water pressure drop characteristics for flow inside the 100 mm duct and the corresponding flow patterns are shown in figures 4.6 and 4.7 respectively.

The onset of entrainment at the sharp-edged inlet, seen in figure 4.7(a) where Re_{sg} = 12012, takes place at approximately the same air flow rate as for propanol. The liquid drains in a wavy rivulet inside the groove cut into the aluminium spacer and cannot be seen. As the air flow rate is increased the entrainment becomes stronger and more and bigger droplets are deposited on the duct walls. Droplets adhering to the walls can be seen in figure 4.7(b) where Re_{sg} = 15056. When comparing figures 4.5(b) and 4.7(b) the different ways in which the propanol and the water wet the acrylic plastic walls can be noticed. While the propanol tends to wet the walls in the form of a wavy film, the water remains in the form of droplets as entrainment and deposition take place.

As the air flow rate is further increased, the droplets adhering to the walls slowly creep upwards and form streaks due to coalescence, as illustrated in figures 4.7(c) and (d) (Re_{sg} = 17071 and 18823 respectively). Figure 4.7(e) illustrates conditions where a vortex, formed at the sharp-edged gas inlet, spans the entire duct height and is propelled upwards. Note the thick rough film at the bottom being swept upwards by the gas flow causing the rotating/rolling motion.

The superficial gas velocity at which the "diameter" of the characteristic rotating motion reached the duct height was 15.5 m/s for propanol and 18.1 m/s for water. In both cases the pressure gradient between points 2 and 3 was equal to the single-phase pressure gradient at $v_{sg} \approx 14.1$ m/s. Upon an increase in the air flow rate a sudden increase in the pressure gradient occurred in the case of propanol. A more gradual increase in the two-phase pressure gradient was experienced for water in the range $14.1 < v_{sg} < 18.1$ m/s before the onset of strong vortex flow and the subsequent sharp increase in the pressure drop occurred.

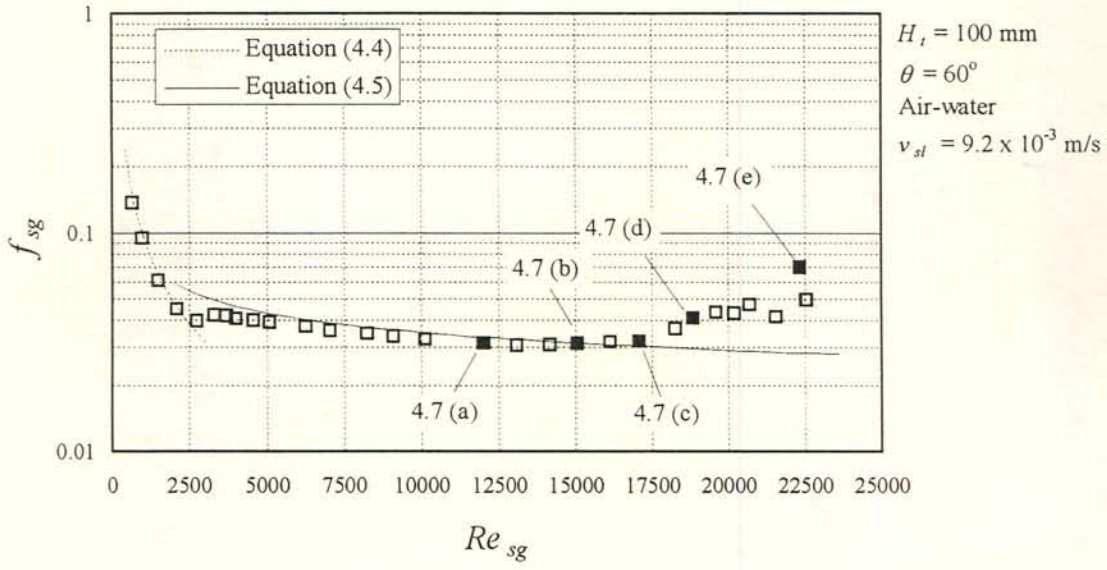

Figure 4.6(a): Two-phase friction factor for air-water flow. The solid symbols represent the gas flow rates at which photos, shown in figure 4.7, were taken.

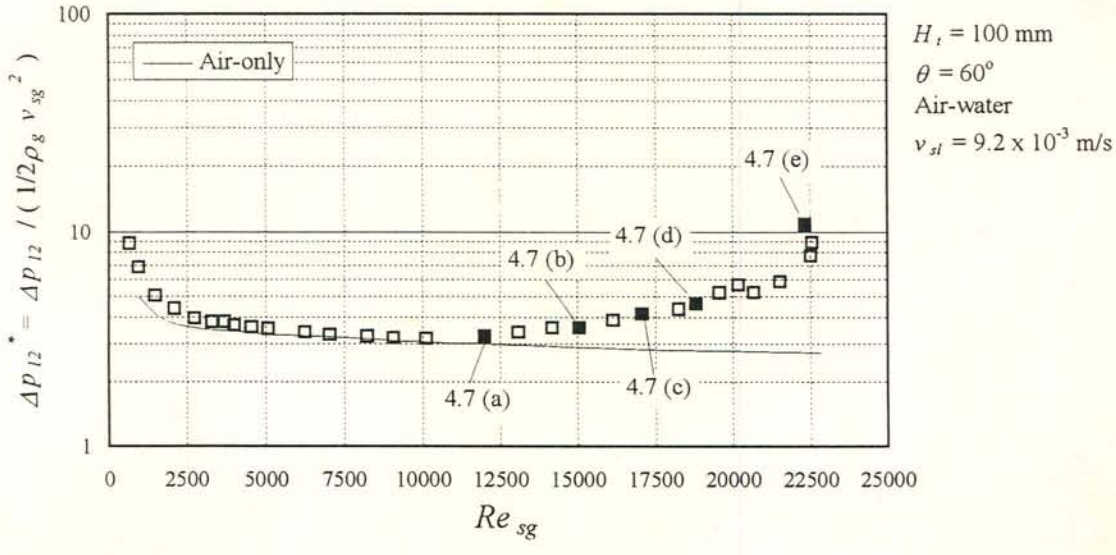

Figure 4.6(b): Dimensionless pressure drop measured across the sharp-edged gas entrance between points 1 and 2 for air-water flow. The solid symbols represent the gas flow rates at which photos, shown in figure 4.7, were taken.

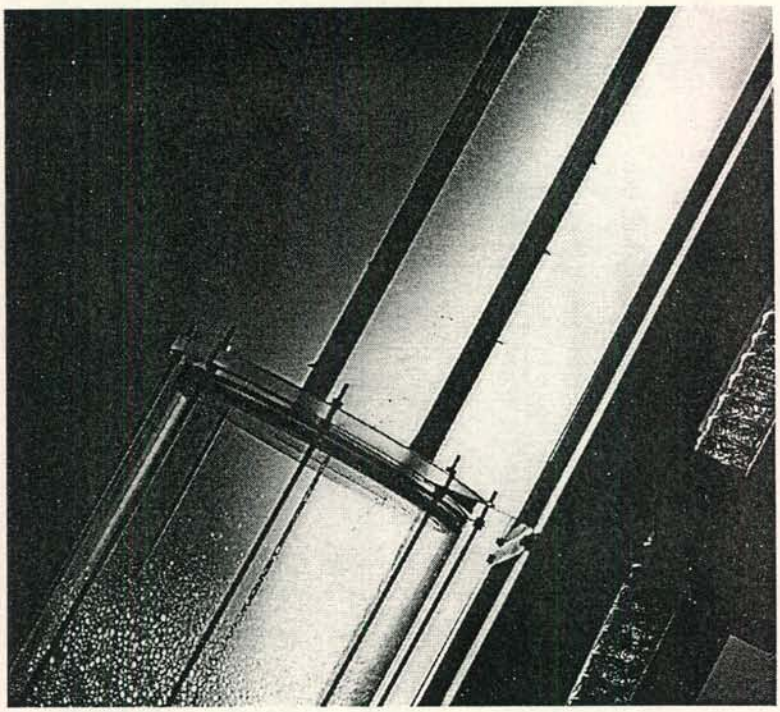

Figure 4.7(a): Air-water flow pattern inside the 100 mm duct inclined at 60° to the horizontal. v_{sg} = 10.0 m/s, v_{sl} = 9.2 x 10^{-3} m/s, Re_{sg} = 12012, Fr_{Hsg} = 0.123.

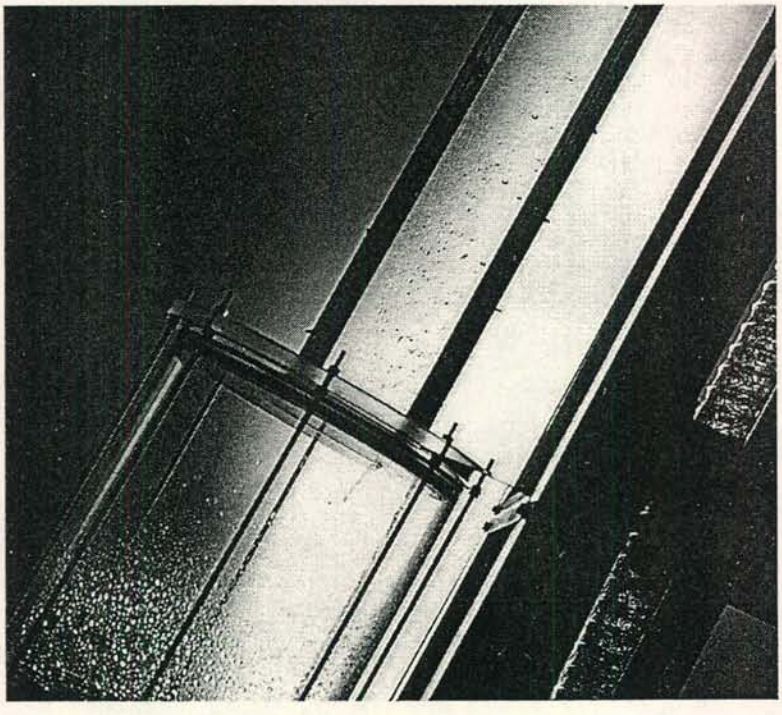

Figure 4.7 (b): Air-water flow pattern inside the 100 mm duct inclined at 60° to the horizontal. v_{sg} = 12.5 m/s, v_{sl} = 9.2 x 10^{-3} m/s, Re_{sg} = 15065, Fr_{Hsg} = 0.193.

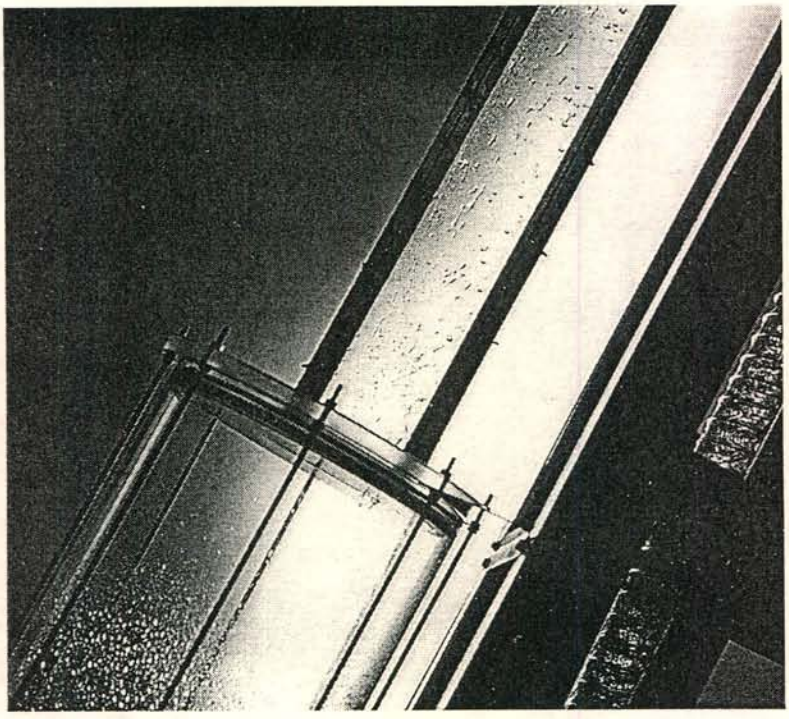

Figure 4.7 (c): Air-water flow pattern inside the 100 mm duct inclined at 60° to the horizontal. v_{sg} = 14.1 m/s, v_{sl} = 9.2 x 10^{-3} m/s, Re_{sg} = 17071, Fr_{Hsg} = 0.246.

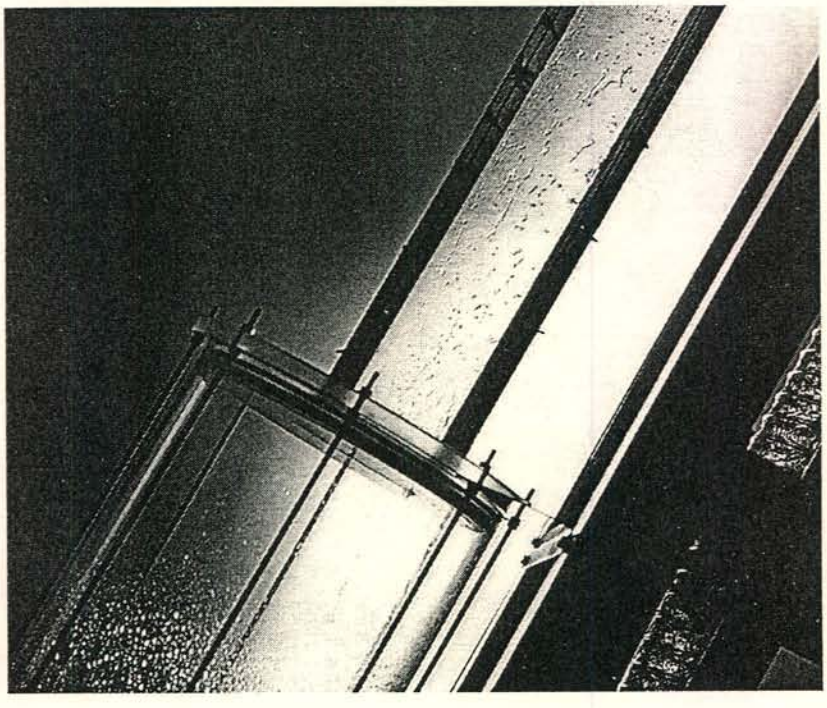

Figure 4.7 (d): Air-water flow pattern inside the 100 mm duct inclined at 60° to the horizontal. v_{sg} = 15.5 m/s, v_{sl} = 9.2 x 10^{-3} m/s, Re_{sg} = 18823, Fr_{Hsg} = 0.298.

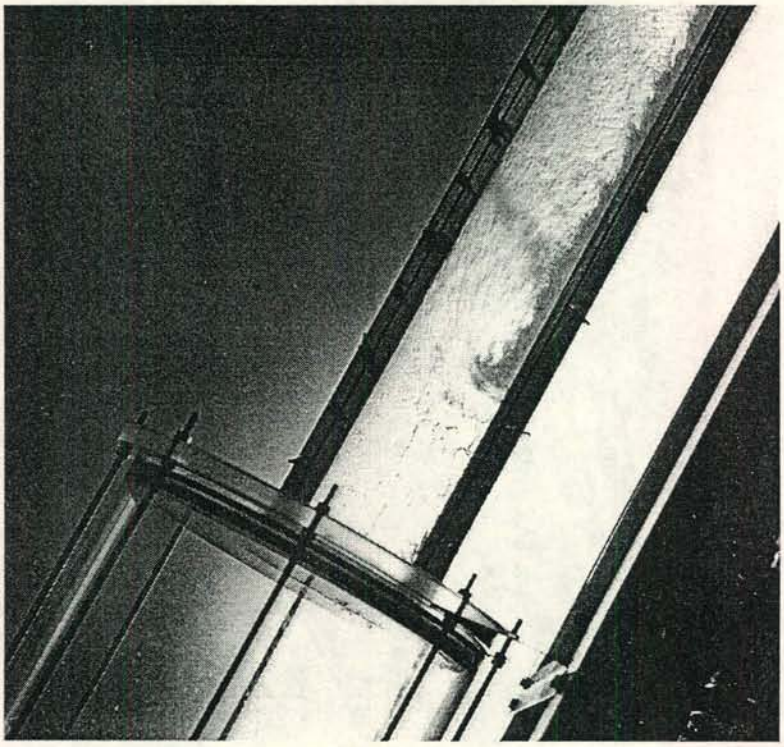

Figure 4.7(e): Air-water flow pattern inside the 100 mm duct inclined at 60° to the horizontal. v_{sg} = 18.1 m/s, v_{sl} = 9.2 x 10^{-3} m/s, Re_{sg} = 22341, Fr_{Hsg} = 0.411.

4.3 Pressure drop characteristics at an inclination of 60° to the horizontal

4.3.1 The effect of the duct geometry

In figure 4.8(a) the frictional pressure gradient for the four different duct geometries is shown. The data are plotted in terms of the two-phase friction factor and the superficial gas Reynolds number Re_{sg}. The superficial liquid velocity for each duct is approximately the same. The same data are plotted in figure 4.8(b) against the superficial densimetric gas Froude number Fr_{Hsg} . According to these two figures the pressure gradient is a function of the gas Reynolds number at low gas flow rates, while the onset of the sharp increase in the pressure gradient at higher gas flow rates is Froude number related. Note that the required length dimension for the superficial gas Reynolds number is the hydraulic diameter while the duct height has been taken as the length dimension for the superficial densimetric gas Froude number.

Similar plots of the two-phase entrance loss coefficient are given in figures 4.9(a) and (b). In the case of single-phase flow such a contraction loss coefficient is independent of the Reynolds number for highly turbulent flow. Such a trend is observed in figure 4.9(b) for low Froude numbers. Above a certain Froude number K_{tp} increases sharply. As in the case of the pressure gradient data, the entrance pressure drop becomes related to the superficial gas Froude number at higher gas flow rates and, according to figure 4.9(a), is not Reynolds number dependent.

4.3.2 The effect of the gas properties

The transition from Reynolds to Froude number governed flow is also illustrated by the pressure drop results obtained for air, helium and hydrogen. Similarly to figures 4.8 and 4.9, air-methanol, helium-methanol and hydrogen-methanol data measured for the 50 mm duct (W_t = 10 mm), are plotted in figures 4.10 and 4.11 against Re_{sg} and Fr_{Hsg}.

In figure 4.10(a) the frictional pressure gradient data correlates in terms of the Reynolds number at low gas flow rates, but as the gas flow rate is increased, it is the Froude numbers which determines when the sudden increase in the pressure gradient occurs.

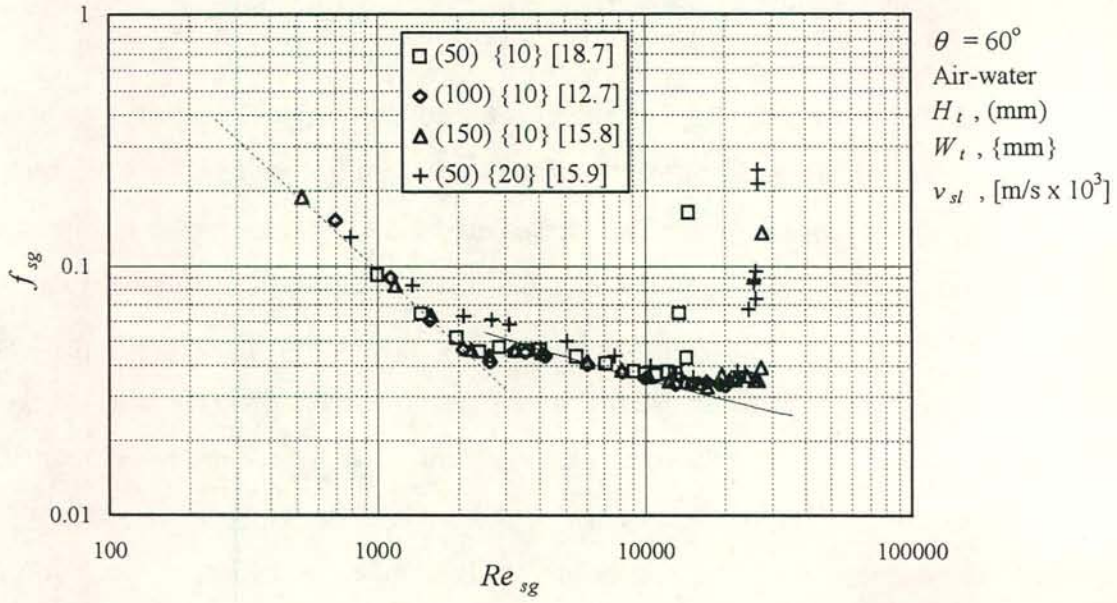

Figure 4.8(a): Two-phase friction factor measured for four different duct geometries, plotted against the superficial gas Reynolds number. Broken and solid line: Laminar and turbulent single-phase friction factor. Data: Short test section

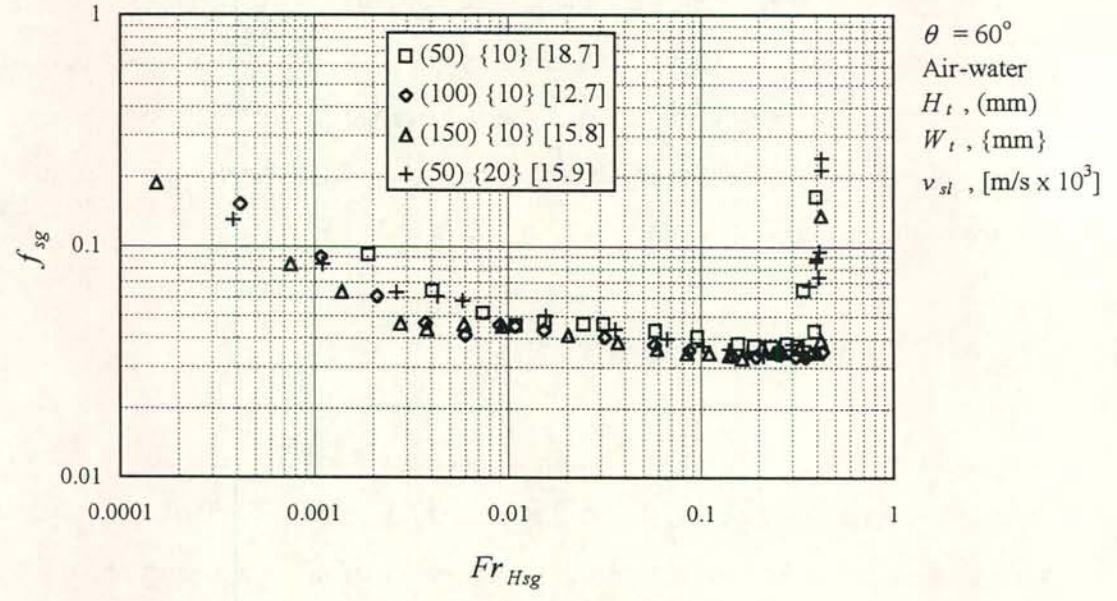

Figure 4.8(b): The pressure gradient data shown in figure 4.8 (a) plotted against the superficial densimetric gas Froude number.

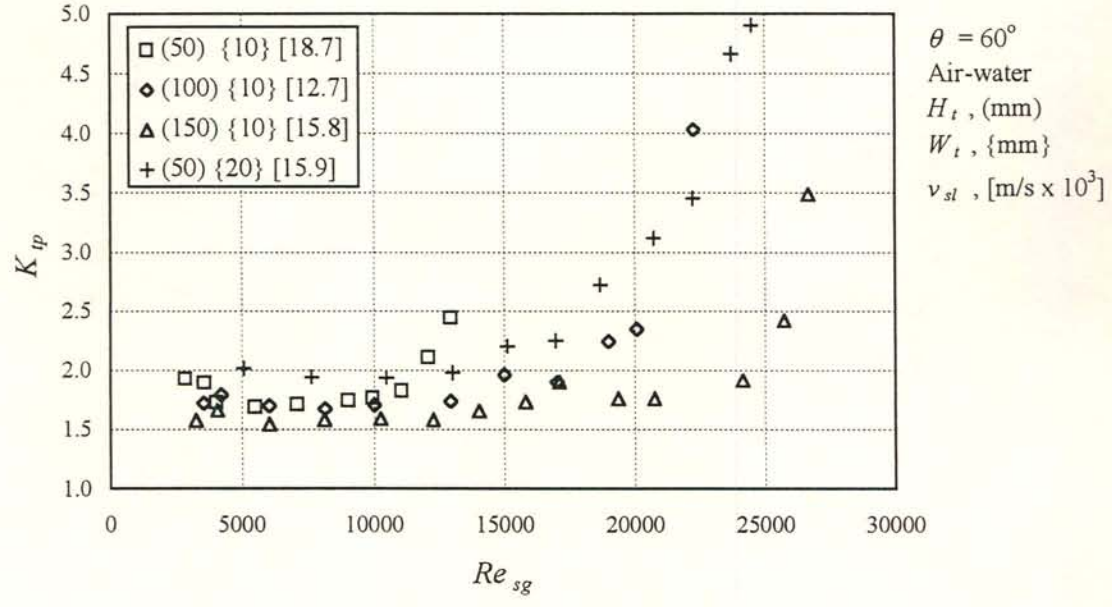

Figure 4.9(a): Two-phase entrance loss coefficient measured for four different ducts, plotted against the superficial gas Reynolds number. The air flow is fully turbulent. Data: Short test section.

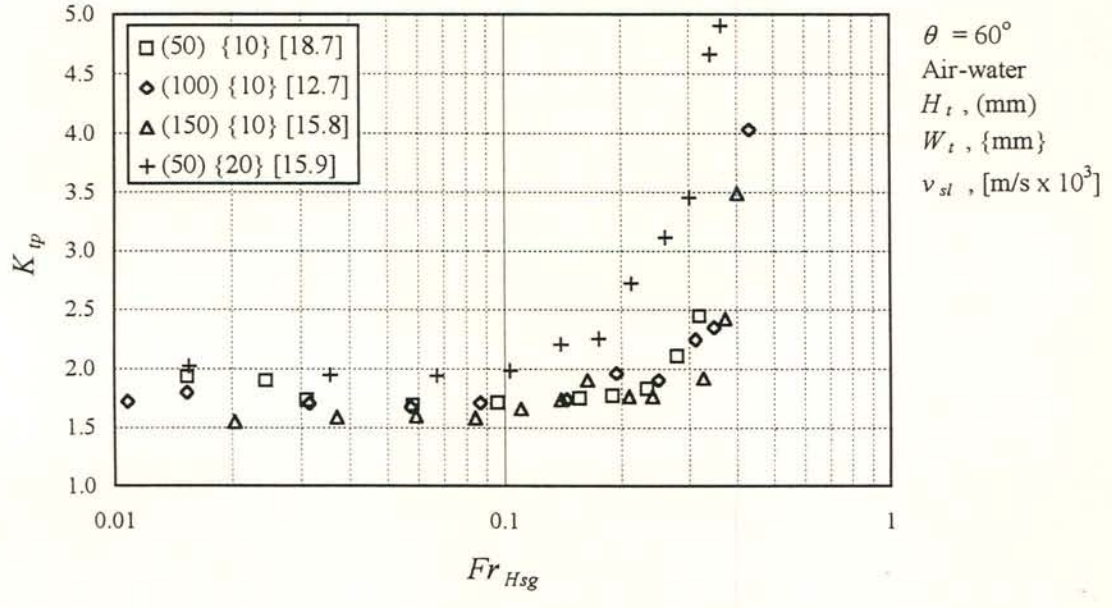

Figure 4.9(b): The entrance pressure drop data of figure 4.9(a) plotted against the superficial densimetric gas Froude number. The gas flow is fully turbulent.

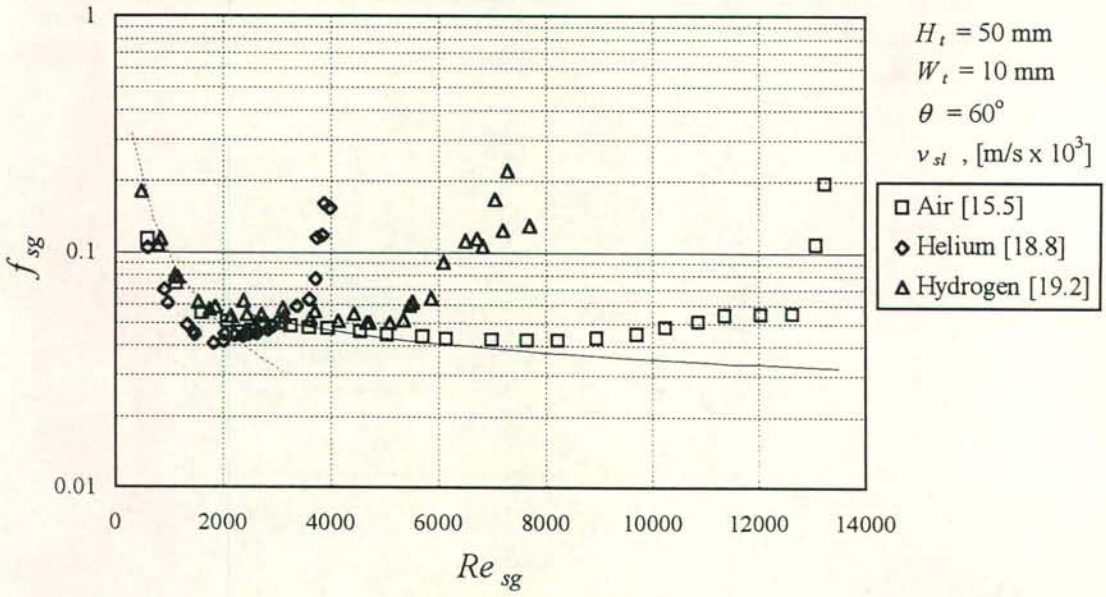

Figure 4.10(a): Two-phase friction factor measured for three different gases and methanol, plotted against the superficial gas Reynolds number. Broken and solid line: Laminar and turbulent single-phase friction factor. Data: Long test section.

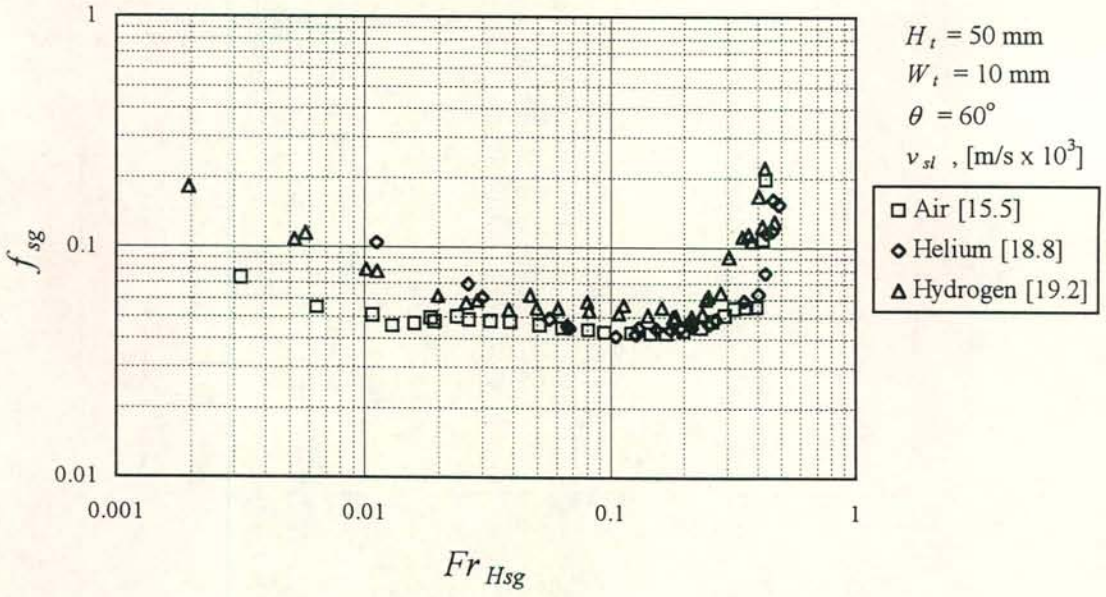

Figure 4.10(b): The two-phase friction factor data of figure 4.10(a) plotted in terms of the superficial densimetric gas Froude number.

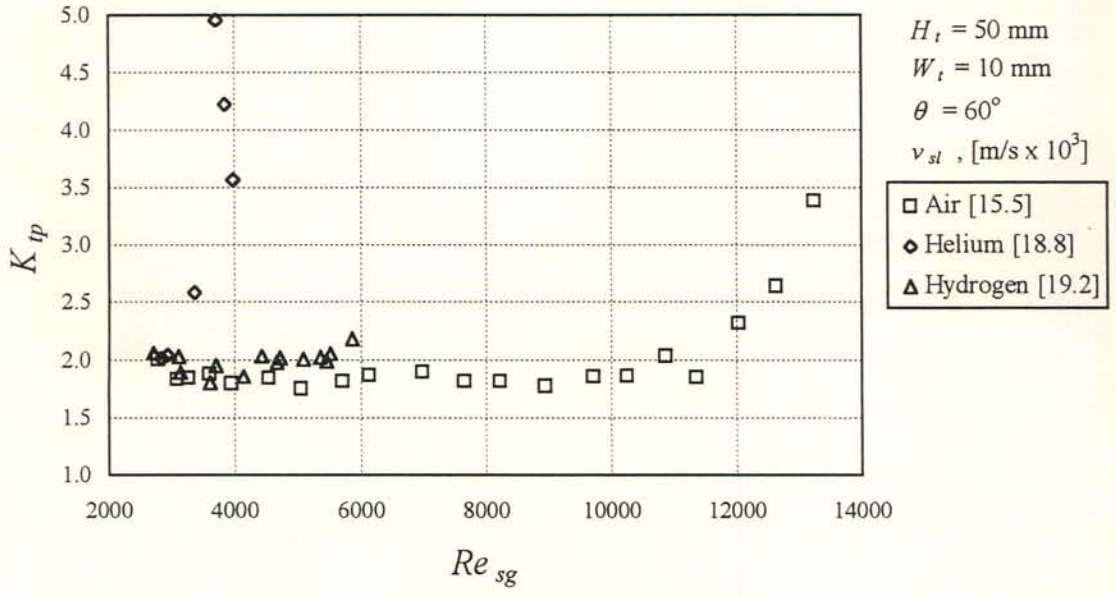

Figure 4.11(a): Two-phase entrance loss coefficient measured for three different gases and methanol, plotted against the superficial gas Reynolds number. The gas flow is turbulent. Data: Long test section.

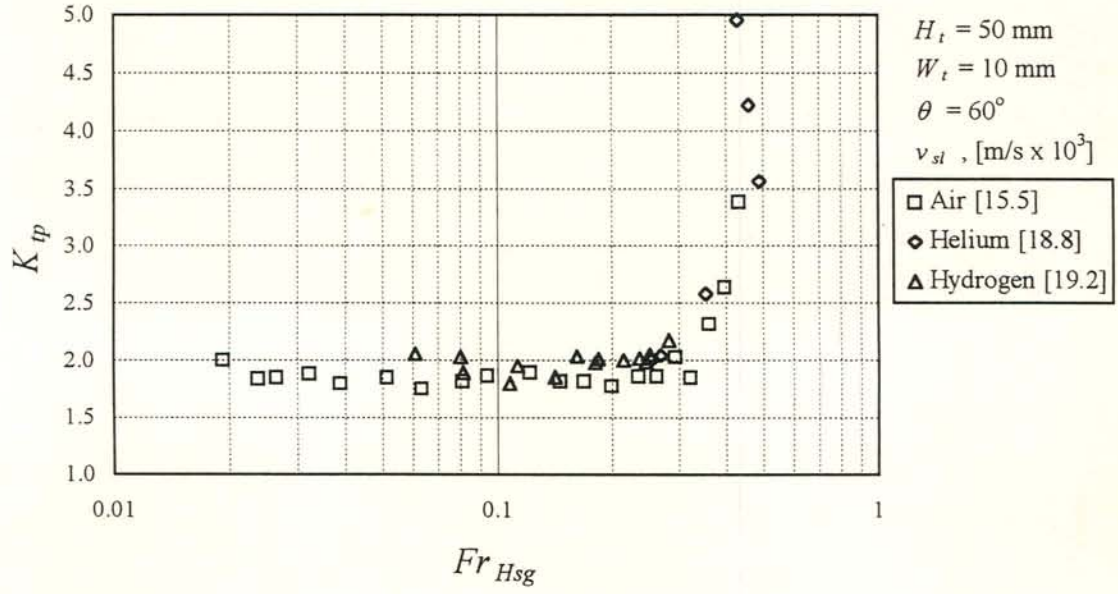

Figure 4.11 (b): The entrance loss coefficient data of figure 4.10(a) plotted against the superficial densimetric gas Froude number.

Similarly the conditions at which the sudden increase in pressure drop across the sharp-edged gas inlet takes place is determined by the superficial densimetric gas Froude number and is not related to the superficial gas Reynolds number.

4.3.3 The effect of the liquid properties and wetting on the pressure drop characteristics

In the Reynolds number region the liquid flow and thus the liquid properties do not affect the pressure drop experienced by the gas significantly. To establish any effects the liquid properties may have at higher gas flow rates where the flow is governed by the superficial densimetric gas Froude number, the pressure gradient ratio for air-water, air-methanol and air-propanol is shown in figures 4.12(a), 4.13(a) and 4.14(a) for the 50, 100 and 150 mm duct respectively.

The gas Froude number at which the pressure gradient data lies practically on a vertical line, i.e. the Froude number at the formation of strong vortex-type flow, is the lowest for propanol. For water and methanol the Froude number at the sharp increase in the pressure gradient is approximately equal. The same trend is observed in the case of the two-phase entrance loss coefficient, shown in figures 4.12(b), 4.13(b) and 4.14(b).

Note that at $Fr_{Hsg} \approx 0.2$ the air-water pressure gradient data obtained with the long configuration for the 150 mm duct rises above the air-water data for the short configuration. The air-water data obtained with the short test section follows the same trend as the alcohols. The tests with the long test section were conducted first (starting with the air-water experiments, then with methanol, followed by the propanol tests), after which the apparatus was modified and the pressure measurements for air-water in the short test section were conducted. It is believed that better wetting of the acrylic plastic duct walls by the water took place after the duct was exposed to the alcohols, causing the apparent inconsistent pressure gradient data for water.

This trend is also present in the case of the 100 mm duct (figure 4.13 a) while it cannot be observed for the 50 mm duct (figure 4.12 a). The gas velocity at the sudden increase in pressure gradient in the 50 mm duct is considerably lower than for the 100 and 150 mm ducts. The combined effect of droplet deposition and weak wetting appears not to

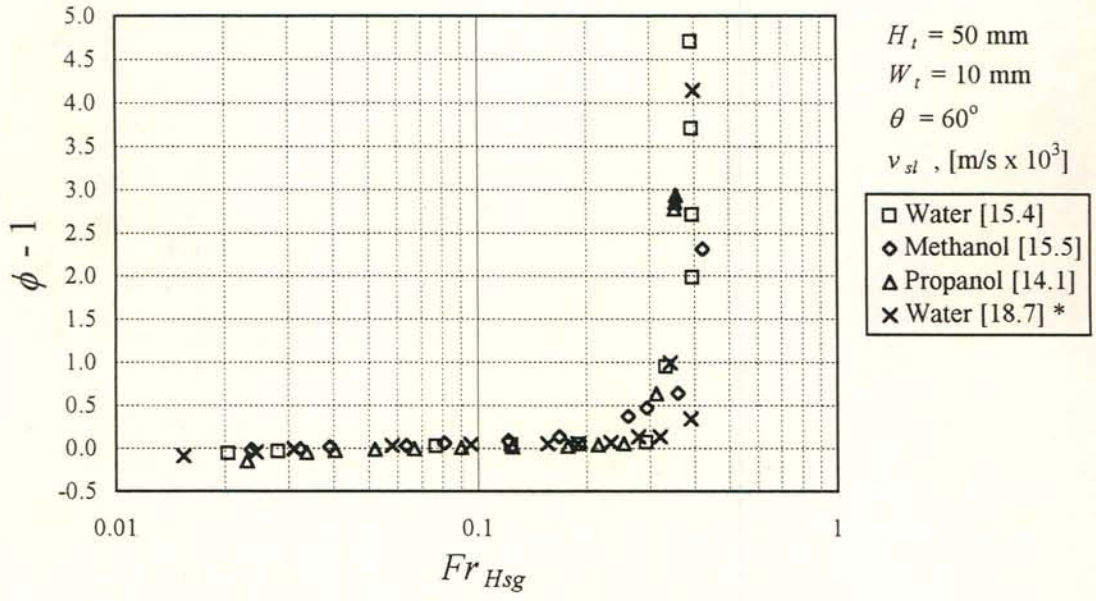

Figure 4.12(a): Pressure gradient ratio for air-water, air-methanol and air-propanol flow in the 50 mm (10 mm wide) duct. Data: Long test section except for water data marked by * which was obtained with the short test section.

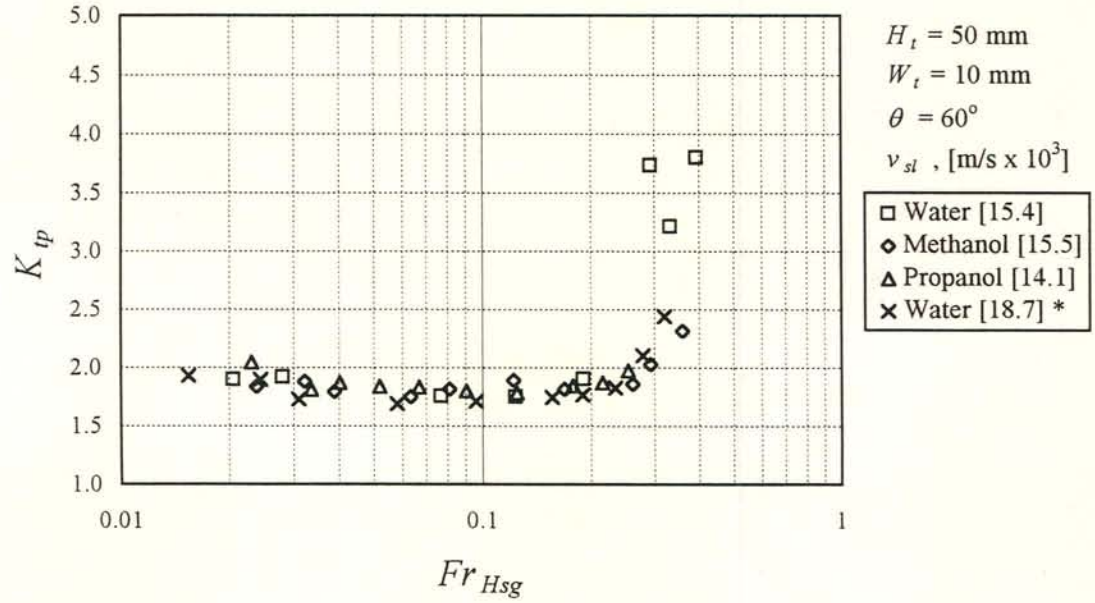

Figure 4.12(b):Entrance pressure drop coefficient for air-water, air-methanol and air-propanol flow in the 50 mm duct (10 mm wide). Data: Long test section except for water data marked by * which was obtained with the short test section.

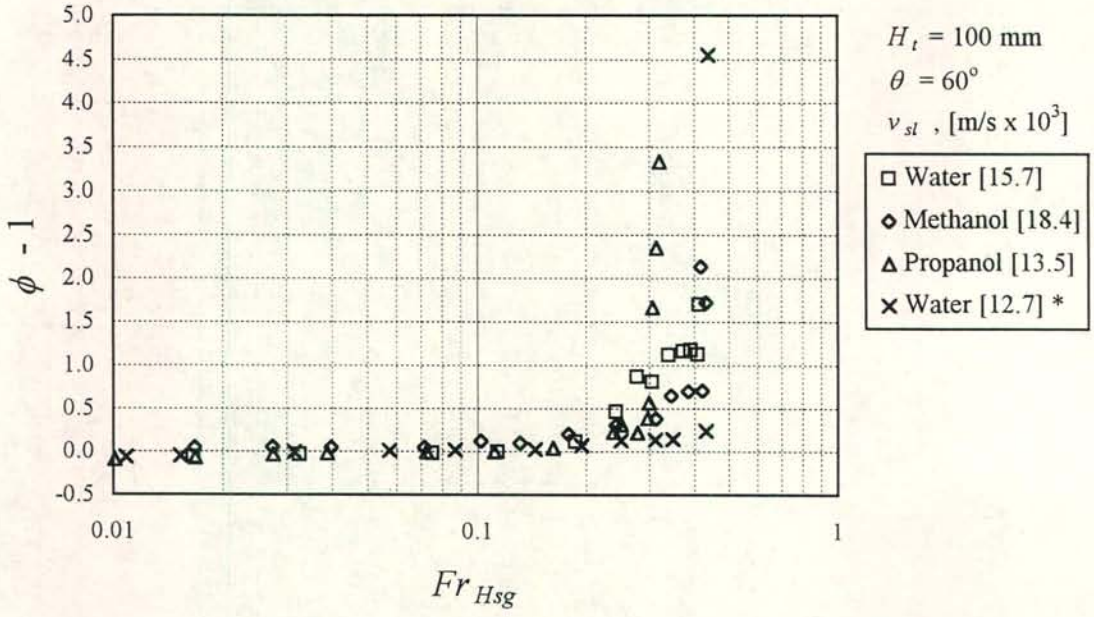

Figure 4.13(a): Pressure gradient ratio for air-water, air-methanol and air-propanol flow in the 100 mm duct. Data: Long test section except for water data marked by * which was obtained with the short test section.

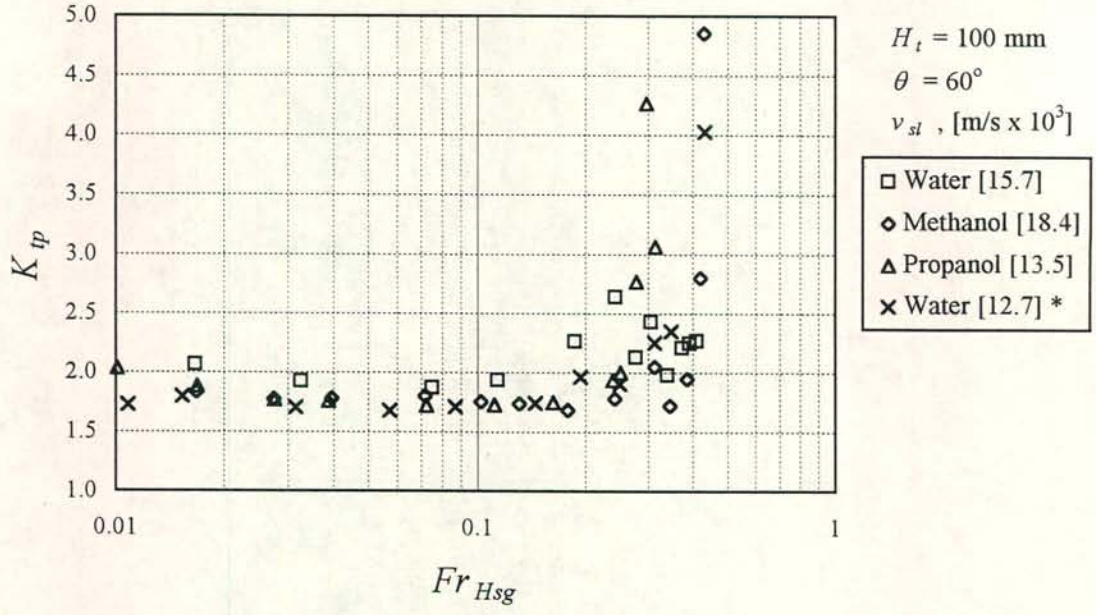

Figure 4.13(b):Entrance pressure drop coefficient for air-water, air-methanol and air-propanol flow in the 100 mm duct. Data: Long test section except for water data marked by * which was obtained with the short test section.

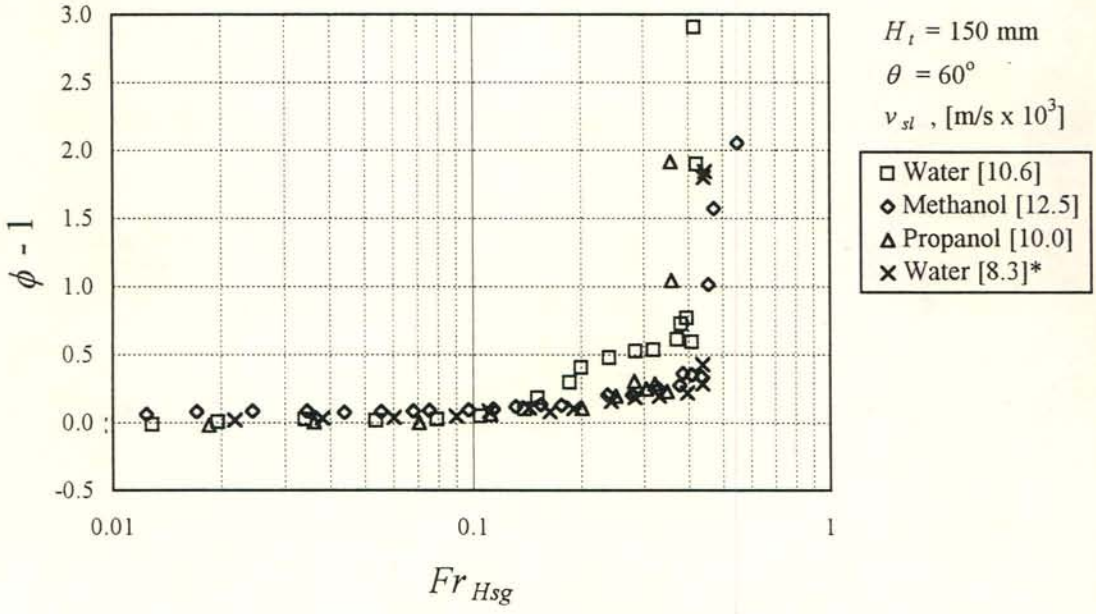

Figure 4.14(a): Pressure gradient ratio for air-water, air-methanol and air-propanol flow in the 150 mm duct. Data: Long test section except for water data marked by * which was obtained with the short test section.

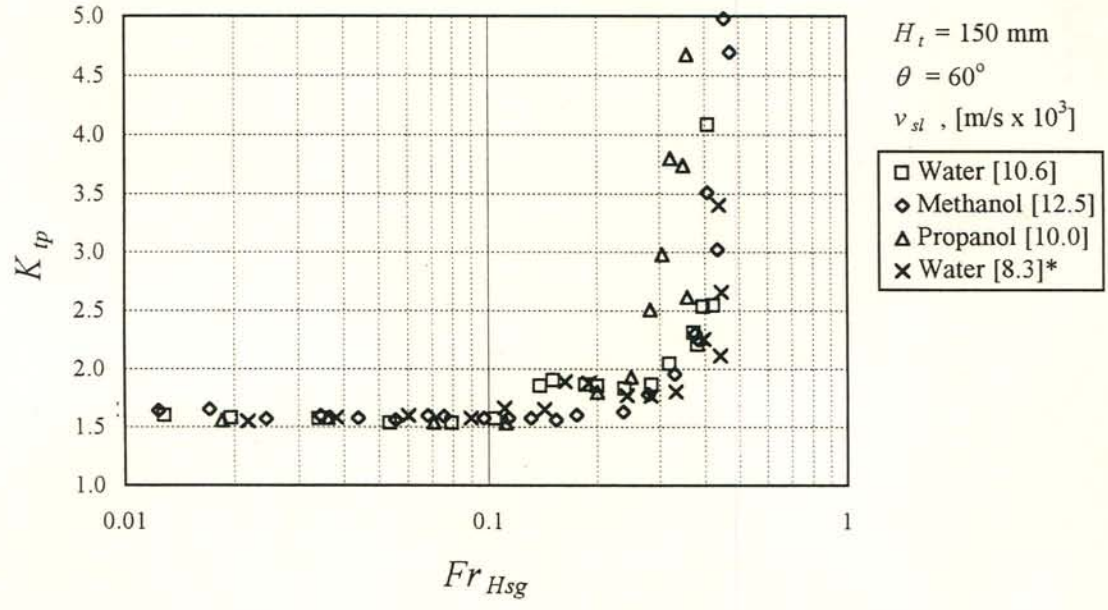

Figure 4.14(b):Entrance pressure drop coefficient for air-water, air-methanol and air-propanol flow in the 150 mm duct. Data: Long test section except for water data marked by * which was obtained with the short test section.

be present at the lower gas velocities present in the 50 mm duct and thus no such early peak in pressure gradient is observed for the water data obtained with the long test section.

4.3.4 The effect of the liquid flow rate on the pressure drop characteristics

Two-phase friction factor data for air-water at various liquid flow rates in the 150 mm duct is shown in figures 4.15(a) and (b) for the long and the short test section respectively. At low liquid flow rates the friction factor follows the characteristic increase present during single-phase flow in the transition region from laminar to turbulent flow. At higher liquid flow rates no such increase inside the transition region is observed.

According to figure 4.15(a) the initial peak caused by poor wetting becomes higher as the liquid flow increases. Also, the peaks are formed earlier at higher liquid flow rates. Note that in figure 4.15 (b) no such peaks exist in the case of the short test section where proper wetting was obtained.

At flooding the sharp increase in the pressure gradient occurs at lower gas flow rates as the liquid flow is increased.

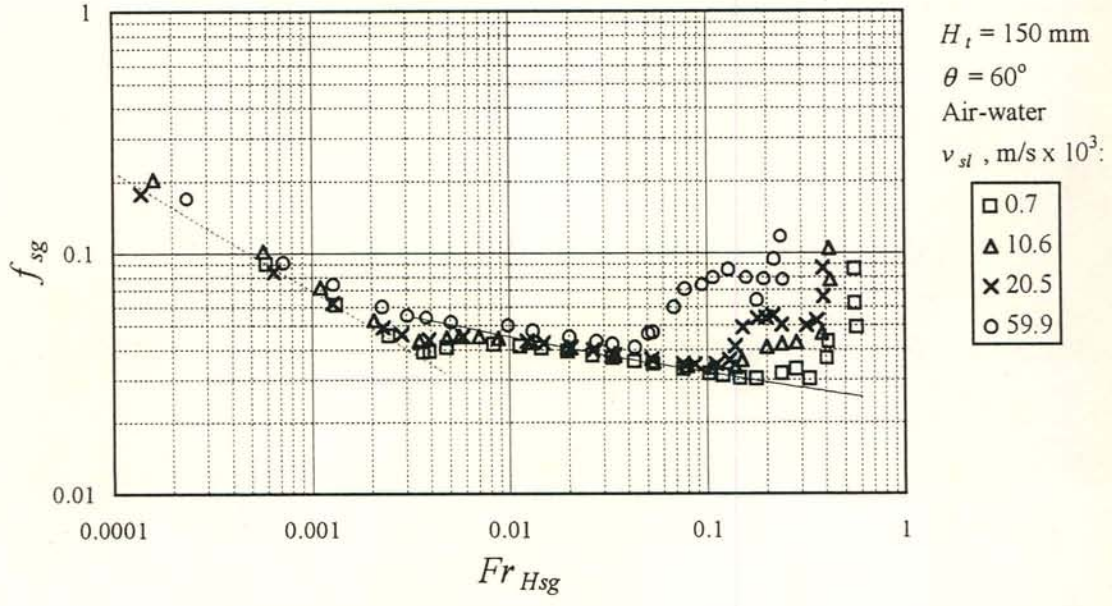

Figure 4.15(a): Two-phase friction factor for air-water flow in the 150 mm duct at various liquid flow rates. Poor wetting is achieved. Data: Long test section.

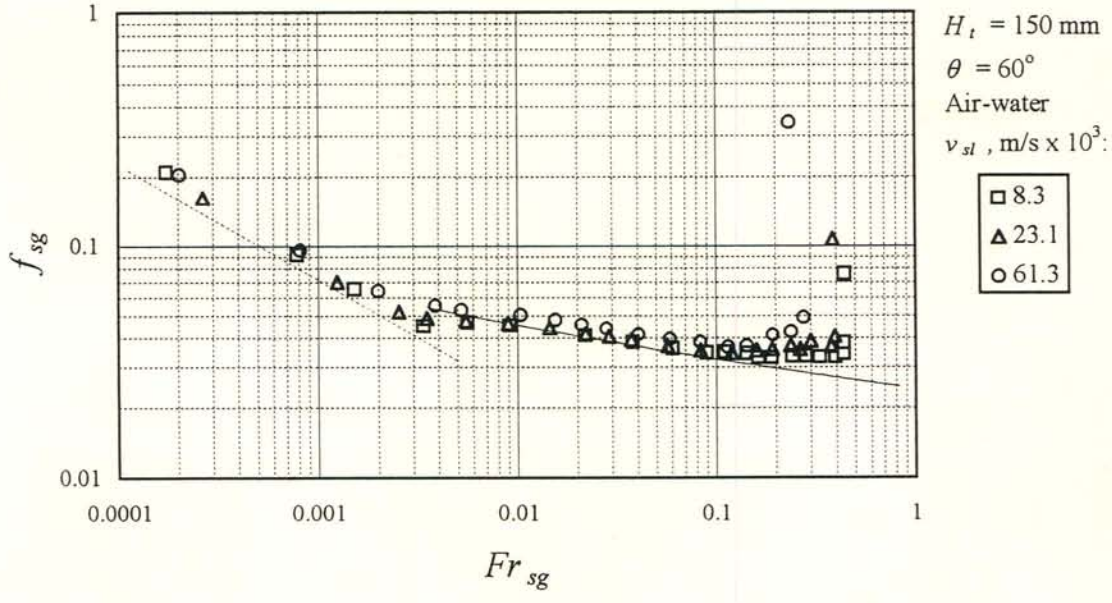

Figure 4.15(b): Two-phase friction factor for air-water flow in the 150 mm duct at various liquid flow rates. Proper wetting is achieved. Data: Short test section.

4.4 Flow patterns observed at a duct inclination of 5° the horizontal

4.4.1 Air-propanol flow inside the 50 mm duct (W_t = 10 mm)

See figures 4.16 and 4.17 for the pressure drop characteristics and the corresponding flow patterns respectively.

At low air flow rates the gas-liquid interface is perfectly smooth. The propanol drains at the bottom of the duct and cannot be seen from the angle of figure 4.17(a), taken at Re_{sg} = 519. At a superficial gas Reynolds number of ≈5600 small ripples are formed on the interface in the region just above the sharp-edged gas inlet. Upon a further increase in the gas flow to $Re_{sg} \approx 6100$ waves with amplitudes of approximately 10 mm, are formed at the gas entrance. These waves travel slowly upwards to the top end of the test section. The formation of such a wave is shown in figure 4.17(b). Here the superficial gas Reynolds number is 6400. The same type of wave can be seen in figure 4.17(c) where Re_{sg} = 6667. Note that at $Re_{sg} \approx 6000$ the pressure gradient is still close to the single-phase frictional pressure gradient, while the two-phase entrance pressure drop is rising above the corresponding single-phase pressure drop. At $Re_{sg} \approx 6000$ the film in the region between points 2 and 3 is still fairly undisturbed, but at the gas inlet, liquid starts to accumulate, as depicted in figure 4.17(c).

Upon a further increase in the air flow rate roll waves are formed at the bottom of the test section, as illustrated in figure 4.17(d) where Re_{sg} = 7041. Initially the roll waves travel approximately 1 m up the duct before being dispersed by the gas flow, causing droplet entrainment in the process. Eventually the roll waves bridge the entire duct height and are propelled upwards to the top end of the test section. Photos taken at the onset of liquid bridging between points 2 and 3 are shown in figure 4.17(e) and (f). In both cases Re_{sg} = 7040. In figure 4.17(e) the wavy film before the formation of a roll wave can be seen and in figure 4.17(f) a roll wave, formed at the gas inlet, is propelled upwards.

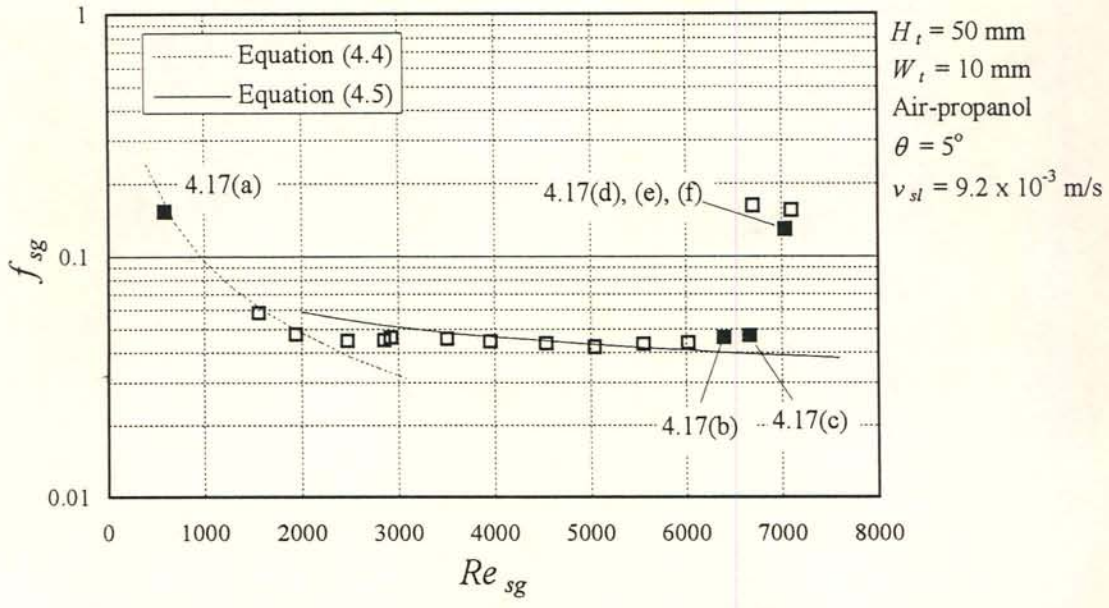

Figure 4.16(a): Two-phase friction factor for air-propanol flow in the 50 mm duct (10 mm wide). The solid symbols represent the gas flow rates at which photos, shown in figure 4.17, were taken.

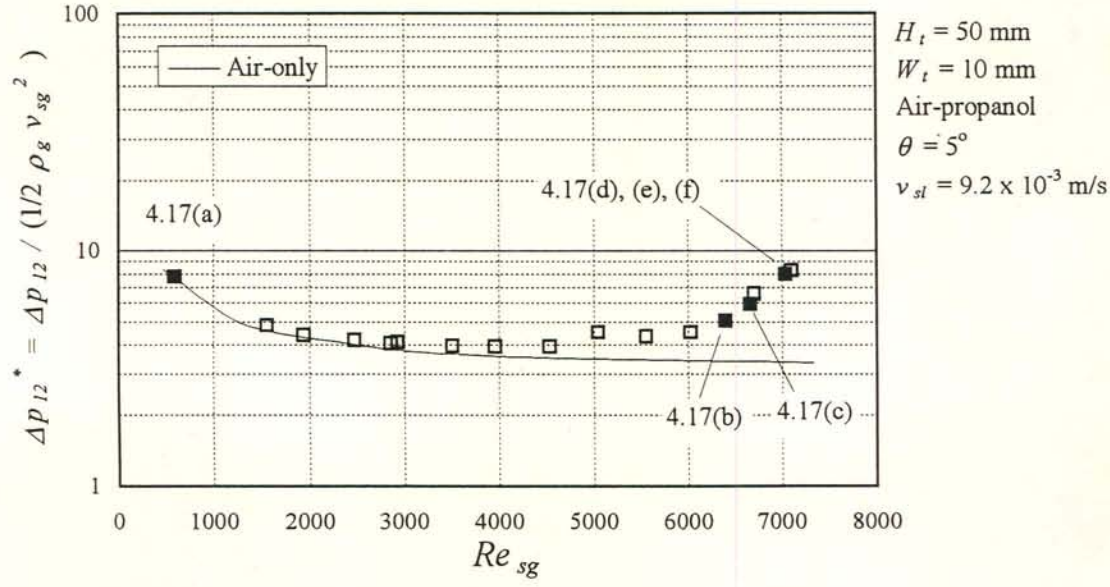

Figure 4.16(b): Dimensionless pressure drop measured across the sharp-edged gas entrance between points 1 and 2 for air-propanol flow in the 50 mm duct (10 mm wide). The solid symbols represent the gas flow rates at which photos, shown in figure 4.17, were taken.

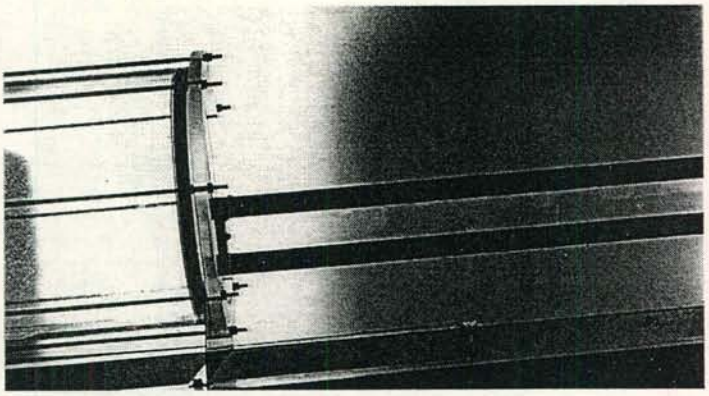

Figure 4.17(a): Air-propanol flow pattern inside the 50 mm (W_t = 10 mm) duct inclined at 5° to the horizontal. v_{sg} = 0.52 m/s, v_{sl} = 9.2 x 10^{-3} m/s, Re_{sg} = 591, Fr_{Hsg} = 0.0008.

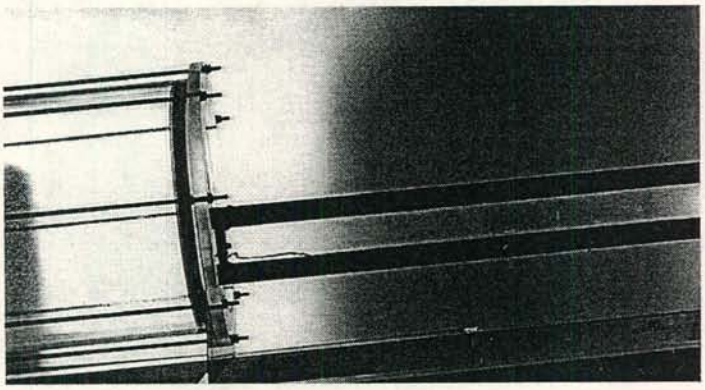

Figure 4.17(b): Air-propanol flow pattern inside the 50 mm (W_t = 10 mm) duct inclined at 5° to the horizontal. v_{sg} = 5.6 m/s, v_{sl} = 9.2 x 10^{-3} m/s, Re_{sg} = 6400, Fr_{Hsg} = 0.100.

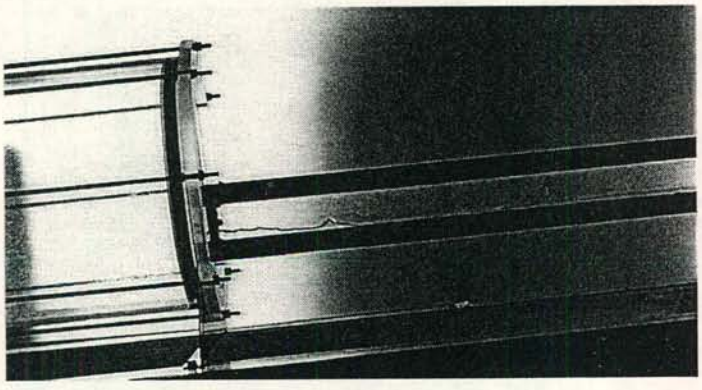

Figure 4.17(c): Air-propanol flow pattern inside the 50 mm duct (W_t = 10 mm) inclined at 5° to the horizontal. v_{sg} = 5.9 m/s, v_{sl} = 9.2 x 10^{-3} m/s, Re_{sg} = 6667, Fr_{Hsg} = 0.108.

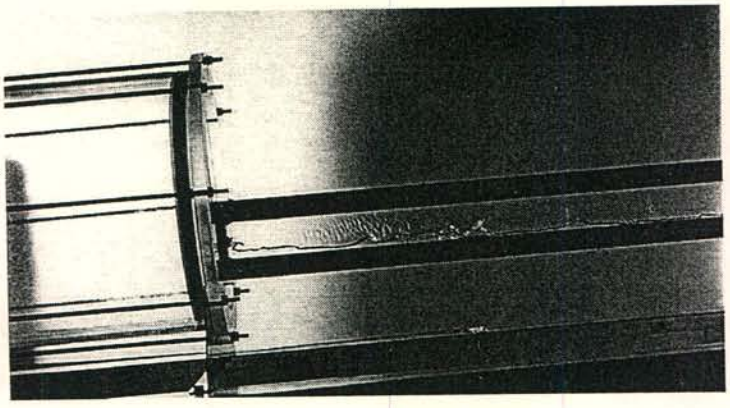

Figure 4.17(d): Air-propanol flow pattern inside the 50 mm duct (W_t = 10 mm) inclined at 5° to the horizontal. v_{sg} = 6.2 m/s, v_{sl} = 9.2 x 10^{-3} m/s, Re_{sg} = 7041, Fr_{Hsg} = 0.120.

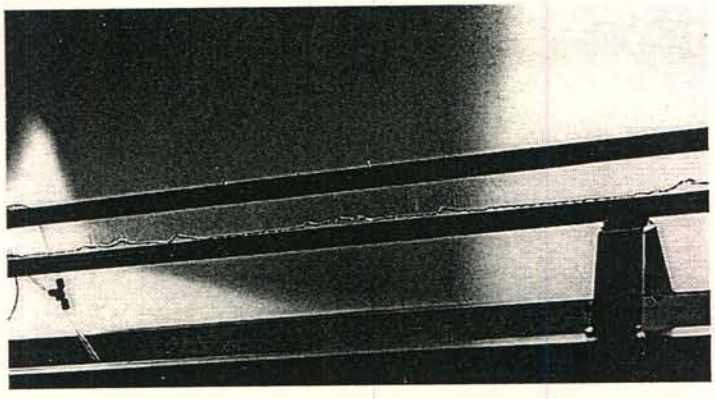

Figure 4.17(e): Air-propanol flow pattern inside the 50 mm duct (W_t = 10 mm) inclined at 5° to the horizontal. v_{sg} = 6.2 m/s, v_{sl} = 9.2 x 10^{-3} m/s, Re_{sg} = 7040, Fr_{Hsg} = 0.120.

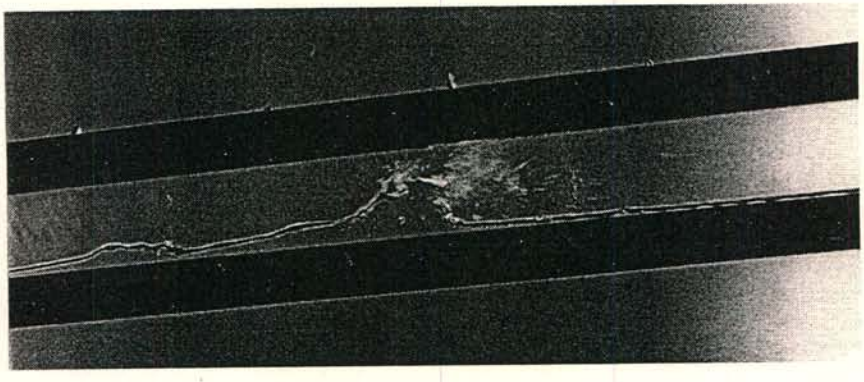

Figure 4.17(f): Air-propanol flow pattern inside the 50 mm duct (W_t = 10 mm) inclined at 5° to the horizontal. v_{sg} = 6.2 m/s, v_{sl} = 9.2 x 10^{-3} m/s, Re_{sg} = 7040, Fr_{Hsg} = 0.120.

4.4.2 Air-propanol flow inside the 100 mm duct

Flow patterns similar to those encountered in the 50 mm duct were observed in the case of the 100 mm duct. The pressure drop characteristics and the corresponding flow patterns are shown in figure 4.18 and 4.19 respectively. In figure 4.19(a) the superficial gas Reynolds number is 564 and the gas-liquid interface is perfectly smooth. The propanol drains in the groove at the bottom of the duct. The part of the test section seen in figure 4.19(a) is located between points 2 and 3. At a superficial gas Reynolds number of approximately 4500 small ripples are formed on the film. As the gas Reynolds number reaches 8500 single waves are formed close to point 2. Upon a small increase in the air flow rate single waves are also formed higher up the duct between points 2 and 3. A wave is shown in figure 4.19(b). Here the superficial gas Reynolds number is 9010. The frictional pressure gradient between points 2 and 3 begins to deviate from the single-phase prediction at the formation of the waves.

At the onset of wave formation they travel downwards but as the gas flow rate is increased, they become stationary, reverse direction of flow and travel upwards. Also, the rate at which the waves are formed increases with an increase in the air flow rate, as illustrated in figure 4.19(c) (Re_{sg} = 10490).

In figure 4.18(b) the pressure drop across the gas entrance rises above the single-phase pressure drop due to the increased liquid hold-up at the sharp-edged flange.

Eventually roll waves appear, which at times bridge the entire duct height as they are propelled upwards by the gas flow. Roll waves are shown in figures 4.19(d) and (e) (Re_{sg} = 11225).

The same sequence of flow patters were encountered in the 150 mm duct, when inclined at 5° to the horizontal. The maximum size of the roll waves was however approximately three quarters of the duct height and did not span across the entire height as in the case of the 50 and 100 mm ducts.

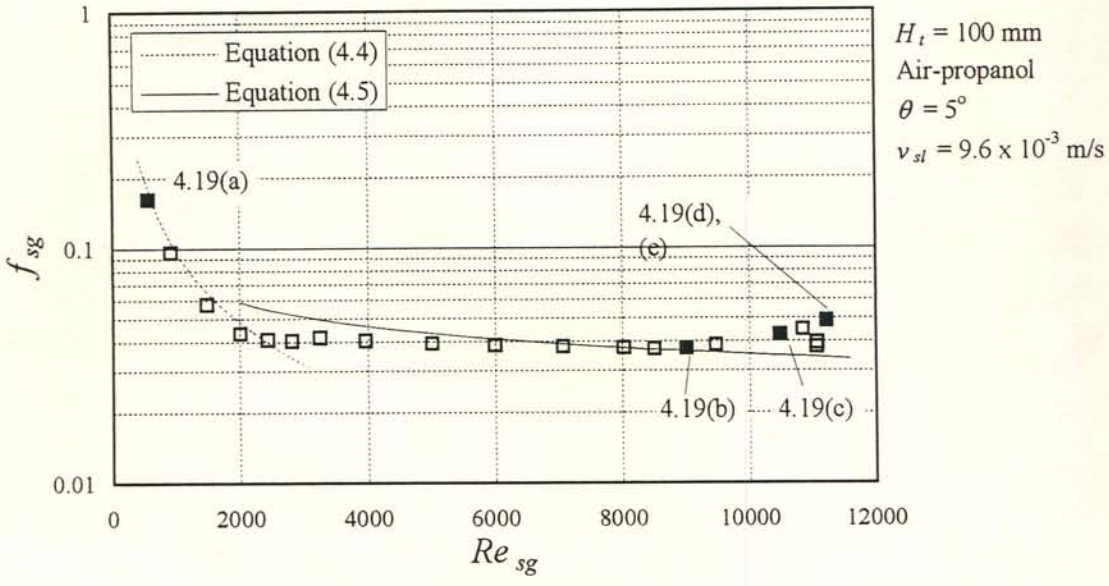

Figure 4.18(a): Two-phase friction factor for air-propanol flow in the 100 mm duct. The solid symbols represent the gas flow rates at which photos, shown in figure 4.19, were taken.

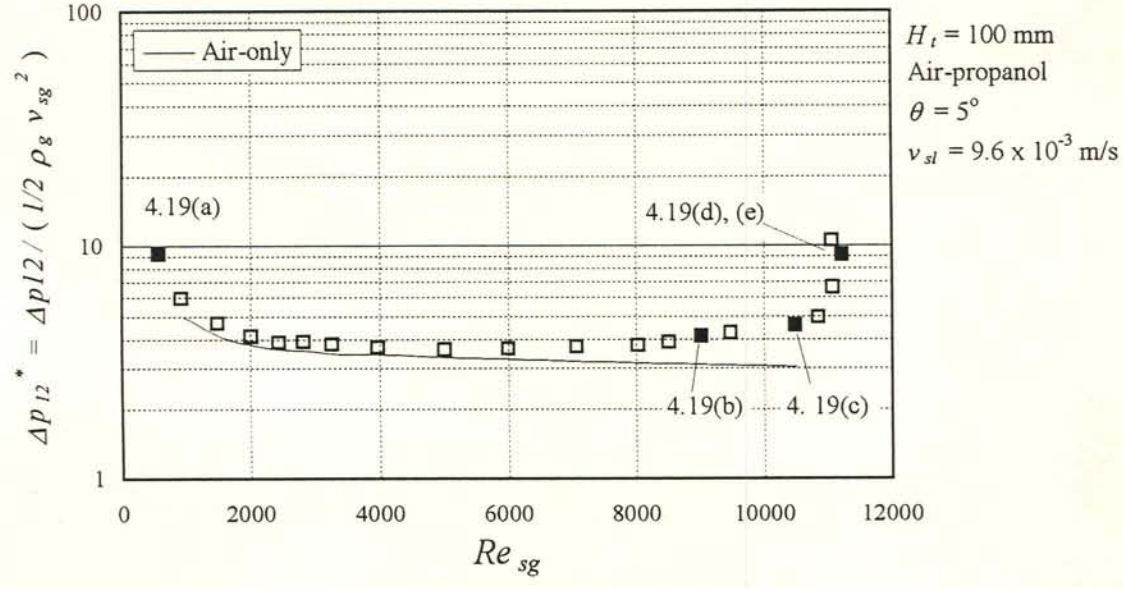

Figure 4.18(b): Dimensionless pressure drop, measured across the sharp-edged gas entrance between points 1 and 2, for air-propanol flow in the 100 mm duct. The solid symbols represent the gas flow rates at which photos, shown in figure 4.19, were taken.

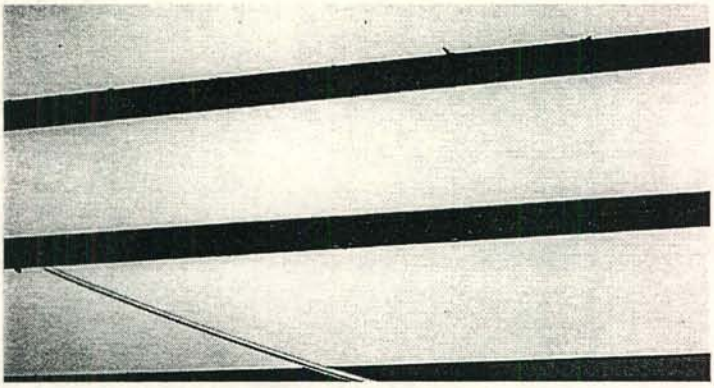

Figure 4.19(a): Air-propanol flow pattern inside the 100 mm duct inclined at 5° to the horizontal. v_{sg} = 0.47 m/s, v_{sl} = 9.6 x 10^{-3} m/s, Re_{sg} = 563, Fr_{Hsg} = 0.0003.

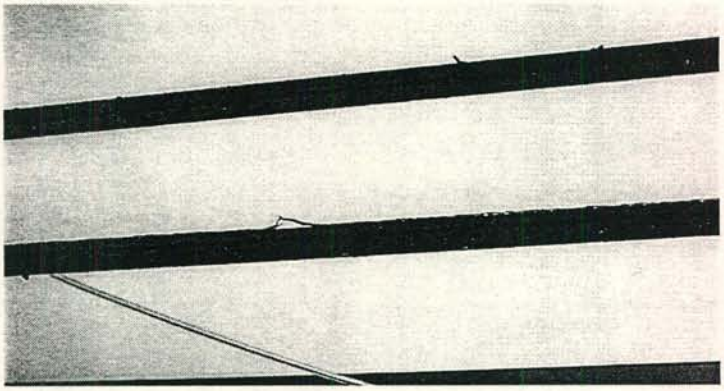

Figure 4.19(b): Air-propanol flow pattern inside the 100 mm duct inclined at 5° to the horizontal. v_{sg} = 7.6 m/s, v_{sl} = 9.6 x 10^{-3} m/s, Re_{sg} = 9010, Fr_{Hsg} = 0.089.

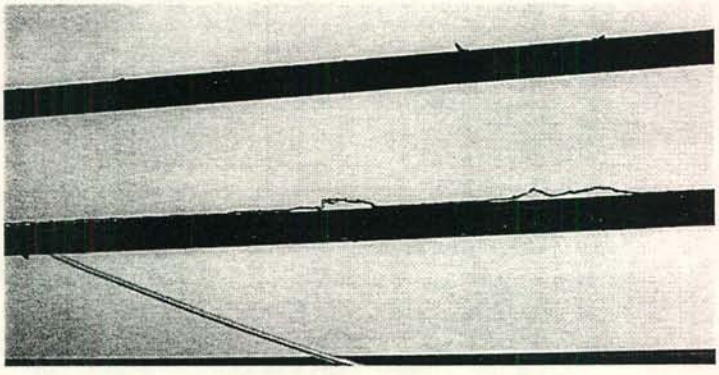

Figure 4.19(c): Air-propanol flow pattern inside the 100 mm duct inclined at 5° to the horizontal. v_{sg} = 8.8 m/s, v_{sl} = 9.6 x 10^{-3} m/s, Re_{sg} = 10490, Fr_{Hsg} = 0.120.

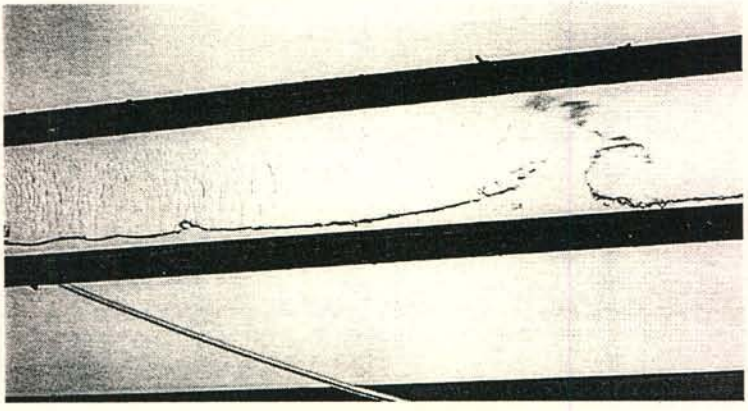

Figure 4.19 (d): Air-propanol flow pattern inside the 100 mm duct inclined at 5° to the horizontal. v_{sg} = 9.4 m/s, v_{sl} = 9.6 x 10^{-3} m/s, Re_{sg} = 11225, Fr_{Hsg} = 0.137.

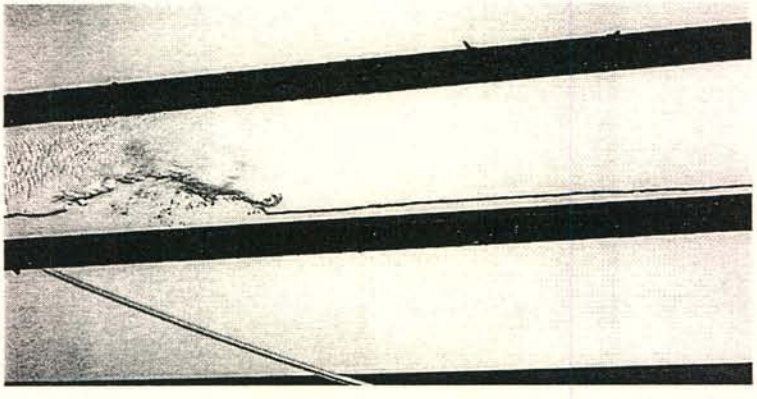

Figure 4.19(e): Air-propanol flow pattern inside the 100 mm duct inclined at 5° to the horizontal. v_{sg} = 9.4 m/s, v_{sl} = 9.6 x 10^{-3} m/s, Re_{sg} = 11225, Fr_{Hsg} = 0.137.

4.5 Flow patterns observed during vertical flow of air-propanol in the 50 mm duct (W_t = 10 mm)

The bottom plenum pressure for air-propanol during vertical flow, measured at point 1 relative to the ambient pressure, is shown in figure 4.20 in a dimensionless form. Photos of the corresponding flow patterns are given in figures 4.21 (a) to (i).

In figure 4.21(a) there is no gas flow and the propanol drains downwards in a wavy film, wetting the entire duct perimeter. At the sharp-edged flange most of the propanol drains at the shorter sides (aluminium spacers) of the duct into the plenum. The next photo was

taken at the onset of entrainment at the gas inlet (Re_{sg} = 3510). The droplet concentration is the highest just above the gas inlet and decreases in the direction of the gas flow as droplets are deposited on the draining film. The biggest droplets are deposited first, the smaller ones being carried further up the duct. At the onset of entrainment the gas velocity is insufficient to carry the drops all the way up past the sintered liquid inlet into the gas-liquid separator.

In figure 4.21(c) a rough film is formed at the bottom of the duct (Re_{sg} = 6121). The entrained droplets shown in figure 4.21(b) cannot be seen in figure 4.21(c) because their speed is too high to be captured on film at the shutter speed of 1/500 s employed. When comparing figures 4.21(a) and (c) it can be seen that the number of waves present on the film flowing down the acrylic plastic duct walls increases at the higher air flow rate. As the air velocity is further increased the rough film region grows upwards. This is illustrated in figures 4.21(d) and (e) taken at superficial gas Reynolds numbers of 6520 and 7140 respectively. A magnification of the rough film is shown in figure 4.21(f).

Once the rough film is formed the propanol does not drain continuously into the bottom plenum anymore. Liquid spurts sporadically exit the duct. A closer look at the region below the sharp-edged flange in figures 4.21(e), (g) and (h) shows that liquid always drains at one of the shorter sides into the plenum. The point of draining oscillates between the two aluminium spacers and during such change from one side to the other no liquid exits the bottom of the duct, as shown in figure 4.21(e).

At the higher gas flow rates rotating gas-liquid mixtures or vortices, similar to those observed for 60° inclined flow, are formed at the gas inlet. While there is only one direction of rotation possible in the case of inclined flow where the liquid always drains at the bottom aluminium spacer, the characteristic vortex can rotate in two directions during vertical flow, depending on the location where the liquid drains into the bottom plenum when the vortex is formed. If it drains on the left-hand side as in figure 4.21(h), the resulting rotation would be anti-clockwise, while it is clockwise if the liquid drains on the right-hand side. Two such vortices can be seen in figure 4.21 (i) (Re_{sg} = 8106), one just being formed at the sharp-edged flange and the other one approximately 250 mm

above. If the point of draining changes after the formation of a vortex, the next one rotates in the opposite direction.

At the flooding air flow rate the film is rough along the entire length of the duct from the sharp-edged flange to the liquid inlet. For low liquid flow rates, liquid is carried above the inlet sinter by upward vortex-type flow at flooding. The carry-over of liquid coincides with a sharp increase in the bottom plenum pressure, as depicted in figure 4.20. In the case of the 60° inclined ducts the "diameter" of the vortices approach the duct height at flooding, but this is not the case for vertical flow. Here the vortex size is some fraction of the duct height. The exact size could not be distinguished.

At higher liquid flow rates flooding occurs due to split flow at the inlet sinter before liquid is carried above the point of liquid injection by vortex type flow. Then flooding does not necessarily coincide with a sharp increase in pressure drop anymore.

The same flow modes were encountered in the 100 mm duct. Once again the exact size of the vortices could not be established.

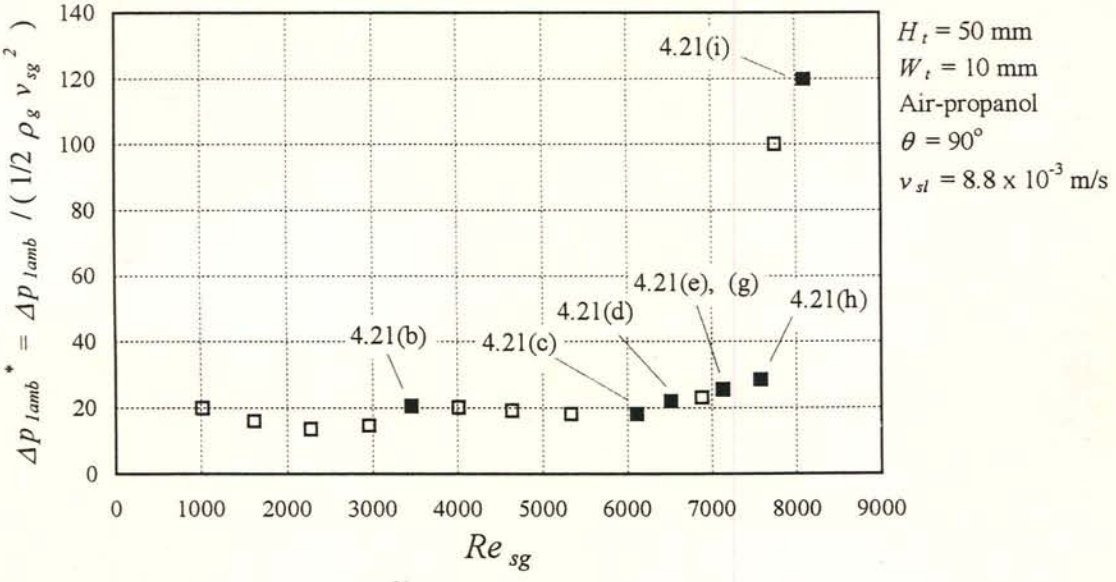

Figure 4.20: Dimensionless bottom plenum pressure (relative to ambient pressure) for air-propanol flow in the 50 mm duct (W_t = 10 mm). The solid symbols represent the gas flow rates at which photos, shown in figure 4.21 , were taken.

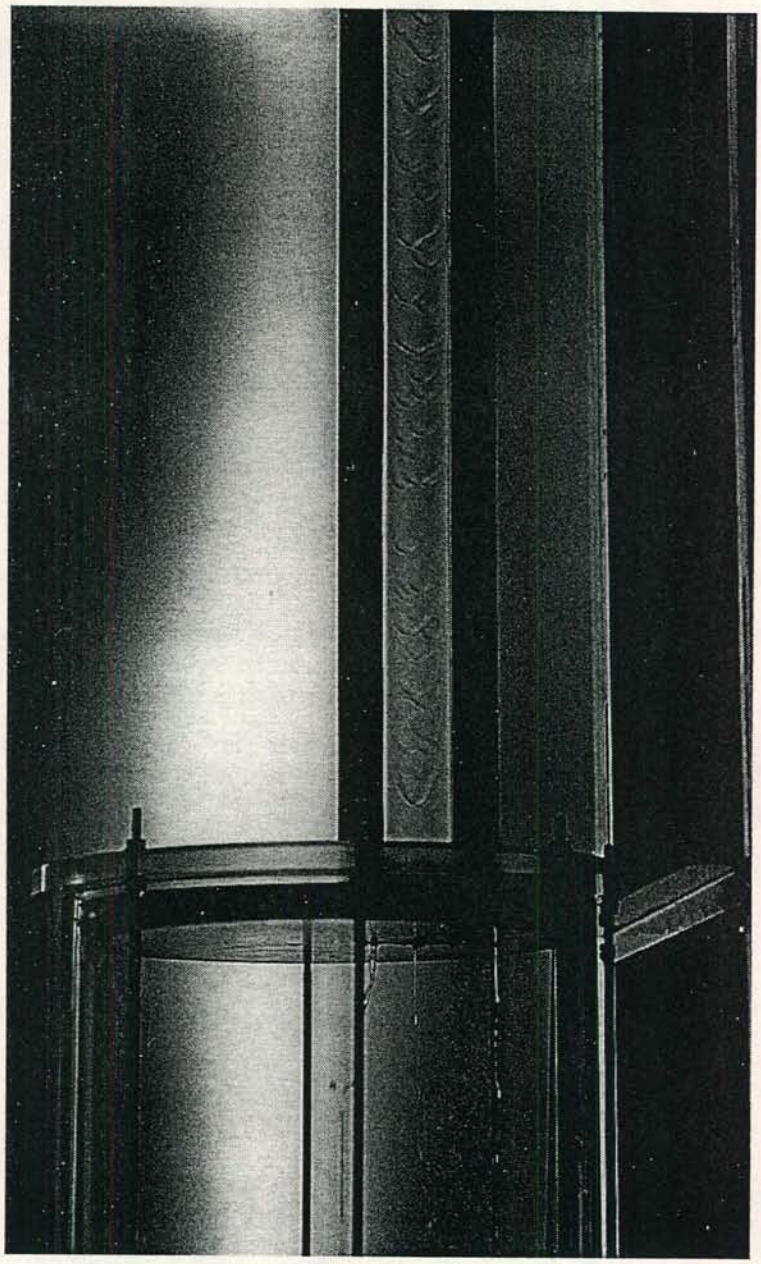

Figure 4.21(a): Air-propanol flow pattern inside the 50 mm duct (W_i = 10 mm) inclined at 90° to the horizontal. v_{sg} = 0 m/s, v_{sl} = 8.8 x 10^{-3} m/s, Re_{sg} = 0, Fr_{Hsg} = 0.

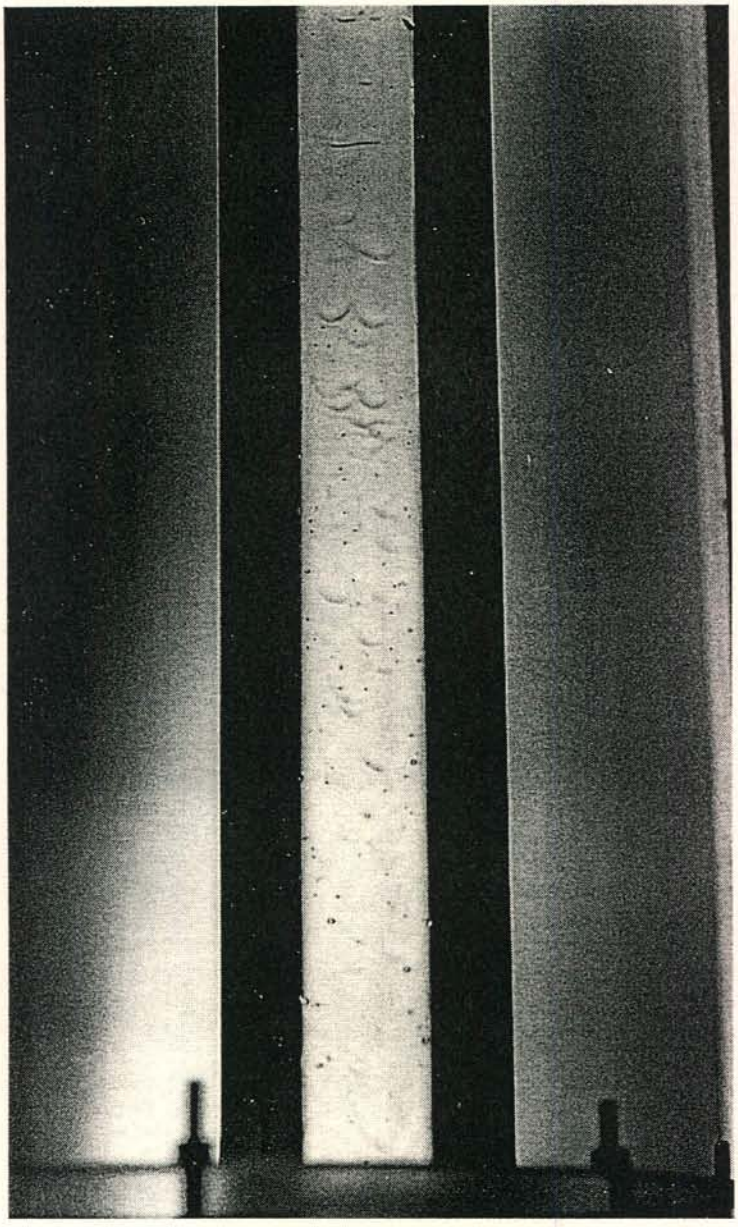

Figure 4.21(b): Air-propanol flow pattern inside the 50 mm duct (W_t = 10 mm) inclined at 90° to the horizontal. v_{sg} = 3.0 m/s, v_{sl} = 8.8 x 10^{-3} m/s, Re_{sg} = 3510, Fr_{Hsg} = 0.029.

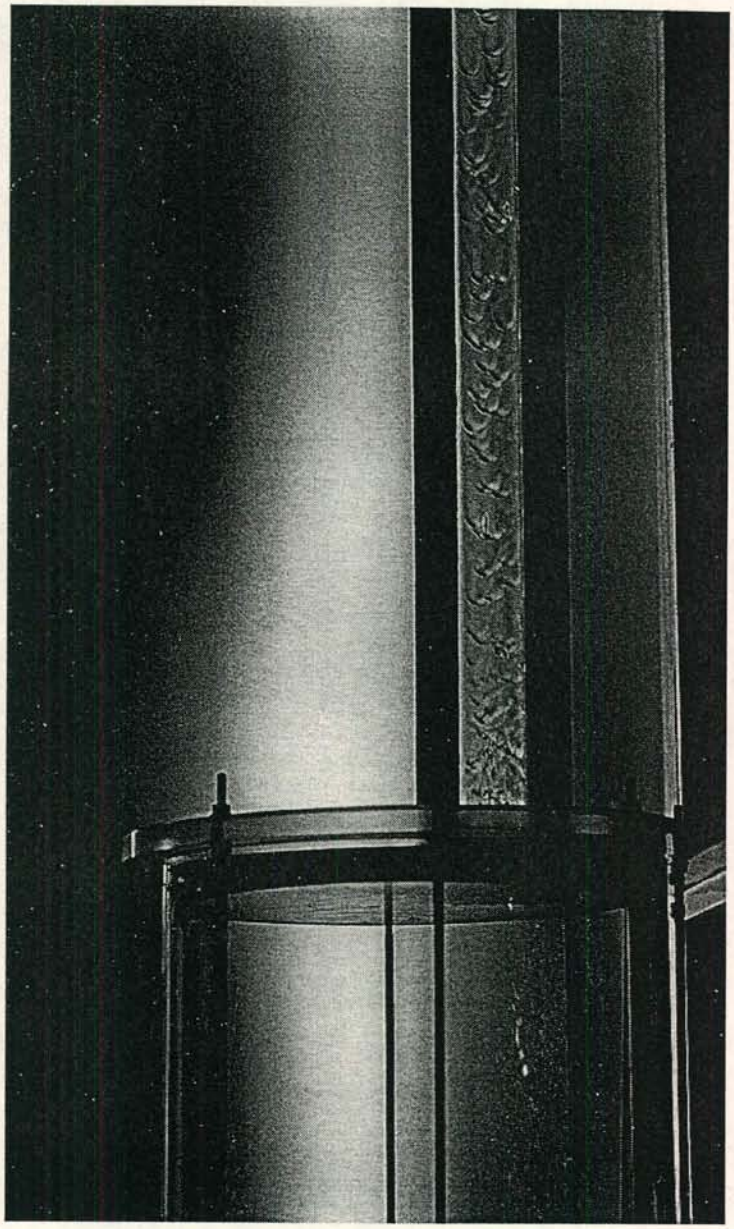

Figure 4.21(c): Air-propanol flow pattern inside the 50 mm duct (W_t = 10 mm) inclined at 90° to the horizontal. v_{sg} = 5.3 m/s, v_{sl} = 8.8 x 10^{-3} m/s, Re_{sg} = 6121, Fr_{Hsg} = 0.088.

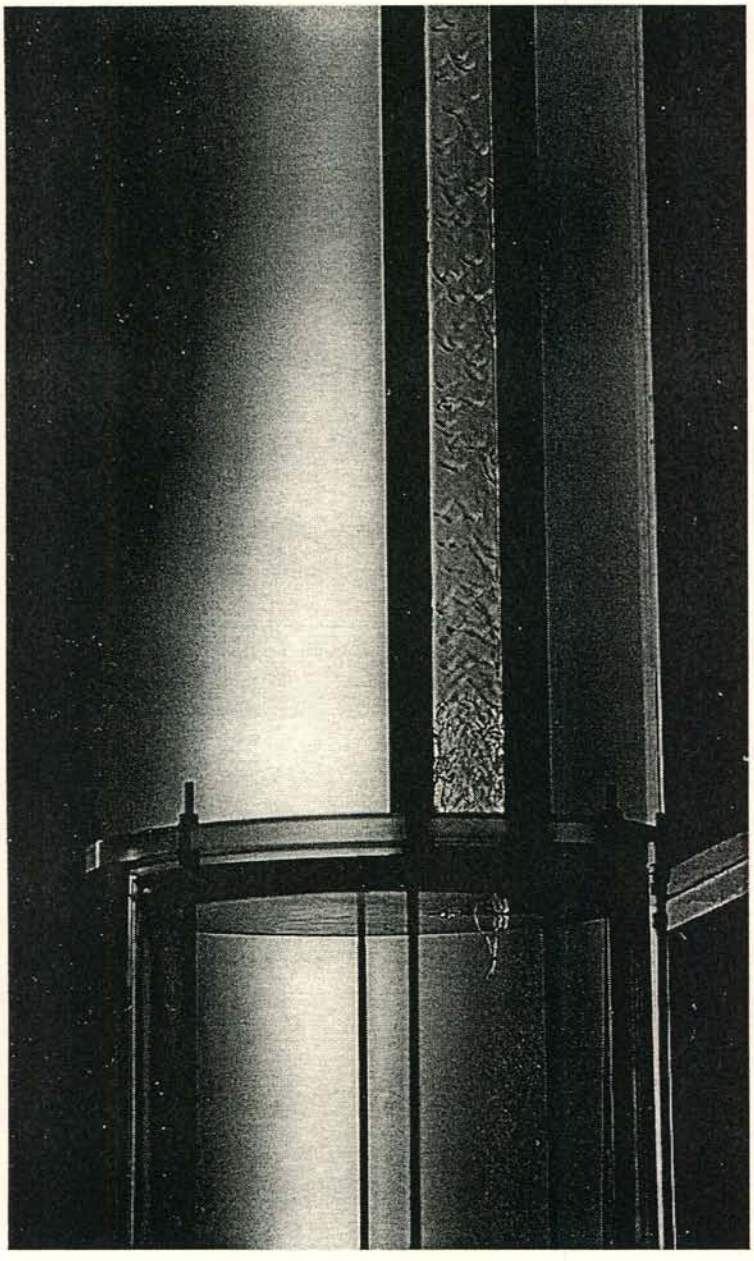

Figure 4.21(d): Air-propanol flow pattern inside the 50 mm duct (W_t = 10 mm) inclined at 90° to the horizontal. v_{sg} = 5.6 m/s, v_{sl} = 8.8 x 10^{-3} m/s, Re_{sg} = 6520, Fr_{Hsg} = 0.100.

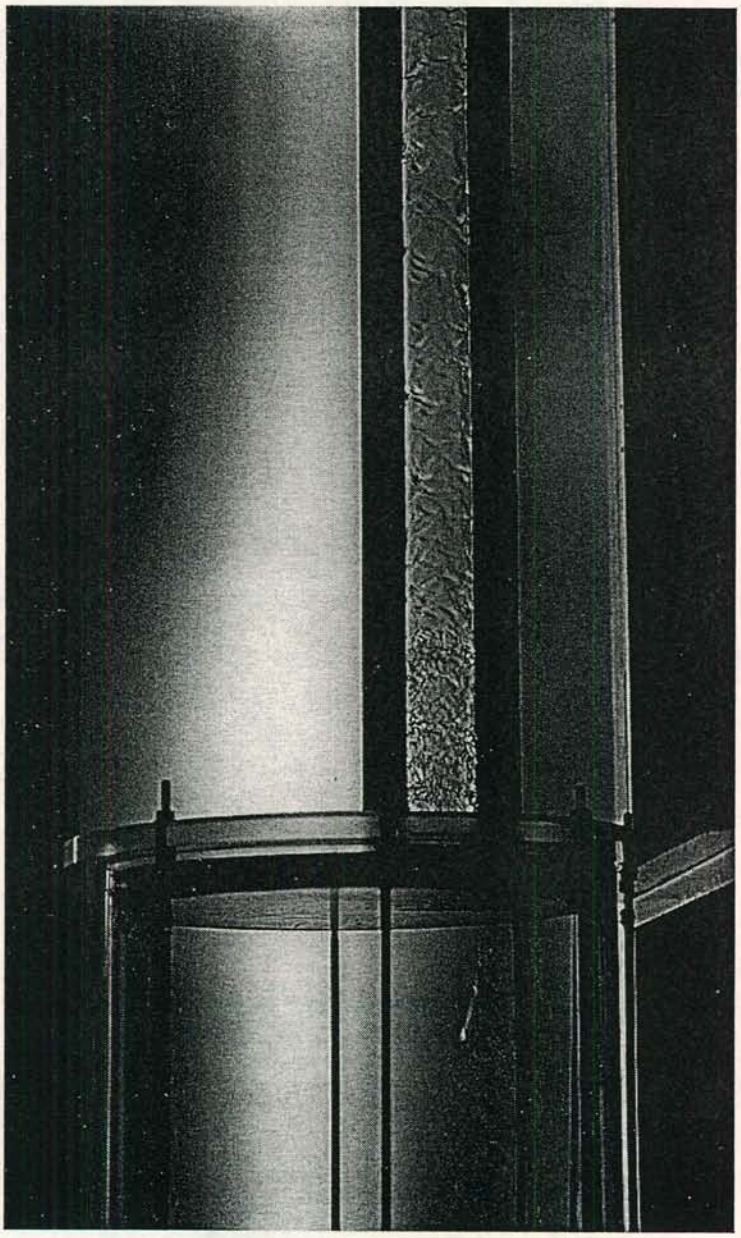

Figure 4.21(e): Air-propanol flow pattern inside the 50 mm duct (W_t = 10 mm) inclined at 90° to the horizontal. v_{sg} = 6.1 m/s, v_{sl} = 8.8 x 10^{-3} m/s, Re_{sg} = 7140, Fr_{Hsg} = 0.112.

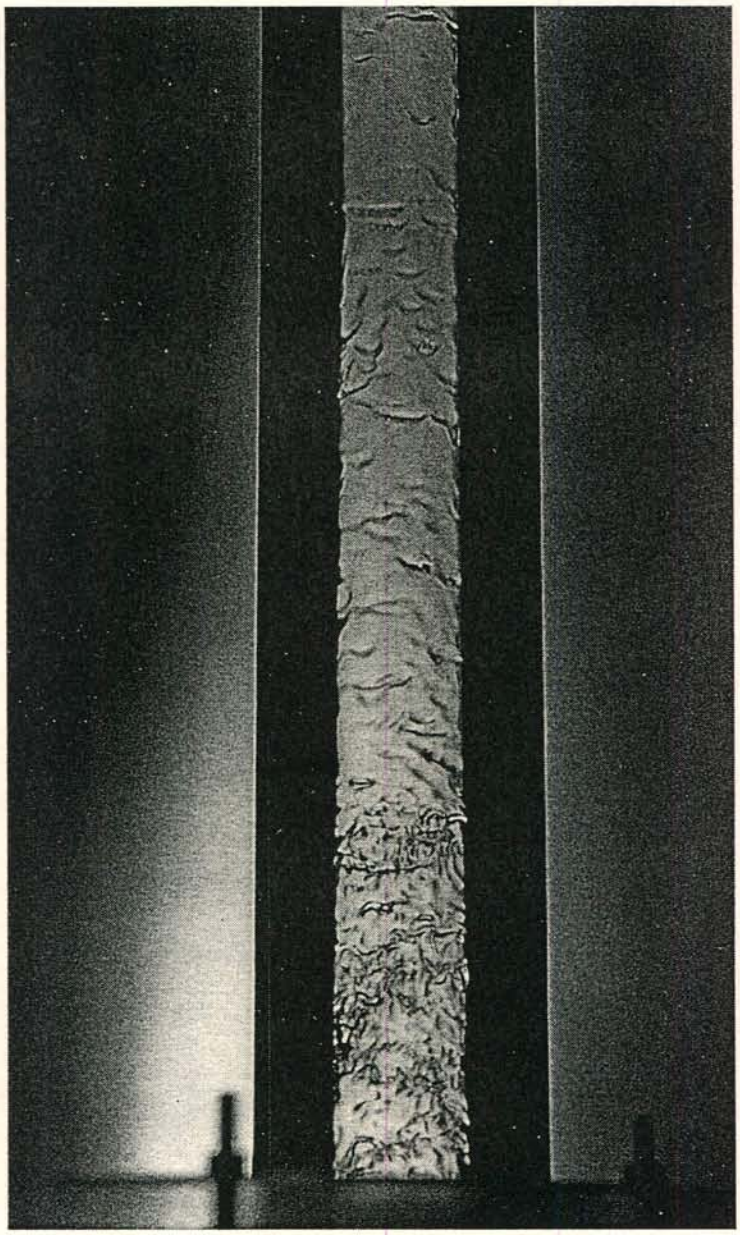

Figure 4.21(f): Air-propanol flow pattern inside the 50 mm duct (W_t = 10 mm) inclined at 90° to the horizontal. v_{sg} = 5.3 m/s, v_{sl} = 8.8 x 10^{-3} m/s, Re_{sg} = 6091, Fr_{Hsg} = 0.088.

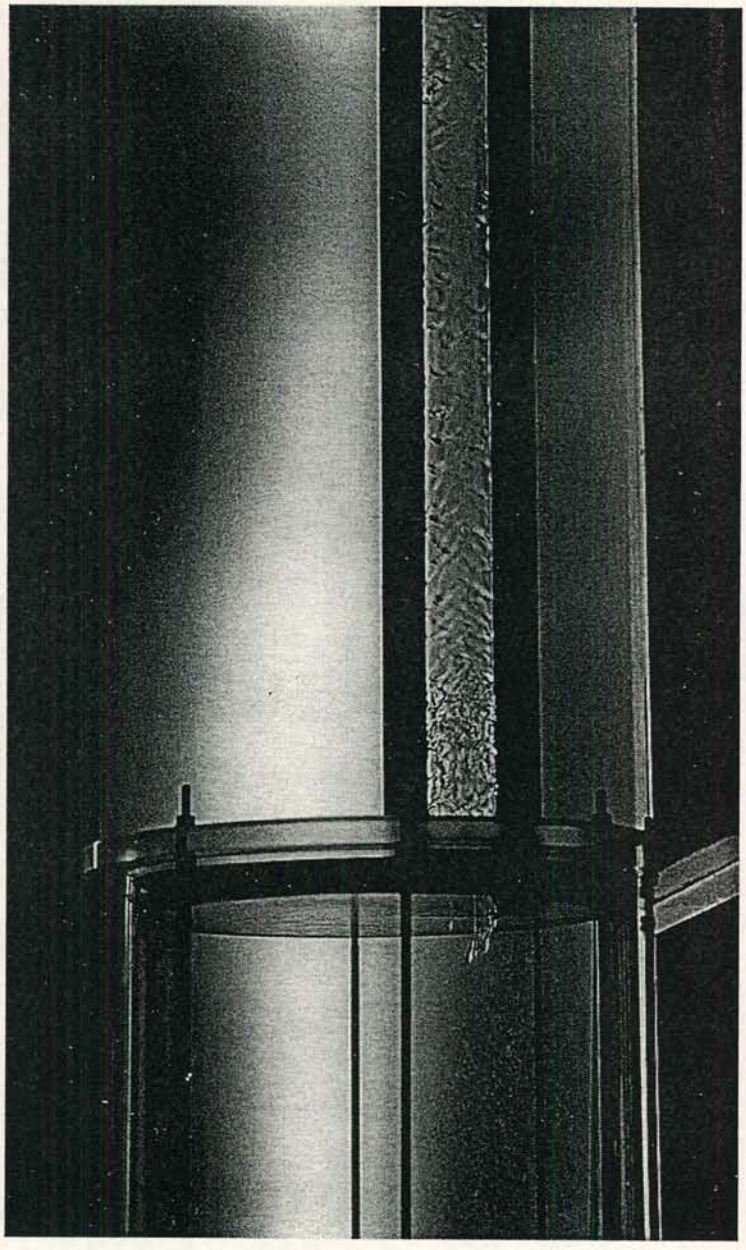

Figure 4.21 (g): Air-propanol flow pattern inside the 50 mm duct (W_t = 10 mm) inclined at 90° to the horizontal. v_{sg} = 6.1 m/s, v_{sl} = 8.8 x 10^{-3} m/s, Re_{sg} = 7140, Fr_{Hsg} = 0.112.

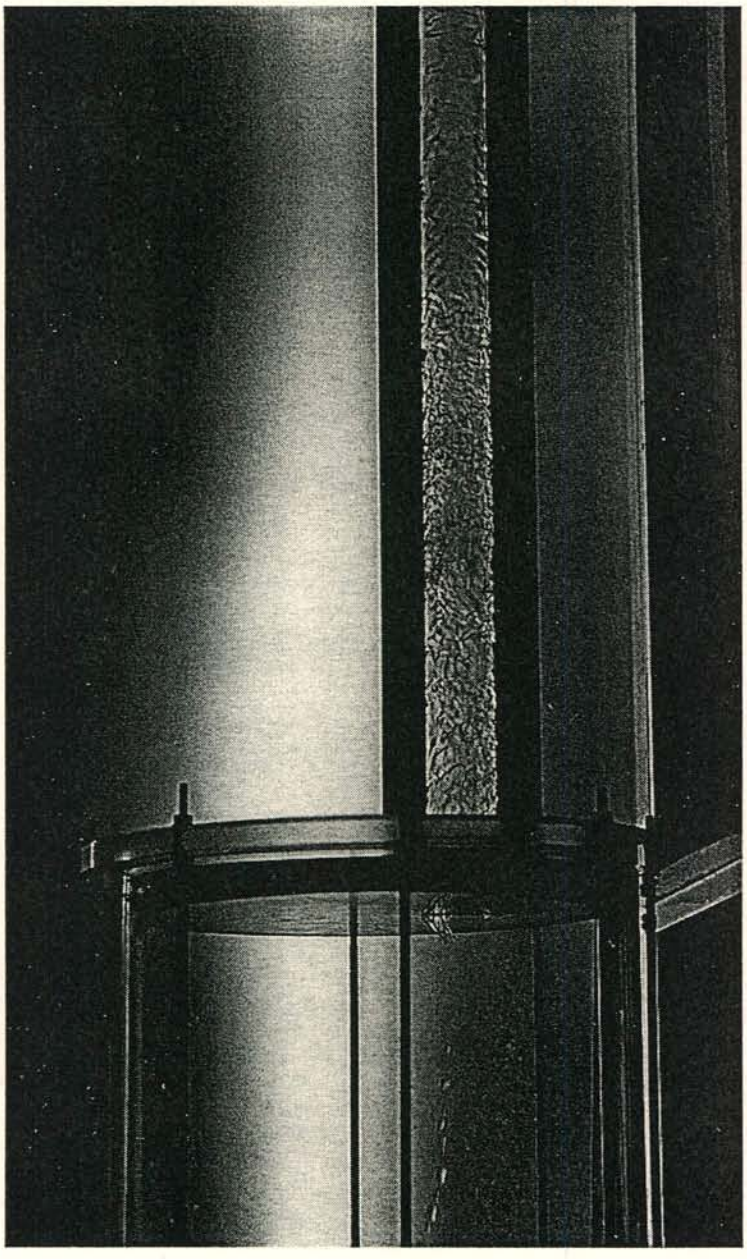

Figure 4.21 (h): Air-propanol flow pattern inside the 50 mm duct (W_t = 10 mm) inclined at 90° to the horizontal. v_{sg} = 6.5 m/s, v_{sl} = 8.8 x 10^{-3} m/s, Re_{sg} = 7585, Fr_{Hsg} = 0.135.

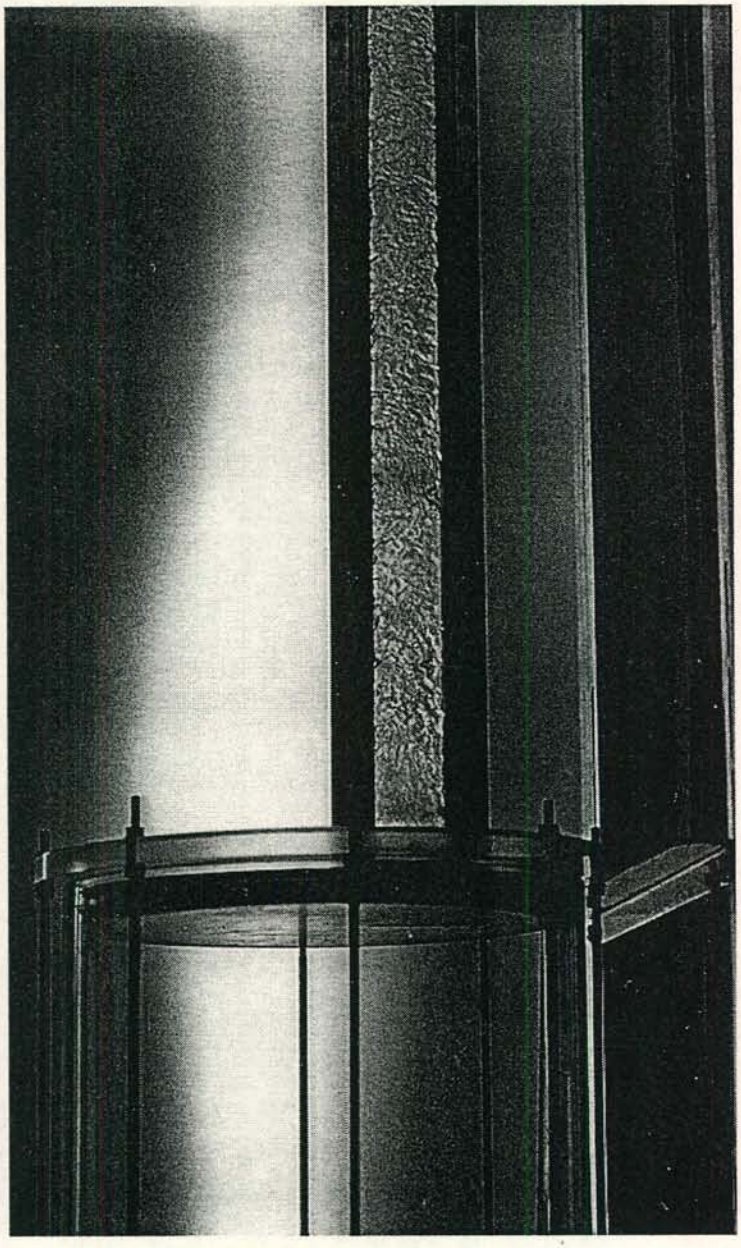

Figure 4.21(i): Air-propanol flow pattern inside the 50 mm duct (W_t = 10 mm) inclined at 90° to the horizontal. v_{sg} = 6.8 m/s, v_{sl} = 8.8 x 10^{-3} m/s, Re_{sg} = 8106, Fr_{Hsg} = 0.151.

4.6 The effect of the duct inclination on the flow patterns and the pressure drop

At small inclinations the stratified flow is perfectly smooth at zero gas flow rate and waves are formed once a gas is flowing over the film. Eventually roll waves are formed and the duct floods. The flooding gas flow rates are small for near horizontal flow causing the gas-liquid interactions to be less intensive.

At higher inclinations, typically 10° and more, the liquid film is always wavy in the absence of gas flow. The downward speed of the waves increases as the duct inclination is increased. While at low gas flow rates the waves travel downwards, they become stationary as the gas flow is increased and subsequently, at sufficiently high gas velocities, they travel upwards. At inclinations of approximately 40° and more no such reversal of the direction of wave motion is observed. Here the waves grow in size as they travel downwards and at a certain gas flow rate the waves suddenly bridge the duct and are immediately dispersed by the gas flow, causing entrainment. This instant bridging occurred especially at higher liquid flow rates ($\approx$ 1 *l*/min and more) but was not so well defined at lower liquid flow rates.

At inclinations of 2 and 5° to the horizontal roll waves are present at flooding but at inclinations of 10° and more the characteristic vortex-type flow is formed, the intensity of rotation growing stronger as the duct inclination is increased. The roll waves always travel upwards upon their formation while a vortex can remain stationary just above the sharp-edged flange, or move upwards and downwards in an oscillating mode causing the flow above the gas inlet to be very transient.

The rate of entrainment is related to the gas velocity. At small inclinations, where flooding takes place at relatively low gas flow rates, entrainment is weaker and the onset of entrainment usually occurs when roll waves are formed and droplets are torn off the wave crests. In other words the onset of entrainment coincides with flooding. At higher inclinations ($> \approx 10°$) droplets are entrained at the gas inlet prior to the formation of the vortices and/or flooding. The entrainment associated with the vortex-type flow is much stronger than for the roll waves present at smaller inclinations. Also, at higher

inclinations droplets are torn off the downward travelling waves prior to flooding, which is not the case for the single waves formed at small inclinations.

The pressure drop ratio and the two-phase entrance pressure drop coefficient for air-water and air-propanol flow at various inclinations are shown in figures 4.22 and 4.23. At low gas flow rates in the Reynolds number region the duct inclination has no effect on the pressure gradient. The gas Froude number at the sharp increase in pressure drop increases, however, as the duct inclination is increased. This trend is stronger at smaller inclinations ($2° < \theta < 20°$) and becomes weaker at higher inclinations. The gravity force acting on the liquid in the direction of flow is proportional to sin (θ). Thus, the change in gravity force acting on the liquid due to a change in inclination is bigger at small inclinations, which explains the observed trend.

The influence of the duct height on the pressure gradient and the entrance pressure drop as found for an inclination of 60° to horizontal, is the same for inclinations from near horizontal to near vertical flow. The two-phase friction factor for the 50 (W_t = 10 mm), 100 and the 150 mm duct inclined at 2° is plotted in figures 4.24 (a) and (b) in terms of the superficial gas Reynolds number and the superficial gas densimetric Froude number respectively. Similar plots of the two-phase entrance pressure drop coefficient are given in figures 4.25(a) and (b). In both cases the densimetric Froude number based on the duct height becomes the governing dimensionless group at higher gas flow rates.

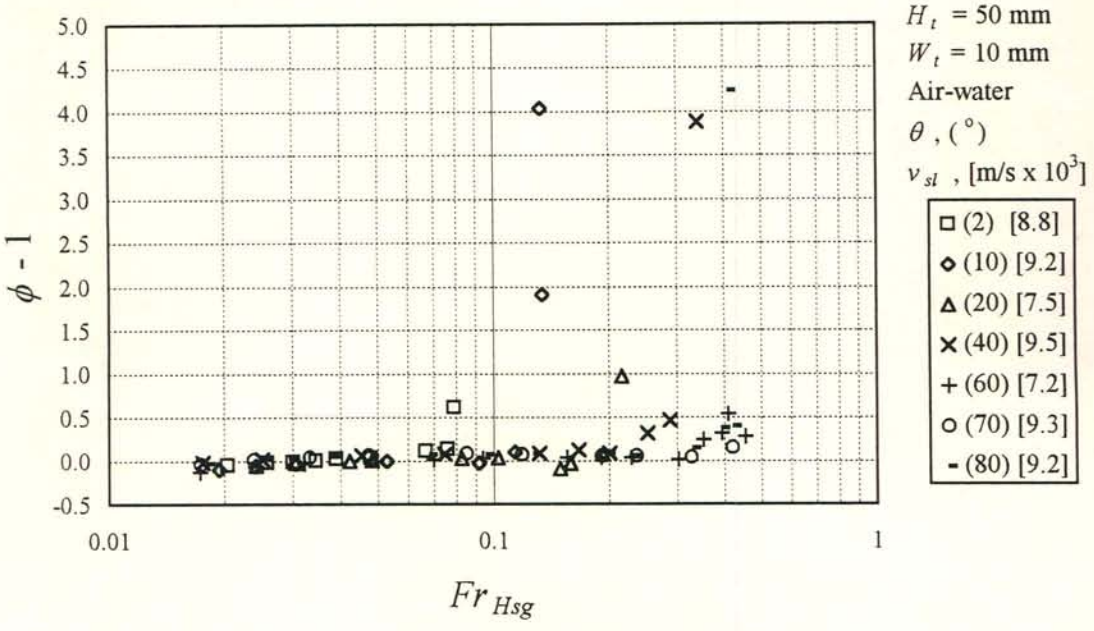

Figure 4.22 (a): Pressure gradient ratio for air-water flow inside the 50 mm duct (W_t = 10 mm) at various duct inclinations. Data: Short test section.

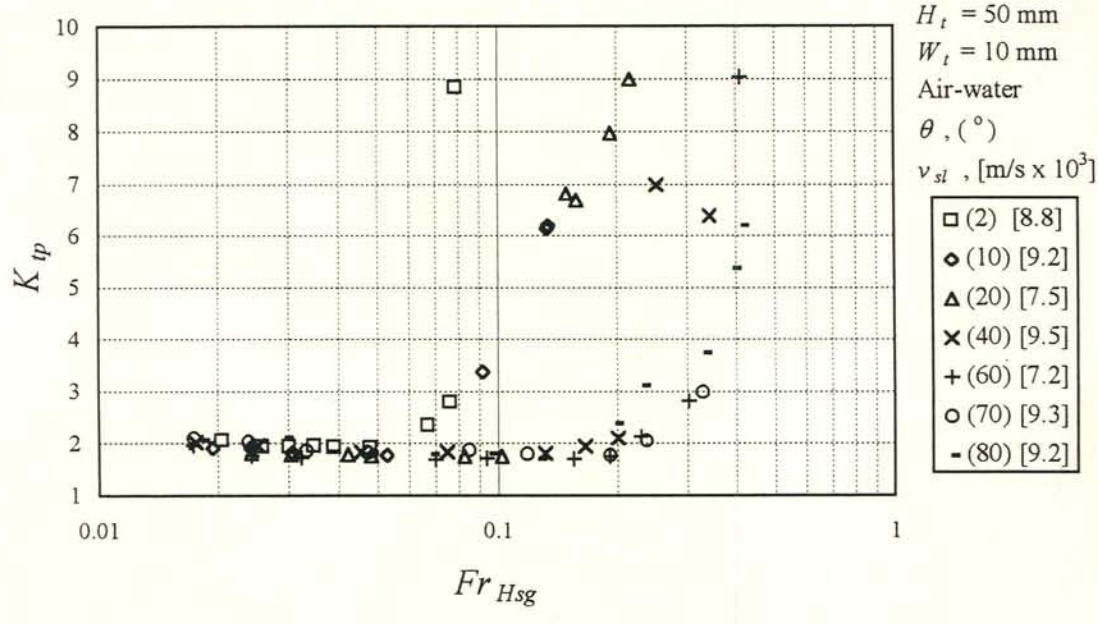

Figure 4.22 (b): Two-phase entrance pressure drop coefficient for air-water flow inside the 50 mm duct at various duct inclinations. Data: Short test section.

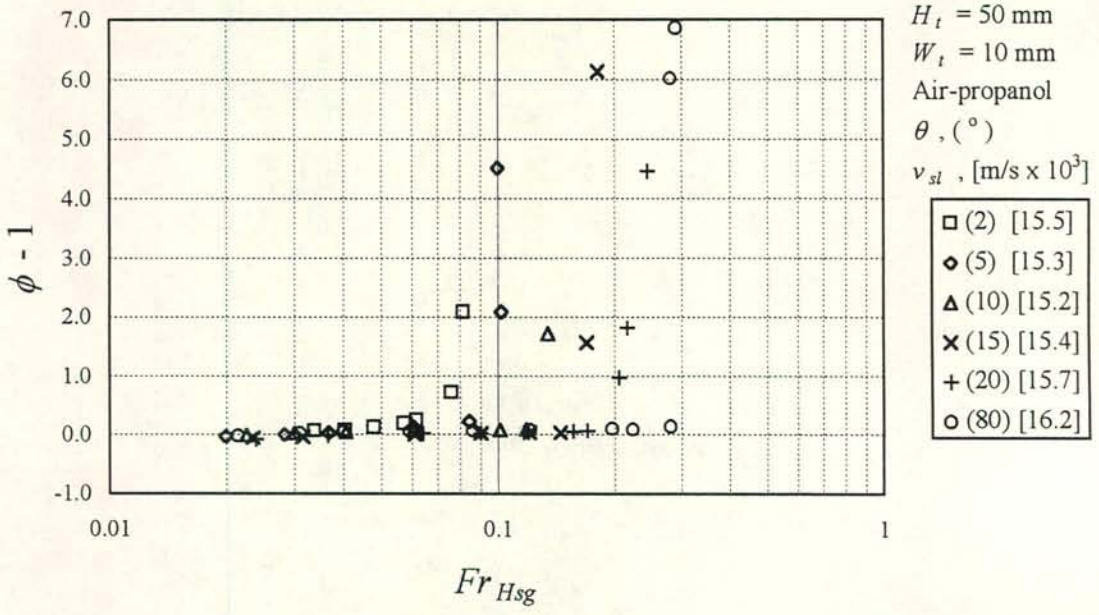

Figure 4.23 (a): Pressure gradient ratio for air-propanol flow inside the 50 mm duct at various duct inclinations. Data: Short test section.

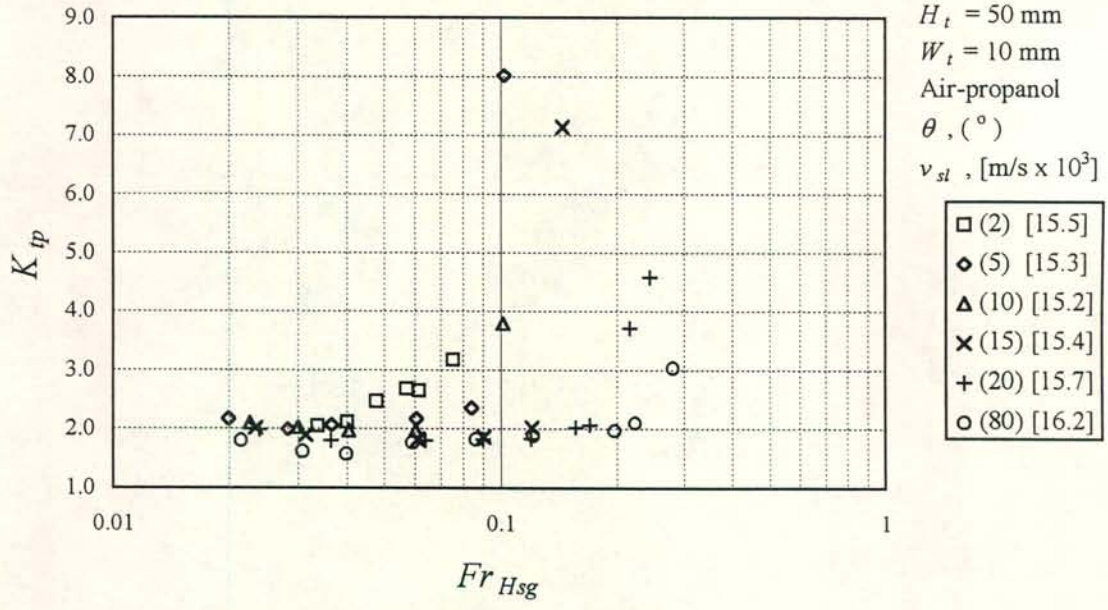

Figure 4.23 (b): Two-phase entrance pressure drop coefficient for air-water flow inside the 50 mm duct at various duct inclinations. Data: Short test section.

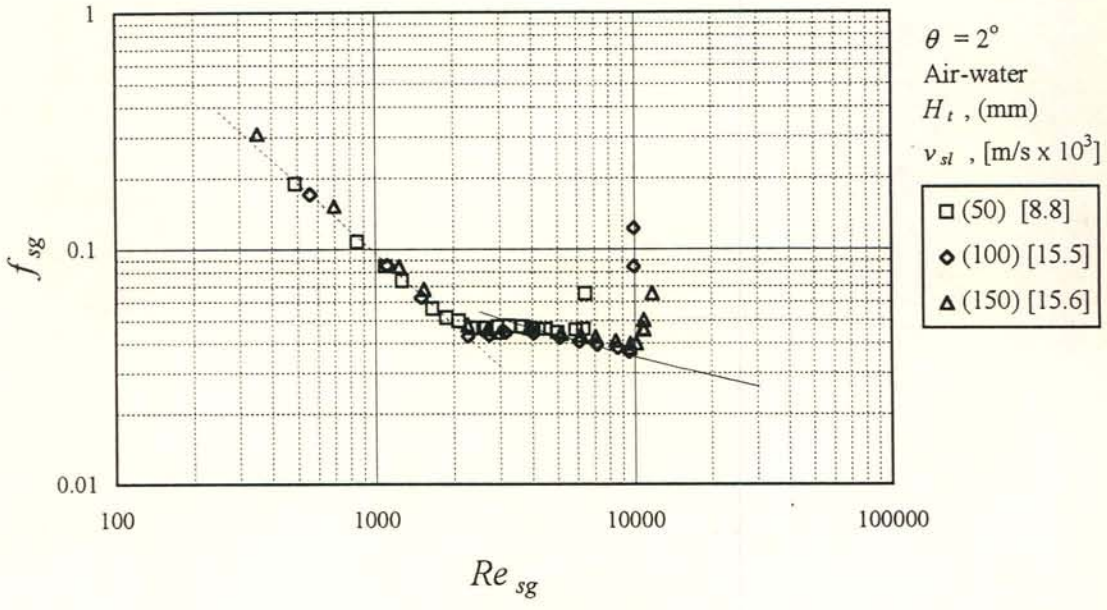

Figure 4.24 (a): Two-phase friction factor for air-water flow measured for three different duct geometries at an inclination of 2° to the horizontal, plotted against Re_{sg}. The width of the 50 mm duct is 10 mm. Broken and solid line: Laminar and turbulent single-phase friction factor. Data: Short test section

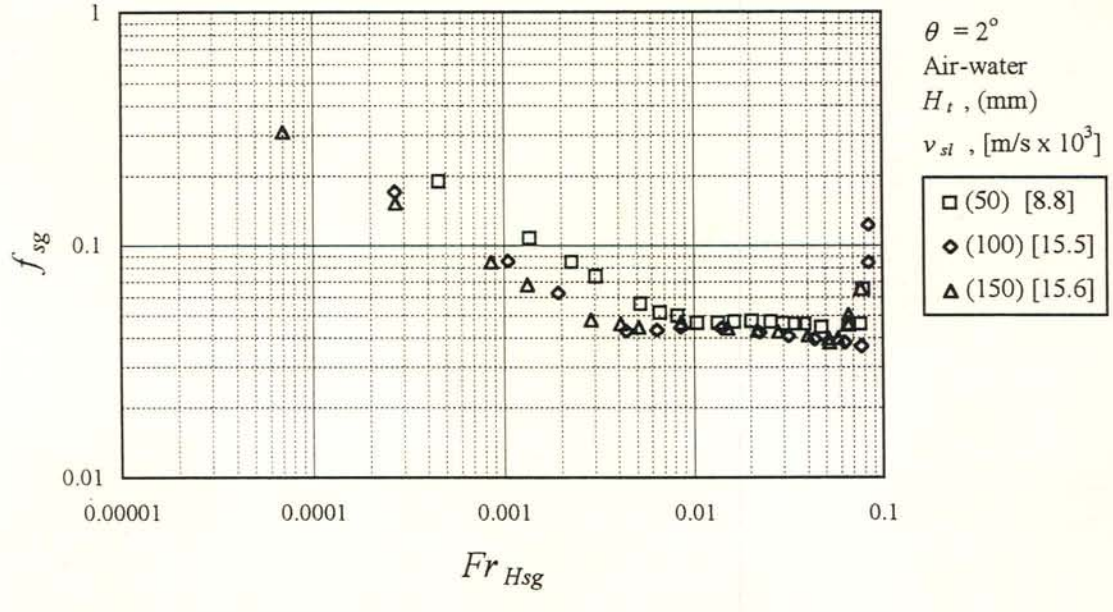

Figure 4.24 (b): The pressure gradient data shown in figure 4.24 (b) plotted against the superficial densimetric gas Froude number.

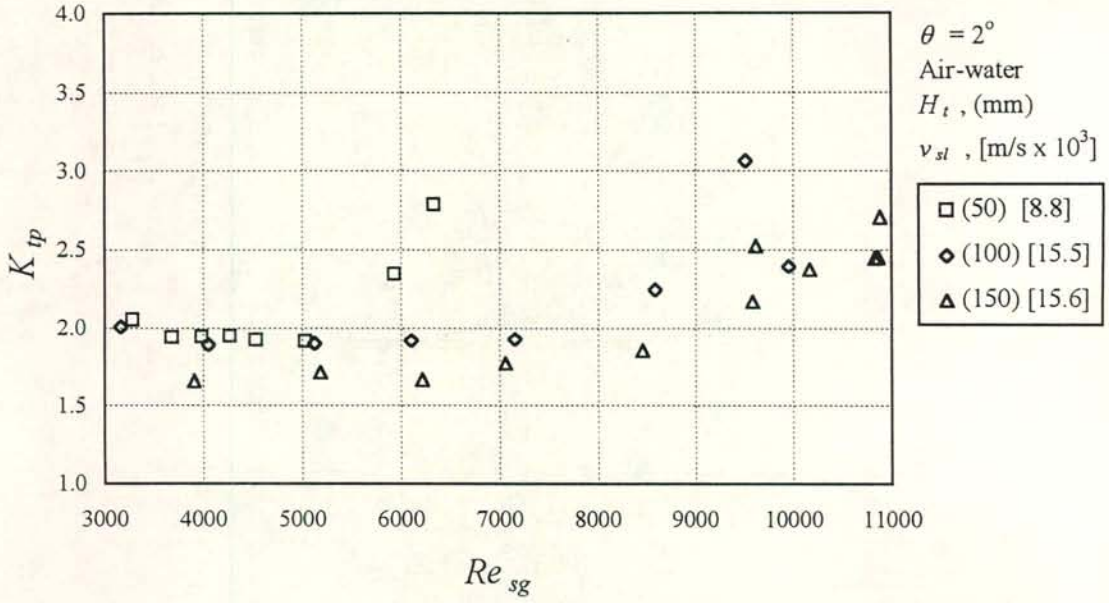

Figure 4.25 (a): Two-phase entrance loss coefficient for air-water flow measured for three different duct geometries at an inclination of 2° to the horizontal, plotted against the superficial gas Reynolds number. The width of the 50 mm duct is 10 mm. The air flow is fully turbulent. Data: Short test section.

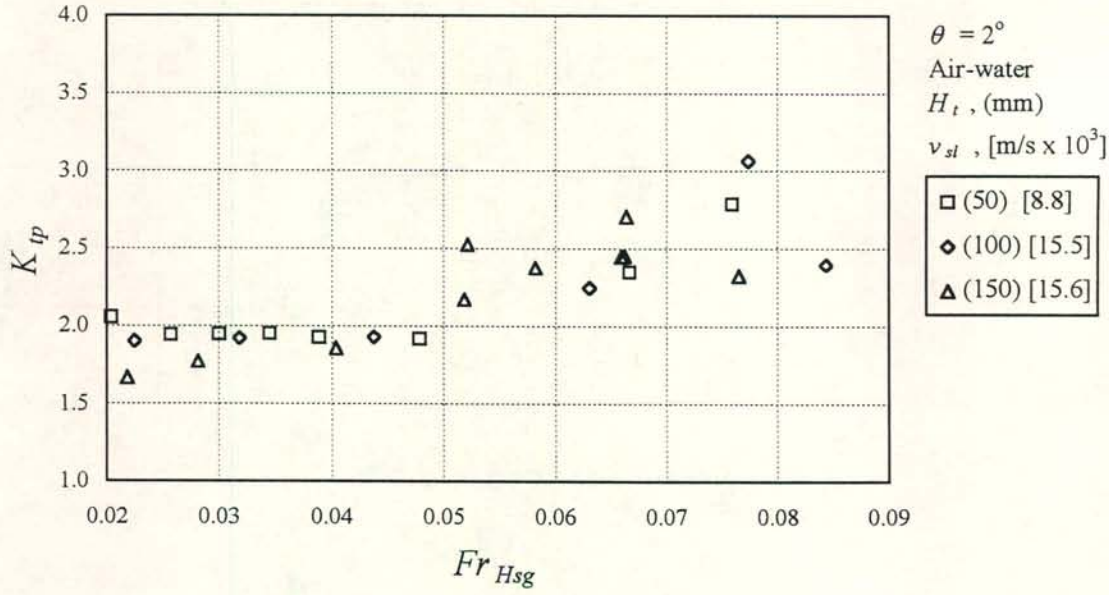

Figure 4.25 (b): The entrance pressure drop data of figure 4.25 (a) plotted in terms of the superficial densimetric gas Froude number. The gas flow is fully turbulent.

4.7 The transient nature of gas-liquid counterflow at intermediate angles

It has been mentioned in previous sections that once a vortex-type flow is formed at the gas inlet, the flow becomes transient. This is a result of the continuous formation and dispersion of vortices. At sufficiently high gas flow rates the vortices translate up and down in the region ($\approx$ 0.5 m) above the gas inlet. Eventually vortices enter the region between points 2 and 3 causing temporary high pressure gradients inside the test section.

For a better illustration of this transient behaviour, the pressure drop across the entrance Δp_{12} and the pressure drop between points 2 and 3 Δp_{23} was monitored over time at constant fluid flow rates. These transient tests were carried out at various gas flow rates, from inside the laminar gas flow region up to flooding.

The results of such a set of transient tests are shown in figures 4.26(a) to (h). In figures 4.26(a) and (b) the flow is steady and only small variations in the measured pressure differentials are observed. In figure 4.26(c) the gas starts to disturb the liquid flow at the gas inlet causing the entrance pressure drop to vary with time, while the pressure drop inside the test section between points 2 and 3 is still fairly constant. In figures 4.26(d) to (f) entrainment and wetting develop at the sharp-edged gas inlet and a vortex is formed. At this stage the size of the vortex is still just a fraction of the duct height. The conditions at which the vortex spans the entire duct height (such as in figure 4.7 e) are illustrated in figure 4.26(g) where the strong pressure pulses above the gas inlet are detected. Here the vortices do not yet reach region 2-3. The flow is stratified wavy between points 2 and 3 and Δp_{23} is still fairly steady. In figure 4.26(g) the vortices are propelled to the top end of the test section and flooding occurs. Note that a peak in the pressure drop across the gas entrance is followed by a pressure pulse in section 2-3 due to the formation of a vortex at the sharp-edged inlet flange and its subsequent upward motion past section 2-3.

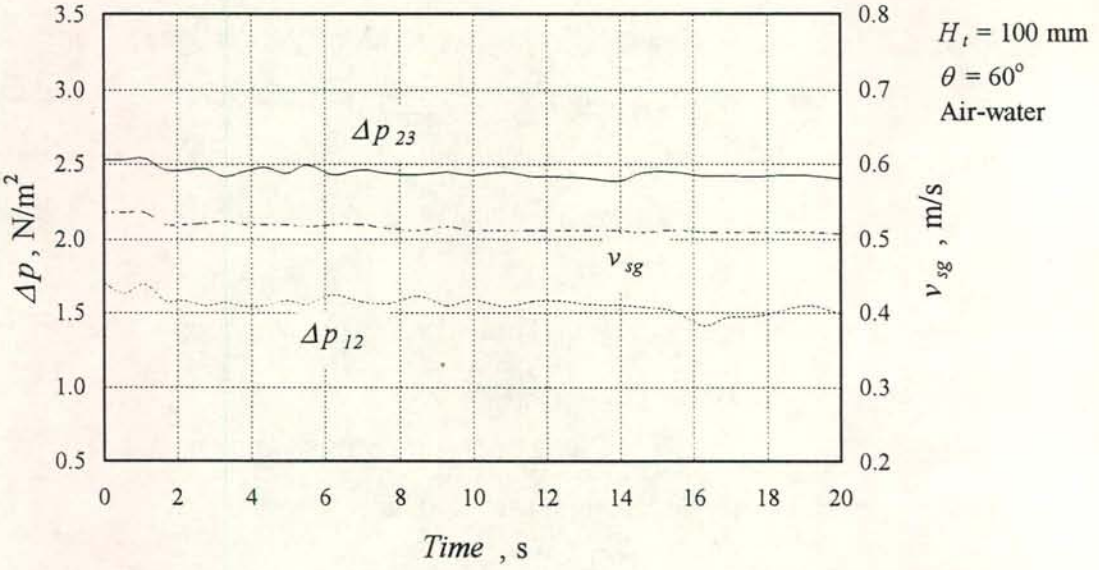

Figure 4.26(a): Transient pressure gradient and entrance pressure drop. Data: Short test section.
v_{sg} = 0.52 m/s, v_{sl} = 8.7 x 10^{-3} m/s, Re_{sg} = 622, Fr_{Hsg} = 0.0003.

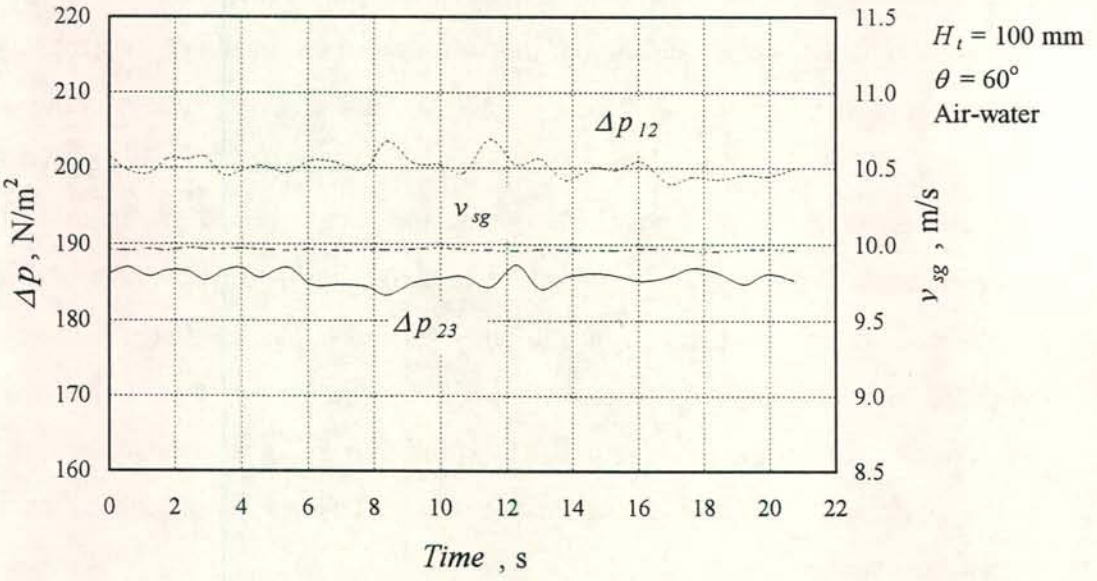

Figure 4.26 (b): Transient pressure gradient and entrance pressure drop. Data: Short test section.
v_{sg} = 10.0 m/s, v_{sl} = 8.7 x 10^{-3} m/s, Re_{sg} = 12639, Fr_{Hsg} = 0.123.

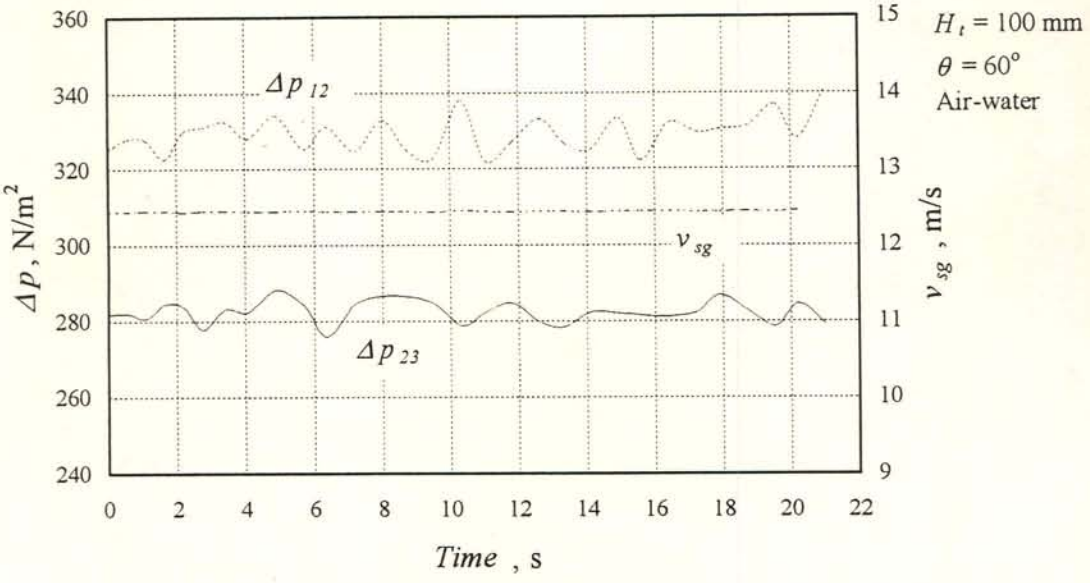

Figure 4.26 (c): Transient pressure gradient and entrance pressure drop. Data: Short test section.
v_{sg} = 12.4 m/s, v_{sl} = 8.7 x 10^{-3} m/s, Re_{sg} = 15068, Fr_{Hsg} = 0.192.

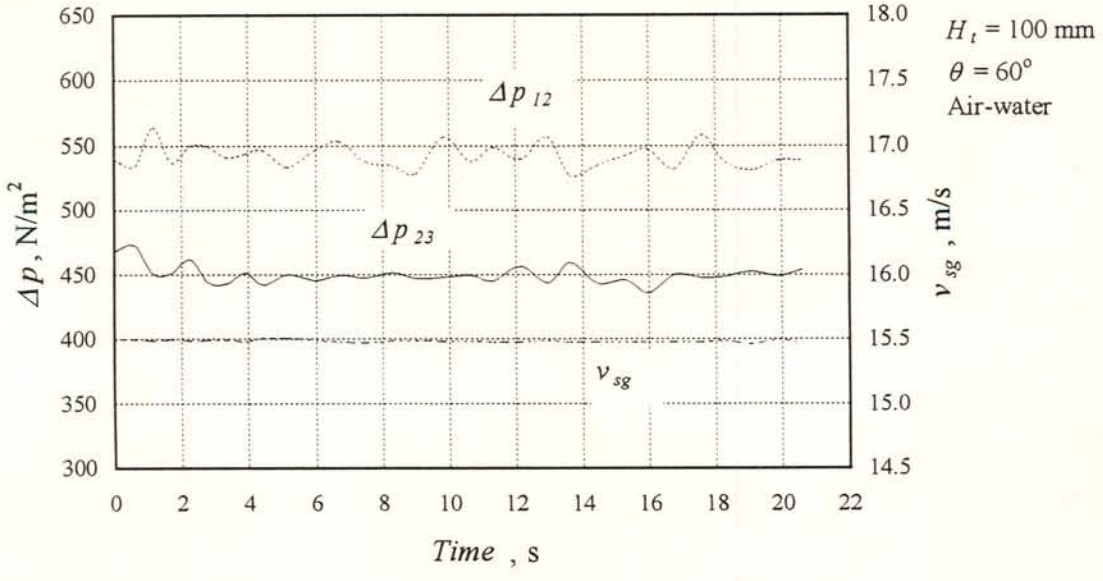

Figure 4.26 (d): Transient pressure gradient and entrance pressure drop. Data: Short test section.
v_{sg} = 15.5 m/s, v_{sl} = 8.7 x 10^{-3} m/s, Re_{sg} = 18831, Fr_{Hsg} = 0.298.

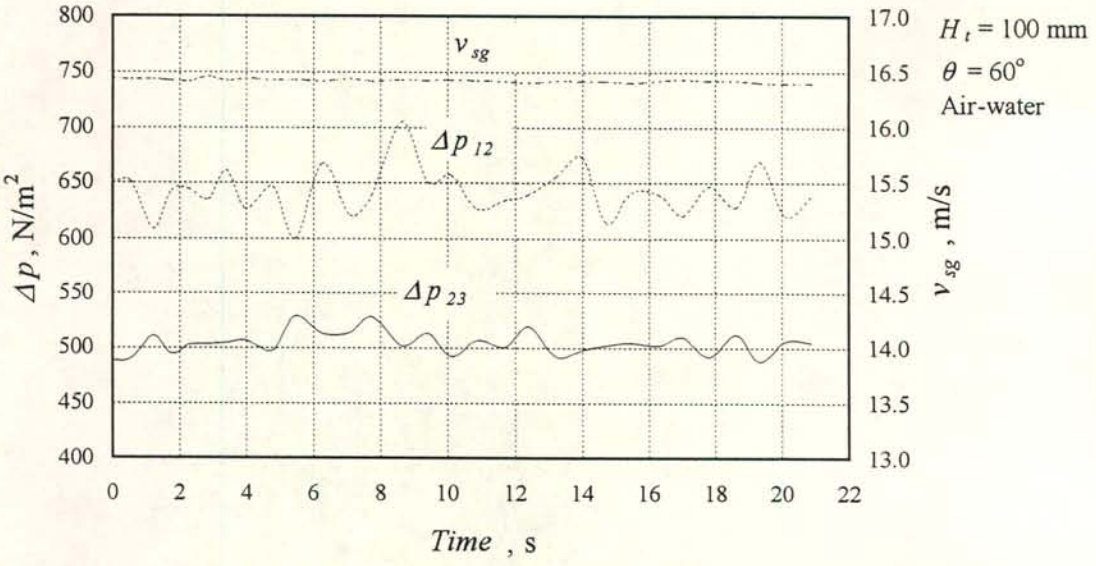

Figure 4.26 (e): Transient pressure gradient and entrance pressure drop. Data: Short test section.
v_{sg} = 16.4 m/s, v_{sl} = 8.7 x 10^{-3} m/s, Re_{sg} = 20004, Fr_{Hsg} = 0.336.

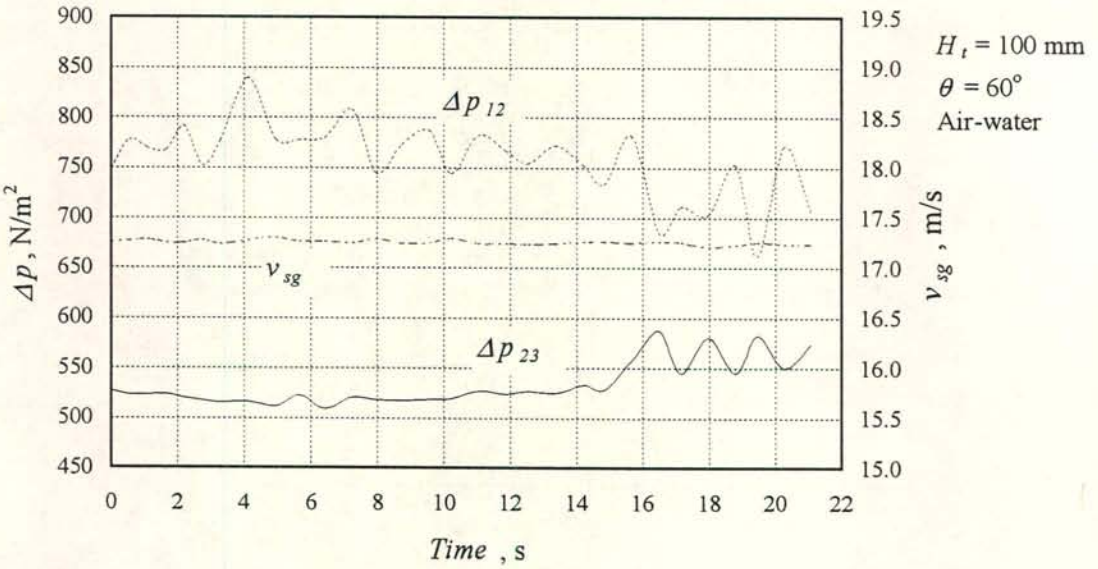

Figure 4.26 (f): Transient pressure gradient and entrance pressure drop. Data: Short test section.
v_{sg} = 17.3 m/s, v_{sl} = 8.7 x 10^{-3} m/s, Re_{sg} = 21040, Fr_{Hsg} = 0.371.

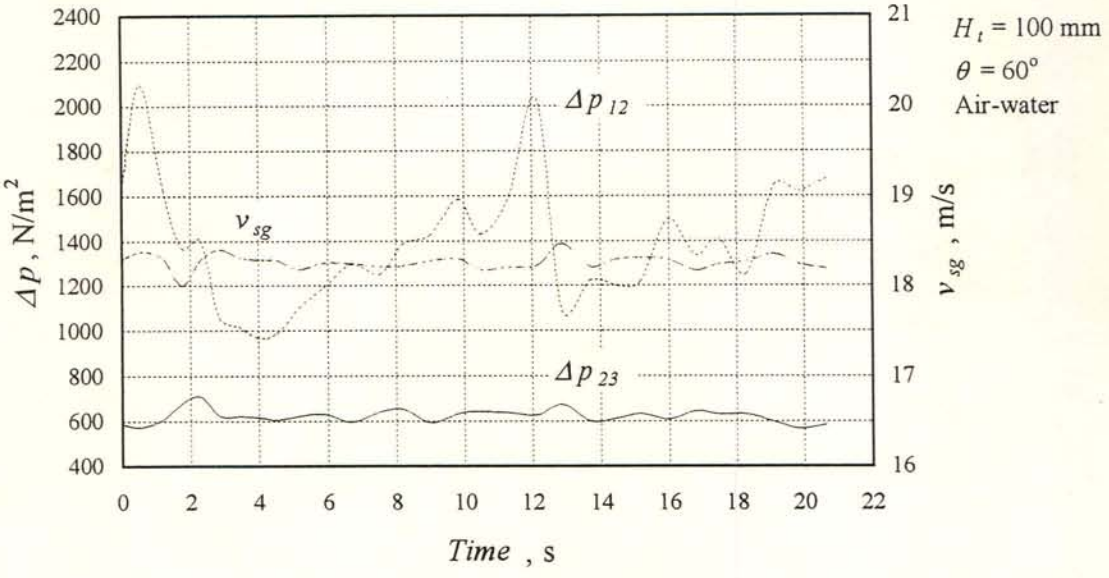

Figure 4.26 (g): Transient pressure gradient and entrance pressure drop. Data: Short test section.
v_{sg} = 18.3 m/s, v_{sl} = 8.7 x 10^{-3} m/s, Re_{sg} =22312, Fr_{Hsg} = 0.416.

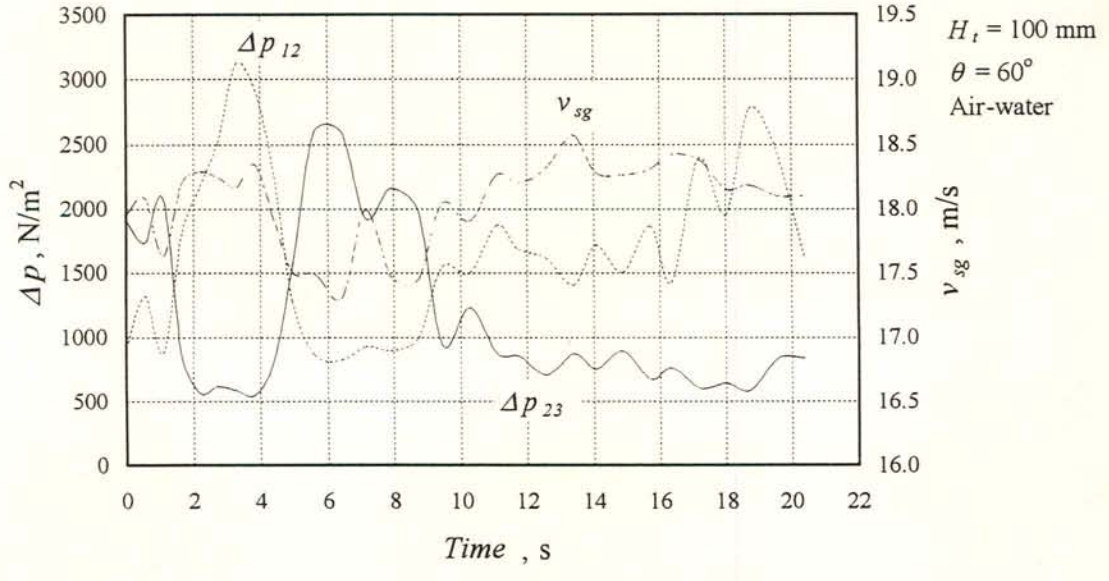

Figure 4.26 (h): Transient pressure gradient and entrance pressure drop. Data: Short test section.
v_{sg} = 18.1 m/s, v_{sl} = 8.7 x 10^{-3} m/s, Re_{sg} =22164, Fr_{Hsg} = 0.409.

Transient pressure drop data for air-propanol flow inside the 50 mm duct (W_t = 10 mm) inclined at 20° to the horizontal are shown in figure 4.27. Here the gas flow rate is gradually increased from just below the inception of vortex formation up to flooding. At a superficial air velocity of approximately 8.5 m/s a vortex, formed just above the gas inlet, spans the duct height causing a sharp increase in the entrance pressure drop. The pressure drop across the entrance decreases immediately as the vortex leaves the entrance and reaches the region between points 2 and 3, causing the pressure gradient inside the test section to rise sharply. The following peaks in the pressure drop across the gas inlet may be caused by the formation of new vortices, or they can be the result of the initial one falling back from inside section 2 -3 into the region just above the gas inlet.

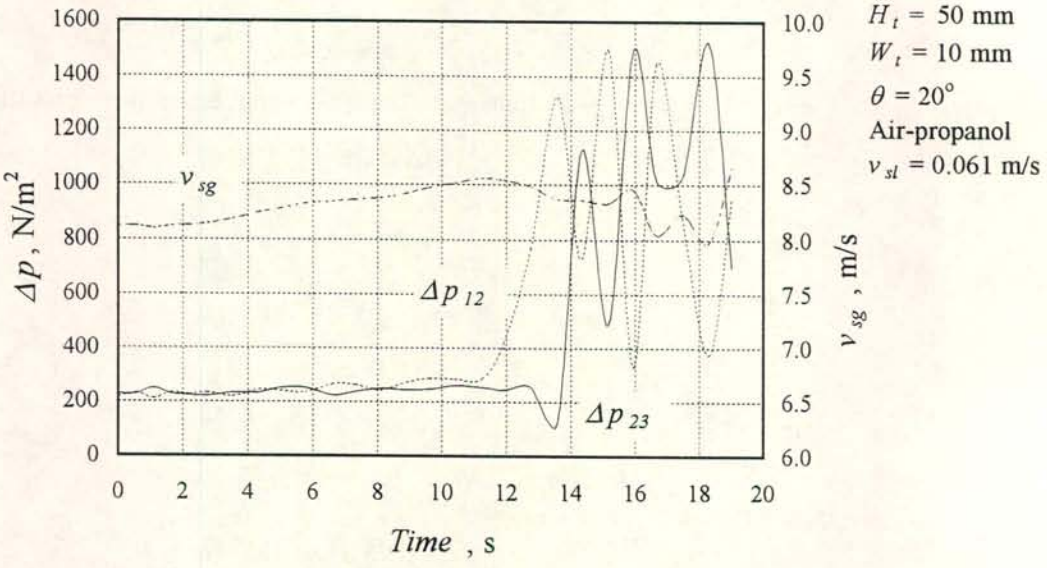

Figure 4.27: Transient pressure gradient and entrance pressure drop for air-propanol flow at an inclination of 20° to the horizontal. Data: Short test section.

4.8 Summary of the results

Three types of flow were identified in the Froude number region. i) At inclinations close to the horizontal roll waves are formed at flooding. Prior to flooding there is no or little entrainment. ii) At intermediate angles the presence of vortices dominates the behaviour of the flow just below and at flooding. The vortices eventually span the duct height and are propelled upwards by the gas. Liquid is entrainment starts before the flooding gas velocity is reached. iii) During vertical flow a vortex-type flow is formed at flooding but

the phase distribution is not as well defined as for the intermediate angles. The rotation of the vortices can be in both directions around the short axis of the duct and the vortex size is some fraction of the duct height. For vertical ducts the gas-liquid interactions and the phase distribution are more complex than for intermediate angles.

Two dimensionless groups, the gas Reynolds number and the gas Froude number, were found to be the major governing variables during counterflow in inclined ducts. At low to moderate gas flow rates the pressure drop is Reynolds number related. As the gas flow rate is increased the two-phase pressure drop starts to rise above the single-phase pressure drop and becomes Froude number dependent. Increased wave action, entrainment and wetting of the acrylic walls cause the deviation from the single-phase pressure drop. It is a gradual process and further investigation of the wave structure and dynamics is required to understand the mechanisms involved at the onset of the deviation from the single-phase pressure drop. Such an investigation on the wave dynamics should include time-varying measurement of the film thickness.

At a certain gas Froude number a sudden increase in pressure drop is experienced and subsequently flooding occurs. The gas Froude number at the sudden increase in pressure drop is a function of the duct inclination, the liquid flow rate and the liquid properties.

For inclined ducts the hydraulic diameter is the length diameter required for the gas Reynolds number while the gas Froude number is based on the height. This implies that the hydraulic diameter is the characteristic dimension at low gas flow rates, while the duct height becomes the characteristic dimension at a certain Froude number.

For low liquid flow rates the two-phase friction factor increases during the transition from laminar to turbulent gas flow, while no such trend was found for higher liquid flow rates. This is in agreement with the results of Feind [60FE1] who conducted similar experiments with vertical tubes.

In the Reynolds number region the pressure gradient is equal or close to the single-phase pressure gradient. This trend can be expected because the gas-liquid interface is very small relative to the dry part of the duct perimeter. To the contrary, Feind [60FE1]

observed a significant difference between the interfacial friction factor and the single-phase friction factor for laminar gas flow in vertical tubes. During countercurrent annular flow a wavy film surrounds the gas core. Separation at the interface and the downward flow of gas in the close proximity of the interface result in a much higher pressure gradient experienced by the gas flow, compared to single-phase flow.

The degree of wetting plays an important role when the Froude number region is entered. Under poor wetting conditions relatively large droplets adhere to the duct wall, while droplets spread to form a thin film when proper wetting is achieved. As a result of the droplets present on the wall during poor wetting the two-phase friction factor f_{sg} experiences an initial peak before it eventually increases sharply at flooding. Such a peak was not found in the case of proper wetting. Similarly poor wetting caused the two-phase entrance loss coefficient to be higher than for proper wetting.

The gas Froude number at the sudden increase in the pressure drop was the lowest for propanol. It can therefore be concluded the gas velocity at the onset of upward liquid transport decreases as the liquid viscosity increases.

The data presented in this chapter and in Appendixes D and C were measured during steady-state conditions prior to flooding except for measurements at the sudden increase in the pressure drop where the flow becomes transient in nature. At and beyond flooding the behaviour of the flow and the pressure drop is very complex. This regime after flooding is beyond the scope of the investigation and was not addressed.

The sharp-edged gas inlet played an important role in the formation of vortices and must have affected the pressure drop characteristics. The gas Froude number at which the sudden increase in pressure drop occurs certainly depends on the bottom geometry. At present one can only speculate on the nature of the flow patterns and the pressure drop characteristics encountered during inclined flow with a rounded gas inlet. The fact that vortex formation and the subsequent upward transport of liquid was not limited to the immediate region above the sharp-edged gas inlet at high liquid flow rates, suggests that the influence of the bottom geometry becomes less as the liquid flow is increased. Consequently the pressure drop characteristics for rounded and sharp-edged inlets may

be similar for high liquid flow. In other words, Reynolds number and Froude number regions may be found in inclined rectangular ducts with rounded inlets. The main difference between counterflow in ducts with different bottom geometries will be the gas Froude number at which the sudden increase in pressure drop occurs at conditions of low liquid flow.

CHAPTER 5

EXPERIMENTAL RESULTS: FLOODING AND ENTRAINMENT

5.1 The flooding definition for counterflow in vertical and inclined ducts

In chapter 2 section 2.3.1 the flooding description and definition by Hewitt and Taylor [70HE1] is given. Their definition was adopted in the present investigation to develop a flooding correlation for rectangular ducts. According to the definition, flooding occurs when the gas flow rate is increased during pure counterflow while the liquid feed rate is kept constant, and a condition is reached when liquid starts to flow up past the point of injection. The gas flow rate at the onset of upward liquid flow past the inlet sinter and the corresponding liquid feed rate into the tube form a set of flooding fluid flow rates. The above-described flooding process for flow in vertical tubes with minimised end effects is illustrated in figure 2.4. Govan *et al.* [91GO1] found that during counterflow in a vertical tube with a porous liquid feed and a sharp-edged gas inlet, droplet entrainment may occur at the gas inlet at flow rates below flooding. At sufficiently high gas flow rates the droplets travel upwards and some are deposited on the tube wall above the liquid feed (see figure 2.7). The deposition of droplets above the liquid feed was not regarded as flooding by Govan *et al.* Flooding was said to occur when liquid is propelled up against the tube wall above the porous feed.

The same criteria were applied in the present investigation for flow inside vertical and inclined rectangular ducts. There is however a fundamental difference between flooding in vertical tubes and inclined rectangular ducts. In the case of flooding in vertical tubes liquid is driven above the feed against the tube wall in the form of a churn-type flow while in inclined rectangular ducts the vortex is the main mechanism by which liquid is transported upwards, the contribution of droplet entrainment and upward film flow being insignificant according to the present investigation. Flooding was subsequently defined as the condition when a vortex, formed inside the test section somewhere below the liquid inlet, is propelled to the top end of the duct, thereby transporting liquid above the feed point.

The liquid feed employed was constructed to eliminate the formation of disturbances in the liquid flow due to entry effects at the point of injection. It was achieved by allowing part of the gas to escape before reaching the porous section in the case of the experiments with inclined ducts, as described in chapter 3. Consequently the characteristic vortex could not be "propelled above the liquid feed", referred to in the definition for flooding because it collapsed as it entered the gas bleed-off zone below the porous section. The flooding gas velocity was therefore defined as the gas flow rate at which liquid is carried by a vortex, or a roll wave in the case of small inclinations, into the bleed-off zone. This may not be regarded as a new or a different definition. The actual "point of liquid injection" is as a matter of fact the location in the constant cross-sectional area test section just below the bleed-off region where the full gas flow is still present. Thus, once a vortex is driven into the bleed-off zone liquid has been per definition "carried upwards above the point of injection" or in other words, flooding has occurred.

A typical flooding process inside rectangular ducts inclined at 60° to the horizontal is described with the aid of the pressure drop characteristics and entrainment data for air-water flow in the 150 mm duct, shown in figure 5.1. At gas flow rates below $Fr_{Hsg} \approx 0.1$ there is no significant gas-liquid interaction. The flow is stratified and the gas-liquid interface is wavy. In this region the pressure gradient multiplier and the entrance pressure drop coefficient are equal to the single-phase air-only pressure drop values. Above $Fr_{Hsg} \approx 0.1$ the interface becomes more wavy and droplets are entrained at the sharp-edged gas inlet. Initially these droplets are deposited onto the acrylic plastic duct walls in the region just above the gas inlet, but as the gas flow is further increased, the droplets are carried to the top of the test section past the porous feed into the cyclone separator. Now both the pressure gradient and the entrance pressure drop start to rise above the corresponding single-phase values. At $Fr_{Hsg} \approx 0.3$ a strong vortex is present at the gas inlet and upon a further increase in the gas flow the "diameter" of the vortex approaches the duct height. At $Fr_{Hsg} \approx 0.4$ the vortex is propelled upwards into the gas bleed-off zone resulting in flooding. When flooding occurs the pressure gradient increases sharply. Note that there is also a strong increase in the entrainment just below flooding, but the percentage entrainment (of the liquid feed) is only 1.1 %. This proves that the mechanism

of upward liquid transport at flooding is the vortex. The decrease in the entrance pressure drop at flooding is the result of the sudden decrease in liquid hold-up as the vortex is propelled upwards away from the gas inlet.

The gas flow rate at the conditions marked "flooding" is taken as the flooding velocity corresponding to, in this case, a liquid flow rate of v_{sl} = 0.011 m/s, because it represents the flow rate at which a vortex was propelled to the top end of the test section into the gas bleed-off zone.

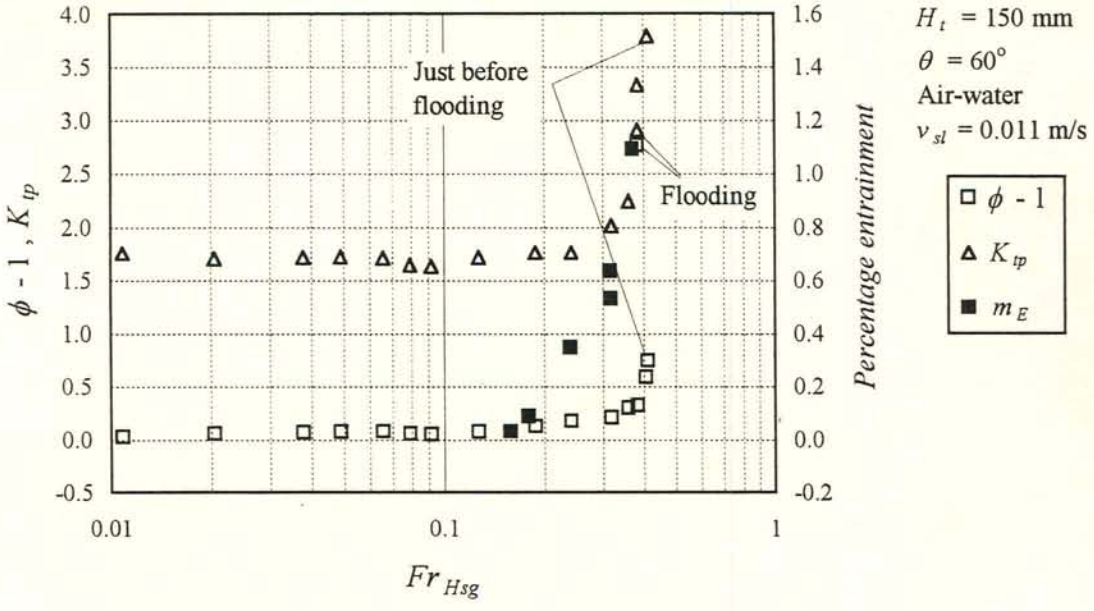

Figure 5.1: Pressure drop characteristics and entrainment data for air-water flow inside the 150 mm duct inclined at 60° to the horizontal.

In the case of vertical flow no gas bleed-off was employed and thus the definition by Hewitt and Taylor [70HE1] and Govan *et al.* [91GO1] could be strictly followed. Although vortex-type flow was present below the porous feed of the vertical ducts, the way in which the liquid flow appeared above the porous section at flooding was very similar to that described for tubes, i.e. liquid was driven upwards against the duct walls in the form of a rough film or a churn-type flow.

5.2 The role of the duct dimensions during flooding

Consider the flooding data for air-water flow inside the rectangular ducts inclined at 60° to the horizontal, as shown in figure 5.2. The flooding gas velocity is strongly dependent on the duct height, experiencing an increase as the height increases. The trend can be explained in terms of the mechanism by which flooding occurs. Flooding takes place when the size of a vortex approaches the duct height and the vortex is subsequently propelled upwards. At flooding the weight of liquid contained in the vortex is proportional to the height of the duct and the density difference between the gas and the liquid. The weight must be overcome by the drag and the lift force exerted by the gas flow, which are related to the momentum flux $\rho_g v_{sg}^2$. The densimetric gas Froude number based on the duct height

$$Fr_{Hsg} = \rho_g v_{sg}^2 \Big/ \left[gH_t \left(\rho_l - \rho_g \right) \right] \tag{4.6}$$

is a ratio of these two forces. The subscript H refers to the height being taken as the required length dimension. During the presence of a vortex the liquid experiences flow between parallel plates and is thus characterised by the hydraulic diameter of the duct. The liquid flow rate should therefore be represented by a densimetric Froude number based on the hydraulic diameter, i.e.

$$Fr_{Dsl} = \rho_l v_{sl}^2 \Big/ \left[gD_e \left(\rho_l - \rho_g \right) \right] \tag{5.1}$$

The data of figure 5.2(a) are plotted in terms of the densimetric Froude numbers Fr_{Hsg} and Fr_{Dsg} in figure 5.2(b). The successful correlation of the data by these two groups is evident. In figure 5.3(a) the same data are plotted in terms of the phase Froude numbers where the hydraulic diameter is taken as the length dimension for both the gas and the liquid phase. This choice to represent the duct dimensions fails to correlate the data. Similarly, taking the duct height as the length dimension for the liquid phase

$$Fr_{Hsl} = \rho_l v_{sl}^2 \Big/ \left[gH_t \left(\rho_l - \rho_g \right) \right] \tag{5.2}$$

does not correlate the data, as illustrated in figure 5.4.

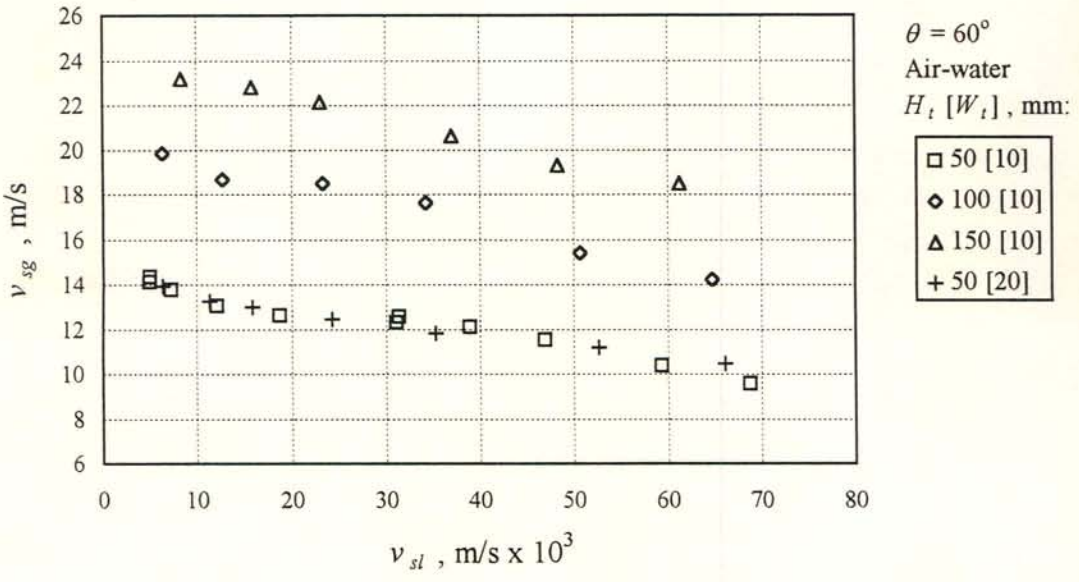

Figure 5.2(a): Flooding superficial velocities for air-water counterflow in rectangular ducts inclined at 60° to the horizontal. Data: Short test section.

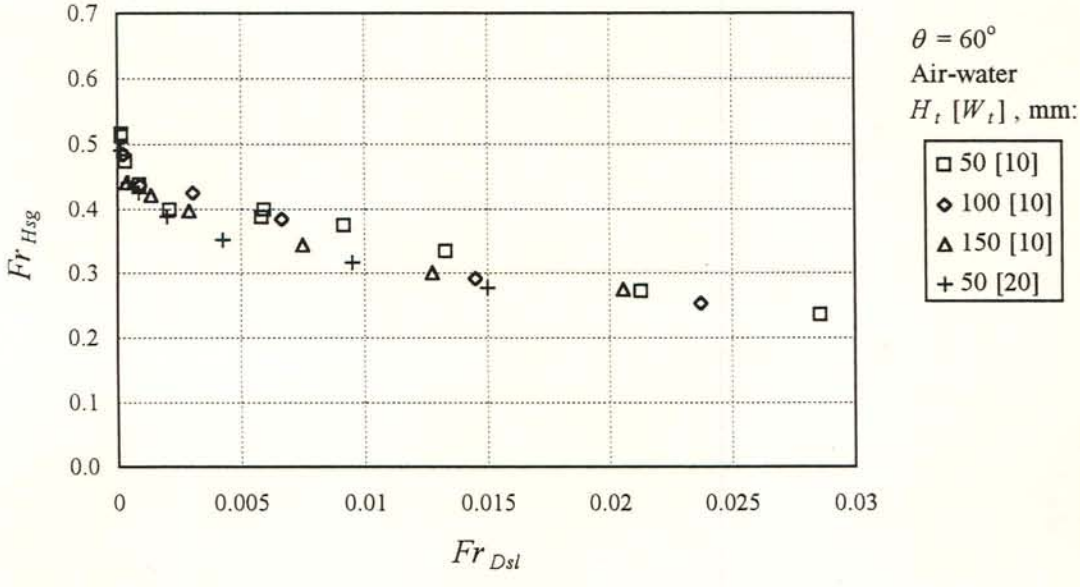

Figure 5.2(b): The flooding data of figure 5.2(a) plotted in terms of the superficial densimetric phase Froude numbers. The duct height and the equivalent diameter are taken as the required length dimension for the gas and liquid Froude numbers respectively.

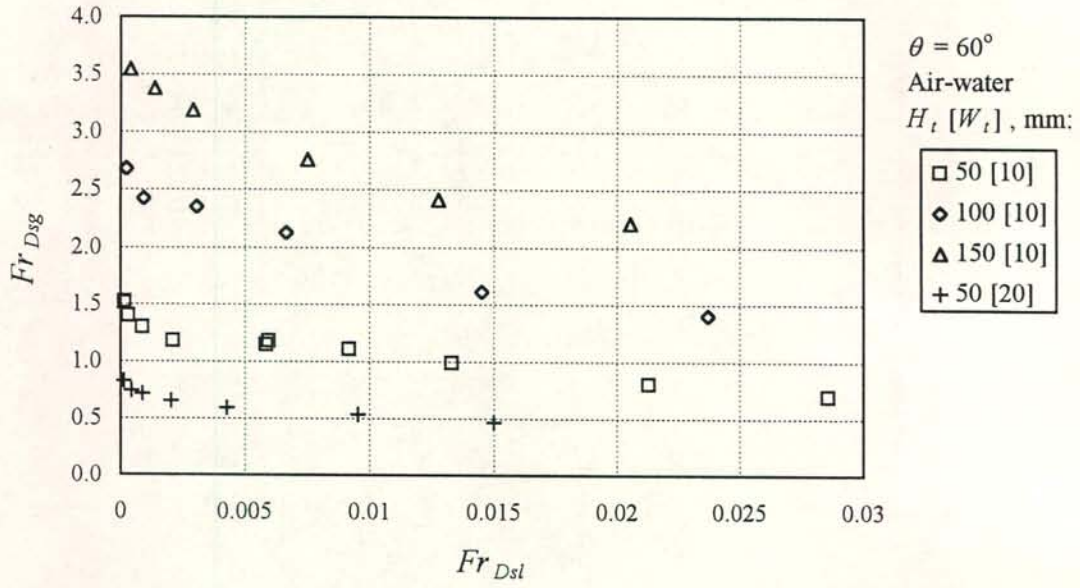

Figure 5.3: The flooding data of figure 5.2(a) plotted in terms of the superficial densimetric phase Froude numbers. The equivalent diameter is taken as the required length dimension for the gas and the liquid Froude number. This choice fails to correlate the data.

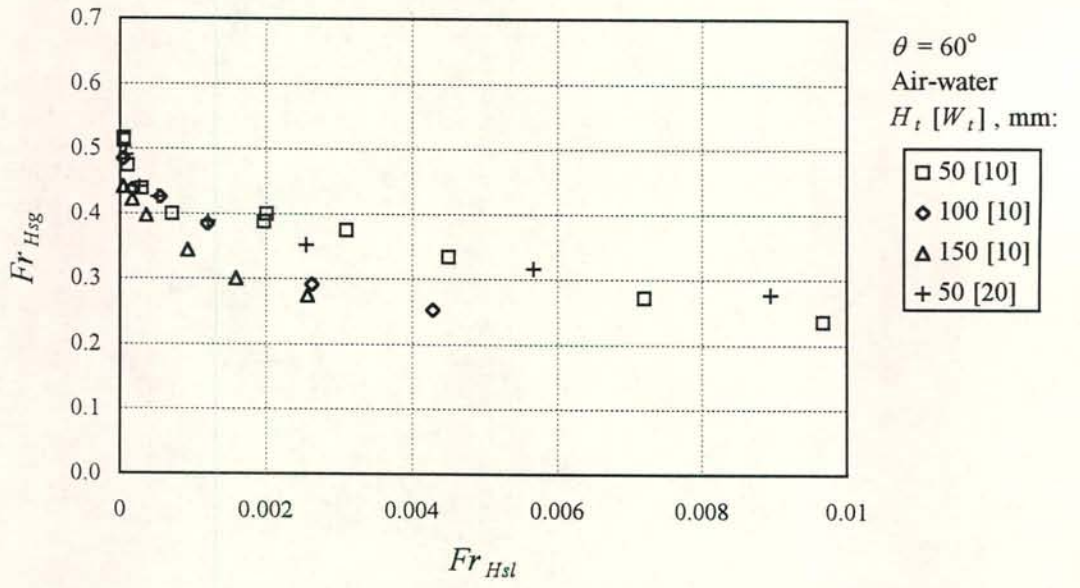

Figure 5.4: The flooding data of figure 5.2(a) plotted in terms of the superficial densimetric phase Froude numbers. The duct height is taken as the required length dimension for the gas and liquid Froude numbers. This choice fails to correlate the data.

The height effect on flooding was observed from near horizontal to vertical flow. Figures 5.5 to 5.10 show air-water data for inclinations of 2, 20, 40, 70, 80 and 90° in both dimensional and dimensionless form. The best correlation is obtained for the intermediate angles 40 to 70°. At these inclinations the vortex "diameter" at flooding was well defined and could clearly be distinguished as the duct height. At near horizontal angles and during vertical flow the nature of the flow was different, as described in chapter 4. In the case of vertical flow the characteristic vortex did not span the entire duct height and it was not possible to estimate its actual size. According to figures 5.10(a) and (b) it appears that the vortex size did increase with an increase in duct height and thus the higher flooding velocities measured for the 100 mm duct. The increase is however not proportional to the duct height because the Froude number defined by equation (4.6) does not correlate the data as well as in the case of the intermediate angles.

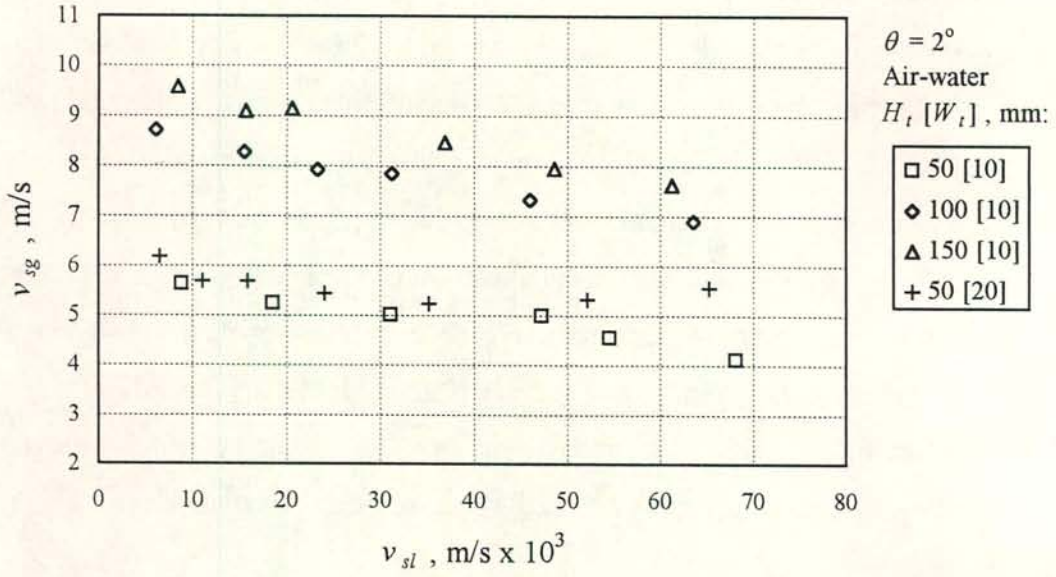

Figure 5.5(a): Flooding data for air-water flow inside the rectangular ducts inclined at 2° to the horizontal plotted in terms of the superficial velocities. Data: Short test section.

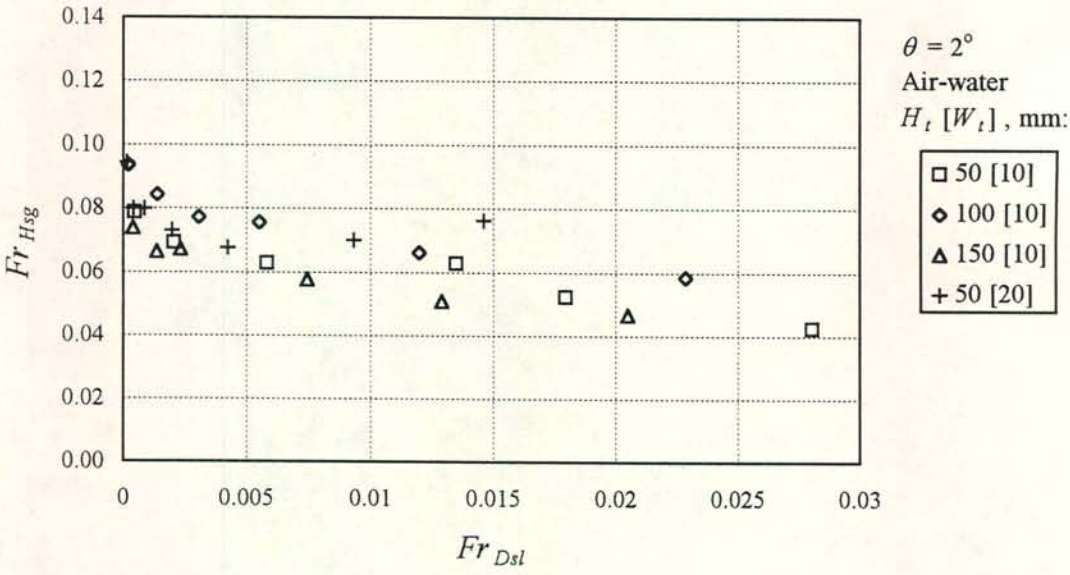

Figure 5.5(b): The flooding data of figure 5.5 (a) plotted in terms of the densimetric superficial phase Froude numbers. The duct height and the equivalent diameter are taken as the required length dimension for the gas and liquid Froude numbers respectively.

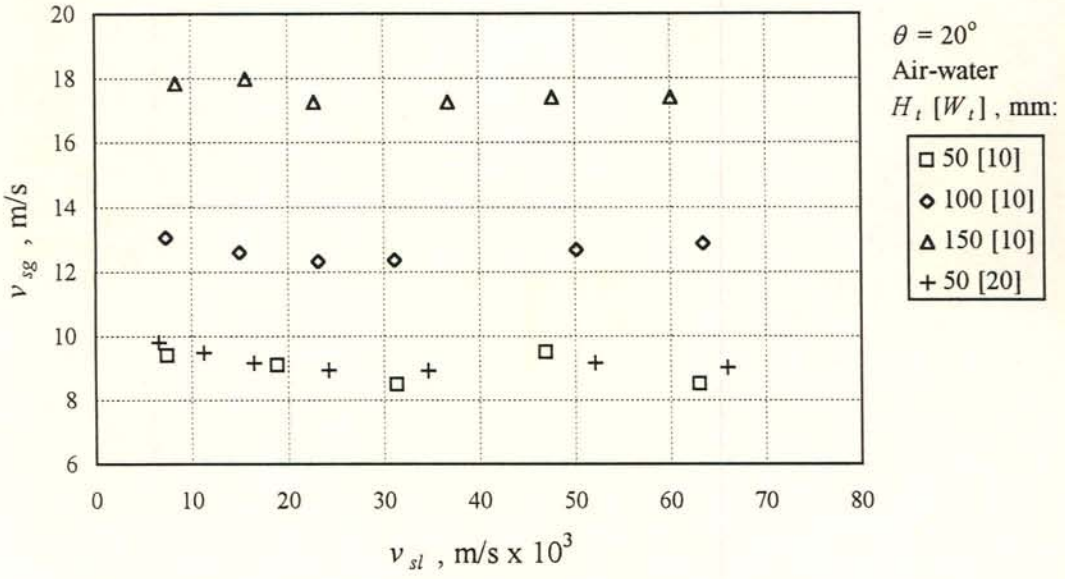

Figure 5.6(a): Flooding data for air-water flow inside the rectangular ducts inclined at 20° to the horizontal plotted in terms of the superficial velocities. Data: Short test section.

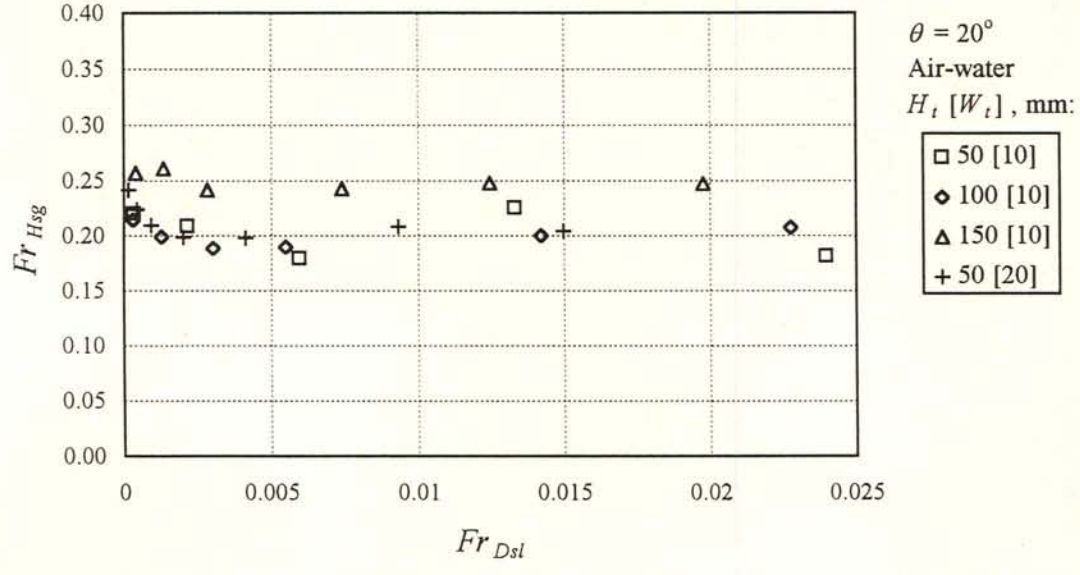

Figure 5.6(b): The flooding data of figure 5.6 (a) plotted in terms of the densimetric superficial phase Froude numbers. The duct height and the equivalent diameter are taken as the required length dimension for the gas and liquid Froude numbers respectively.

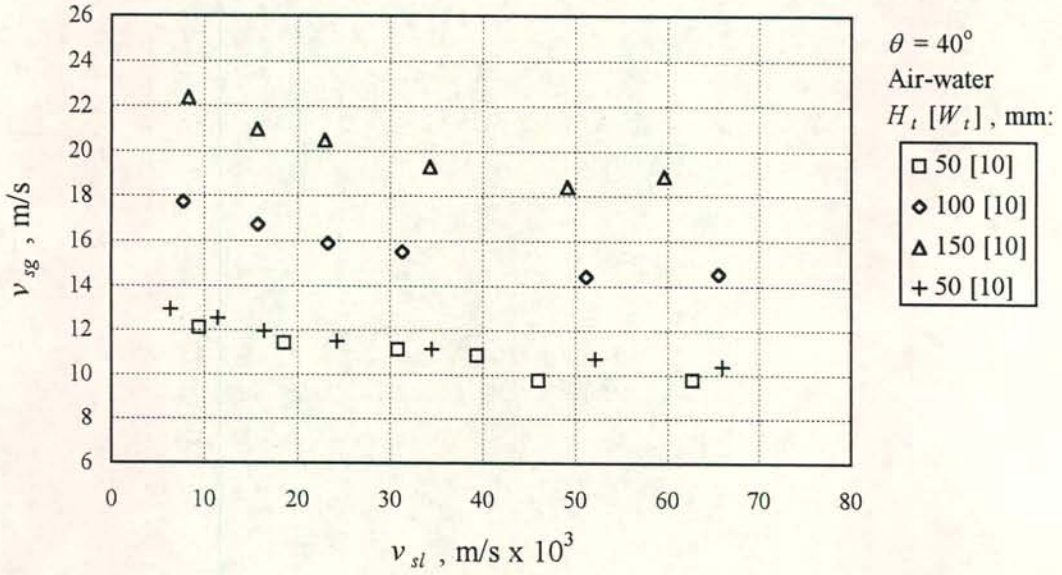

Figure 5.7(a): Flooding data for air-water flow inside the rectangular ducts inclined at 40° to the horizontal plotted in terms of the superficial velocities. Data: Short test section.

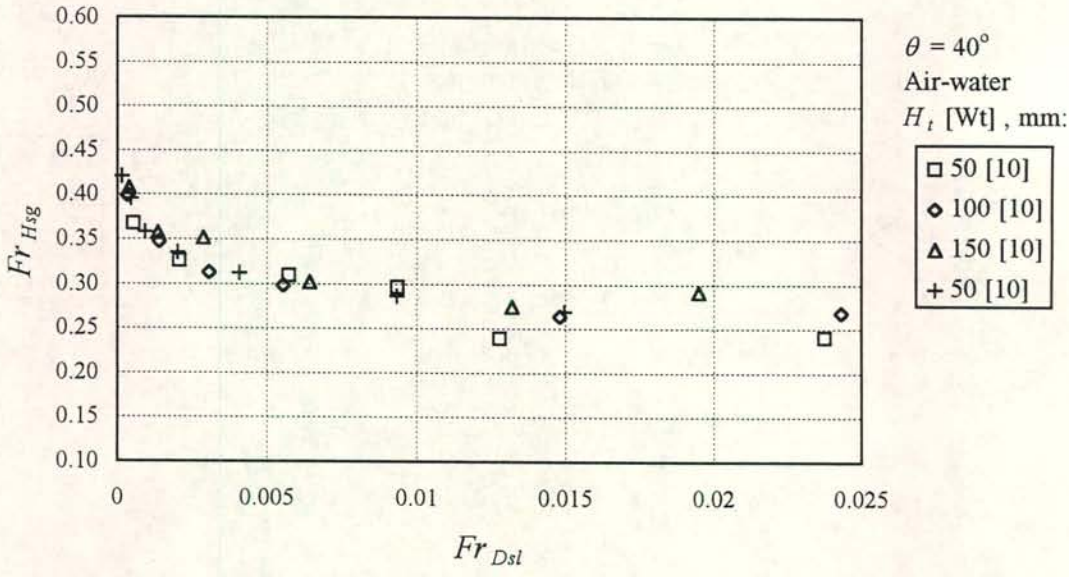

Figure 5.7(b): The flooding data of figure 5.7 (a) plotted in terms of the densimetric superficial phase Froude numbers. The duct height and the equivalent diameter are taken as the required length dimension for the gas and liquid Froude numbers respectively.

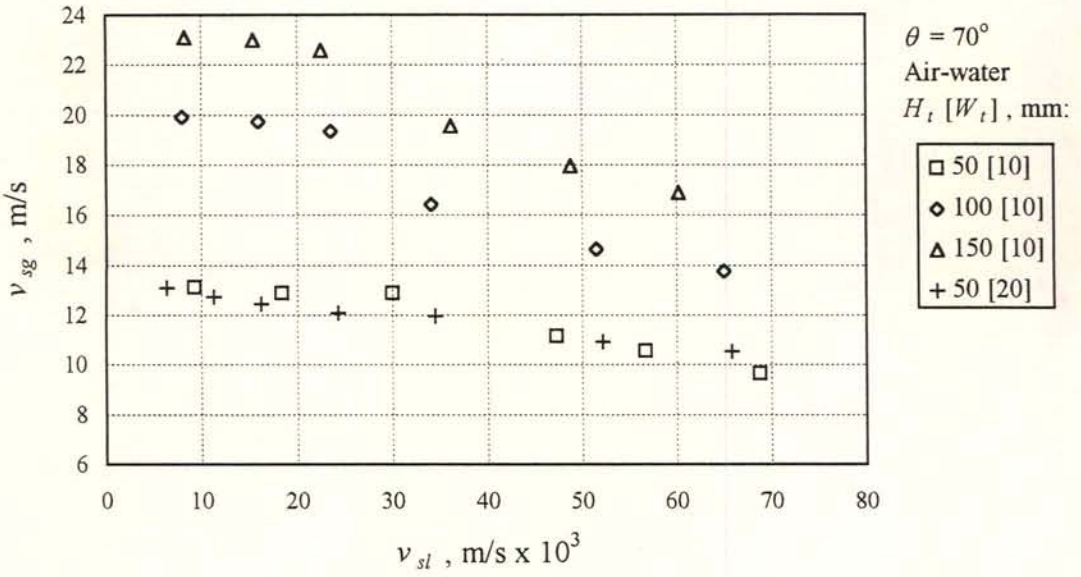

Figure 5.8(a): Flooding data for air-water flow inside the rectangular ducts inclined at 70° to the horizontal plotted in terms of the superficial velocities. Data: Short test section.

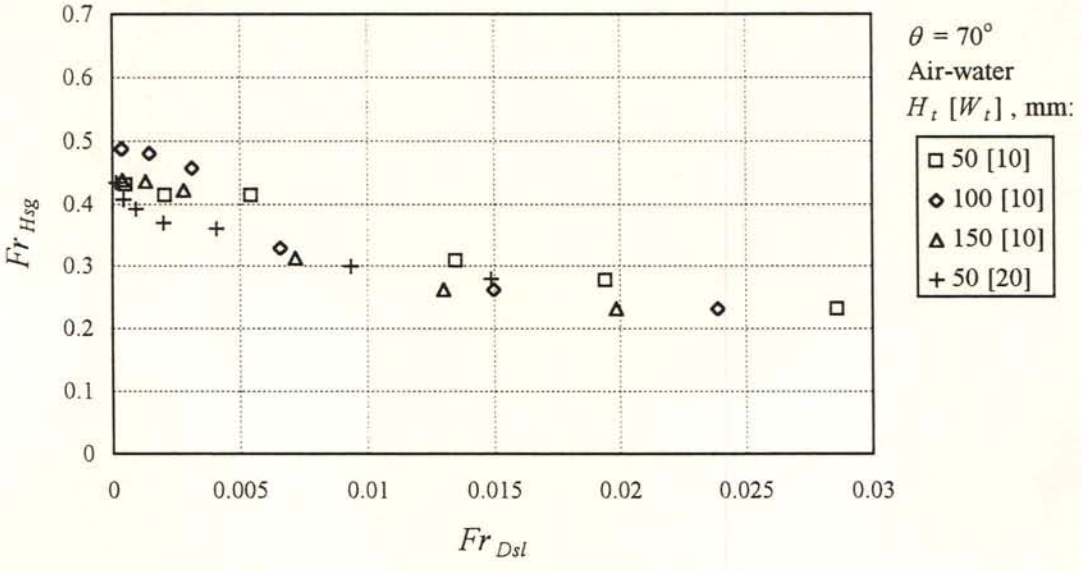

Figure 5.8(b): The flooding data of figure 5.8 (a) plotted in terms of the densimetric superficial phase Froude numbers. The duct height and the equivalent diameter are taken as the required length dimension for the gas and liquid Froude numbers respectively.

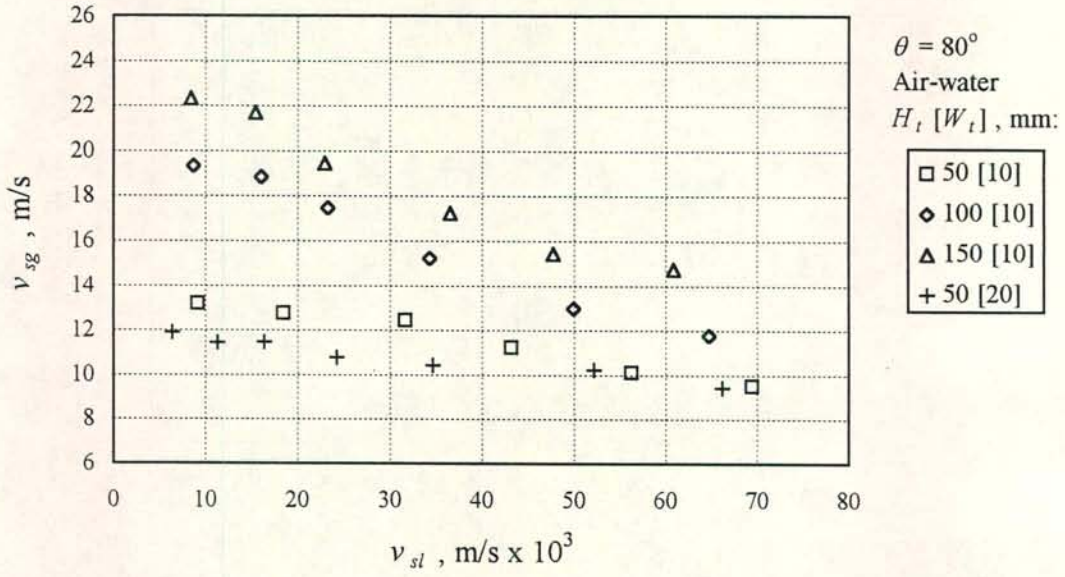

Figure 5.9(a): Flooding data for air-water flow inside the rectangular ducts inclined at 80° to the horizontal plotted in terms of the superficial velocities. Data: Short test section.

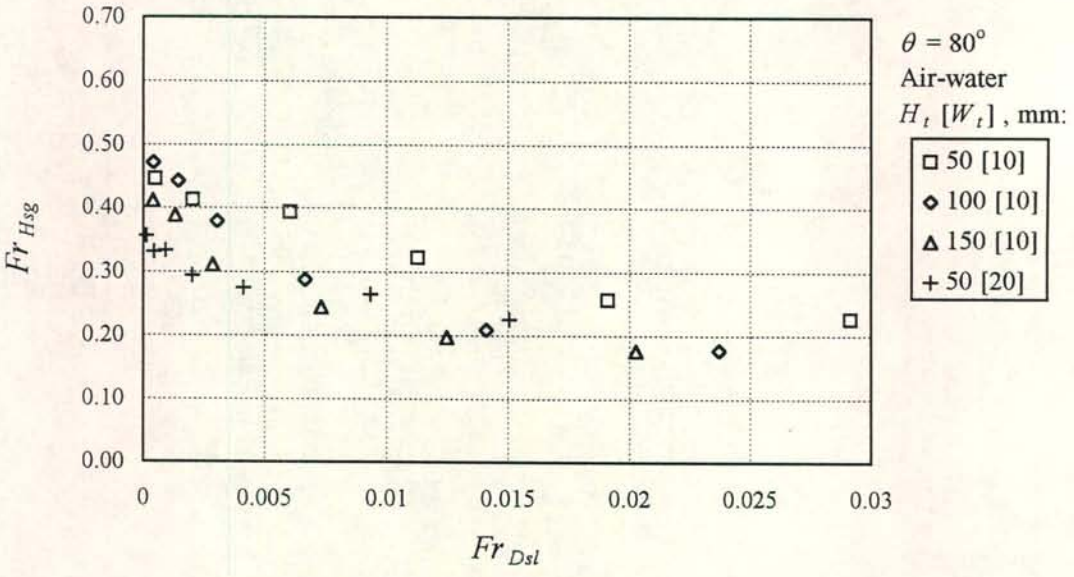

Figure 5.9(b): The flooding data of figure 5.9 (a) plotted in terms of the densimetric superficial phase Froude numbers. The duct height and the equivalent diameter are taken as the required length dimension for the gas and liquid Froude numbers respectively.

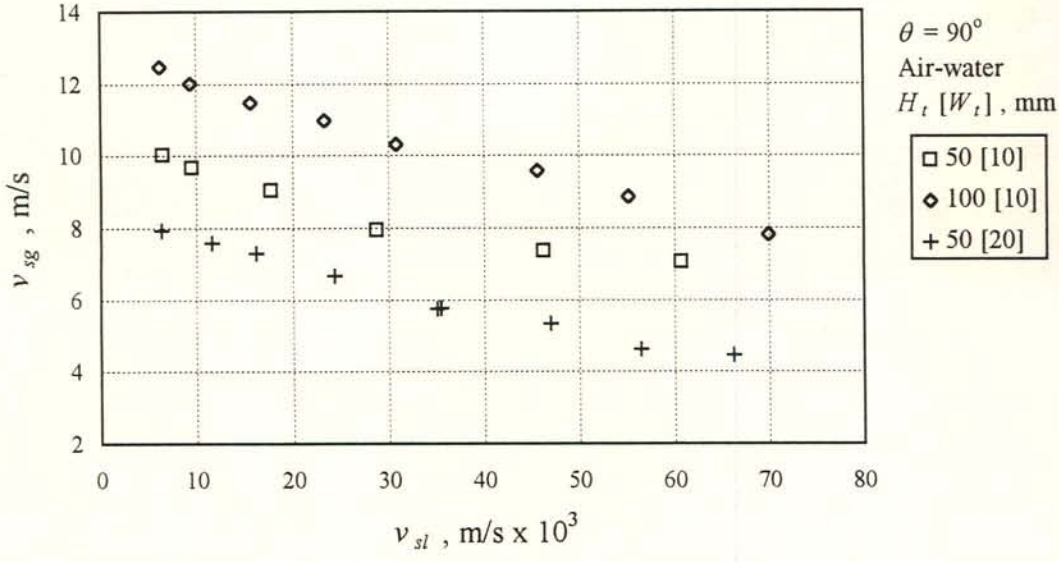

Figure 5.10(a): Flooding data for air-water flow inside the rectangular ducts inclined at 90° to the horizontal plotted in terms of the superficial velocities. Data: Short test section.

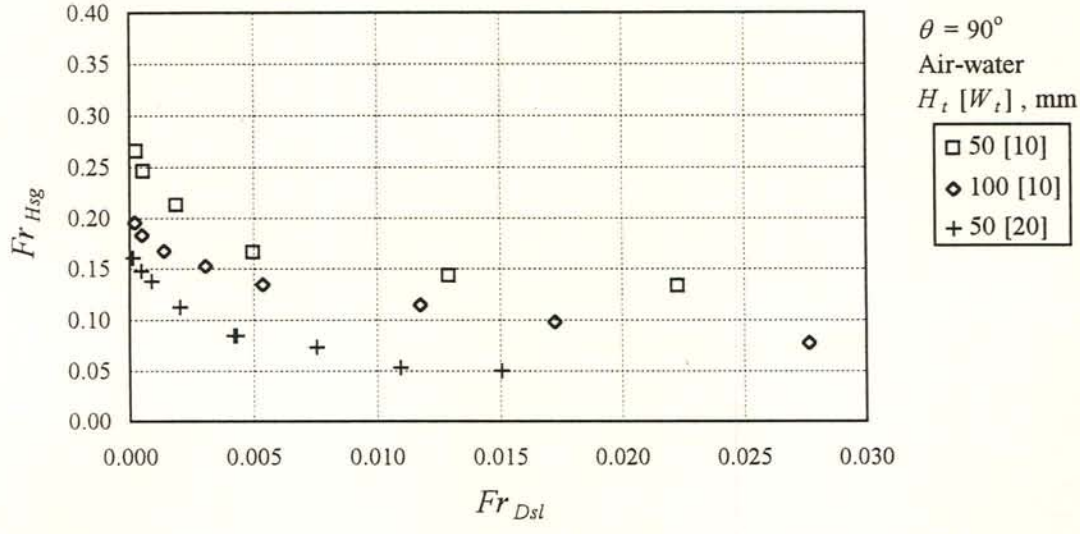

Figure 5.10(b): The flooding data of figure 5.10 (a) plotted in terms of the densimetric superficial phase Froude numbers. The duct height and the equivalent diameter are taken as the required length dimension for the gas and liquid Froude numbers respectively.

5.3 The effect of the fluid properties on flooding inside inclined ducts

5.3.1 The effect of the gas properties

A number of tests were carried out with air, hydrogen, helium and argon to establish the role of the gas properties during flooding. Flooding superficial velocities for air-methanol, helium-methanol and hydrogen-methanol are shown in figure 5.11. A wide range of velocities, varying from ≈10 m/s to ≈45 m/s, were measured. The data are presented in figure 5.12 in terms of the superficial gas Reynolds number. At a superficial liquid velocity of $\approx 10 \times 10^{-3}$ m/s for example, flooding takes place at superficial gas Reynolds numbers of 4000 and 14000 for air and hydrogen respectively. Flooding is therefore not related to the gas Reynolds number. The same data are plotted in terms of the superficial gas momentum flux $\rho_g v_{sg}^2$ in figure 5.13. According to the plot flooding takes place at a certain gas momentum flux, which in turn is related to other parameters such as the liquid flow rate and properties. Figure 5.14 presents the data in the form of the dimensionless phase Froude numbers defined by equations (4.6) and (5.1). Similar plots are shown in figures 5.15 to 5.17 for air-water, helium-water and argon-water.

5.3.2 The effect of the liquid properties

Flooding data for air-water, air-methanol and air-propanol flow are shown in figure 5.18. For each duct the propanol flooding velocities are the lowest. Thus, the flooding gas velocity decreases with an increase in the liquid viscosity. This conclusion is based on the fact that the density and the surface tension of propanol and methanol are approximately equal while the propanol viscosity is approximately three to four times that of methanol.

The same data are plotted in terms of the phase Froude numbers in figure 5.19. The water and methanol data correlate (empty and solid symbols), while the propanol data (crosses) are below the water and the methanol data. This is in agreement with the findings by Zapke and Kröger [96ZA1] according to which the Froude numbers should suffice to correlate water and methanol data because these two liquids have approximately equal *Zk* numbers

$$Zk_D = \left(\rho_l D_e \sigma\right)^{0.5} / \mu_l \qquad (5.3)$$

The fact that the phase Froude numbers correlate the water and the methanol data of figure 5.18 proves that the lower flooding gas velocities for methanol are primarily a result of the difference between the water and the methanol density and that the surface tension does not affect flooding significantly.

To account for the combined influence of the liquid properties on flooding in a dimensionless form, the *Zk* number is introduced as shown in figure 5.20. It effectively shifts the propanol data in figure 5.19 more to the right relative to the water and the methanol data, to achieve better correlation. According to a trial-and-error regression analysis the best curve fit is obtained by an exponential curve of the form

$$Fr_{Hsg} = K_o \, exp\left(- n Fr_{Dsl}^{0.6} / Zk_D^{0.2}\right) \qquad (5.4)$$

where the mean deviation reaches a minimum at the exponents of 0.6 and 0.2 for the liquid Froude and the *Zk* number respectively. K_o and n are empirical constants.

In figure 5.21 the flooding data obtained with the different liquids and air are plotted in terms of the phase Kutateladze numbers. The plot fails to correlate the data because the duct height, which proved to be one of the characteristic dimensions for flooding in inclined ducts, is not included in these dimensionless numbers. Also, the Kutateladze numbers cannot account for the effect of the liquid viscosity on flooding. The same data are shown in figure 5.22 in terms of the gas Froude number and the superficial liquid Reynolds number. According to figure 5.22 the gas Froude number at flooding is not related to the superficial liquid Reynolds number.

All the flooding data obtained for the ducts inclined at 60° to the horizontal are shown in figure 5.23 in terms of the superficial velocities, to illustrate the wide range of values correlated by the proposed dimensionless groups. The same data are plotted in figure 5.24 in the dimensionless form. Considering figures 5.2(b), 5.12, 5.20, 5.21 and 5.22 the Froude and the *Zk* number prove to be the most successful dimensionless groups to represent the fundamental physics of flooding inside inclined rectangular ducts with a sharp-edged gas inlet.

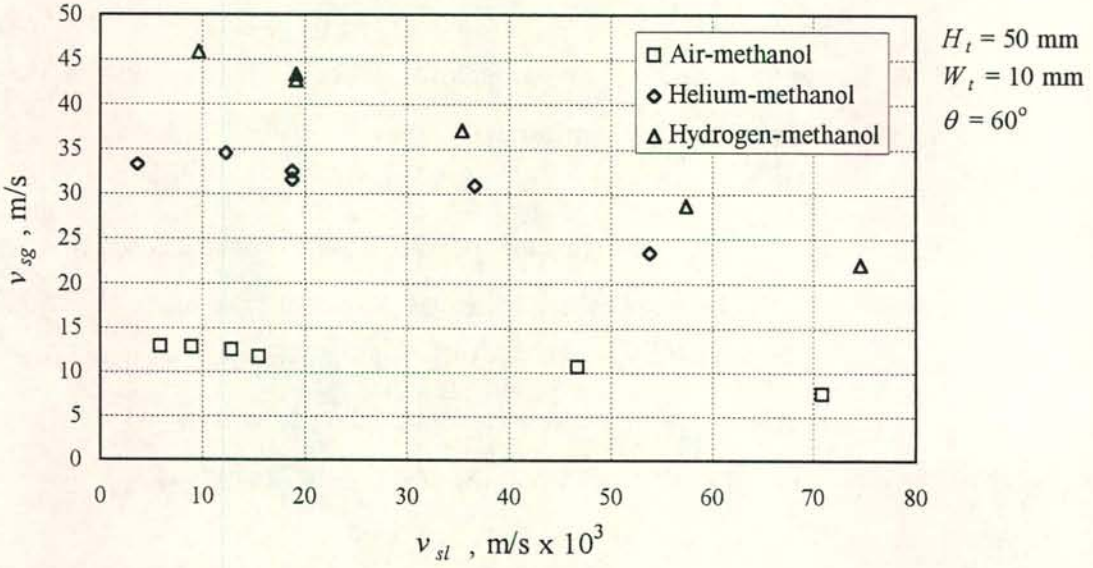

Figure 5.11: Superficial gas flooding velocities for air, helium and hydrogen tested with methanol inside the 50 mm duct (W_t = 10 mm). Data: Long test section.

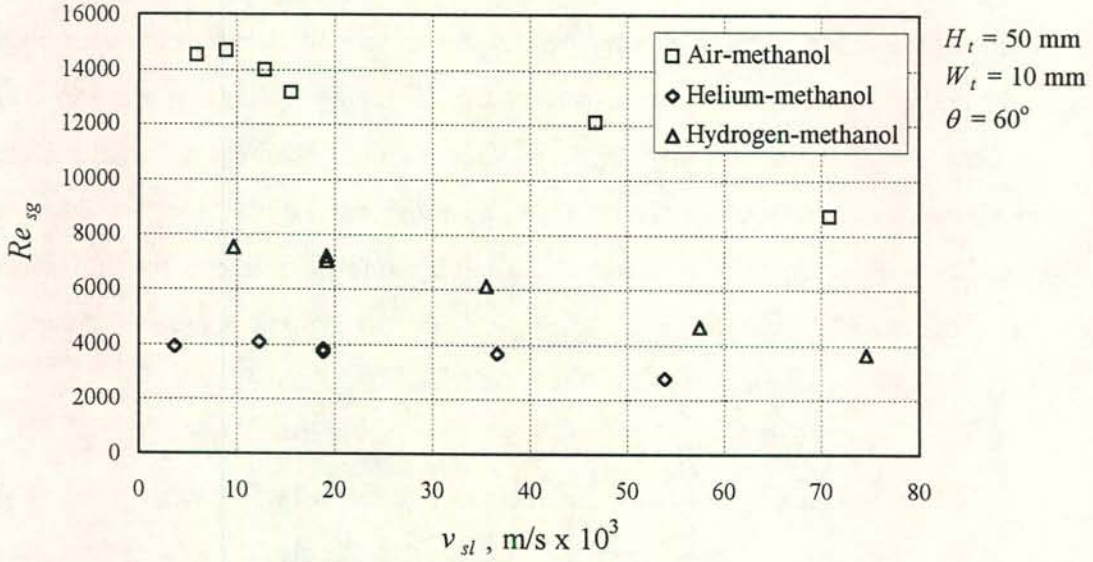

Figure 5.12: The flooding data of figure 5.11 obtained with the different gases plotted in terms of the superficial gas Reynolds number and the superficial liquid velocity.

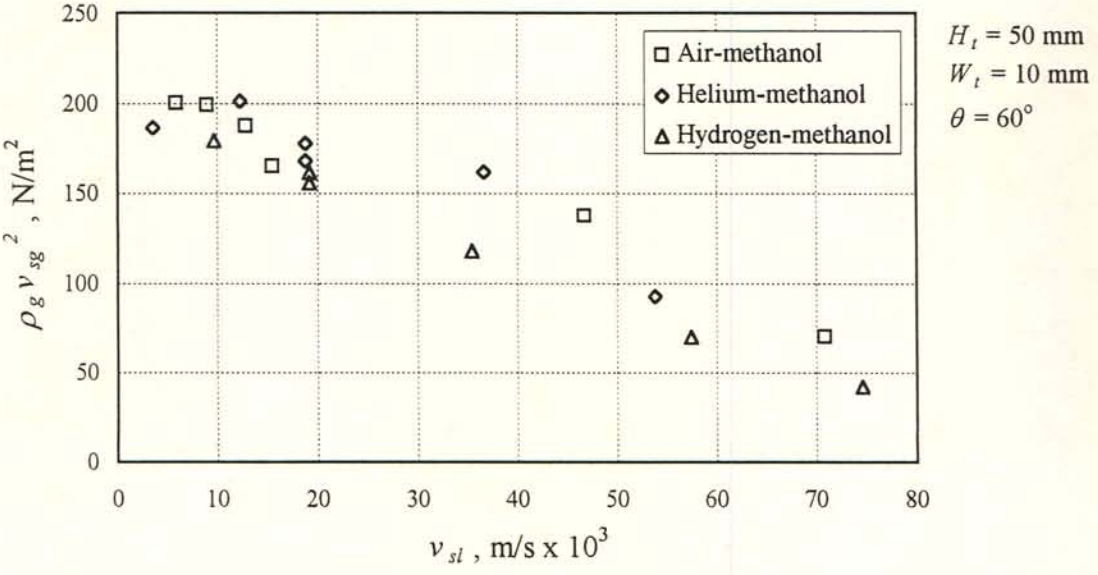

Figure 5.13: The flooding data of figure 5.11 presented in terms of the gas superficial momentum flux and the superficial liquid velocity.

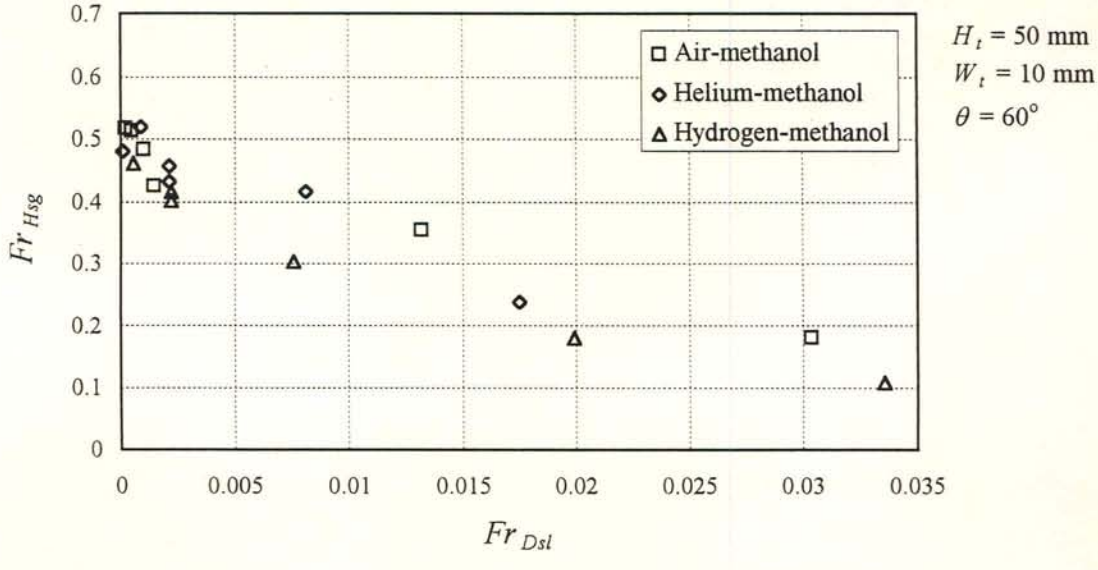

Figure 5.14: The flooding data of figure 5.11 obtained with the different gases plotted in terms o the superficial phase Froude numbers.

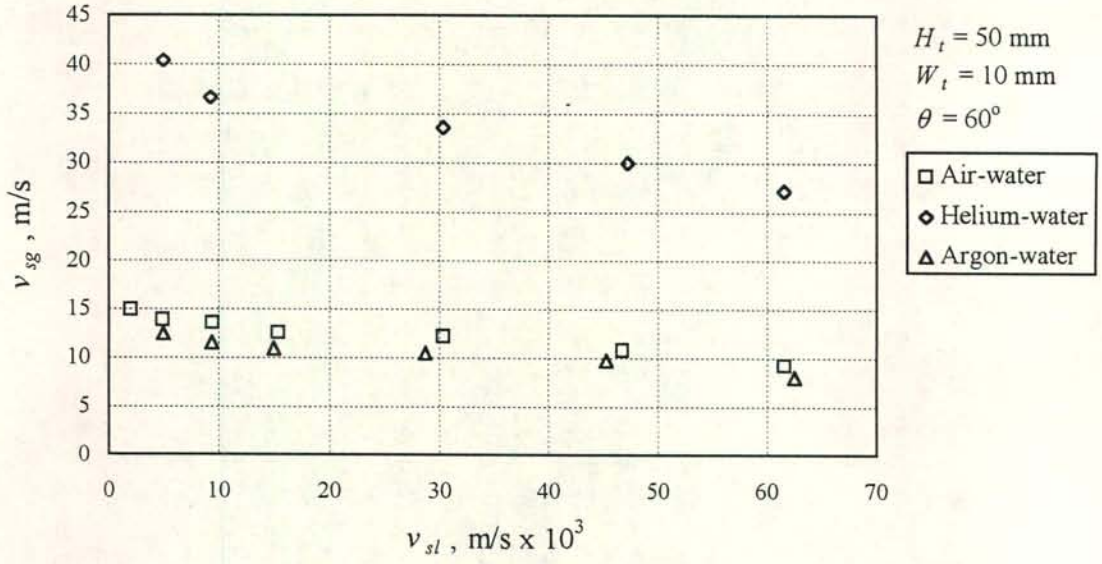

Figure 5.15: Superficial gas flooding velocities for air, helium and argon tested with water inside the 50 mm duct (W_t = 10 mm). Data: Long test section.

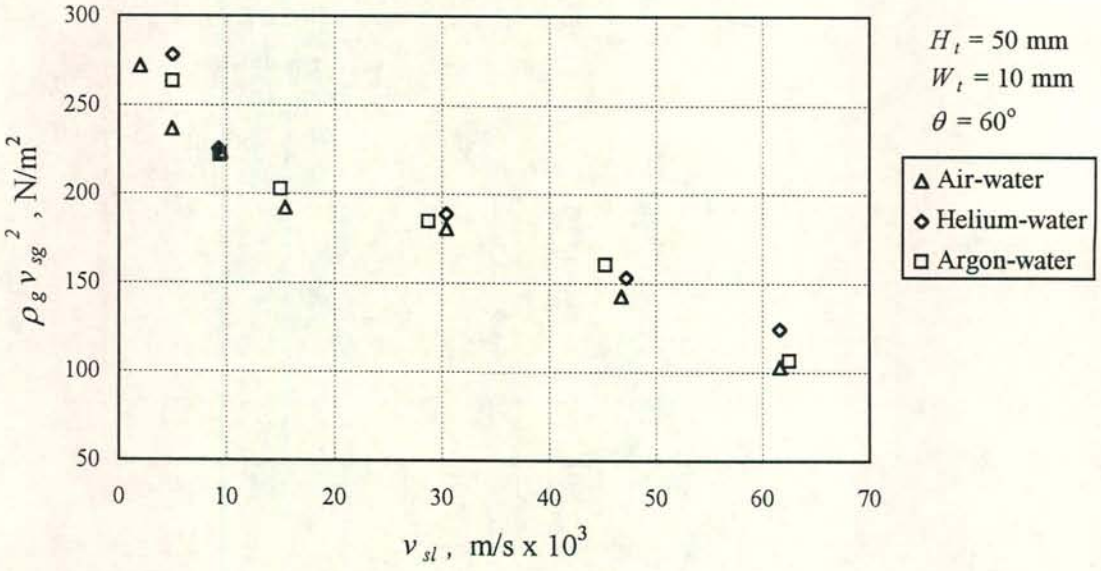

Figure 5.16: The flooding data of figure 5.15 presented in terms of the gas superficial momentum flux and the superficial liquid velocity.

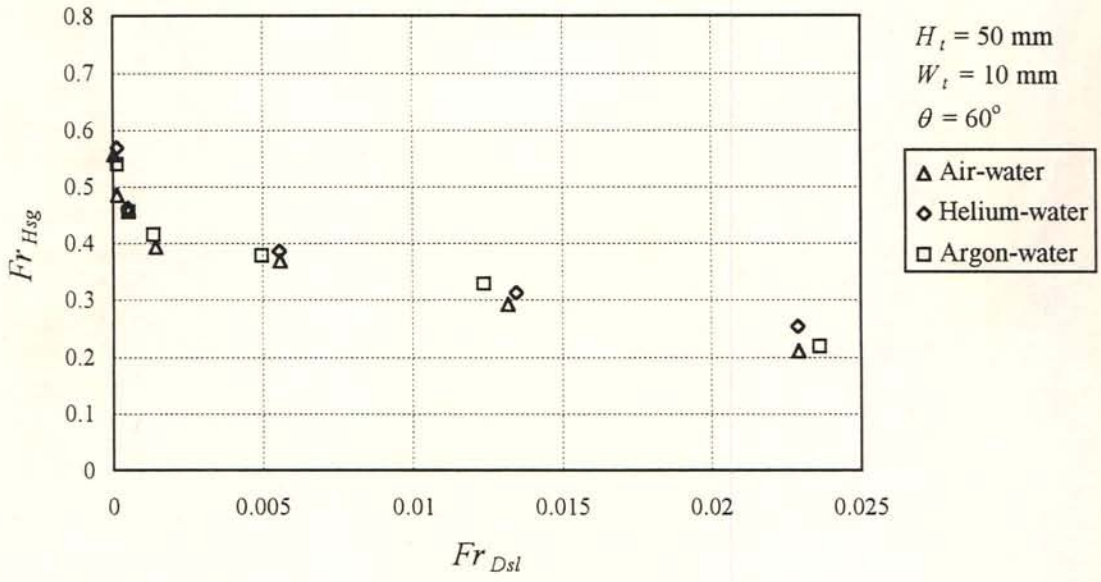

Figure 5.17: The flooding data of figure 5.15 obtained with the different gases plotted in terms o the superficial phase Froude numbers.

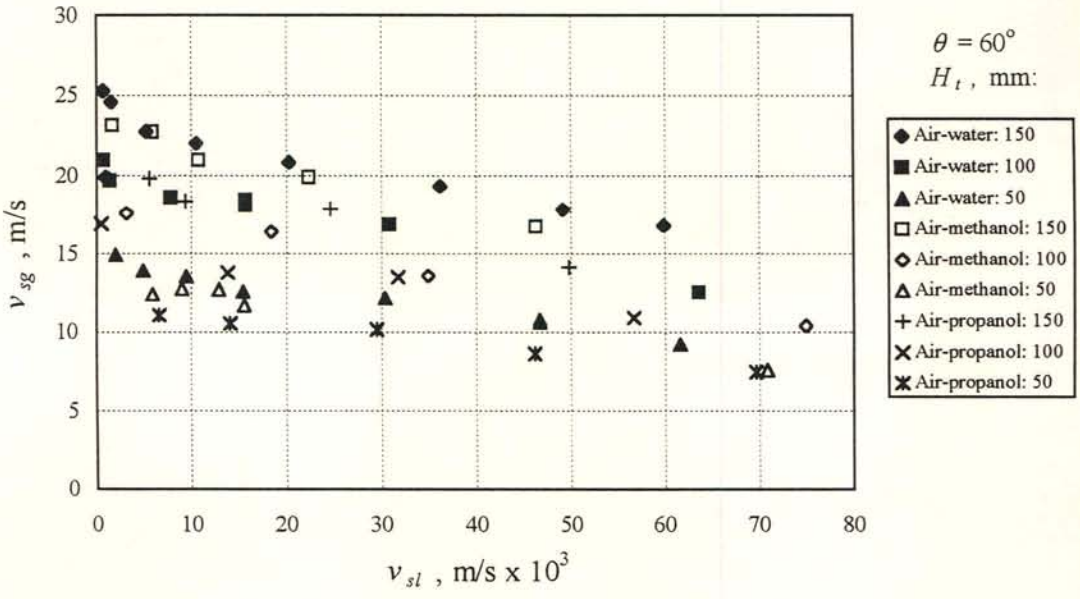

Figure 5.18: Flooding superficial velocities for air-water, air-methanol and air-propanol flow inside the 150, 100 and 50 mm ducts (W_t = 10 mm) to illustrate the effect of the liquid properties. Data: Long test section.

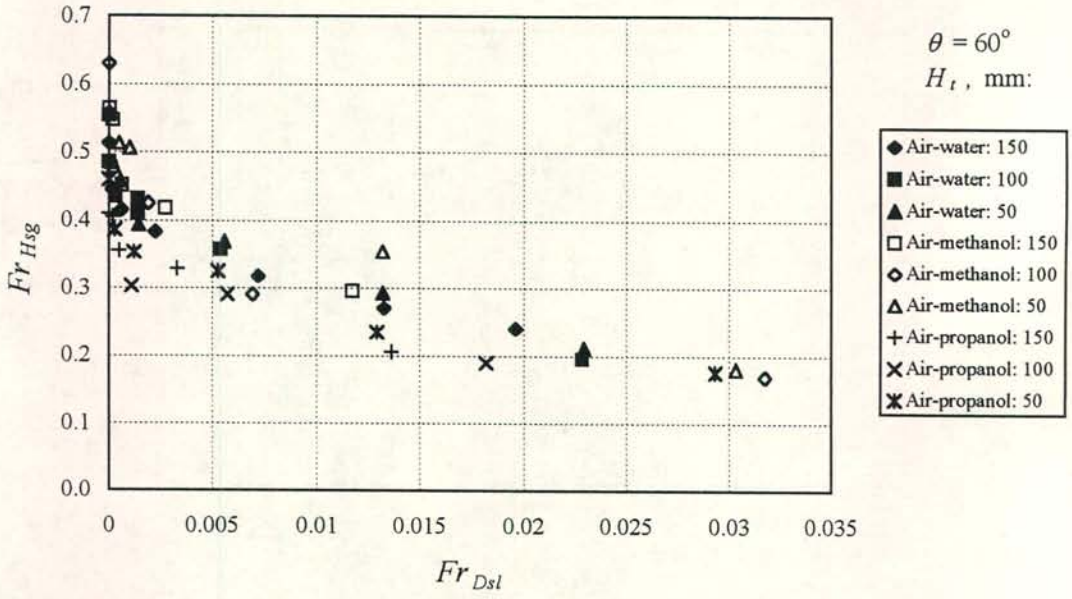

Figure 5.19: The flooding data of figure 5.23 plotted in terms of the phase Froude numbers.

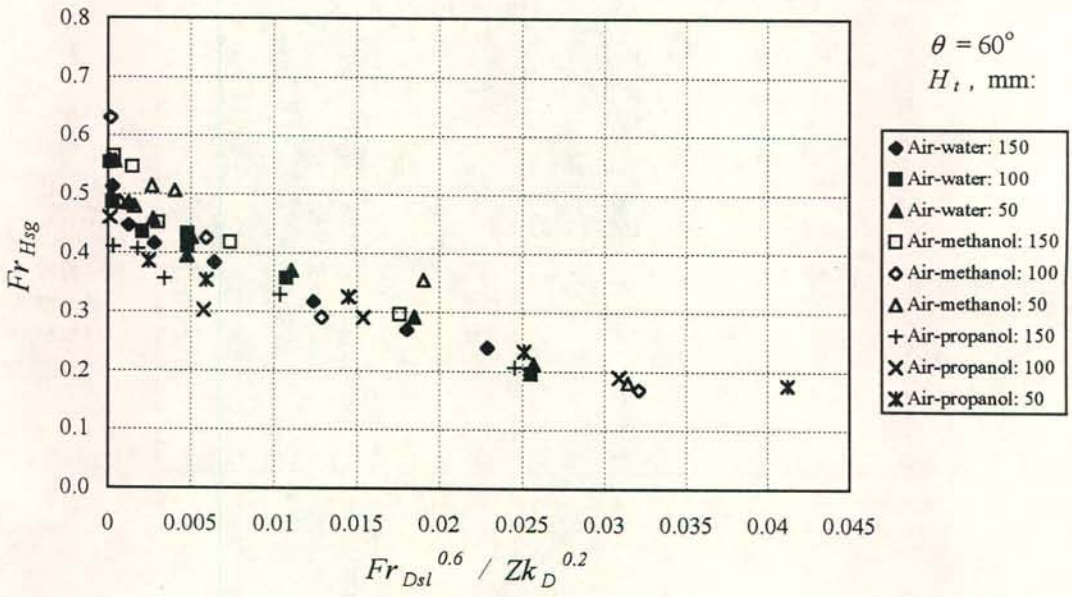

Figure 5.20: The flooding data of figure 5.23 plotted in terms of the phase Froude numbers and the Zk number.

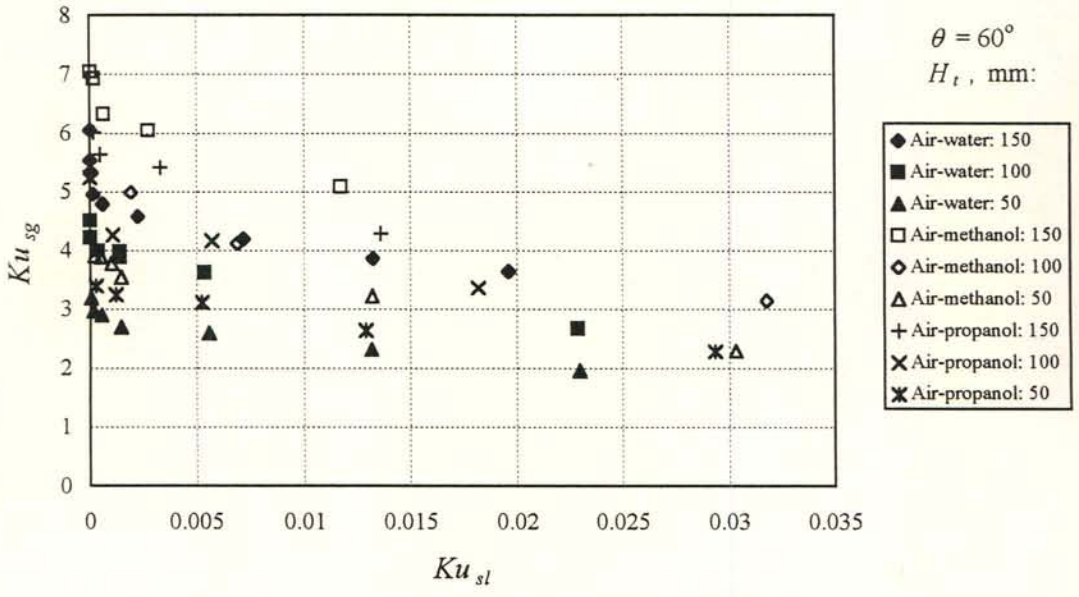

Figure 5.21: The flooding data of figure 5.23 plotted in terms of the superficial phase Kutateladze numbers.

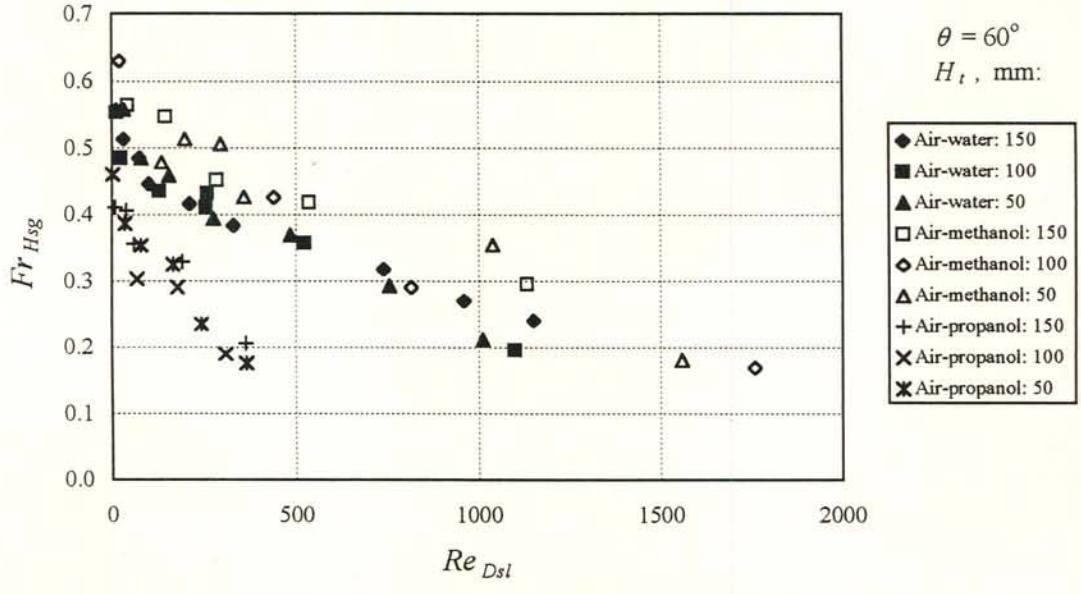

Figure 5.22: The flooding data of figure 5.23 plotted in terms of the superficial gas Froude number and the superficial liquid Reynolds number.

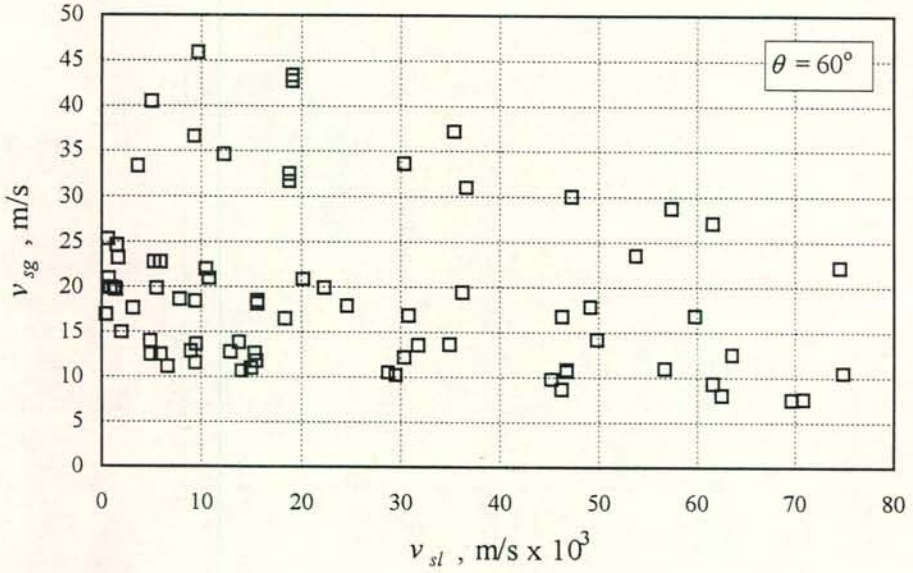

Figure 5.23: All the flooding data obtained with the different gases and liquids tested in the long test section inclined at 60° to the horizontal.

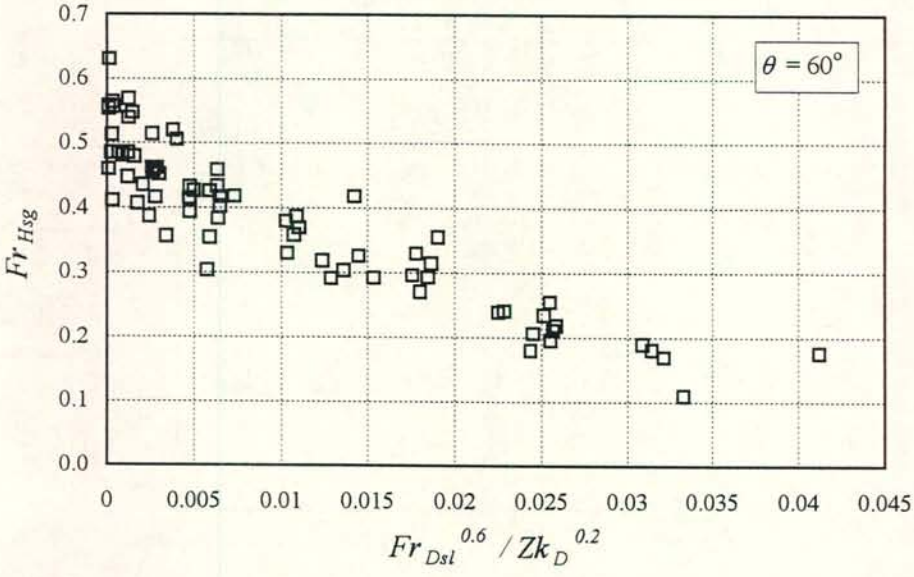

Figure 5.24: The flooding data presented in figure 5.23 plotted in terms of the proposed combination of dimensionless groups.

5.4 The effect of the duct inclination on flooding

Flooding data for the 50 mm (W_t = 10 mm), 100 mm and the 150 mm duct measured at various inclinations from near horizontal to vertical, are shown in figures 5.25 to 5.28. Each data set is presented in two different ways. In the first plot the superficial gas velocity at flooding is presented against the superficial liquid velocity with the duct inclination as a parameter. The second plot shows the flooding superficial gas velocity versus the inclination angle with the liquid flow rate as the parameter.

At small inclinations the flooding gas velocity is almost independent of the liquid flow rate. At steeper inclinations the gradient of the v_{sg} - v_{sl} plots becomes steeper.

Higher gas velocities are required to cause flooding at steeper inclinations due to increased gravity component acting on the liquid in the direction of the duct axis. A relatively sharp drop in the flooding gas velocity occurs from near vertical to the vertical for two reasons. i) The vortex size becomes smaller than the duct height and thus the corresponding weight of the liquid inside the vortex becomes less, compared to inclined flow where the vortex "diameter" is equal to the duct height at flooding. Thus, while the gravity component $g \sin \theta$ acting on the liquid may not differ significantly for vertical and near vertical flow, the amount of liquid to be carried upwards in the form of the vortex becomes less, causing the observed decrease in flooding gas velocity as 90° is approached. ii) During stratified flow in inclined ducts gravity tends to stabilise the draining film. The gas flow has to lift the liquid against the stabilising gravity component to form a vortex. This gravity component vanishes in vertical ducts.

For smaller inclinations the flooding gas velocity is well above zero although one would expect it to become very small because the gravity component $g \sin \theta$ vanishes. Consider the liquid draining down an slightly inclined duct as shown in figure 5.29. A wave is present on the interface similar to those shown in figures 4.17 and 4.19. The conditions are valid for small inclinations in the absence of a vortex-type flow where the gas-liquid interface and the film height δ is well defined.

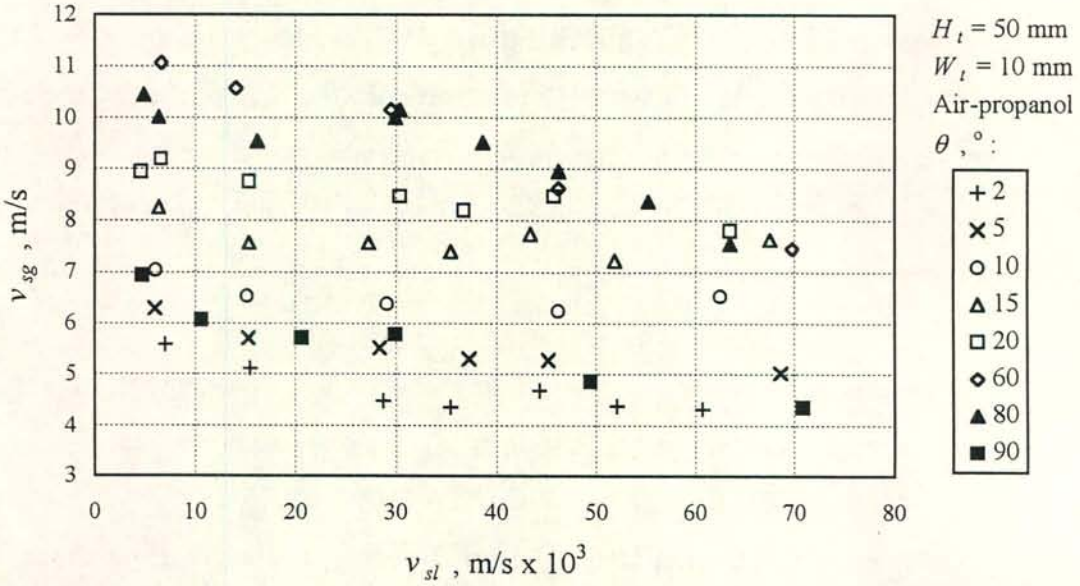

Figure 5.25(a): Air-propanol flooding superficial velocities for the 50 mm duct (W_t = 10 mm) measured at various inclinations. Data: Short test section except for the 60° inclination.

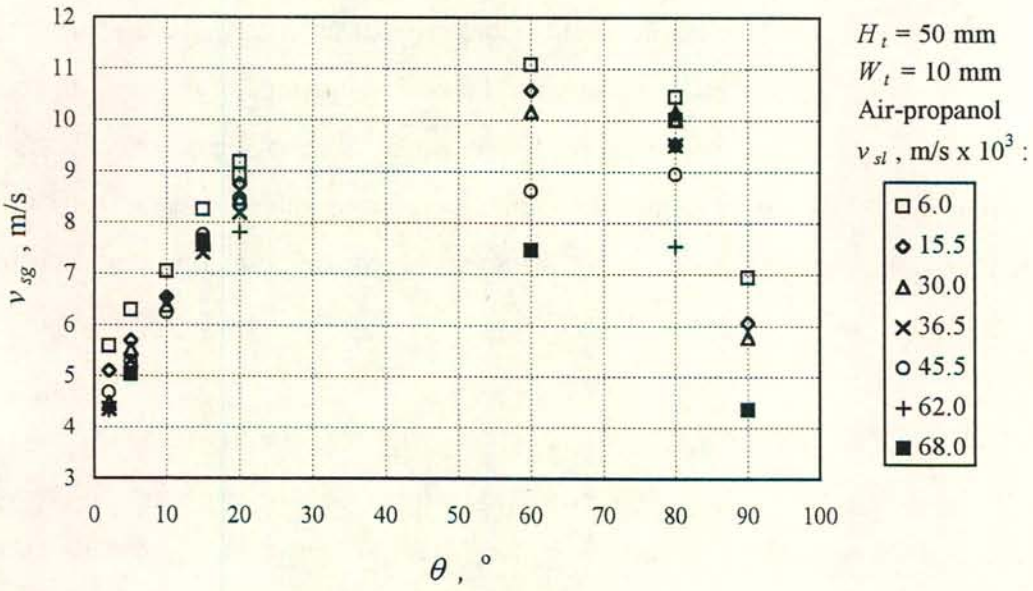

Figure 5.25(b): The data of figure 5.25(a) plotted in terms of the air flooding superficial velocity against the duct inclination with the liquid flow rate as the parameter.

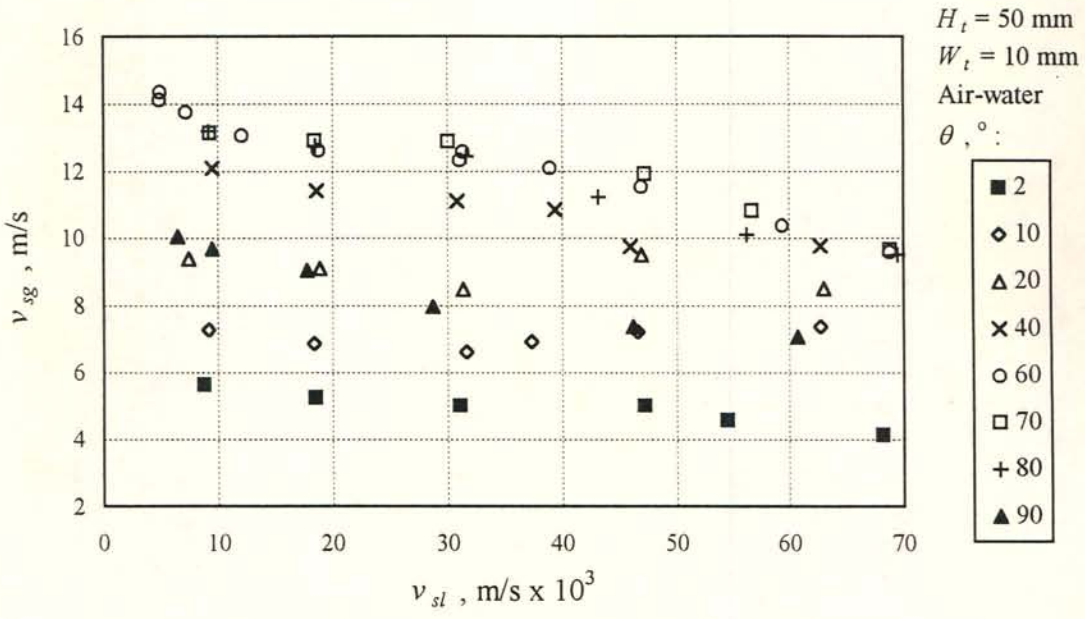

Figure 5.26(a): Air-water flooding superficial velocities for the 50 mm duct (W_t = 10 mm) measured at various inclinations. Data: Short test section.

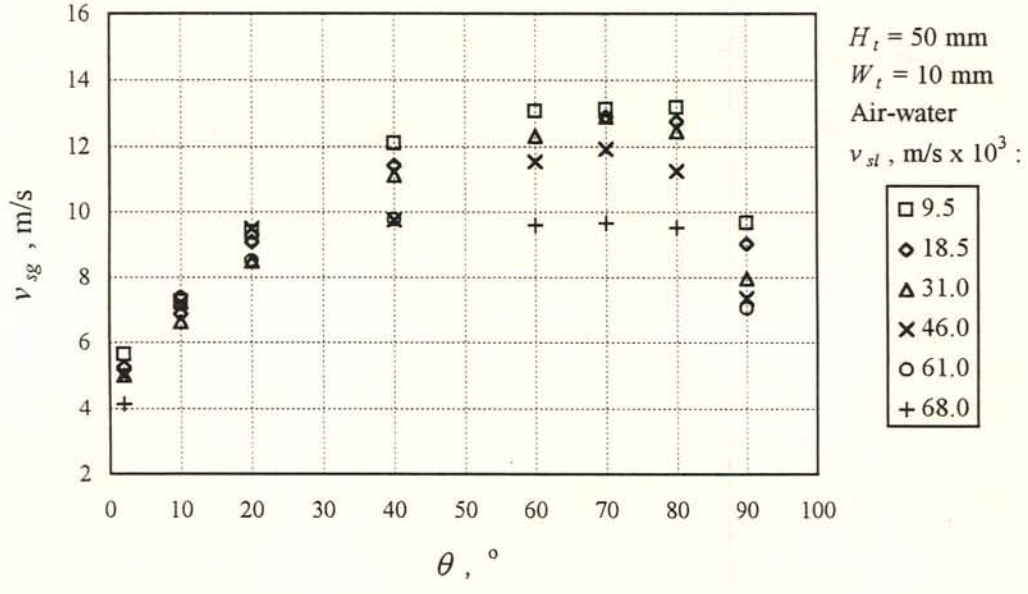

Figure 5.26(b): The data of figure 5.26(a) plotted in terms of the air flooding superficial velocity against the duct inclination with the liquid flow rate as the parameter.

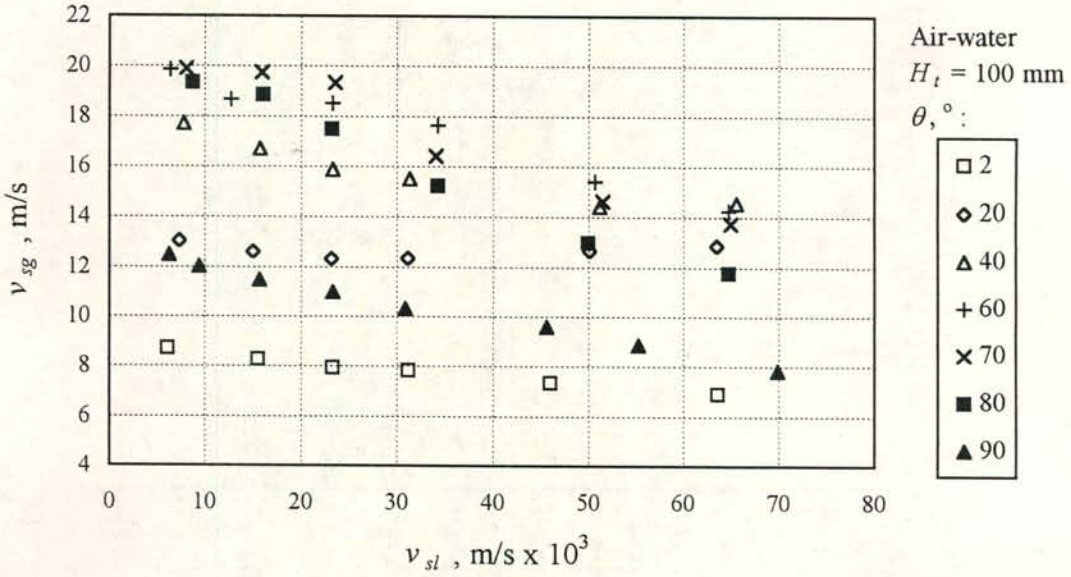

Figure 5.27(a): Air-water flooding superficial velocities for the 100 mm duct measured at various inclinations. Data: Short test section.

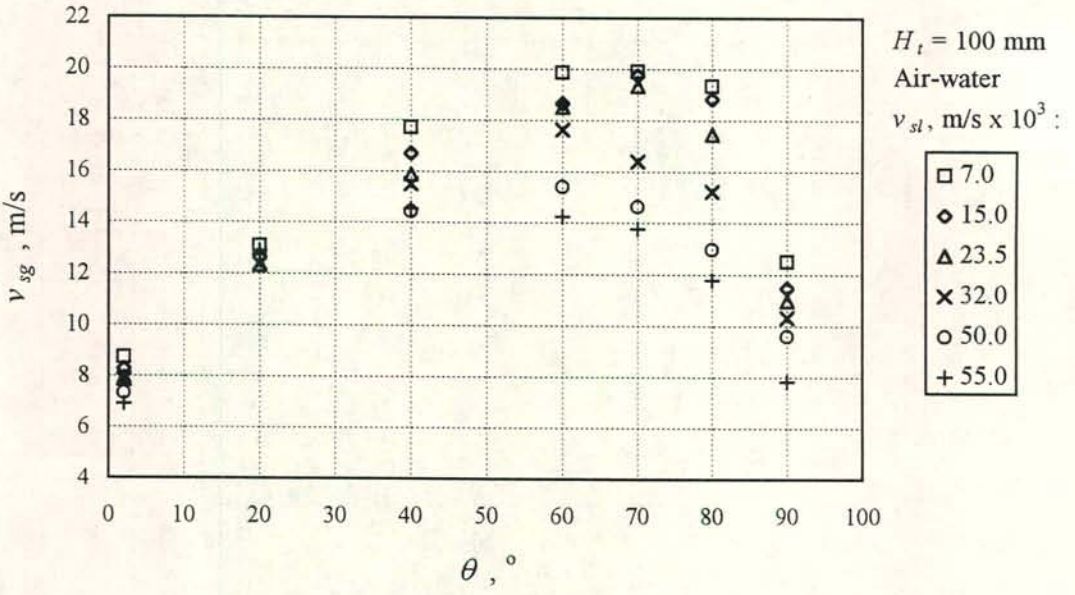

Figure 5.27(b): The data of figure 5.27 (a) plotted in terms of the air flooding superficial velocity against the duct inclination with the liquid flow rate as the parameter.

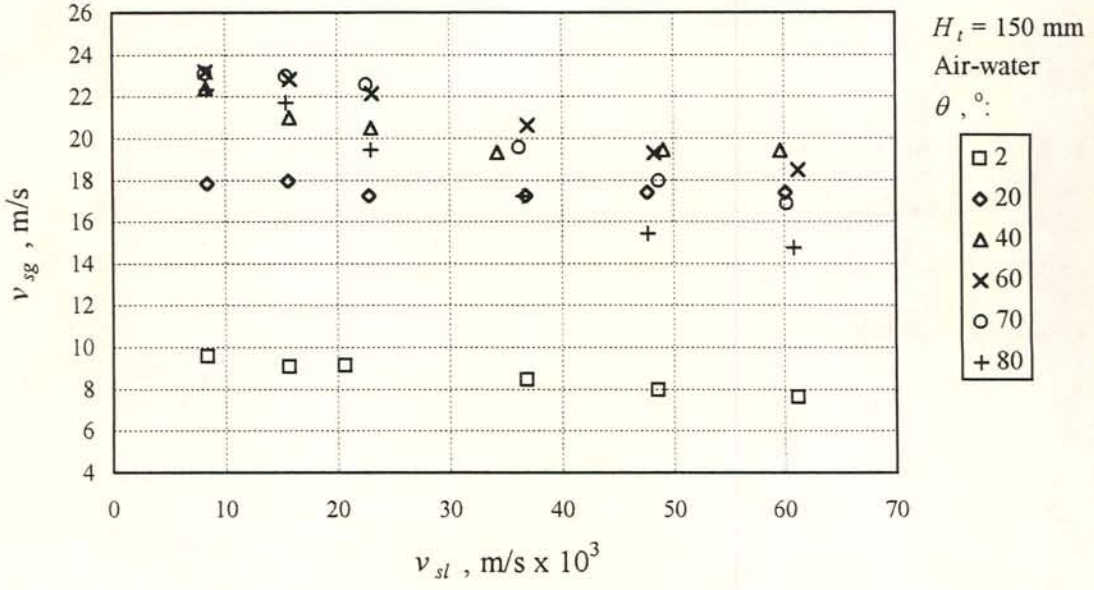

Figure 5.28(a): Air-water flooding superficial velocities for the 150 mm duct measured at various inclinations. Data: Short test section.

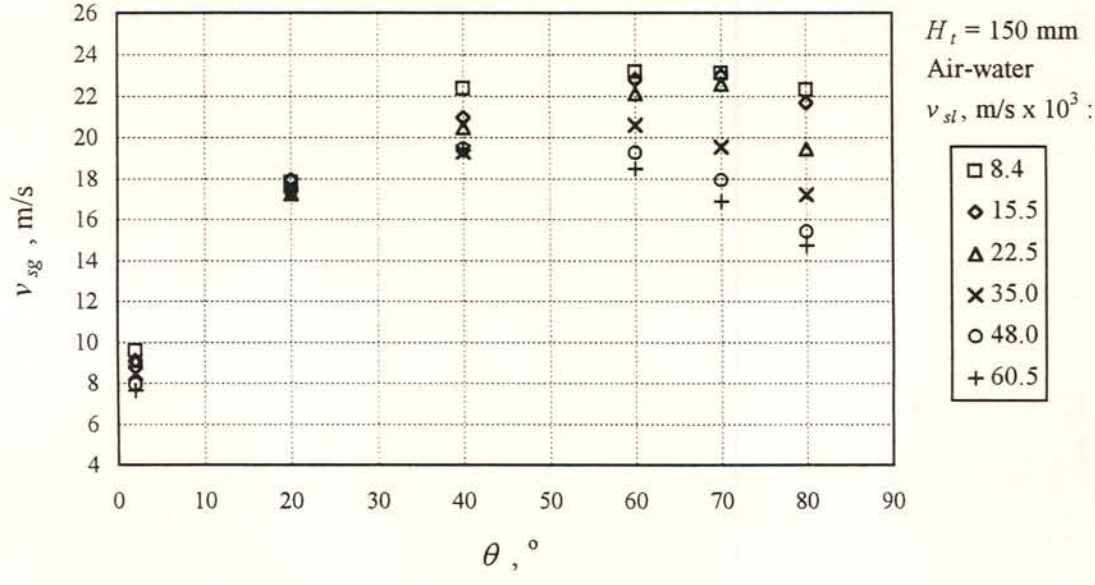

Figure 5.28(b): The data of figure 5.28 (a) plotted in terms of the air flooding superficial velocity against the duct inclination with the liquid flow rate as the parameter.

The net body force acting on the liquid inside the control volume consists of the sin θ component and the hydrostatic pressure due to the change in film thickness

$$F_B = W_t \, \delta \, \Delta z \, g \left(\rho_l - \rho_g\right) \sin\theta + \frac{d\delta}{dz} \Delta z \, W_t \delta \, g \left(\rho_l - \rho_g\right) \cos\theta \tag{5.5}$$

Thus for small inclinations there is an added gravity component once liquid accumulates or in the case of wave formation. The net body force acting in the liquid does not approach zero for near horizontal ducts and for this reason the flooding gas velocity does not become zero.

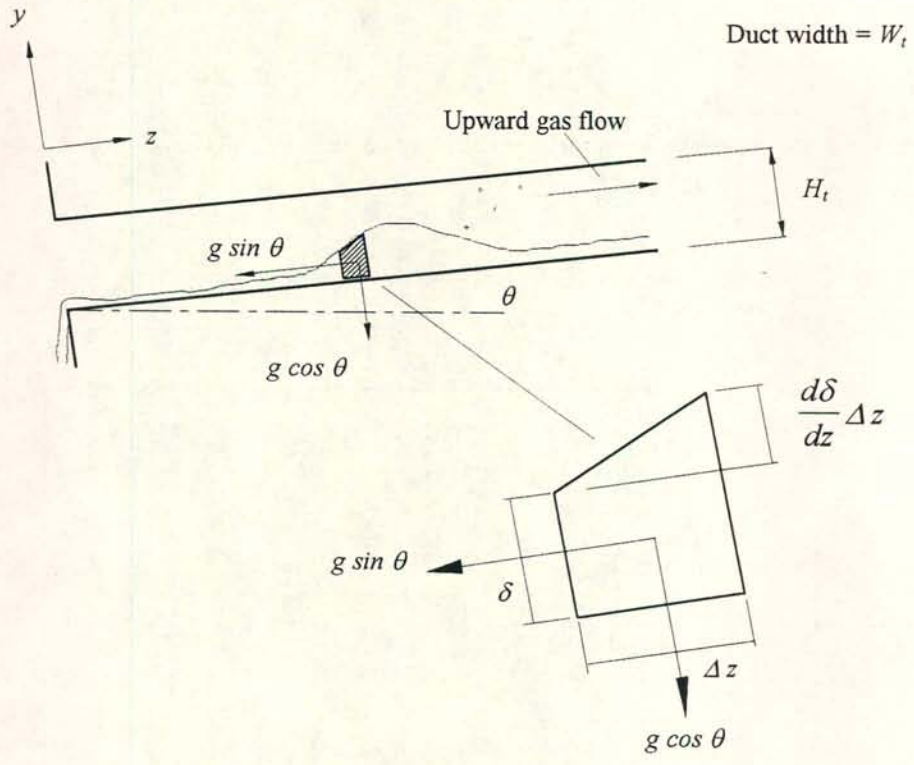

Figure 5.29: Gravity force on wavy film for near horizontal inclinations.

5.5 Correlation for flooding inside inclined rectangular ducts

Separate correlations are developed for inclined and vertical flow due to the difference in the nature of the flow observed in these two cases. Flooding inside vertical ducts is addressed in section 5.6.

The air-water and air-propanol flooding data obtained at various inclinations can be correlated by equation (5.3) where K_o and n are related to the duct inclination. At Fr_{Dsl} = 0 the gas Froude number is equal to K_o, while n determines the gradient in the Fr_{Dsl} - Fr_{Hsg} plane. Curve fits were carried out for each inclination tested to obtain expressions for K_o and n as functions of the duct inclination. The graphs illustrating the fitted curves are given in Appendix F figures F.1 to F.9. The resulting values for K_o and n are shown in figure 5.30 together with their correlating equations

$$K_o = 7.9143 x 10^{-2} + 4.9705 x 10^{-3}\,\theta + 1.5183 x 10^{-4}\,\theta^2 - 1.9852 x 10^{-6}\,\theta^3 \qquad (5.5)$$

$$n = 1.8149 x 10^{1} - 1.9471\theta + 6.7058 x 10^{-2}\,\theta^2 - 5.3227 x 10^{-4}\,\theta^3 \qquad (5.6)$$

Equations (5.5) and (5.6) are valid for $2° \leq \theta \leq 80°$.

All the data on which equation (5.4) are based is shown in figure 5.31 in terms of the superficial velocities. The measured gas flooding velocities vary from as low as 5 m/s to a maximum of approximately 45 m/s, which represents a range of almost an order of magnitude. The same data is shown in figure 5.32 in terms of the dimensionless groups of equation (5.4), representing a scatter of ±20%.

In figure 5.33 the data are presented in terms of the measured versus the predicted superficial velocities. Here the deviation is less because the superficial velocity is proportional to the square root of the Froude number. When applying equation (5.4) one ultimately aims to predict the gas flow rate at flooding for the purpose of sizing equipment for example. According to figure 5.33 predictions accurate to approximately 10% can be achieved. In Appendix F figures F.1 to F.9 equation (5.4) is plotted separately for each inclination together with the experimental data. Good correlation is obtained across the entire range of inclinations tested.

The gradient of the flooding line, as depicted in figure 5.30, has a minimum at an inclination of 10° to the horizontal and reaches a maximum at 60°. The inclinations at the minimum and the maximum values of n correspond to boundaries according to which the flooding process can be divided into three regions. At small angles (region 1), typically less than 10°, roll waves are formed at flooding. In the range of intermediate angles (region 2) the characteristic vortex-type flow is present just before and at flooding. In region 3 ($60° < \theta < 90°$) the transition to flooding in vertical ducts takes place.

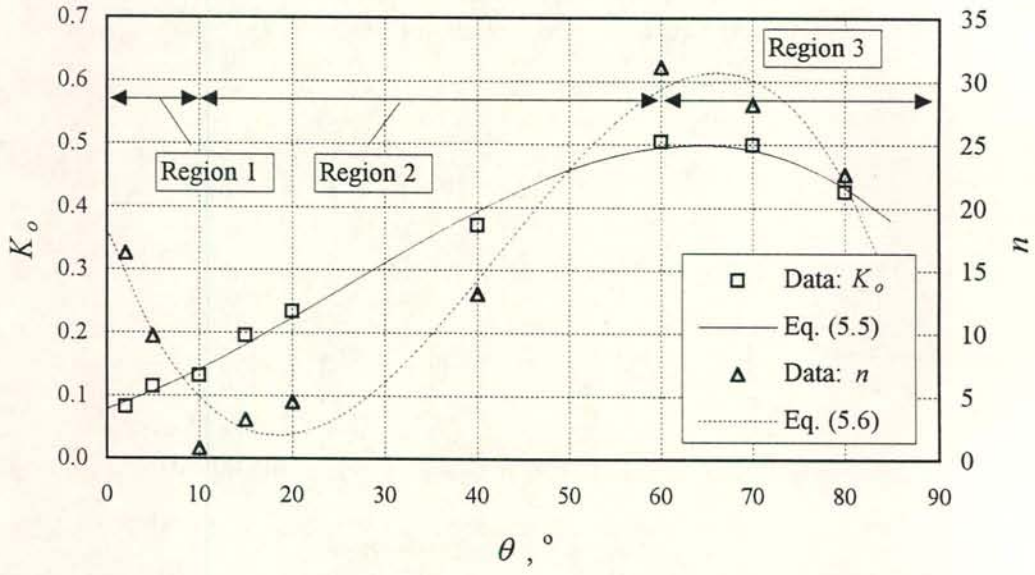

Figure 5.30: The empirical constants plotted against the duct inclination.

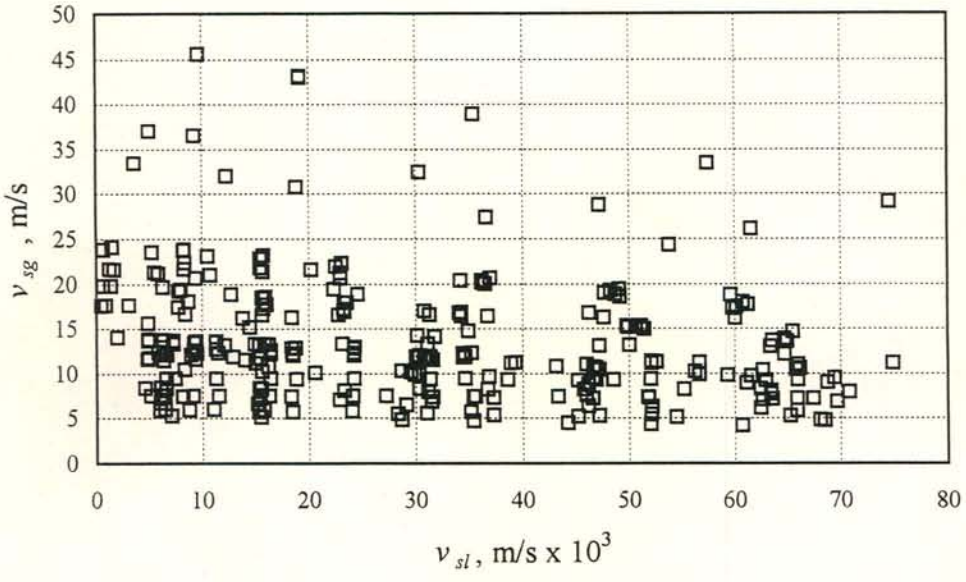

Figure 5.31: Flooding data obtained with various gas-liquid combinations and four different rectangular ducts for inclinations from near horizontal to 80°.

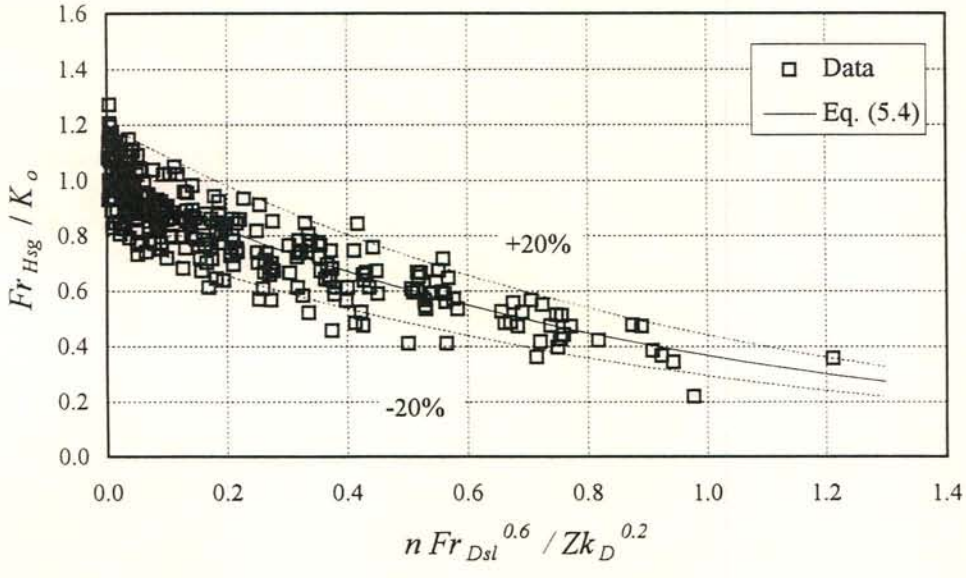

Figure 5.32: The flooding data presented in figure 5.31 plotted in terms of the dimensionless groups of the proposed correlation given by equation (5.4)

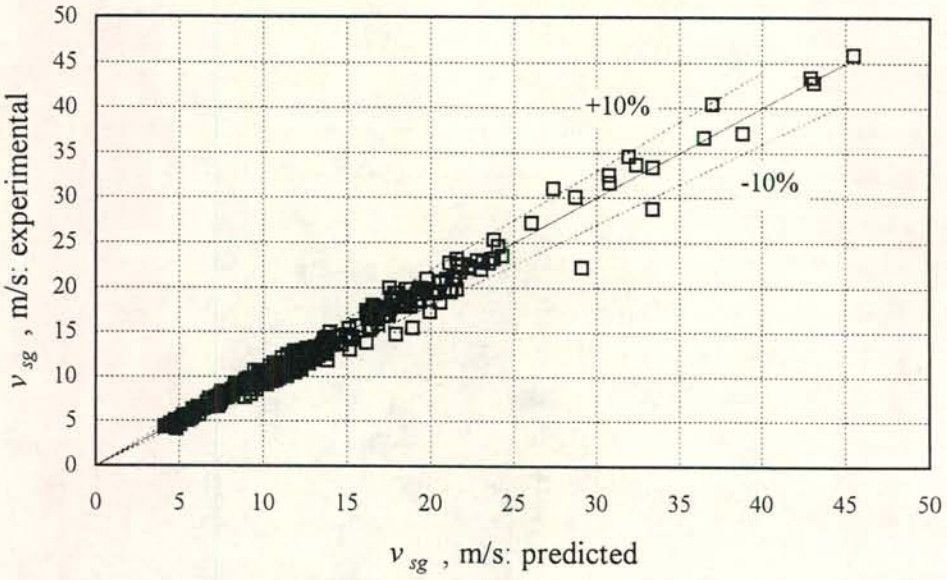

Figure 5.33: Experimental superficial gas velocities at flooding in inclined ducts versus the predicted values according to equation (5.4).

5.6 The effect of the liquid properties on flooding inside vertical rectangular ducts

Flooding data obtained with air-water, air-methanol and air-propanol flow inside the 50 mm duct (10 mm wide) are shown in figure 5.34. In the case of the methanol and propanol tests, flooding did not occur as a result of the vortex formation at high liquid flow rates. Prior to the formation of a disturbed liquid flow at the sharp-edged gas inlet, as illustrated in figure 4.21 for a typical low liquid flow rate, flooding took place due to split flow at the liquid feed upon which only part of the liquid drained downwards. This will be referred to as *top flooding* and is indicated by the solid symbols in figure 5.34. The empty symbols, called *bottom flooding*, represent flooding conditions as illustrated in figure 4.21, i.e. vortex formation at the gas inlet followed by flooding. According to figure 5.34 the flooding gas velocity decreases with a decrease in the liquid density and/or viscosity, similar to the results for inclined flow. Inside the range of liquid flow rates where top flooding occurs the liquid viscosity in particular shows a strong effect.

In figure 5.35 the data are plotted in terms of the proposed Froude-*Zk* number combination. A similar plot for data obtained with the 100 mm duct is given in figure 5.36.

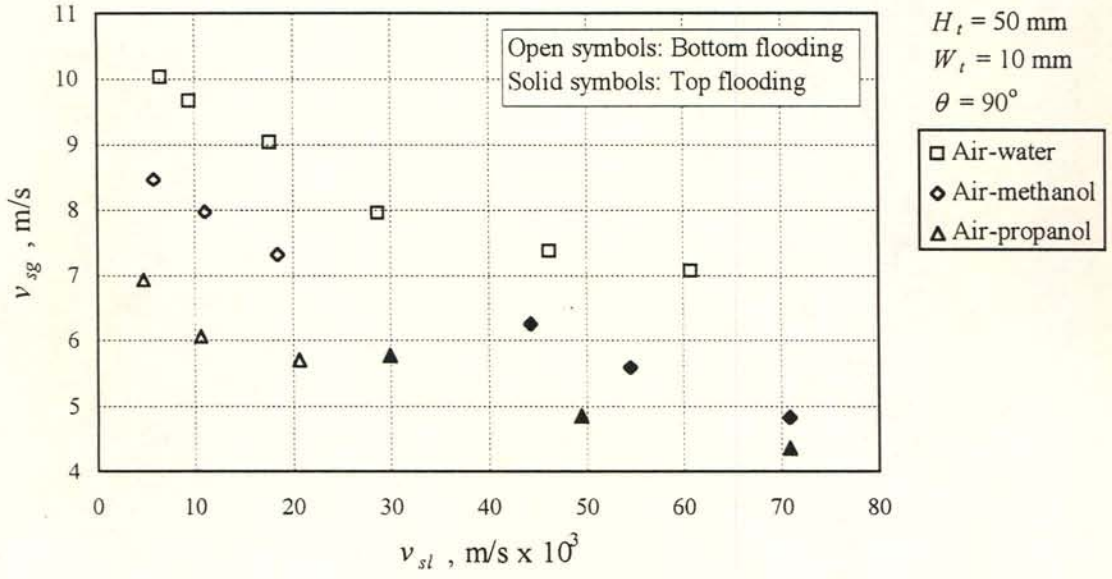

Figure 5.34: Superficial flooding velocities obtained with different liquids to illustrate the effect of the liquid properties on flooding inside vertical rectangular ducts.

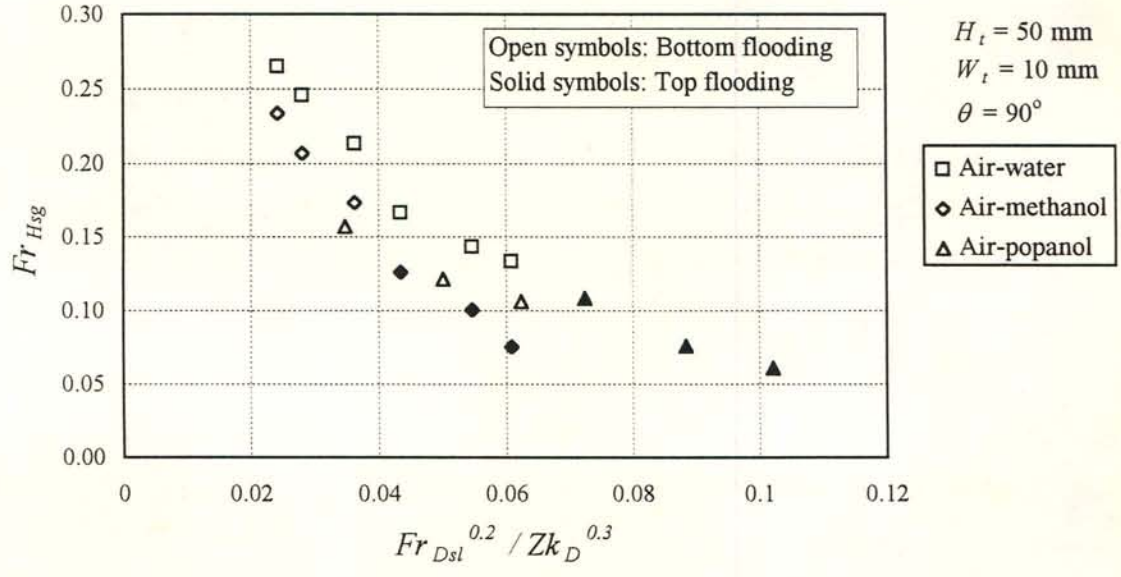

Figure 5.35 The flooding data of figure 5.34 plotted in terms of the phase Froude numbers and the *Zk* number.

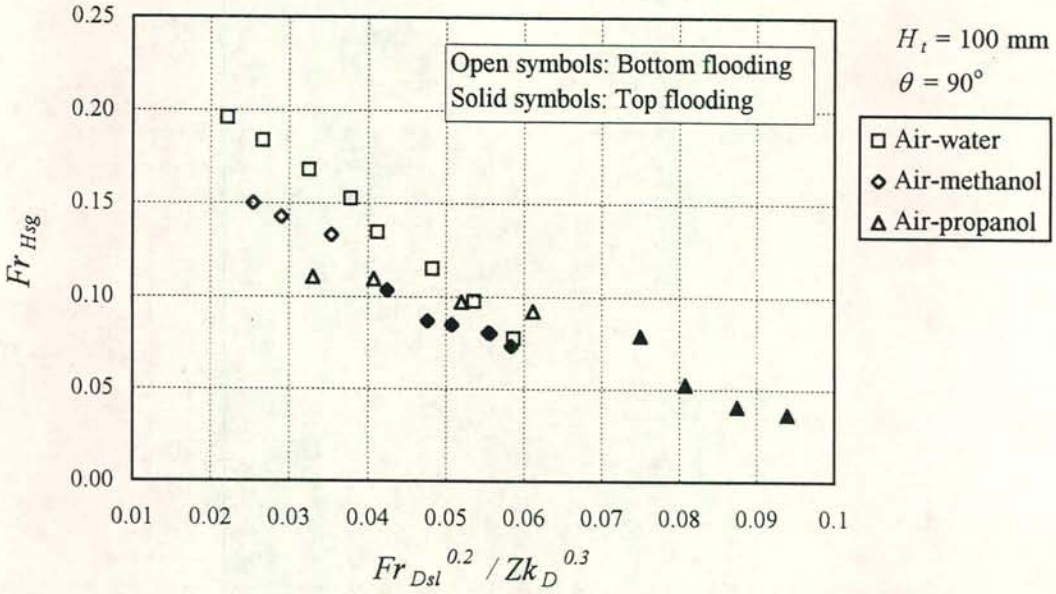

Figure 5.36 Flooding data for the 100 mm duct plotted in terms of the phase Froude numbers and the *Zk* number.

The data for flooding in vertical rectangular ducts are correlated by the expression

$$Fr_{Hsg} = 0.0055 / \left(Fr_{Dsl}^{0.2} / Zk_D^{0.3} \right) \tag{5.7}$$

The exponents 0.2 and 0.3 were determined independently by plotting the densimetric gas Froude number against different values of Fr_{Dsl} at constant values of *Zk* and repeating the procedure by keeping Fr_{Dsl} constant while varying the *Zk* number, thereby obtaining the functional relations $Fr_{Hsg} = f(Fr_{Dsl})$ and $Fr_{Hsg} = f(Zk_D)$ respectively. All the data obtained for vertical flow on which equation (5.7) is based, is shown in figure 5.37 in terms of the superficial velocities and in figure 5.38 the same data are presented in terms of the appropriate dimensionless groups. The measured superficial velocities at flooding versus the predictions by equation (5.7) are shown in figure 5.38. An accuracy of ±15% is achieved.

No flooding experiments were carried out with the 150 mm duct in its vertical flow. Here no vortex formation occurred, resulting in a fundamentally different type of flow which is beyond the scope of the present investigation of rectangular ducts.

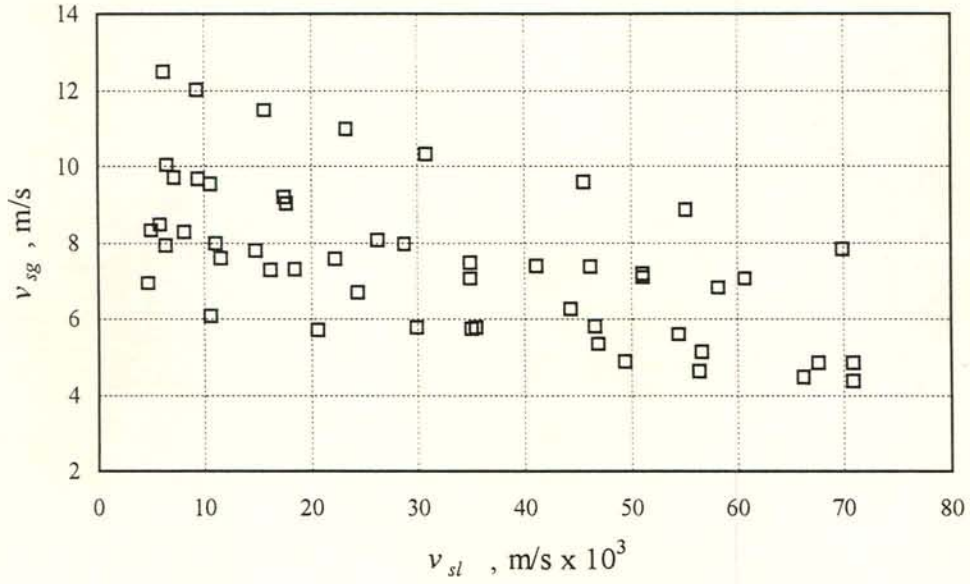

Figure 5.37: Flooding superficial velocities for vertical rectangular ducts used to obtain the correlation given by equation (5.7).

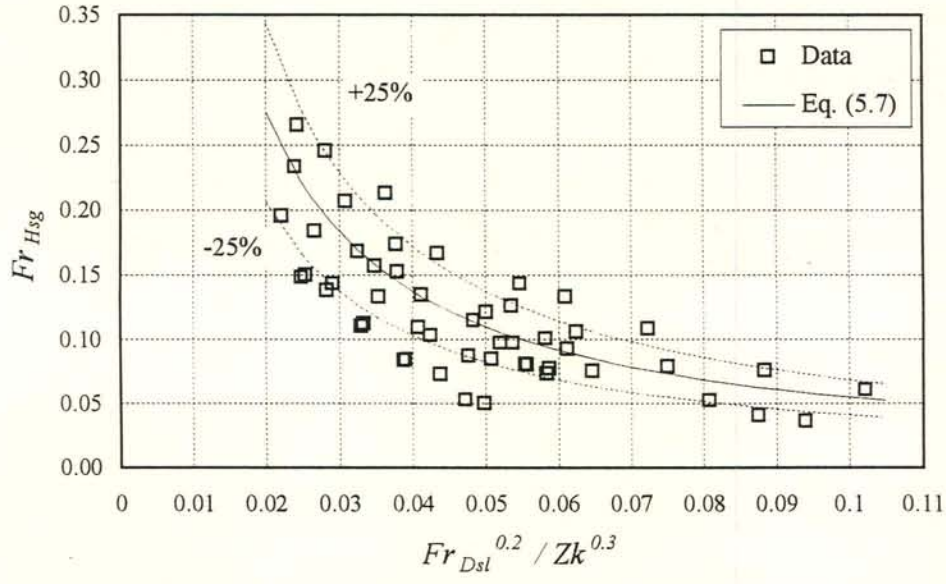

Figure 5.38: The flooding data of figure 5.37 plotted in terms of the dimensionless groups of the correlating equation.

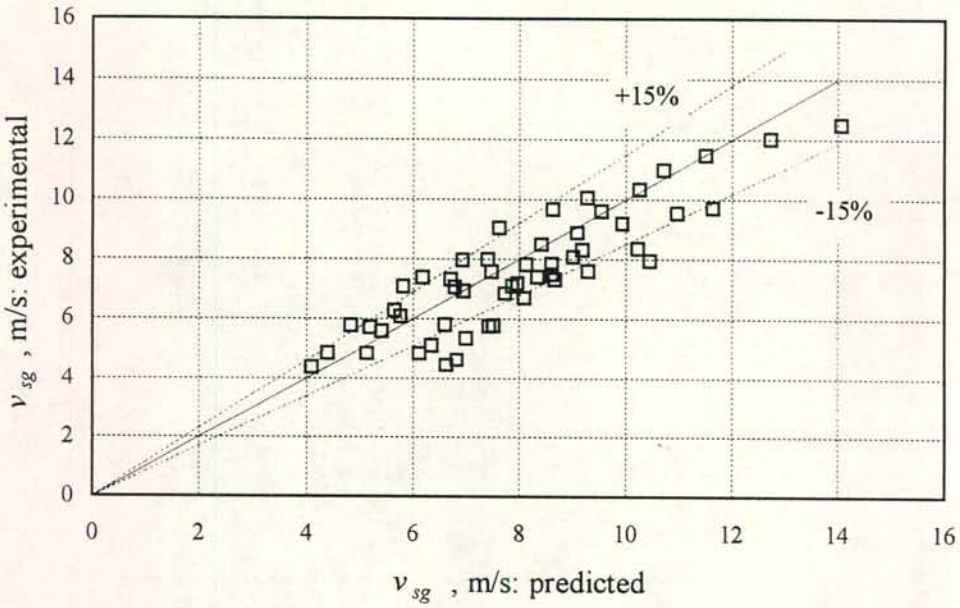

Figure 5.39: Experimental superficial gas velocities at flooding in vertical ducts versus the predicted values according to equation (5.7).

5.7 Entrainment during counterflow in the 150 mm duct inclined at 60°

Similar to the pressure drop and flooding experiments, entrainment tests were conducted by measuring the rate of entrainment at different gas flow rates while keeping the liquid feed into the test section constant. Entrainment was measurement for three liquid flow rates, i.e. v_{sl} = 0.0049, 0.0105 and 0.0204 m/s. The entrainment data are shown in figures 5.40 and 5.41 in terms of the superficial gas velocity and the superficial densimetric gas Froude number respectively. The liquid flow rate did not have a significant effect on the nature of entrainment in the range of flow rates tested. A detailed description of the observations during the tests for v_{sl} = 0.0105 m/s is presented in following paragraph.

Below Fr_{Hsg} = 0.09 no entrainment was observed at the sharp-edged gas inlet, nor were any droplets observed higher up the duct. At Fr_{Hsg} = 0.09 droplets were entrained at the gas inlet and deposited in an ≈0.5 m long region above the sharp-edged flange. The liquid jet inside the bottom plenum was slightly deflected upwards but was not sucked into the duct at this stage. Stratified wavy flow was present between points 2 and 3 in the test section. No droplets were torn off the wave crests. At a superficial densimetric

Froude number of 0.127 the lower parts of duct walls in the region between the inlet flange and point 2 were wetted. At a densimetric gas Froude number of 0.157 droplets began to enter the cyclone separator. At Fr_{Hsg} = 0.187 approximately 30% of the duct height was wetted at the gas inlet, resulting in a thin liquid film creeping upwards from just above the inlet flange. Now droplets were torn off the waves crests in section 2-3 and some adhered, upon deposition along the entire duct length, to the walls. The liquid jet was sporadically broken up resulting in droplets being sucked into the duct from inside the bottom plenum. Upon a further increase in the air flow rate the wetting in the immediate region above the inlet increased and at Fr_{Hsg} = 0.241, 50% of the duct height was wetted.

At Fr_{Hsg} = 0.319 a strong vortex was present just above the sharp-edged inlet flange where it remained stationary. The vortex "diameter" was approximately half the duct height. In section 2-3 waves travelling downwards were frequently dispersed by the gas flow causing droplet formation and entrainment. Part of the droplets were deposited on the duct walls at the point of entrainment. At the gas inlet the liquid drained in the form of spurts sporadically falling into the plenum. As the air flow rate was further increased, the "diameter" of the vortex grew, reaching approximately 90% of the duct height at Fr_{Hsg} = 0.384. At this stage similar but smaller vortices appeared in section 2-3 but were immediately dispersed by the gas flow upon formation. At Fr_{Hsg} = 0.410 vortices formed at the sharp-edged gas inlet were propelled up the duct causing a sharp increase in the pressure gradient and resulting in flooding.

Note that entrainment was observed already at Fr_{Hsg} = 0.09 at the gas inlet, but most of these droplets were deposited onto the duct walls in the immediate region above the gas inlet. Only at Fr_{Hsg} = 0.157 the entrained liquid was carried upwards beyond the porous sinter. Just before the flooding the entrainment measured represented only 1.1 % of the liquid fed into the system.

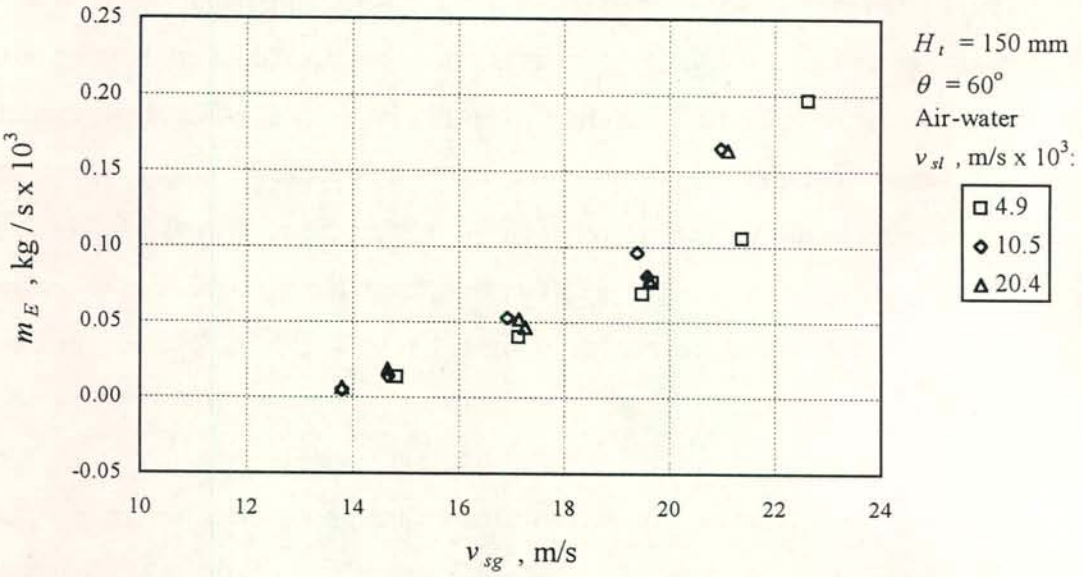

Figure 5.40: Entrainment rate for air-water flow inside the 150 mm duct inclined at 60° to horizontal, plotted against the superficial gas velocity.

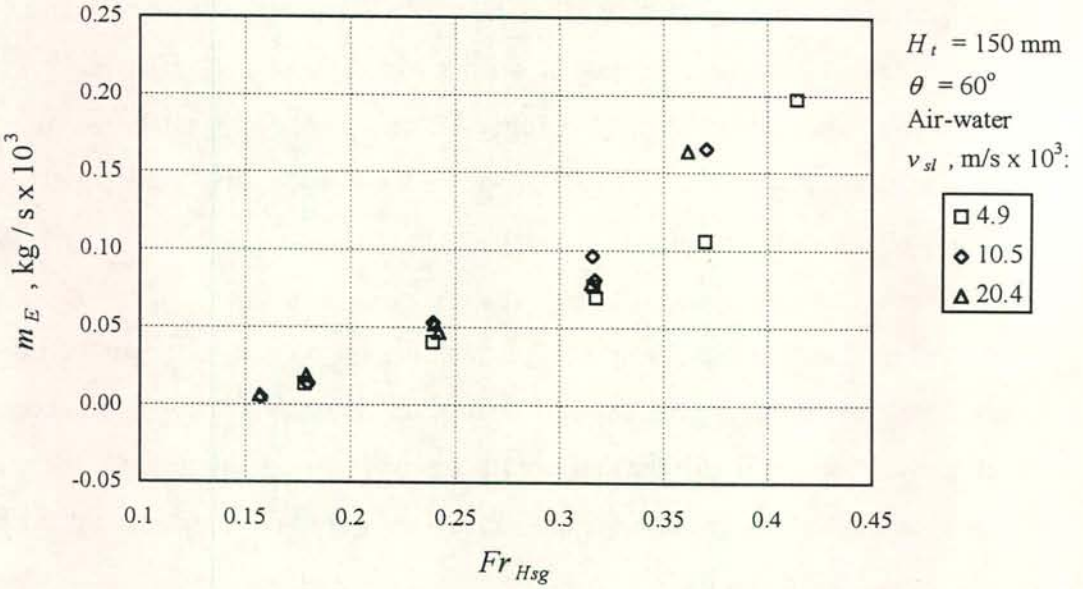

Figure 5.41: Entrainment rate for air-water flow inside the 150 mm duct inclined at 60° to horizontal, plotted against the superficial densimetric gas Froude number.

5.8 Discussion of the flooding results

At low liquid flow rates ($0.005 < v_{sl} < 0.015$ m/s) the two phases interacted strongly in the immediate vicinity of the gas entrance to form a vortex, while stable stratified flow prevailed higher up the test section. At moderate liquid flow rates and intermediate inclinations the point of inception of the vortex could however not always be identified as the bottom entrance. At $v_{sl} \approx 0.07$ m/s and higher flow rates the vortex formation was not limited to sharp-edged gas inlet anymore, but took place somewhere between the gas inlet and point 3 in the test section. It can therefore be speculated that the influence of the bottom configuration on flooding becomes less at higher liquid flow rates.

The draining liquid appeared to be very stable at low liquid flow rates and strong localised interactions at the gas inlet were required to initiate flooding. At higher liquid flow rates the stratified liquid layer tended to be unstable along the entire duct length in the presence of a flowing gas.

The densimetric Froude numbers were found to be the major dimensionless groups governing flooding in the duct configurations tested. In the past researchers generally assumed the hydraulic diameter to be the characteristic dimension during flooding. According to the results reported here the flooding gas velocity is strongly dependent on the duct height. It has furthermore been found that both the duct height and the hydraulic diameter play a role in the flooding process. Consequently the gas and the liquid Froude number do not have the same characteristic dimension and according to the physics of flooding, the gas Froude number should contain the duct height while the hydraulic diameter should be employed for the liquid Froude number. This is a new concept in contrast to the method employed in the past where the same type of dimension was chosen for both Froude numbers.

A dimensionless group containing the liquid density and viscosity, the hydraulic diameter and the surface tension originally propose by Zapke and Kröger [96ZA1] was introduced to correlate the effect of the liquid properties on the flooding gas velocity. According to the dimensionless group the liquid viscosity and the surface tension have opposite effects

on flooding. Consider the correlation for flooding in vertical ducts given by equation (5.7). Assume that $(\rho_l - \rho_g) \approx \rho_l$ and solve for the superficial gas velocity, i.e.

$$v_{sg} \propto \frac{g^{0.6} H_t^{0.5} D_e^{0.175} \rho_l^{0.575} \sigma^{0.075}}{\mu_l^{0.15} v_{sl}^{0.2}} \tag{5.8}$$

Equation (5.8) illustrates how the different parameters influence flooding. While an increase in surface tension results in an increase in the flooding gas velocity, an increase in the liquid viscosity causes the flooding velocity to decrease.

The qualitative trend given by equation (5.8) is in agreement with existing theoretical models on two-phase flow associated instabilities. According to the Kelvin-Helmholtz instability theory [92CA1] for inviscid two-phase flow, the surface tension acts as a restoring force on a disturbed interface. Higher gas velocities are thus required for the break-up of the liquid film and subsequent upward liquid transport as the surface tension increases.

Cetinbudaklar and Jameson [69CE1] conducted a linearized small-amplitude stability analysis for viscous film flow. The resulting Orr-Sommerfeld equations for each phase were then solved to find the conditions at which the surface disturbance amplifies and the interface becomes unstable. Their theory predicts decreasing flooding gas velocities for an increase in the liquid viscosity. It was argued that viscous damping occurs due to dissipation near the wall. This wall effect decreases with an increase in the film thickness. Because the film thickness increases with an increase in the liquid viscosity, the damping effect decreases with an increase in the viscosity. Less energy is then required to cause instability and flooding occurs at lower gas velocities.

The *Zk* number appears to be related to the surface tension and liquid viscosity effects which determine the stability of the liquid film and therefore succeeds in correlating the experimental data.

The author would like to stress the point that equations (5.4) and (5.7) do not represent flow rates during partial liquid delivery. The fluid flow rates just below the predictions of

these correlations represent the maximum attainable flow rates, without liquid ejection at the top end of the test section, when approached from conditions below flooding.

In chapter 4 section 4.3.3 it is mentioned that the wetting of the acrylic plastic duct walls by water changed after the propanol tests were completed and that the wetting properties of the duct walls influenced the pressure gradient during counterflow. No such an effect was found in the case of flooding.

CHAPTER 6

EVALUATION OF THE VALIDITY OF THE FROUDE-ZK NUMBER COMBINATION AND CONCLUSIONS

The general validity of the Froude-*Zk* number can be evaluated by considering the data of other investigations. Care must however be taken when comparing flooding data of different researchers. The strong influence of the test section configuration does not permit direct comparison unless the data have been generated under identical conditions. Furthermore, proper interpretation of the flooding definitions employed in the past is essential to prevent the comparison of data which represent different flow phenomena.

Because very few, if any, of the past investigations were carried out under identical conditions (test section configuration, flooding definition, experimental procedure), the author decided not to compare existing data of different investigations directly. Instead, data sets by other researchers are plotted individually in terms of the proposed Froude-*Zk* number combination to establish whether it applies in general or only under certain conditions.

6.1 Flooding data of other investigations

6.1.1 Clift et al. [66CL1]

Clift *et al.* investigated the effect of the liquid viscosity on flooding in a vertically inclined tube of diameter D = 31.8 mm. Water and aqueous glycerol solutions were used as working fluids. The properties of the solutions tested are given in table 6.1. Liquid was injected through a porous section and air entered the tube at the bottom through a bell-mouth inlet. The flooding definition and flow patterns observed are described in section 2.3 and the flooding superficial velocities are shown in figure 2.17(a). The data are replotted in figure 6.1 in terms of the proposed Froude and *Zk* numbers proposed for vertical rectangular ducts. Excellent correlation is achieved.

Table 6.1: Properties of the liquids tested by Clift *et al.* [66CL1].

% Glycerol	μ_l [kg/ms x 10^3]	ρ_l [kg/m^3]	σ [N/m x 10^3]
Water	1.32	1000	72.0
25 %	2.18	1060	70.2
59 %	10.4	1150	68.0
70 %	23.4	1180	66.4
77 %	46.0	1200	65.8
82 %	82.5	1210	65.0

6.1.2 Suzuki and Ueda [77SU1]

Experiments similar to those of Clift *et al.* [66CL1] were conducted by Suzuki and Ueda. Air, water and aqueous glycerol solutions were tested. The properties are given in table 6.2. A detailed description of their experiments is presented in section 2.3. The flooding data are shown in figures 2.10(b) and 6.2 in terms of the superficial velocities and the Froude-*Zk* number combination respectively. Good correlation is achieved in the case of the solutions but the data for pure water deviate at high liquid flow rates.

Table 6.2: Properties of the liquids tested by Suzuki and Ueda. [77SU1].

Aqueous glycerol solution no.	μ_l [kg/ms x 10^3]	ρ_l [kg/m^3]	σ [N/m x 10^3]
Water	0.9	997	68.0
1	2.0	1090	56.0
2	5.1	1140	53.0
3	10.0	1180	53.0
4	24.0	1210	53.0

6.1.3 Chung et al. [80CH1, 79TI1]

Chung et *al.* conducted experiments with pure water, water treated with surfactants, and silicon oil to establish the role of the surface tension during flooding. They also tested three different kinds of oils to investigate the effect of the liquid viscosity.

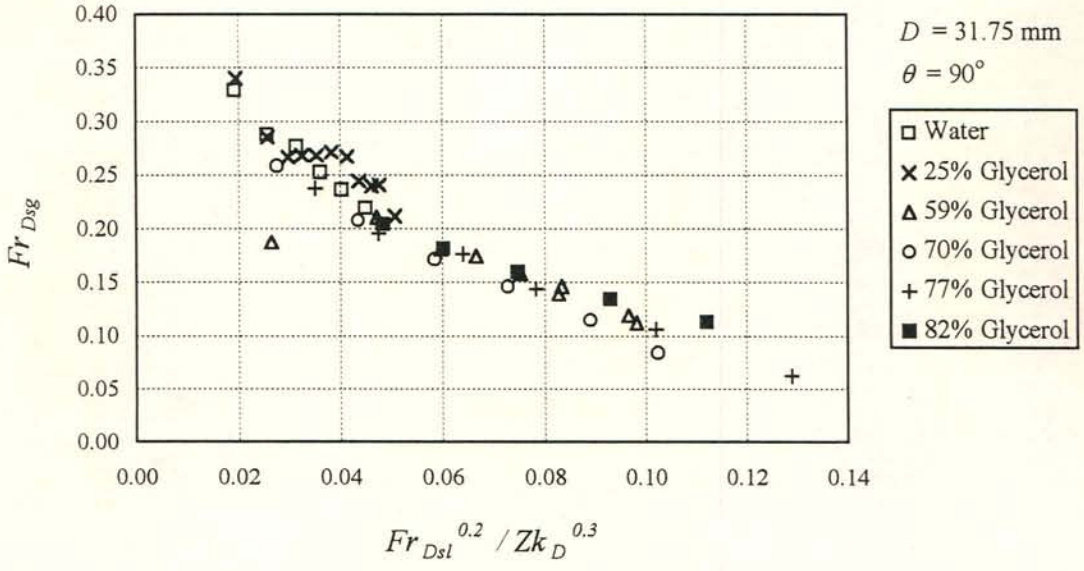

Figure 6.1: The flooding superficial velocities by Clift *et al.* [66CL1] shown in figure 2.17(a), presented in terms of the proposed Froude-*Zk* number combination for vertical ducts.

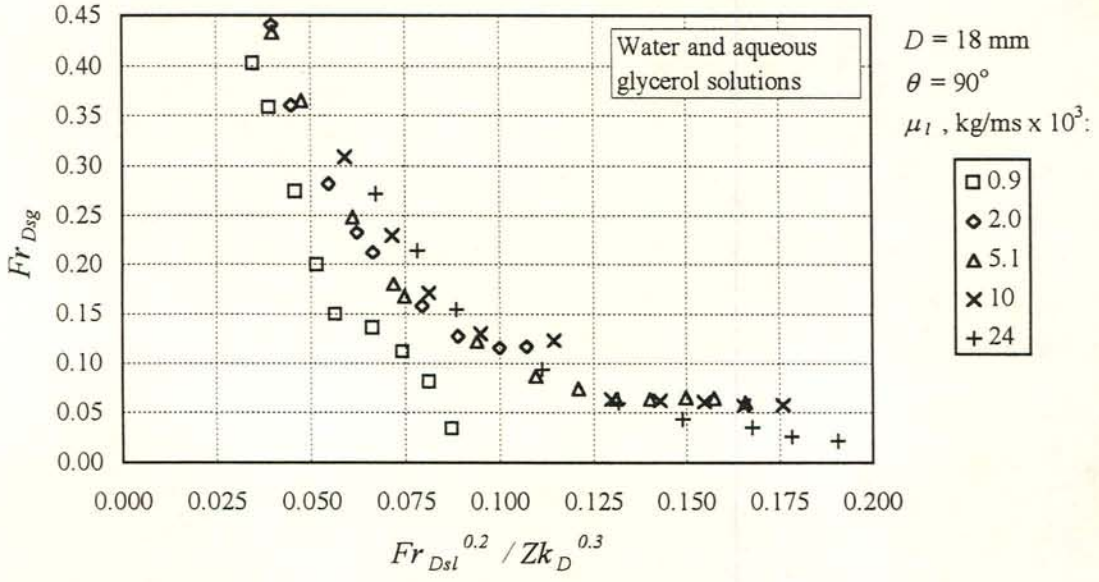

Figure 6.2: The flooding superficial velocities by Suzuki and Ueda [77SU1], shown in figure 2.10(b), presented in terms of the proposed Froude-*Zk* number combination for vertical ducts.

The data of the two sets of experiments are shown in figures 2.18(a) and 2.19(a) respectively and the corresponding liquid properties are given in tables 6.3 and 6.4. In figure 6.3 both sets are shown together in terms of the superficial velocities. Note the low air flow rates at which the oils flood as the result of their high viscosities.

Table 6.3: Liquids tested by Chung et *al.* [80CH1, 79TI1] to investigate the effect of the surface tension. The flooding superficial velocities are shown figure 2.18(a).

Liquid	μ_l [kg/ms x 10^3]	ρ_l [kg/m^3]	σ [N/m x 10^3]
Water; 22°	1.00	1000	72.7
Water with Surfynol SE 0.1% by weight; 20°	1.00	1000	35.0
Water with Surfynol TG 0.1% by weight; 20°	1.00	1000	0.028
Silicon oil; 20°	0.82	820	17.4

Table 6.4: Oils tested by Chung et *al.* [80CH1, 79TI1] to investigate the effect of the liquid viscosity. The flooding superficial velocities are shown figure 2.19(a).

Oil	μ_l [kg/ms x 10^3]	ρ_l [kg/m^3]	σ [N/m x 10^3]
Chevron white oil 3; 20°	3.85	844.3	31.0
Chevron white oil 5; 20°	5.25	850.8	35.0
Chevron white oil 9; 20°	10.60	863.6	36.0

When Zapke and Kröger [96ZA1] initially discovered that the *Zk* number successfully correlates the combined effect of the liquid properties on flooding, they proposed a flooding correlation in terms of the dimensionless groups $Fr_{Dsi}^{1/4} / Zk_D^{0.05}$, given by equation (2.12). The ratio $Fr_{Dsi}^{1/4} / Zk_D^{0.05}$ correlates the data by Chung *et al.* in figures 2.18(a) and 2.19(a) individually, as shown in figures 2.18(b) and 2.19(b) respectively. It fails, however, for both sets simultaneously. This is illustrated in figure 6.4. The newly proposed form of dimensionless groups correlates the entire set of data as can be seen in figure 6.5.

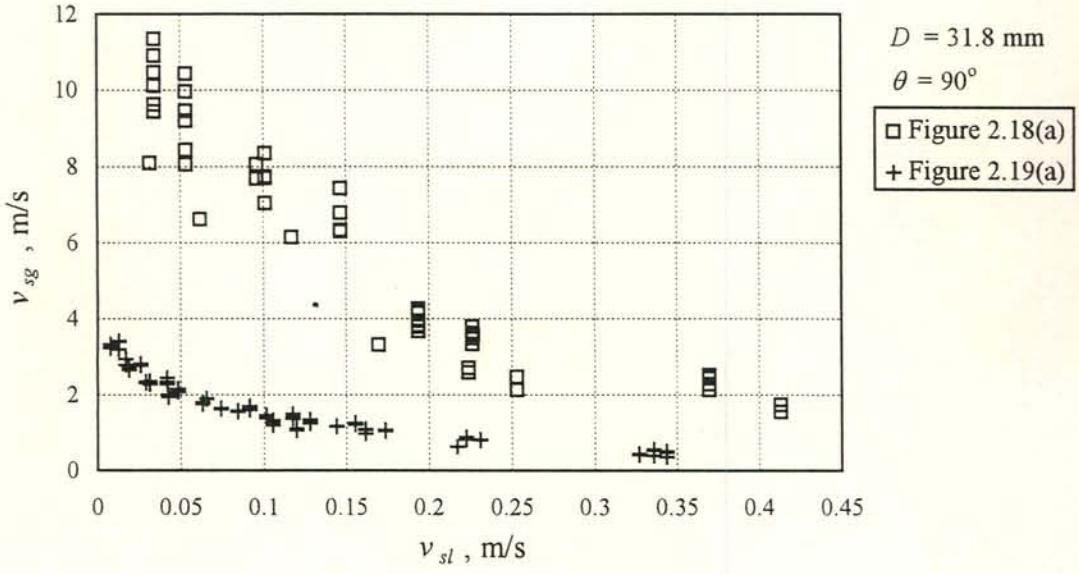

Figure 6.3: Flooding data by Chung *et al.* [80CH1, 79TI1] to investigate the effect of the liquid viscosity (crosses) and surface tension (squares) on flooding. The squares are the data of figure 2.18(a) and the crosses represent the data shown in figure 2.19(a).

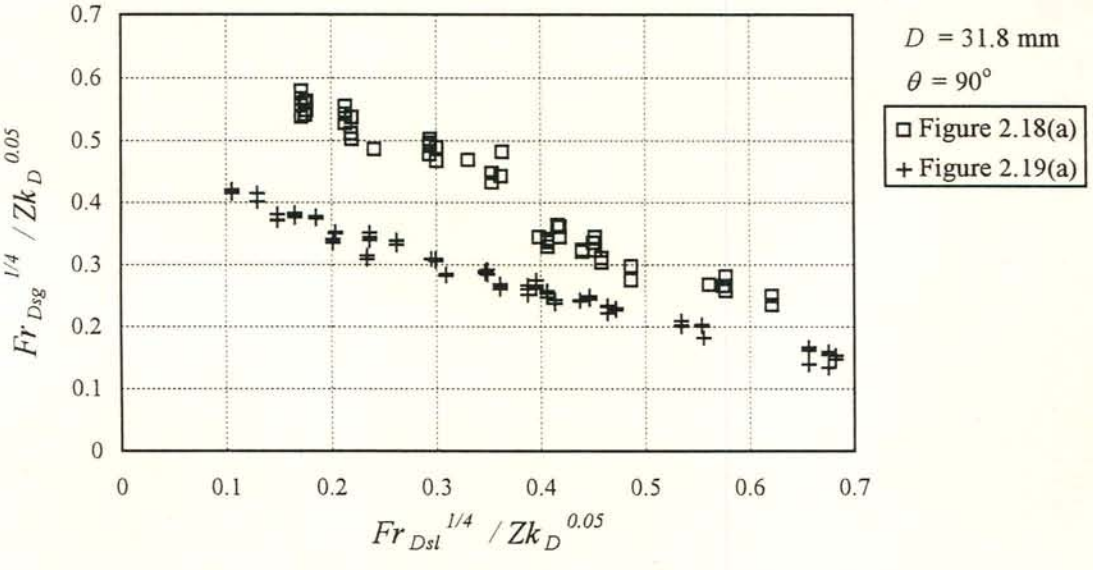

Figure 6.4: The flooding superficial velocities by Chung *et al.* [80CH1, 79TI1] shown in figure 6.3, plotted in the form of the correlation originally proposed by Zapke and Kröger [96ZA1]. The method fails to correlate the entire set of data. The squares are the data of figure 2.18(a) and the crosses represent the data shown in figure 2.19(a).

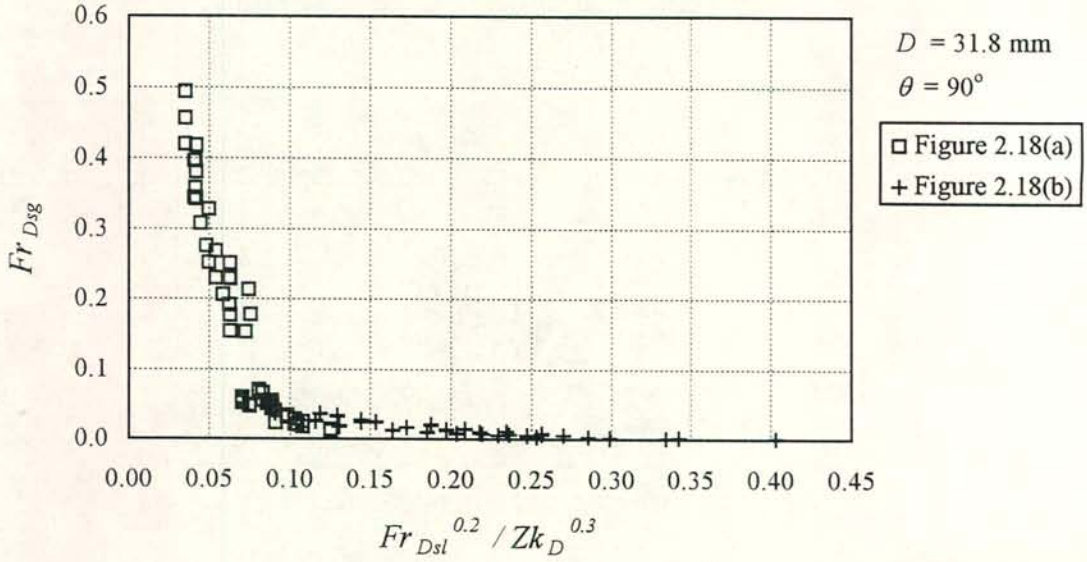

Figure 6.5: The flooding superficial velocities by Chung *et al.* [80CH1, 79TI1] shown in figure 6.3, presented in terms of the newly proposed Froude-*Zk* number combination for vertical ducts. The squares are the data of figure 2.18(a) and the crosses represent the data shown in figure 2.19(a). The data are shown in figure 6.6 on a log-log scale.

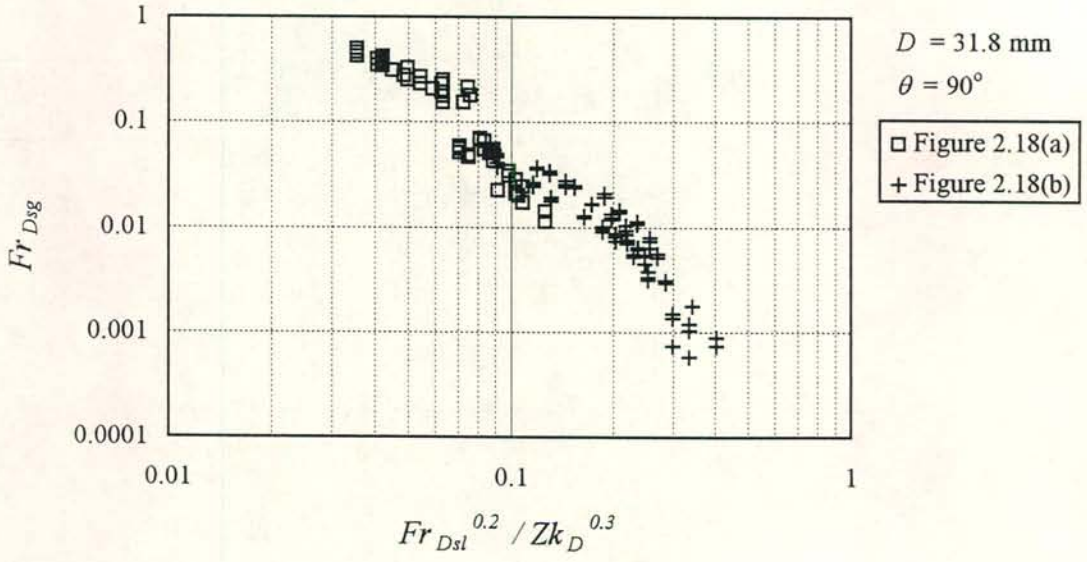

Figure 6.6: The data of figure 6.5 replotted on a log-log scale.

6.1.4 Zapke and Kröger [96ZA1]

Zapke and Kröger investigated the effect of the liquid properties on flooding by making use of water, methanol and propanol. The tests were carried out in a vertical tube of diameter D = 30 mm with a sharp-edged gas inlet and a porous injection unit for the liquid feed. The data is shown in figures 6.7 and 6.8 in terms of the superficial velocities and the Froude-*Zk* number respectively. Good correlation is achieved.

Air-water flooding data for the 30 mm tube inclined at 60° to the horizontal are shown in figure 6.9 together with air-water data obtained in the present investigation for rectangular ducts. Here direct comparison is permitted because the data are based on the same definition for flooding. Also, in both cases, round and rectangular, the gas inlet geometry is the same, i.e. square-edged. The rectangular ducts flood at higher velocities. The data are replotted in figure 6.10 in terms of the proposed dimensionless groups for flooding in inclined ducts. Both Froude numbers (gas and liquid) are based on the diameter in the case of the tube. The correlation achieved is remarkable, indicating a similarity between flooding in tubes and rectangular ducts..

During flooding in the inclined tube an upward rolling action was observed, which at times was dispersed and the liquid flowed back and accumulated near the sharp-edged gas inlet only to be propelled up again. Thus, the flooding mechanism for inclined tubes and rectangular ducts appear to be same, i.e. upward liquid transport in the form of roll waves or vortex-type flow at sufficiently high gas flow rates. The critical dimension for the flooding process is the duct height, which is the diameter for tubes, according to figure 6.10.

Because the flooding gas velocity is proportional to the square root of the duct height, the 30 mm tube floods at relatively low gas flow rates compared to the 50, 100 and 150 mm ducts. For this reason roll waves were formed at flooding in the tube (similar to the roll waves observed at flooding in the rectangular ducts at small inclinations), instead of the intensive vortex-type flow present at high gas velocities in the rectangular ducts.

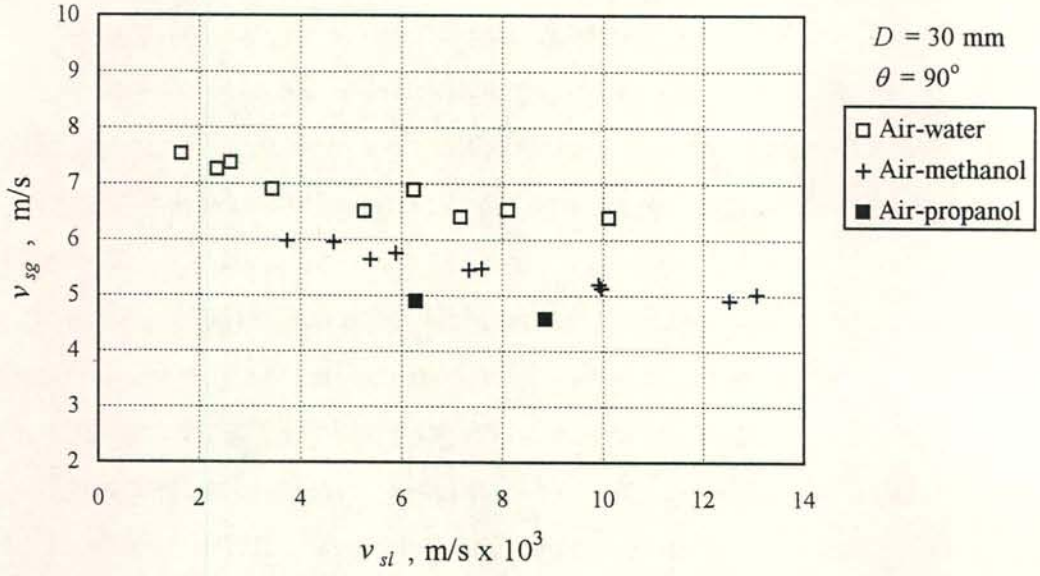

Figure 6.7: Flooding data by Zapke and Kröger [96ZA1] for air-water, air-methanol and air-propanol flow in a vertical tube with sharp-edged gas inlet.

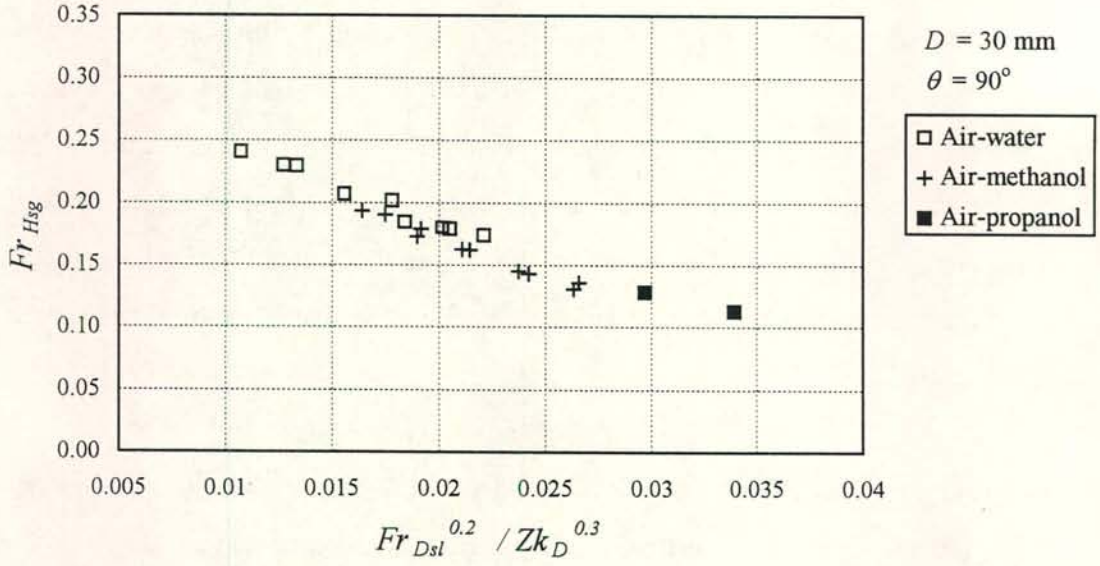

Figure 6.8: The flooding superficial velocities by Zapke and Kröger [96ZA1], shown in figure 6.7, plotted in terms of the proposed Froude-*Zk* number combination for vertical ducts.

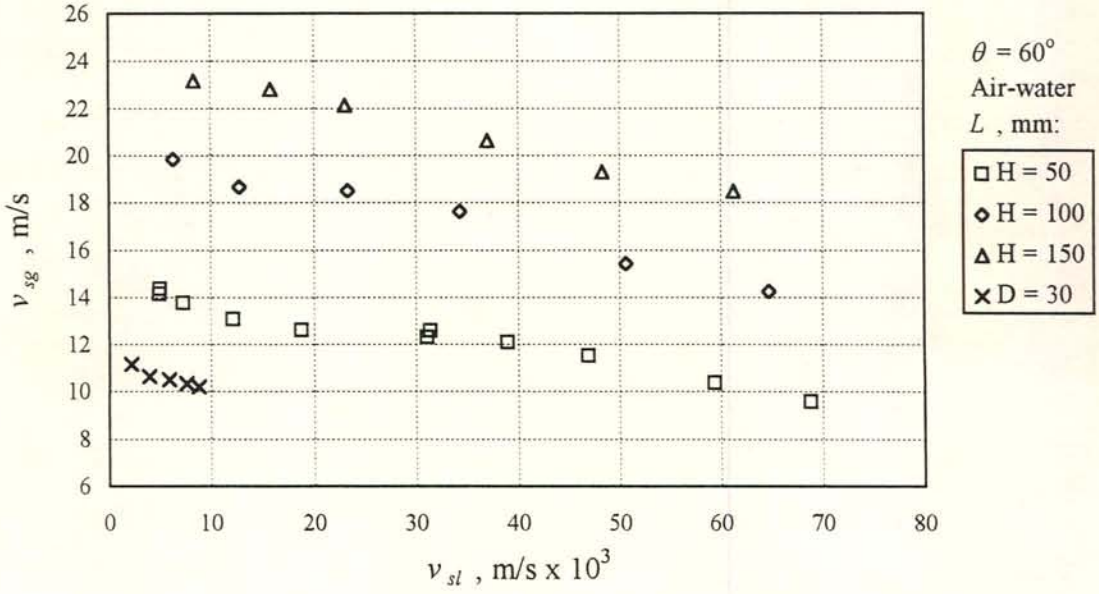

Figure 6.9: Air-water flooding superficial velocities for rectangular ducts and a tube [96ZA1] inclined at 60° to the horizontal. L is the characteristic dimension for the gas Froude number. The width of the 50 mm duct is 10 mm.

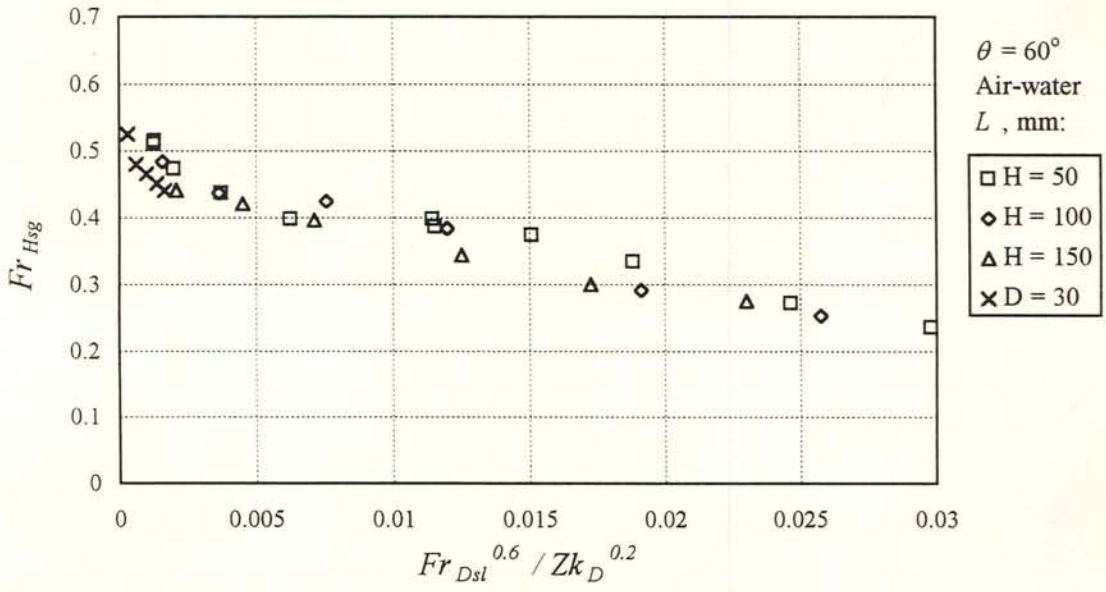

Figure 6.10: Air-water flooding data for rectangular ducts and a tube shown in figure 6.9, presented in terms of the proposed Froude-Zk number combination for inclined ducts.

A similar comparison between flooding data for a vertical tube [96ZA1] and rectangular ducts is illustrated in figures 6.11 and 6.12. The correlation achieved is not as good as for inclined ducts. The gas-liquid distribution in vertical ducts is complex under flooding conditions and not as well defined as for inclined ducts. Consequently the data correlate only to some extent because the duct height is not fully representative of the flow modes anymore. More insight is needed to fully understand the complex nature of counterflow in vertical ducts and tubes.

6.2 General remarks and conclusions

The most well known flooding correlation for annular countercurrent flow is the Wallis [69WA1] model. Wallis argued that the body forces acting on the phases are balanced by dissipative effects or turbulent stresses which are related to the average momentum fluxes $\rho_g v_g^2$ and $\rho_l v_l^2$ and that the dynamic processes of such a balance relate the phase flow rates to the film thickness. The proposed correlation or model is based on the dimensionless groups

$$v_{sg}^* = \rho_g^{1/2} v_{sg} \Big/ \left[gD\left(\rho_l - \rho_g\right) \right]^{1/2} \tag{6.1}$$

$$v_{sl}^* = \rho_l^{1/2} v_{sl} \Big/ \left[gD\left(\rho_l - \rho_g\right) \right]^{1/2} \tag{6.2}$$

which, according to Wallis, relate the momentum fluxes to the hydrostatic forces. A question here is, why seek dimensionless groups which represent force ratios and then take the square root of the groups ? Equations (6.1) and (6.2) are in actual fact square roots of the Froude number, which relates inertia forces to body forces, i.e.

$$Fr = inertia\ force / body\ force = \left(\rho v^2 L^2\right) / \left(\rho g L^3\right) \tag{6.3}$$

where L is a representative length dimension. During flooding the inertia forces, represented by $\rho_g v_{sg}^2 L^2$ and $\rho_l v_{sl}^2 L^2$, are related to the body force $gL^3(\rho_l - \rho_g)$ acting on the liquid, resulting in the densimetric Froude numbers

$$Fr_{Lsg} = \rho_g v_{sg}^2 \Big/ \left[gL\left(\rho_l - \rho_g\right) \right] \tag{6.4}$$

$$Fr_{Lsl} = \rho_l v_{sl}^2 \Big/ \left[gL\left(\rho_l - \rho_g\right) \right] \tag{6.5}$$

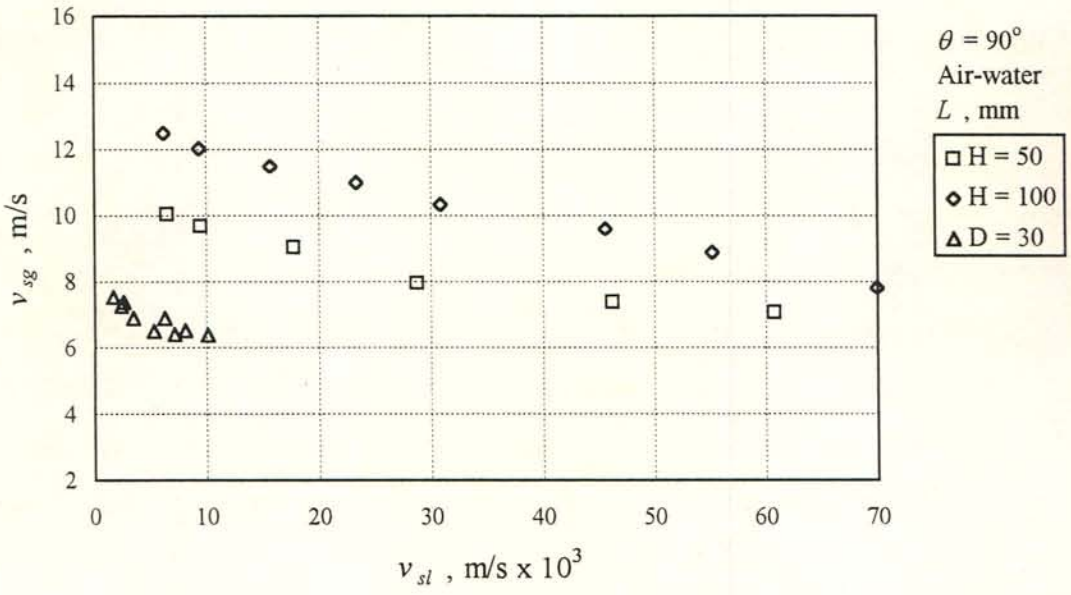

Figure 6.11: Air-water flooding superficial velocities for vertical rectangular ducts and a tube [96ZA1]. L is the characteristic dimension for the gas Froude number.

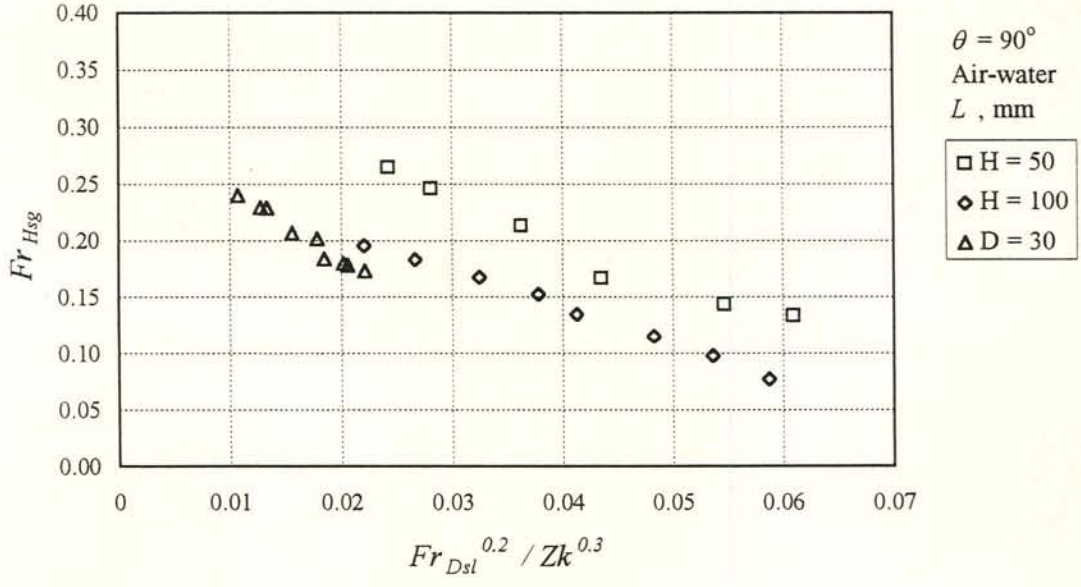

Figure 6.12: Air-water flooding data for rectangular ducts and a tube shown in figure 6.11, presented in terms of the proposed Froude-Zk number combination for vertical ducts.

Wallis correlated flooding data in terms of the square root of the dimensionless velocities, in other words the fourth root of the densimetric Froude numbers. The parameters $v_{sg}^{*1/2}$ and $v_{sl}^{*1/2}$ were probably chosen to present flooding data because of their linear relationship.

The author does not agree with this particular method of presenting flooding data. Flooding is caused by a force exerted by gas flow on a draining liquid and should therefore be presented in terms of the relevant force ratios, which are the densimetric *Froude numbers*. Furthermore, a $v_{sg}^{*1/2}$ - $v_{sl}^{*1/2}$ plot hides secondary effects and reduces the actual scatter artificially. Consequently such a plot is not a true reflection of the physics of flooding. Still, at present it has become general practice by researchers to present flooding data in terms of the square root of the dimensionless superficial velocities. Since Wallis [69WA1] proposed the dimensionless velocities, the hydraulic diameter is usually taken as the required length dimension for conditions where the duct geometry affects the flooding gas velocity.

Lee and Bankoff [83LE1] proposed a modified Wallis parameter

$$v_{msi}^{*} = \rho_l^{1/2} v_{si} \Big/ \left[2H\, g \sin\theta \left(\rho_l - \rho_g \right) \right]^{1/2} \tag{6.6}$$

for flooding in inclined ducts, where H is the channel height. Here $2H$ represents the hydraulic diameter because of the large channel width of 380 mm compared to the heights of 38 and 76 mm tested. The flooding mechanism observed is described in section 2.4.3. The flooding steam velocities increased with an increase in the channel height and the modified Wallis parameter was found to correlate the height effect by employing the hydraulic diameter. For such a wide channel where the hydraulic diameter is directly proportional to the height, the flooding data will correlate in terms of the hydraulic diameter by coincidence. The present investigation has, however, revealed that the flooding gas velocity for inclined ducts is related to the duct height and not to the hydraulic diameter. The three ducts of width W_t = 10 mm tested have equal hydraulic diameters, but do not flood at equal gas velocities because their heights differ (see figures 5.2(b) and 5.3). It appears that the form of the modified dimensionless velocity by

Bankoff and Lee was based on the hydraulic diameter concept for vertical tubes which, however, does not apply in the case of inclined ducts.

According to Lee and Bankoff [83LE1] the $\sin\theta$ term in the modified Wallis parameter incorporates the effect of gravity for steep angles, but $v_{msg}^{*1/2}$ rises as the inclination decreases towards zero. The same trend was encountered in the present investigation and it is caused by the added gravity component illustrated by equation (5.5). The air-water flooding data for the 50 mm duct (W_t = 10 mm) shown in figure 5.26(b) are plotted in figure 6.13 in terms of the gas Froude number divided by $\sin\theta$, analogous to the modified Wallis parameter. For angles between the 40 and 60° it correlates the gravity effect but increases strongly at smaller inclinations. A Froude number which incorporates the gravity effect for small angles can be derived as follows: The force on the liquid is

$$F_B = W_t\,\delta\,\Delta z\,g\left(\rho_l-\rho_g\right)\sin\theta+\frac{d\delta}{dz}\Delta z\,W_t\delta\,g\left(\rho_l-\rho_g\right)\cos\theta \tag{5.5}$$

The combined upward drag and lift exerted by the gas flow is proportional to the momentum flux and the interface area of the control volume depicted in figure 5.29 and can expressed as

$$F_D = C_D\,\rho_g\,v_{sg}^2\,W_t\,\Delta z \tag{6.7}$$

The ratio of these two forces form a densimetric gas Froude number for wavy flow in a duct at inclinations close to the horizontal, i.e.

$$Fr'_{Hsg} = \frac{\rho_g\,v_{sg}^2}{g\,H_t\,\alpha_l\left(\rho_l-\rho_g\right)\left(\sin\theta+H_t\,\alpha_l\dfrac{d\alpha_l}{dz}\cos\theta\right)} = \frac{1}{C_D} \tag{6.8}$$

where α_l is the liquid hold-up

$$\alpha_l = \delta/H_t \tag{6.9}$$

When flooding is about to occur the roll waves bridge the duct height and the liquid hold-up is close to unity. The gradient of the wave $d\alpha_l/dz$ can vary from small to very steep. If we assume an intermediate gradient of approximately 60° then $d\alpha_l/dz \approx 2$.

Substituting these values into equation (6.8) for the 50 mm duct, the Froude number becomes

$$Fr'_{Hsg} = \frac{\rho_g v_{sg}^2}{g H_t \left(\rho_l - \rho_g\right)\left(\sin\theta + 0.1\cos\theta\right)} = Fr_{Hsg} \Big/ \left(\sin\theta + 0.1\cos\theta\right) \qquad (6.10)$$

In figure 6.14 the data of figure 6.13 are replotted in terms of the densimetric gas Froude number and the angle correction according to equation (6.10). Now good correlation is obtained for inclinations close to the horizontal as well as inclinations up to ≈60°. At the steeper inclinations there is no well defined interface once vortices have been formed. Thus the conditions depicted in figure 5.29 do not apply. The cosine term however vanishes for steeper inclinations and according to figure 6.14, the sine term alone correlates the data. It can be concluded that the gravity term containing the sine term becomes the primary weight component as the duct inclinations is increased.

Rearranging equation (6.8) yields

$$Fr_{Hsg} = \frac{\rho_g v_{sg}^2}{g H_t \left(\rho_l - \rho_g\right)} = \frac{\left(\sin\theta + 0.1\cos\theta\right)}{C_D} \qquad (6.11)$$

for flooding conditions in the 50 mm duct. By inspection of equations (5.4) and (6.11) one finds that

$$K_o = C\left(\sin\theta + 0.1\cos\theta\right) \qquad (6.12)$$

where C is a constant of proportionality which is related to the drag coefficient. The values for K_o determined according to experiment are shown in figure (6.15) together with the relation according to equation (6.12) where a value of 0.55 has been taken for the constant C. The trend predicted by the function for the angle/gravity effect on flooding is in good agreement with the experimental results. Note that the choice of C is purely empirical because one has to rely on experiment due to the complexity of the flow. The functional relation (6.12) for the angle/gravity effect is, however, based on theory and appears to present a good explanation for the observed trend.

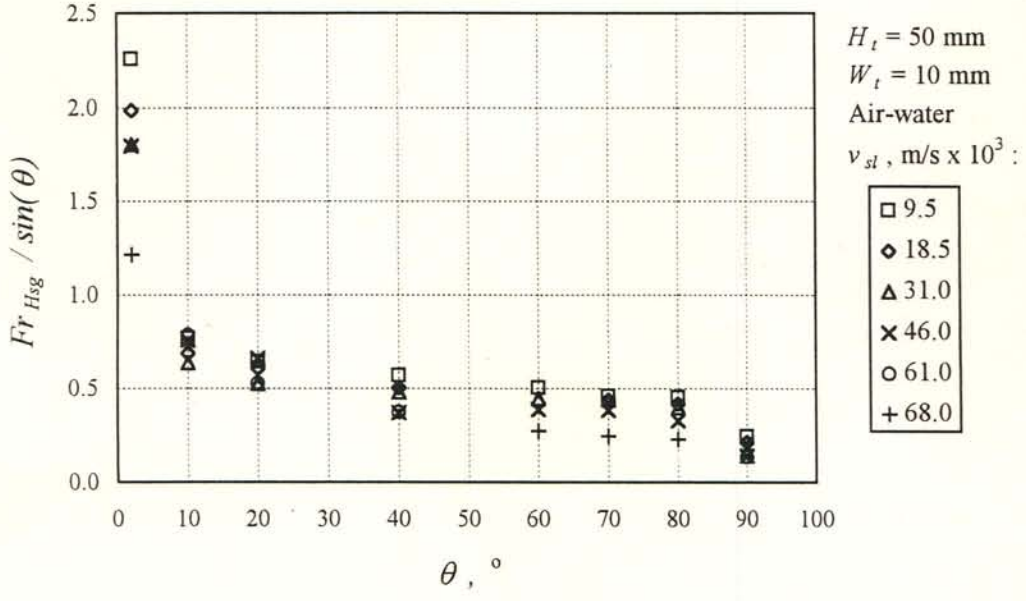

Figure 6.13: Air-water flooding data measured at various inclinations, plotted in terms of the Froude number divided by sin θ analogous to the modified Wallis parameter proposed by Lee and Bankoff [83BA1].

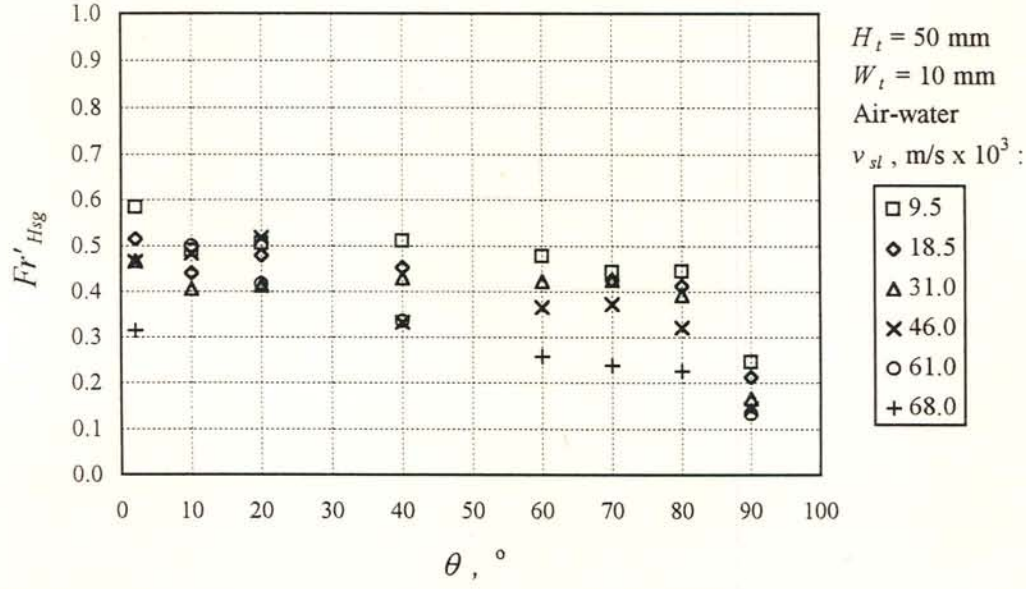

Figure 6.14: The flooding data shown in figure 6.13 replotted in terms of the gas Froude number and the angle correction according to equation (6.10).

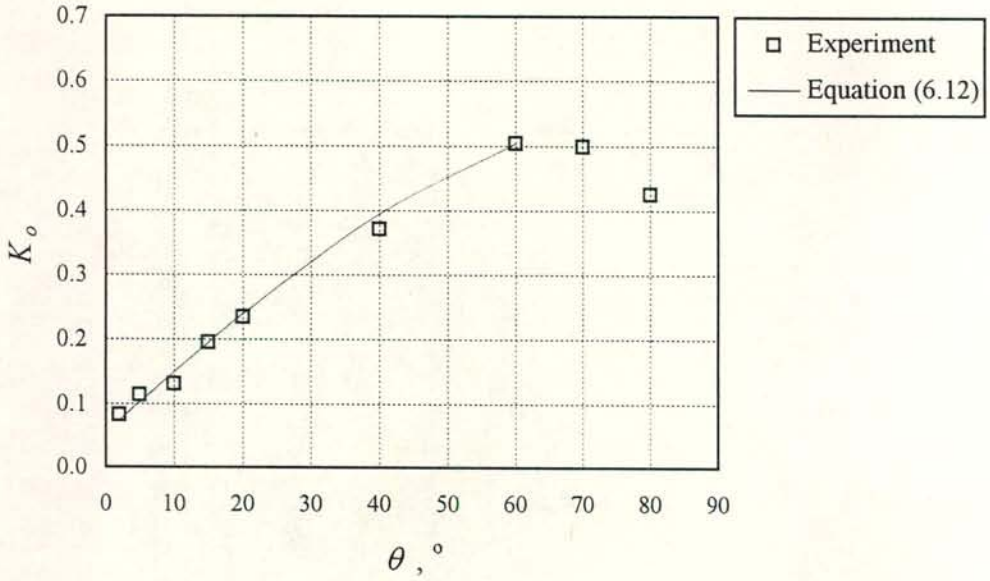

Figure 6.14: Comparison of the experimental values for K_o and the prediction according to equation (6.12).

Above 60° the transition region to the flooding mode in vertical ducts is entered and a decrease in the flooding gas velocity occurs. Equation (6.8) does not apply in the transition region and therefore cannot predict the downward trend. The third degree polynomial equation (5.5), which is purely a curve fit, can be employed for the purpose of predicting flooding velocities below 60° and inside the transition region up to 80°.

The height effect on the flooding gas velocity found in the present investigation differs from that found by Jayanti and Hewitt [96JA1]. See section 2.4.2 for detail on their study. The present height effect is related to the liquid distribution just before and at flooding, while Jayanti and Hewitt investigated the effect of the duct dimension on the gas boundary layer in the presence of a wave and the resultant pressure and shear stress distribution across the wave. There is a fundamental difference. Their height effect is related to the gas velocity profile while in the present investigation the height effect is related to the weight of the liquid contained in a vortex or a roll wave.

At present a number of flooding models and correlations exist containing dimensionless groups which were not verified by experiment. Feind [60FE1] proposed a correlation containing the gas Reynolds number. The correlation is based on experiments for air only

and the effect of the gas properties were never tested. The correlation creates the impression that flooding is Reynolds number related, which is not the case. Similarly Lee and Bankoff [83LE1] developed an envelope theory based on a gas Reynolds number related friction factor. The friction factor was expressed in terms of the steam Reynolds number for stratified flow at low steam flow rates as well as for the roll wave region closer to flooding. Because only steam was used as a working fluid the gas properties could not be varied to substantiate the Reynolds model. At higher gas flow rates the pressure drop characteristics become Froude number related and the Reynolds number model is not valid anymore!

Chung *et al.* [80CH1, 79TI1] proposed a Kutateladze-Bond number correlation based on a Kelvin-Helmholtz instability analysis for inviscid two-phase flow. Their own data indicated a liquid viscosity effect, which in fact was stronger than the influence of the surface tension, yet for some reason the liquid viscosity was never incorporated in the correlation (given by equation (2.9)). Faghri *et al.* [89FA1,95FA1] proposed exactly the same type of Kutateladze number correlation. Their modelling was based on the critical assumption that the Wallis- and the Kutateladze-type correlation are simultaneously valid for flooding. Existing results prove that this assumption may be wrong (compare figures 2.21(a) and 6.8). After all there is a trend to differentiate between these two models where the Wallis correlation is applied for conditions when the duct dimensions affect flooding while the Kutateladze correlation is applied when the duct dimensions do not play a significant role. It is not surprising then, that Faghri *et al.* had to introduce a density correction to achieve better correlation for fluids other than air and water.

More recently Sudo *et al.* [91SU1] developed a correlation for countercurrent flow limitation for air-water flow in tubes and rectangular ducts. The data were correlated in terms of the Wallis parameters and a Bond number. The effect of the fluid properties, gas and liquid, contained in the correlation, was however not verified by experiment.

The general validity of the Froude-*Zk* number combination has been confirmed by results of other researchers. Although equation (5.7), based on data for vertical rectangular ducts with a sharp-edged gas inlet, does not necessarily predict flooding for tubes with a rounded inlet for example, the proposed form and the relative magnitude of the

exponents for Fr_{Dsl} and Zk_D were found to apply for geometries other than rectangular ducts. The functional relationship of the Froude-Zk number combination may be not the same for different geometries or inclinations, but they remain the fundamental groups which govern flooding.

According to existing experimental findings the influence of the duct dimensions (diameter, width or height) in flooding becomes less as the dimensions increase. The proposed correlation method is therefore only valid for conditions where the dimensions play a role.

CHAPTER 7

BACKGROUND ON THE CONDENSER-DEPHLEGMATOR SYSTEM

In a power generating cycle, direct air-cooled condensers make use of finned tubes to condense the turbine exhaust steam. The finned tubes of the system under investigation are arranged in an A-type configuration. A condenser unit is illustrated in figure 7.1. It consists of eight finned tube bundles placed in an A-frame above a fan. The fan forces cooling air through the bundles. Each bundle contains two tube rows. Air at ambient temperature enters the bundles and is heated as it flows past row (1), after which it enters row (2). A decrease in temperature difference between the condensing steam and the cooling air is experienced by consecutive rows in such a multi-row condenser, resulting in a decrease in heat rejected by each row in the direction of the air flow. This so-called tube-row-effect results in steam backflow at the bottom end of the condenser bundles.

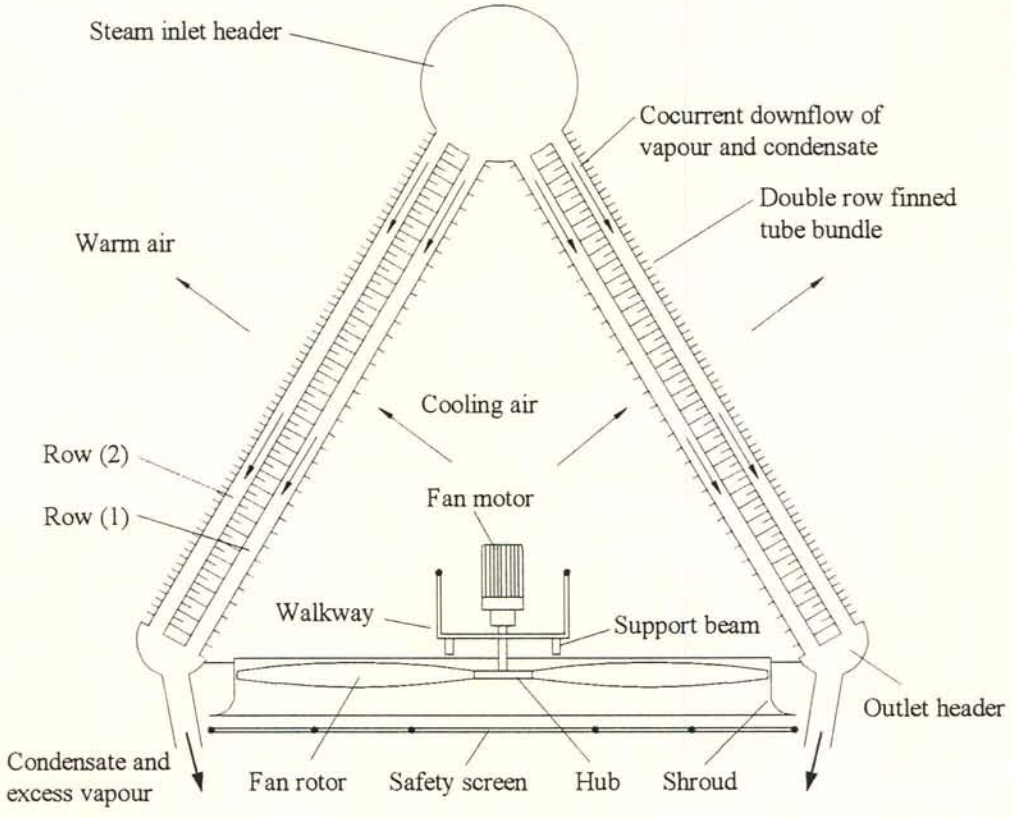

Figure 7.1: Schematic of an air-cooled condenser unit.

A schematic of a multi-row condenser experiencing steam backflow and the corresponding pressure distribution is shown in figure 7.2. The rows have common distributing (inlet) and collecting (outlet) headers, imposing equal pressure drops across individual rows. Because the condensation rate and thus the vapour inlet flow in each row decreases in the direction of the air flow, steam exits row (3) and enters row (1) and (2) at the bottom. This is referred to as backflow. Backflow reduces the vapour inlet flow of certain rows at the distributing header to satisfy the equal pressure drop condition.

Turbine exhaust steam contains inert gases due to boiler feed water treatment and air which leaks into the low pressure part of the cycle. These noncondensable gases flow with the steam into the backflow region where they are trapped and subsequently accumulate to fill the entire backflow region. Accumulation of noncondensable gases renders part of the condenser unavailable for heat rejection. The ineffective region is called a dead zone. Such a dead zone and the resultant steamside pressure drop distribution is shown in figure 7.3. Dead zones have been described by a number of researchers [67FO1, 70SC1, 74RO1, 78LA1, 81SC1, 84SC1].

Methods to counter or prevent the formation of dead zones have been discussed and analysed by, amongst others, Schrey and Kern [81SC1]. To obtain the same pressure drop across each row in the absence of steam backflow, flow restrictions can be inserted at the inlet of the row with the smallest vapour inflow such that the added resistance has an equalising effect on the pressure drop. Another method to prevent backflow is to select different heat transfer characteristics for each tube row such that the heat rejected by each row is the same. Equal heat transfer rates can be achieved by decreasing the fin pitch in the direction of the air flow. The resulting increase in the airside surface area compensates for the decrease in the driving temperature difference.

Both above-mentioned methods have the disadvantage that backflow is eliminated at one operating point only. To overcome this problem a secondary condenser can be added in series to the main condenser, as illustrated in figure 7.4. The secondary condenser acts as a dephlegmator by facilitating a outflow of steam at the bottom of the main condenser, thus preventing the formation of dead zones. A dephlegmator is a better alternative than

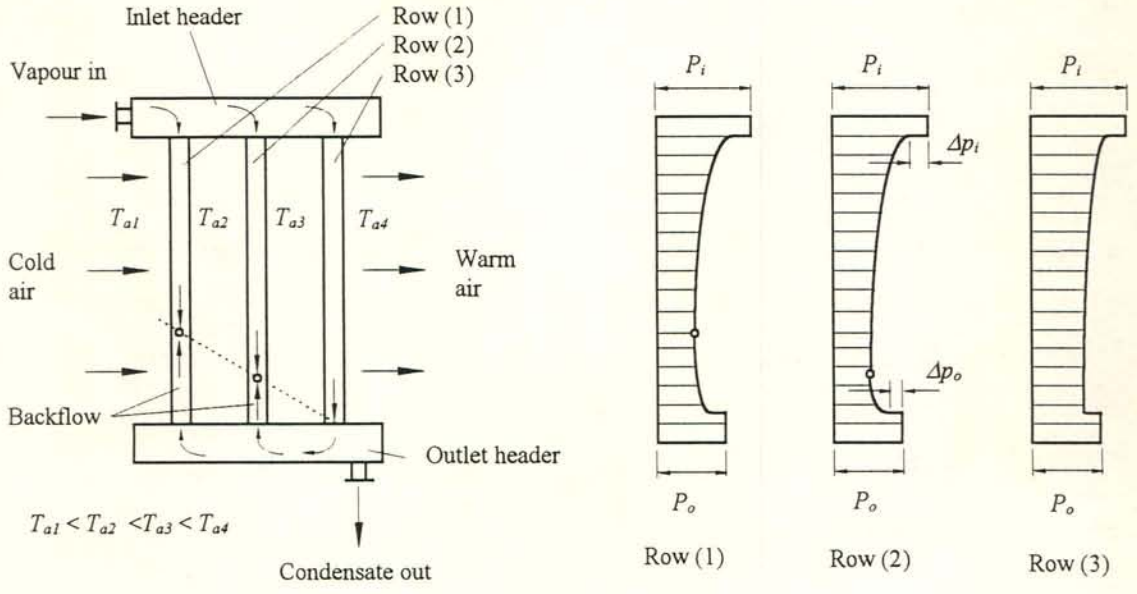

Figure 7.2: Schematic of a multi-row condenser experiencing steam backflow and the corresponding steamside pressure distribution.

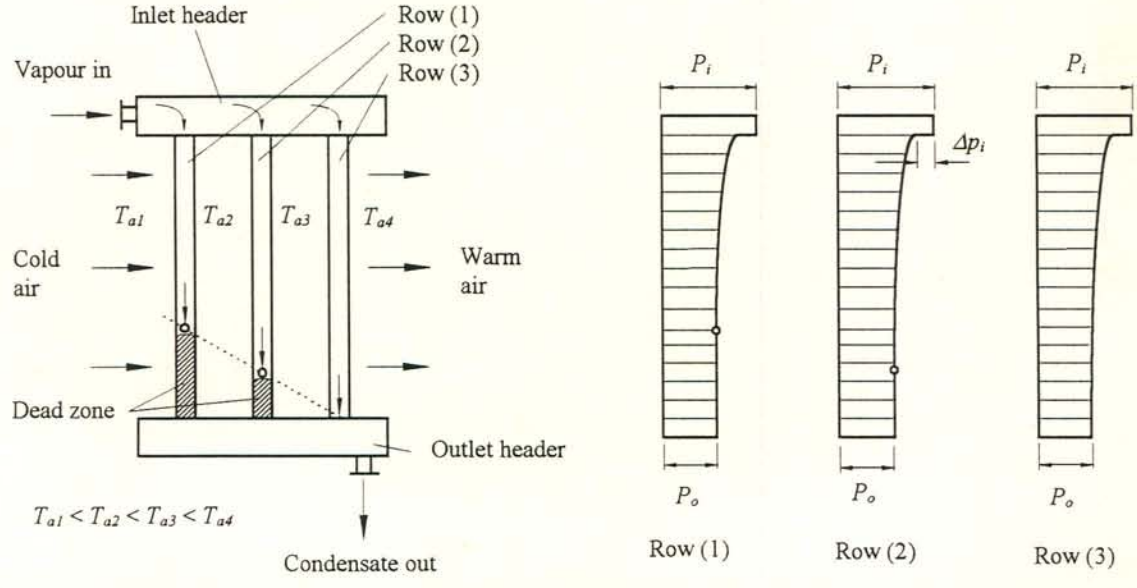

Figure 7.3: Schematic of a multi-row condenser containing a dead zne and the corresponding steamside pressure distribution.

the first two methods because air-cooled heat exchangers can be exposed to extreme variations in the atmospheric or ambient conditions. A correctly sized dephlegmator can

prevent the formation of dead zones across the entire range of operating conditions during full-load turbine output.

More recently the multi-row concept has been replaced by a single-row of flattened tubes in some air-cooled systems. While it certainly solves the backflow problem to a large extent, noncondensable gases may still be trapped inside such condensers, hence requiring the service of a dephlegmator [94SC1]. Backflow can of course be eliminated by simply employing separate outlet headers, i.e. each row has it own outlet header. The concept however requires separate vacuum systems or first stage ejectors for each row, which makes it very costly.

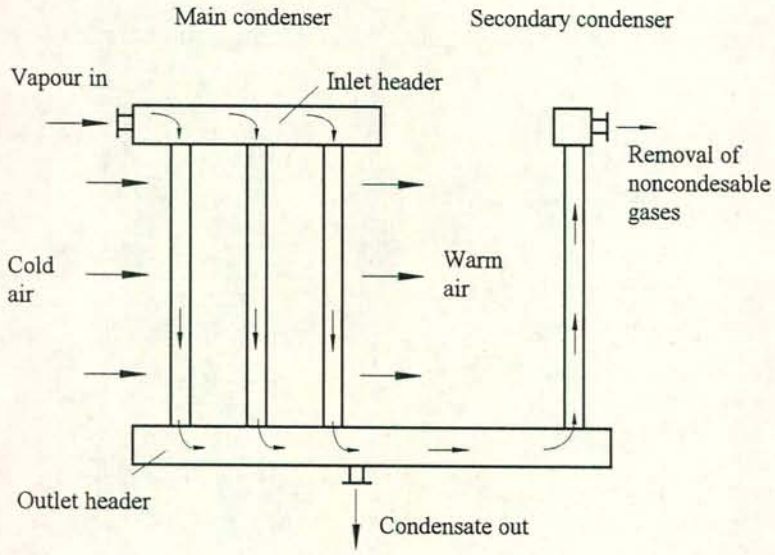

Figure 7.4: A secondary condenser or dephlegmator added to the main condenser to prevent the formation of a dead zone.

In the cooling system under investigation two methods are employed to ensure effective performance of the main condenser. Firstly, the fin pitch of the second row is approximately double the pitch of row (1) to achieve approximately equal condensation rates in each row and secondly a dephlegmator is employed. The condenser excess steam enters the dephlegmator at the bottom and is condensed countercurrent to the downward draining condensate. A schematic of the dephlegmator is shown in figure 7.5.

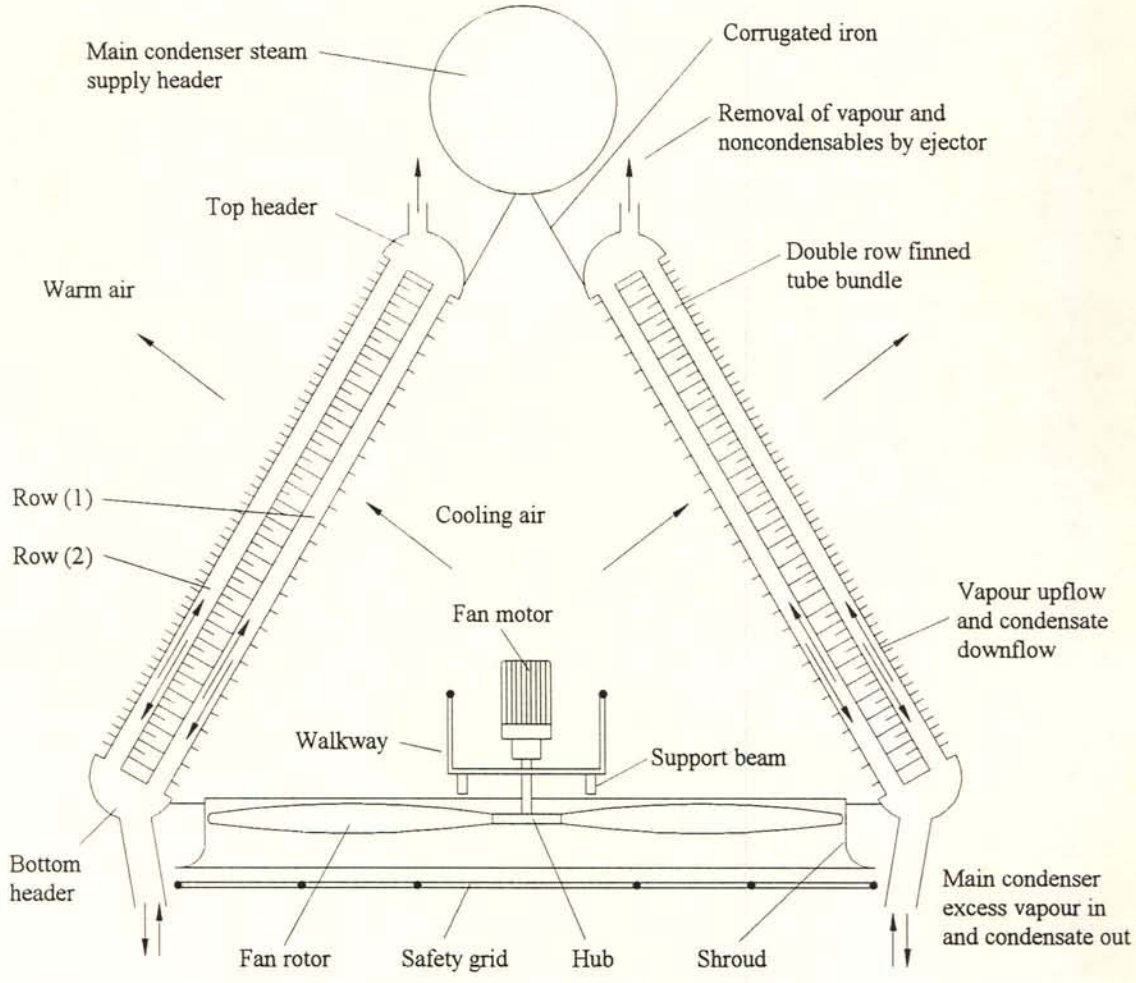

Figure 7.5: Schematic of a dephlegmator unit.

A vacuum system is connected to the top header of the dephlegmator bundles. The vacuum system for normal turbine operating conditions consists of a two-stage steam driven ejector pump and water-cooled shell-and-tube condensers after each stage. The noncondensable gases should ideally accumulate inside the top header of the dephlegmator, from where they are removed by the vacuum system together with a certain amount of steam. The purpose of the ejector, also referred to as the holding ejector, is to maintain vacuum conditions in the low pressure part of the cycle by continuously removing the noncondensables. During turbine start-up procedures a so-called hogging ejector evacuates the condenser. The hogger has a higher suction rate than the holding ejector and can achieve vacuum conditions in a shorter time period. It consumes more steam and is not operated under normal operating conditions.

Each dephlegmator unit serves five condenser units, three on the one side and two on the other side of the dephlegmator. This combination of six units, also referred to as fan units, is called a fan row. Such a row of fan units is illustrated in figure 7.6. The entire cooling system serving one turbo-generator set consists of eight rows. The combination of A-frames or fan units perpendicular to a row is called a fan bay. In other words, there are six fan bays with eight fans per bay. A schematic of the entire cooling system is shown in figure 7.7.

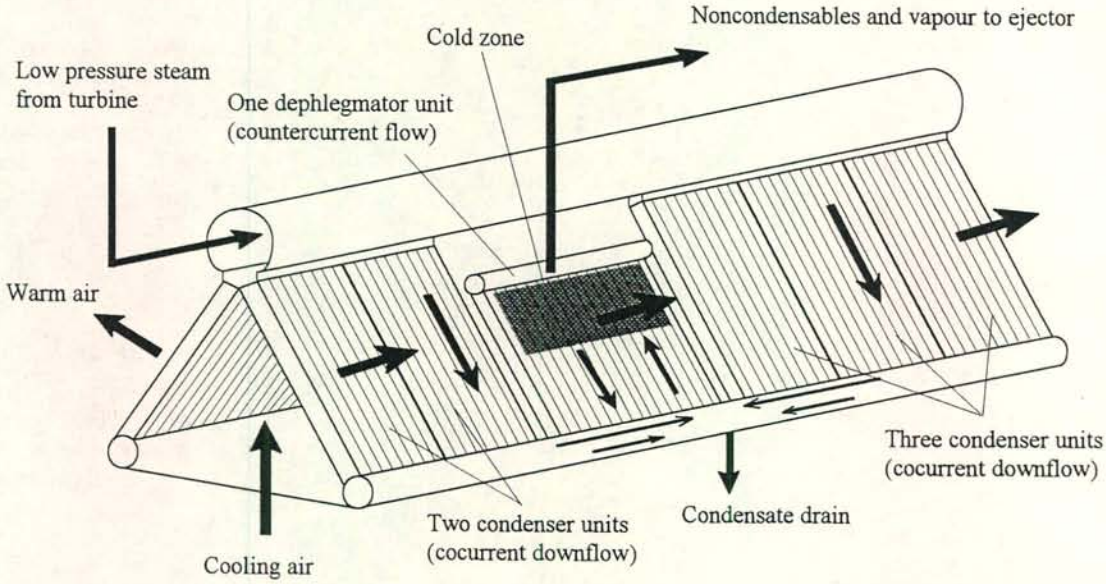

Figure 7.6: Schematic of a row of five condenser units and one dephlegmator unit.

The dephlegmator units can experience steam backflow and dead zone formation if the ejector suction rate is insufficient. Hence the added dephlegmator may ensure 100% effective performance of the condenser units, but it does not imply that effective system performance is achieved.

Dead zones do indeed appear on the dephlegmator under investigation, as indicated in figure 7.6. The loss in turbine output due to the ineffective dephlegmator functioning can be significant. It is the purpose of the present study to find the causes of the dead zones and to propose solutions. Three possible problem areas were identified:

1) The dephlegmator operates in a countercurrent mode. Flooding and entrainment inside the finned tubes and thus countercurrent flow limitation can lead to the accumulation of condensate and subsequently cause maldistribution of the steamside flow. The maldistribution or undesirable steamside flow patterns render the removal of noncondensable gases ineffective, causing the formation of dead zones.

2) The steamside flow may not be countercurrent limited, but a combination of steam backflow and insufficient ejector suction can result in the accumulation of noncondensables and the subsequent formation of dead zones.

3) Condensate accumulation inside the bottom D-type headers causes blockage at the inlet of the finned tubes, resulting in a high pressure drop across the headers and ineffective ejector performance.

The present system ineffectiveness appears to be caused by undesirable steamside flow conditions inside the dephlegmator. Therefore the research undertaken in this dissertation, presented in part A, concentrated on gas-liquid counterflow in inclined ducts. The loss in turbine output can, however, only be quantified by analysing the entire cooling system. A complete performance analysis was therefore carried out as part of the dephlegmator and adiabatic counterflow investigation. Such an analysis includes the modelling of the airside flow and fan performance, the condenser units, the dephlegmator units and the vacuum system, the ambient conditions and the turbine characteristics.

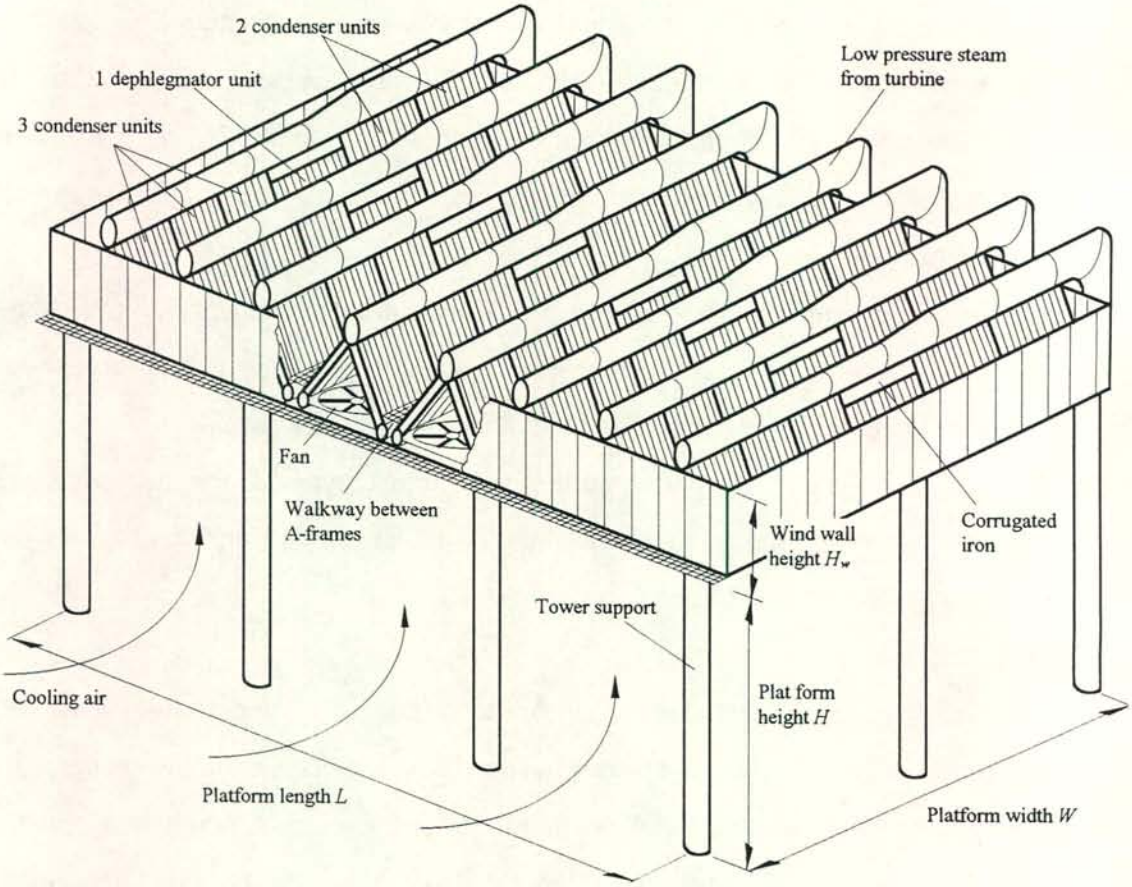

Figure 7.7: Schematic of the forced-draft air-cooled condenser system, consisting of six fan bays (five condenser units and one dephlegmator unit) with eight fan units per bay (i.e. eight fan rows). Not to scale.

CHAPTER 8

DESCRIPTION OF THE FULL SCALE TEST PROCEDURE

Measurements were conducted at the full scale cooling system to evaluate the heat rejected to the air by condenser and dephlegmator units and to gain insight regarding the steamside flow. Dephlegmator tests were carried out at various fan blade angles and at different times during the course of the day to establish under what conditions cold zones are formed.

8.1 Airside measurements and instrumentation

The heat rejected by a heat exchanger bundle can be determined according to the heat transfer relation

$$\begin{aligned} Q_{ab} &= m_{ab} c_{pam} \left(T_{ao(2)} - T_{ai(1)} \right) \\ &= \rho_{ao(2)} v_{ao(2)} A_{fr(2)} c_{pam} \left(T_{ao(2)} - T_{ai(1)} \right) \end{aligned} \tag{8.1}$$

The air outlet temperature distribution of row (2) $T_{ao(2)}$ and the air inlet temperature $T_{ai(1)}$ at row (1) were measured with copper-constantan thermocouples. Two thermocouples, attached to the walkway above the fan, monitored the inlet temperature. The thermocouples were located at a distance of approximately 3 m from the centre of the fan rotor.

The bundle frontal area was divided into rectangular area elements as shown in figure 8.1. By taking readings at the centre of each area element the air outlet velocity and temperature distribution were determined. The dephlegmator bundles were divided into 45 area elements (5 in the horizontal direction and 9 in the direction of the finned tubes) while 40 elements per bundle were used in the case of the condenser bundles (5 in the horizontal direction and 8 along the finned tubes). The air outlet temperature distribution was uniform in the case of the condenser bundles, which allowed for bigger area elements.

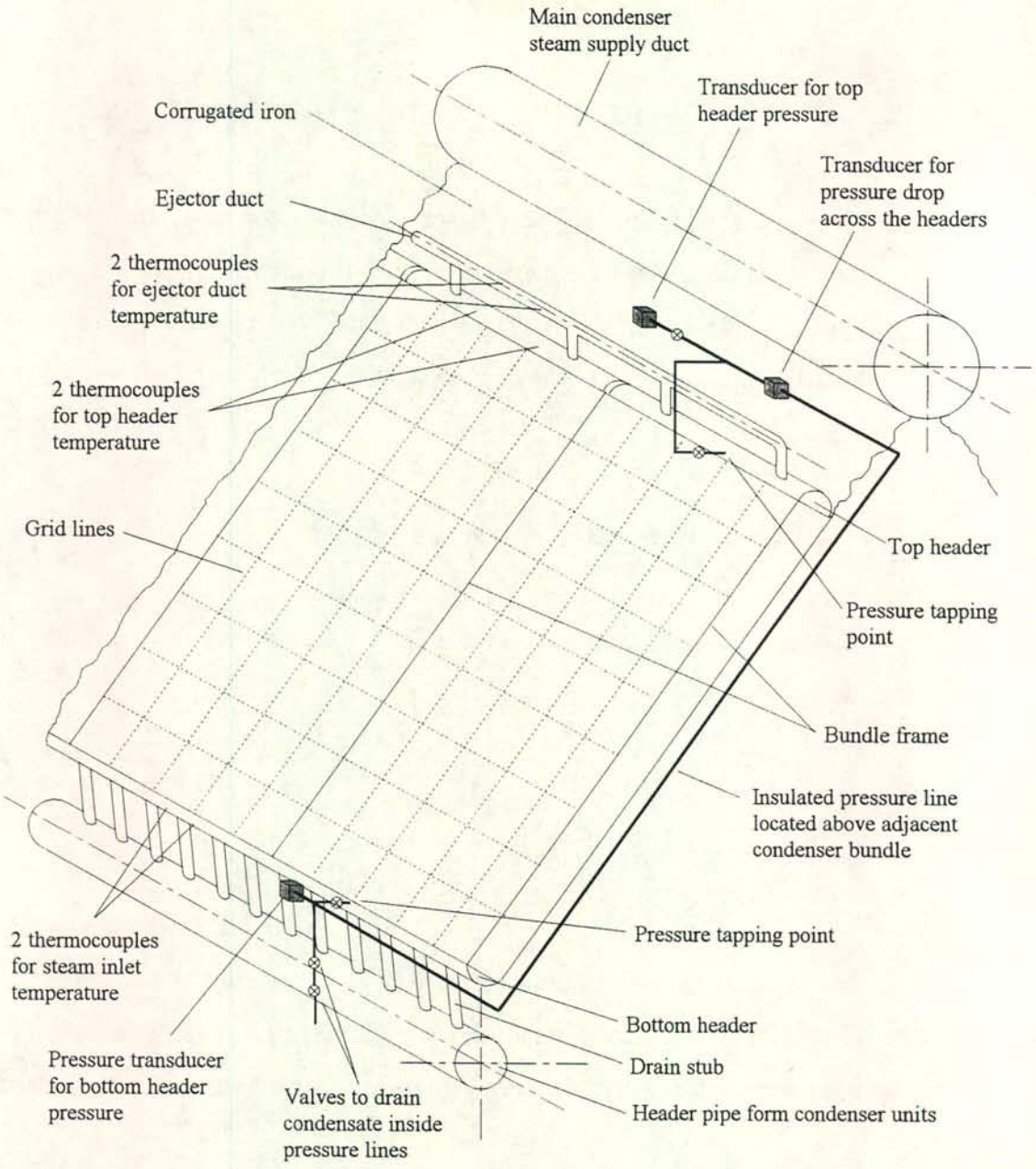

Figure 8.1: Pressure transducer arrangement and thermocouple locations at full scale dephlegmator.

The air mass flow rate passing through such an area element is

$$\Delta m_{aj} = \rho_{ao(2)j} v_{ao(2)j} \Delta A_{fr(2)j} \tag{8.2}$$

where $\Delta A_{fr(2)\,j}$ is the j-th element. The total mass flow rate per bundle is obtained by summation of the incremental flow rates.

$$m_{ab} = \sum_{j=1}^{n_A} \rho_{ao(2)j} v_{ao(2)j} \Delta A_{fr(2)j} \tag{8.3}$$

n_A is the number of area elements per bundle. The corresponding heat rejected by the bundle to the ambient air is

$$Q_{ab} = \sum_{j=1}^{n_A} \Delta m_{aj} c_{pamj} \left(T_{ao(2)j} - T_{ai(1)} \right) \tag{8.4}$$

The density of air $\rho_{ao(2)}$ was evaluated at the outlet temperature and the ambient pressure measured at ground level, which was approximately 91330 N/m^2 at the time of testing.

An aluminium beam fitted with ten propeller-type anemometers and ten thermocouples was constructed to traverse the heat exchanger frontal area at the air outlet side. The beam was supported in the middle and at the ends. Each support was fitted with wheels which rested on the bundle frame, as shown in figure 8.2. The beam was manually held in a horizontal position by ropes attached to the supports via a pulley system.

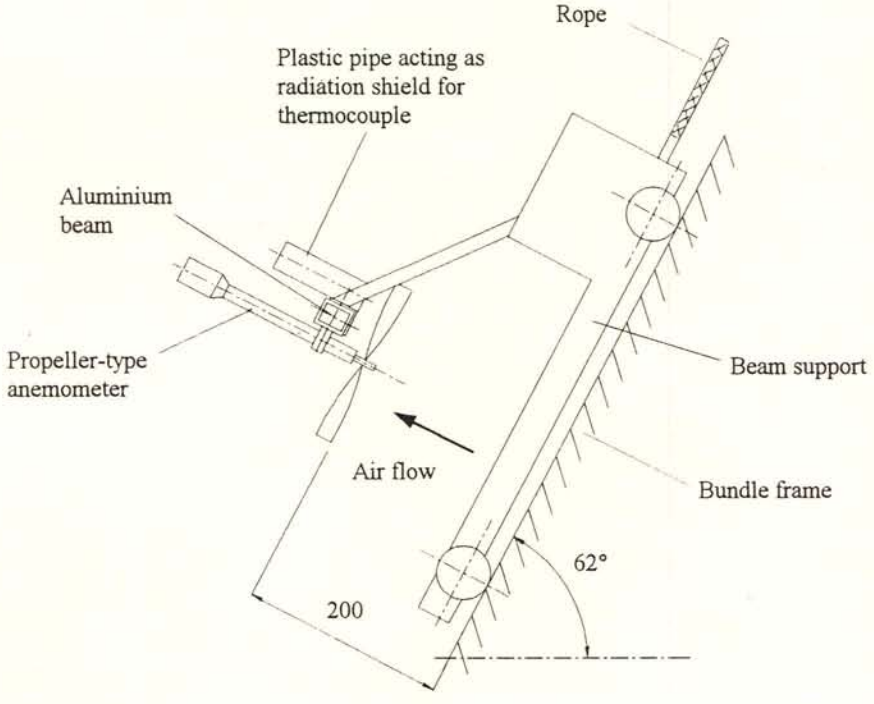

Figure 8.2: Instrumentation beam detail.

8.2 Steamside measurements and instrumentation

The absolute pressure inside the bottom and top header of the dephlegmator was measured with *Foxboro* differential pressure transducers relative to the ambient pressure. A third *Foxboro* pressure transducer monitored the pressure drop across the headers. The transducer arrangement is illustrated in figure 8.1.

The absolute steamside pressure was typically 20 000 to 30 000 N/m^2 or approximately 60 000 to 70 000 N/m^2 below the ambient pressure. Transducers with a range of 0-200 000 N/m^2 were employed to measure the steamside pressure relative to the ambient pressure, while a transducer with a smaller range (0-25 000 N/m^2) was selected for the pressure drop across the headers, to achieve accurate results in the range of 200-10 000 N/m^2 encountered.

The transducers were connected by insulated copper tubing to the pressure tapping points. The copper tube connecting the transducer to the top and bottom headers was placed in the warm outlet air above an adjacent condenser bundle to minimise measurement errors as a result of condensation inside the pressure lines. The condensate inside the pressure lines was drained by two valves located in the pressure lines below the transducer at the bottom of the bundle. Double valves were required, where only one was opened at a time because the system operates at conditions close to vacuum. Practically no condensate accumulated inside the pressure lines during the course of a test run. Hence accurate readings could be achieved.

Three steamside temperatures were monitored, namely the bottom header, top header and ejector duct temperature. Each of the three temperatures was monitored by two thermocouples. The thermocouple locations are shown in figure 8.1. The thermocouple junctions were soldered onto the duct sheeting after the paint was ground off at the particular locations. The thermocouple junctions were then covered with insulating material to minimise the temperature gradient inside the duct walls at the junctions. The measured temperatures can therefore be regarded as representative of the temperature inside the headers/ducts.

8.3 Data acquisition and test procedure

Two 20-channel *Schlumberger IMP*s (Isolated Measurement Pod) performed the data logging. The data loggers take voltage readings and convert voltage signals of thermocouples to temperatures. The pressure transducers, anemometers and the thermocouples were connected to the *Schlumberger IMP*s, which in turn were connected to a personnel computer via a communication cable. All the connected channels were scanned and read every second. The data logger digitises the signals before communicating them to the *PC* where the data were stored on disk for later retrieval and processing.

The instrumentation beam spanned two bundles and therefore the air outlet velocity and temperature distribution of two adjacent bundles were determined simultaneously. At the beginning of a traverse the beam was pulled to the top of the bundles and positioned at the first row of area elements. Once in position, the thermocouples were usually given one minute to stabilise at the outlet temperature after which approximately 30 sets of readings were taken and averaged. After storing the set of average velocities and temperatures on disk the beam was lowered to the next row of area elements for the routine to be repeated. Such a traverse of two adjacent bundles usually took about 20 minutes to complete. At every beam position the steamside data (pressures and temperatures) were recorded, averaged and stored as well.

The fin surface temperature distribution was captured with the aid of infra-red thermography. An *AVIO Thermal Video System* (*TVS-200*) was used for this purpose. The positioning of the camera is shown in figure 8.3. Images were taken of the first row from inside the A-frame and of the second row from outside. The system, consisting of a camera head and a processor unit, was placed in wooden casings for protection. When taking pictures from outside the A-frame, cold air was blown through a flexible tube from inside the plenum into the casings to prevent the camera from being exposed to temperatures above the permissible limit.

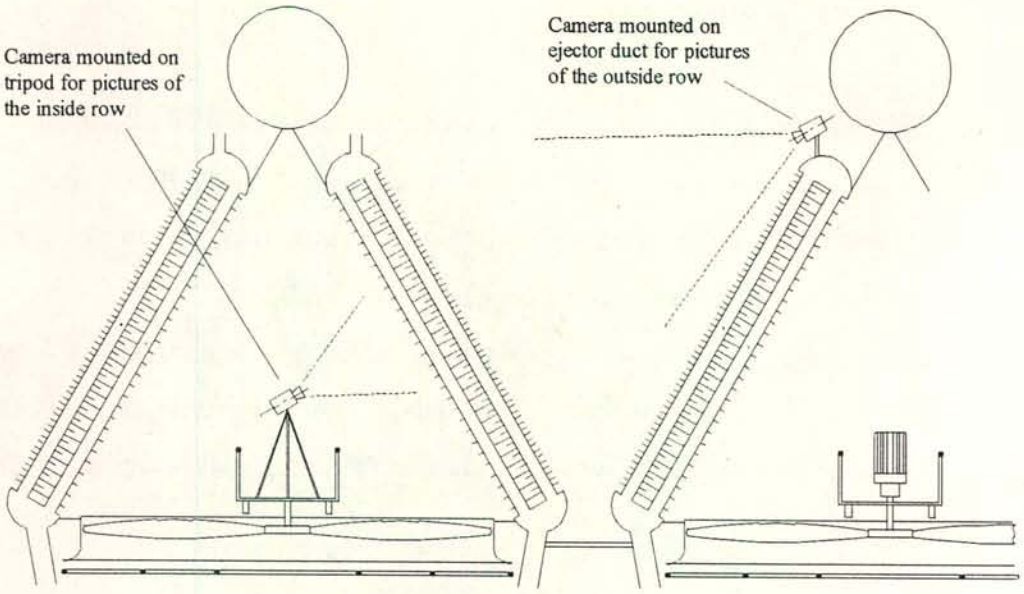

Figure 8.3: Positioning of the infra-red camera.

CHAPTER 9

ANALYSIS OF A DIRECT DRY-COOLED FORCED DRAFT CONDENSER

9.1 Introduction

The turbine output is a function of the turbine exhaust pressure, also referred to as the backpressure. The backpressure is related to the saturation temperature of the vapour inside the condenser, which in turn is dependent on the heat rejection capability of the cooling tower. The operating point of a turbine-condenser system and the corresponding turbine output is evaluated by:

1) Solving for the air flow through the cooling system.
2) Solving for the heat dissipated to the atmosphere.
3) Obtaining the condensation rate from the heat transfer calculations and solving for the corresponding steamside flow distribution and the backpressure.
4) Solving for the turbine operating point by matching the turbine characteristics and the heat rejection rate of the cooling system. The turbine characteristics relate the turbine output and the heat to be dissipated to the backpressure.

The solution procedure for the set of non-linear modelling equations effectively seeks a condenser temperature at which the heat rejected by the cooling tower is equal to the rejection rate required by the turbine characteristics. The required rate is basically the difference between the energy input at the boiler and the output by the turbine.

The analysis of forced draft direct dry-cooled heat exchangers and condensers forms part of an ongoing research and development program at the University of Stellenbosch [85BE1, 86KO1, 91CO1, 94KR1, 95CO1, 95CO2]. The main contribution of this dissertation is the study on the dephlegmator consisting of the analysis presented in section 9.2.2 and the full scale tests described and discussed in chapter 10.

9.2 Steamside flow analysis

9.2.1 Condenser unit

Consider the schematic of a condenser unit containing double-row finned tube bundles as shown in figure 9.1. It is assumed that the excess vapour condensed by the dephlegmator is sufficient to prevent the formation of dead zones caused by the tube-row-effect and that the vapour flow distribution is uniform. The latter implies that for each row the amount of vapour entering each duct is the same, but the vapour flow into ducts of row (1) and (2) may differ.

Conservation of mass. Consider each row separately. The outflow of condensate at the bottom must be equal to the net inflow of vapour, i.e.

$$m_{v2(1)} - m_{v3(1)} = m_{c(1)} \tag{9.1}$$

$$m_{v2(2)} - m_{v3(2)} = m_{c(2)} \tag{9.2}$$

The excess vapour entering the dephlegmator is

$$m_{dephlegmator} = 5\left(m_{v3(1)} + m_{v3(2)}\right) \tag{9.3}$$

One dephlegmator serves five condenser units and here a uniform outflow is assumed amongst the condenser units.

Momentum equations. The absolute pressure p_{vl} in the supply duct or distributing manifold is calculated by subtracting the losses in the exhaust ducting Δp_{vd} from the turbine backpressure p_{vt},

$$p_{vl} = p_{vt} - \Delta p_{vd} = p_{vt} - K_{vd}\, \rho_{v(1)} v^2_{svs(1)}/2 \tag{9.4}$$

K_{vd} is a loss coefficient for the steam duct system. The decrease in pressure experienced by the vapour on its way form the turbine outlet to the distributing header of the finned tube bundles results in a decrease in the saturation temperature. A value of 0.6 for K_{vd} is representative of the pressure losses corresponding to the decrease in the saturation temperature typically observed at the full scale system.

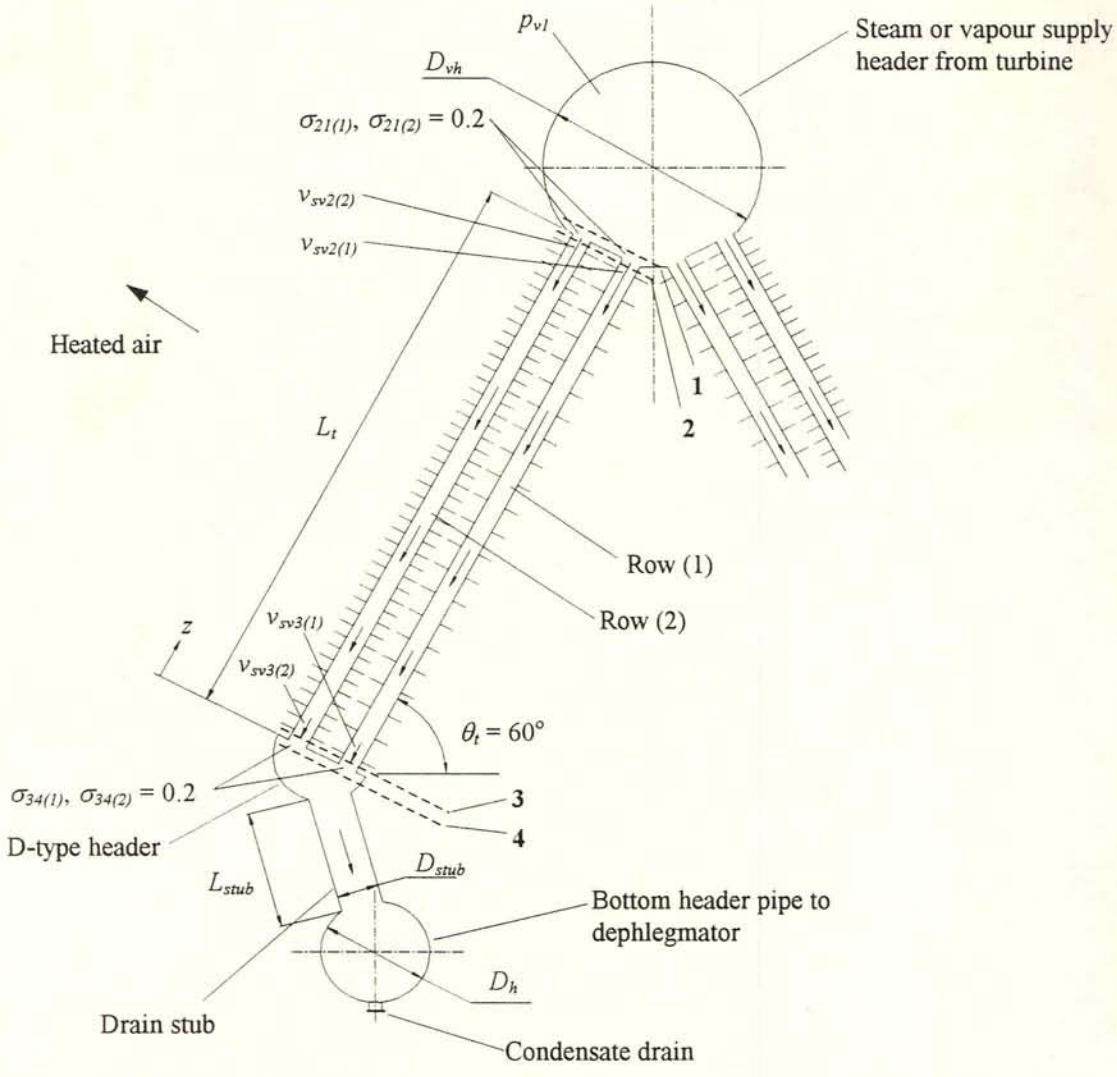

Figure 9.1: Steamside flow distribution inside a double-row condenser unit.

Consider the vapour flow in row (1). Take a decrease in pressure as positive in the z-direction and assume constant vapour properties. The total pressure drop across a finned tube is

$$\Delta p_{14(1)} = \Delta p_{12(1)} + \Delta p_{23(1)} + \Delta p_{34(1)} \tag{9.5}$$

$\Delta p_{12(1)}$ is the change in static pressure across the sudden contraction at the top where the vapour enters the finned tube. It can be expressed according to equation (4.8) in terms of a single-phase loss coefficient

$$\Delta p_{12(1)} = \frac{1}{2}\rho_{v(1)} v_{sv2(1)}^2 \left[\left(1-\sigma_{21}^2\right) + K_{csp}\right] \tag{9.6}$$

where $K_{csp} \approx 0.41$ for the square-edged inlet when assuming flow between parallel plates [50KA1].

The resultant pressure drop inside the finned tube $\Delta p_{23(1)}$ is the sum of the frictional, gravitational and the momentum component:

$$\begin{aligned}\Delta p_{23(1)} &= \Delta p_{f(1)} + \Delta p_{g(1)} + \Delta p_{m(1)} \\ &= \int_0^{L_t} \beta \left(\frac{dp}{dz}\right)_{ftp} dz \;+\; \int_0^{L_t} g\rho_{v(1)} \sin(\theta_t)\, dz \;+\; \int_0^{L_t} -\frac{d}{dz}\left(\rho_{v(1)} v_{sv(1)}^2\right) dz\end{aligned} \tag{9.7}$$

$(dp/dz)_{ftp}$ is the frictional pressure gradient experienced by a gas during adiabatic cocurrent gas-liquid flow. β accounts for the increased frictional pressure drop due to condensation and the subsequent deformation of the vapour boundary layer, similar to boundary layer flow with suction. At the duct inlet where the vapour velocity is the highest, the amount of condensate is small. The condensate flow rate reaches a maximum at the bottom of the duct where the vapour flow is at its minimum. Under such conditions there are no significant vapour-condensate interactions along the entire length of the finned tube and $(dp/dz)_{ftp}$ may be approximated [95GR1] by a relation for single-phase flow

$$\left(\frac{dp}{dz}\right)_{ftp} = f_{sv} \frac{1}{D_e} \frac{1}{2} \rho_g v_{sv}^2 \tag{9.8}$$

f_{sv} is the Darcy friction factor based on the superficial vapour velocity. It is a function of the superficial vapour Reynolds number and may be expressed in terms of a Blasius-type relation

$$f_{sv} = K\, Re_{sv}^n \tag{9.9}$$

where $K = 0.5046$ and $n = -0.2883$ for turbulent flow between parallel plates. Equation (9.9) approximates the implicit *f-Re* function given by equation (4.5) in the range $2500 \leq Re \leq 25\,000$. It underpredicts equation (4.5) by 2.8% at $Re = 2500$ while it overpredicts by 1.1% at $Re = 25\,000$.

Groenewald and Kröger [95GR1] presented a function for β for condensation during turbulent flow inside flattened tubes or rectangular ducts of high aspect ratio:

$$\beta = a_1 + a_2 / Re_{sv} \tag{9.10}$$

a_1 and a_2 are functions of the suction Reynolds number Re_{vn}:

$$a_1 = 1.0649 + 1.041 x 10^{-3}\, Re_{vn} - 2.011 x 10^{-7}\, Re_{vn}^3 \tag{9.11a}$$
$$a_2 = 290.1479 + 59.3153\, Re_{vn} + 1.5995 x 10^{-2}\, Re_{vn}^3 \tag{9.11b}$$

for $0 \le Re_{vn} \le 40$. The suction Reynolds number is expressed as

$$Re_{vn(1)} = m_{c(1)} D_e \Big/ \left(\mu_{v(1)} n_{tb(1)} n_b L_t A_{ti}\right) \tag{9.12}$$

The variation in the vapour velocity along the axial direction of the finned tube may be approximated by a linear relation

$$v_{sv(1)} = \left(v_{sv3(1)} - v_{sv2(1)}\right) z / L_t + v_{sv2(1)} \tag{9.13}$$

Substitute equations (9.8) to (9.11) and (9.13) in equation (9.7) and integrate to obtain

$$\Delta p_{23(1)} = \frac{1}{2}\rho_{v(2)} v_{sv2(1)}^2 \left[\frac{L_t}{D_e}\frac{K\, Re_{sv2(1)}^n}{\left(1 - v_{sv3(1)}/v_{sv2(1)}\right)}\left(\frac{a_1\left(1-\left(v_{sv3(1)}/v_{sv2(1)}\right)^{n+3}\right)}{n+3} + \frac{a_2\left(1-\left(v_{sv3(1)}/v_{sv2(1)}\right)^{n+2}\right)}{(n+2)\, Re_{sv2(1)}}\right)\right] + \rho_{v(1)} g\, L_t \sin\left(\theta_t\right) + \left(\rho_{v(1)} v_{sv2(1)}^2 - \rho_{v(1)} v_{sv3(1)}^2\right) \tag{9.14}$$

Note that a transition from turbulent to laminar flow may occur close to the bottom end of the elliptical tube. The pressure drop in the laminar region is negligibly small compared to the pressure drop across the headers and is approximated by the relation for turbulent flow for the purpose of the present analysis.

The pressure drop at the bottom of row (1) where the vapour enters the D-type header is calculated with the aid of an expansion loss coefficient for single-phase flow between parallel plates [50KA1]

$$\Delta p_{34(1)} = \frac{1}{2}\rho_{v(1)} v_{sv3(1)}^2 \left[\left(\sigma_{34}^2 - 1\right) + K_{esp}\right] \tag{9.15}$$

where $K_{esp} \approx 0.64$.

By adding the respective components, equation (9.5) for the total pressure drop across the headers yields

$$\begin{aligned}\Delta p_{14(1)} = {} & \frac{1}{2}\rho_{v(1)} v_{sv2(1)}^2 \left[\left(1-\sigma_{21}^2\right) + K_{csp}\right] \\ & + \frac{1}{2}\rho_{v(2)} v_{sv2(1)}^2 \left[\frac{L_t}{D_e}\frac{K\,Re_{sv2(1)}^n}{\left(1 - v_{sv3(1)}/v_{sv2(1)}\right)}\left(\frac{a_1\left(1-\left(v_{sv3(1)}/v_{sv2(1)}\right)^{n+3}\right)}{n+3}\right.\right. \\ & \left.\left. + \frac{a_2\left(1-\left(v_{sv3(1)}/v_{sv2(1)}\right)^{n+2}\right)}{(n+2)\,Re_{sv2(1)}}\right)\right] \\ & + \rho_{v(1)} g\, L_t \sin\left(\theta_t\right) + \left(\rho_{v(1)} v_{sv2(1)}^2 - \rho_{v(1)} v_{sv3(1)}^2\right) \\ & + \frac{1}{2}\rho_{v(1)} v_{sv3(1)}^2 \left[\left(\sigma_{34}^2 - 1\right) + K_{esp}\right]\end{aligned} \tag{9.16}$$

The same expression is valid for row (2). The common bottom and top header requires that

$$\Delta p_{14(1)} = \Delta p_{14(2)} \tag{9.17}$$

Equations (9.1) to (9.3) and (9.17) form a set of four equations which can be solved for the four variables $m_{v2(1)}$, $m_{v3(1)}$, $m_{v2(2)}$ and $m_{v3(2)}$ once the condensation rates $m_{c(1)}$ and $m_{c(2)}$ and the mass flow rate entering the dephlegmator $m_{dephlegmator}$ are known.

Heat transfer relations. The heat transfer from the condensing steam to the air passing through the finned tube bundles of a fan unit is

$$Q_a = \sum_{i=1}^{n_{tr}} Q_{a(i)} = \sum_{i=1}^{n_{tr}} m_a c_{pam(i)} \left(T_{ao(i)} - T_{ai(i)} \right)$$
$$= \sum_{i=1}^{n_{tr}} m_{c(i)} i_{lg(i)} = \sum_{i=1}^{n_{tr}} m_a c_{pam(i)} \left(T_{vm(i)} - T_{ai(i)} \right) e_{(i)} \qquad (9.18)$$

The effectiveness for each tube row is [86HO1]

$$e_{(i)} = 1 - exp\left[-(UA)_{(i)} / \left(m_a c_{pam(i)} \right) \right] \qquad (9.19)$$

where the overall thermal conductance is

$$(UA)_{(i)} = \left[1/h_{ae(i)} A_{a(i)} + 1/h_{c(i)} A_{c(i)} \right]^{-1} \qquad (9.20)$$

$h_{ae}A_a$ is the effective airside thermal conductance and may be expressed as

$$h_{ae(i)} A_{a(i)} = \left[1/h_{a(i)} e_{f(i)} A_{a(i)} + \sum_n \frac{R_n}{A_n} \right]^{-1} \qquad (9.21)$$

The summation term represents the thermal resistances other than the airside and steamside values.

The inside duct surface area of row (i) exposed to the steam is

$$A_{c(i)} = n_b n_{tr(i)} A_{ti} L_t \qquad (9.22)$$

A correlation developed by Groenewald [93GR1] for flattened tubes is employed to determine the condensation heat transfer coefficient, i.e.

$$h_{c(i)} = 0.9245 \left[\frac{L_t k_{c(i)}^3 \rho_{c(i)}^2 g \cos\left(\theta_t\right) i_{lg(i)}}{\mu_{c(i)} m_{al(i)} c_{pam(i)} \left(T_{v(i)} - T_{ai(i)} \right) \left[1 - exp\left\{ -\left(U_{c(i)} H_t L_t \right) / \left(m_{al(i)} c_{pam(i)} \right) \right\} \right]} \right]^{0.333} \qquad (9.23)$$

m_{al} is the air mass flow rate flowing on one side of a duct:

$$m_{al(i)} = m_a / \left(2 n_{tb(i)} n_b \right) \qquad (9.24)$$

The overall heat transfer coefficient based on the condensation surface area may be approximated by

$$U_{c(i)} H_t L_t = \left(h_{ae(i)} A_{a(i)}\right) \Big/ \left(2 n_{tb} n_b\right) \tag{9.25}$$

where the thermal resistance of the condensate film has been neglected.

The heat transfer performance characteristic for each tube row was obtained in a standard wind-tunnel (see Appendix J) and is presented in the dimensional form proposed by Kröger [86KR1]

$$h_{ae(i)} A_{a(i)} = Ny_{(i)} k_{am(i)} Pr_{am(i)}^{1/3} A_{fr(i)} \tag{9.26}$$

where the characteristic heat transfer parameters $Ny_{(i)}$ [m^{-1}] are expressed as

Row (1): $Ny_{(1)} = 583.830\, Ry_{(1)}^{0.4031}$ (9.27a)

Row (2): $Ny_{(2)} = 1277.7255\, Ry_{(2)}^{0.3806}$ (9.27b)

$Ry_{(i)}$ [m^{-1}] is the heat exchanger flow parameter

$$Ry_{(i)} = \frac{m_a}{\mu_{am(i)} A_{fr(i)}} \tag{9.28}$$

The rate of condensation in each row can be calculated by making use of equations (9.18) to (9.28), with the air flow rate and inlet temperature as input values.

The mean vapour temperature $T_{vm(i)}$ in equation (9.18) is approximated by the saturation temperature corresponding to the mean row pressure

$$p_{vm(i)} = p_{v1} - \Delta p_{12(i)} - \frac{1}{L_t} \int_0^{L_t} \left(\Delta p_f(z) + \Delta p_g(z) + \Delta p_m(z)\right)_{(i)} dz \tag{9.29}$$

The change in the frictional, gravitational and momentum pressure components along the duct axis are respectively

$$\Delta p_f(z) = \int_0^z \left(dp/dz\right)_{ftp} dz \tag{9.30a}$$

$$\Delta p_g(z) = \rho_v \, g \, z \, sin\left(\theta_t\right) \tag{9.30b}$$

$$\Delta p_m(z) = \rho_v \left(v_{sv}(z)\right)^2 - \rho_v \, v_{sv2}^2 \tag{9.30c}$$

Substitution of the appropriate equations into (9.30) and then into equation (9.29) yields upon integration

$$p_{vm} = p_{v1} - \Delta p_{12(i)} - \frac{1}{2}\rho_{v(i)} v_{sv2(i)}^2 \frac{L}{D_e} \frac{K \, Re_{sv2(i)}^n}{\left(1 - v_{sv3(i)}/v_{sv2(i)}\right)} \left[\frac{a_1}{n+3} x \right.$$

$$\left\{ 1 - \frac{v_{sv3(i)}^{n+4} - v_{sv2(i)}^{n+4}}{v_{sv2(i)}^{n+3}\left(n+4\right)\left(v_{sv3(i)} - v_{sv2(i)}\right)} \right\} + \frac{a_2}{\left(n+2\right) Re_{sv2(i)}} \left\{ 1 - \frac{v_{sv3(i)}^{n+3} - v_{sv2(i)}^{n+3}}{v_{sv2(i)}^{n+2}\left(n+4\right)\left(v_{sv3(i)} - v_{sv2(i)}\right)} \right\} \Bigg]$$

$$+ 1/2 \, \rho_{v(i)} \, g \, L_t \, sin\left(\theta_t\right) + \rho_{v(i)} \left(1/3 \, v_{sv3(i)}^2 + 1/3 \, v_{sv2(i)} v_{sv3(i)} + 2/3 \, v_{sv2(i)}^2\right) \tag{9.31}$$

The vapour and condensate thermophysical properties for each row are evaluated at the saturation temperature corresponding to the mean vapour pressure.

9.2.2 Dephlegmator unit

The steamside flow distribution of a dephlegmator unit is shown in figure 9.2. For the purpose of the present analysis the noncondensable gases present in the dephlegmator are not considered separately. They are included in the mass flow rate $m_{dephlegmator}$ entering the dephlegmator and $m_{ejector}$ removed from the top header by the vacuum system and are treated as vapour.

The heat transfer characteristics of the rows are such that row (1) condenses slightly more steam than row (2). It can therefore be assumed that steam backflow from the top of row (2) into the top of row (1) will occur. The length of the backflow region is denoted as L_b. The assumption is based on the fact that the ejector suction rate is small and does not influence the steamside flow distribution significantly.

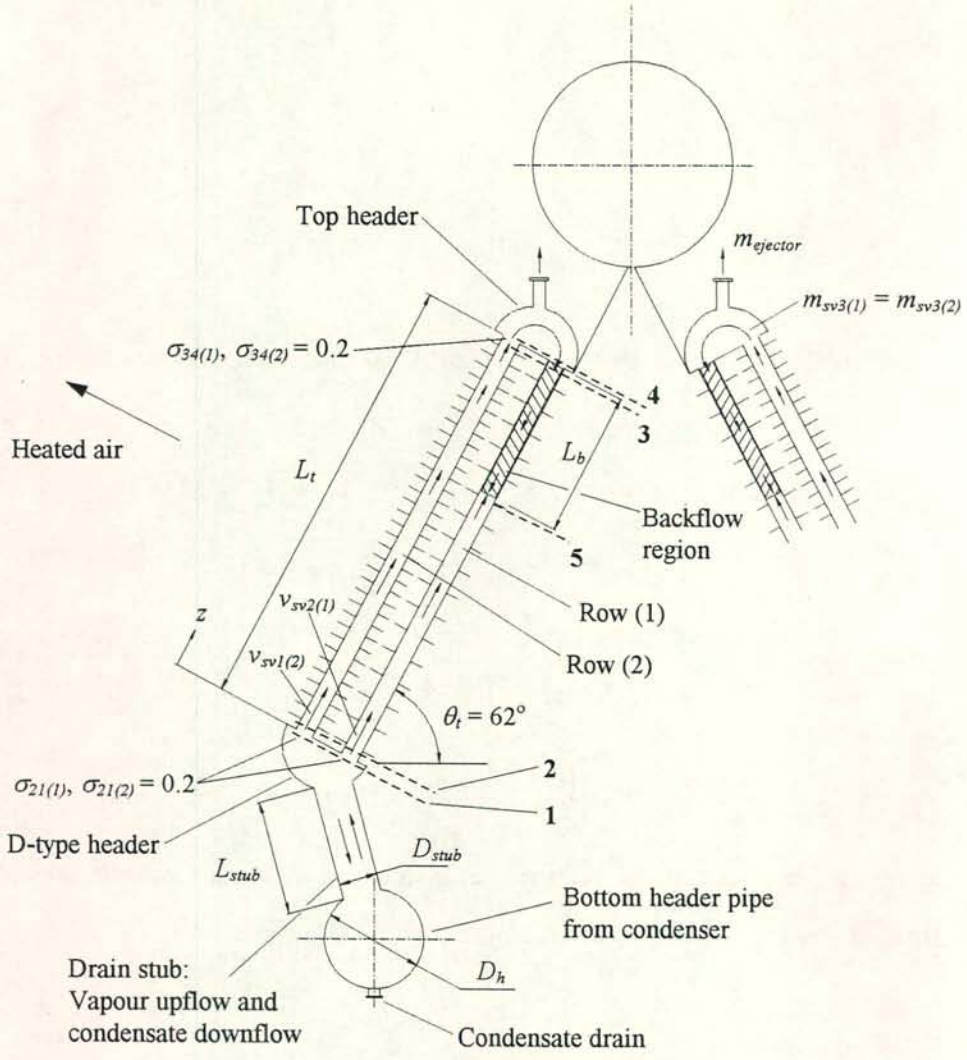

Figure 9.2: Steamside flow distribution inside a double-row dephlegmator unit.

Conservation of mass. The following balance of the mass flow rates applies for each row respectively:

$$m_{v2(1)} + m_{v3(1)} = m_{c(1)} \tag{9.32}$$

$$m_{v2(2)} - m_{v3(2)} = m_{c(2)} \tag{9.33}$$

where m_v and m_c are the vapour and the condensate flow rates. Excess vapour at the top of row (2) enters row (1) via the top header and at the same time vapour is removed by the ejector. Therefore we have

$$m_{v3(1)} + m_{ejector} = m_{v3(2)} \tag{9.34}$$

The heat transfer along the finned tubes can be considered as a constant heat flux process and thus:

$$m_{v3(1)}/m_{c(1)} = L_b/L_t \tag{9.35}$$

Momentum equations. Consider the vapour flow of row (1). The pressure drop across a finned tube is

$$\Delta p_{14(1)} = \Delta p_{15(1)} + \Delta p_{54(1)} = \left(\Delta p_{12(1)} + \Delta p_{25(1)}\right) + \left(\Delta p_{53(1)} + \Delta p_{34(1)}\right) \tag{9.36}$$

$\Delta p_{15(1)}$ is the change in pressure experienced by the vapour entering from the bottom while $\Delta p_{54(1)}$ represents the pressure rise in the backflow region.

According to equation (4.10) the entrance pressure drop in the presence of draining condensate can be expressed as

$$\Delta p_{12(1)} = \frac{1}{2}\rho_{v(1)} v_{sv2(1)}^2 \left[K_{tp} - \sigma_{21}^2\right] \tag{9.37}$$

where the two-phase entrance loss coefficient K_{tp} is a function of the densimetric gas Froude number Fr_{Hsg}. During filmwise condensation as found in the finned tubes the entire tube wall is wetted. For this reason data from the short test section configuration where better wetting was achieved, are used for the modelling of the steamside flow. Air-water entrance pressure drop data are shown in figure 9.2. The data were obtained with the 100 mm duct inclined at 60° to the horizontal. The water flow rate of the data in figure 9.2 typically represents the condensate flow rates encountered in the dephlegmator. The loss coefficient is correlated by

$$K_{tp} = 1.622 + 2.078\, Fr_{Hsg} \tag{9.38}$$

for $0.03 \leq Fr_{Hsg} \leq 0.4$. Equation (9.38) is valid for steady counterflow. It does not incorporate the strong increase in pressure drop when the vortex size at the vapour inlet approaches the duct height and the subsequent unsteady nature of the pressure drop.

The resultant pressure drop $\Delta p_{25(1)}$ inside the duct across the length (L_t - L_b), i.e. from the bottom of the duct to the point where the backflow region begins, is

$$\Delta p_{25(1)} = \Delta p_f + \Delta p_g + \Delta p_m$$
$$= \int_0^{L_t - L_b} \beta \left(\frac{dp}{dz}\right)_{ftp} dz + \int_0^{L_t - L_b} g\rho_{v(1)} \sin(\theta_t)\, dz$$
$$+ \int_0^{L_t - L_b} -\frac{d}{dz}\left(\rho_{v(1)} v_{sv(1)}^2\right) dz \qquad (9.39)$$

At low vapour flow rates the two-phase friction factor f_{sg} required to evaluate $(dp/dz)_{ftp}$ is related to the vapour Reynolds number as illustrated in chapter 4 of part A.

Adiabatic air-water friction factor data for counterflow are shown in figure 9.4 against the superficial gas Reynolds number. At higher vapour flows wave action and entrainment cause the two-phase friction factor to rise above the single-phase prediction. Inside the operating range of the dephlegmator the two-phase friction factor should not deviate significantly from the single-phase friction factor and may be correlated in the form of a Blasius-type relation given by equation (9.9), where K = 0.2259 and n = -0.2088.

Although the pressure drop in the presence of a draining liquid becomes strictly speaking Froude number related, it can be correlated in terms of the Reynolds number in the transition region from Reynolds to Froude number governed flow where the friction factor remains constant. This can be seen in figure 9.4 where f_{sg} is practically constant inside the range 15 000 < Re_{sg} < 24 000. In other words, in the transition region the two-phase friction factor is independent of the gas Reynolds and Froude number and only at higher gas flow rates closer to flooding it becomes Froude number related (see figures 4.10a and b). The condensate flow rate is not in incorporated in the correlation for the two-phase friction factor because it has no effect at the low liquid flow rates achieved during condensation in the air-cooled reflux condenser.

A dephlegmator design should be safe against flooding and pulsating conditions. For this reason the present analysis will be based on the Reynolds number region only. Conditions at higher vapour flow rates are of no practical interest and are not modelled. The inception of flooding is however addressed.

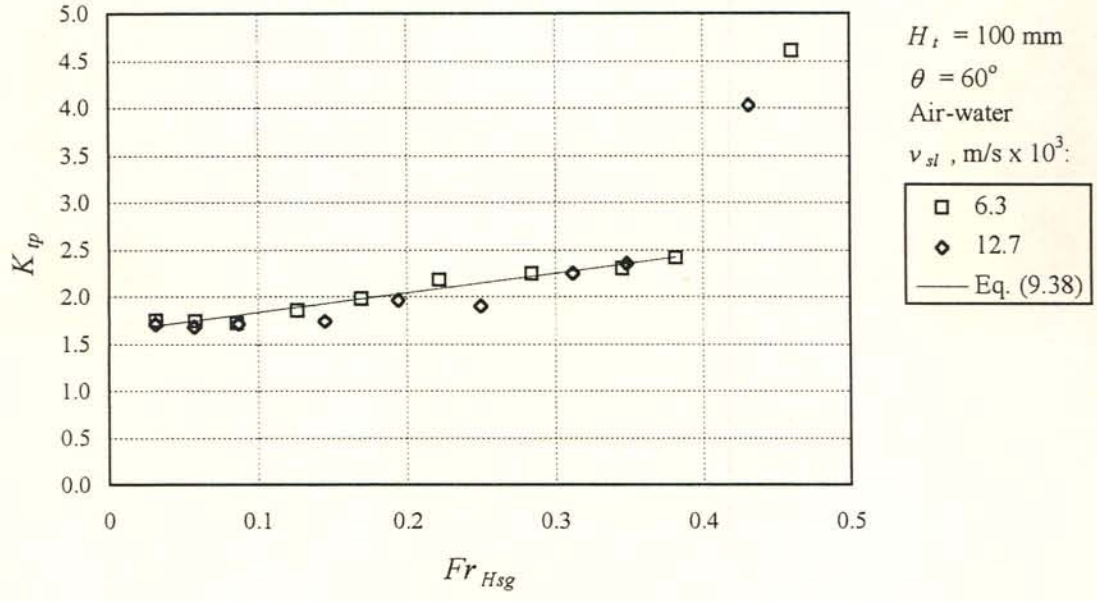

Figure 9.3: Adiabatic air-water entrance pressure drop data for the modelling of the dephlegmator steamside flow. The data were obtained with the short test section configuration where better wetting was achieved.

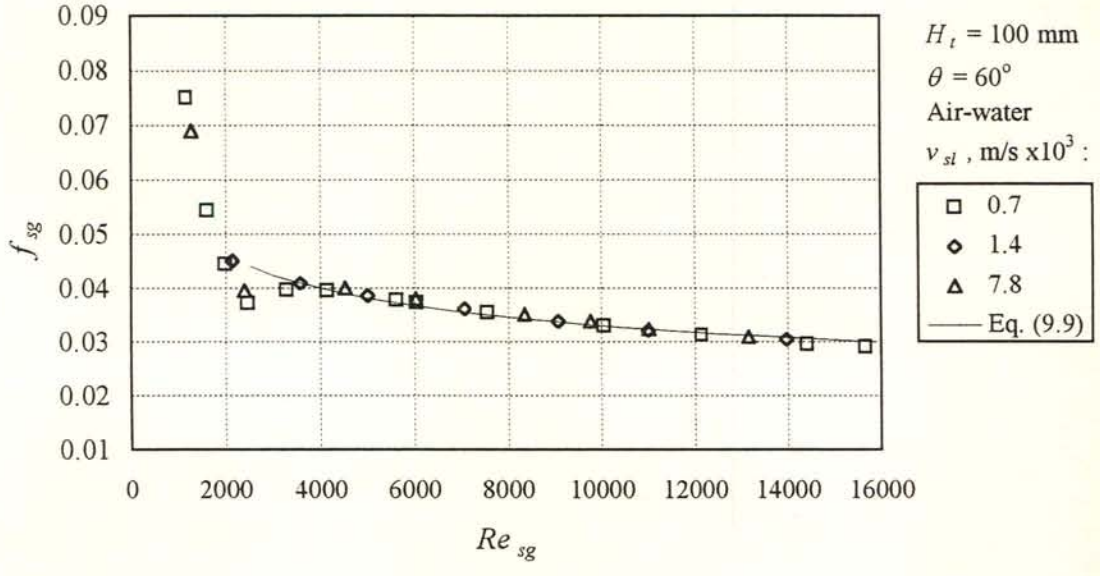

Figure 9.4: Adiabatic air-water friction factor data obtained with the 100 mm duct inclined at 60° to the horizontal. The solid line represents a Blasius-type relation (equation (9.9)) with K = 0.2259 and n = -0.2088.

The variation of the vapour velocity in the upflow region of row (1) is given by

$$v_{sv(1)} = v_{sv2(1)}\left(1 - z/\left(L_t - L_b\right)\right) \tag{9.40}$$

Upon substitution of equations (9.8) to (9.11) and (9.40) into equation (9.39) and integration, the pressure drop from inside the header to the backflow region is obtained, i.e.

$$\begin{aligned}\Delta p_{25(1)} = {} & \frac{1}{2}\rho_{v(1)}v_{sv2(1)}^2\left[\frac{\left(L_t - L_b\right)}{D_e}K\,Re_{sv2(1)}^n\left(\frac{a_1}{n+3} + \frac{a_2}{(n+2)\,Re_{sv2(1)}}\right)\right] \\ & + \rho_{v(1)}g\left(L_t - L_b\right)sin(\theta_t) - \rho_{v(1)}v_{sv2(1)}^2\end{aligned} \tag{9.41}$$

The same procedure can be carried out for the backflow region where the vapour and condensate flow cocurrently downwards. Exactly the same governing equations are used for this region except that the entrance pressure drop at the top of the finned tube may be calculated with a single-phase loss coefficient. Equation (4.8) applies, i.e.

$$\Delta p_{34(1)} = -\frac{1}{2}\rho_{v(1)}v_{sv3(1)}^2\left[\left(1-\sigma_{34}^2\right) + K_{csp}\right] \tag{9.42}$$

Equation (9.36) for the total pressure drop across the headers can now be obtained by adding the respective components, resulting in

$$\begin{aligned}\Delta p_{14(1)} = {} & \frac{1}{2}\rho_{v(1)}v_{sv2(1)}^2\left[\left(K_{tp(1)} - \sigma_{21}^2\right) + \frac{\left(L_t - L_b\right)}{D_e}K\,Re_{sv2(1)}^n\left(\frac{a_1}{n+3} + \frac{a_2}{(n+2)\,Re_{sv2(1)}}\right)\right] \\ & - \frac{1}{2}\rho_{v(1)}v_{sv3(1)}^2\left[\left(1 - \sigma_{34}^2 + K_{csp}\right) + \frac{L_b}{D_e}K\,Re_{sv3(1)}^n\left(\frac{a_1}{n+3} + \frac{a_2}{(n+2)\,Re_{sv3(1)}}\right)\right] \\ & + \rho_{v(1)}g\,L_t\sin(\theta_t) - \left(\rho_{v(1)}v_{sv2(1)}^2 + \rho_{v(1)}v_{sv3(1)}^2\right)\end{aligned} \tag{9.43}$$

A similar expression can be derived for row (2), keeping in mind that there is an outflow of steam at the top. The entrance pressure drop is evaluated according to equation (9.37) while the pressure drop at the top where the vapour enters the header is determined with the aid of a single-phase expansion loss coefficient. The resultant pressure drop across a finned tube of row (2) is

$$\Delta p_{14(2)} = \frac{1}{2}\rho_{v(2)} v_{sv2(2)}^2 \left(K_{tp(2)} - \sigma_{21}^2\right) + \frac{1}{2}\rho_{v(2)} v_{sv2(2)}^2 \left[\frac{L_t}{D_e}\frac{K\,Re_{sv2(2)}^n}{\left(1 - v_{sv3(2)}/v_{sv2(2)}\right)}\left(\frac{a_1\left(1-\left(v_{sv3(2)}/v_{sv2(2)}\right)^{n+3}\right)}{n+3} + \frac{a_2\left(1-\left(v_{sv3(2)}/v_{sv2(2)}\right)^{n+2}\right)}{(n+2)\,Re_{sv2(2)}}\right)\right] + \rho_{v(2)}\, g\, L_t \sin\left(\theta_t\right) - \left(\rho_{v(2)} v_{sv2(2)}^2 - \rho_{v(2)} v_{sv3(2)}^2\right) + \frac{1}{2}\rho_{v(2)} v_{sv3(2)}^2 \left[\left(\sigma_{34}^2 - 1\right) + K_{esp}\right] \qquad (9.44)$$

The common bottom and top header configuration requires that

$$\Delta p_{14(1)} = \Delta p_{14(2)} \qquad (9.45)$$

Similar to the condenser unit, equations (9.32) to (9.35) and the equal pressure drop condition equation (9.45) form a set of five equations which can be solved for the five variables $v_{sv2(1)}$, $v_{sv3(1)}$, $v_{sv2(2)}$, $v_{sv3(2)}$ and L_b , once the condensations rates $m_{c(1)}$ and $m_{c(2)}$ and the ejector suction rate $m_{ejector}$ are known.

Heat transfer relations. Below flooding conditions the heat transfer equations derived for the condenser unit are applicable to the dephlegmator. The mean vapour pressure is determined according to equation (9.31). In the case of row (1) L_t is replaced by (L_t - L_b) and $v_{sv3(1)}$ is set equal to zero in equation (9.31). The pressure drop in the backflow region is small and its effect on the mean vapour pressure is ignored.

9.3 Airside flow

As the cooling air passes through the system it has to overcome flow resistances imposed by the heat exchanger bundles and other flow obstacles causing a decrease in the total pressure. At the heat exchanger operating point the decrease in total pressure is balanced by the total pressure rise across the fan. The equation describing this balance is called the draft equation. The derivation of such a draft equation has been outlined by Kröger [94KR1]. The method is followed in Appendix G to derive a draft equation for the system under consideration. The final equation is briefly discussed in this section.

Consider the schematic of a fan unit shown in figure 9.5. Stagnant air rises from somewhere near ground level (1). It flows past the heat exchanger supports (2) and enters the fan at (3) before crossing upstream obstacles such as the safety grid. The air exits the fan at (4) where downstream obstacles such as the fan drive support bridge and the walkway are located. Before reaching the finned tube bundles at (5) the air flow experiences losses in the plenum. (5) denotes the average bundle height. Having passed the bundles, the air turns upwards between (6) and (7) and enters the atmosphere.

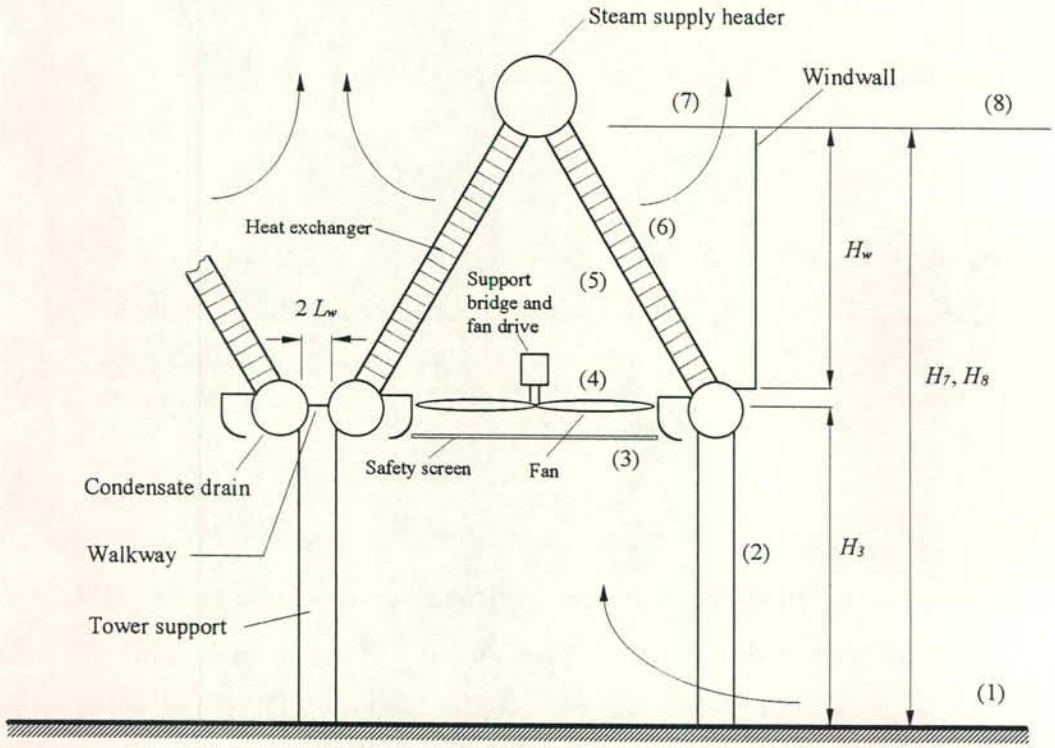

Figure 9.5: Schematic of a fan unit illustrating the air flow.

Take consecutive flow losses into account to obtain the draft equation

$$p_{a1}\left[\left\{1-0.00975\left(H_7-H_6\right)/T_{a6}\right\}^{3.5}-\left\{1-0.00975\left(H_7-H_6\right)/T_{a1}\right\}^{3.5}\right]=$$
$$K_{ts}\left(m_a/A_2\right)^2/\left(2\rho_{a1}\right)+K_{up}\left(m_a/A_{Fe}\right)^2/\left(2\rho_{a3}\right)-K_{Fs}\left(m_a/A_{Fc}\right)^2/\left(2\rho_{a3}\right)$$
$$+K_{do}\left(m_a/A_{Fe}\right)/\left(2\rho_{a3}\right)+K_{\theta t}\left(m_a/A_{fr}\right)/\left(2\rho_{a56}\right) \qquad \text{(G.72)}$$

The left-hand side of equation (G.72) represents the buoyancy force experienced by the air flow as result of a decrease in density at the heat exchanger bundles where the air is heated.

The right-hand side contains the pressure losses and the pressure rise across the fan in terms of dimensionless coefficients K and their dynamic head $(m_a/A)^2/(2\rho_a) = 1/2\rho_a v_a^2$. See Appendix G for a detailed description of each term.

The first term on the right-hand side represents the pressure loss across the support structure. K_{ts} is the tower support loss coefficient while A_2 is the free flow area into the condenser at the supports. An expression for K_{ts} is given by equation (G.80). For the present system as value of 1.6 is assumed [94KR1, 95CO1].

K_{up} and K_{do} are the loss coefficients due to obstacles at the upstream and downstream sides of the fan. Venter and Kröger [91VE1] simulated the air flow past a fan safety grid, a fan support structure and a walkway in a scale model and evaluated the effective flow resistances of these obstacles located immediately upstream and downstream of the fan rotor. It was found that direct measurement of the effective loss coefficients is the most reliable approach, but that satisfactorily predictions of pressure loss coefficients can be obtained from the bulk method [85VE1]. The bulk method expresses the loss coefficients

$$K_{up} = \Delta p_{up} \Big/ \left(1/2\, \rho_{a3} v_{a3}^2\right) = 2\Delta p_{up} \rho_{a3} \Big/ \left(m_a / A_{Fe}\right)^2 \qquad \text{(G.81a)}$$

$$K_{do} = \Delta p_{do} \Big/ \left(1/2\, \rho_{a4} v_{a4}^2\right) = 2\Delta p_{do} \rho_{a4} \Big/ \left(m_a / A_{Fe}\right)^2 \qquad \text{(G.81b)}$$

as a function of the distance between the fan rotor and the flow obstacle and its projected blockage area. For the specifications on the flow obstacles (Appendix A) find, according to the bulk method, $K_{up} = 0.312$ and $K_{do} = 0.376$. The flow area in equation (G.81) is defined as $A_{Fe} = A_{Fc} - A_{Fh}$, where A_{Fc} and A_{Fh} are the fan casing and fan hub cross-sectional areas respectively.

The third term on the right-hand side of equation (G.72) represents the pressure rise across the fan. K_{Fs} is the fan static pressure coefficient defined as

$$K_{Fs} = 2\,\Delta p_{Fs}\, \rho_{a3} \Big/ \left(m_a / A_{Fc}\right)^2 \qquad \text{(G.69)}$$

and is obtained from the performance characteristics of the fan. Δp_{Fs} is the fan static pressure. The performance characteristics are shown in figures 9.6(a) and (b) against the

volume flow rate through the fan V_F. The fan static pressure and power consumption P_F are shown in figure 9.6(a) and the corresponding fan static efficiency, defined as

$$\eta_{Fs} = \frac{\Delta p_{Fs} V_F}{P_F} \tag{G.55}$$

is shown in figure 9.6(b). The heat exchanger should operate at a volume flow rate slightly above the optimum flow rate so that a decrease in flow results in an increase in efficiency and improved system performance. Thus, further deterioration can be countered.

The last term on the right-hand side of equation (7.2) represents the pressure loss experienced at the heat exchanger bundles. It includes oblique flow losses at the inlet to the bundles, turning and jetting losses between locations (6) and (7) and the kinetic energy loss at elevation (7). A_{fr} is the heat exchanger frontal area.

9.4 Ejector characteristics

A flow diagram of the vacuum system is shown in figure 9.7(a). One two-stage ejector driven by steam (primary fluid) at 1500 kN/m^2 serves eight dephlegmator units. The suction side of the first stage is connected to the dephlegmator top header and expands into an inter-condenser which in turn is evacuated by the second stage. The discharge pressure or pressure of the after-condenser serving the second stage is just above the ambient pressure, so that the accumulated noncondensable gases are blown into the atmosphere. Water-cooled shell-and-tube heat exchangers are employed as inter- and after condensers.

The suction rate or secondary flow rate of an ejector can be expressed as a function of the suction pressure. Such a relationship forms the ejector characteristics, as shown in figure 9.7(b). The characteristics are valid for a vapour-air mixture flow rate containing air at a rate of 30 kg/h. For the purpose of the present investigation the entire suction flow is treated as vapour and the presence of air is ignored.

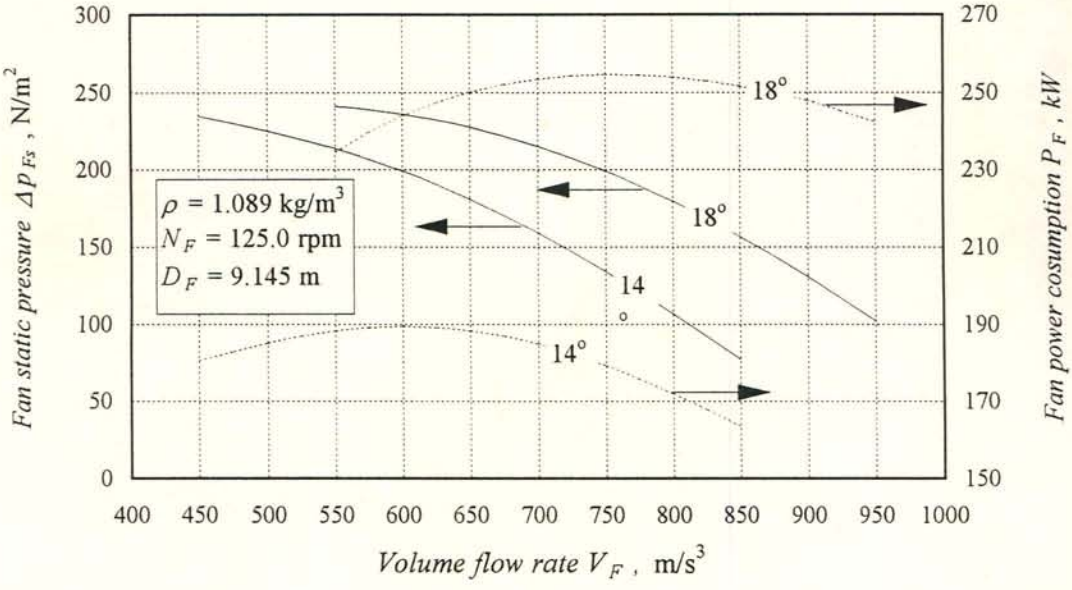

Figure 9.6(a): Fan static pressure and power consumption of the axial flow fans employed for blade angles of 14° and 18°.

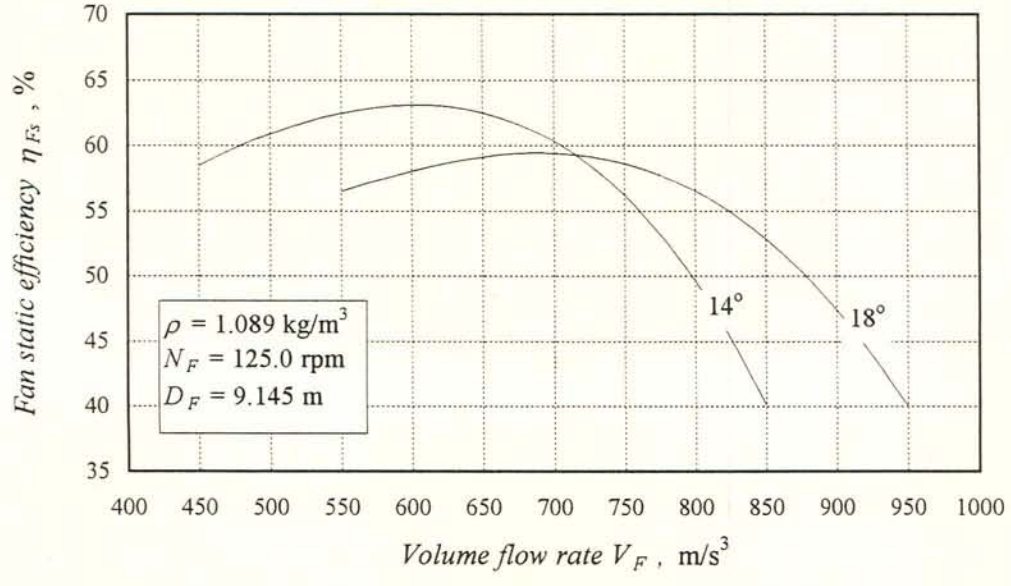

Figure 9.6(b): Fan static efficiency of the axial flow fans employed for blade angles of 14° and 18°.

The suction pressure at the first stage ejector is obtained by subtracting the pressure drop along the ejector ducting from the pressure inside the top header of the dephlegmator.

$$p_{ejector} = p_{v4} - \Delta p_{4-ejector} = p_{v4} - K_{ejector}\, 1/2\, \rho_{v4} v_{ejector}^2 \tag{9.46}$$

$K_{ejector}$ is an ejector ducting loss coefficient and is estimated at 22 for the system under investigation. $v_{ejector}$ is the vapour velocity inside the ejector ducting of diameter $D_{ejector}$ = 150 mm and is determined by

$$v_{ejector} = m_{ejector} \Big/ \left(\rho_4\, \pi\, D_{ejector}^2 / 4\right) \tag{9.47}$$

$m_{ejector}$ is the mass flow rate removed per dephlegmator, i.e.

$$m_{ejector} = m_{tot}/8 \tag{9.48}$$

where m_{tot} is the suction flow rate per first stage ejector shown in figure 9.7(b).

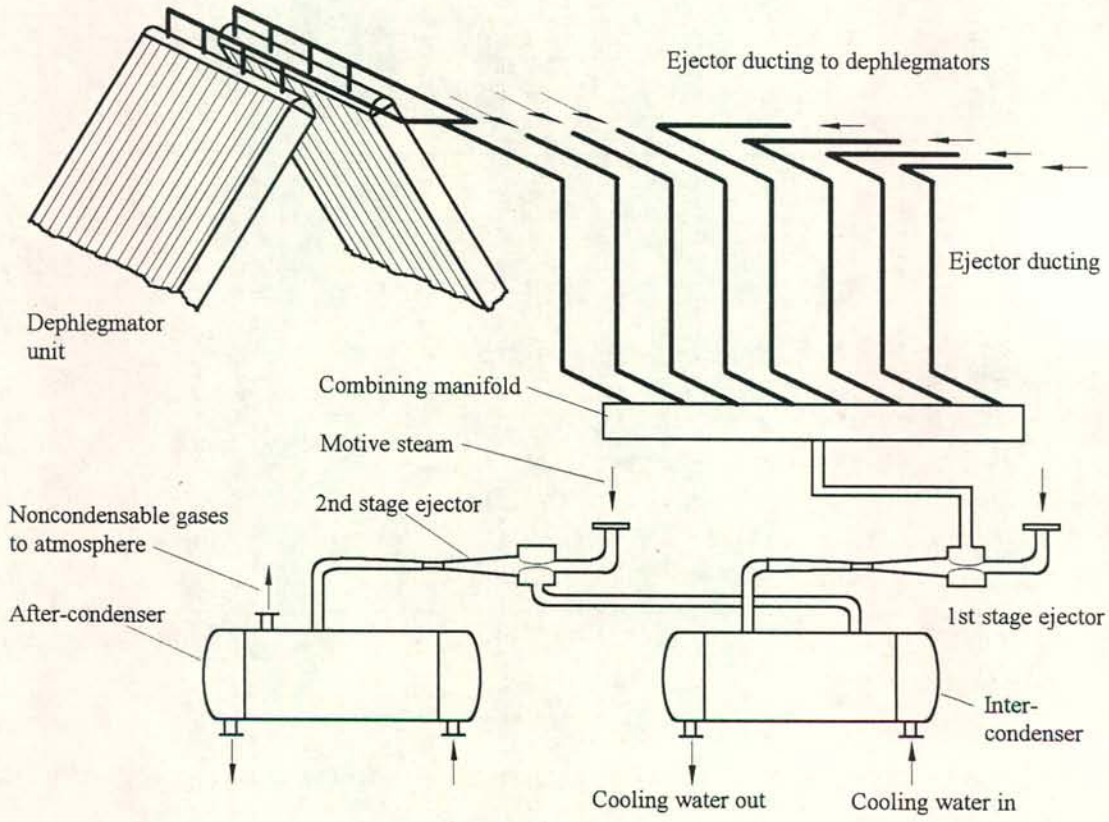

Figure 9.7(b): Flow diagram of the vacuum system.

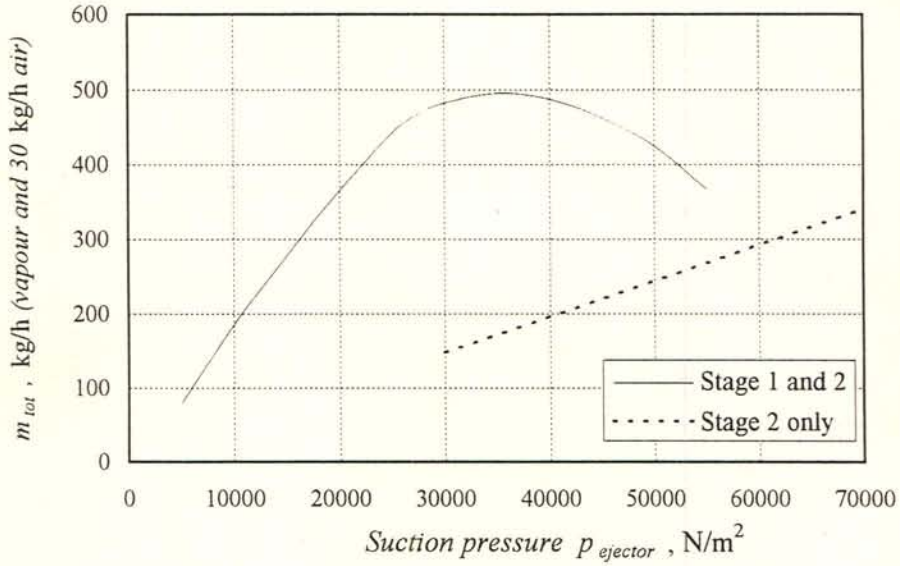

Figure 9.7(b): Ejector characteristics. One two-stage ejector serves eight dephlegmator units.

9.5 Turbine characteristics

The turbine characteristics are shown in figure 9.8. The shaft work produced by a turbine or turbine output is a function of the steam flow rate passing through the turbine and the exhaust pressure or backpressure. The turbine output increases with a rise in the steam flow rate and a decrease in the backpressure. The difference in the energy input at the boiler and the turbine output has to be rejected by the cooling system where the atmosphere acts as a heat sink. The power output and the required heat rejection rate form the turbine characteristics and are expressed in terms of the turbine backpressure or the corresponding vapour saturation temperature for a given steam flow rate passing through the turbine.

The ambient temperature determines the vapour saturation temperature and hence the backpressure. For a given steam flow rate driving the turbine and a given turbine output P_t, the condenser stabilises at a certain steam temperature so that the required heat rejection rate is achieved. Consequently extreme variations in the ambient temperature result in a wide fluctuation of the turbine backpressure. According to the turbine characteristics a rise in the system temperature caused by an increase in the ambient temperature reduces the turbine output. If the output is to be maintained under such

conditions more steam has to be generated by the boiler and more energy is required for the same output. Thus, higher system temperatures imply less efficient system performance.

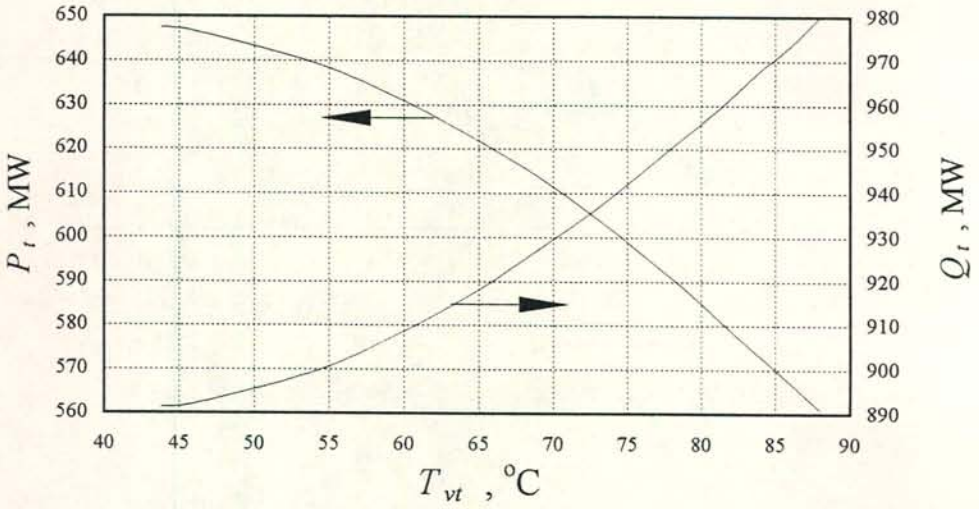

Figure 9.8: Turbine characteristics: Power output P_t and the required heat rejection rate Q_t versus the saturation temperature T_{vt} at the turbine exit.

9.6 System solution

When searching for the turbine-condenser operating point for a given ambient temperature and pressure the modelling equations presented in sections 9.1 to 9.3 are applied to solve for a air mass flow rate m_a and a vapour saturation temperature T_{vt} which satisfy the heat transfer equations and the draft equation simultaneously and in addition the heat rejection rate prescribed by figure 9.8, i.e.

$$n_{Fcondenser}\left(\sum_{i=1}^{n_{tr}} m_a c_{pam(i)}\left(T_{vm(i)}-T_{ai(i)}\right)e_{(i)}\right)_{condenser} + n_{Fdephlegmator}\left(\sum_{i=1}^{n_{tr}} m_a c_{pam(i)}\left(T_{vm(i)}-T_{ai(i)}\right)e_{(i)}\right)_{dephlegmator} = Q_t \qquad (9.49)$$

$n_{Fcondenser}$ and $n_{Fdephlegmator}$ are the number of operating condenser and dephlegmator fan units respectively. The turbine output corresponding to T_{vt} can be obtained from figure

9.8. The solution is valid for the steam flow corresponding to the characteristics employed.

For given steamside conditions the performance of a single fan unit can be evaluated by employing the equations in section 9.2.1 or 9.2.2 and the draft equation. The air flow rate m_a passing through the unit and the corresponding heat transfer Q_a are then solved for.

If m_a is known from measurements for example, section 9.2 alone can be applied to obtain the heat rejection rate by a unit.

9.7 Closing remarks

The backflow phenomenon in single-pass multi-row condensers and the subsequent vapour blanketing by nocondensable gases have been analysed in a number of publications [74RO1, 80BE1, 81SC1, 84SC1, 97FA1]. The emphasis of existing theories is on the quantification of the decrease in the system effectiveness due to the accumulation of noncondensables. Often simplifying assumptions are required when striving for closed analytical solutions. The pressure drop at the inlet of the tubes is ignored for example and the pressure gradient inside the tubes is assumed to be the product of some constant and the square of the vapour velocity.

While such theories provide much needed insight regarding the performance and row interaction, more detailed and comprehensive modelling is required for accurate prediction of the steamside flow distribution. The backflow analysis presented in section 9.2.2 is in principle not new, but the fundamental flow dynamics are not compromised by simplifying assumptions in order to achieve maximum accuracy.

CHAPTER 10

COMPARISON BETWEEN FIELD TEST RESULTS AND THEORY

10.1 Performance evaluation of a single condenser unit

The air outlet temperature and velocity distribution measured at a condenser unit are shown in tables H.1 to H.4. Measurements were conducted at all the eight bundles of the fan unit to determine the air flow rate m_a and heat transfer Q_a according to equation (8.1). The data of two adjacent bundles are presented by a set of three tables, i.e. (a) to (c). Tables (a) and (b) represent the grid on the bundle as illustrated in figure 8.2 and show the air outlet temperature and velocity measured at the centre of each area element respectively. A set of ten horizontal values (temperature and velocity) was measured simultaneously. The time period during which each set was recorded is given in table (c).

No steamside measurements were carried out. The saturation pressure at the turbine exit was obtained from the control room of the power station and is used as an input for the simulation model. The modelling equations of sections 9.2.1 and 9.3 are applied to predict the air flow rate and heat transfer.

10.1.1 Air inlet temperature for equation (8.1)

A weather mast at the power station monitors the ambient temperature at heights of 1.2, 2.5, 5, 10, 20, 40, 64 and 96 m. A typical 24 hour cycle encountered during the winter season, measured on the day when the condenser unit was tested, is shown in figure 10.1.

The ambient temperature at 40 m elevation is taken as the air inlet temperature $T_{ai(1)}$ required in equation (8.1) in order to be consistent with the model which incorporates the dry adiabatic lapse rate. The inlet temperature at 40 m corresponding to each set of outlet temperatures is given in tables H.1(c) to H.4(c).

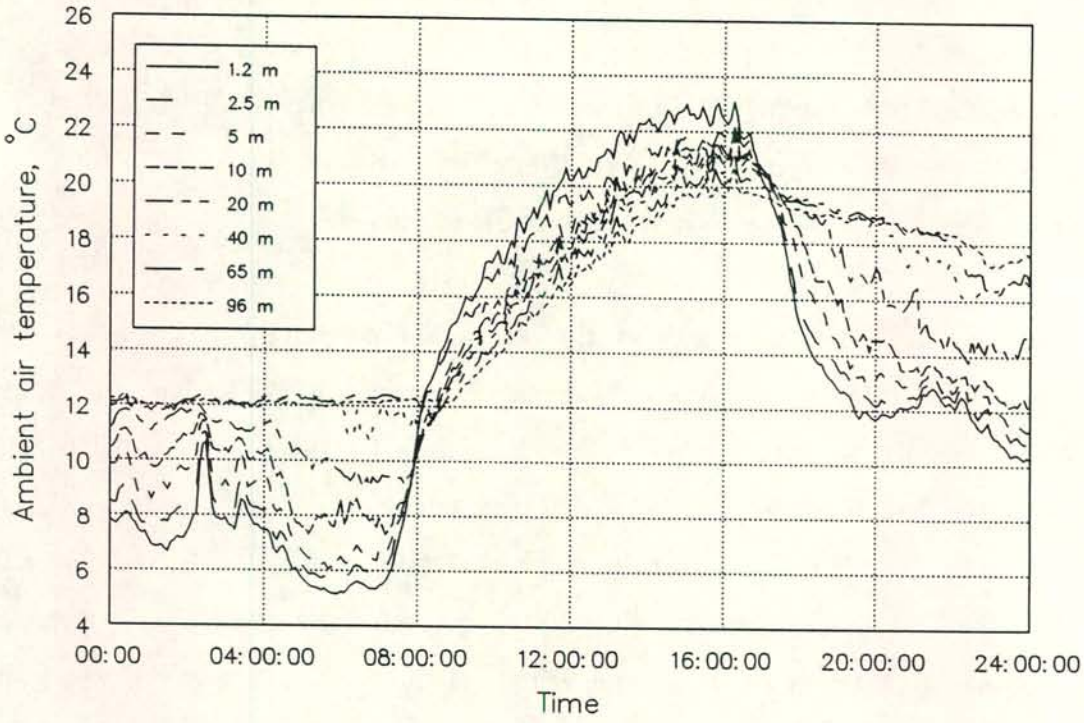

Figure 10.1: Ambient temperature at various elevations recorded by the weather mast.

10.1.2 Input data for simulation model

During day time when the ambient air is heated by the surface of the earth the temperature gradient in the lower layers is steeper than predicted by the dry adiabatic lapse rate. Thus, the temperature close to the surface, for example the temperature at 1.2 m, cannot be employed as the ground level temperature T_{al} (defined by the derivation in Appendix G) together with the dry adiabatic lapse rate. It would underpredict the actual performance because the estimated temperature at the inlet of finned tube bundles T_{as} would be too high.

Measurements of the air temperature at the inlet of a number of fans showed that air mainly from layers above ≈10 m is sucked into the cooling system [95ZA1]. The high temperature lower layer is not representative of the conditions at the cooling tower inlet. The ground level temperature T_{al} in the draft equation should therefore be taken as the temperature at 10 m elevation. Above 10 m the dry adiabatic lapse rate prevails. This choice for T_{al} is therefore consistent with the model. The ambient temperature at 10 m

elevation corresponding to the periods of testing are shown in tables H.1(c) to 10.4(c). The average of the tabulated values for the 10 m elevation is taken as T_{al}.

From the beginning to the end of the condenser test the turbine exhaust pressure and turbine output varied from 19090 to 19630 N/m^2 and 651.2 to 653.1 MW respectively, without any significant fluctuations in between. The condenser operating conditions during the period of testing can therefore be regarded as steady.

The averaged data for the input of the analysis is:

Ambient pressure	p_{al} =	91330 N/m^2
Tower inlet temperature	T_{al} =	20.02 °C
Saturation pressure at turbine exit	p_{vt} =	19360 N/m^2

10.1.3 Airside flow prediction according to theory

An air mass flow rate of m_a = 694.5 kg/s satisfies the draft and heat transfer equations simultaneously. The corresponding air temperatures at each row are:

Row (1)

Air inlet temperature	$T_{ai(1)}$ =	19.56 °C
Air outlet temperature	$T_{ao(1)}$ =	35.52 °C
Mean air temperature	$T_{am(1)}$ =	27.54 °C

Row (2)

Air inlet temperature	$T_{ai(2)}$ =	35.52 °C
Air outlet temperature	$T_{ao(2)}$ =	49.11 °C
Mean air temperature	$T_{am(2)}$ =	42.32 °C

The fan performance detail is:

Volume flow rate through fan	V_F =	640.6 m^3/s

Fan shaft power	P_F	=	227.4 kW
Density of air at fan	ρ_{a3}	=	1.084 kg/m^3
Fan static pressure	Δp_{Fs}	=	228.5 N/m^2

Losses experienced by the air flow:

Tower support loss	Δp_{ts}	=	7.3682 N/m^2	eq. (G.80)
Losses due to upstream obstacles	Δp_{up}	=	16.3273 N/m^2	eq. (G.81a)
Losses due to downstream obstacles	Δp_{do}	=	19.6819 N/m^2	eq. (G.81b)
Heat exchanger oblique flow loss	Δp_{θ}	=	19.9136 N/m^2	eq. (G.82)
Heat exchanger normal loss	Δp_{he}	=	111.3096 N/m^2	eq. (G.82)
Turning and jetting loss	Δp_{dj}	=	13.0105 N/m^2	eq. (G.90)
Outlet kinetic energy loss	Δp_o	=	44.7875 N/m^2	eq. (G.91)

The pressure rise across the fan and the individual losses can be divided by the dynamic pressure at the heat exchanger inlet $(m_a/A_{fr})/(2\rho_{a56})$ for direct comparison in a dimensionless form:

Fan static pressure	46.791	98.28 %
Buoyancy potential (left-hand side of eq. (G.72))	0.821	1.72 %
Sum	**47.612**	**100.00 %**

Tower support loss	1.508	3.17 %
Upstream losses	3.342	7.02 %
Downstream losses	4.029	8.46 %
Heat exchanger oblique flow loss	4.076	8.56 %
Heat exchanger normal loss	22.811	47.91 %
Turning and jetting loss	2.667	5.60 %
Outlet kinetic energy loss	9.180	19.28 %
Sum	**47.612**	**100.00 %**

Note that the normal pressure drop across the heat exchanger bundles contributes only 47% to the total loss. Second highest is the kinetic energy dissipated above the A-frame. The secondary losses make up a significant 30% of the total.

10.1.4 Heat transfer and steamside flow prediction according to theory

The predicted heat transfer is 20.67 MW and steam is condensed at a rate of 8.750 kg/s. The steamside conditions and flow rates are:

Saturation pressure at turbine exit (input value)	p_{vt}	=	19630.0 N/m^2
Saturation temperature at turbine exit	T_{vt}	=	59.57 °C
Steam ducting pressure drop	Δp_{vd}	=	167.9 N/m^2
Supply header pressure	p_{vl}	=	19192.1 N/m^2
Supply header temperature	T_{vl}	=	59.38 °C
Row (1)			
Heat transfer	$Q_{a(1)}$	=	11.164 MW
Condensation heat transfer coefficient	$h_{c(1)}$	=	15597.0 W/m^2 K
Condensation rate	$m_{c(1)}$	=	4.725 kg/s
Mean vapour pressure	$p_{vm(1)}$	=	18258.6 N/m^2
Mean vapour temperature	$T_{vm(1)}$	=	58.31 °C
Inlet vapour mass flow rate	$m_{v2(1)}$	=	4.989 kg/s
Outlet vapour mass flow rate	$m_{v3(1)}$	=	0.264 kg/s
Inlet vapour velocity	$v_{sv2(1)}$	=	68.00 m/s
Outlet vapour velocity	$v_{sv3(1)}$	=	3.59 m/s
Inlet vapour Reynolds number	$Re_{sv2(1)}$	=	19392
Outlet vapour Reynolds number	$R_{esv3(1)}$	=	1024
Suction Reynolds number	$Re_{vn(1)}$	=	12.6
Inlet contraction pressure drop	$\Delta p_{12(1)}$	=	383.14 N/m^2
Frictional pressure drop	$\Delta p_{f(1)}$	=	1287.12 N/m^2
Gravitational pressure drop	$\Delta p_{g(1)}$	=	-9.91 N/m^2
Momentum pressure drop	$\Delta p_{m(1)}$	=	-557.76 N/m^2

Exit pressure drop	$\Delta p_{34(1)}$	=	-0.25 N/m^2
Total pressure drop	$\Delta p_{14(1)}$	=	1102.3 N/m^2

Row (2)

Heat transfer	$Q_{a(2)}$	=	9.510 MW
Condensation heat transfer coefficient	$h_{c(2)}$	=	16520.3 W/m^2 K
Condensation rate	$m_{c(2)}$	=	4.025 kg/s
Mean vapour pressure	$p_{vm(2)}$	=	18298.9 N/m^2
Mean vapour temperature	$T_{vm(2)}$	=	58.36°C
Inlet vapour mass flow rate	$m_{v2(2)}$	=	4.720 kg/s
Outlet vapour mass flow rate	$m_{v3(2)}$	=	0.694 kg/s
Inlet vapour velocity	$v_{sv2(2)}$	=	63.23 m/s
Outlet vapour velocity	$v_{sv3(2)}$	=	9.33 m/s
Inlet vapour Reynolds number	$Re_{sv2(2)}$	=	18036
Outlet vapour Reynolds number	$Re_{sv3(2)}$	=	2660
Suction Reynolds number	$Re_{vn(2)}$	=	10.5
Inlet contraction pressure drop	$\Delta p_{12(2)}$	=	331.4 N/m^2
Frictional pressure drop	$\Delta p_{f(2)}$	=	1255.8 N/m^2
Gravitational pressure drop	$\Delta p_{g(2)}$	=	-473.3N/m^2
Momentum pressure drop	$\Delta p_{m(2)}$	=	-9.91 N/m^2
Exit pressure drop	$\Delta p_{34(2)}$	=	-1.68 N/m^2
Total pressure drop	$\Delta p_{14(2)}$	=	1102.3 N/m^2

The results presented above are based on a vapour outflow $m_{dephlegmator}$ = 4.8 kg/s corresponding to a heat rejection rate of ≈11.0 MW typically achieved by the dephlegmator (see section 10.2 please).

10.1.5 Comparison of the predicted and measured performance

The predicted and measured performance results are compared in table 10.1. Good agreement is obtained. The predicted and measured air mass flow rate differ by 0.7 % while a deviation of 1.8 % is found in the case of the total heat transfer. The measured

heat transfer is slightly overpredicted by the model, a reason being the predicted air mass flow rate which is too high.

High cross-flow velocities encountered below arrays of fan units and the presence of the ground level cause flow distortions at the fan inlets [95SA1, 96DU1]. The negative effect by the distortions is not incorporated in the fan characteristics for individual fans which are generally obtained under ideal conditions. It can therefore be expected that the model will tend to overpredict the performance of individual units. Considering, however, the complexity of the airside flow and the fact that the draft equation is based on scale model tests, the agreement is very satisfactorily.

Table 10.1: Predicted and measured condenser performance.

	Field tests	Theory	% dif.
Air outlet velocity $v_{ao(2)}$, m/s	3.19	3.22	1.1
Air outlet temperature $T_{ao(2)}$, °C	48.79	49.11	0.7
Bundle 1 and 2 air flow rate, kg/s	178.7	173.6	-2.9
Bundle 3 and 4 air flow rate, kg/s	171.7	173.6	1.1
Bundle 5 and 6 air flow rate, kg/s	172.7	173.6	0.6
Bundle 7 and 8 air flow rate, kg/s	166.9	173.6	4.0
Total air flow rate m_a , kg/s	689.9	694.5	0.7
Bundle 1 and 2 heat transfer, W	5200103	5168694	-0.6
Bundle 3 and 4 heat transfer, W	5187042	5168694	-0.4
Bundle 5 and 6 heat transfer, W	4949436	5168694	4.4
Bundle 7 and 8 heat transfer, W	4967758	5168694	4.0
Total heat transfer Q_a, MW	20.30	20.67	1.8

The measured air flow rate and heat transfer per bundle are practically equal. The heat rejected by bundles 5 to 8 is slightly less than by bundles 1 to 4. Bundles 1 to 4 form one side of the A-frame configuration while bundles 5 to 8 are on the opposite side. The air flow distribution may not be symmetrical, perhaps causing the observed deviation. On the other hand, the measurements at bundles 5 to 8 were recorded almost and hour after completion of the tests at bundles 1 to 4. Changes in the ambient conditions such as the

wind speed, wind direction and the temperature or in turbine performance during the interval may have caused the deviation.

For the purpose of the full scale investigation the air mass flow rate and heat transfer per bundle can be regarded as equal and subsequently further tests were conducted only on one side of the A-frames, either on all four bundles or only on two adjacent bundles.

10.2 Performance evaluation of a single dephlegmator unit

In an attempt to establish under what conditions cold zones are formed and the corresponding heat transfer rate achieved, a series of performance tests were conducted for various air flow rates. The condensation rate is proportional to the air flow rate if there are no cold zones. Thus, by varying the air flow rate a wide range of vapour velocities entering the bottom of the finned tubes can be obtained. Air flow rates from well below the design rate up to the maximum were tested. This was accomplished by adjusting the fan blades to predetermined angles. Five fan blade angles were tested, namely α = -2°, 2°, 10°, 13° and 16°.

For each blade angle setting the air outlet velocity and temperature distribution as well as the air inlet temperature to the bundles were measured. While the bundles were traversed by the instrumentation beam the steamside temperatures and pressures (bottom and top header), the ejector duct temperature and the pressure drop across the D-type headers were recorded. Seven complete sets of data are presented in this chapter, i.e.

1) Case 1: α = -2°
2) Case 2(a): α = 2°
3) Case 2(b): α = 2° (repeat of case 2a)
4) Case 3: α = 10°
5) Case 4(a): α = 13°
6) Case 4(b): α = 13° (repeat of case 4a)
7) Case 5: α = 16°

The dephlegmator is designed to operate at fan blade angles close to 16°.

The theory on the steamside flow and heat transfer given in section 9.2.2 is applied to predict the condensation rate and the corresponding pressure drop across the headers. Here the emphasis is on the steamside flow. The draft equation analysis is not considered because no fan characteristics could be obtained for the smaller fan blade angles.

The measured air mass flow rate and air temperature recorded inside the plenum are employed as input values to predict the condensation rate, instead of applying the draft equation and making use of the weather mast data as in the case of the condenser unit. The good agreement between theory and experiment in section 10.1 proves that the data acquisition system yields reliable air flow rates required for the steamside analysis.

During some of the dephlegmator tests infra-red pictures were taken of the bundles. The pictures are presented in the next section to illustrate the distribution of cold zones on the dephlegmator. Normal photos taken from the same angles are also shown to assist the reader in the interpretation of the infra-red frames.

10.2.1 Infra-red images of the dephlegmator bundles

Detail such as the air flow rate and the turbine exhaust conditions corresponding to the infra-red images is given in table 10.2.

A photo of the outside finned tube row of on one side of the A-frame is shown in figure 10.2(a). The top half of two adjacent bundles appear on the photo. The small duct just above the top header of the dephlegmator leads to the ejector after having joined the duct from the bundles on the other side of the A-frame. Above the bundles corrugated steel sheeting covers the remaining part of the A-frame up to the condenser supply header. Part of a condenser bundle can be seen to the right of the dephlegmator. Infra-red images of the outside row, i.e. row (2), are shown in figures 10.2(b) and (c).

Figure 10.2(b) was taken at a relatively low air flow rate. The temperature distribution of the finned tubes is uniform as expected for isothermal conditions during condensation of

saturated steam in the absence of inert gases. The blue zone above the dephlegmator bundles is the corrugated sheeting. In figure 10.2(c) the air flow rate is representative of the design rate. A typical cold zone is present in the dephlegmator. Almost the entire top third of the tubes is close to the ambient temperature. At the bottom of the cold zone a distinctive tooth pattern can be seen. It appears that the tubes directly above the drain stubs are more susceptible to cold zone formation than the tubes in between. A photo of the drain stubs connecting the D-type header to the bottom header pipe is shown in figure 10.2(d). The photo was taken from inside the plenum. Each bundle contains six drain stubs.

A similar set of images of the inside row is shown in figures 10.3(a) to (c). The I-beam construction forming the A-frame can be seen in figure 10.3(a). The top half of one bundle is depicted in the centre of the photo.

The infra-red image of the inside row, corresponding to that of the outside in figure 10.2(b), is given in figure 10.3(b). The temperature distribution is uniform. Because row (1) is exposed to inlet air at ambient temperature, the fin temperature distribution is lower in figure 10.3(b) than in figure 10.2(b) where row (2) is shown. In figure 10.3(c) cold zones appear in row (1). Note that there are a few tubes which are hot along the entire length of the bundle.

Throughout the investigation it was observed that the temperature of the ejector duct is usually well above the ambient temperature notwithstanding the presence of cold zones. This is illustrated in figures 10.4(a) and (b). In figure 10.4(a) the ejector ducts enter the plenum through the corrugated iron from either side of the A-frame and are joined by a T-piece. An infra-red image taken from a similar angle is shown in figure 10.4(b). Although there are cold zones on the bundles, the ejector duct is at a relatively high temperature. Figure 10.4(c) shows a closer image of an ejector duct taken during conditions of uniform bundle temperature such as in figure 10.2(b). Here the temperature of the duct is close to the steam saturation temperature.

A closer look at the inside row revealed that small cold spots are formed at low air flow rates in the absence of the intensive cold zones typically observed at higher air flow rates.

Such cold spots are shown in figure 10.5(a). The figure covers a region of approximately 1 m along the tubes directly below the top header. While the big cold zones shown in previous figures were steady in nature, the small spots disappeared, only to be formed again in a few seconds. An image taken 30 seconds later than 10.5(a) is shown in figure 10.5(b). Some spots have disappeared.

Table 10.1: Infra-red image detail.

Figure	m_a, kg/s	$T_{ai(1)}$, °C	T_{vl}, °C
10.2(b)	250.0	20.5	57.0
10.2(c)	590.7	14.7	49.3
10.3(b)	250.0	20.5	57.0
10.3(c)	520.0	20.0	62.0
10.4(b)	354.2	19.2	55.2
10.4(c)	250.0	20.5	57.0
10.5(a)	163.4	23.4	67.0
10.5(b)	163.4	23.4	67.0

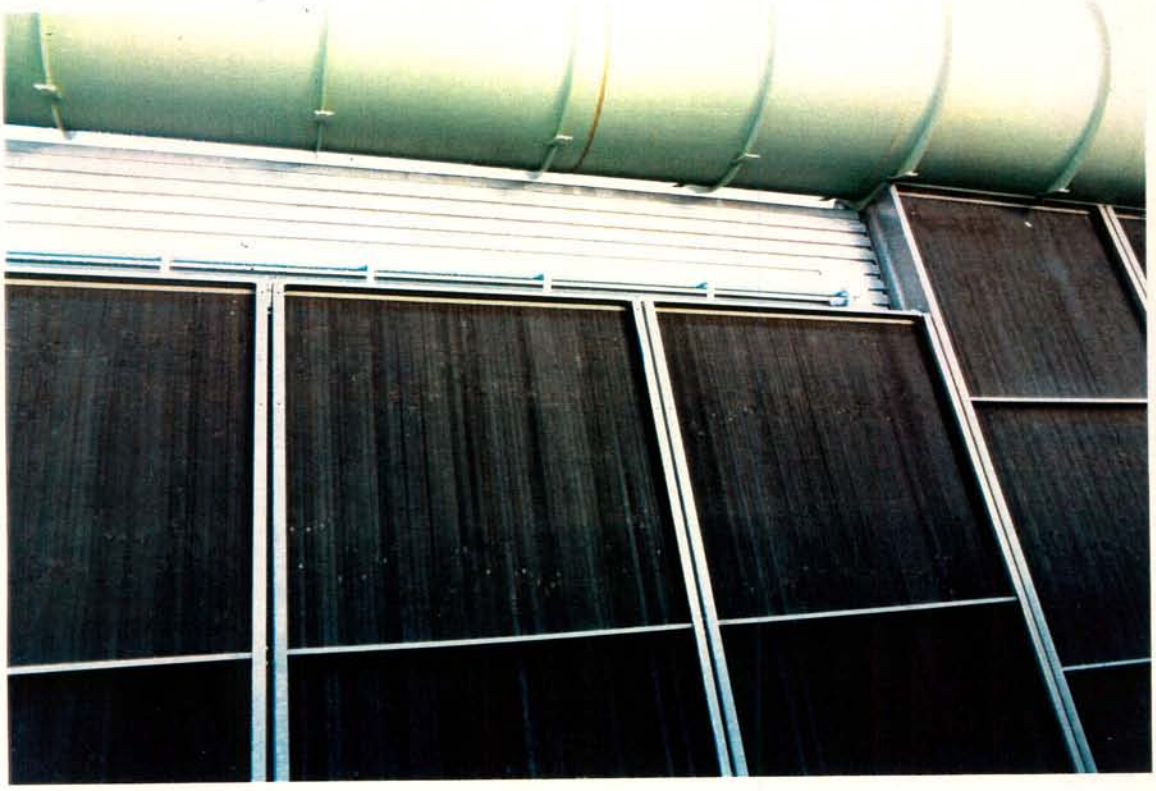

Figure 10.2(a): Photo of the dephlegmator taken from the outside of the A-frame.

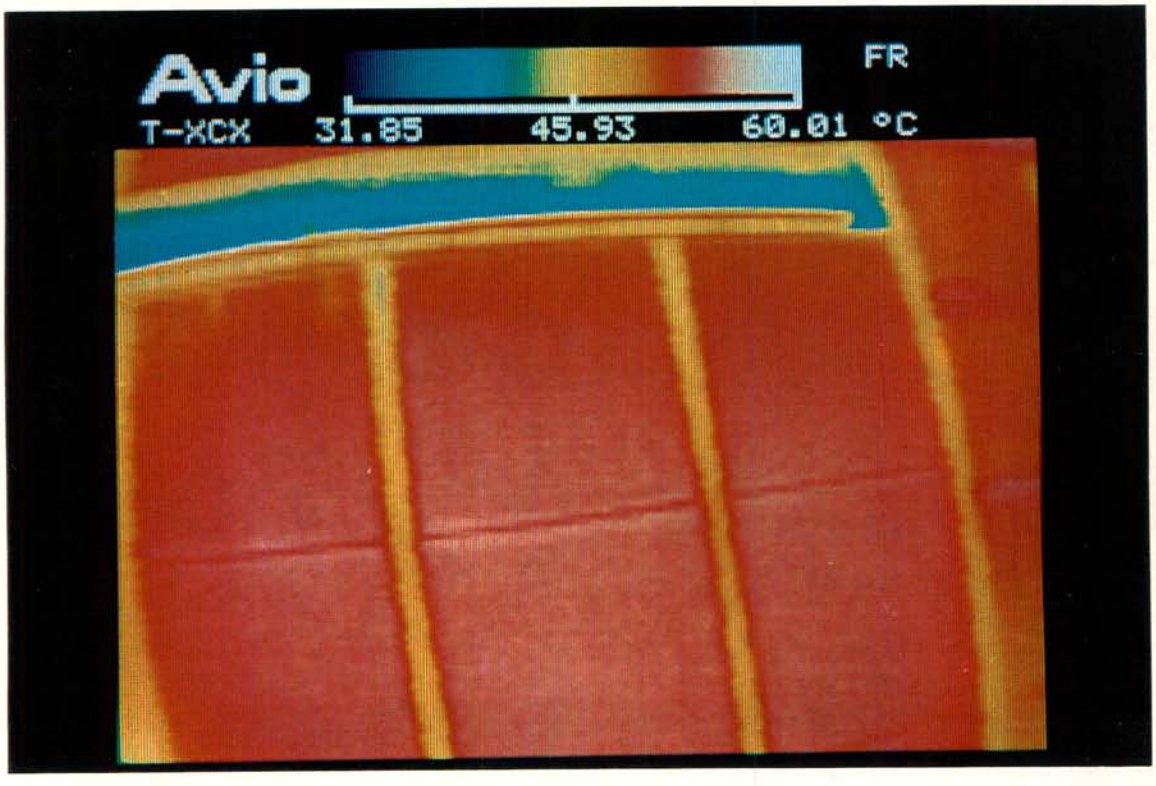

Figure 10.2(b): Infra-red image of the outside row taken at relatively low air flow rate.

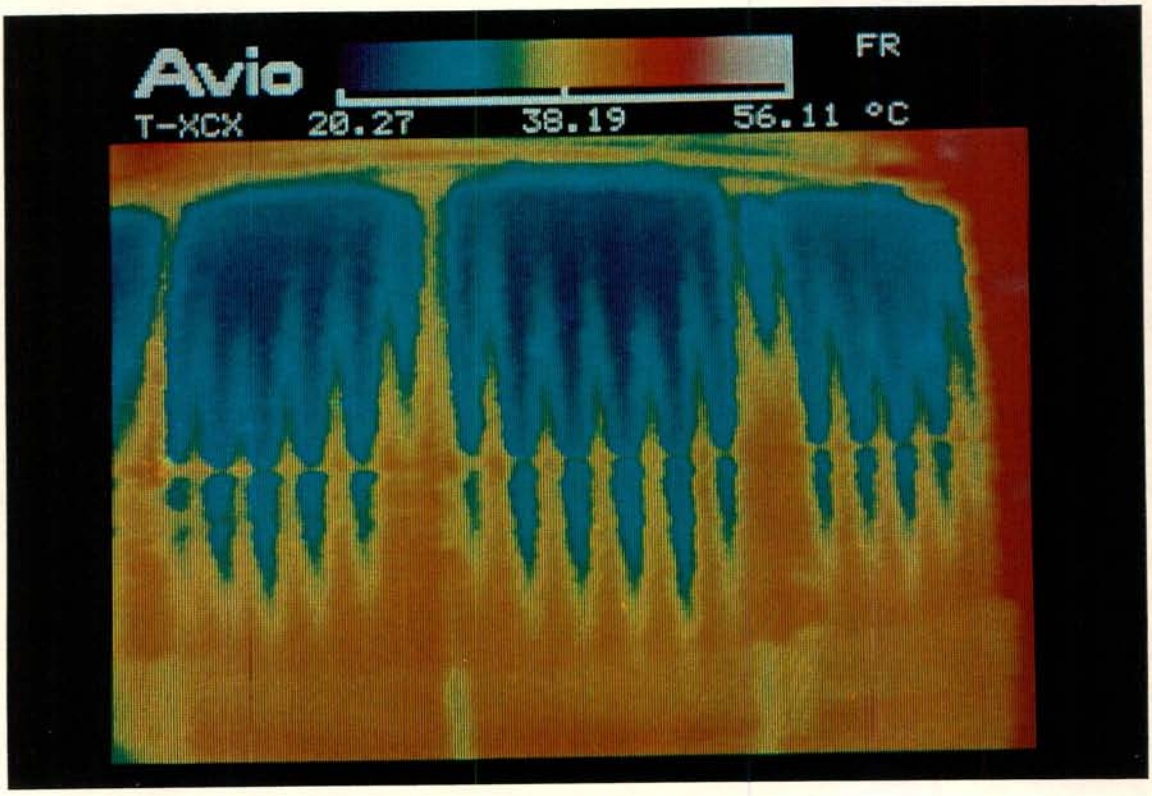

Figure 10.2(c): Infra-red image of the outside row taken at the design air flow rate.

Figure 10.2(d): Photo of drain stubs and bottom header pipe. There are six stubs per bundle.

Figure 10.3(a): Photo of dephlegmator bundles taken from inside the A-frame.

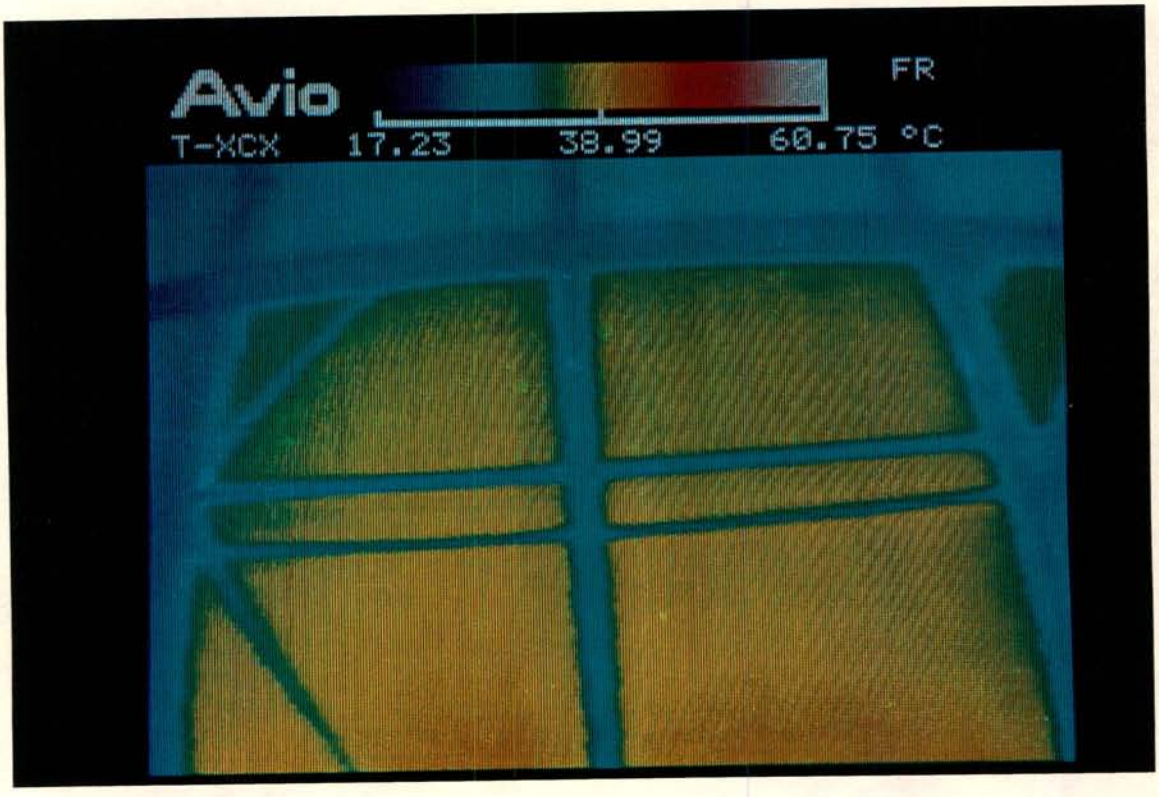

Figure 10.3(b): Infra-red image of the inside row taken at relatively low air flow rate.

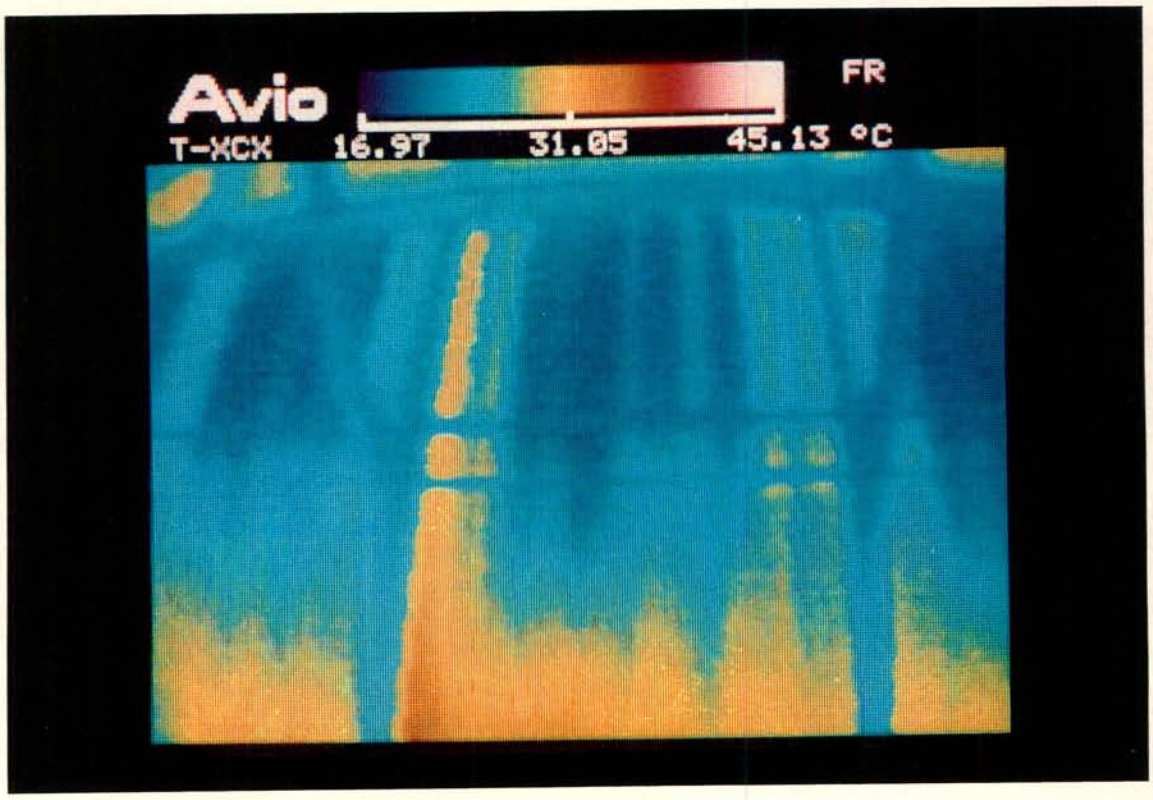

Figure 10.3(c): Infra-red image of the inside row taken at the design air flow rate.

Figure 10.4(a): Photo of the ejector ducts inside the A-frame.

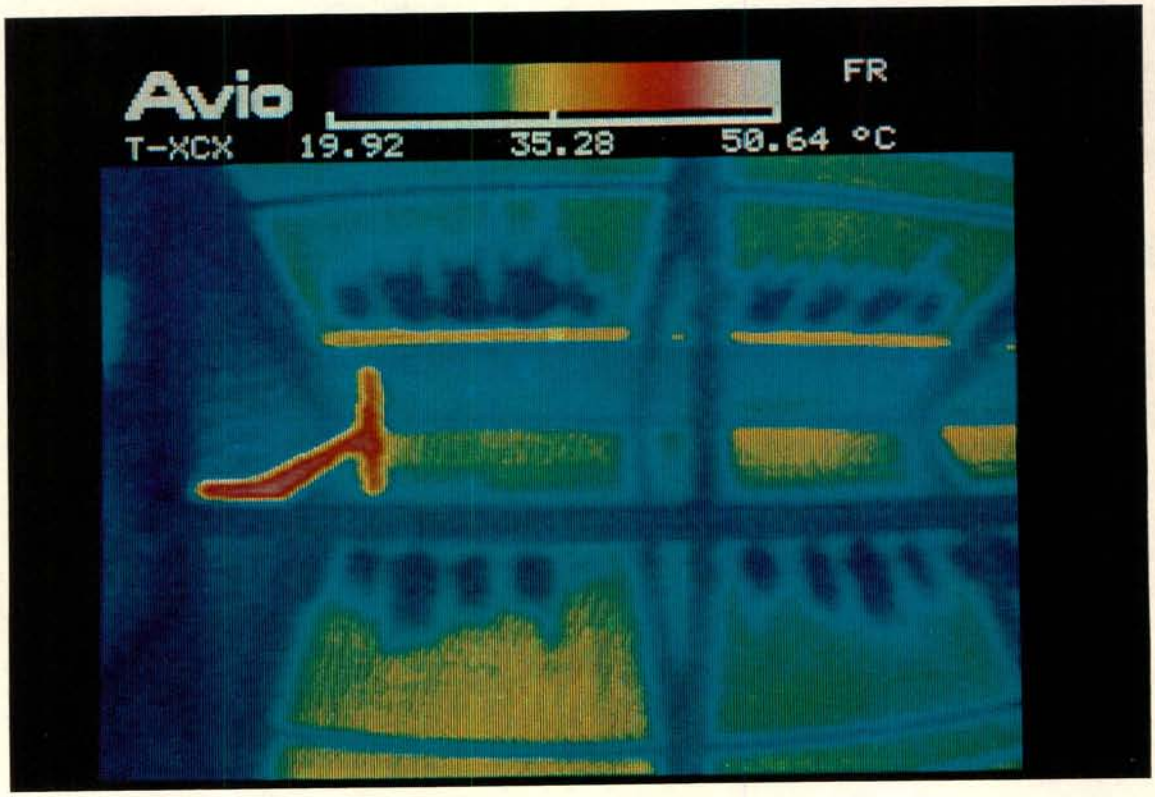

Figure 10.4(b): Infra-red image of the ejector ducts.

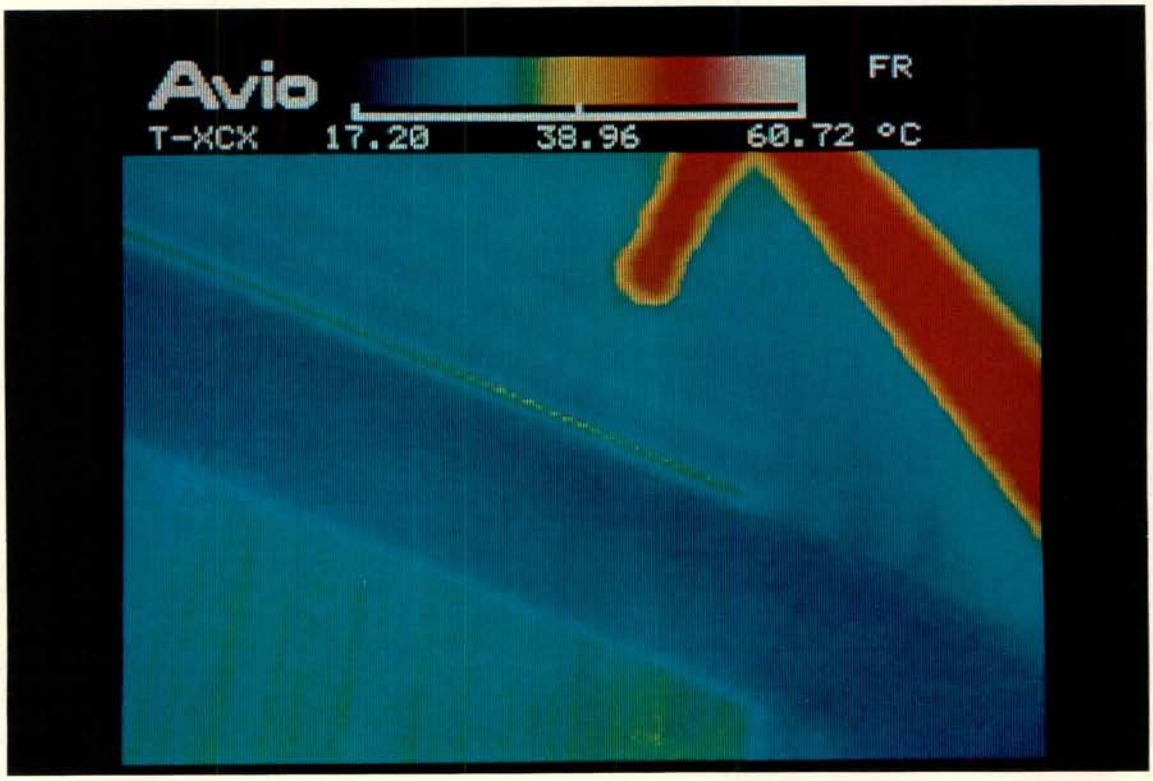

Figure 10.4(c): Zoomed infra-red image of the ejector ducts.

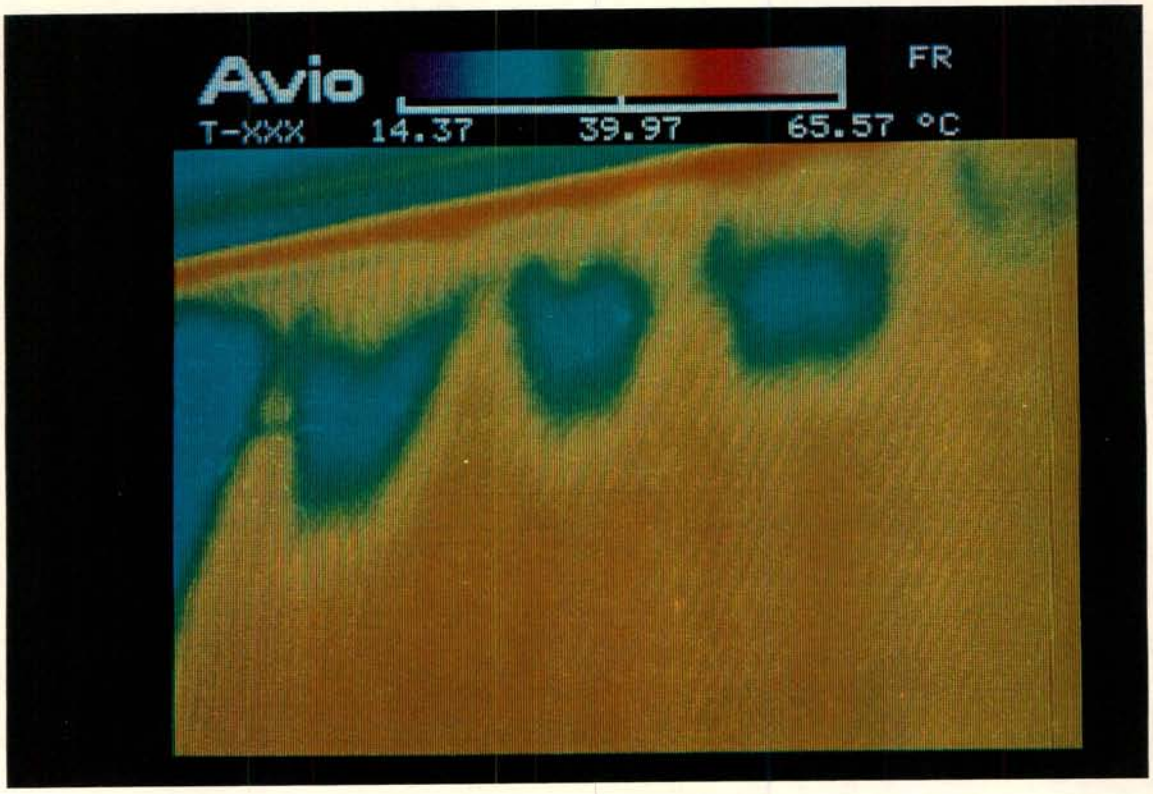

Figure 10.5(a): Infra-red image of small cold spots formed at relatively low air flow rates.

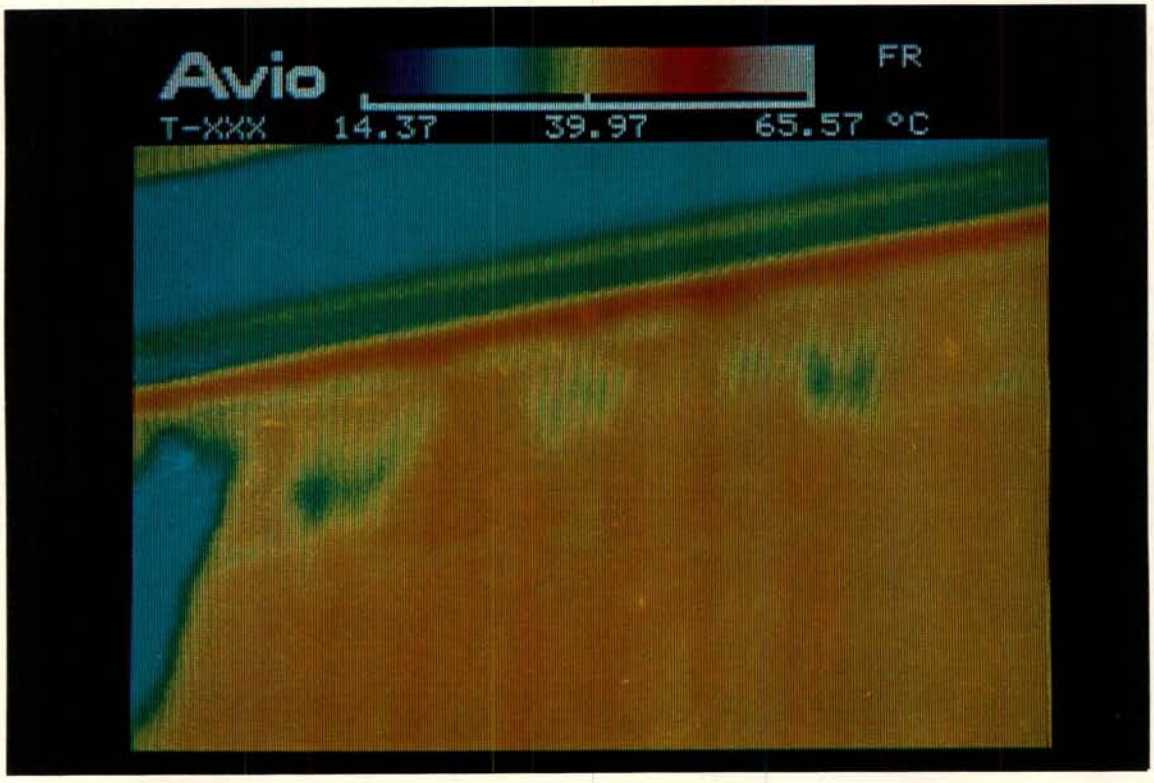

Figure 10.5(b): The cold spots in figure 10.5(a) disappearing after 30 seconds.

10.2.2 Comparison of the predicted and measured dephlegmator performance

The dephlegmator tests were conducted only on one side of the A-frame on two or four bundles. The air flow passing through and the heat rejected by two (or four bundles) is multiplied by 4 (or 2) to evaluate the performance of the entire unit.

The air outlet temperature and velocity data are presented in Appendix H in the same way as for the condenser unit, where tables (a) and (b) represent the grid across two adjacent bundles. The third table of each traverse (table c), contains the time at which each row of air outlet temperatures and velocities were recorded together with the steamside data and the air temperature inside the plenum measured at that time. The average values of the steamside data and air inlet temperatures recorded while traversing the bundles are given in table 10.3. These averages of T_{vl} and $T_{ai(1)}$ together with the measured air flow rate form the input for the performance prediction by the model in section 9.2.2.

A comparison between the theoretical and experimental performance is summarised in table 10.4. The actual superficial vapour velocity v_{sv2} entering at the bottom of the finned tubes can be approximated by

$$v_{sv2\,(measured)} = \frac{Q_{a\,(measured)}}{i_{lg(1)}\,\rho_{v(1)}\left(n_{tb(1)} + n_{tb(2)}\right) n_b\, A_{tc}} \tag{10.1}$$

and is shown in table 10.5 together with predicted superficial velocities and the flooding velocity according to equation (5.4). The superficial liquid velocity required in equation (5.4) to predict flooding, can be expressed in terms of the condensate flow rate

$$v_{sc2(i)} = \frac{m_{c(i)}}{\rho_{c(i)} n_{tb(i)} n_b A_{tc}} = \frac{Q_{a(i)}}{i_{lg(i)} \rho_{c(i)} n_{tb(i)} n_b A_{tc}} \tag{10.2}$$

Substitute equation (10.2) into equation (5.4) to solve for the flooding superficial velocity of row (i)

$$v_{sv(i)flooding} = K_o \left(\frac{gH_t\left(\rho_{c(i)} - \rho_{v(i)}\right)}{\rho_{v(i)}} \right)^{1/2}$$

$$x \left[-n \left\{ \frac{1}{gD_e\rho_{c(i)}\left(\rho_{c(i)} - \rho_{v(i)}\right)} \left(\frac{Q_{a(i)}}{i_{lg(i)} n_{tb(i)} n_b A_{tc}} \right)^2 \right\}^{0.6} \Big/ Zk_D^{\,0.2} \right] \qquad (10.3)$$

Detailed data of the performance analysis for each case study are given in tables 10.6(a) to (c) at the end of section 10.2.

Table 10.3: Averages of the measured steamside temperatures, pressures and air inlet temperature.

	Case 1	Case 2(a)	Case 2(b)	Case 3	Case 4(a)	Case 4(b)	Case 5
p_{v1}, N/m^2	17063	18213	15008	14800	16737	27206	14946
p_{v4}, N/m^2	16318	17273	9203	10839	13251	27153	10688
Δp_{v14}, N/m^2	558	710	6289	3912	4174	588	4399
T_{v1}, °C	55.11	55.29	48.62	48.94	56.62	66.55	49.30
T_{v4}, °C	54.99	56.44	40.85	34.95	25.75	65.79	26.97
$T_{ejector}$, °C	55.03	56.47	40.90	41.98	32.77	65.87	40.79
$T_{ai(1)}$, °C	19.25	19.07	11.52	15.32	19.55	27.11	14.72

Table 10.4: Predicted and measured dephlegmator heat transfer and pressure drop.

Case	α, °	Air flow m_a, kg/s	Heat transfer Q_a, MW			Pressure drop Δp_{14}, N/m^2		
		Measured	Predicted	Measured	% differ.	Predicted	Measured	% differ.
1	-2	264.4	8.61	7.95	7.6	208	558	-168.5
2(a)	2	341.5	10.71	10.61	0.9	304	710	-133.2
2(b)	2	358.6	11.24	9.23	17.9	458	6289	-1271.6
3	10	514.8	13.29	10.40	21.8	634	3912	-517.2
4(a)	13	543.0	15.48	10.73	30.7	586	4174	-611.8
4(b)	13	506.1	15.92	15.51	2.6	397	588	-48.2
5	16	590.7	14.97	10.92	27.0	806	4399	-445.8

Table 10.5: Summary of the predicted and measured vapour velocities and Froude numbers.

	Case 1	Case 2(a)	Case 2(b)	Case 3	Case 4(a)	Case 4(b)	Case 5
$v_{sv2(1)}$, m/s (predicted)	31.8	38.2	54.6	62.5	50.7	34.1	69.4
$v_{sv2(2)}$, m/s (predicted)	25.5	32.7	47.8	58.2	47.4	31.3	66.0
v_{sv2}, m/s (measured)	26.1	34.6	40.6	45.1	33.0	31.5	46.6
$v_{sv2(1)}$, m/s (flooding)	66.9	66.7	78.6	78.4	65.0	51.9	78.2
$v_{sv2(2)}$, m/s (flooding)	66.9	66.7	78.5	78.3	65.0	52.0	78.1
$Fr_{sv2(1)}$, m/s (predicted)	0.112	0.162	0.238	0.313	0.298	0.212	0.388
$Fr_{sv2(2)}$, m/s (predicted)	0.072	0.119	0.183	0.272	0.262	0.179	0.352
Fr_{sv2}, m/s (measured)	0.076	0.135	0.136	0.151	0.130	0.183	0.185
$Fr_{sv2(1)}$, m/s (flooding)	0.494	0.493	0.493	0.492	0.491	0.491	0.492
$Fr_{sv2(2)}$, m/s (flooding)	0.496	0.495	0.495	0.494	0.491	0.491	0.492

10.2.3 Discussion of the dephlegmator performance

Important aspects regarding the performance are:

1) Cold zones were observed on the dephlegmator in cases 3, 4(a) and 5 while the temperature distribution of the finned tubes and the outlet air was uniform in cases 1, 2(a), 2(b) and 4(b). A graphic representation of the air outlet temperature measured in cases 4(a) and (b) is given in figure 10.5 to illustrate the outlet temperature distribution under the influence of cold zones.
2) When there are cold zones the pressure drop across the headers is an order of magnitude above the prediction.
3) Good agreement is achieved between theory and experiment in the case of the heat rejection rate and vapour inlet velocities if the temperatures are uniform. In the presence of cold zones the measured heat transfer is well below the prediction.
4) The predicted and measured pressure drop is of the same order of magnitude under uniform temperature conditions. Except for case 2(b), where no cold zones were observed but the pressure drop was $\approx$6000 N/m^2 while the model predicts 458 N/m^2.
5) Although the measured and predicted pressure drop in cases 1, 2(a) and 4(b) are of the same order, the measured values are approximately double the theoretical value. There is a consistent trend that the theory underpredicts the actual pressure drop.

6) For all the test cases the actual vapour velocity at the bottom of the finned tubes is well below the flooding superficial velocity. The same is true for the predicted superficial velocities, except in case 5 where the predicted vapour velocity and the flooding velocity are fairly close, especially when considering that the scatter of the flooding correlation is ±10%.
7) In cases 1, 2(a), 2(b) and 4(b) all the measured steamside temperatures, including the ejector duct temperature, are practically equal to the saturation temperatures corresponding to the measured pressures.
8) In the presence of cold zones the temperature of the top header is well below the steam saturation temperature at the bottom header. Furthermore, it does not correspond to saturation temperature of the measured pressure. The ejector duct temperature is higher than the top header temperature, but it too differs significantly from the bottom header temperature.
9) At fan blade angles below 0° cold zones were never found to occur on the dephlegmator. The onset of the high pressure drop appears to occur at $\alpha \approx 2°$, illustrated by cases 2(a) and (b) where both steamside flow modes were encountered. The fact that the dephlegmator can function satisfactorily close to the design point, as found in case 4(b), was discovered by coincidence in the process when the turbine load was increased from part load to full load. As a rule cold zones were always present during steady-state full-load turbine operation. Then the heat transfer rate measured varied between 9 and 11 MW whereas approximately 16 to 17.5 MW should ideally have been rejected.

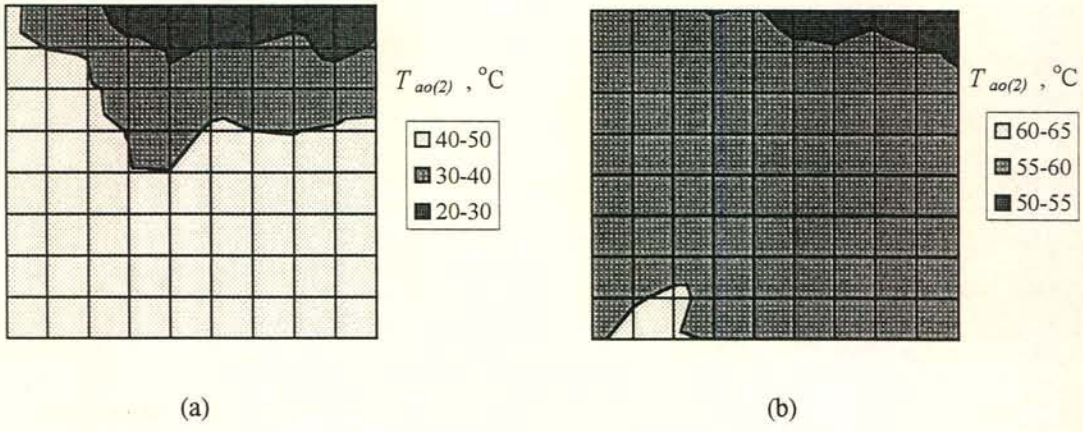

(a) (b)

Figure 10.5: Air outlet temperature distribution. (a): Case 4(a) where cold zones were present in the dephlegmator. (b): Uniform finned tube and air outlet temperature distribution as found in case 4(b).

10.2.3 Conclusions on the dephlegmator performance

In a concurrent study Schoenfeld [97SC1] investigated condensation of steam at sub-atmospheric pressures in a single-duct inclined at 60° to the horizontal. Exactly the same type of finned tube employed in the dephlegmator was tested in a reflux mode. The pressure drop and flooding characteristics observed by Schoenfeld [97SC1] are described in Appendix I where the analysis presented in section 9.2.2 is applied to predict the performance of the single-duct. The pressure drop model in chapter 9, based on the theory by Groenewald and Kröger [95KR1] and the present adiabatic counterflow investigation, shows excellent agreement with the reflux condensation results by Schoenfeld [97SC1]. Furthermore, the flooding correlation in equation (5.4) accurately predicts the performance limit of the elliptical duct during reflux condensation. See Appendix I for more detail on the performance of the elliptical duct.

While the present analysis successfully models reflux condensation in a single-duct, it fails in the case of a multi-duct configuration such as the dephlegmator. It can be concluded that flooding as found during countercurrent flow in a single-duct is not the cause of the ineffective dephlegmator performance encountered at the power plant.

It is postulated that counterflow limitation inside the drain stubs and the D-type header leads to excessive entrainment at the sharp-edged vapour inlet. The subsequent accumulation of condensate inside the ducts results in the high pressure drop measured. Most of the ducts are then partially blocked causing a maldistribution of the steamside flow. It renders the removal of noncondensable gases ineffective and air gets trapped inside the dephlegmator. This can in particular be seen in figure 10.3(c) where a few of the finned tubes are warm along the entire length. Steam passes upwards through these ducts at excessively high rates. Part of the steam continuously feeds the ejector while the remainder enters other finned tubes from the top where it is condensed. In the process air accumulates in the dephlegmator. Of course the system eventually stabilises at conditions where air reaches the ejector duct and is removed at the leak rate, otherwise the entire cooling system would tend to fill with air, which is obviously not the case.

During flooding in sharp-edged single-ducts liquid accumulates and the pressure drop rises sharply. The high pressure drop encountered across the dephlegmator header may hence lead one to believe that flooding and the subsequent accumulation of condensate imposes performance limitations well below the intended operating point. Consider case 5 for example. The actual inlet vapour Froude number is 0.185 and the measured pressure drop is 4399 N/m^2. According to figure 4.7(e) in part A such high pressure drops can only be expected at Fr_{Hsg} = 0.411 when the characteristic vortex-type flow is formed. A further look at the flow modes depicted in figure 4.7 reveals that at Froude numbers close to 0.185 the condensate should drain freely and the corresponding pressure drop should be relatively small. This in particular is illustrated by figures 4.7(a) and 4.7(b) where the gas Froude number is 0.123 and 0.193 respectively. These figures show no significant gas-liquid interaction and the corresponding pressure drop (figure 4.6a) is equal to the single-phase prediction while the entrance pressure drop (figure 4.6b) is close to the single-phase value. Yet the measured pressure drop of 4399 N/m^2 is too high by an order of magnitude. This discrepancy substantiates the idea that the flow phenomena encountered in the single-duct experiments cannot explain the observations at the dephlegmator.

Significant sub-cooling occurring in the single-phase liquid region, which is formed as a result of flooding [83BA1] may suggest that the cold zones are due to the presence of

liquid plugs. This can, however, not be the case because firstly the length of the cold zones, measured in the direction of the finned tubes, was at times 2 to 3 metres. The corresponding pressure drop across such a single-phase column is ≈20 000 N/m^2, but such high pressure differentials were never recorded. Secondly the formation of single-phase regions and the subsequent sub-cooling of condensate is unlikely to occur in inclined flattened ducts of high aspect ratio [97SC1].

The cold zones appear to be regions containing mainly air. The accumulated condensate causing the high pressure drop is most probably located just above the duct inlets in the warm part of the dephlegmator where it is continually heated by the incoming vapour.

The fact that a uniform finned tube temperature distribution can be achieved during steady-state conditions as in case 1, proves that the suction rate of the ejector is sufficient to remove noncondensable gases in such a way that no major cold zones can be formed as a result of the tube-row-effect. The presence of smaller cold spots illustrated in figure 10.5(a) substantiates, however, that backflow is caused by the tube-row-effect and that the ejector suction rate is insufficient to prevent backflow.

Under desirable operating conditions the ejector duct temperature was found be to equal to the saturation temperature of the steam. This is an indication that mainly steam is removed by the vacuum system in the absence of counterflow limitations, as prescribed by the ejector performance characteristics shown in figure 9.7(b). Modelling the flow to the ejector in terms of vapour only is therefore permissible.

Table 10.6(a): Detailed dephlegmator performance data according to theory: Cases 1 and 2.

	Case 1		Case 2(a)		Case 2(b)	
	Row (1)	Row (2)	Row (1)	Row (2)	Row (1)	Row (2)
T_{vm}, °C	54.84	54.91	54.92	54.99	47.8	48.0
p_{vm}, N/m^2	15490	15539	15548	15601	11011	11084
T_{ao}, °C	39.85	51.60	37.80	50.22	29.93	42.69
T_{am}, °C	29.55	45.72	28.43	44.01	20.73	36.31
Q_a, W	5484420	3131131	6436628	4278055	6647429	4608588
Q_a, MW	8.62		10.71		11.26	
m_c, kg/s	2.313	1.320	2.715	1.804	2.784	1.930
m_{v2}, kg/s	1.998	1.635	2.412	2.107	2.487	2.226
m_{v3}, kg/s	0.315	0.305	0.303	0.293	0.296	0.289
$m_{ejector}$, kg/s	0.010		0.010		0.007	
v_{sv2}, m/s	31.8	25.5	38.2	32.7	54.6	47.8
v_{sv3}, m/s	5.0	4.8	4.8	4.5	6.5	6.2
Fr_{Hsv2}	0.112	0.072	0.162	0.119	0.238	0.183
Re_{sv2}	7845	6301	9469	8127	9968	8764
Re_{sv3}	1237	1176	1188	1128	1187	1139
L_b, m	1.081	---	0.885	---	0.844	---
p_{v1}, N/m^2	15690		15830		11437	
Δp_{12}, N/m^2	95.0	58.3	145.9	101.9	232.7	167.9
Δp_{23f}, N/m^2	195.4	188.6	279.1	276.9	408.4	413.5
Δp_{23g}, N/m^2	7.1	7.1	7.2	7.2	5.2	5.2
Δp_{23m}, N/m^2	-107.8	-65.2	-154.5	-109.6	-227.3	-169.3
Δp_{34}, N/m^2	-1.8	-0.4	-1.6	-0.3	-2.2	-0.5
Δp_{14}, N/m^2	188.4	188.4	276.0	276.0	416.8	416.8
p_{v4}, N/m^2	15501		15579		11020	
$\Delta p_{ejector}$, N/m^2	34.6		34.8		23.1	
$p_{ejector}$, N/m^2	15465		15544		10997	

Table 10.6(b): Detailed dephlegmator performance data according to theory: Cases 3 and 4.

	Case 3		Case 4(a)		Case 4(b)	
	Row (1)	Row (2)	Row (1)	Row (2)	Row (1)	Row (2)
T_{vm}, °C	47.94	48.05	55.96	56.02	66.25	66.28
p_{vm}, N/m^2	11057	11113	16341	16389	26259	26298
T_{ao}, °C	29.47	41.00	35.07	47.90	44.53	58.35
T_{am}, °C	22.39	35.24	27.31	41.48	35.82	51.44
Q_a, W (per row)	7335604	5981202	8482890	7018522	8877593	7053362
Q_a, MW	13.32		15.50		15.93	
m_c, kg/s	3.072	2.505	3.582	2.963	3.789	3.010
m_{v2}, kg/s	2.858	2.719	3.348	3.196	3.511	3.288
m_{v3}, kg/s	0.214	0.207	0.233	0.222	0.278	0.262
$m_{ejector}$, kg/s	0.007		0.011		0.016	
v_{sv2}, m/s	62.5	58.2	50.7	47.4	34.1	31.3
v_{sv3}, m/s	4.7	4.4	3.5	3.3	2.7	2.5
Fr_{Hsv2}	0.313	0.272	0.298	0.262	0.212	0.179
Re_{sv2}	11450	10703	13105	12292	13339	12278
Re_{sv3}	858	815	912	856	1057	980
L_b, m	0.554	---	0.517	---	0.583	---
p_{v1}, N/m^2	11621		16861		26611	
Δp_{12}, N/m^2	328.9	274.0	307.9	260.3	199.4	162.8
Δp_{23f}, N/m^2	541.4	553.9	500.2	510.4	348.0	351.2
Δp_{23g}, N/m^2	5.2	5.2	7.5	7.5	11.7	11.7
Δp_{23m}, N/m^2	-296.3	-254.9	-281.0	-244.3	-198.5	-165.8
Δp_{34}, N/m^2	-1.1	-0.2	-0.9	-0.2	-0.9	-0.2
Δp_{14}, N/m^2	578	578	533.6	533.6	359.8	359.8
p_{v4}, N/m^2	11043		16327		26251	
$\Delta p_{ejector}$, N/m^2	23.1		36.4		50.8	
$p_{ejector}$, N/m^2	11020		16291		26200	

Table 10.6(c): Detailed dephlegmator performance data according to theory: Case 5.

	Case 5	
	Row (1)	Row (2)
T_{vm}, °C	48.05	48.14
p_{vm}, N/m^2	11115	11167
T_{ao}, °C	28.27	39.94
T_{am}, °C	21.49	34.11
Q_a, W (per row)	8060680	6945962
Q_a, MW	15.01	
m_c, kg/s	3.376	2.909
m_{v2}, kg/s	3.188	3.097
m_{v3}, kg/s	0.188	0.181
$m_{ejector}$, kg/s	0.007	
v_{sv2}, m/s	69.4	66.0
v_{sv3}, m/s	4.1	3.9
Fr_{Hsv2}	0.388	0.352
Re_{sv2}	12769	12187
Re_{sv3}	753	712
L_b, m	0.442	---
p_{v1}, N/m^2	11827	
Δp_{12}, N/m^2	435.5	281.2
Δp_{23f}, N/m^2	663.2	680.7
Δp_{23g}, N/m^2	5.2	5.2
Δp_{23m}, N/m^2	-366.1	-329.9
Δp_{34}, N/m^2	-0.9	-0.2
Δp_{14}, N/m^2	737.0	737.0
p_{v4}, N/m^2	11090	
$\Delta p_{ejector}$, N/m^2	23.2	
$p_{ejector}$, N/m^2	110067	

10.3 Reduction in turbine output due to ineffective dephlegmator performance

It has been explained in section 9.5 how the heat rejection rate required by the turbine characteristics has to be achieved by the cooling system. When cold zones are formed on the dephlegmators the available airside surface is reduced. Subsequently the system temperature rises to maintain the heat rejection rate. The corresponding increase in the backpressure results in a decrease in the turbine output.

Note that the condenser units, making up 85.6% of the total airside surface, primarily determine the turbine backpressure and the pressure in the bottom header pipe of the dephlegmators. Consequently the strong increase in the pressure drop across the dephlegmator in the presence of cold zones has no direct adverse effect on the turbine backpressure but it significantly affects the suction pressure to the ejectors. In other words, an increased pressure drop across the dephlegmators results in a decrease in the absolute pressure downstream of the dephlegmator and it does not cause a rise in the system pressure upstream of the dephlegmator towards the turbine exit.

The primary adverse effect of the cold zones is the increased system temperature and the correspondingly higher backpressure which ultimately reduces the turbine efficiency.

To estimate the loss in power generated due to the ineffective dephlegmator performance, a system analysis incorporating the turbine characteristic was carried out by

1) assuming 100% dephlegmator performance
2) and by reducing the heat transfer prediction according to section 9.2.2 to 60% when solving for the heat rejected by the entire system in equation (9.49).

The loss in output was evaluated for the entire range of ambient temperatures prevailing at the power station. The mean hourly frequency of ambient temperatures over a period of one year is shown in figure 10.6. The turbo-generator performance and the percentage loss are shown against the ambient temperature in figure 10.7. At the highest ambient temperatures the loss is the biggest. At very low ambient temperatures the heat rejection capability of the cooling system exceeds the required heat rejection rate and the adverse

effect of the cold zones abates. Taking the conditions at an ambient temperature of 20°C as representative of an entire year, the corresponding decrease of 0.5% in the turbine output amounts to an estimated annual loss of 18.9 MW in power generation capacity. This estimate is based on full-load conditions and will be less when taking part-load periods into account where cold zones do not necessarily reduce the efficiency.

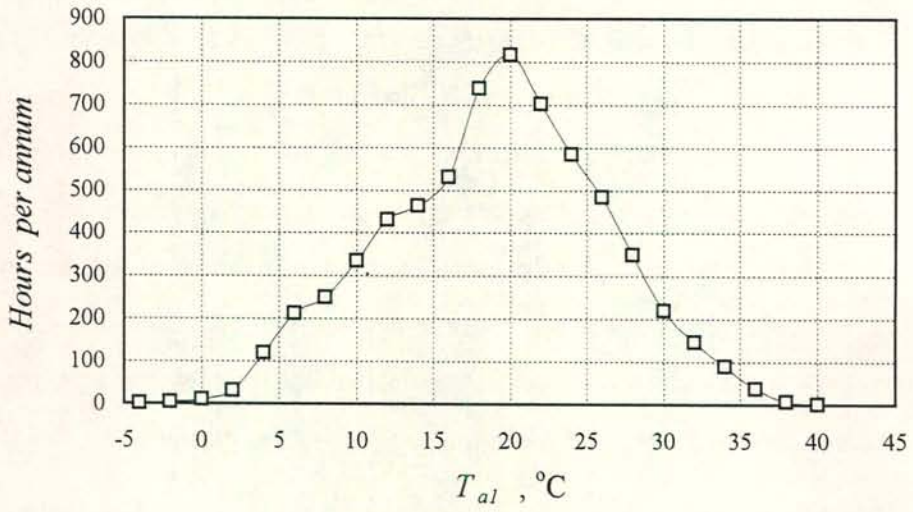

Figure 10.6: Frequency of the ambient temperature at the power station.

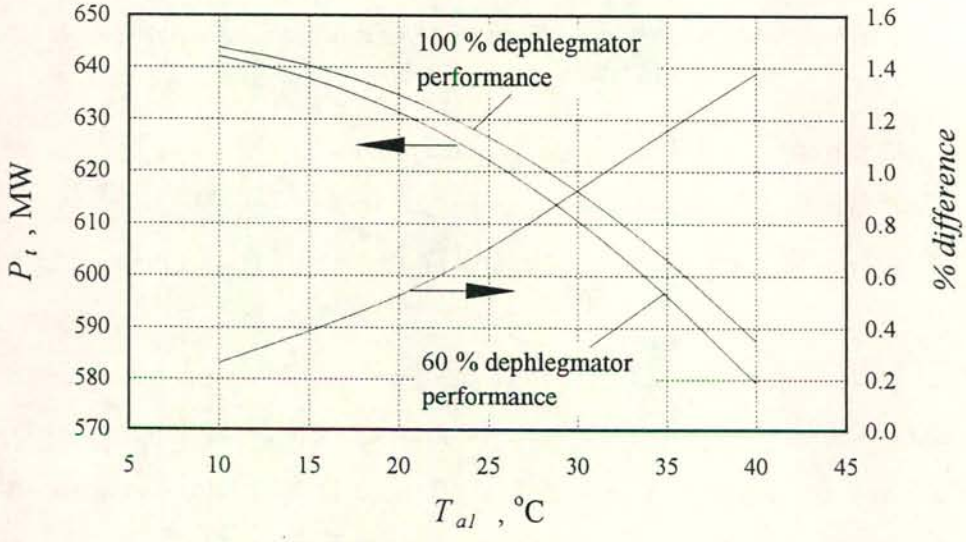

Figure 10.7: Reduction in turbine output due to ineffective dephlegmator performance.

It must however be kept in mind that environmental effects such as wind and inversions and the recirculation of hot air can strongly influence the performance of the cooling system [93DU1, 95DU5], which can result in output losses well above the average of 0.5%.

Another adverse effect due to the reduced condensation rate inside the dephlegmator is the potential formation of secondary flow patterns in the condenser units. When the dephlegmator does not succeed in its primary objective to facilitate a net outflow of vapour at the bottom of the condenser units, air is trapped resulting in dead zones. Such cold zones were indeed observed in the bottom corners of some condenser units.

10.4 Closing remarks

The present adiabatic counterflow investigation cannot provide adequate explanations for the ineffective dephlegmator performance. Much needed insight regarding counterflow phenomena in single-ducts has however been gained in Part A, which leads to the conclusion that the D-type header and the drain stubs are potential locations of counterflow limitation. It is therefore recommended that the next step towards a solution should involve the investigation of the flow distribution inside the bottom header and drain stubs. The tooth pattern at the bottom of the cold zones shown by the infra-red image in figure 10.2(c) suggests that the drain stub configuration may strongly effect the flow distribution inside the finned tube bundles.

If free drainage of the condensate is indeed restricted inside the header, additional drain stubs should be inserted between the existing ones. This would lower the vapour velocity entering the header and a more uniform flow will be achieved to the inlet of the finned tubes.

Due to the essentially low suction rate of the ejector system backflow at the top of the dephlegmator rows occurs. To eliminate this problem the dephlegmator should be provided with an after-condenser which in turn is connected to the evacuation system. Such an after-condenser can be constructed of horizontally oriented finned tubes located above the existing bundles where the corrugated iron is at present. Only the condensation

or heat rejection capability of an after-condenser can effectively keep the dephlegmator free of noncondensables. And as the number of finned tubes decreases towards the evacuation system by employing and after-condenser, the noncondensables become more concentrated while the ejector suction rate per finned tube becomes more significant.

CHAPTER 11

SUMMARY

Observation of an existing inclined reflux condenser revealed that only up to 60% of the design heat rejection rate is achieved under steady-state full-load turbine operating conditions of the power generating cycle. Cold zones are present in the reflux condenser or dephlegmator, resulting in ineffective performance. The accumulation of condensate associated with countercurrent flow can possibly lead to be the observed inefficiencies.

Elliptical finned tubes inclined at 62° to the horizontal are employed in the cooling system under investigation. The inside duct height and width are 97 mm and 20 mm respectively. An extensive literature survey on countercurrent gas-liquid flow showed, however, that experimental research has so far concentrated on vertical tubes. The test sections employed in these investigations were found to have a strong effect on the flow modes during counterflow, which therefore ruled out the application of existing information to model the dephlegmator in an attempt to identify the cause of cold zone formation.

An experimental apparatus was constructed to investigate adiabatic gas-liquid counterflow and flooding. The reflux condenser geometry was followed as a guide line for this purpose, but a much wider range of the relevant parameters was covered to gain a better understanding of the fundamental characteristics of countercurrent flow. Three rectangular ducts of 10 mm width and heights of 50 mm, 100 mm and 150 mm respectively and a fourth duct of 20 mm width and 50 mm height were tested. The entrance pressure drop at the sharp-edged gas inlet and the frictional pressure drop inside the ducts were measured for inclined flow. Flooding curves were generated for inclinations from close to the horizontal to vertical.

The pressure drop during counterflow was found to be governed by the superficial gas Reynolds number and the superficial densimetric gas Froude number. At low to moderate gas flow rates the pressure drop is Reynolds number related while it becomes Froude number dependent as the gas flow is increased. The role of these two dimensionless

groups was independently confirmed by i) keeping the fluid properties constant and varying the duct dimensions and ii) by testing with different working fluids in one duct, i.e. varying the fluid properties, while keeping the dimensions the same.

The length dimension in the gas Reynolds number was found to be the hydraulic diameter while the length dimension required for the gas Froude number is the duct height.

At flooding in ducts inclined at intermediate angles a vortex-type churning flow was the primary mechanism of upward liquid flow. In the case of vertical ducts the phase distribution at flooding was less defined compared to inclined flow.

The flooding data correlated well in terms of a Froude-*Zk* number combination where the *Zk* number accounts for the liquid properties. It was furthermore found that flooding is not related to the gas Reynolds number. The validity of the Froude-*Zk* number combination was confirmed by vertical tube flooding data of other researchers and thus should not to be limited to inclined rectangular ducts.

.The duct height, fluid densities and duct inclination have the strongest influence on the flooding gas velocity while the gas viscosity appears not to play a role. The effect of the liquid viscosity and surface tension is of secondary nature. The liquid viscosity was found to have a stronger effect on the flooding gas velocity than the surface tension.

The performance of the entire condenser-turbine system was modelled. The performance prediction by the model was compared to the results of field tests carried out on the full scale plant. Good agreement was achieved between theory and experiment in the case of a condenser unit.

An analysis of a dephlegmator unit, based on the phenomenological findings of the adiabatic counterflow investigation, revealed that flooding as found in single-ducts should not limit the performance inside the intended operating range. This was confirmed by the reflux condensation experiments carried out in an inclined finned tube by Schoenfeld [97SC1].

System effects such as counterflow limitation in the bottom header and drain stubs and maldistribution of the vapour flow amongst the finned tubes appear to cause the high steamside pressure drop and the subsequent formation of cold zones in the dephlegmator.

As a result of the cold zone formation the theory fails to model the dephlegmator performance satisfactorily. It is recommended that further research should focus on the bottom header and the drain stubs.

REFERENCES

00WE1 Weisbach, J., *Die Experimental-Hydraulik*, J.S. Engelhardt, Freiberg, 1855.

50KA1 Kays, W.M., Loss Coefficients for Abrupt Changes in Flow Cross Section with Low Reynolds Number Flow in Single and Multiple-Tube Systems, *Transactions of the ASME*, Vol. 72, No. 8, pp. 1067-1074, 1950.

54KA1 Kamei, S., Onishi, J. and Okane, T., Flooding in a Wetted Wall Tower, *Chemical Engineering (Japanese)*, Vol. 18, pp. 364-368, 1954.

60FE1 Feind, K., Falling Liquid Films with Countercurrent Air Flow in Vertical Tubes, *VDI Forschungsheft 481*, 1960.

63EN1 English, K.G., Jones, W.T., Spillers, R.C. and Orr, V., Flooding in a Vertical Updraft Partial Condenser, *Chemical Engineering Progress*, Vol. 59, No. 7, pp. 51-53, 1963.

65SH1 Shires, G.L. and Pickering, A.R., The Flooding Phenomenon in Counter-Current Two-Phase Flow, *Proceedings of the Symposium on Two-Phase Flow*, Exeter. 2, pp. B501-B538, 1965.

65ZU1 Zuber, N. and Findlay, J.A., Average Volumetric Concentration in Two-Phase Flow Systems, *Journal of Heat Transfer*, Vol. 87, pp. 453-468, 1965.

66CL1 Clift, R., Pritchard, C.L. and Nedderman, R.M., The Effect of Viscosity on the Flooding Conditions in Wetted Wall Columns, *Chemical Engineering Science*, Vol. 21, pp. 87-95, 1966.

66VD1 *Verein Deutscher Ingenieure*, VDI-Richtlinien, Abnahme- und Leistungsversuche an Ventilatoren, VDI 2044. Berlin und Köln, 1966.

67FO1 Forgó, L., Die Ursachen für schlechte Wärmeübertragung in Rohrbündel-Wärmetauscher bei kondensierendem Sattdampf, *Brennst.-Wärme-Kraft*, Vol. 19, No. 1, pp. 20-23, 1967.

69CE1 Cetinbudaklar, A.G. and Jameson, G.J., The Mechanism of Flooding in Vertical Countercurrent Two-Phase Flow, *Chemical Engineering Science*, Vol. 24, pp. 1669-1680, 1969.

69DI1 Diehl, J.E. and Koppany, C.R., Flooding Velocity Correlation for Gas-Liquid Counterflow in Vertical Tubes, *Chemical Engineering Progress Symposium Series*, Vol. 65, No. 92, pp. 77-83, 1969.

69PU1 Pushkina, O.L. and Sorokin, Yu.L., Breakdown of Liquid Film Motion in Vertical Tubes, *Heat Transfer-Soviet Research*, Vol. 1, No. 5, pp. 56-64, 1969.

69WA1 Wallis, G.B., *One-Dimensional Two-Phase Flow*, McGraw Hill Book Company, 1969.

70HE1 Hewitt, G.F. and Hall-Taylor, N.S., *Annular Two-Phase Flow*, Pergamon Press, Oxford, 1970.

70SC1 Schulenberg, F., Wärmeübergang und Druckverlust bei der Kondensation von Kältemitteldämpfen in Luftgekühlten Kondensatoren, *Kältetechnik - Klimatisierung*, Vol. 22, No. 3, pp. 75-81, 1970.

74OS1 Oshinowo, T. and Charles, M.E., Vertical Two-Phase Flow, *The Canadian Journal of Chemical Engineering*, Vol. 52, pp. 23-35, 1974.

74RO1 Rozenman, T. and Pundyk, J., Effect of Unequal Heat Loads on the Performance of Air Cooled Condensers, *AIChE Symposium Series*, Vol. 70, No. 138, pp. 178-184, 1974.

74WA1 Wallis, G.B. and Makkenchery, S., The Hanging Film Phenomenon in Vertical Annular Two-phase Flow, *Journal of Fluids Engineering*, Vol. 96, pp. 297-298, 1974.

76TA1 Taitel, Y. and Dukler, A.E., A Model for Predicting Flow Regime Transitions in Horizontal and Near Horizontal Flow, *AIChE Journal*, Vol. 22, No.1, pp. 47-55, 1976.

76ZU1 Zucrow, M.J. and Hoffman, J.D., *Gas Dynamics*, Volume 1, John Wiley and Sons, New York, p. 132, 1976.

77HE1 Hewitt, G.F., Influence of End Conditions, Tube Inclination and Physical Properties on Flooding in Gas Liquid Flows, *Harwell Report No. HTFS-RS 222*, 1977.

77IM1 Imura, H., Kusuda, H. and Funatsu, S., Flooding Velocity in a Counter-Current Annular Two-Phase Flow, *Chemical Engineering Science*, Vol. 32, pp. 97-87, 1977.

77SU1 Suzuki, S. and Ueda, T., Behaviour of Liquid Films and Flooding in Counter-Current Two-Phase Flow - Part 1. Flow in Circular Tubes, *International Journal of Multiphase Flow*, Vol. 3, pp. 517-532, 1977.

78LA1 Larinoff, M.W., Moles, W.E. and Reichhelm, R., Design and Specification of Air-Cooled Steam Condensers, *Chemical Engineering*, May 22, pp. 86-94, 1978.

78UE1 Ueda, T, and Suzuki, S., Behaviour of Liquid Films and Flooding in Counter-Current Two-Phase Flow. Part 2. Flow in Annuli and Rod Bundles, *International Journal of Multiphase Flow*, Vol. 4, pp. 157-170, 1978.

79BH1 Bharathan, D., Wallis, G.B. and Richter, H.J., Air-Water Countercurrent Annular Flow, *Electric Power Research Institute Report EPRI-NP-1165*, Palo Alto, California, 1979.

79TI1 Tien, C.L. and Liu, C.P., Survey on Vertical Two-Phase Countercurrent Flooding, *Electric Power Research Institute Report EPRI-NP-984*, Palo Alto, California, 1979.

79TI2 Tien, C.L., Chung, K.S. and Liu, C.P., Flooding in Two-Phase Countercurrent Flows, *Electric Power Research Institute Report EPRI-NP-1283*, Palo Alto, California, 1979.

80BA1 Barnea, D., Shoham, O., Taitel, Y. and Dukler, A.E., Flow Pattern Transition for Horizontal and Inclined Pipes; Experimental and Comparison with Theory, *International Journal of Multiphase Flow*, Vol. 6, p. 217, 1980.

80BE1 Berg, W.F. and Berg, J.L., Flow Patterns for Isothermal Condensation in One-Pass Air-Cooled Heat Exchangers, *Heat Transfer Engineering*, Vol. 1, No. 4, pp. 21-31, 1980.

80BS1 *British Standards Institution*, Fans for General Purposes, Part 1, Methods of Testing Performance, BS848, 1980.

80CH1 Chung, K.S., Liu, C.P. and Tien, C.L., Flooding in Two-Phase Countercurrent Flows - II. Experimental Investigation, *PhysicoChemical Hydrodynamics*, Vol. 1, pp. 209-220, 1980.

80RU1 Russell, C.M.B., Condensation of Steam in a Long Reflux Tube, *Heat Transfer and Fluid Flow Service*, AERE Harwell and National Engineering Laboratory, 1980.

80SP1 Spedding, P.L. and Nguyen, V.T., Regime Maps for Air-Water Two-phase Flow, *Chemical Engineering Science*, Vol. 35, pp. 779-793, 1980.

80TA1 Taitel, Y., Barnea, D. and Dukler, A.E., Modelling Flow Pattern Transitions for Steady Upward Gas-Liquid Flow in Vertical Tubes, *AIChE Journal*, Vol. 26, No. 3, pp. 345-354, 1980.

81RI1 Richter, H.J., Flooding in Tubes and Annuli, *International Journal of Multiphase Flow*, Vol. 7, No. 6, pp. 647-658, 1981.

81SC1 Schrey, H.G. and Kern, J., Zum Rohrreiheneffekt bei Gasbeaufschlagten Kondensatoren, *International Journal of Heat Mass Transfer*, Vol. 24, pp. 335-342, 1981.

82HE1 Hewitt, G.F., Flow Regimes, in *Handbook of Multiphase Systems*, ed. Hetsroni, G., Chapter 2.1, 1982.

82TA1 Taitel, Y., Barnea, D. and Dukler, A.E., A Film Model for the Prediction of Flooding and Flow Reversal For Gas-Liquid Flow in Vertical Tubes, *International Journal of Multiphase Flow*, Vol. 8, No. 1, pp. 1-10, 1982.

83BH1 Bharathan, D. and Wallis, G.B., Air-Water Countercurrent Annular Flow, *International Journal of Multiphase Flow*, Vol. 9, No. 4, pp. 349-366, 1983.

83BA1 Banerjee, S., Chang, J.S., Girard, R. and Krishnan, V.S., Reflux Condensation and Transition to Natural Circulation in a Vertical U-Tube, *Journal of Heat Transfer*, Vol. 105, pp. 719-727, 1983.

83LE1 Lee, S.C. and Bankoff, S.G., Stability of Steam-Water Countercurrent Flow in an Inclined Channel, *Journal of Heat Transfer*, Vol. 105, pp. 713-718, 1983.

83TA1 Taitel, Y. and Barnea, B., Counter-Current Gas-Liquid Vertical Flow, Model for Flow Pattern Transition and Pressure Drop, *International Journal of Multiphase Flow*, Vol. 9, No. 6, pp. 673-647, 1983.

84DU1 Dukler, A.E., Smith, L. and Chopra, A., Flooding and Upward Film Flow in Tubes - I, *International Journal of Multiphase Flow*, Vol. 10, No. 5, pp. 585-597, 1984.

84LE1 Lee, S.C. and Bankoff, S.G., Parametric Effects on the Onset of Flooding in Flat-Plate Geometries, *International Journal of Heat Mass Transfer*, Vol. 27, No. 10, pp. 1691-1700, 1984.

84MI1 Mishima, K. and Nishihara, H., Flooding Velocities for Countercurrent Air-Water Flow in Thin Rectangular Channels, *Annual Reports of the Research Reactor Institute*, Kyoto University, Vol. 17, pp. 1-14, 1984.

84SC1 Schrey, H.G., Zur Bestimmung des Leistungsverhaltens bei mehrreihigen, luft- bzw. gasgekühlten Kondensatoren mit Inerten, *Wärme- und Stoffübertragung*, Vol. 18, No. 3, pp. 185-191, 1984.

85BA1 Barnea, D., Shoham, O., Taitel, Y. and Dukler, A.E., Gas-Liquid Flow in Inclined Tubes: Flow Pattern Transitions for Upward Flow., *Chemical Engineering Science*, Vol. 40, No. 1, pp. 131-136, 1985.

85BE1 Bellstedt, M.O., Performance Prediction of Dry Cooling Towers, *M.Eng, Thesis*, Department of Mechanical Engineering, University of Stellenbosch, Stellenbosch, South Africa, 1985.

85MC1 McQuillan, K.W., Whalley, P.B. and Hewitt, G.F., Flooding in Vertical Two-Phase Flow, *International Journal of Multiphase Flow*, Vol. 11, No. 6, pp. 741-760, 1985.

85MC3 McQuillan, K.W. and Whalley, P.B., Flow Patterns in Vertical Two-Phase Flow, *International Journal of Multiphase Flow*, Vol. 11, No. 2, pp. 161-175, 1985.

85MU1 Mukherjee, H. and Brill, J.P., Empirical Equations to Predict Flow Patterns in Two-Phase Inclined Flow, *International Journal of Multiphase Flow*, Vol. 11, No. 3, pp. 299-315, 1985.

85WH1 Whalley, P.B. and McQuillan, K.W., Flooding in Two-Phase Flow: The Effect of Tube Length and Artificial Wave Injection, *PhysicoChemical Hydrodynamics*, Vol. 6, No. 1/2, pp. 3-21, 1985.

85VE1 *Ventilatoren Stork Hengelo*, General Instructions for E-Type Fans, V.960874, 1985.

86BA1 Bankoff, S.G. and Lee S.C., A Critical Review of the Flooding Literature, in *Multiphase Science and Technology* (Edited by Hewitt, G.F., Delhaye, J.M. and Zuber, N.), Hemisphere Publishing Corporation, New York, Vol. 2, Chapter 2, pp. 95-180, 1986.

86BA2 Barnea, D., Ben Yoseph, N. and Taitel, Y., Flooding in Inclined Pipes - Effect of Entrance Section, *The Canadian Journal of Chemical Engineering*, Vol. 64, pp. 177-184, 1986.

86DU1 Dukler, A.E. and Taitel, Y., Flow Pattern Transitions in Gas-Liquid Systems: Measurement and Modeling, in *Multiphase Science and Technology* (Edited by Hewitt, G.F., Delhaye, J.M. and Zuber, N.), Hemisphere Publishing Corporation, New York, Vol. 2, Chapter 1, pp. 1-94, 1986.

86HO1 Holman, J.P., *Heat Transfer*, McGraw-Hill Book Company, New York, 1986.

86KO1 Kotzé, J.C.B., Ontwerp van Droë Direk Geforseerde en Indirek Natuurlike Konveksie Koeltorings, *M.Eng, Thesis*, Department of Mechanical Engineering, University of Stellenbosch, Stellenbosch, South Africa, 1986.

86KO2 Kotzé, J.C.B., Bellstedt, M.O. and Kröger, D.G., Pressure Drop and Heat Transfer Characteristics of Inclined Finned Tube Heat Exchanger Bundles, *Proceedings of the 8th International Heat Transfer Conference*, San Francisco, 1986.

86KR1 Kröger, D.G., Performance Characteristics of Industrial Tubes Presented in Dimensional Form, *International Journal of Heat and Mass Transfer*, Vol. 29, No. 8, pp. 1119-1125, 1986.

86ST1 Stanislav, J.F., Kokal, S. and Nicholson, M.K., Intermittent Gas-Liquid Flow in Upward Inclined Pipes, *International Journal of Multiphase Flow*, Vol. 12, No. 3, pp. 325-335, 1986.

87BA1 Barnea, D., A Unified Model for Predicting Flow-Pattern Transitions for the Whole Range of Pipe Inclinations, *International Journal of Multiphase Flow*, Vol. 13, No. 1, pp. 1-12, 1987.

88ZA1 Zabaras, G.J. and Dukler, A.E., Countecurrent Gas-Liquid Annular Flow, Including the Flooding State, *AIChE Journal*, Vol. 34, No. 3, pp. 389-396, 1988.

89FA1 Faghri, A., Chen, M.-M. and Morgan, M., Heat Transfer Characteristics in Two-Phase Closed Conventional and Concentric Annular Thermosyphons, *Journal of Heat Transfer*, Vol. 111, pp. 611-618, 1989.

89FU1 Fürst, J., Kondensation in Geneigten Ovalen Rohren, *Fortschritt-Berichte VDI*, VDI Verlag, Düsseldorf, Vol. 19, No. 36, 1989.

89OS1 Osakabe, M. and Kawasaki, Y., Top Flooding in Thin Rectangular and Annular Passages, *International Journal of Multiphase Flow*, Vol. 15, No. 5, pp. 747-754, 1989.

89SU1 Sudo, Y. and Kaminaga, M., A CHF Characteristic for Downward Flow in a Narrow Vertical Rectangular Channel Heated from both Sides, *International Journal of Multiphase Flow*, Vol. 15, No. 5, pp. 755-766, 1989.

90ST1 Stephan, M., Untersuchungen zur Gegenstrombegrenzung in Vertikalen Gas-Flüssigkeits-Strömungen, *Ph. D. Thesis*, Technische Universität München, Munich, Germany, 1990.

90VE1 Venter, S.J., The Influence of Distorted Flow Patterns on the Overall Performance of Axial Flow Fans, *Ph.D Thesis*, Department of Mechanical Engineering, University of Stellenbosch, Stellenbosch, South Africa, 1990.

91CO1 Conradie, A.E., Evaluation of the performance Characteristics of Forced Draft Air-Cooled Heat Exchangers and the Effect of Plume Recirculation thereon, *M.Eng. Thesis*, Department of Mechanical Engineering, University of Stellenbosch, Stellenbosch, South Africa, 1991.

91BE1 Bellstedt, M.O., Condensation of Low Pressure Steam in Inclined Air-Cooled Tubes, *Ph.D. Thesis*, Department of Mechanical Engineering, University of Stellenbosch, Stellenbosch, South Africa, 1991.

91FU1 Funnell, R.C., Prediction of Flow Patterns and Pressure Gradient in Inclined Two-Phase Flow Systems, *M.Eng. Thesis*, Department of Mechanical Engineering, University of Stellenbosch, Stellenbosch, South Africa, 1991.

91GO1 Govan, A.H., Hewitt, G.F., Richter, H.J., and Scott, A., Flooding and Churn Flow in Vertical Pipes, *International Journal of Multiphase Flow*, Vol. 17, No. 1, pp. 27-44, 1991.

91SU1 Sudo, Y., Usui, T. and Kaminaga, M., Experimental Study of Falling Water Limitation under a Counter-Current Flow in a Vertical Rectangular Channel (1st Report, Effect of Flow Channel Configuration and Introduction of CCFL Correlation), *JSME International Journal*, Series II, Vol. 34, No. 2, 1991.

91VE1 Venter, S.J. and Kröger, D.G., An Evaluation of Methods to Predict the System Effect Present in Air-Cooled Heat Exchangers, *Heat Recovery Systems and CHP*, Vol. 11, No. 5, pp. 431-440, 1991.

91WH1 White, F.M., *Viscous Fluid Flow*, McGraw Hill Book Company, p. 424, 1991.

92CA1 Carey, Van P., *Liquid-Vapor Phase-Change Phenomena*, Hemisphere Publishing Corporation, p. 90, 1992.

92GI1 Girard, R. and Chang, J.S., Reflux Condensation Phenomena in Single Vertical Tubes, *International Journal of Heat Mass Transfer*, Vol. 35, No. 9, pp. 2203-2218, 1992.

92JA1 Jayanti, S. and Hewitt, G.F., Prediction of the Slug-to-Churn Flow Transition in Vertical Two-Phase flow, *International Journal of Multiphase Flow*, Vol. 18, No. 6, pp. 847-860, 1992.

92ST1 Stephan, M. and Mayinger, F., Experimental and Analytical Study of Countercurrent Flow Limitation in Vertical Gas/Liquid Flows, *Chemical Engineering Technology*, Vol. 15, pp. 51-62, 1992.

93DU1 Du Toit, C.G., Thiart, G.D. and Kröger, D.G., Analysis of Recirculation in Mechanical-Draught Heat Exchangers, *Proceedings of the Third World Conference on Experimental Heat Transfer, Fluid Mechanics and Thermodynamics*, Honolulu, Hawaii, USA, Vol. 1, pp.377-383, 1993.

93GR1 Groenewald, W., Heat Transfer and Pressure Change in an Inclined Air-Cooled Flattened Tube during Condensation of Steam, *M.Eng. Thesis*, Department of Mechanical Engineering, University of Stellenbosch, Stellenbosch, 1993.

93HE1 Hewitt, G.F. and Jayanti, S., To Churn or not to Churn, *International Journal of Multiphase Flow*, Vol. 19, No. 3, pp. 527-529, 1993.

93JA1 Jayanti, S., Hewitt, G.F., Low, D.E.F. and Hervieu, E., Observation of Flooding in the Taylor Bubble of Co-Current Upwards Slug Flow, *International Journal of Multiphase Flow*, Vol. 19, No. 3, pp. 531-534, 1993.

93MA1 Mao, Z.S. and Dukler, A.E., The Myth of Churn Flow?, *International Journal of Multiphase Flow*, Vol. 19, No. 2, pp. 377-383, 1993.

93VA1 Van Aarde, D.J. and Kröger, D.G., Flow Losses Through an Array of A-Frame Heat Exchangers, *Heat Transfer Engineering*, Vol. 14, No. 1, pp. 43-51, 1993.

94HE1 Hewitt, G.F., Shires, G.L. and Bott, T.R., *Process Heat Transfer*, CRC Press, London, Chapter 10, pp. 391-396, 1994.

94KR1 Kröger, D.G., Fan Performance in Air-Cooled Steam Condensers, *Heat Recovery Systems and CHP*, Vol. 14, No. 4, pp. 391-399, 1994.

94LA1 Lacy, C.E. and Dukler, A.E., Flooding in Vertical Tubes - I Experimental Studies of the Entry Region, *International Journal of Multiphase Flow*, Vol. 20, No. 2, pp. 219-233, 1994.

94OB1 Obinelo, I.F., Round, G.F. and Chang, J.S., Condensation Enhancement by Steam Pulsation in a Reflux Condenser, *International Journal of Heat and Fluid Flow*, Vol. 15, No. 1, 1994.

94RE1 Reuter, H.C.R., Flow Modes and Pressure Change in an Inclined Tube during Reflux Condensation of Steam, *M.Eng. Thesis*, Department of Mechanical Engineering, University of Stellenbosch, Stellenbosch, South Africa, 1994.

94SC1 Schrey, H.G., Operational Considerations for Air-cooled Steam Condensers with One or Higher Numbers of Tube Rows, *Paper presented at the 9th IAHR Cooling Tower and Spraying Pond Symposium*, von Karman Institute, Brussels, Belgium, September 1994.

94ZA1 Zapke, A., Pressure Gradient and Flooding during Two-Phase Countercurrent Flow in Inclined Tubes, *M.Eng. Thesis*, Department of Mechanical Engineering, University of Stellenbosch, Stellenbosch, South Africa, 1994.

95CO1 Conradie, A.E., Performance Optimization of Engineering Systems with Particular Reference to Dry-cooled Power Plants, *Ph.D Thesis*, Department of Mechanical Engineering, University of Stellenbosch, Stellenbosch, South Africa, 1995.

95CO2 Conradie, A.E. and Kröger, D.G., Performance Evaluation of Dry-Cooling Systems for Power Plant Applications, *Applied Thermal Engineering*, Vol. 16, No. 3, pp. 219-232, 1995.

95DU1 Duvenhage, K. and Kröger, D.G., Plume Recirculation in Mechanical-Draft Air-Cooled Heat Exchangers, *Heat Transfer Engineering*, Vol. 16, No. 4, pp. 42-49, 1995.

95GR1 Groenewald, W. and Kröger, D.G., Effect of Mass Transfer on Turbulent Friction during Condensation inside Ducts, *International Journal of Heat Mass Transfer*, Vol. 38, No. 18, pp. 3385-3392, 1995.

95SA1 Salta, C.A. and Kröger, D.G., Effect of Inlet Flow Distortions on Fan Performance in Forced Draught Air-Cooled Heat Exchangers, *Heat Recovery Systems and CHP*, Vol. 15, No. 6, pp. 555-561, 1995.

95ZA1 Zapke, A., Report on Full Scale Condenser Performance Evaluation, Department of Mechanical Engineering, University of Stellenbosch, Stellenbosch, South Africa, 1995.

96DU1 Duvenhage, K., Vermeulen, J.A., Meyer, C.J. and Kröger, D.G., Flow Distortions at the Fan Inlet of Forced-Draught Air-Cooled Heat Exchangers, Applied Thermal Engineering, Vol. 16, Nos 8/9, pp. 741-752, 1996.

96JA1 Jayanty, S., Tokarez, A. and Hewitt, G.F., Theoretical Investigation of the Diameter Effect on Flooding in Countercurrent Flow, *International Journal of Multiphase Flow*, Vol. 22, No. 2, pp. 307-324, 1996.

96JE1 Jeong, J.H. and No, H.C, Experimental Study of the Effect of Pipe Length and Pipe-End Geometry on Flooding, *International Journal of Multiphase Flow*, Vol. 22, No. 3, pp. 499-514, 1996.

96OS1 Osakabe, M. and Futamata, H., Effect of Inserted Rod and Cross Flow on Top Flooding of Pipe, *International Journal of Multiphase Flow*, Vol. 22, No. 5, pp. 883-891, 1996.

96RE1 Reuter, H.C. and Kröger, D.G., Pressure Change and Flooding in Vertical and Inclined Tubes during Reflux Condensation of Steam, *The Ninth International Symposium on Transport Phenomena in Thermal-Fluids Engineering*, Singapore, pp. 727-732, 1996.

96SU1 Sudo, Y., Mechanism and Effects of Predominant Parameters Regarding Limitation of Falling Water in Vertical Countercurrent Two-Phase Flow, *Journal of Heat Transfer*, Vol. 118, pp. 715-724, 1996.

96WA1 Wallis, G.B, Thayer School of Engineering, Dartmouth College, Personal Communication, 1996.

96ZA1 Zapke, A. and Kröger, D.G., The Influence of Fluid Properties and Inlet Geometry on Flooding in Vertical and Inclined Tubes, *International Journal of Multiphase Flow*, Vol. 22, No. 3, pp. 461-472, 1996.

97FA1 Fabbri, G., Analysis of the Noncondensable Contaminant Accumulation in Single-Pass Air-Cooled Condensers, *Heat Transfer Engineering*, Vol. 18, No. 2, pp. 50-60, 1997.

97SC1 Schoenfeld, P., Personal Communication, Investigation on reflux condensation to be submitted for a M.Eng. degree, Department of Mechanical Engineering, University of Stellenbosch, Stellenbosch, South Africa, 1997.

APPENDIX A

SPECIFICATIONS AND DETAIL DRAWINGS OF THE FULL SCALE FORCED DRAFT AIR-COOLED CONDENSER

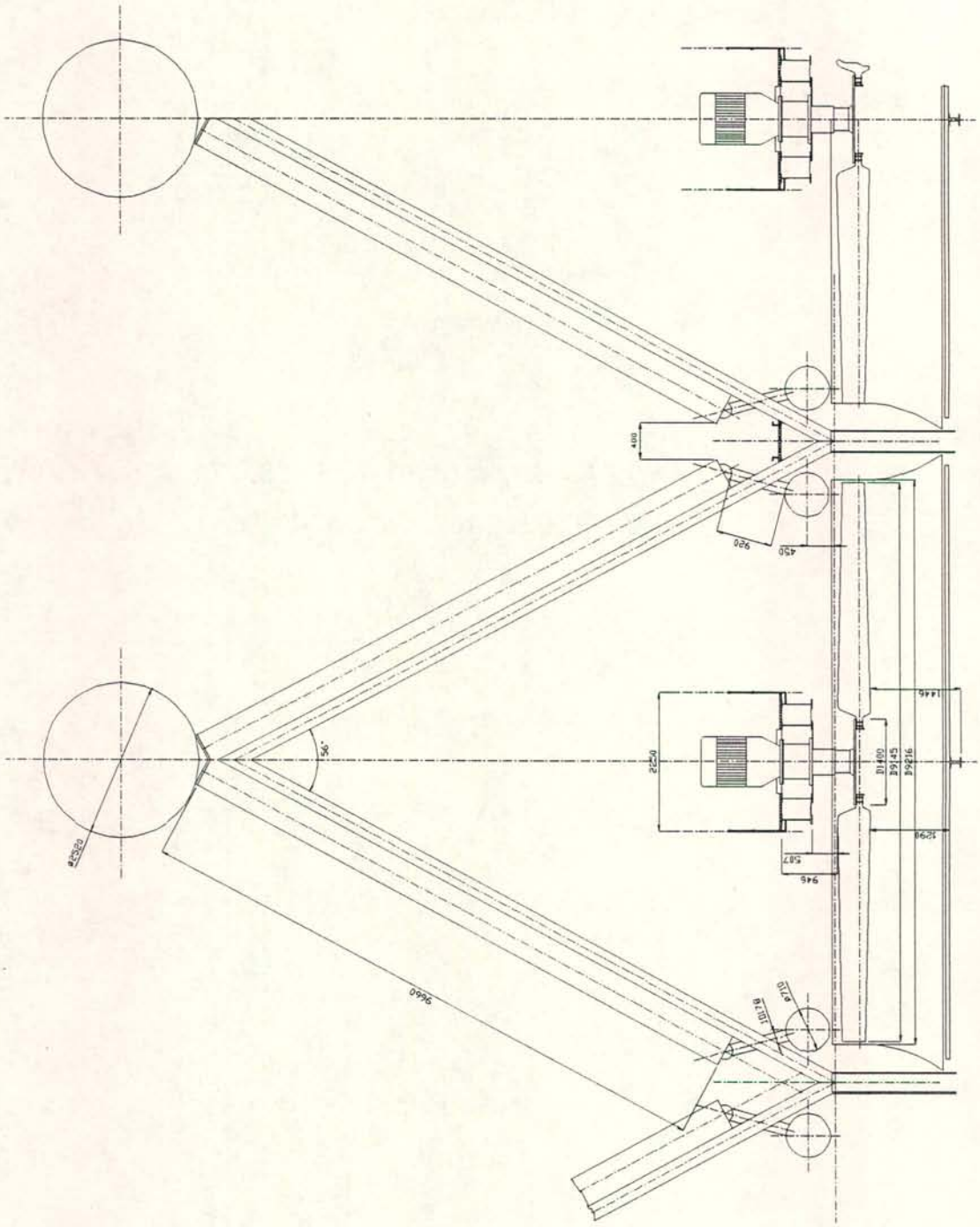

Figure A.1: Condenser A-frame and fan drive dimensions.

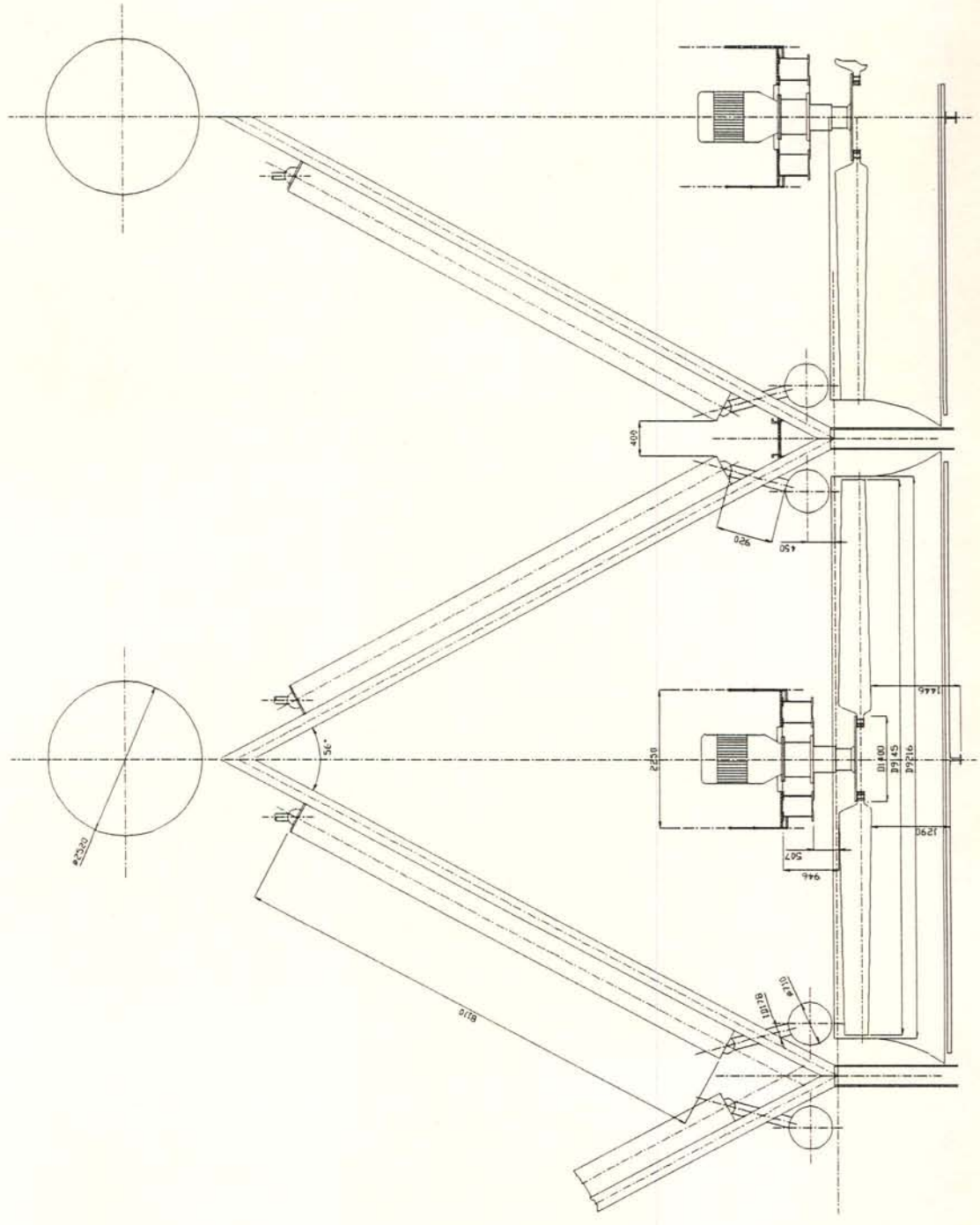

Figure A.2: Dephlegmator A-frame and fan drive dimensions.

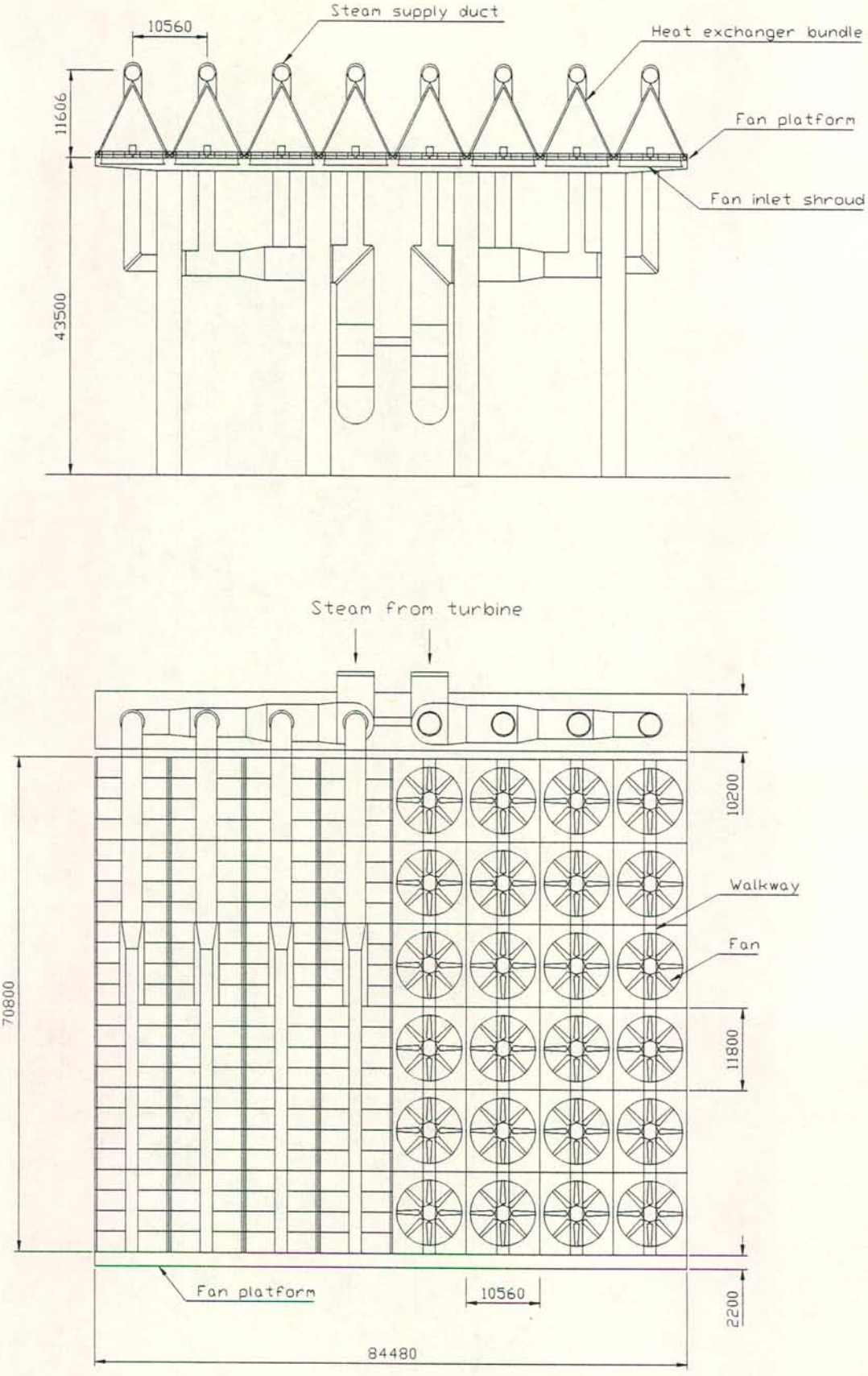

Figures A.3(a) and (b): Frontal and plan view of the air-cooled condenser.

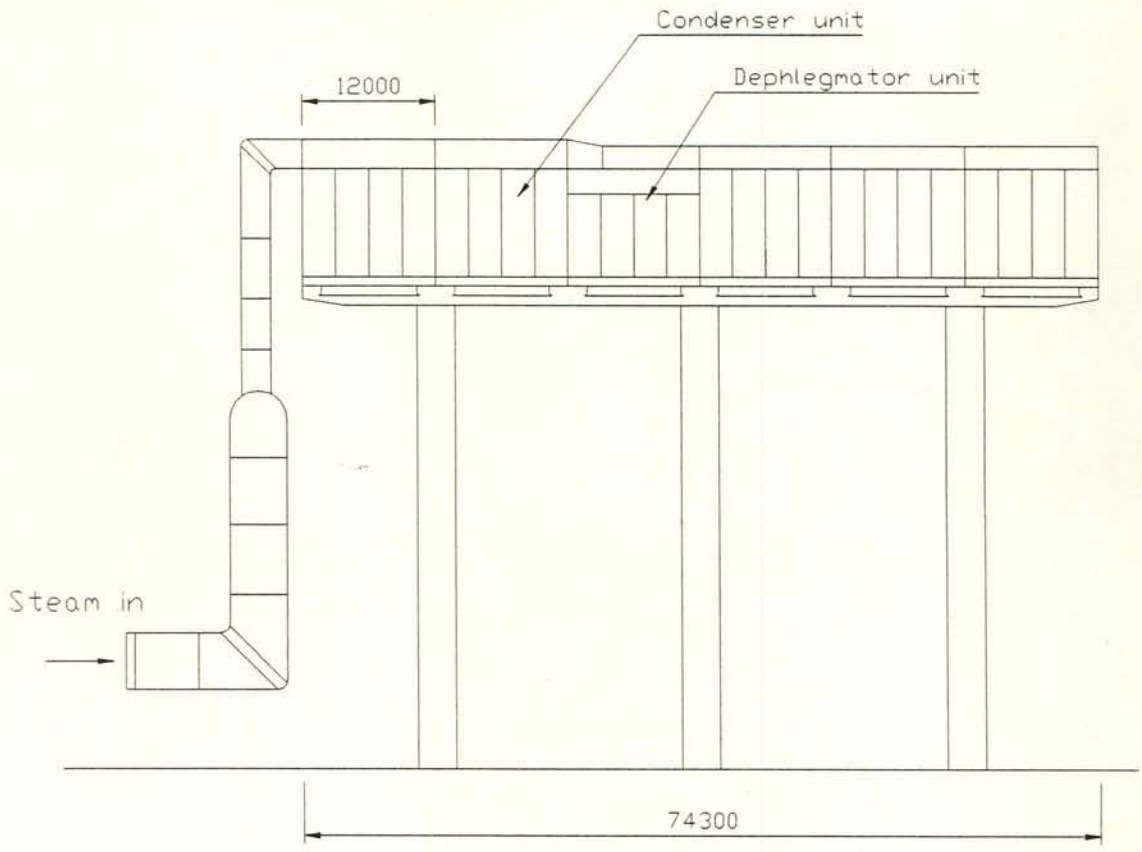

Figure A.3(c): Side view of the air-cooled condenser.

Air-cooled condenser specifications

The cooling system of one turbo-generator set consists of forty condenser units and eight dephlegmator units. Each unit contains eight tube bundles. A bundle consists of two rows of staggered elliptical finned tubes, as shown schematically in figure A.4. The heat exchanger specifications are as follows:

Hydraulic diameter of tube	D_e	=	0.02593 m
Inside area of tube per unit length	A_{ti}	=	0.20524 m^2/m
Inside cross-sectional tube flow area	A_{tc}	=	0.00133 m^2
Inside height of tube	H_t	=	0.097 m
Length of finned tube (condenser unit)	L_t	=	9.46 m
Length of finned tube (dephlegmator unit)	L_t	=	7.94 m
Number of tube rows	n_{tr}	=	2

Number of tubes per bundle (first row)	$n_{tb(1)}$	=	57
Number of tubes per bundle (second row)	$n_{tb(2)}$	=	58
Number of steam passes	n_{vp}	=	1
Frontal area of a condenser bundle (second row	$A_{fr(2)}$	=	27.434 m^2
Frontal area of a dephlegmator bundle (second row)	$A_{fr(2)}$	=	23.026 m^2
Bundle apex angle	$2\theta_b$	=	56°
Duct inclination to the horizontal	θ_t	=	62°
Fin height	H_f	=	0.12 m
Fin width	W_f	=	0.05 m
Root width (short axis)	W_r	=	0.02 m
Fin pitch (first row)	$P_{f(1)}$	=	0.004 m
Fin pitch (second row)	$P_{f(2)}$	=	0.0025 m
Ratio of minimum to free steam flow area at inlet to finned tube bundle	σ_{in}	=	0.86
Ratio of minimum to free stream flow area through finned tube bundle	σ_{min}	=	0.41
Effective steam header diameter	D_{sh}	=	2.52 m
Condenser and dephlegmator D-type header radius	r_h	=	0.1305 m
Condensate drain stub inside diameter	D_{stub}	=	0.178 m
Drain stub length	L_{stub}	=	0.915 m
Number of drain stubs per condenser bundle	n_{stub}	=	3
Number of drain stubs per dephlegmator bundle	n_{stub}	=	6
Inside diameter of bottom header pipe	D_h	=	0.698 m

Eight-bladed axial flow fans are employed in the system to achieve the desired air flow rate. The fan installation specifications are:

Fan diameter	D_F	=	9.145 m
Fan casing diameter	D_{Fc}	=	9.216 m
Fan hub diameter	D_{Fh}	=	1.4 m
Number of fan rows	n_{Fr}	=	8
Number of fan bays	n_{Fb}	=	6

Rotational speed	N_F	=	125 rpm
Efficiency of fan drive system	η_F	=	0.9
Inlet screen distance from fan blade	x_{si}	=	1.29 m
Screen support beam distance from fan blade (upstream)	x_{bi}	=	1.446 m
Walkway grid distance from fan blade (downstream)	x_{so}	=	0.946 m
Support beam distance from fan blade (downstream)	x_{bo}	=	0.507 m
Inlet screen projected area (upstream)	A_{si}	=	8.270 m^2
Support beam projected area (upstream)	A_{bi}	=	9.300 m^2
Walkway grid projected area (downstream)	A_{so}	=	5.283 m^2
Support beam projected area (downstream)	A_{bo}	=	4.880 m^2
Height of fan platform above ground level	H_3	=	43.5 m
Platform length	L	=	85.0 m
Platform width	W	=	74.3 m
Half-width of walkway between A-frames	L_w	=	0.2 m

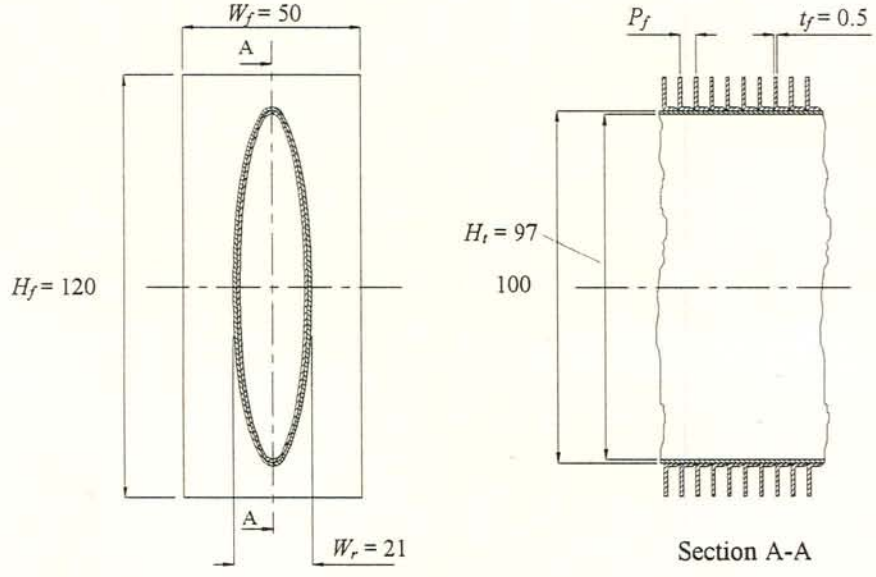

Figure A.4: Elliptical finned tubes employed in the air-cooled condenser under investigation.

APPENDIX B

ORIFICE PLATE DESIGN AND FLOW RATE CALCULATION

B.1 Orifice plate design and gas flow rate calculation procedure

The gas flow rate was measured with three existing orifice plates, designed according to the guidelines outlined by the *British Standards* BS 1042: Sections 1.1 (1981) and 1.2 (1984). Such a standard orifice plate is shown in figure B.1. A wide range of volume flow rates can be measured with the bank of three orifice plates with a maximum uncertainty better than approximately 3%. The orifice plates are fitted with corner tappings. Detail drawings of the orifice plates and their installation are shown in figures B.2 to B.4. A summary of the orifice dimensions is given in table B.1.

Table B.1: Orifice dimensions.

D [m]	d [m]	β [--]	E [--]	F_A [--]	X_{FA} [%]	X_{FB} [%]
0.0470	0.03016	0.6417	1.0974	1.0113	2.9	1.46
0.0470	0.01985	0.4223	1.0163	1.0058	2.1	1.06
0.0364	0.01154	0.3170	1.0051	1.0064	1.9	0.95

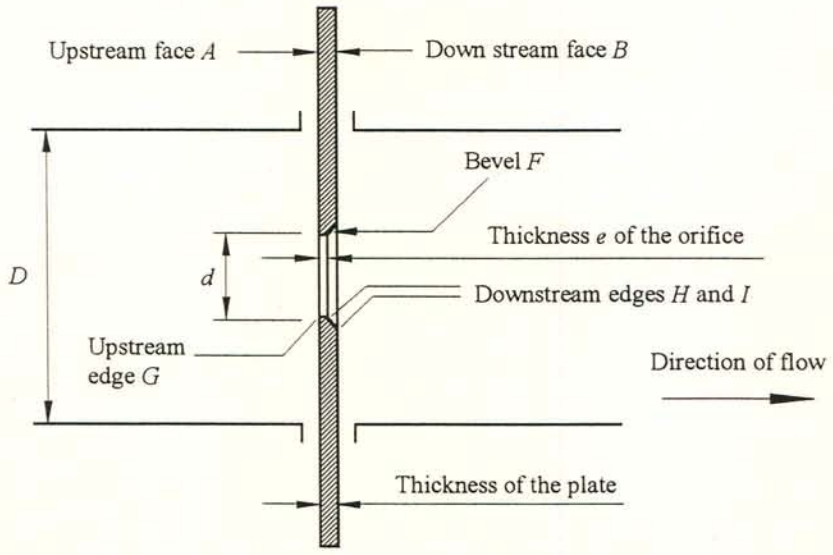

Figure B.1: Standard square-edged orifice plate according to the *British Standards*.

The mass flow rate passing through an orifice is expressed as

$$m = F_B\, C\, E\, \varepsilon\, \frac{\pi}{4} d^2 \sqrt{2\, \Delta p_o\, \rho_{up}} \tag{B.1}$$

F_B is a correction factor for square-edged orifice plates installed in type B pipes of diameters $25\ \text{mm} \le D < 50\ \text{mm}$. Type B includes plastics and applies in this case. F_B is expressed in terms of the correction factor F_A for type A pipes, i.e.

$$F_B = \left(F_A - 1\right)/2 + 1 \tag{B.2}$$

F_A and its percentage uncertainty are given in figures 1(a) and 1(b) of BS 1042: Section 1.2: 1984.

The discharge coefficient C for orifice plates with corner tappings is given by

$$C = 0.5959 + 0.031\,\beta^{2.1} - 0.1480\,\beta^{8} + 0.0029\,\beta^{2.5}\left[10^6/Re_D\right]^{0.75} \tag{B.3}$$

where β is the diameter ratio

$$\beta = d/D \tag{B.4}$$

Re_D is the upstream Reynolds number

$$Re_D = 4\,m/\left(\pi\, D\, \mu_{up}\right) \tag{B.5}$$

where the viscosity μ_{up} is evaluated at the upstream conditions.

The velocity of approach factor E is defined as

$$E = \left(1 - \beta^4\right)^{-0.5} \tag{B.6}$$

A relation for the expansion factor ε is given by the empirical formula

$$\varepsilon = \left(0.41 + 0.35\,\beta^4\right) \Delta p_o / \left(k\, p_{up}\right) \tag{B.7}$$

According to the British Standards equation (B.7) may be used for gases other than air, steam and natural gas if the isentropic exponent k is known. It is applicable only if

$p_{do}/p_{up} \geq 0.75$ where p_{do} and p_{up} are the orifice downstream and upstream pressures respectively.

The orifice plates were installed in smooth walled plastic pipes. The relative roughness therefore conforms to the specified upper limits of the standards. When the values of β, D, Re_D and the relative roughness are known without error, the percentage uncertainty X_C of the discharge coefficient C for corner tappings is

1) $X_C = 0.6\%$ for $\beta \leq 0.6$ (B.8a)
2) $X_C = \beta\,\%$ for $0.6 \leq \beta \leq 0.8$ (B.8b)

When β, $\Delta p_o/p_{up}$ and the isentropic coefficient k are known without error, the percentage uncertainty of the value of the expansion factor ε is equal to

$$X_\varepsilon = 4\,\Delta p_o/p_u \ \% \text{ for } \beta \leq 0.75 \tag{B.9}$$

The uncertainty X_{FB} of F_B is related to the uncertainty of F_A by

$$X_{FB} = X_{FA}/\left(1+1/F_A\right) \ \% \tag{B.10}$$

The resultant uncertainty of the mass flow rate in equation (B.1) X_m, upon substitution of the individual uncertainties and linearisation, becomes

$$X_m = X_C + X_\varepsilon + X_{FB} \quad \% \tag{B.11}$$

The following general limits of use are prescribed for square-edged orifice plates installed in pipes of diameter $25\text{ mm} \leq D \leq 50\text{ mm}$:

1) $d \geq 6\text{ mm}$
2) $0.23 \leq \beta \leq 0.7$
3) $0.023 \leq C\,E\,\beta^2 \leq 0.35$
4) $10000 \leq Re_D \leq 10^8$ for $0.45 < \beta \leq 0.77$
5) $5000 \leq Re_D \leq 10^8$ for $0.23 \leq \beta \leq 0.45$

The flow rate ranges of the orifice plates, based on the limitations 1) to 5) and the pressure ratio limit $p_{do}/p_{up} \geq 0.75$, are given in tables B.2 to B.5 for air, argon, helium and hydrogen respectively. $CE\beta^2{}_{min}$ and $CE\beta^2{}_{max}$ refer to the minimum and maximum flow rate conditions respectively.

Table B.2: Flow rate ranges air at 290 K and 105 000 N/m^2.

Orifice	m_{min} kg/s x 10^3	m_{max} kg/s x 10^3	Δp_{min} N/m^2	Δp_{max} N/m^2	Re_{Dmin}	Re_{Dmax}	$CE\beta^2{}_{min}$	$CE\beta^2{}_{max}$
1	6.6467	112.7479	70	26250	10000	169629	0.274	0.286
2	3.3234	45.2924	115	26250	5000	68142	0.109	0.112
3	2.5738	15.1068	642	26250	5000	29347	0.061	0.061

Table B.3: Flow rate ranges for argon at 290 K and 105 000 N/m^2.

Orifice	m_{min} kg/s x 10^3	m_{max} kg/s x 10^3	Δp_{min} N/m^2	Δp_{max} N/m^2	Re_{Dmin}	Re_{Dmax}	$CE\beta^2{}_{min}$	$CE\beta^2{}_{max}$
1	8.1509	134.3494	77	26250	10000	164827	0.286	0.274
2	4.0755	53.8824	125	26250	5000	66106	0.112	0.109
3	3.1563	17.9673	700	26250	5000	28462	0.061	0.061

Table B.4: Flow rate ranges for helium at 290 K and 105 000 N/m^2.

Orifice	m_{min} kg/s x 10^3	m_{max} kg/s x 10^3	Δp_{min} N/m^2	Δp_{max} N/m^2	Re_{Dmin}	Re_{Dmax}	$CE\beta^2{}_{min}$	$CE\beta^2{}_{max}$
1	8.8344	42.9076	903	26250	10000	48569	0.286	0.277
2	4.4172	17.1623	1481	26250	5000	19427	0.112	0.110
3	3.4210	5.7200	8525	26250	5000	8360	0.061	0.061

Table B.5: Flow rate ranges for hydrogen at 290 K and 105 000 N/m^2.

Orifice	m_{min} kg/s x 10^3	m_{max} kg/s x 10^3	Δp_{min} N/m^2	Δp_{max} N/m^2	Re_{Dmin}	Re_{Dmax}	$CE\beta^2{}_{min}$	$CE\beta^2{}_{max}$
1	3.2340	29.8627	239	26250	10000	92339	0.286	0.275
2	1.6170	11.9834	197	26250	5000	37054	0.112	0.110
3	1.2523	3.9961	1104	26250	5000	15955	0.061	0.061

The maximum pressure differentials measured across the orifice plates were typically 3000 N/m^2 for orifice 1 and up to 25 000 N/m^2 for orifice 2 and 3 at an upstream pressure of approximately 105 000 N/m^2. The estimated maximum uncertainties according equations (B.8) to (B.11) at these conditions are

1) X_m = 2.2 % for orifice 1

2) $X_m = 2.6$ % for orifice 2 and

3) $X_m = 2.5$ % for orifice 3.

At the lowest gas flow rates tested the Reynolds number in the pipe of orifice 3 was below the prescribed minimum value. Comparison of the air-only friction factor data generated for the ducts with existing correlations (see figure 3.14) proved, however, that accurate measurement outside the lower limits were achieved.

The conditions in the orifice bank corresponding to the gas flow rates at flooding were always within the prescribed limits.

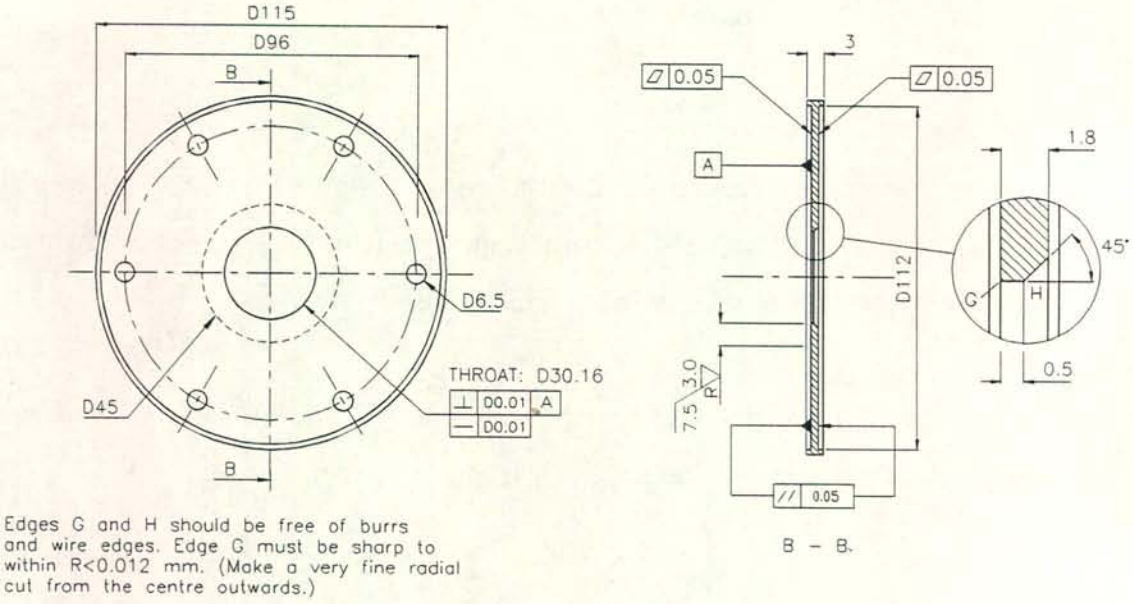

Figure B.2 (a): Detail drawing of orifice plate 1.

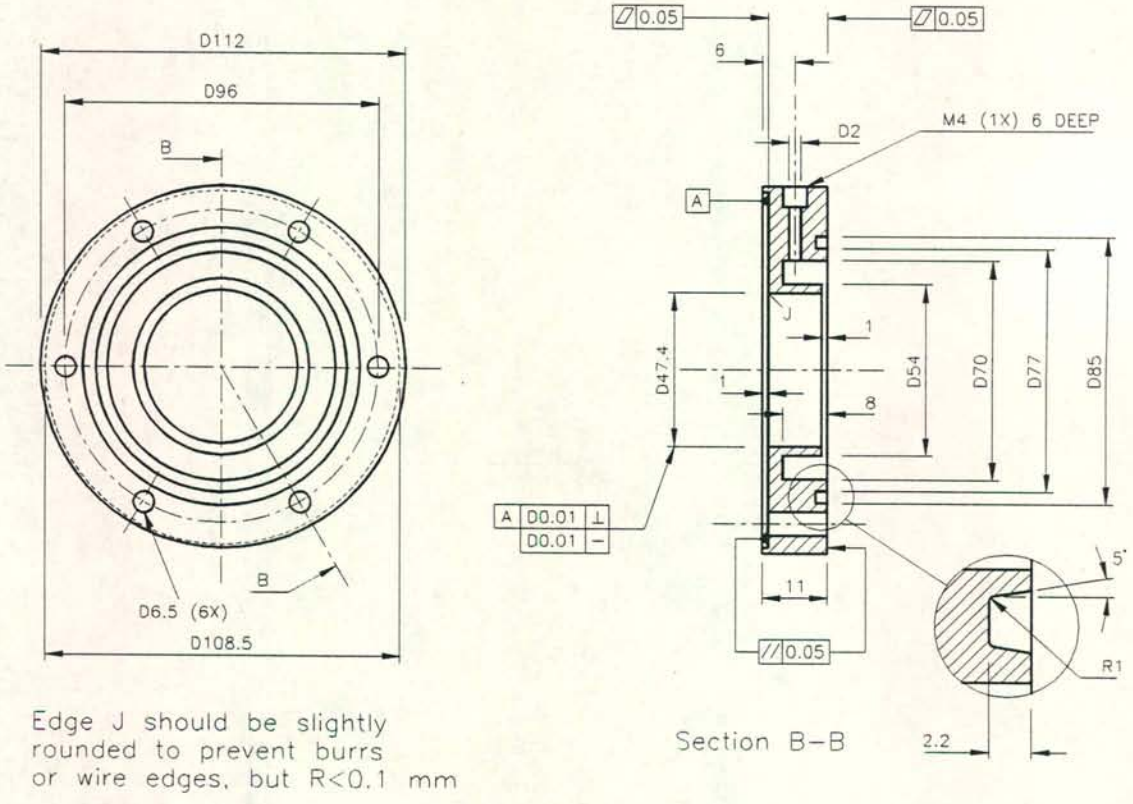

Figure B.2 (b): Orifice 1 carrier ring: Detail drawing.

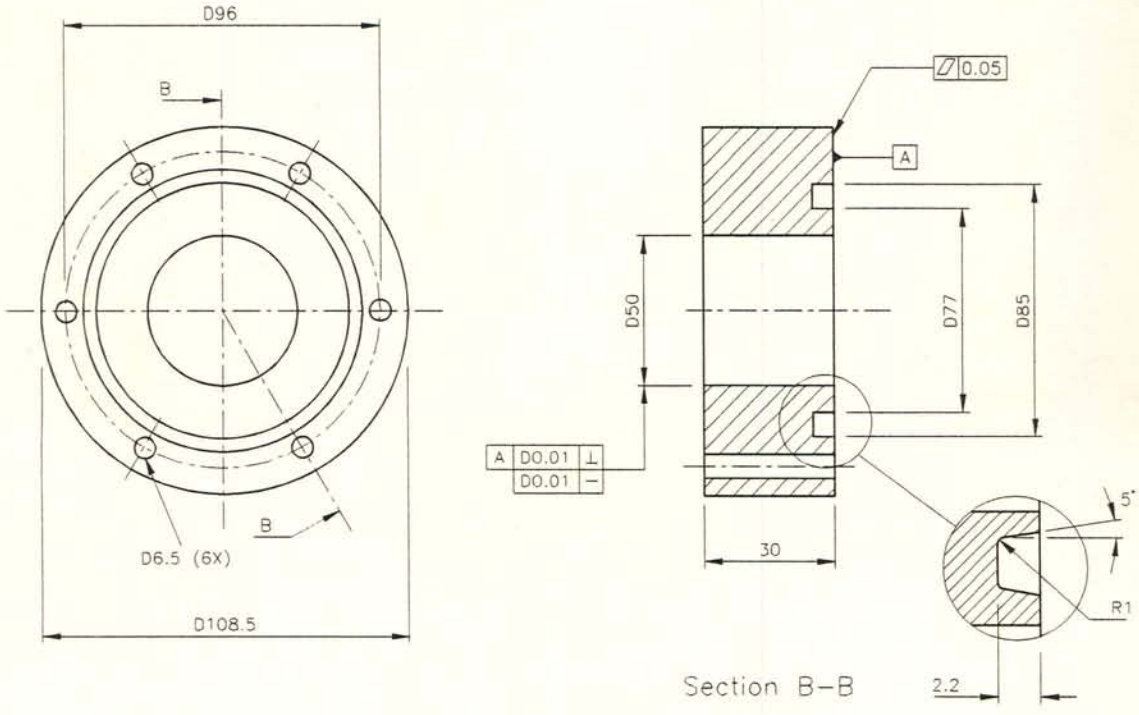

Figure B.2 (c): Orifice 1 pipe flange: Detail drawing.

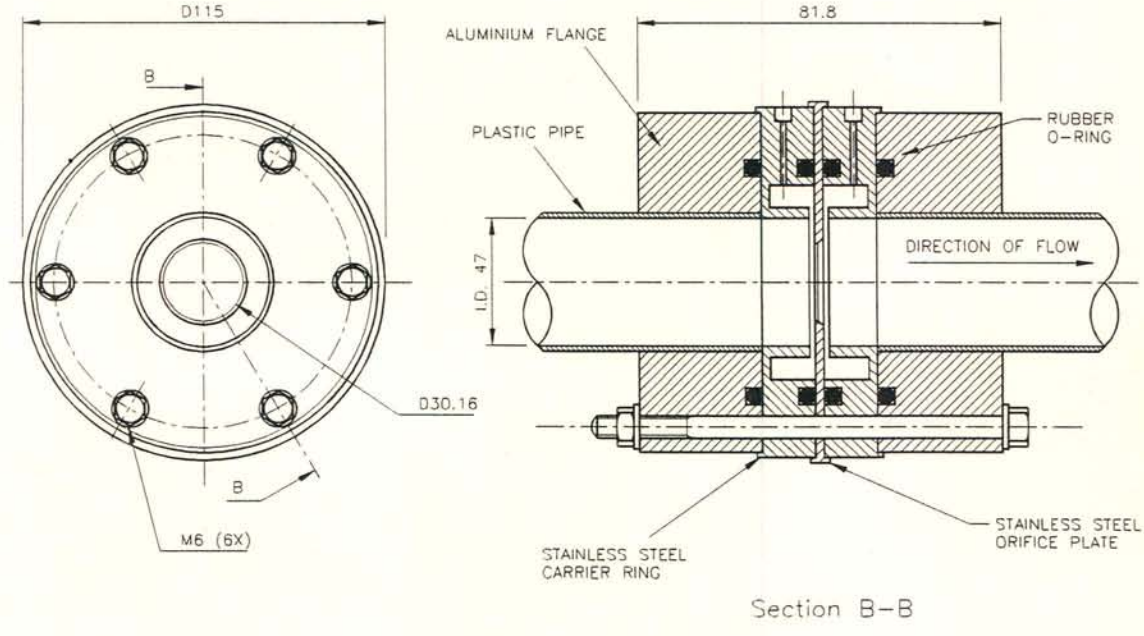

Figure B.2 (d): Assembly drawing of orifice 1 installation.

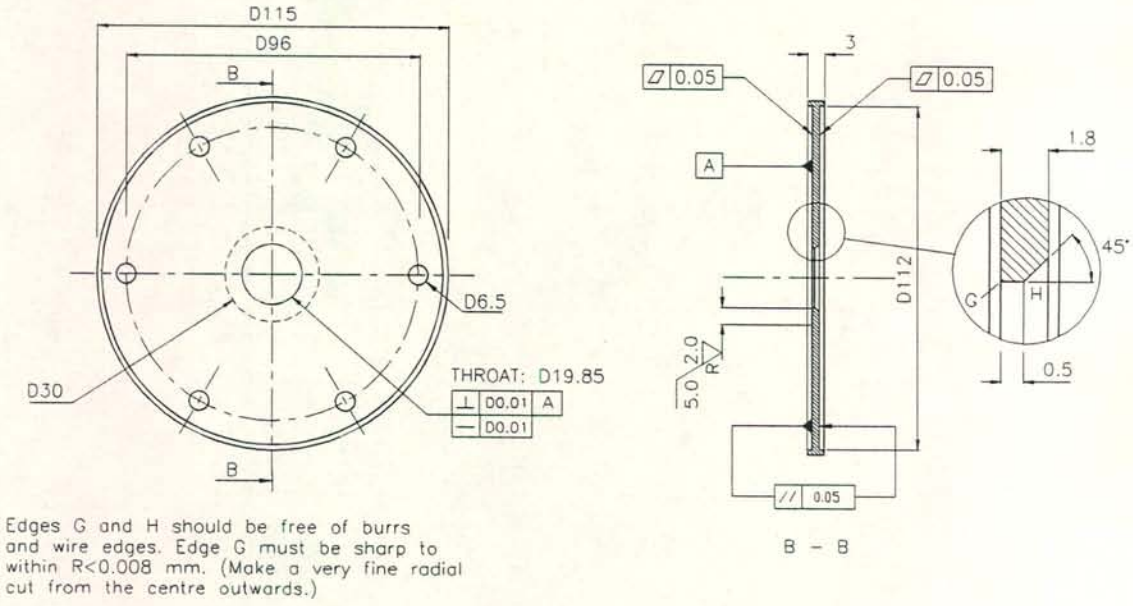

Figure B.3 (a): Detail drawing of orifice plate 2.

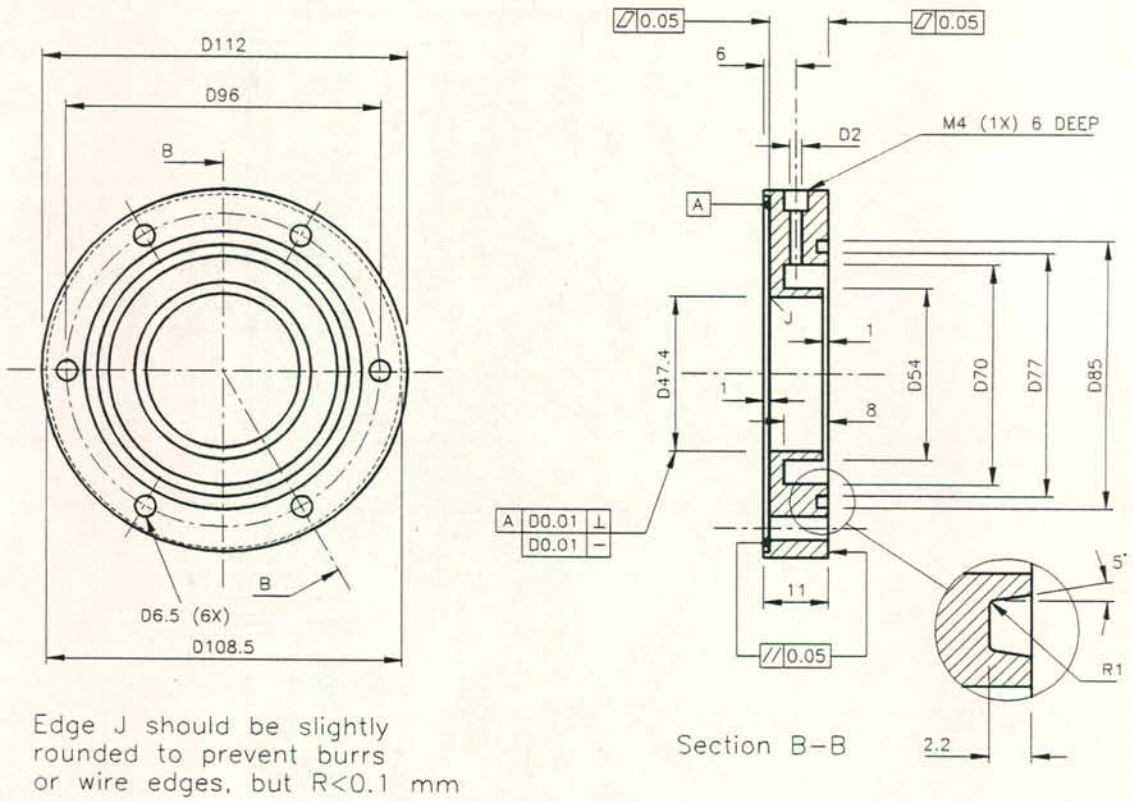

Figure B.3 (b): Orifice 2 carrier ring: Detail drawing.

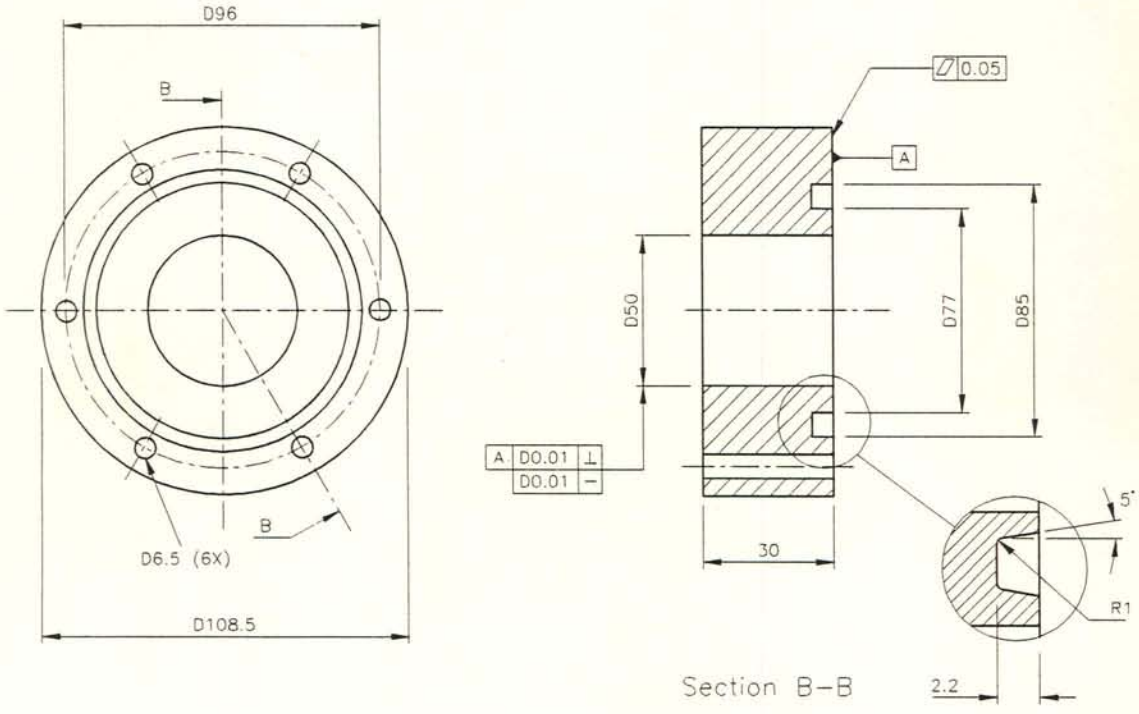

Figure B.3 (c): Orifice 2 pipe flange: Detail drawing.

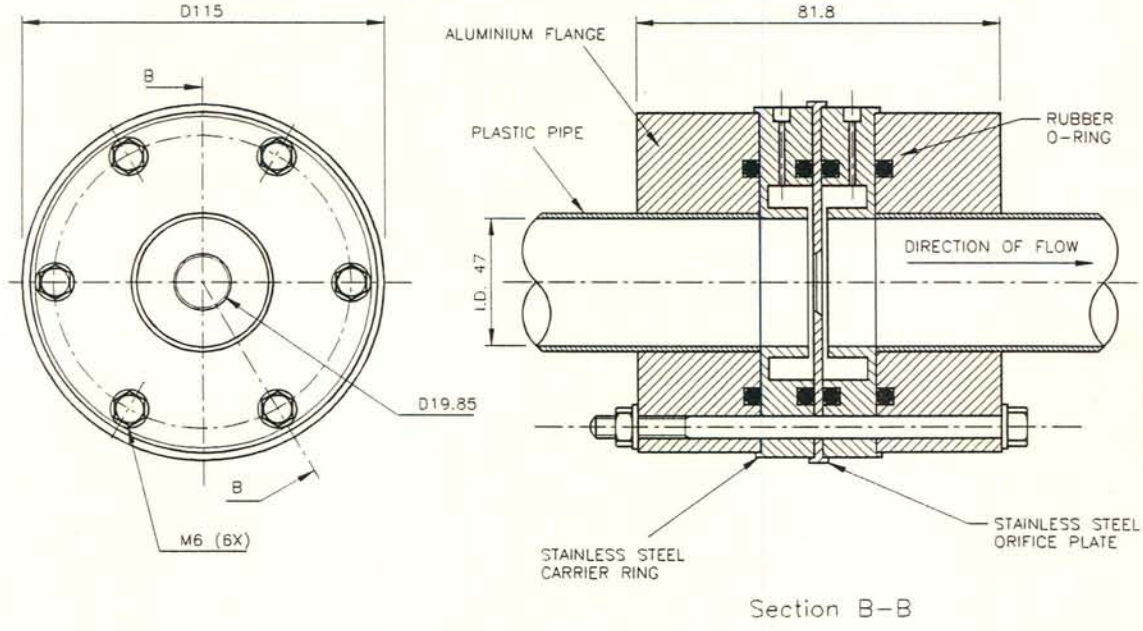

Figure B.3 (d): Assembly drawing of orifice 2 installation.

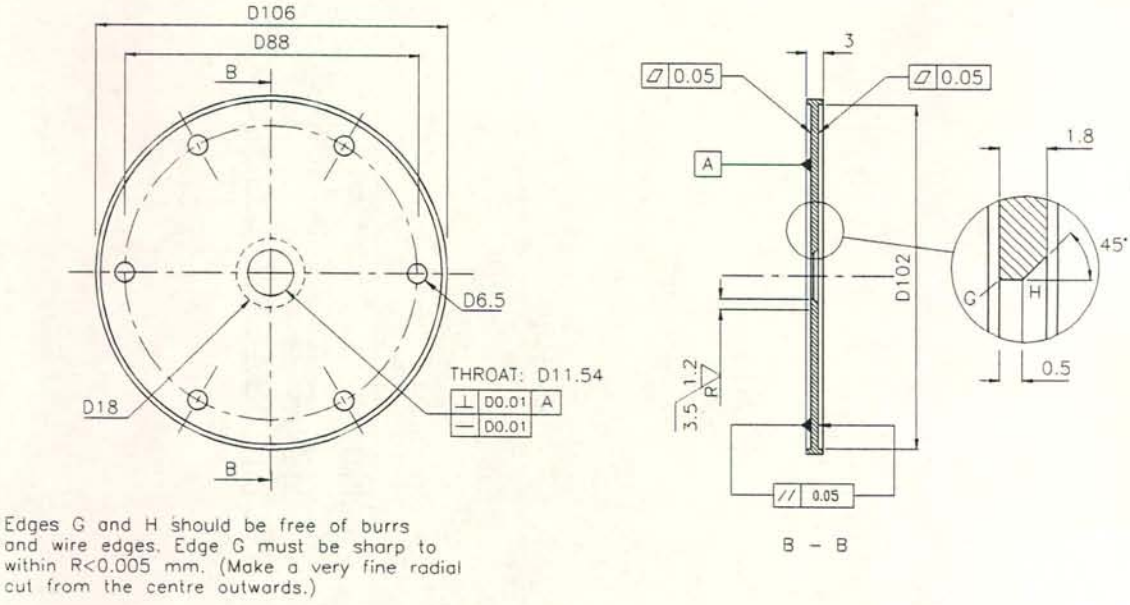

Figure 4 (a): Detail drawing of orifice plate 3.

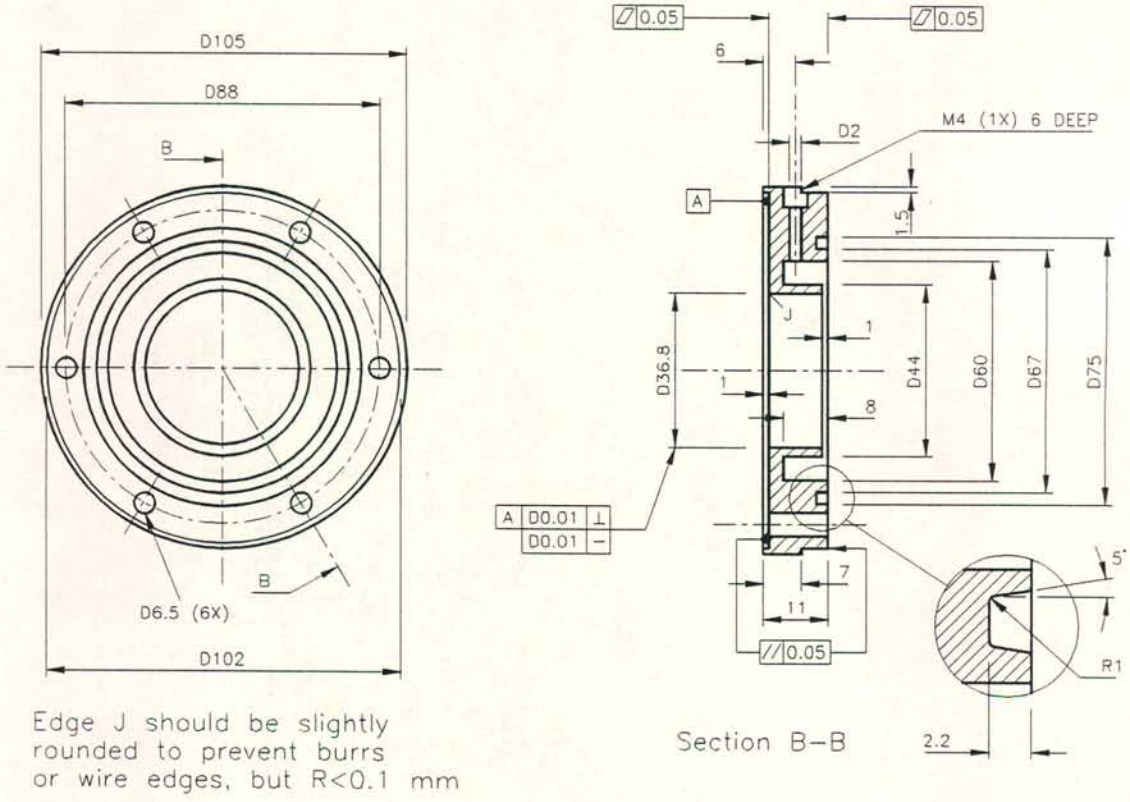

Figure 4 (b): Orifice 3 carrier ring: Detail drawing.

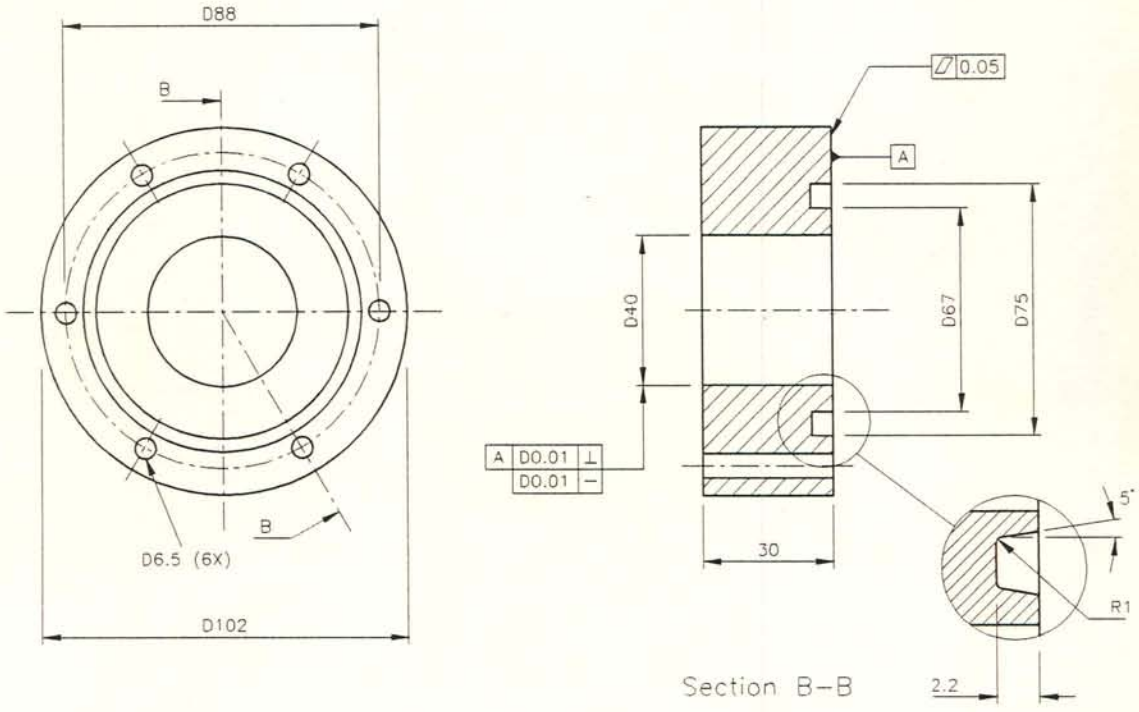

Figure B.4 (c): Orifice 3 pipe flange: Detail drawing.

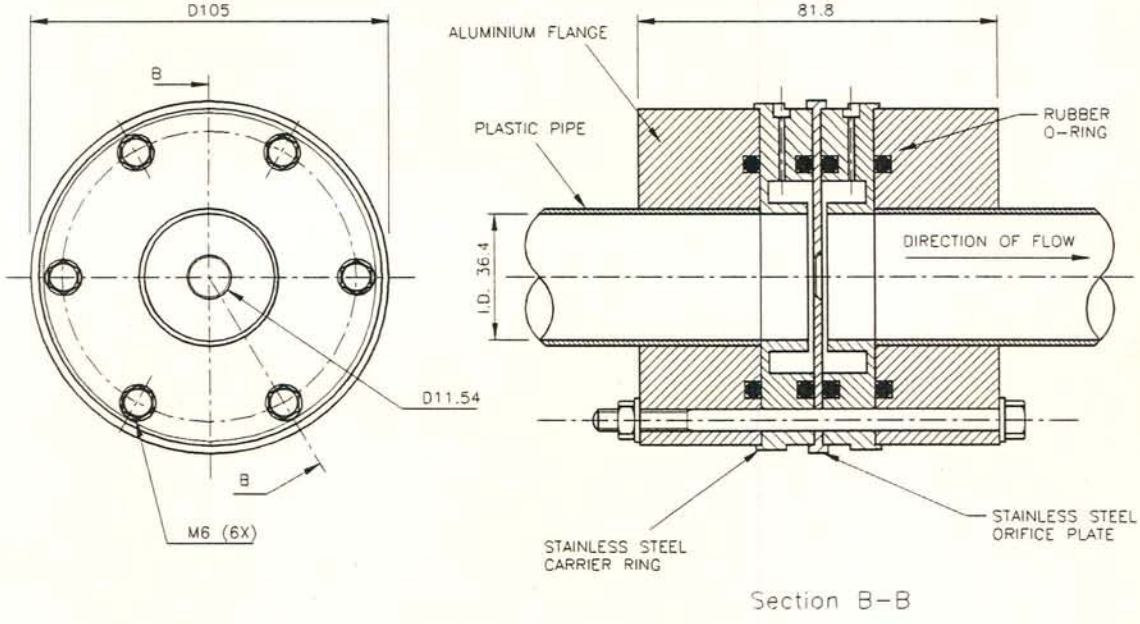

Figure B.4 (d): Assembly drawing of orifice 3 installation.

B.2 Sample calculation of the gas flow rate

The measured data for the sample calculation are:

Gas : Air (single-phase flow)

Orifice : 1

Duct : 1 (See table 3.3 for the dimensions)

p_{amb} = 101300 N/m^2

T_{amb} = 15 °C

T_a = 13.9945 °C (Air temperature at orifice plates and in test section)

$\Delta p_{up\text{-}amb}$ = 3690.5133 N/m^2 (Orifice upstream pressure relative to the ambient pressure)

Δp_o = 1347.6911 N/m^2 (Pressure drop across the orifice plate)

Δp_{2amb} = 2076.9810 N/m^2 (Pressure at point 2 relative to the ambient pressure)

Δp_{23} = 365.0470 N/m^2 (Pressure drop between points 2 and 3)

According to the user's manual of the manometer, the ambient pressure reading must be corrected for temperature effects as follows:

$$p_{amb}\,(\text{corrected}) = p_{amb}\left(1 - 1.62\,x\,10^{-4}\,T_{amb}\right) \tag{B.12}$$

where T_{amb} is in °C.

The corrected ambient pressure is

$$p_{amb}\,(\text{corrected}) = 101300\,x\left(1 - 1.62\,x\,10^{-4}\,x\,15\right)$$
$$101053.8410\ \text{N/m}^2$$

Add the relative upstream orifice pressure to the ambient pressure to obtain the absolute orifice upstream pressure

$$p_{up} = p_{amb} + \Delta p_{up-amb} \tag{B.13}$$
$$= 101053.8410 + 3690.5133 = 104744.3543\ \text{N/m}^2$$

The air temperature in Kelvin is

$$T_a[\mathrm{K}] = T_a[^\circ\mathrm{C}] + 273.15 \qquad (B.14)$$
$$= 13.9945 + 273.15 = 287.1445\ \mathrm{K}$$

According to equation (C.1.1) the air density at the upstream orifice face is

$$\rho_{up} = \frac{104744.3543}{287.08\,x\,287.1445} = 1.2707\ \mathrm{kg/m^3}$$

The air viscosity at the upstream orifice face is evaluated with equation (C.1.3):

$$\mu_{up} = 2.287973\,x\,10^{-6} + 6.259793\,x\,10^{-8}\,x\,287.1445 - 3.131956\,x\,10^{-11}\,x\,287.1445^2$$
$$+ 8.15068\,x\,10^{-15}\,x\,287.1445^3 = 1.7873\,x\,10^{-5}\ \mathrm{kg/ms}$$

According to equation (B.2) the correction factor F_B is

$$F_B = 0.5\,x\,(1.00113 - 1) + 1 = 1.0057$$

The velocity of approach factor is given by equation (B.6):

$$E = \left(1 - 0.6417^4\right)^{-0.5} = 1.0974$$

The expansion factor is according to equation (B.7)

$$\varepsilon = 1 - \left(0.41 + 0.35\,x\,0.6417^4\right)\frac{1347.6911}{1.4021\,x\,104744.3543} = 0.9957$$

Assume a value of 0.6165 for the discharge coefficient C and determine the mass flow rate by employing equation (B.1):

$$m = 1.0057\,x\,0.6165\,x\,1.0974\,x\,0.9957\,x\,\frac{\pi}{4}0.03016^2\,x\,\sqrt{2\,x\,1347.6911\,x\,1.2707}$$
$$= 28.3256\,x\,10^{-3}\ \mathrm{kg/s}$$

The pipe Reynolds number (equation (B.5) is

$$Re_D = \frac{4\,x\,28.3256\,x\,10^{-3}}{\pi\,x\,0.047\,x\,1.7873\,x\,10^{-5}} = 42933$$

Evaluate the discharge coefficient with equation (B.3)

$$C = 0.5959 + 0.0312x0.6417^{2.1} - 0.184x0.6417^{8} + 0.0029x0.6417^{2.5}x\left[\frac{10^6}{42933}\right]^{0.75}$$
$$= 0.6130$$

which is in good agreement with the initial value of C.

The percentage uncertainty for the air mass flow rate is, according to equation (B.11),

$$X_m = 0.6417 + 4x\frac{1347.6911}{104744.3543} + 1.46 = 2.2\ \%$$

The test section pressure is

$$p_2 = p_{amb} + \Delta p_{2amb} \qquad (B.15)$$
$$= 101053.8410 + 2076.981 = 103130.822\ \mathrm{N/m^2}$$

and the corresponding density is, according to equation (C.1.1),

$$\rho_2 = \frac{103130.822}{287.08x287.1445} = 1.2511\,\mathrm{kg/m^3}$$

Inside the test section the air velocity is

$$v = m/(\rho_2 A_{tc}) \qquad (B.16)$$
$$= 28.1661x10^{-3}/(1.2511x1452.9x10^{-6}) = 15.4955\ \mathrm{m/s}$$

The test section Reynolds number is evaluated according to equation (4.3), i.e.

$$Re = 1.2511x15.4955x0.018673/17.873x10^{-6} = 20254$$

The Darcy friction factor is expressed as

$$f = (\Delta p_{23}/L_{23})D_e/(1/2\rho v^2) \qquad (B.17)$$
$$= (365.0470/1.6)x0.018673/(0.5x1.2511x15.4955^2) = 0.0284$$

The friction factor for parallel plates evaluated according equation (4.5) is 0.0291. The percentage difference between the measured and the predicted value is 2.4%.

APPENDIX C

PROPERTIES OF FLUIDS

C.1 The thermophysical properties of dry air from 220 K to 380 K at standard atmospheric pressure (101325 N/m^2)

Density (ideal gas law):

$$\rho_a = p/\left(R_a T\right), \text{ kg/m}^3 \qquad \text{(C.1.1)}$$

where R_a = 287.08 J/kg K

Specific heat [82AN1]:

$$c_{pa} = a + b\,T + c\,T^2 + d\,T^3, \text{ J/kg K} \qquad \text{(C.1.2)}$$

a = 1.045356 x 10^{3}

b = -3.161783 x 10^{-1}

c = 7.083814 x 10^{-4}

d = -2.705209 x 10^{-7}

Dynamic viscosity [82AN1]:

$$\mu_a = a + b\,T + c\,T^2 + d\,T^3, \text{ kg/ms} \qquad \text{(C.1.3)}$$

a = 2.287973 x 10^{-6}

b = 6.259793 x 10^{-8}

c = -3.131955 x 10^{-11}

d = 8.150380 x 10^{-15}

Thermal conductivity:

$$k_a = a + b\,T + c\,T^2 + d\,T^3, \text{ W/m K} \qquad \text{(C.1.4)}$$

a = -4.937787 x10^{-4}

$b = 1.018087 \times 10^{-4}$

$c = -4.627937 \times 10^{-8}$

$d = 1.250603 \times 10^{-15}$

Isentropic coefficient:

$$k_a = 1.4021 \qquad \text{(C.1.5)}$$

C.2 The thermophysical properties of saturated water vapour from 273.15 K to 380 K

Vapour pressure [65GO1]:

$$p_v = 10^{z}, \text{ N/m}^2 \qquad \text{(C.2.1)}$$
$$z = a\,(1-x) + b \log_{10}(x) + c\,[1-10^{d\{(1/x)-1\}}] + e\,(10^{f(1-x)}-1) + g$$
$$x = 273.16/T$$

$a = 1.079586 \times 10$

$b = 5.028080$

$c = 1.504740 \times 10^{-4}$

$d = -8.296920$

$e = 4.287300 \times 10^{-4}$

$f = 4.769550$

$g = 2.786118312$

Dynamic viscosity:

$$\mu_v = a + b\,T + c\,T^2 + d\,T^3, \text{ kg/ms} \qquad \text{(C.2.2)}$$

$a = 2.562435 \times 10^{-6}$

$b = 1.816683 \times 10^{-8}$

$c = 2.579066 \times 10^{-11}$

$d = -1.067299 \times 10^{-14}$

Thermal conductivity [82AN1]:

$$k_v = a + b\,T + c\,T^2 + d\,T^3, \text{ W/m K} \qquad \text{(C.2.3)}$$

$a = 1.3046 \times 10^{-2}$

$b = -3.756191 \times 10^{-5}$

$c = 2.217964 \times 10^{-7}$

$d = -1.111562 \times 10^{-10}$

Vapour density [70UK1]:

$$\rho_v = a + b\,T + c\,T^2 + d\,T^3 + e\,T^4 + f\,T^5 \text{ , kg/m}^3 \qquad \text{(C.2.4)}$$

$a = -4.062329056$

$b = 0.10277044$

$c = -9.76300388 \times 10^{-4}$

$d = 4.475240795 \times 10^{-6}$

$e = -1.004596894 \times 10^{-8}$

$f = 8.9154895 \times 10^{-12}$

C.3 The thermophysical properties of saturated water liquid from 273.15 K to 380 K

Density:

$$\rho_w = (a + b\,T + c\,T^2 + d\,T^6)^{-1} \text{ , kg/m}^3 \qquad \text{(C.3.1)}$$

$a = 1.49343 \times 10^{-3}$

$b = -3.7164 \times 10^{-6}$

$c = 7.09782 \times 10^{-9}$

$d = -1.90321 \times 10^{-20}$

Specific heat:

$$c_{pw} = a + b\,T + c\,T^2 + d\,T^3 \text{ , J/kg K} \qquad \text{(C.3.2)}$$

$a = 8.15599 \times 10^{3}$

$b = -2.80627 \times 10$

$c = 5.11283 \times 10^{-2}$

$d = -2.17582 \times 10^{-13}$

Dynamic viscosity [82AN1]:

$$\mu_w = a\ 10^{\,b/(T-c)}\ \text{, kg/ms} \qquad \text{(C.3.3)}$$

$a = 2.414 \times 10^{-5}$

$b = 247.8$

$c = 140$

Thermal conductivity:

$$k_w = a + b\,T + c\,T^2 + d\,T^3\ \text{, W/m K} \qquad \text{(C.3.4)}$$

$a = -6.14255 \times 10^{-1}$

$b = 6.9962 \times 10^{-3}$

$c = -1.01075 \times 10^{-5}$

$d = 4.74737 \times 10^{-12}$

Latent heat of vaporisation:

$$i_{fgw} = a + b\,T + c\,T^2 + d\,T^3\ \text{, J/kg} \qquad \text{(C.3.5)}$$

$a = -3.4831814 \times 10^{6}$

$b = -5.8627703 \times 10^{3}$

$c = 12.139568$

$d = -1.40290431 \times 10^{-2}$

Surface tension [70UK1]:

$$\sigma_w = a + b\,T + c\,T^2 + d\,T^3\ \text{, N/m} \qquad \text{(C.3.6)}$$

$a = 5.148103 \times 10^{-2}$

$b = 3.998714 \times 10^{-4}$

$c = -1.4721869 \times 10^{-6}$

$d = 1.21405335 \times 10^{-9}$

C.4 The thermophysical properties of helium from 144 K to 477 K at standard atmospheric pressure (101325 N / m²)

Density (ideal gas law):

$$\rho_{He} = p/R_{He}T \text{ , kg/m}^3 \qquad \text{(C.4.1)}$$

where $R_{He} = 2078.2$ J / kg K

Dynamic viscosity [89HO1]:

$$\mu_{He} = a + b\,T + c\,T^2 \text{ , kg/ms} \qquad \text{(C.4.2)}$$

$a = 4.54 \times 10^{-6}$

$b = 5.976 \times 10^{-8}$

$c = 2.452 \times 10^{-11}$

Isentropic coefficient:

$$k_{He} = 1.667 \qquad \text{(C.4.3)}$$

C.5 The thermophysical properties of argon from 225 K to 300 K at standard atmospheric pressure (101325 N / m²)

Density (ideal gas law):

$$\rho_{Ar} = p/R_{Ar}T \text{ , kg/m}^3 \qquad \text{(C.5.1)}$$

where $R_{Ar} = 208.15$ J/kg K

Dynamic viscosity [89HO1]:

$$\mu_{Ar} = a + b\,T + c\,T^2 \text{ , kg/ms} \qquad \text{(C.5.2)}$$

$a = -1.467 \times 10^{-6}$

$b = 9.976 \times 10^{-8}$

$c = -6.4 \times 10^{-11}$

Isentropic coefficient:

$$k_{Ar} = 1.667 \qquad \text{(C.5.3)}$$

C.6 The thermophysical properties of hydrogen from 150 K to 500 K at standard atmospheric pressure (101325 N/m^2)

Density (ideal gas law):

$$\rho_{Hy} = p/R_{Hy}T, \text{ kg/m}^3 \qquad \text{(C.6.1)}$$

where $R_{Hy} = 4124.2$ J/kg K

Dynamic viscosity [89HO1]:

$$\mu_{Hy} = a + b\,T + c\,T^2 + d\,T^3 + e\,T^4, \text{ kg/ms} \qquad \text{(C.6.2)}$$

$a = 1.099077 \times 10^{-6}$

$b = 3.554584 \times 10^{-8}$

$c = -4.432311 \times 10^{-11}$

$d = 5.202525 \times 10^{-14}$

$e = -2.651515 \times 10^{-17}$

Isentropic coefficient:

$$k_{Hy} = 1.409 \qquad \text{(C.6.3)}$$

C.7 The thermophysical properties of methyl alcohol (CH_3OH)

Density [84GR1]:

$$\rho = a + b\,T + c\,T^2 + d\,T^3, \text{ kg/m}^3 \text{ (273.15 K to 293.15 K)} \qquad \text{(C.7.1)}$$

$a = -3.018574 \times 10^{4}$

$b = 3.305739 \times 10^{2}$

$c = -1.171741$

$d = 1.380000 \times 10^{-3}$

Dynamic viscosity [92LI1]:

$$\mu = a + b\,T + c\,T^2 + d\,T^3 \text{, kg/ms (228.62 K to 323.15 K)} \qquad \text{(C.7.2)}$$

$a = 5.367041 \times 10^{-2}$

$b = -4.970945 \times 10^{-4}$

$c = 1.565356 \times 10^{-6}$

$d = -1.662434 \times 10^{-9}$

Surface tension [92LI1]:

$$\sigma = a + b\,T + c\,T^2 \text{, N/m (273.15 K to 323.15 K)} \qquad \text{(C.7.3)}$$

$a = 6.885000 \times 10^{-2}$

$b = -2.261367 \times 10^{-4}$

$c = 2.333333 \times 10^{-7}$

C.8 The thermophysical properties of isopropyl alcohol (C_3H_7OH)

Density [84GR1]:

$$\rho = a + b\,T + c\,T^2 + d\,T^3 \text{, kg/m}^3 \text{ (273.15 K to 303.15 K)} \qquad \text{(C.8.1)}$$

$a = -6.755164 \times 10^{2}$

$b = 1.653948 \times 10^{1}$

$c = -5.896333 \times 10^{-2}$

$d = 6.666667 \times 10^{-5}$

Dynamic viscosity [92LI1]:

$$\mu = a + b\,T \text{, kg/ms (288.15 K to 303.15 K)} \qquad \text{(C.8.2)}$$

$a = 2.379890 \times 10^{-2}$

$b = -7.2667 \times 10^{-5}$

Surface tension [92LI1]:

$$\sigma = 0.0217 \text{ N/m at } 293.15 \text{ K} \qquad \text{(C.8.3)}$$

APPENDIX D

PRESSURE DROP DATA FOR THE LONG CONFIGURATION INCLINED AT 60° TO THE HORIZONTAL

D.1 Two-phase pressure gradient and entrance pressure drop for the 50 mm duct (W_t = 10 mm)

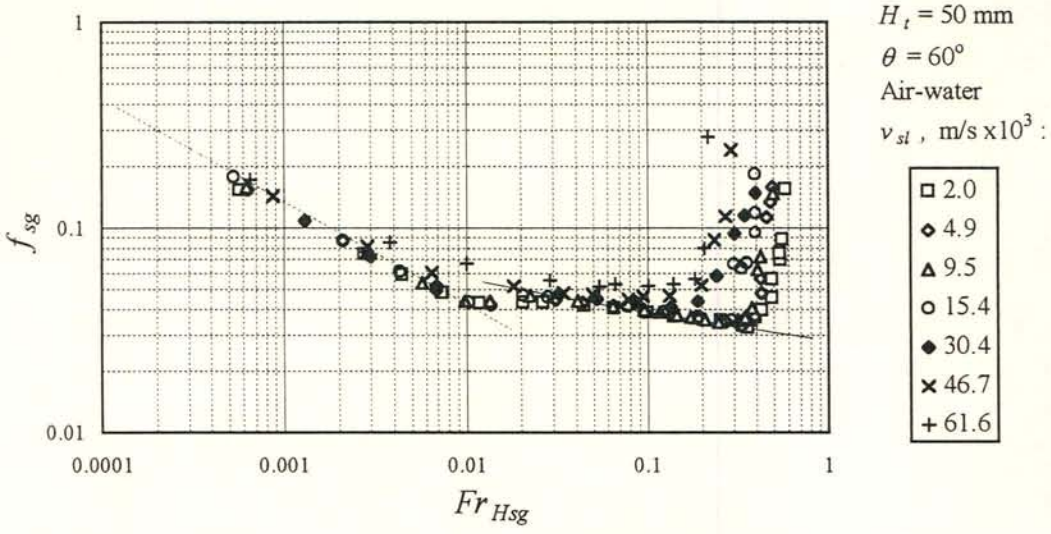

Figure D.1 (a): Friction factor for air-water plotted against the superficial gas densimetric Froude number. Broken and solid line: Single-phase laminar and turbulent friction factor.

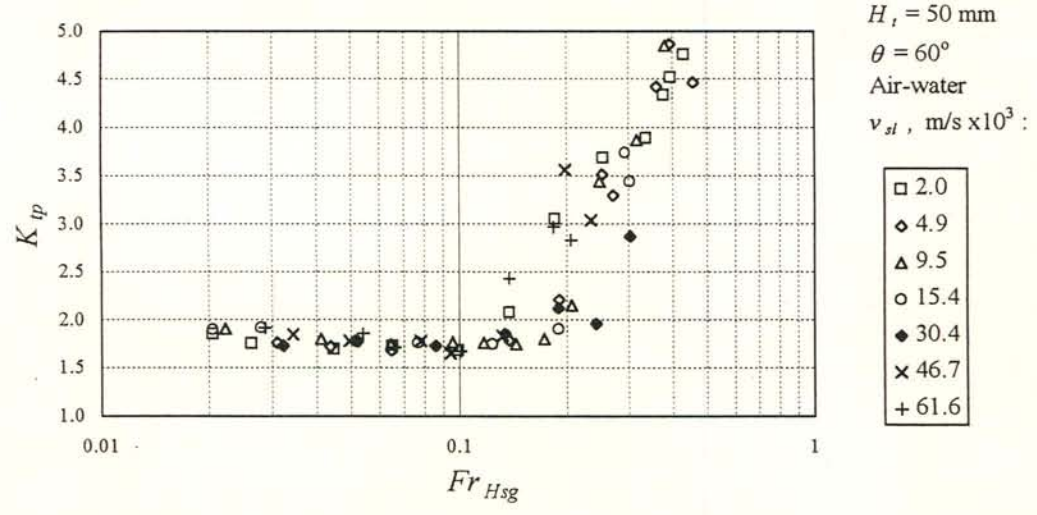

Figure D.1 (b): The two-phase entrance pressure drop coefficient for air-water plotted against the superficial gas densimetric Froude number. The gas flow is fully turbulent.

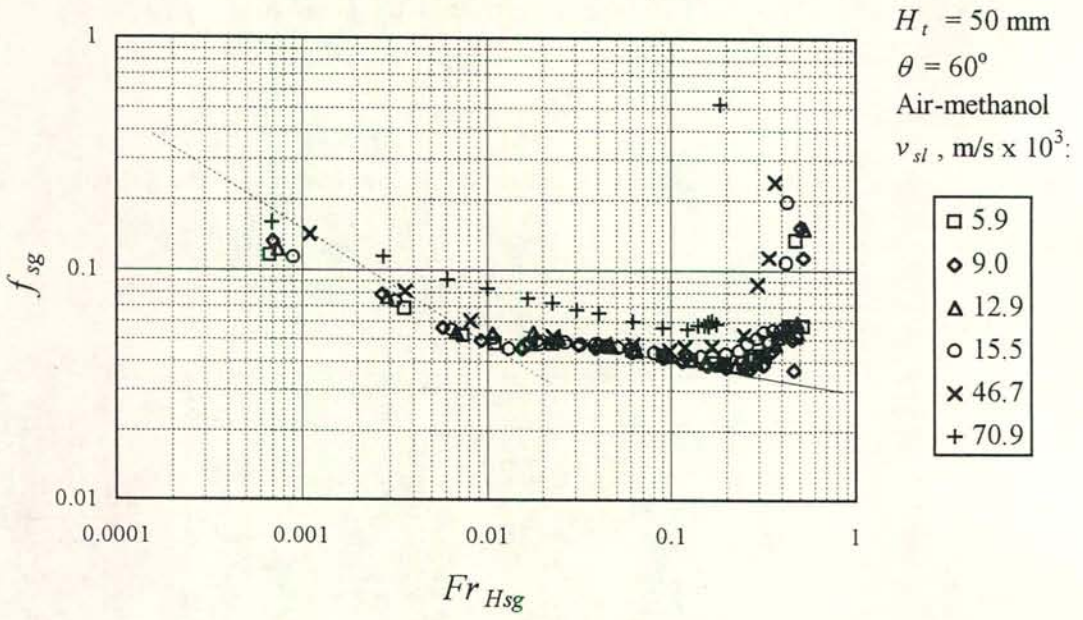

Figure D.2 (a): Friction factor for air-methanol plotted against the superficial gas densimetric Froude number. Broken and solid line: Single-phase laminar and turbulent friction factor.

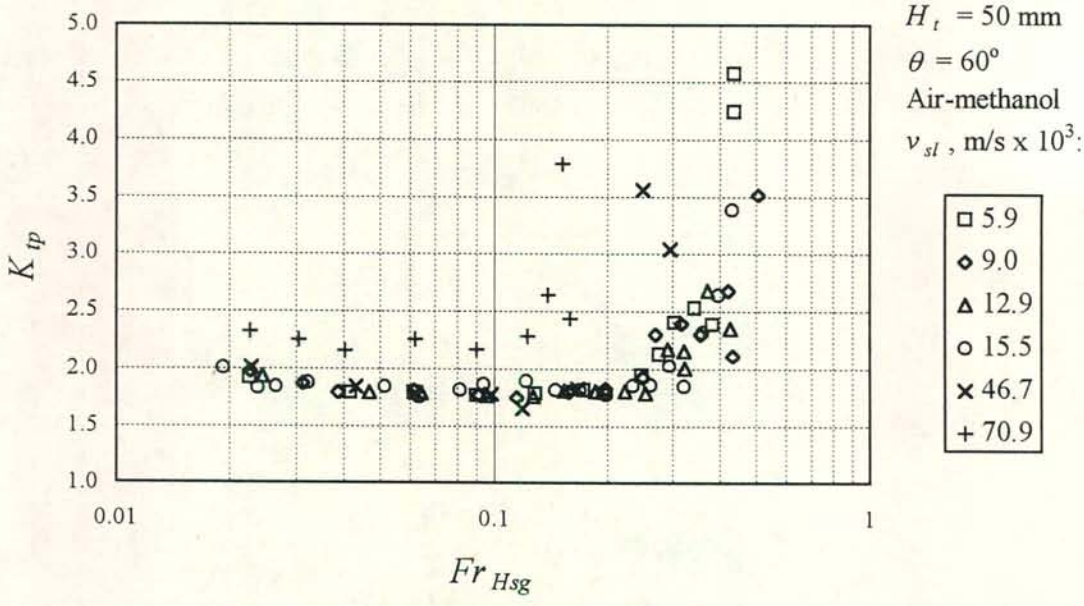

Figure D.2 (b): Two-phase entrance pressure drop coefficient for air-methanol plotted against the superficial gas densimetric Froude number. The gas flow is fully turbulent.

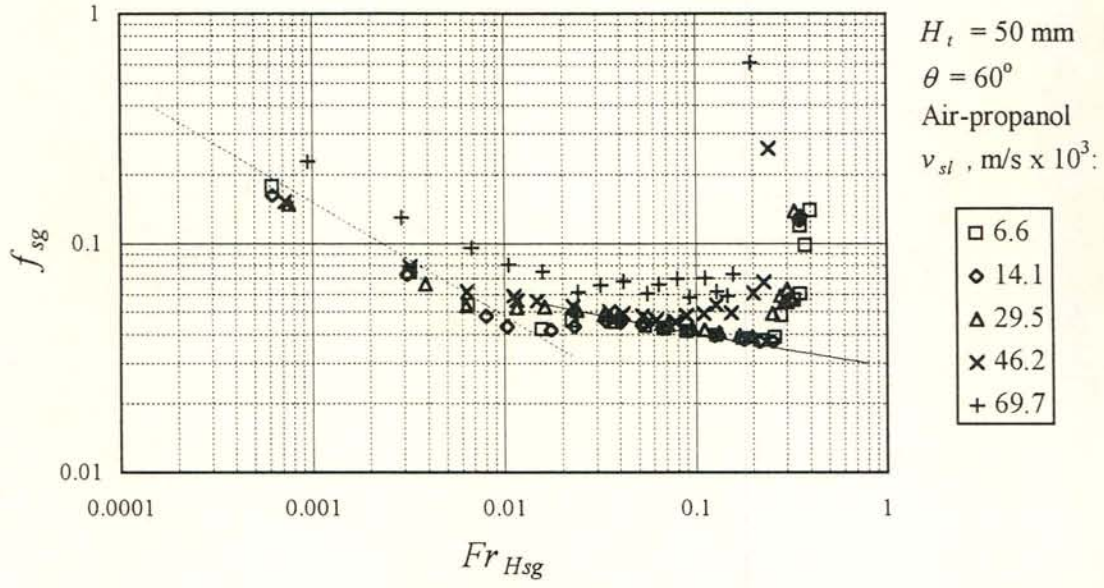

Figure D.3 (a): Friction factor for air-propanol plotted against the superficial gas densimetric Froude number. Broken and solid line: Single-phase laminar and turbulent friction factor.

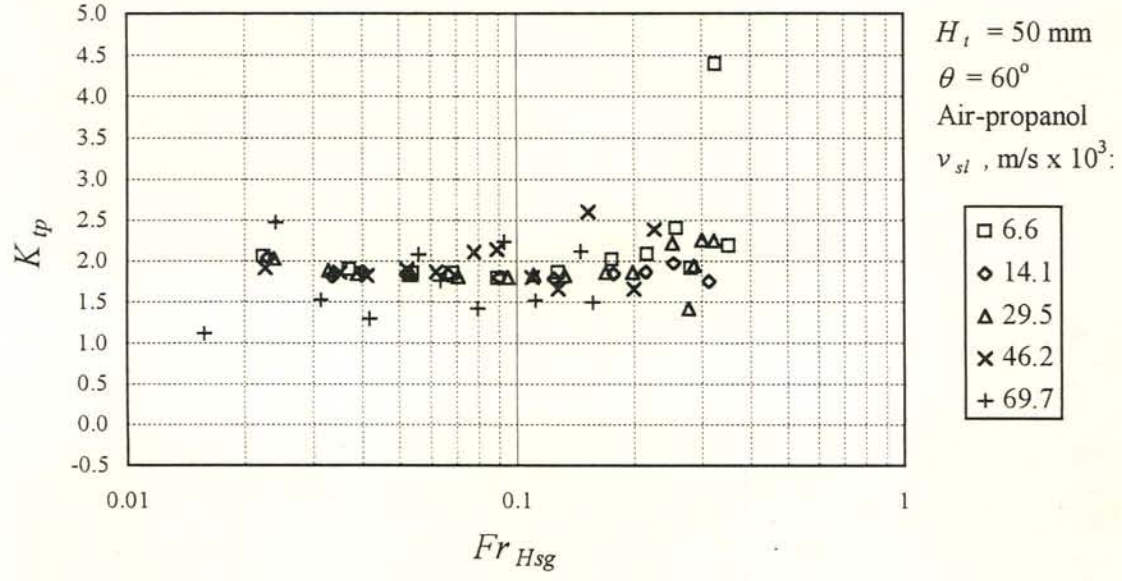

Figure D.3 (b): Two-phase entrance pressure drop coefficient for air-propanol plotted against the superficial gas densimetric Froude number. The gas flow is fully turbulent.

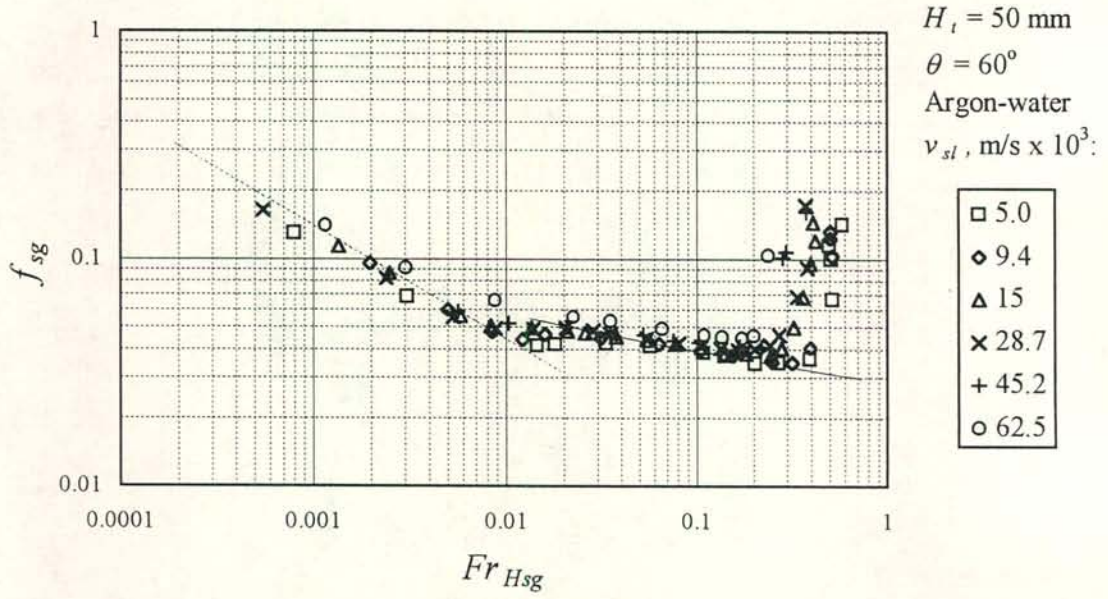

Figure D.4 (a): Friction factor for argon-water plotted against the superficial gas densimetric Froude number. Broken and solid line: Single-phase laminar and turbulent friction factor.

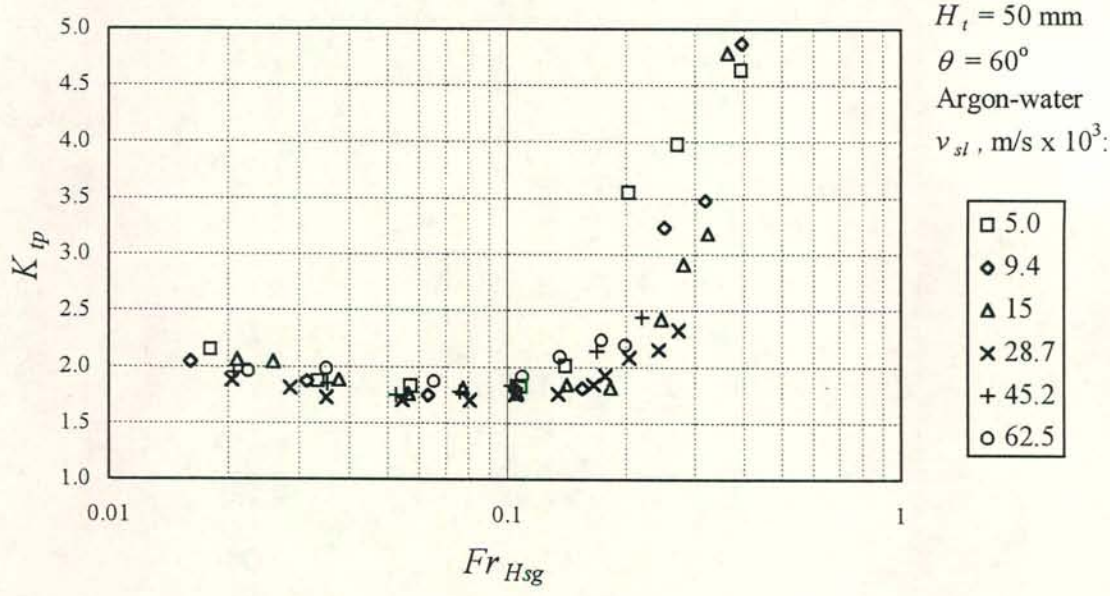

Figure D.4 (b): Two-phase entrance pressure drop coefficient for argon-water plotted against the superficial gas densimetric Froude number. The gas flow is fully turbulent.

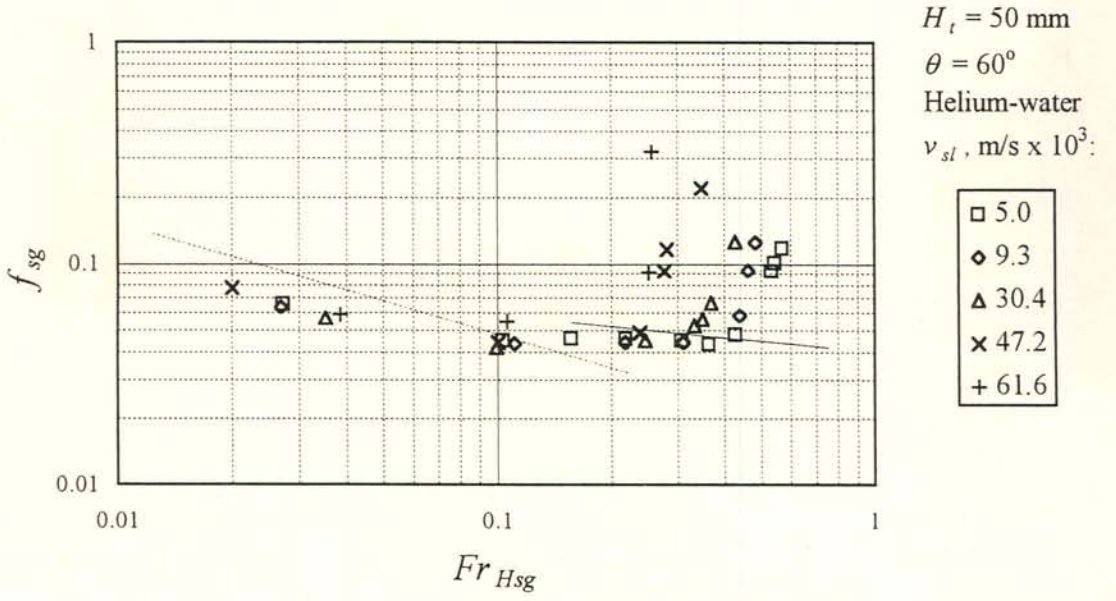

Figure D.5 (a): Friction factor for helium-water plotted against the superficial gas densimetric Froude number. Broken and solid line: Single-phase laminar and turbulent friction factor.

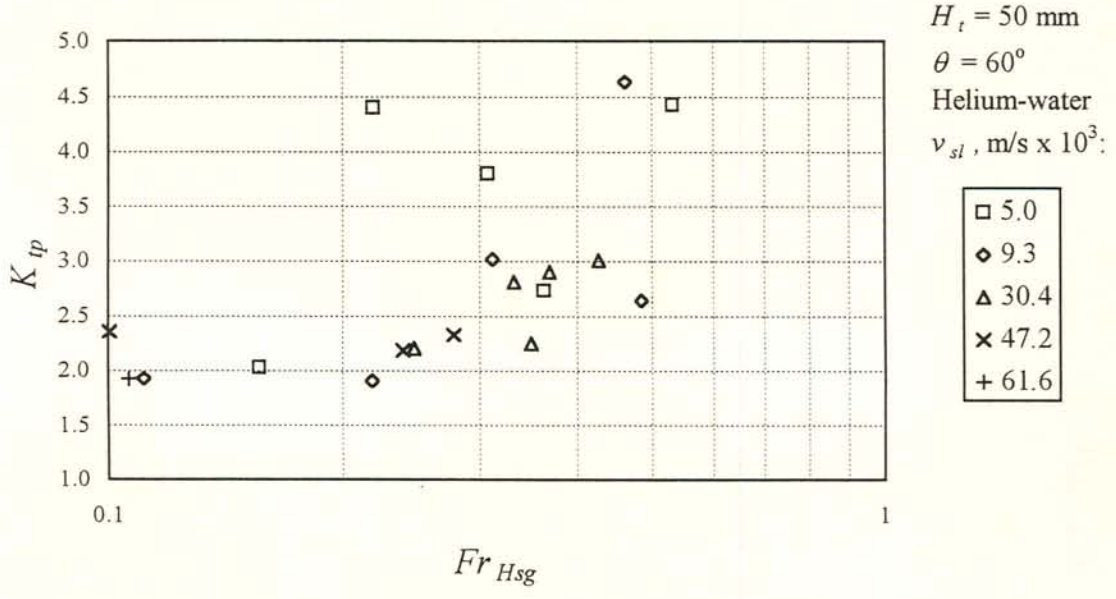

Figure D.5 (b): Two-phase entrance pressure drop coefficient for helium-water plotted against the superficial gas densimetric Froude number. The gas flow is fully turbulent.

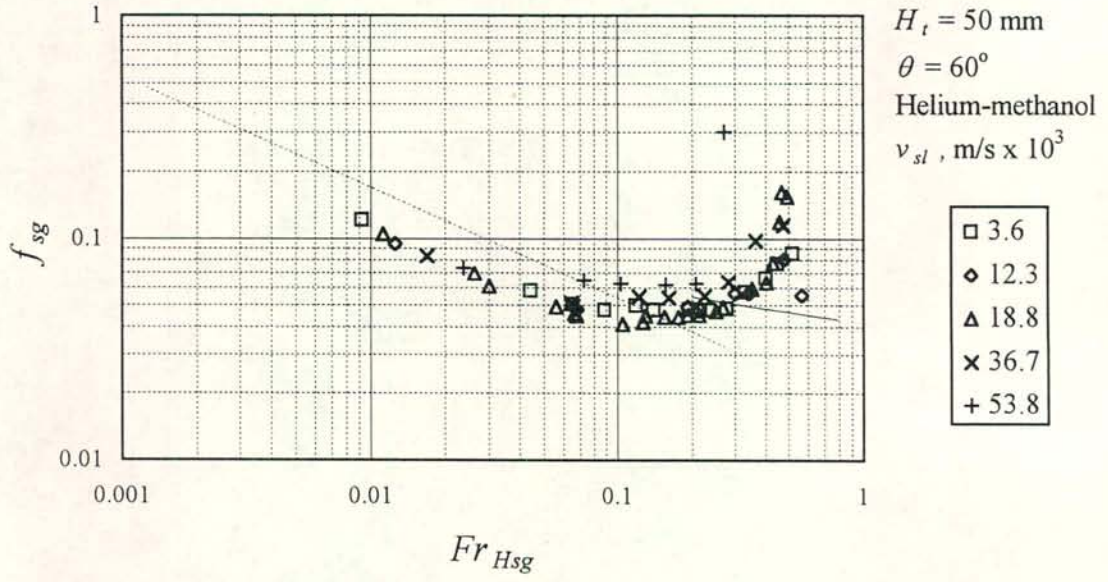

Figure D.6 (a): Friction factor for helium-methanol plotted against the superficial gas densimetric Froude number. Broken and solid line: Single-phase laminar and turbulent friction factor.

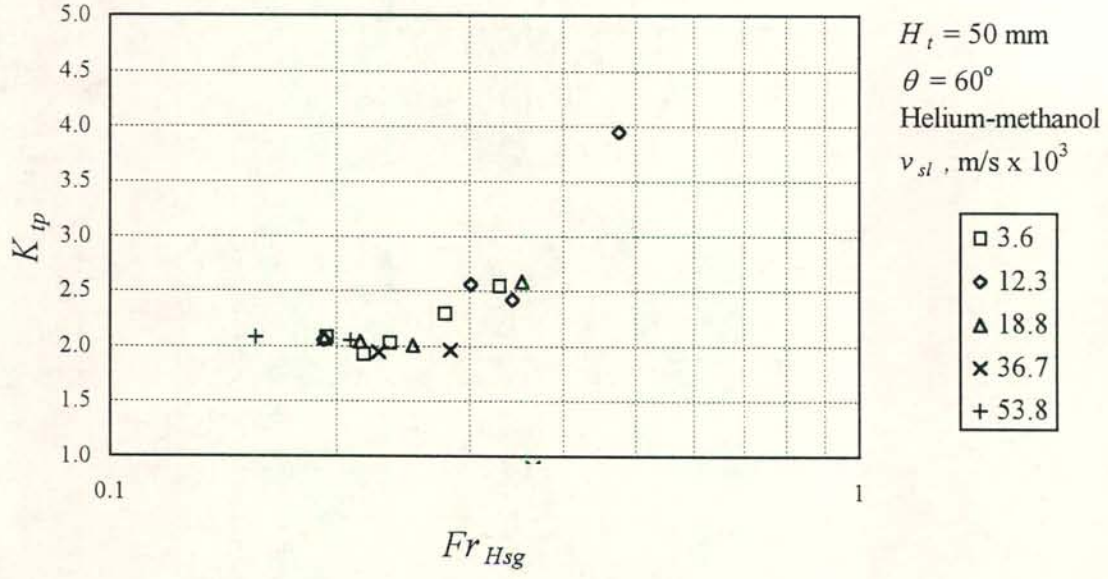

Figure D.6 (b): Two-phase entrance pressure drop coefficient for helium-methanol plotted against the superficial gas densimetric Froude number. The gas flow is fully turbulent.

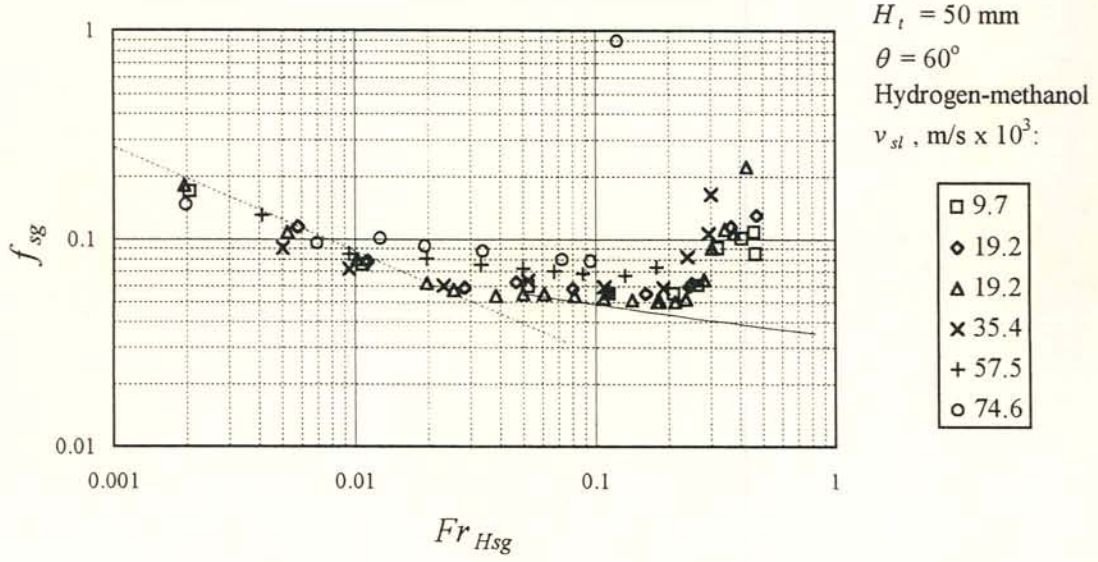

Figure D.7 (a): Friction factor for hydrogen-methanol plotted against the superficial gas densimetric Froude number. Broken and solid line: Single-phase laminar and turbulent friction factor.

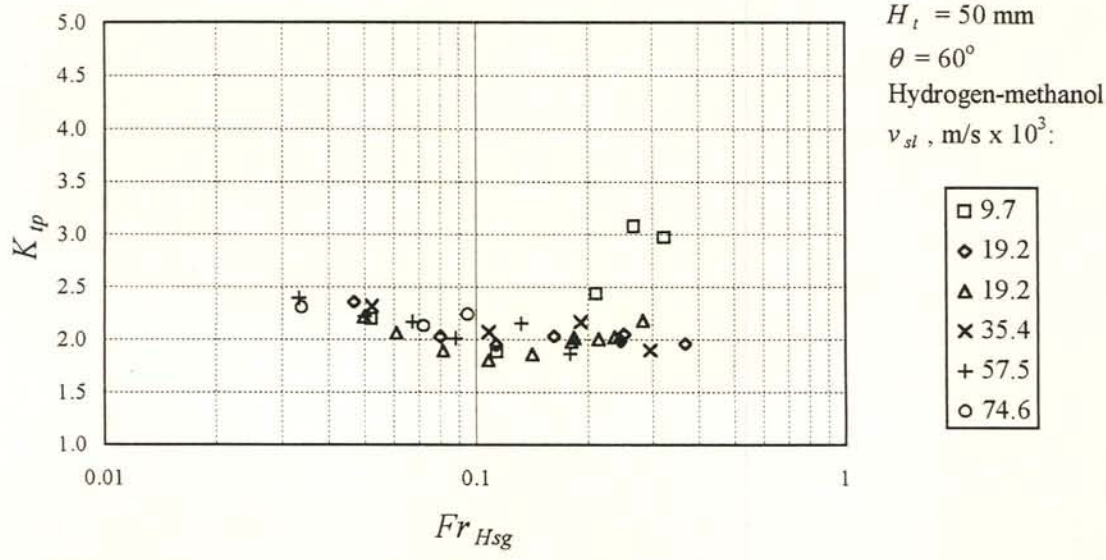

Figure D.7 (b): Two-phase entrance pressure drop coefficient for hydrogen-methanol plotted against the superficial gas densimetric Froude number. The gas flow is fully turbulent.

D.2 Two-phase pressure gradient and entrance pressure drop for the 100 mm (H_t) duct

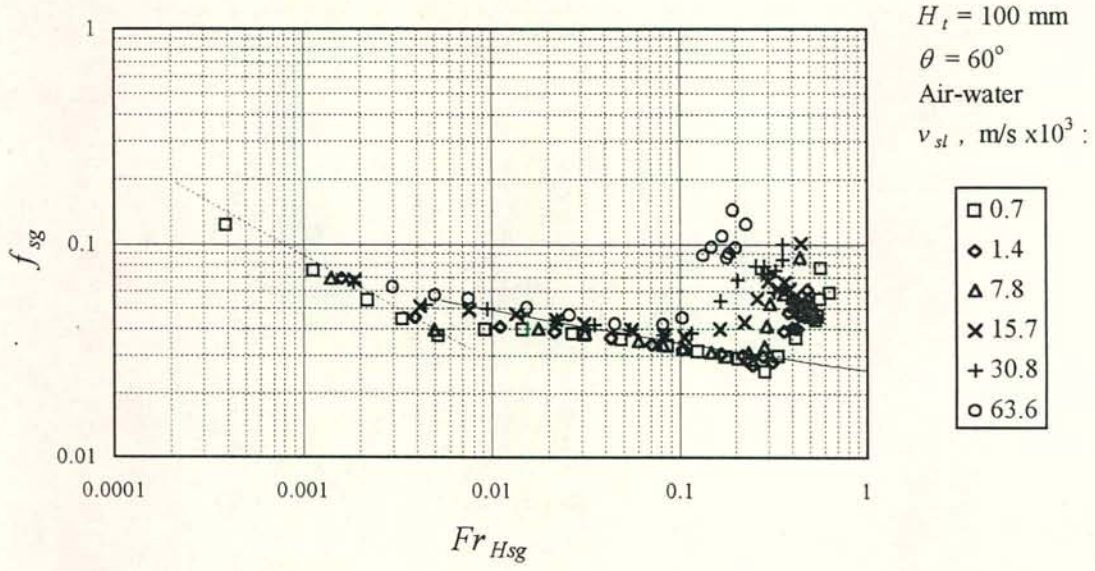

Figure D.8 (a): Friction factor for air-water plotted against the superficial gas densimetric Froude number. Broken and solid line: Single-phase laminar and turbulent friction factor.

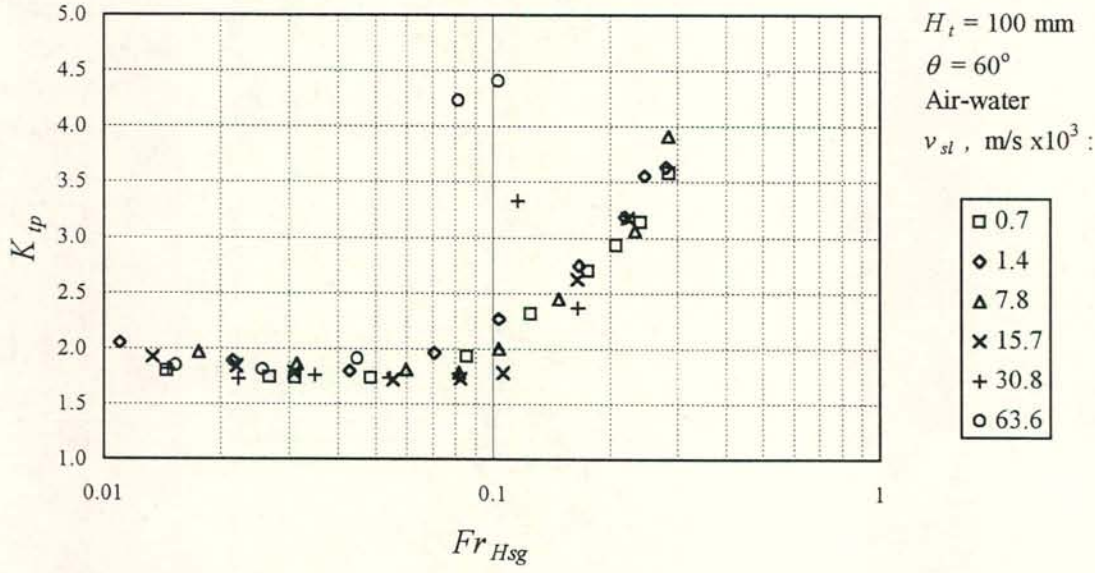

Figure D.8 (b): Two-phase entrance pressure drop coefficient for air-water plotted against the superficial gas densimetric Froude number. The gas flow is fully turbulent.

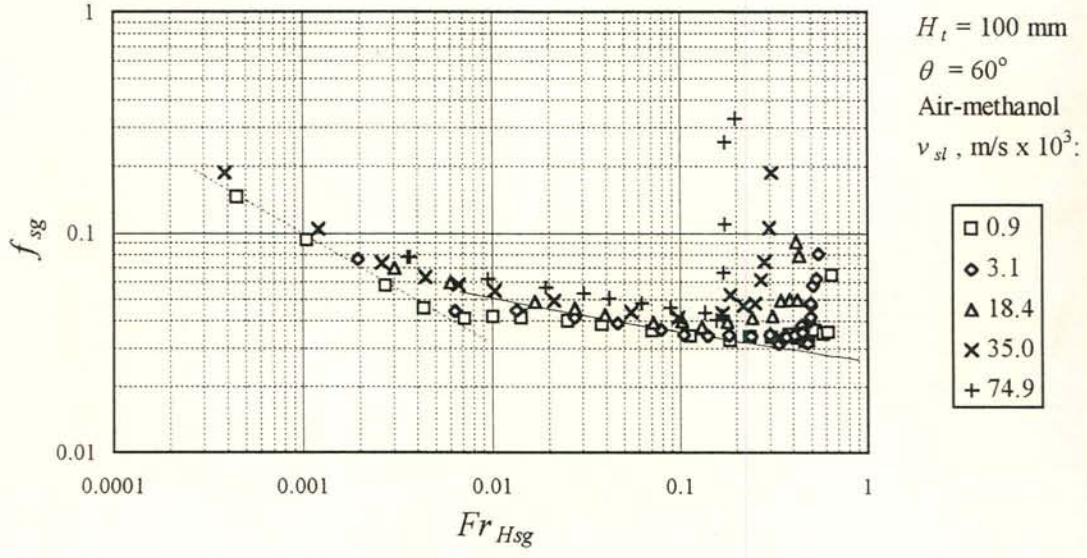

Figure D.9 (a): Friction factor for air-methanol plotted against the superficial gas densimetric Froude number. Broken and solid line: Single-phase laminar and turbulent friction factor.

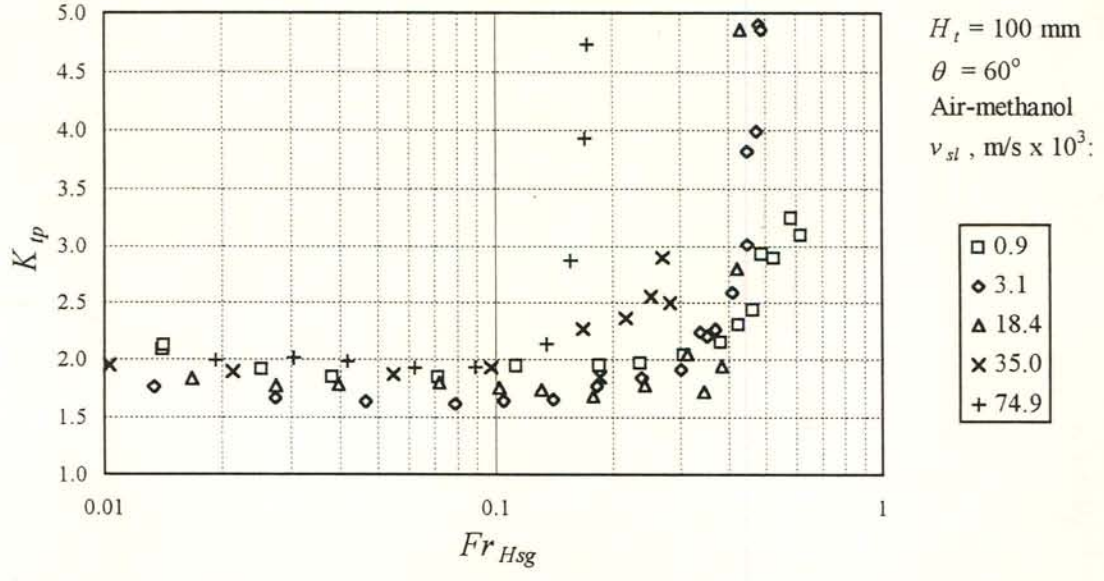

Figure D.9 (b): Two-phase entrance pressure drop coefficient for air-methanol plotted against the superficial gas densimetric Froude number. The gas flow is fully turbulent.

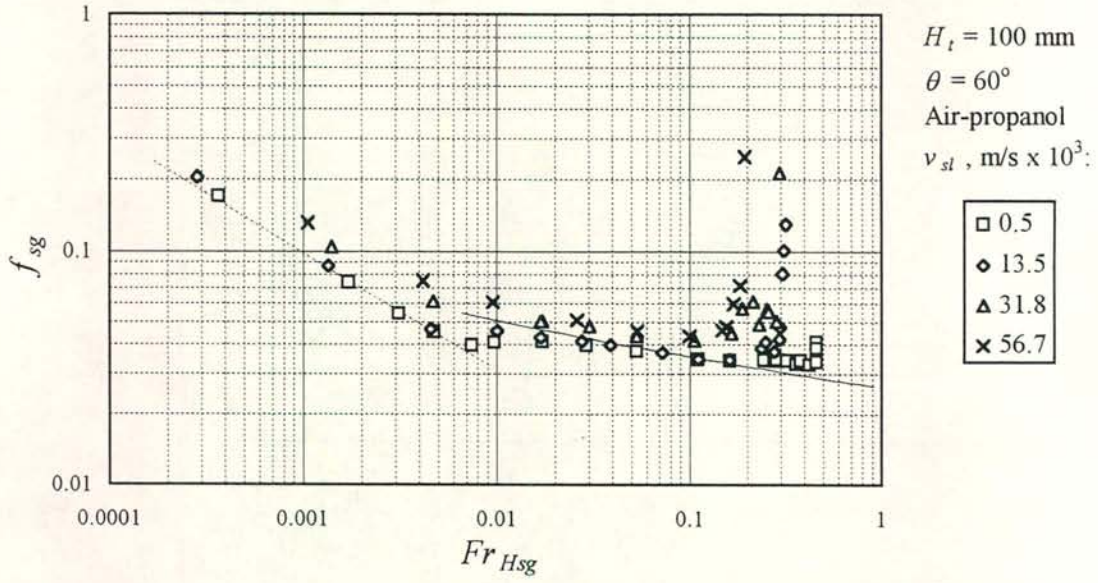

Figure D.10 (a): Friction factor for air-propanol plotted against the superficial gas densimetric Froude number. Broken and solid line: Single-phase laminar and turbulent friction factor.

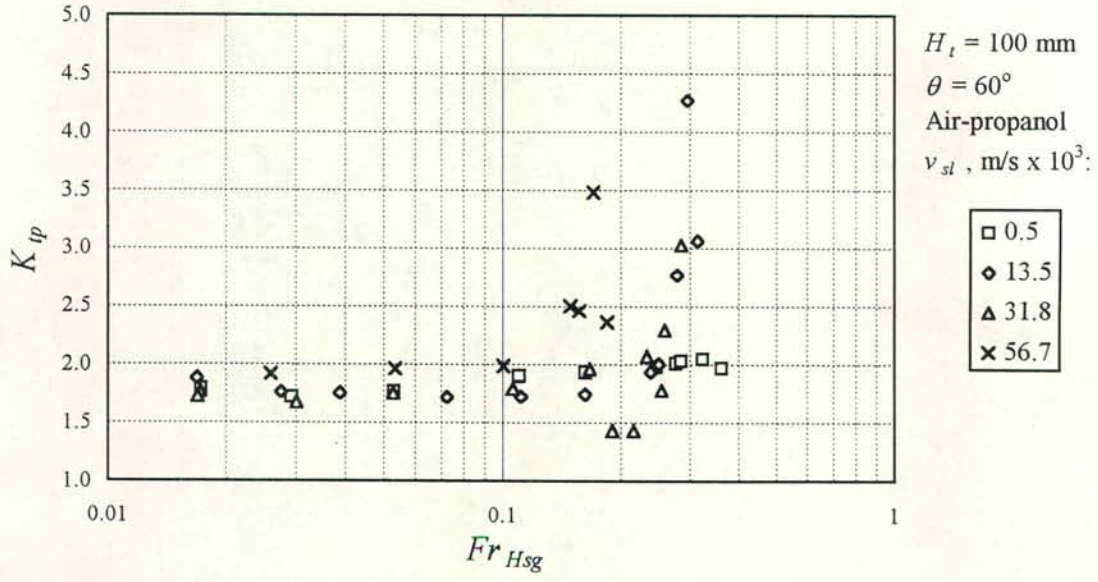

Figure D.10 (b): Two-phase entrance pressure drop coefficient for air-propanol plotted against the superficial gas densimetric Froude number. The gas flow is fully turbulent.

D.3 Two-phase pressure gradient and entrance pressure drop for the 150 mm (H_t) duct

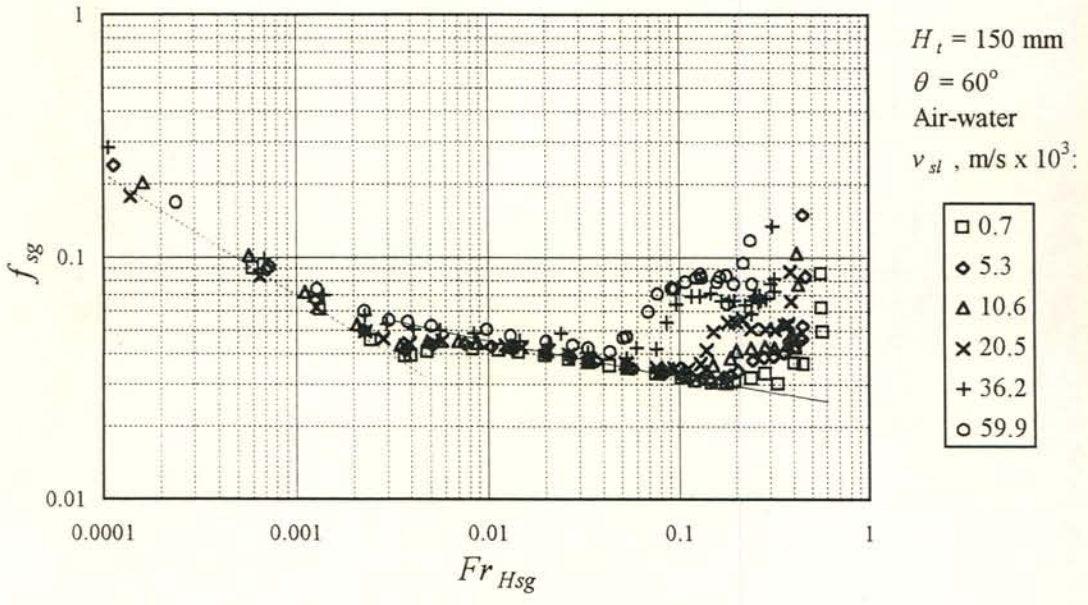

Figure D.11 (a): Friction factor for air-water plotted against the superficial gas densimetric Froude number. Broken and solid line: Single-phase laminar and turbulent friction factor.

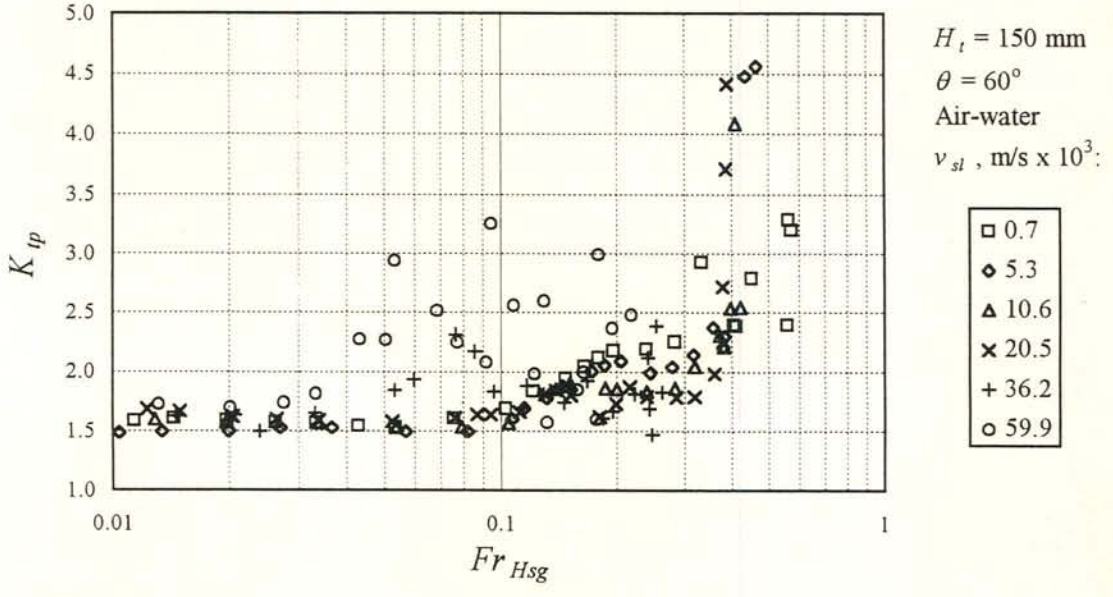

Figure D.11 (b): Two-phase entrance pressure drop coefficient for air-water plotted against the superficial gas densimetric Froude number. The gas flow is fully turbulent.

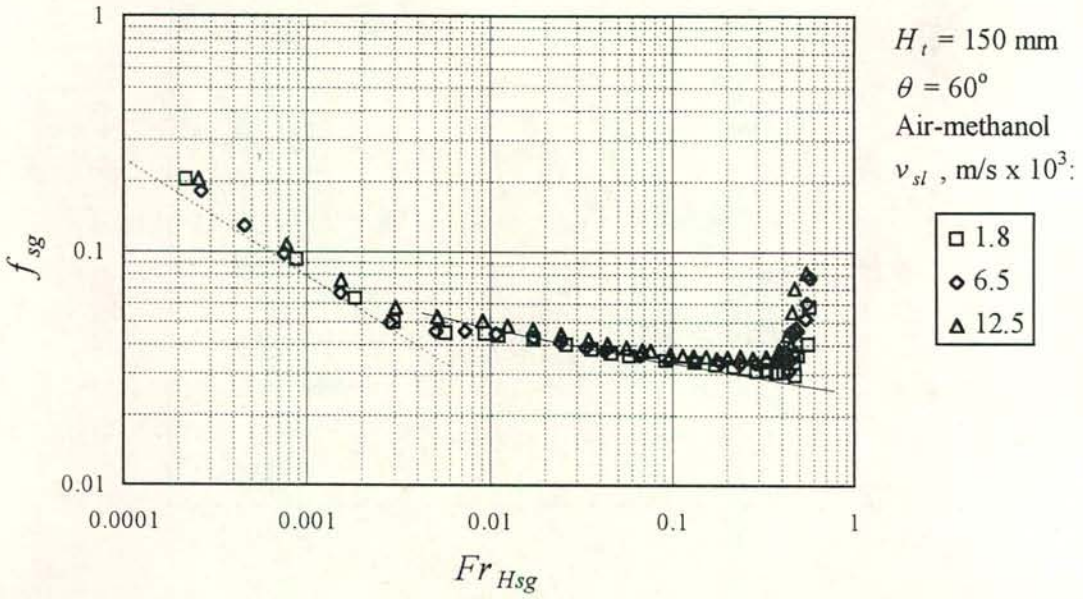

Figure D.12 (a): Friction factor for air-methanol plotted against the superficial gas densimetric Froude number. Broken and solid line: Single-phase laminar and turbulent friction factor.

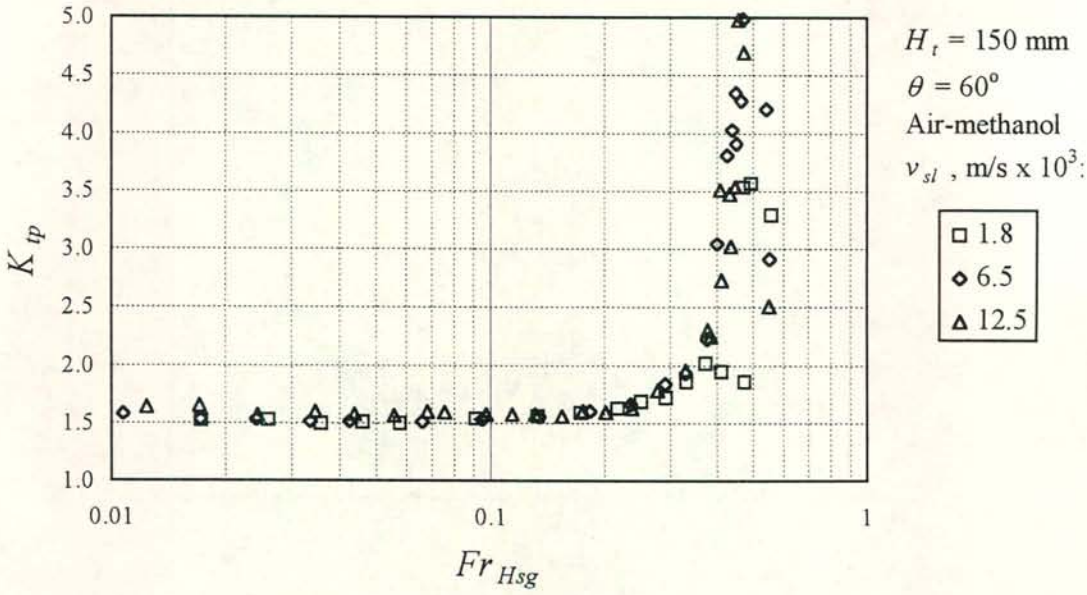

Figure D.12 (b): Two-phase entrance pressure drop coefficient for air-methanol plotted against the superficial gas densimetric Froude number. The gas flow is fully turbulent.

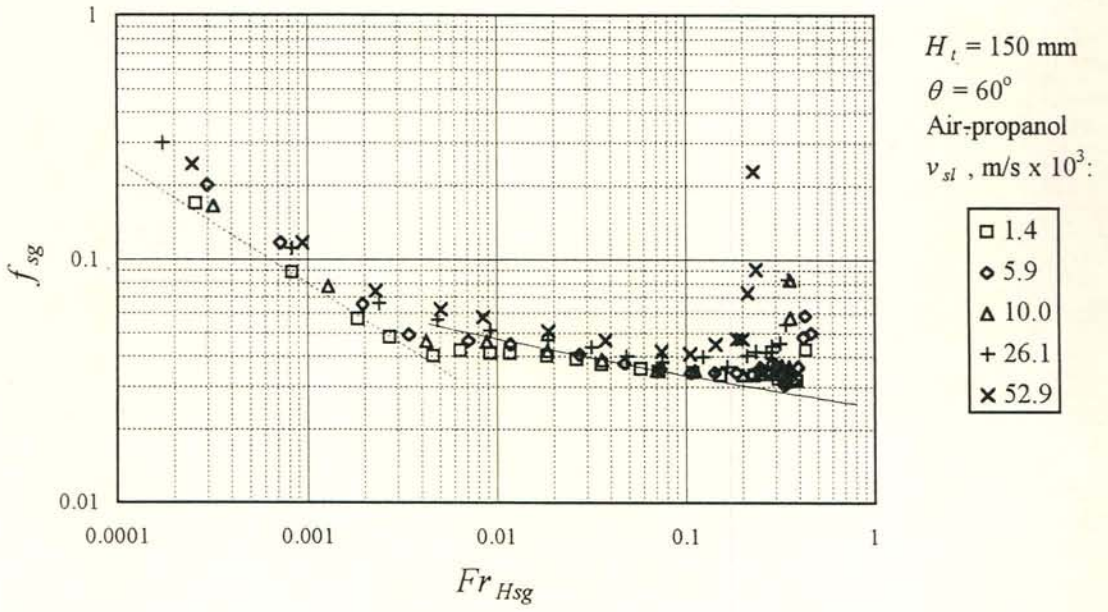

Figure D.13 (a): Friction factor for air-propanol plotted against the superficial gas densimetric Froude number. Broken and solid line: Single-phase laminar and turbulent friction factor.

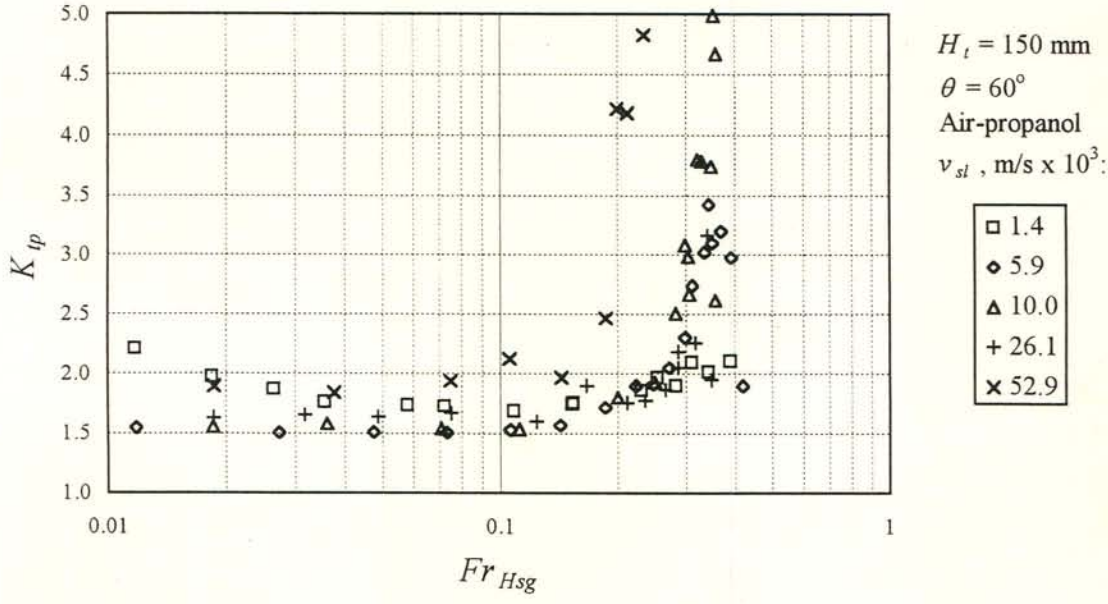

Figure D.13 (b): Two-phase entrance pressure drop coefficient for air-propanol plotted against the superficial gas densimetric Froude number. The gas flow is fully turbulent.

APPENDIX E

PRESSURE DROP DATA FOR THE SHORT CONFIGURATION

E.1 Air-water pressure gradient and entrance pressure drop for the 50 mm duct (W_t = 10 mm)

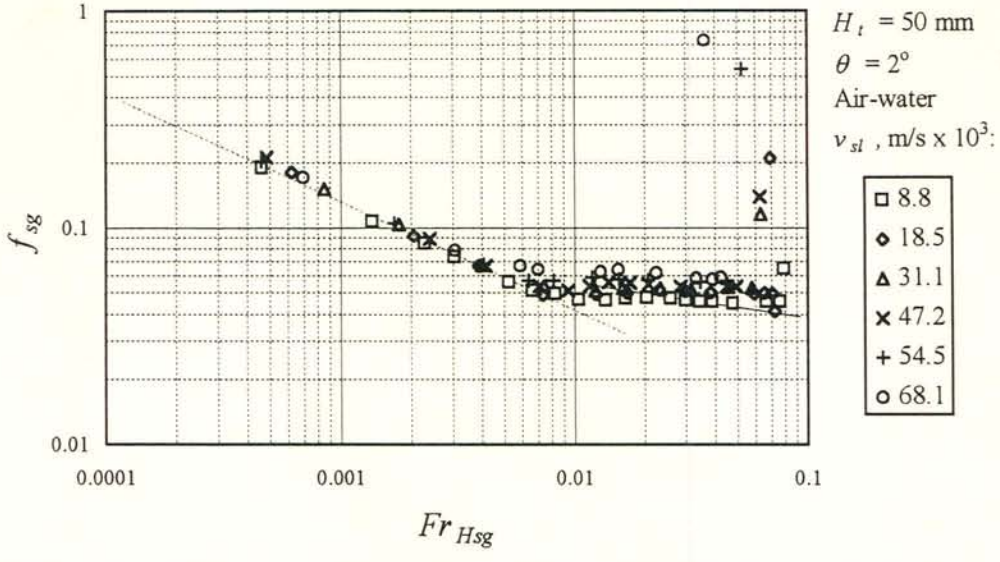

Figure E.1 (a): Friction factor for air-water flow at 2° inclination plotted against the superficial gas densimetric Froude number. Broken and solid line: Single-phase laminar and turbulent friction factor.

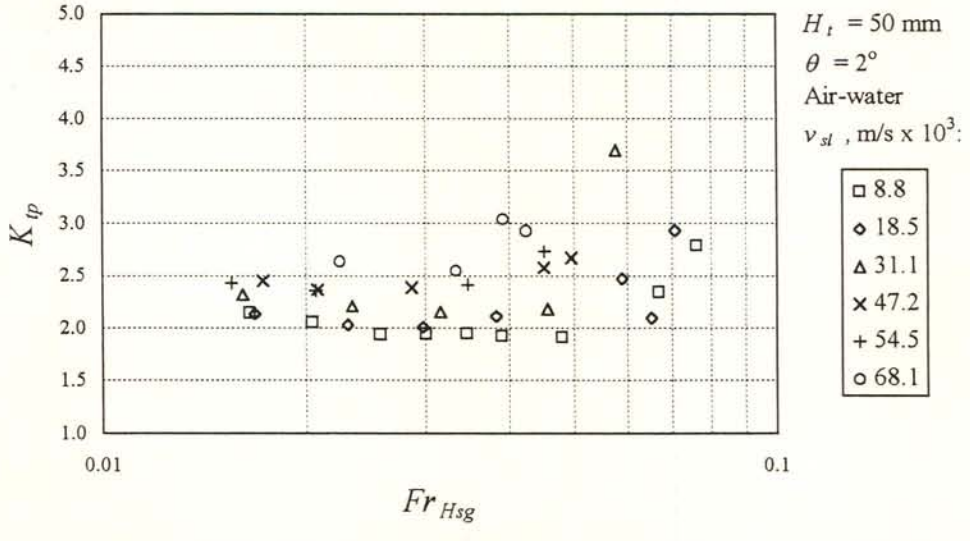

Figure E.1 (b): Two-phase entrance pressure drop coefficient for air-water flow at 2° inclination plotted against the superficial gas densimetric Froude number. The gas flow is fully turbulent.

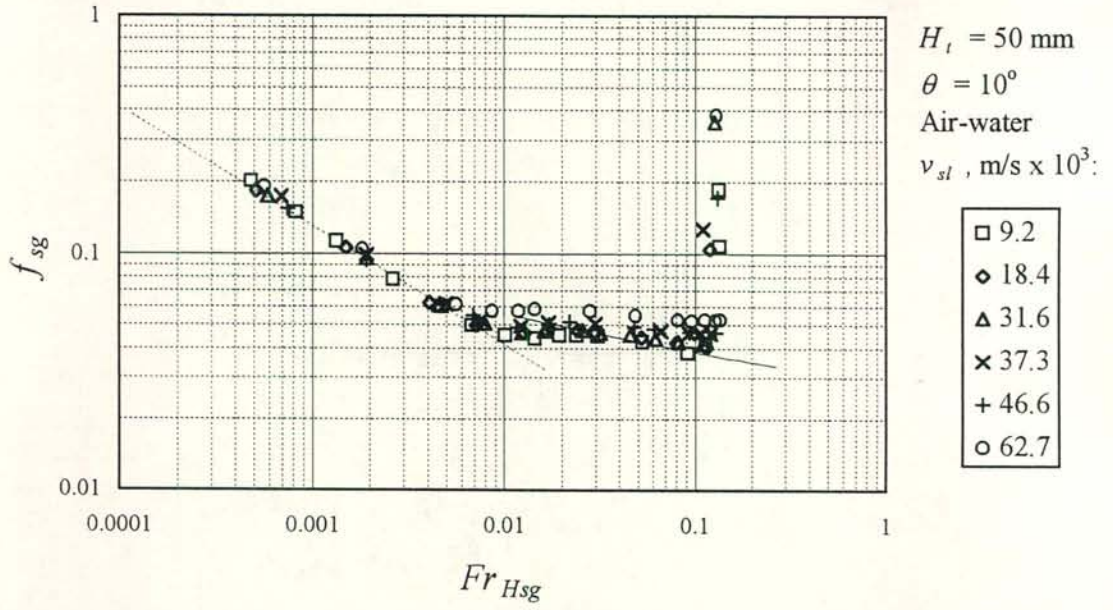

Figure E.2 (a): Friction factor for air-water flow at 10° inclination plotted against the superficial gas densimetric Froude number. Broken and solid line: Single-phase laminar and turbulent friction factor.

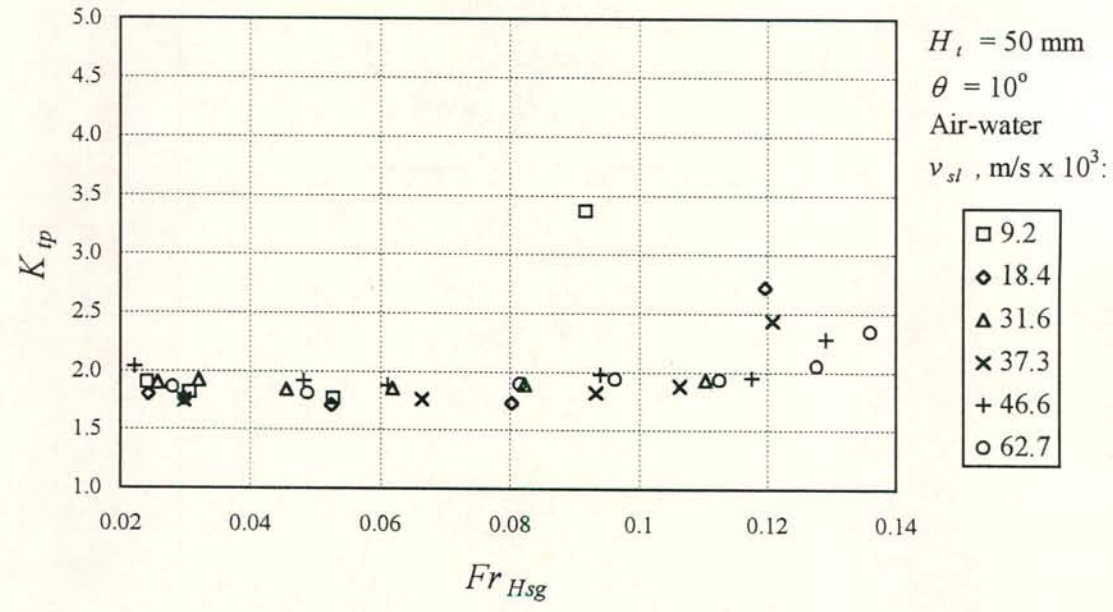

Figure E.2 (b): Two-phase entrance pressure drop coefficient for air-water flow at 10° inclination plotted against the superficial gas densimetric Froude number. The gas flow is fully turbulent.

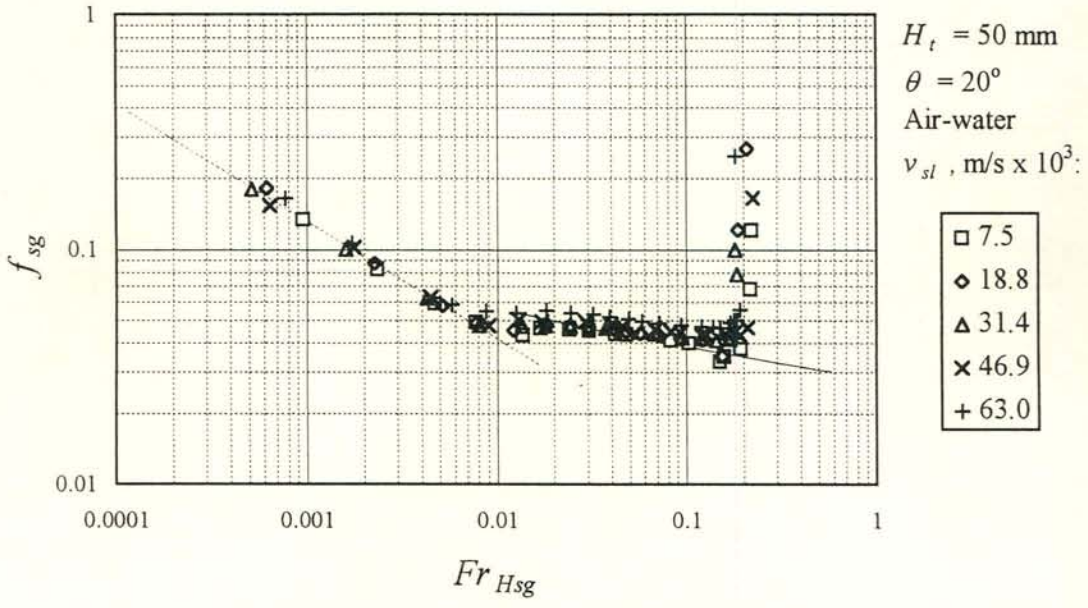

Figure E.3 (a): Friction factor for air-water flow at 20° inclination plotted against the superficial gas densimetric Froude number. Broken and solid line: Single-phase laminar and turbulent friction factor.

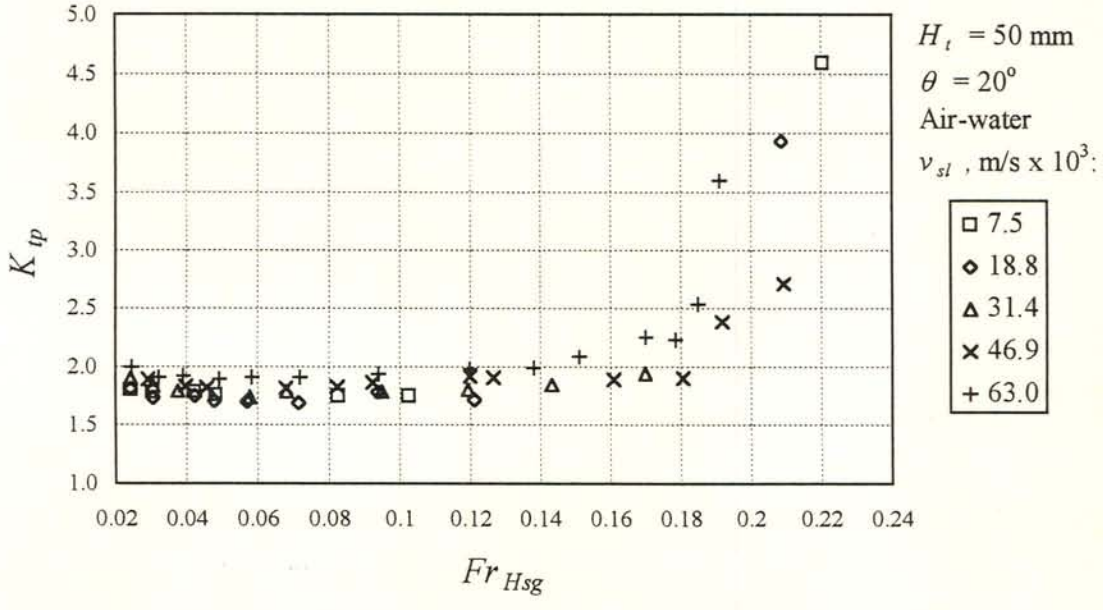

Figure E.3 (b): Two-phase entrance pressure drop coefficient for air-water flow at 20° inclination plotted against the superficial gas densimetric Froude number. The gas flow is fully turbulent.

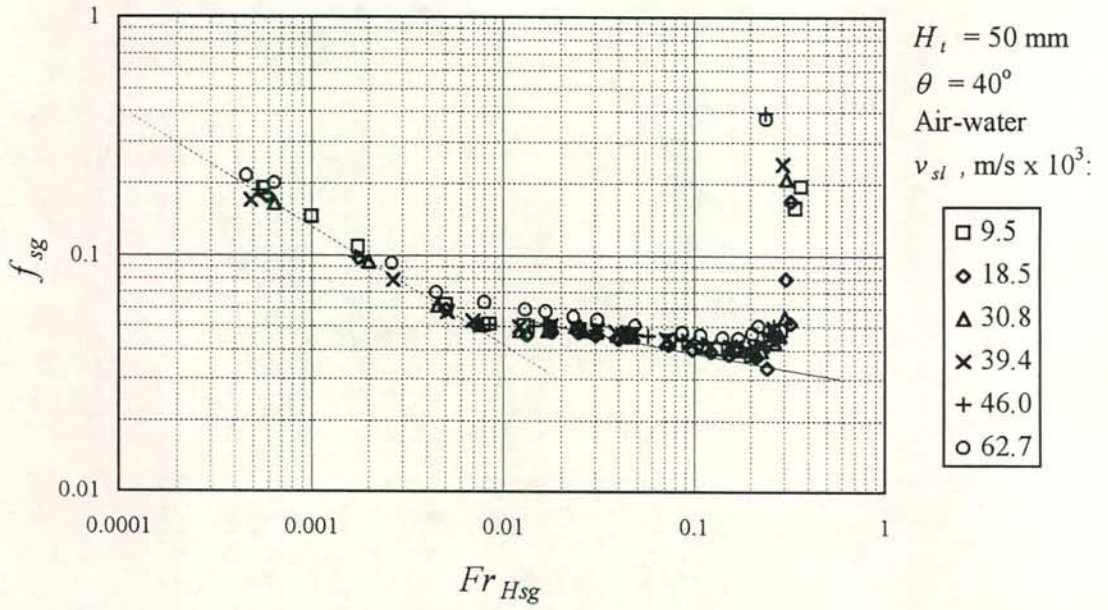

Figure E.4 (a): Friction factor for air-water flow at 40° inclination plotted against the superficial gas densimetric Froude number. Broken and solid line: Single-phase laminar and turbulent friction factor.

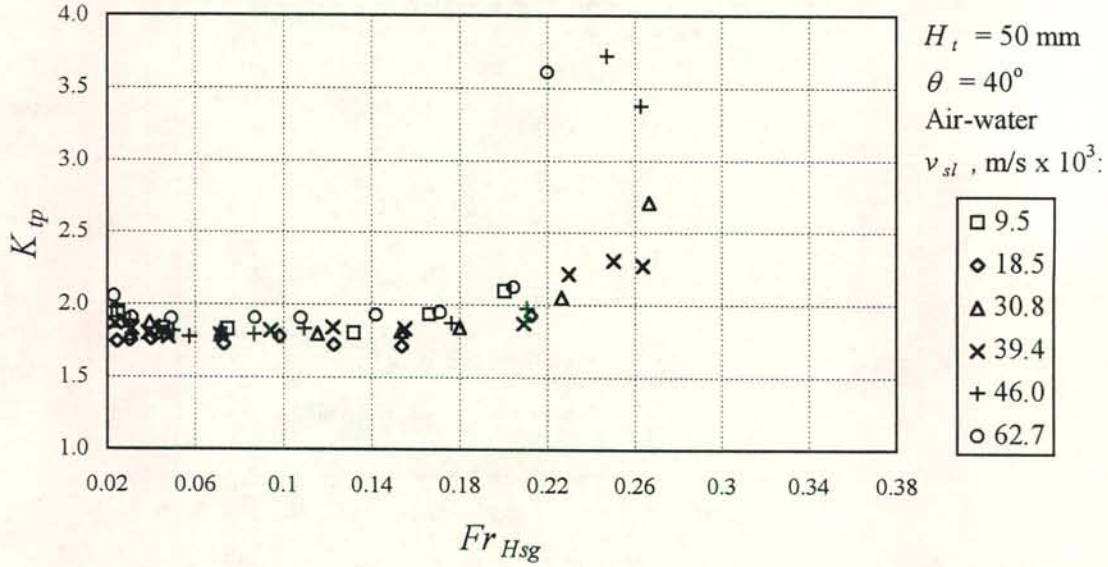

Figure E.4 (e): Two-phase entrance pressure drop coefficient for air-water flow at 40° inclination plotted against the superficial gas densimetric Froude number. The gas flow is fully turbulent.

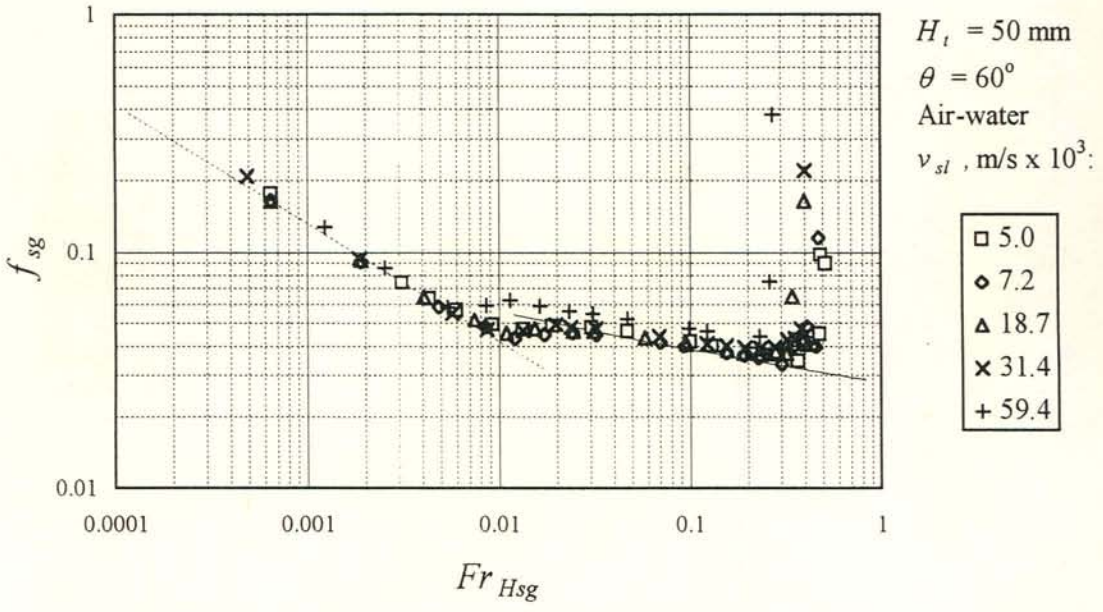

Figure E.5 (a): Friction factor for air-water flow at 60° inclination plotted against the superficial gas densimetric Froude number. Broken and solid line: Single-phase laminar and turbulent friction factor.

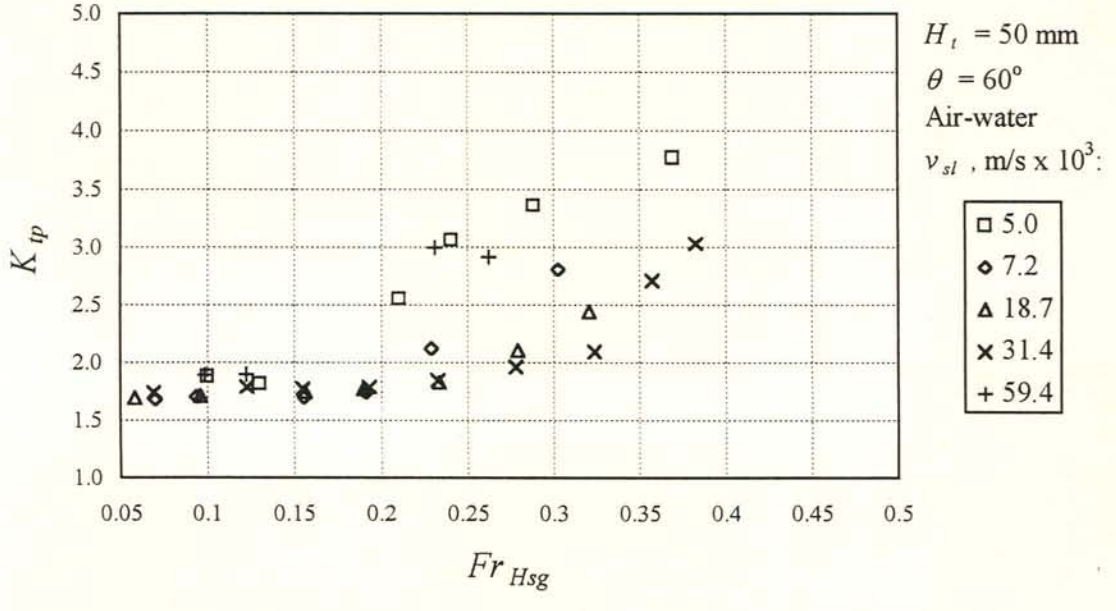

Figure E.5 (b): Two-phase entrance pressure drop coefficient for air-water flow at 60° inclination plotted against the superficial gas densimetric Froude number. The gas flow is fully turbulent.

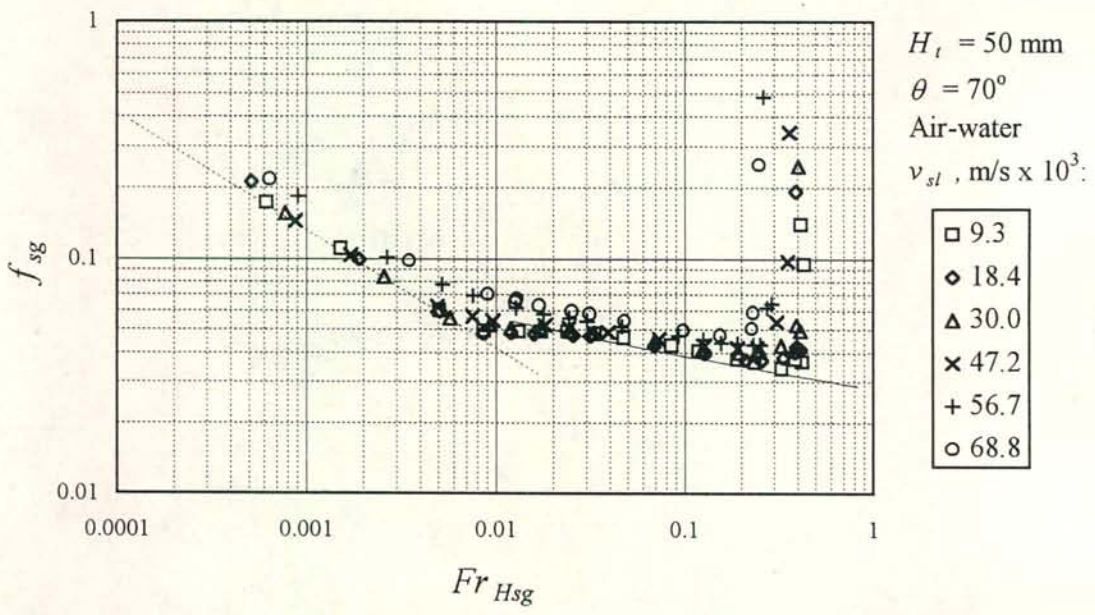

Figure E.6 (a): Friction factor for air-water flow at 70° inclination plotted against the superficial gas densimetric Froude number. Broken and solid line: Single-phase laminar and turbulent friction factor.

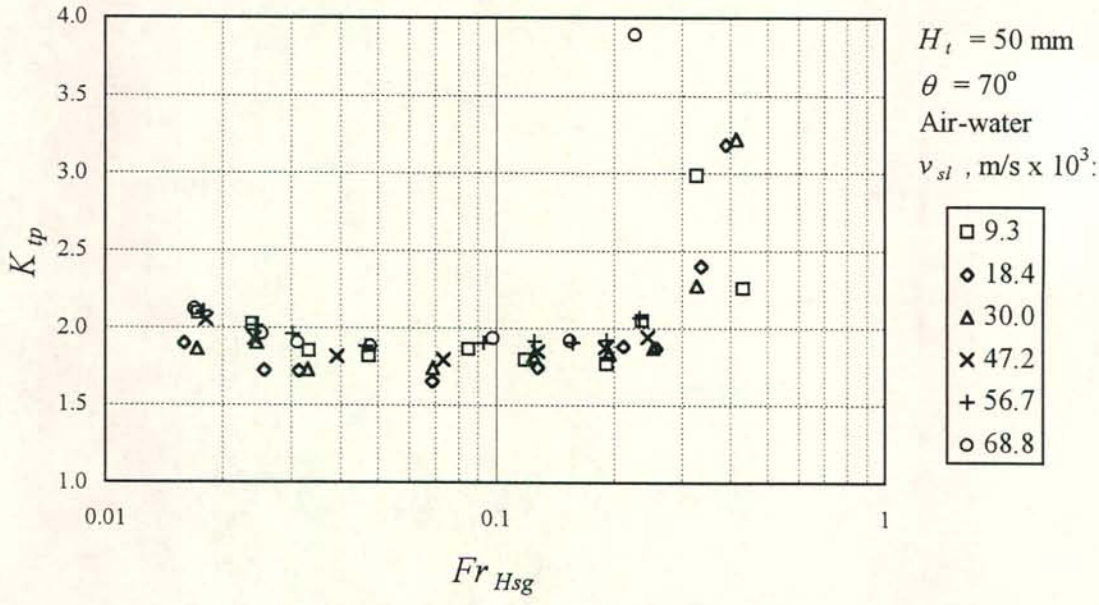

Figure E.6 (b): Two-phase entrance pressure drop coefficient for air-water flow at 70° inclination plotted against the superficial gas densimetric Froude number. The gas flow is fully turbulent.

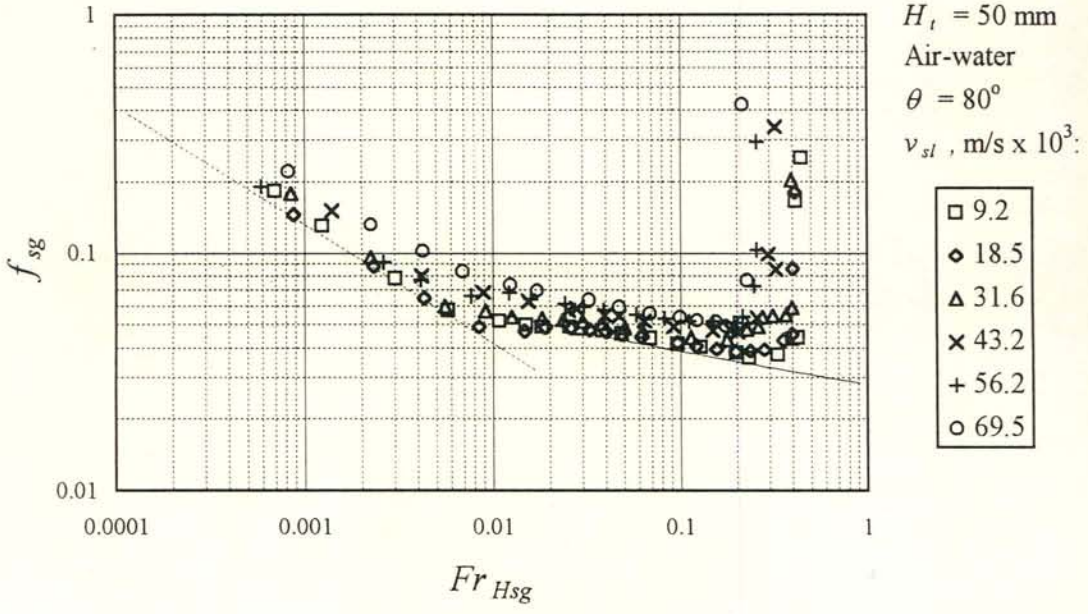

Figure E.7 (a): Friction factor for air-water flow at 80° inclination plotted against the superficial gas densimetric Froude number. Broken and solid line: Single-phase laminar and turbulent friction factor.

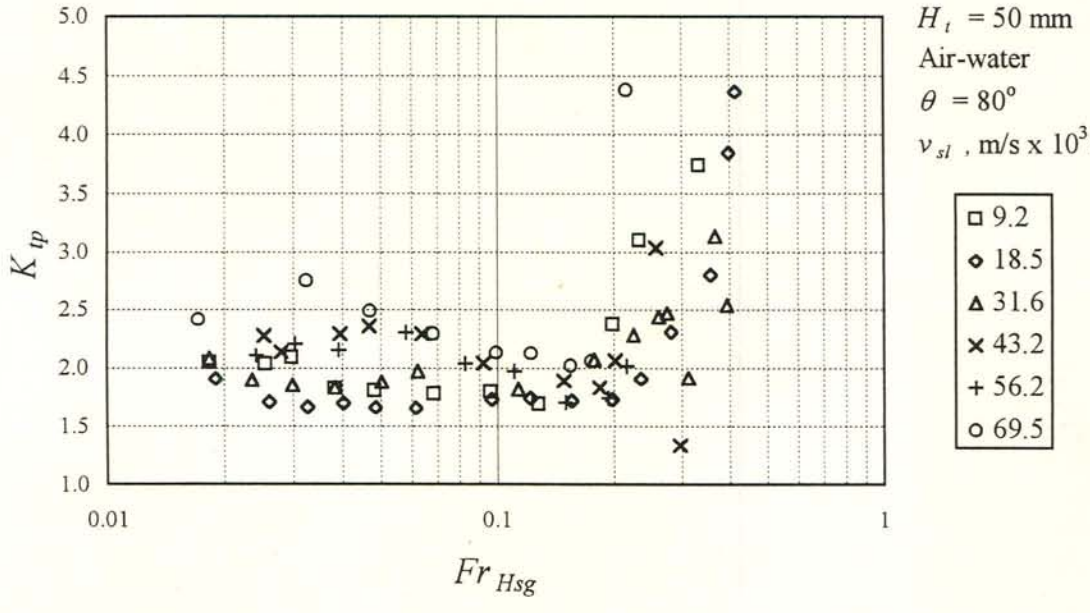

Figure E.7 (b): Two-phase entrance pressure drop coefficient for air-water flow at 80° inclination plotted against the superficial gas densimetric Froude number. The gas flow is fully turbulent.

E.2 Air-propanol pressure gradient and entrance pressure drop for the 50 mm duct (W_t = 10 mm)

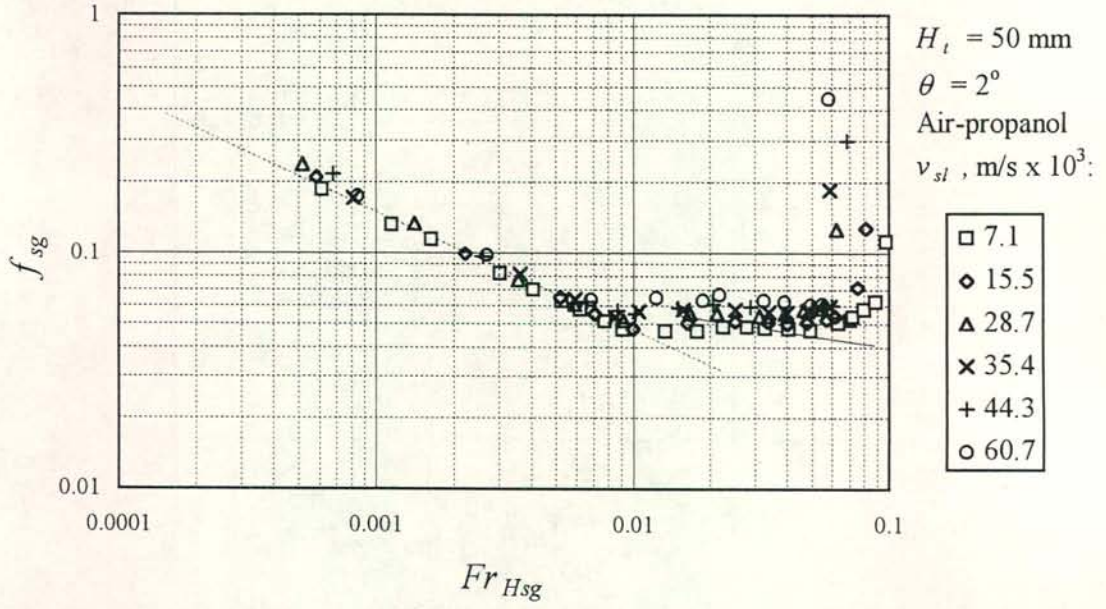

Figure E.8 (a): Friction factor for air-propanol flow at 2° inclination plotted against the superficial gas densimetric Froude number. Broken and solid line: Single-phase laminar and turbulent friction factor.

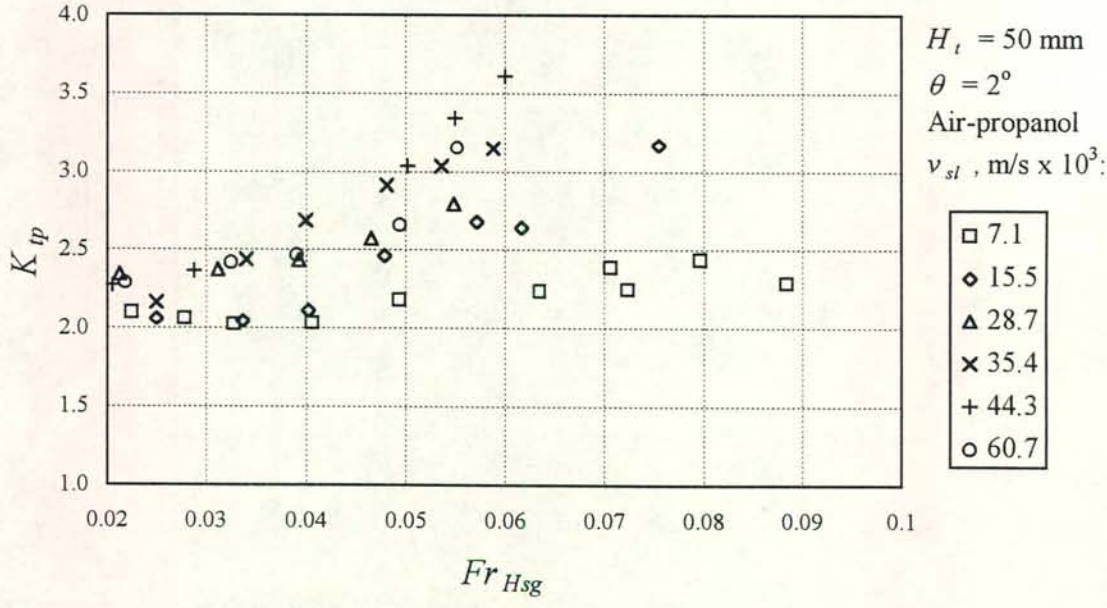

Figure E.8 (b): Two-phase entrance pressure drop coefficient for air-propanol flow at 2° inclination plotted against the superficial gas densimetric Froude number. The gas flow is fully turbulent.

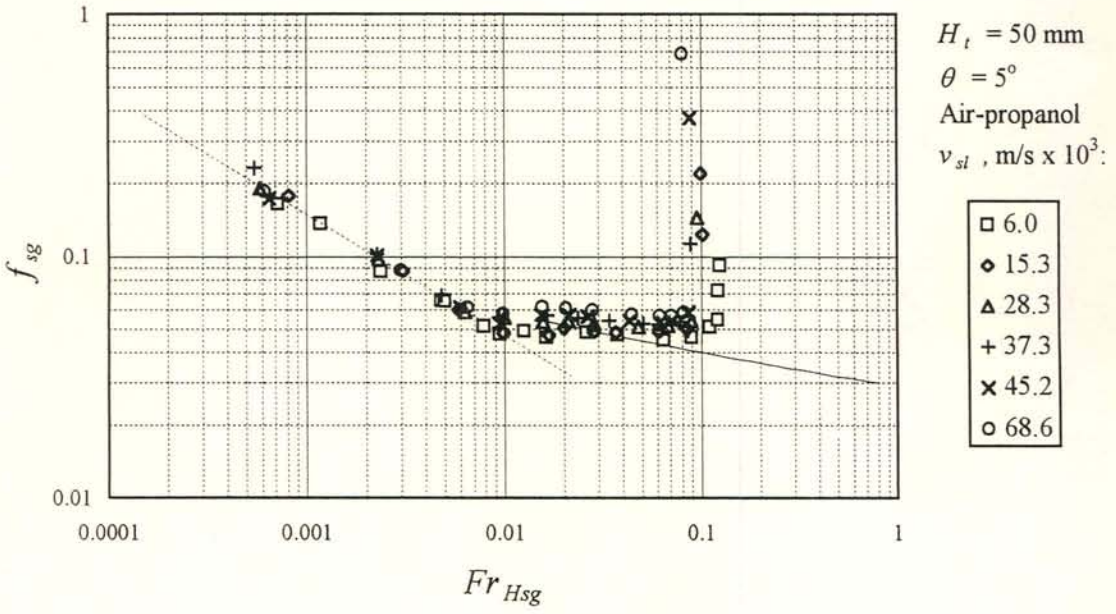

Figure E.9 (a): Friction factor for air-propanol flow at 5° inclination plotted against the superficial gas densimetric Froude number. Broken and solid line: Single-phase laminar and turbulent friction factor.

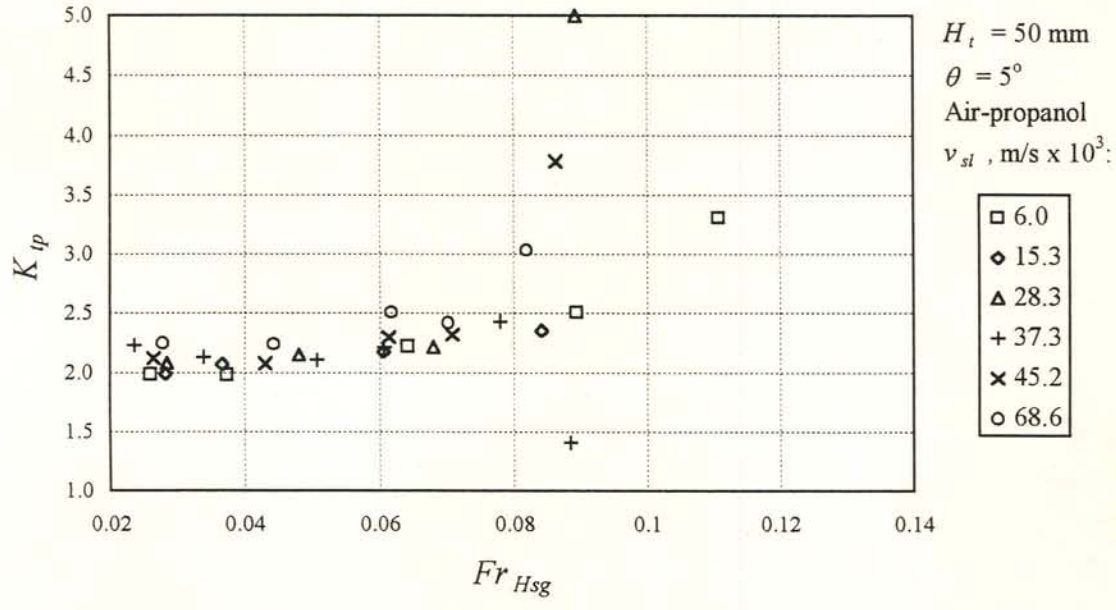

Figure E.9 (b): Two-phase entrance pressure drop coefficient for air-propanol flow at 5° inclination plotted against the superficial gas densimetric Froude number. The gas flow is fully turbulent.

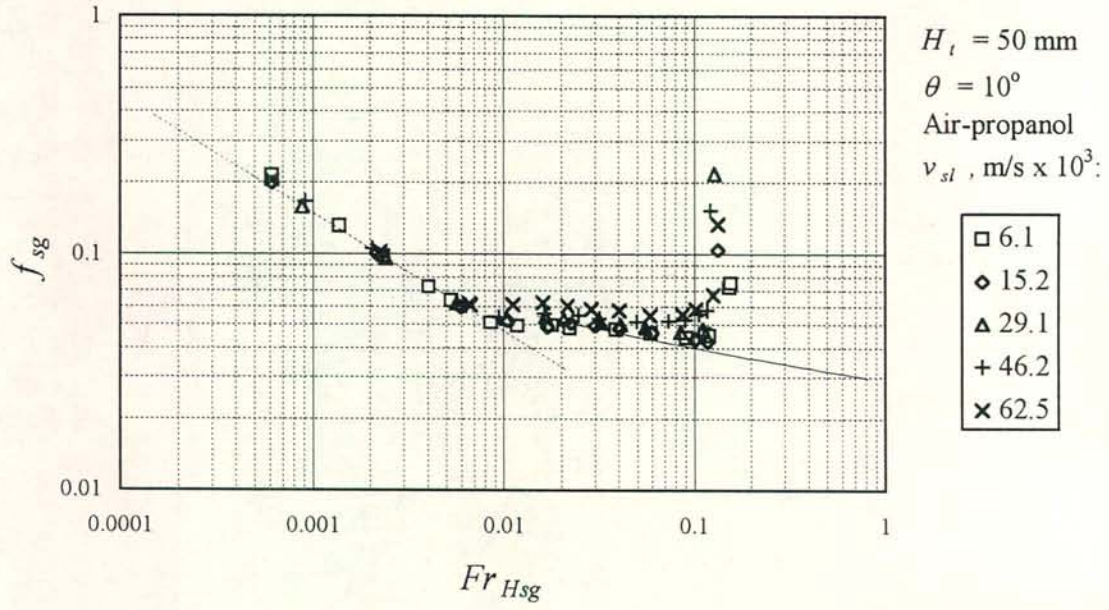

Figure E.10 (a): Friction factor for air-propanol flow at 10° inclination plotted against the superficial gas densimetric Froude number. Broken and solid line: Single-phase laminar and turbulent friction factor.

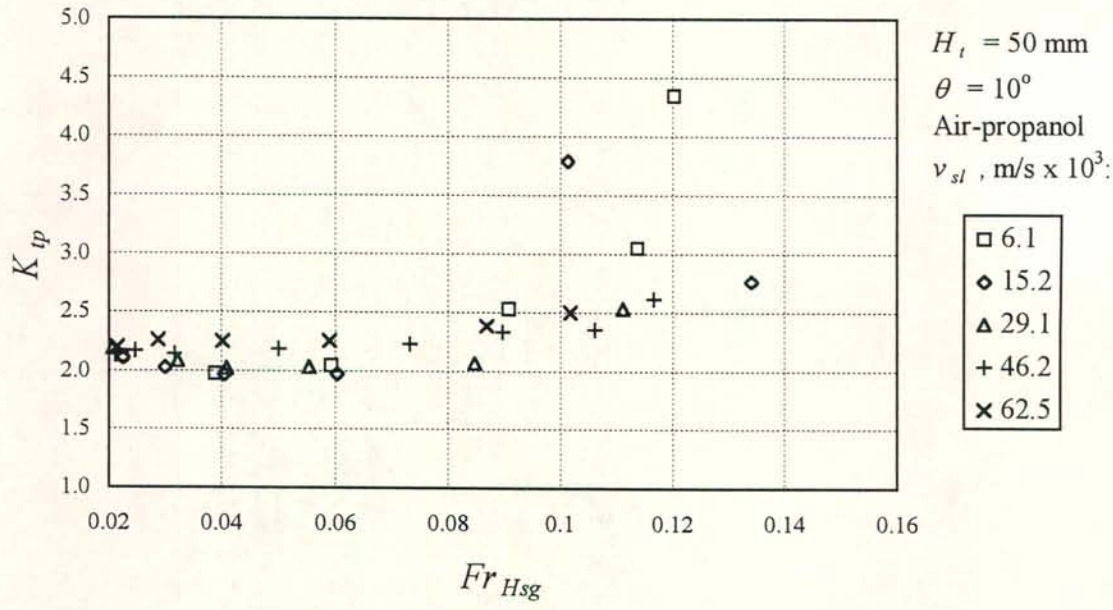

Figure E.10 (b): Two-phase entrance pressure drop coefficient for air-propanol flow at 10° inclination plotted against the superficial gas densimetric Froude number. The gas flow is fully turbulent.

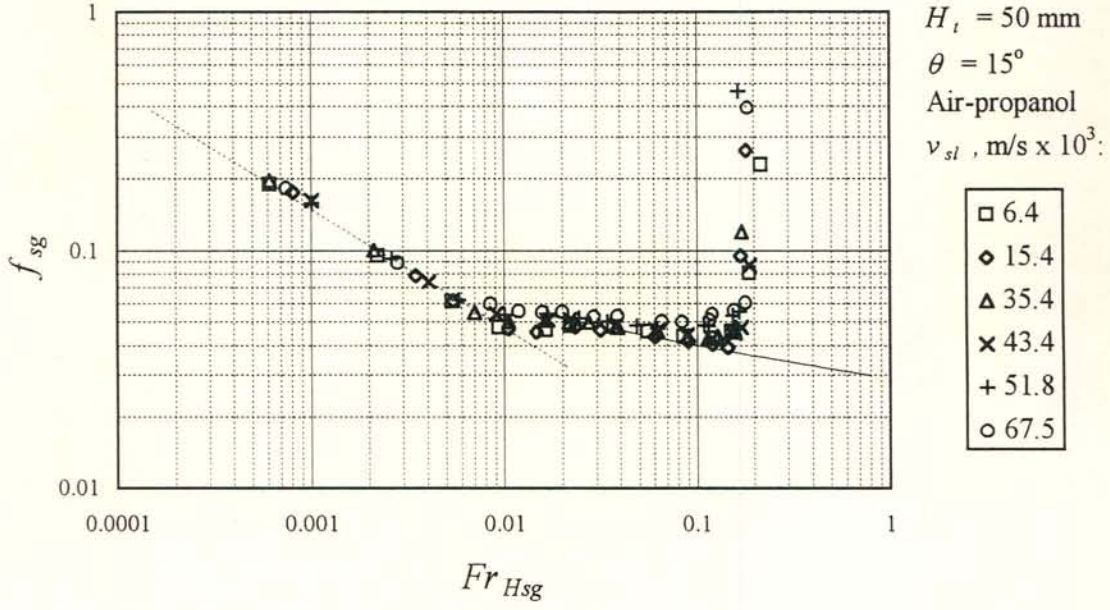

Figure E.11 (a): Friction factor for air-propanol flow at 15° inclination plotted against the superficial gas densimetric Froude number. Broken and solid line: Single-phase laminar and turbulent friction factor.

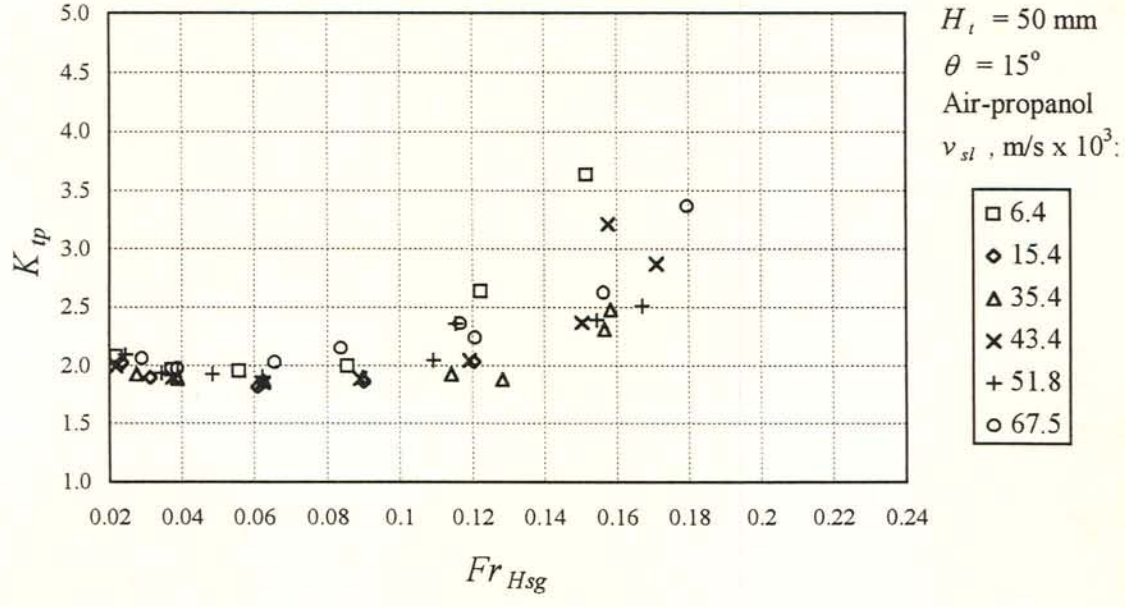

Figure E.11 (b): Two-phase entrance pressure drop coefficient for air-propanol flow at 15° inclination plotted against the superficial gas densimetric Froude number. The gas flow is fully turbulent.

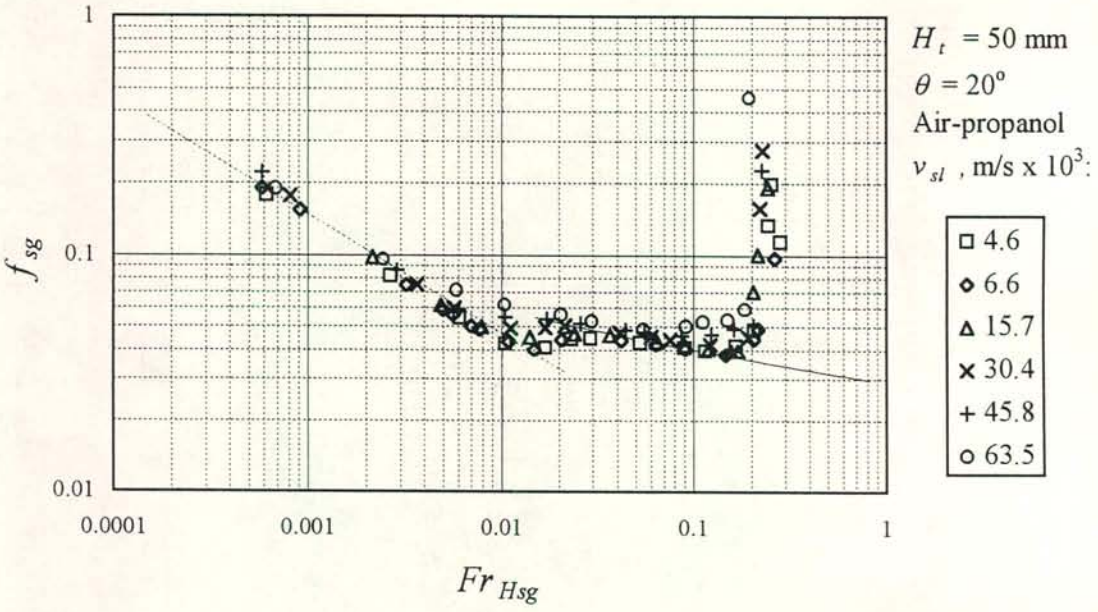

Figure E.12 (a): Friction factor for air-propanol flow at 20° inclination plotted against the superficial gas densimetric Froude number. Broken and solid line: Single-phase laminar and turbulent friction factor.

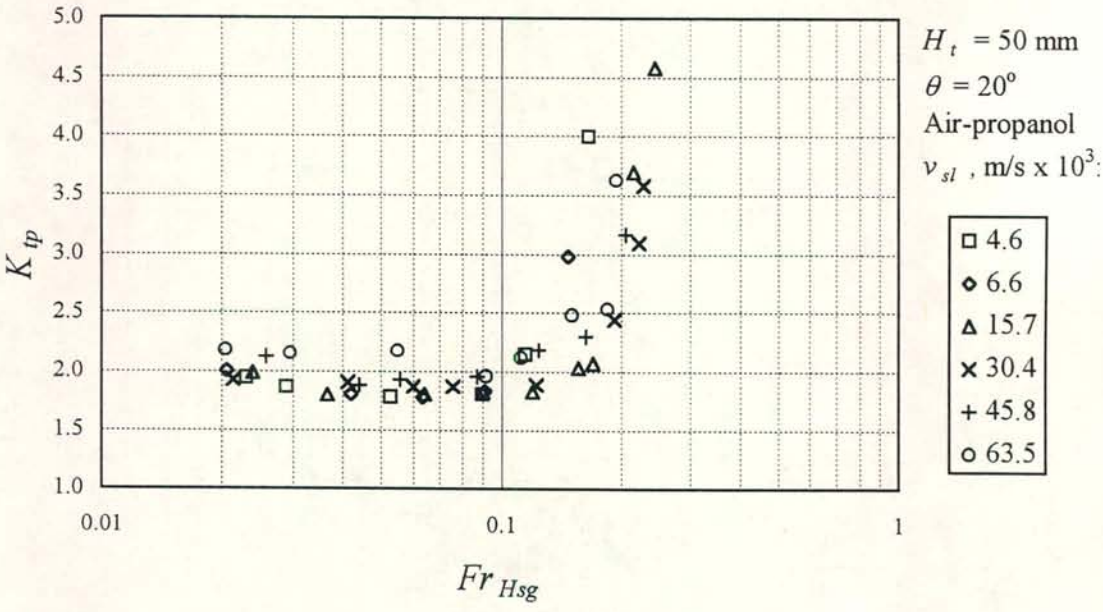

Figure E.12 (b): Two-phase entrance pressure drop coefficient for air-propanol flow at 20° inclination plotted against the superficial gas densimetric Froude number. The gas flow is fully turbulent.

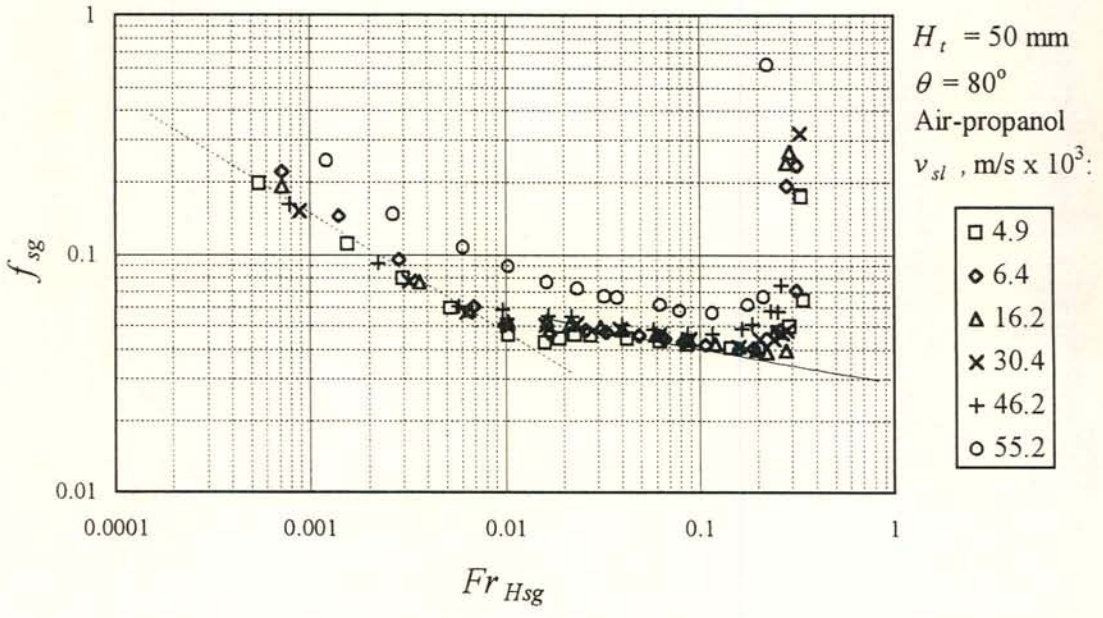

Figure E.13 (a): Friction factor for air-propanol flow at 80° inclination plotted against the superficial gas densimetric Froude number. Broken and solid line: Single-phase laminar and turbulent friction factor.

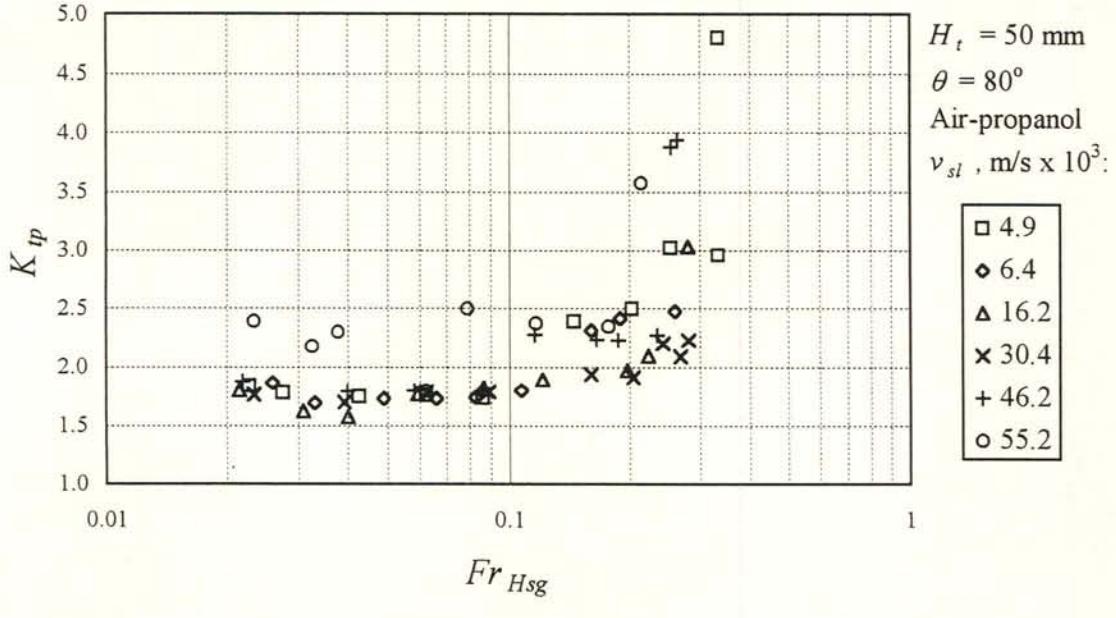

Figure E.13 (d): Two-phase entrance pressure drop coefficient for air-propanol flow at 80° inclination plotted against the superficial gas densimetric Froude number. The gas flow is fully turbulent.

E.3 Air-water pressure gradient and entrance pressure drop for the 100 mm (H_t) duct

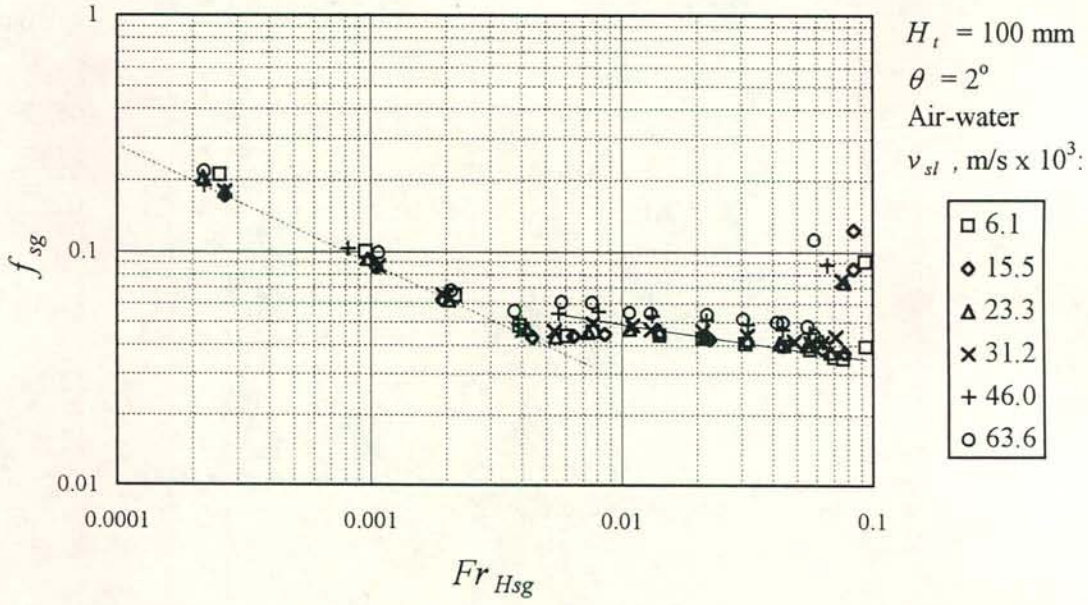

Figure E.14 (a): Friction factor for air-water flow at 2° inclination plotted against the superficial gas densimetric Froude number. Broken and solid line: Single-phase laminar and turbulent friction factor.

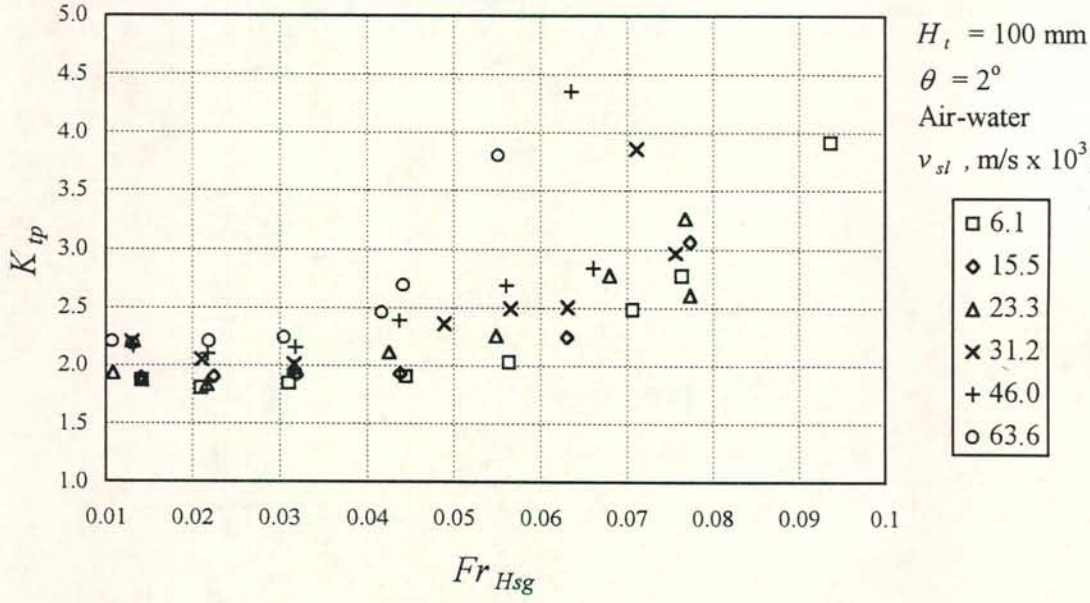

Figure E.14 (b): Two-phase entrance pressure drop coefficient for air-water flow at 2° inclination plotted against the superficial gas densimetric Froude number. The gas flow is fully turbulent.

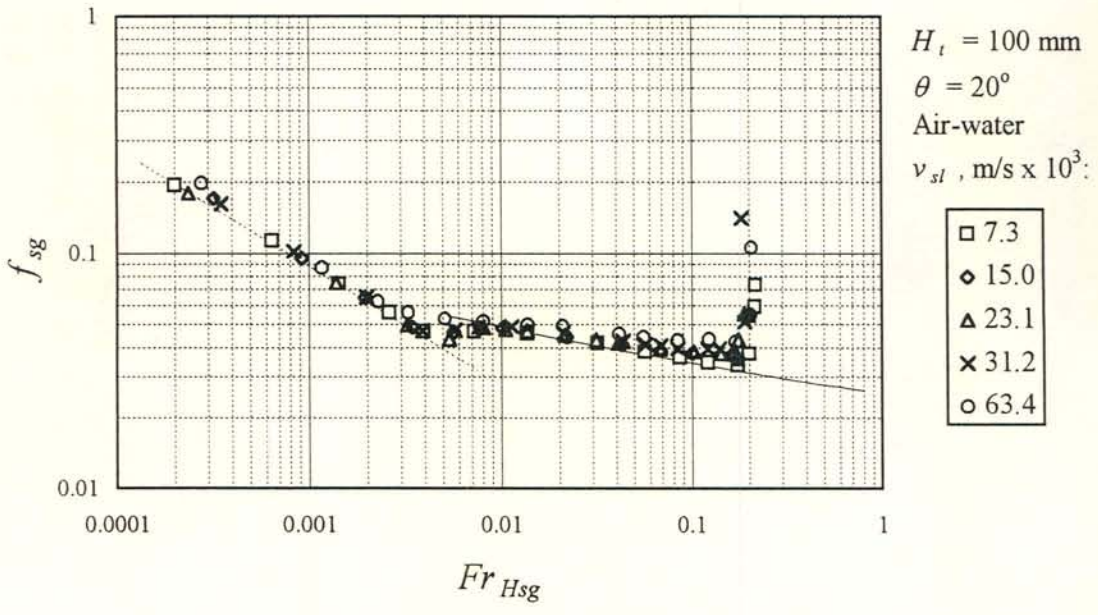

Figure E.15 (a): Friction factor for air-water flow at 20° inclination plotted against the superficial gas densimetric Froude number. Broken and solid line: Single-phase laminar and turbulent friction factor.

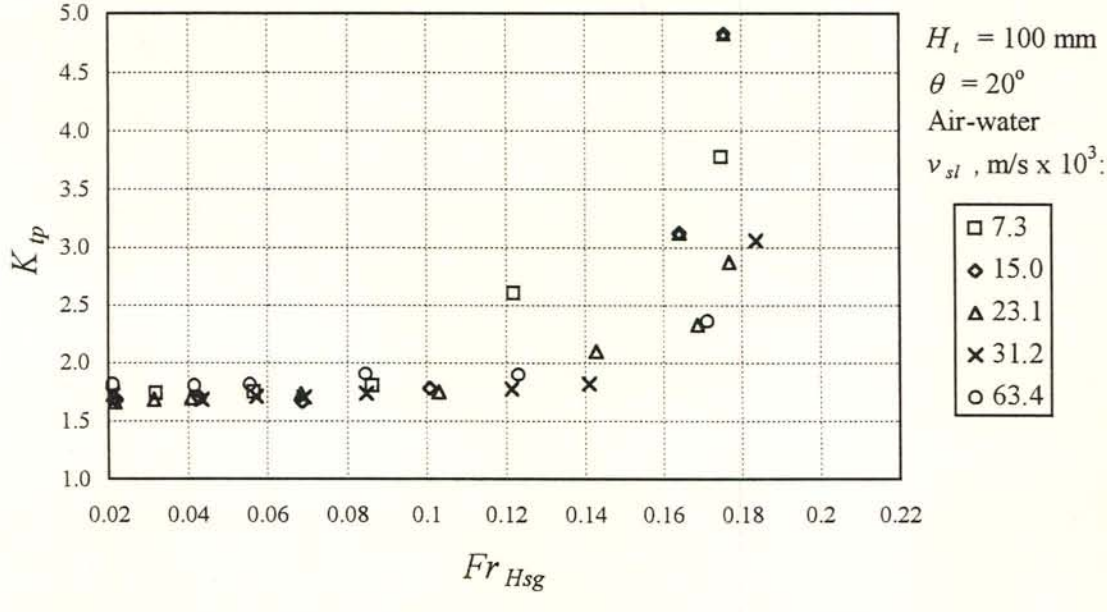

Figure E.15 (b): Two-phase entrance pressure drop coefficient for air-water flow at 20° inclination plotted against the superficial gas densimetric Froude number. The gas flow is fully turbulent.

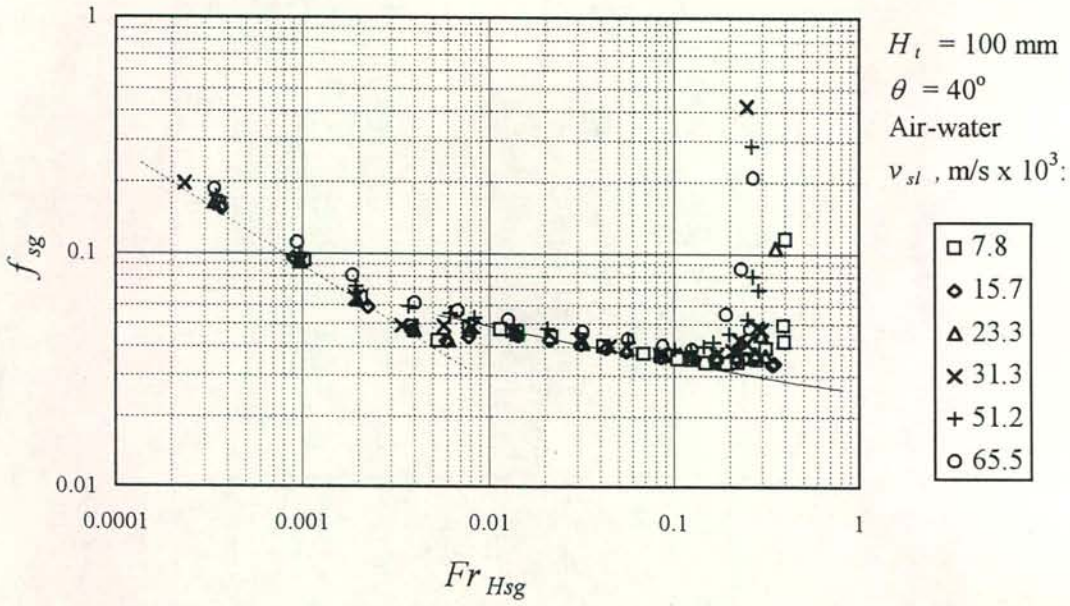

Figure E.16 (a): Friction factor for air-water flow at 40° inclination plotted against the superficial gas densimetric Froude number. Broken and solid line: Single-phase laminar and turbulent friction factor.

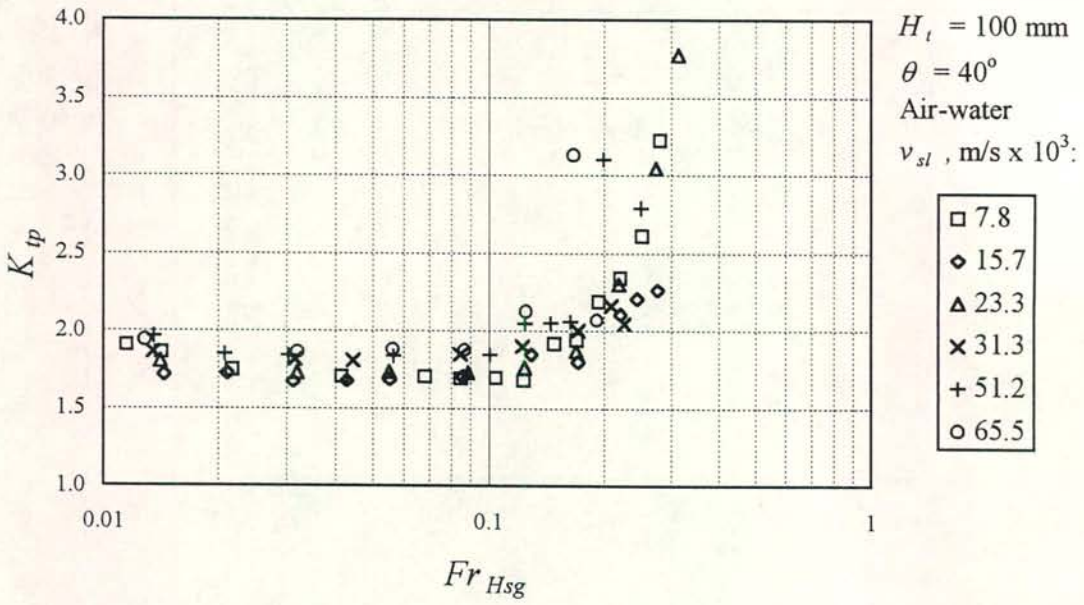

Figure E.16 (b): Two-phase entrance pressure drop coefficient for air-water flow at 40° inclination plotted against the superficial gas densimetric Froude number. The gas flow is fully turbulent.

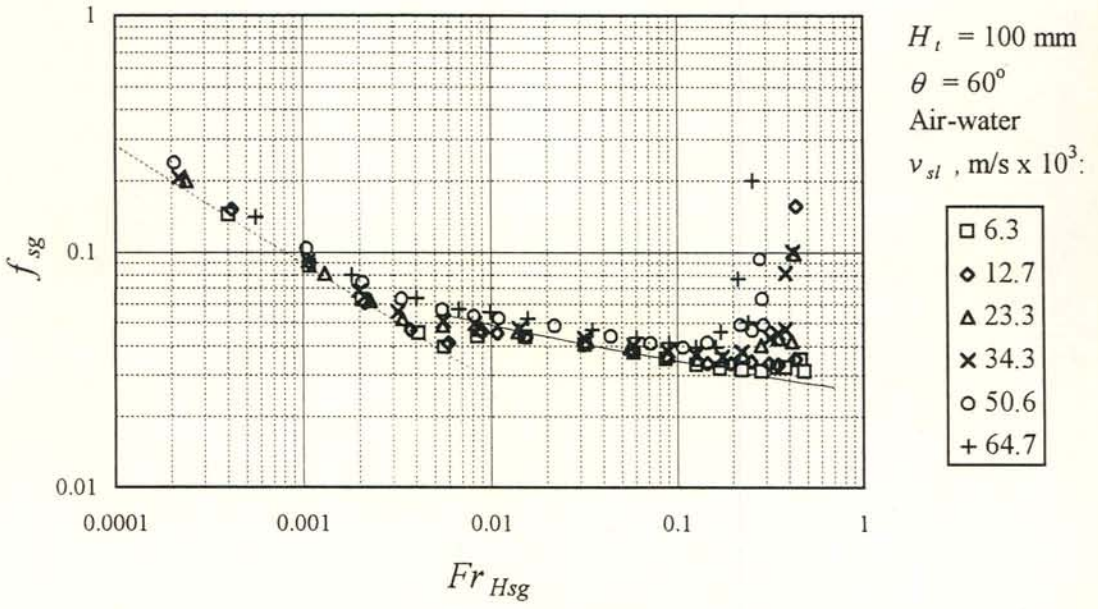

Figure E.17 (a): Friction factor for air-water flow at 60° inclination plotted against the superficial gas densimetric Froude number. Broken and solid line: Single-phase laminar and turbulent friction factor.

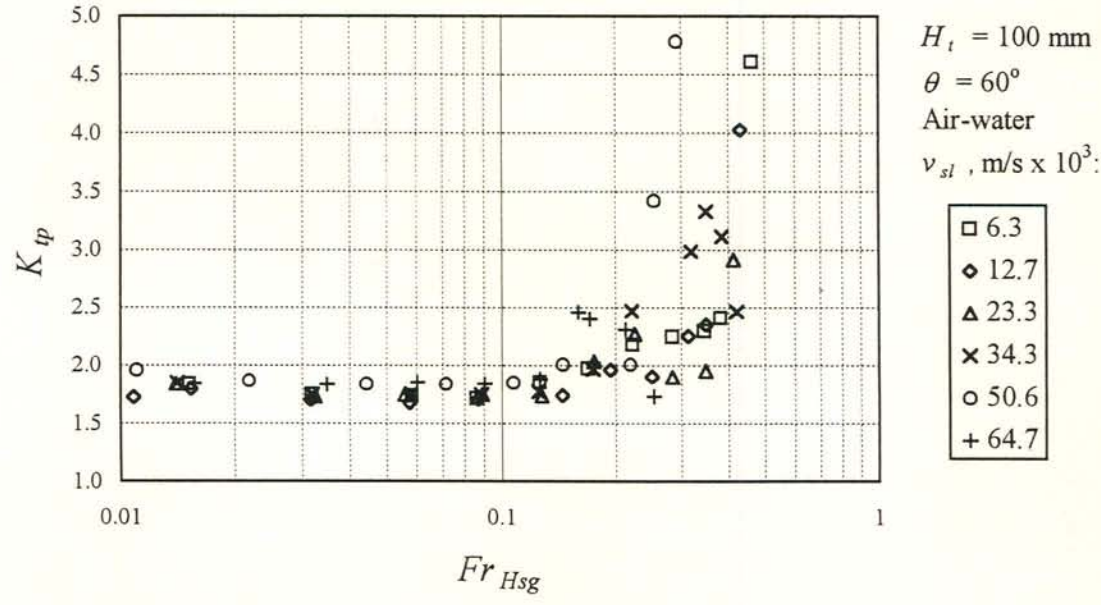

Figure E.17 (b): Two-phase entrance pressure drop coefficient for air-water flow at 60° inclination plotted against the superficial gas densimetric Froude number. The gas flow is fully turbulent.

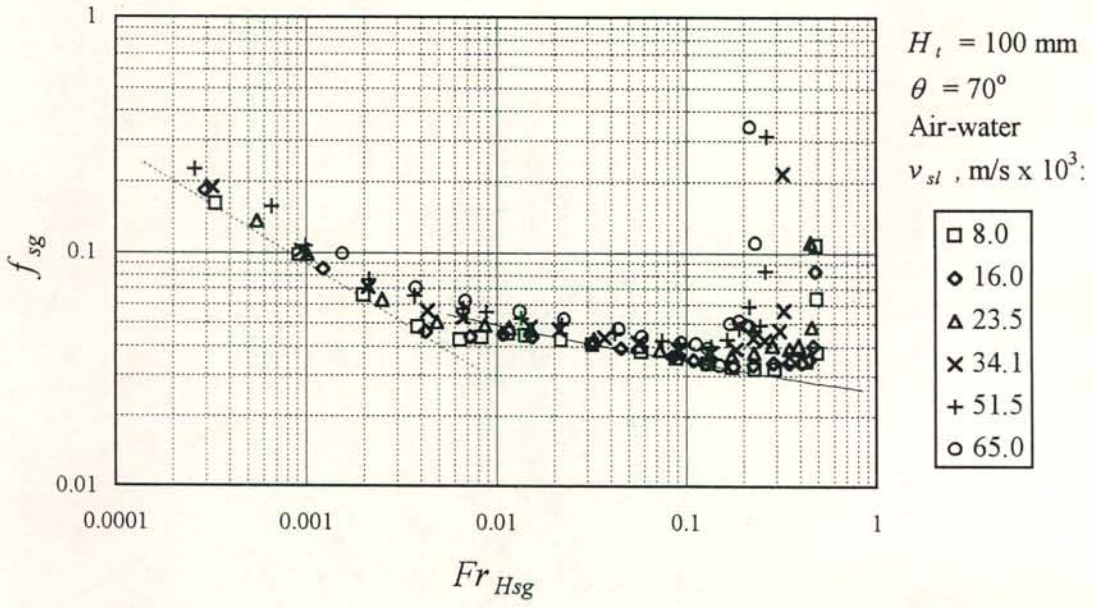

Figure E.18 (a): Friction factor for air-water flow at 70° inclination plotted against the superficial gas densimetric Froude number. Broken and solid line: single-phase laminar and turbulent friction factor.

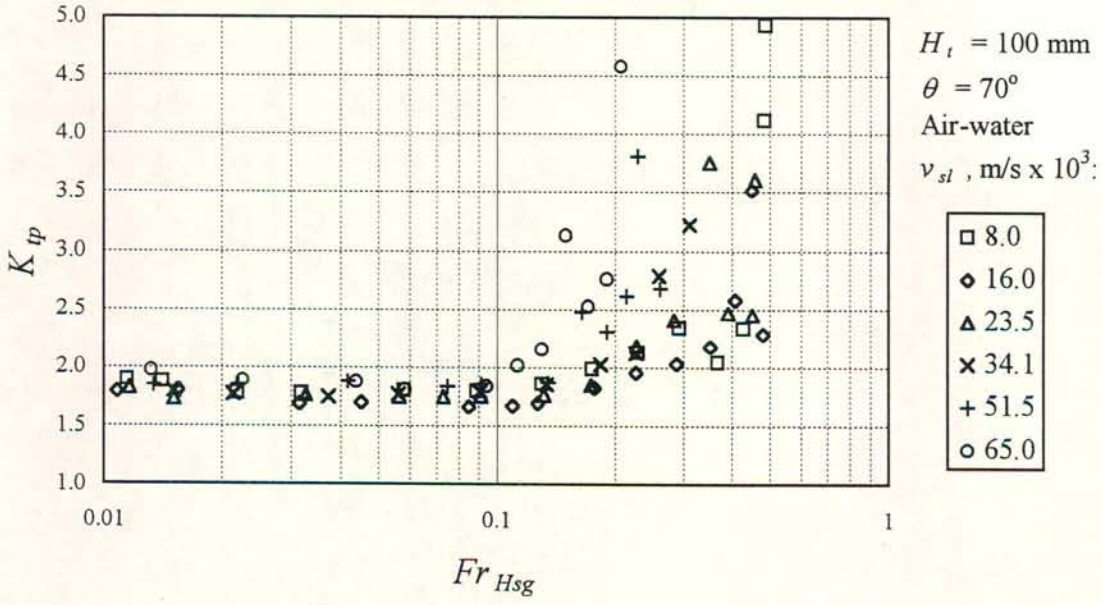

Figure E.18 (b): Two-phase entrance pressure drop coefficient for air-water flow at 60° inclination plotted against the superficial gas densimetric Froude number. The gas flow is fully turbulent.

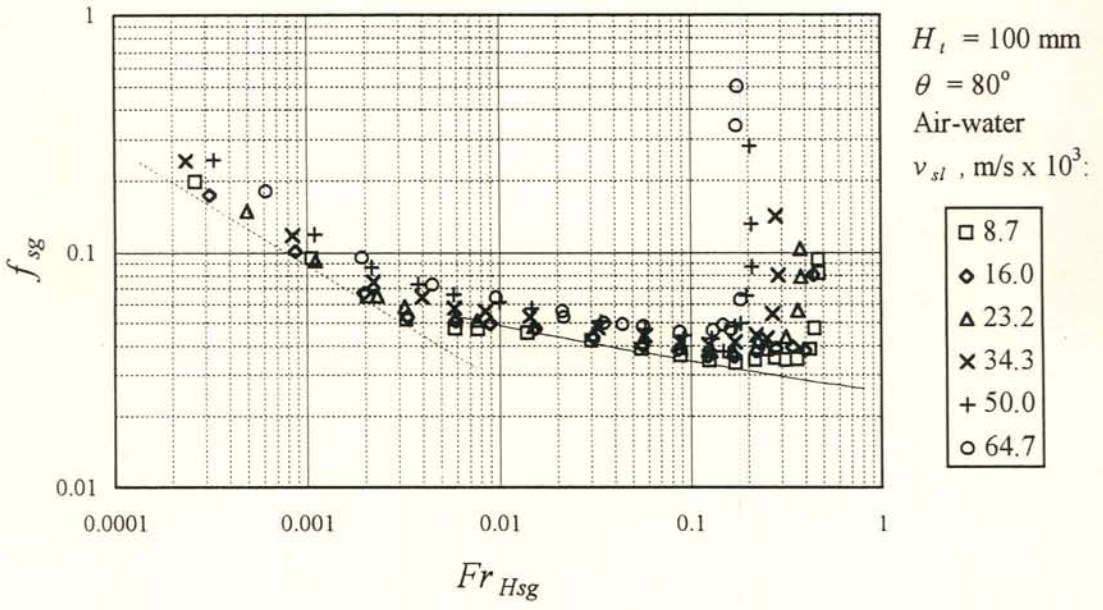

Figure E.19 (a): Friction factor for air-water flow at 80° inclination plotted against the superficial gas densimetric Froude number. Broken and solid line: Single-phase laminar and turbulent friction factor.

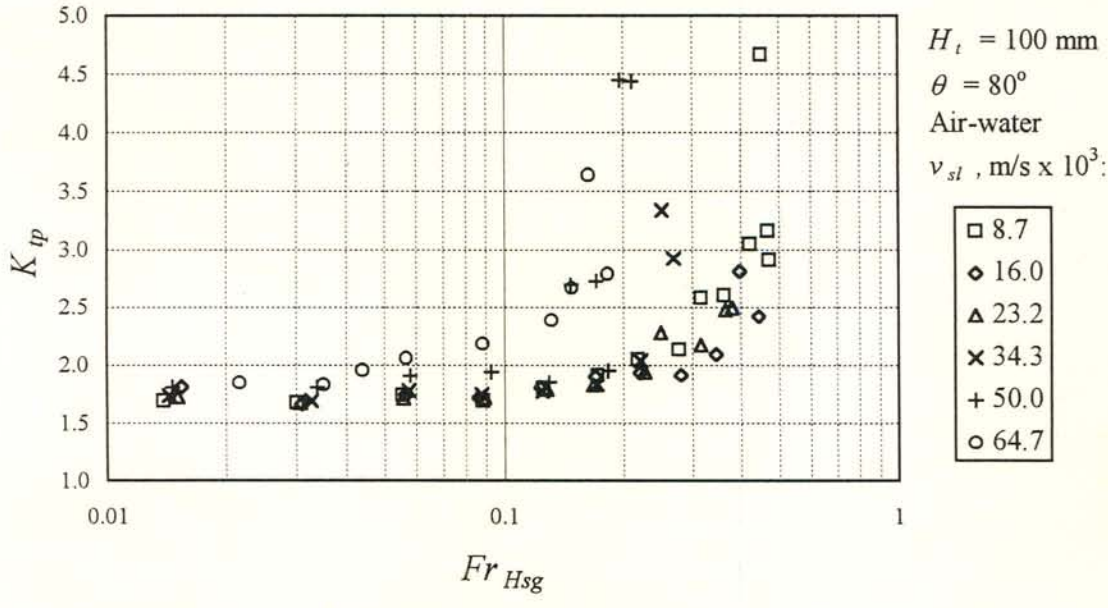

Figure E.19 (d): Two-phase entrance pressure drop coefficient for air-water flow at 80° inclination plotted against the superficial gas densimetric Froude number. The gas flow is fully turbulent.

E.4 Air-propanol pressure gradient and entrance pressure drop for the 100 mm (H_t) duct

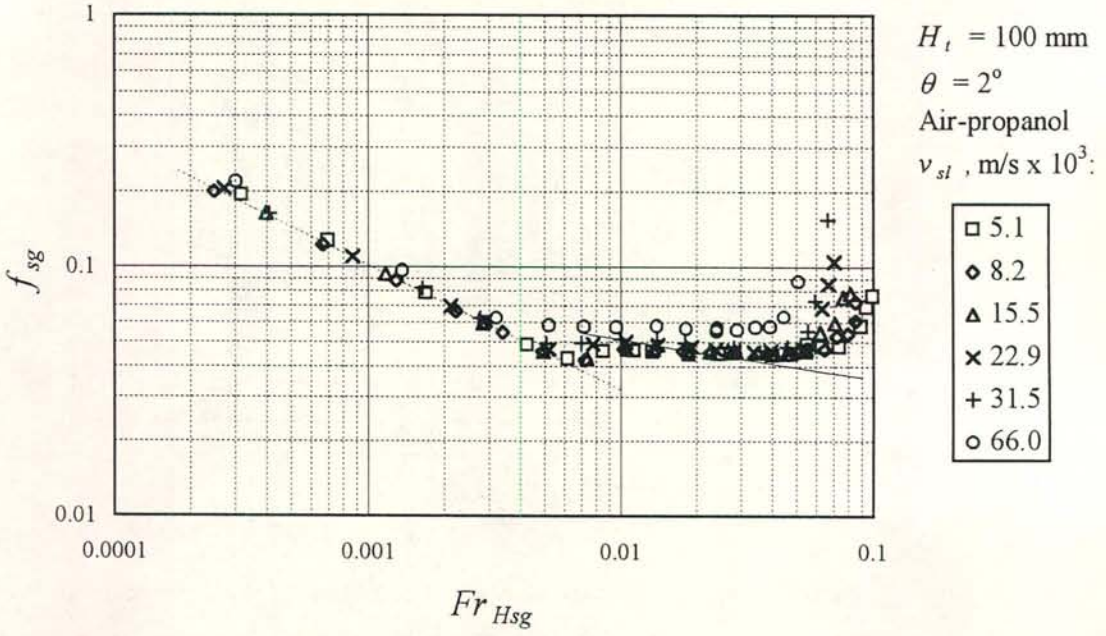

Figure E.20 (a): Friction factor for air-propanol flow at 2° inclination plotted against the superficial gas densimetric Froude number. Broken and solid line: Single-phase laminar and turbulent friction factor.

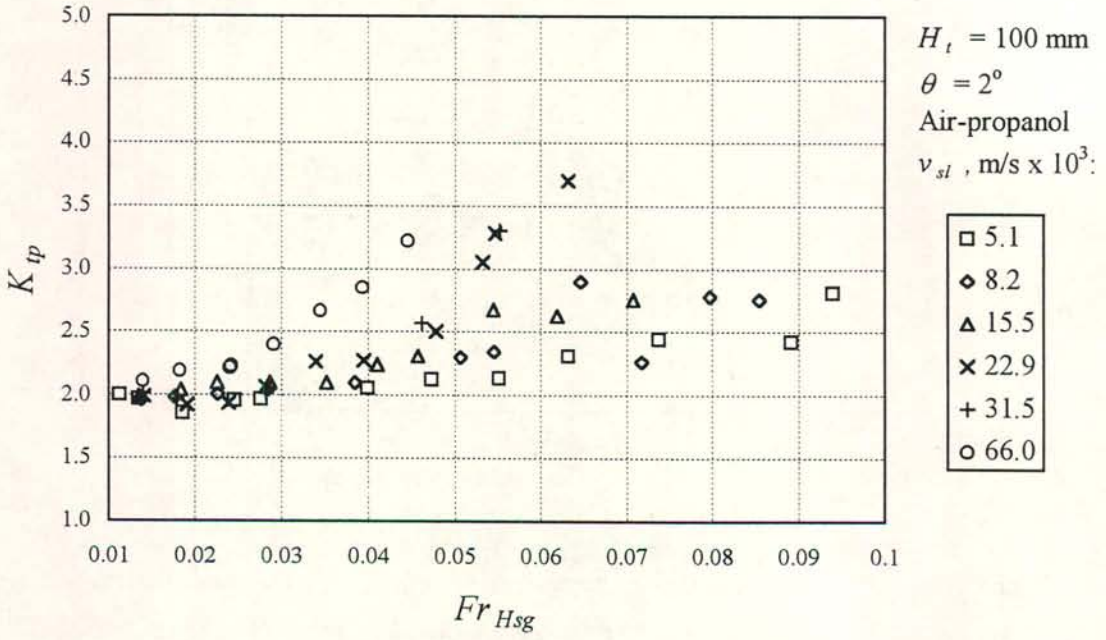

Figure E.20 (b): Two-phase entrance pressure drop coefficient for air-propanol flow at 2° inclination plotted against the superficial gas densimetric Froude number. The gas flow is fully turbulent.

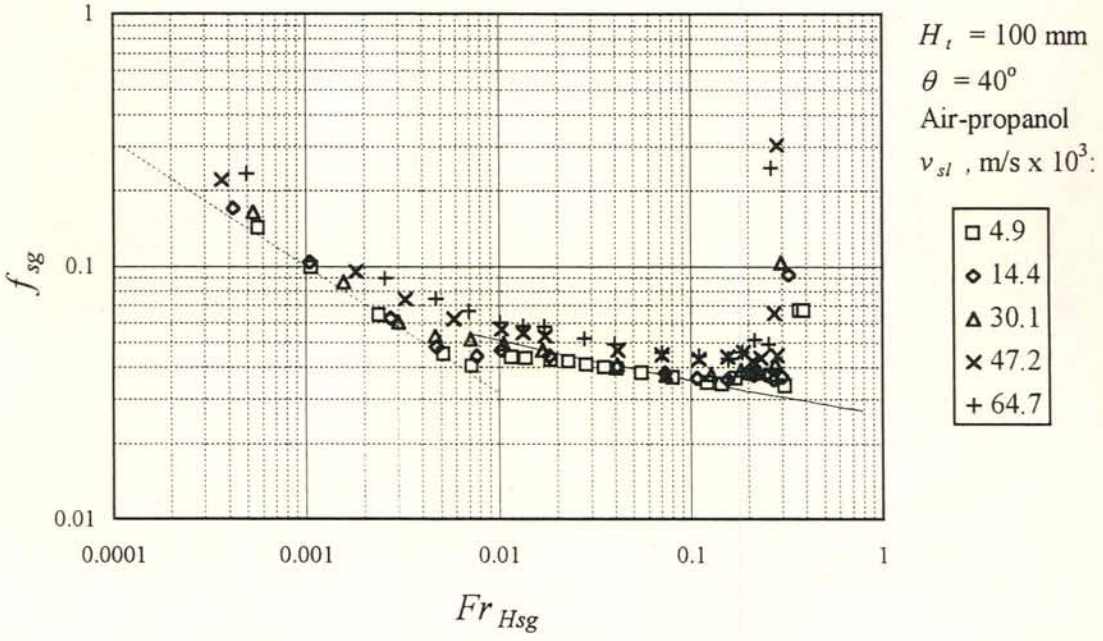

Figure E.21 (a): Friction factor for air-water flow at 40° inclination plotted against the superficial gas densimetric Froude number. Broken and solid line: Single-phase laminar and turbulent friction factor.

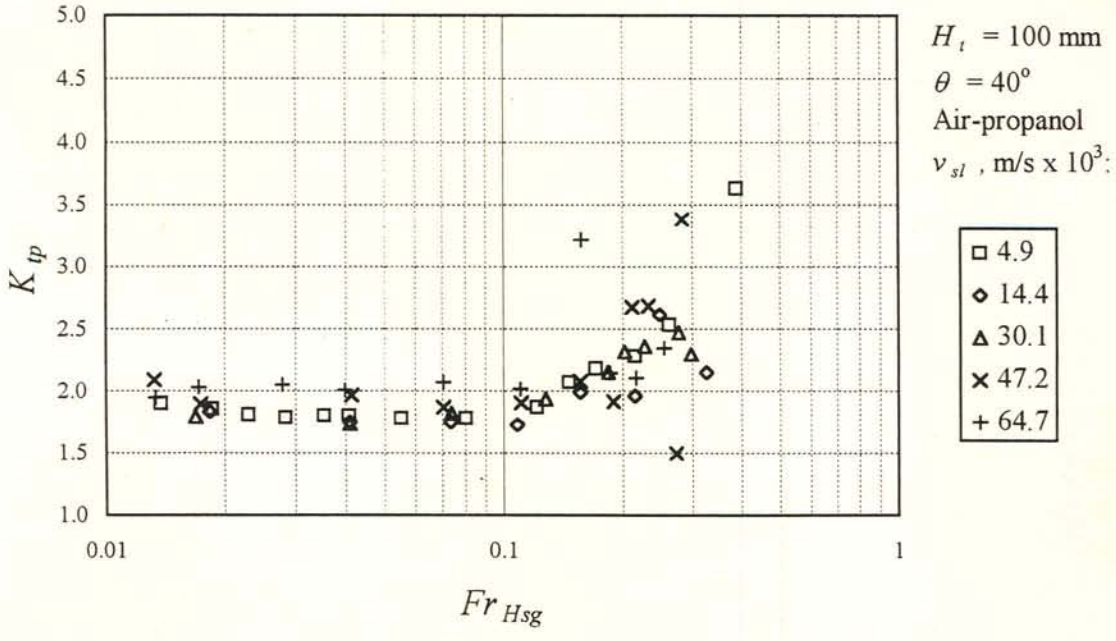

Figure E.21 (b): Two-phase entrance pressure drop coefficient for air-propanol flow at 40° inclination plotted against the superficial gas densimetric Froude number. The gas flow is fully turbulent.

E.5 Air-water pressure gradient and entrance pressure drop for the 150 mm (H_t) duct

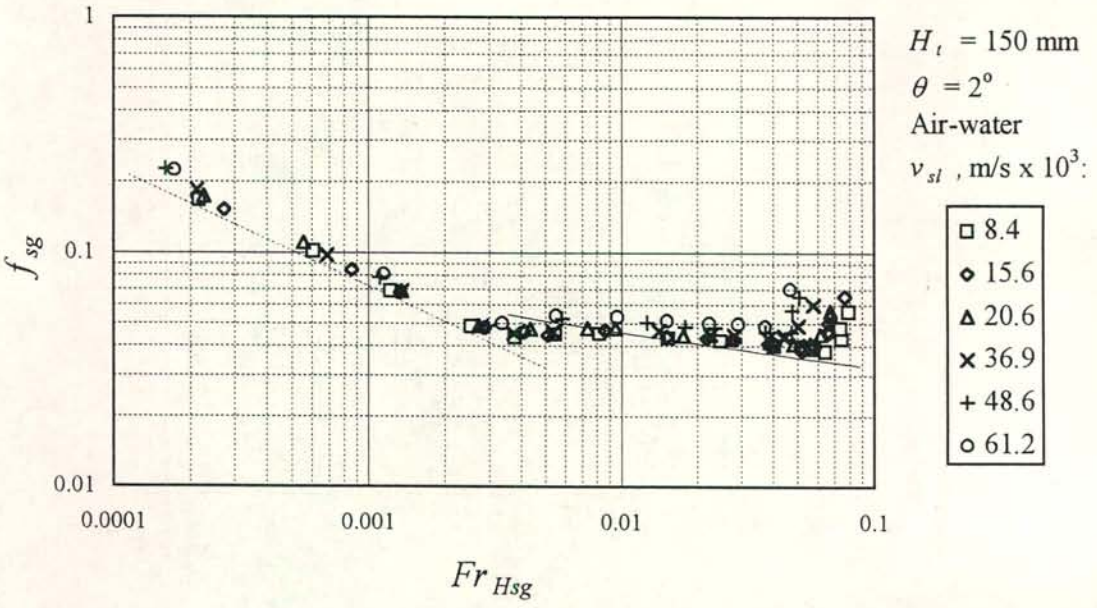

Figure E.22 (a): Friction factor for air-water flow at 2° inclination plotted against the superficial gas densimetric Froude number. Broken and solid line: Single-phase laminar and turbulent friction factor.

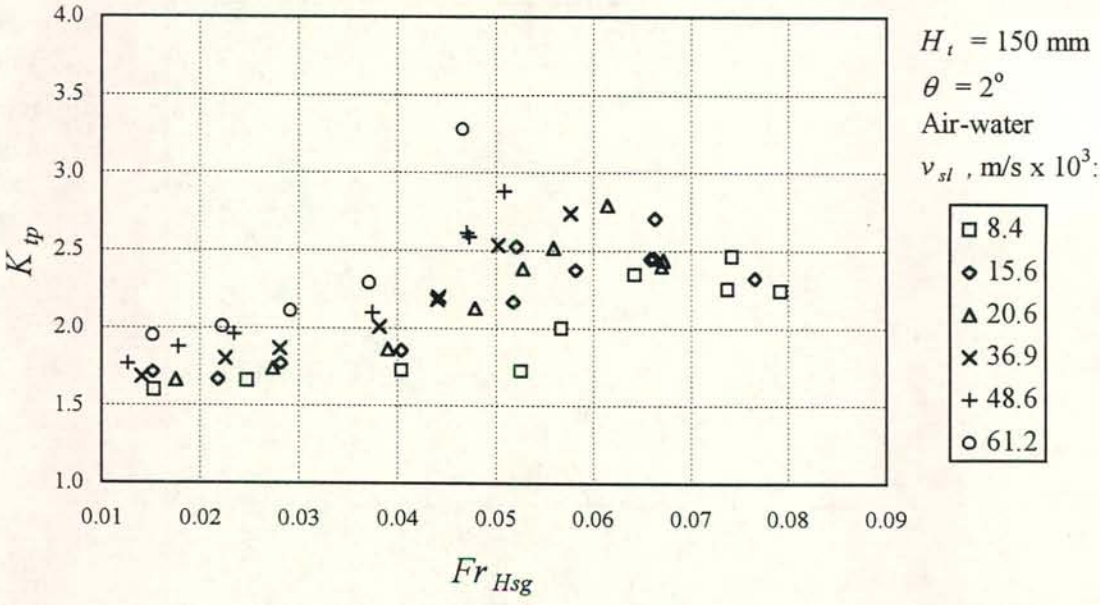

Figure E.22 (b): Two-phase entrance pressure drop coefficient for air-water flow at 2° inclination plotted against the superficial gas densimetric Froude number. The gas flow is fully turbulent.

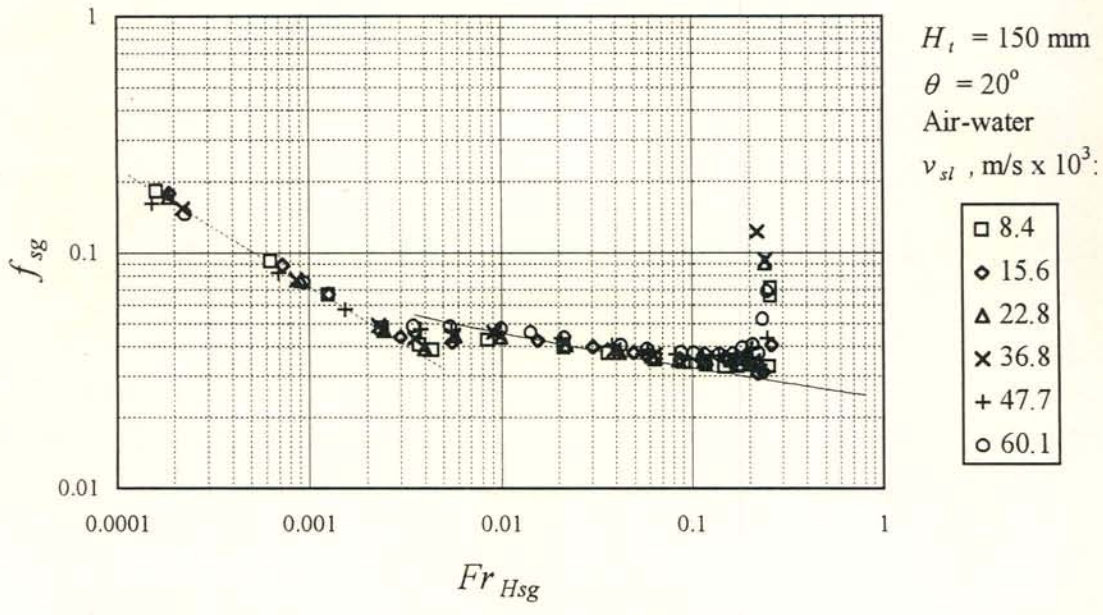

Figure E.23 (a): Friction factor for air-water flow at 20° inclination plotted against the superficial gas densimetric Froude number. Broken and solid line: Single-phase laminar and turbulent friction factor.

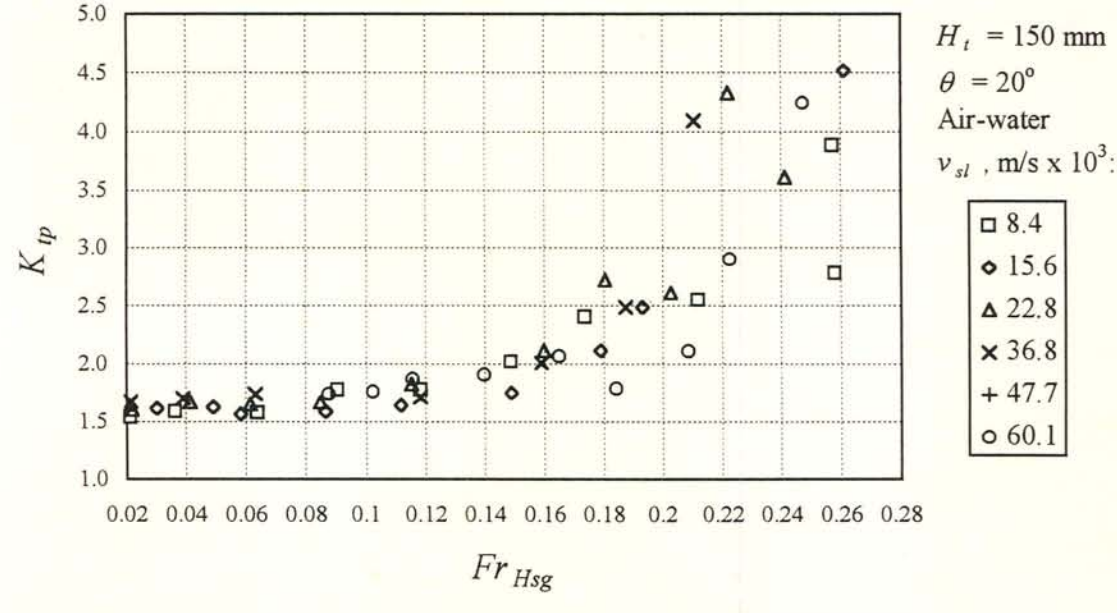

Figure E.23 (b): Two-phase entrance pressure drop coefficient for air-water flow at 20° inclination plotted against the superficial gas densimetric Froude number. The gas flow is fully turbulent.

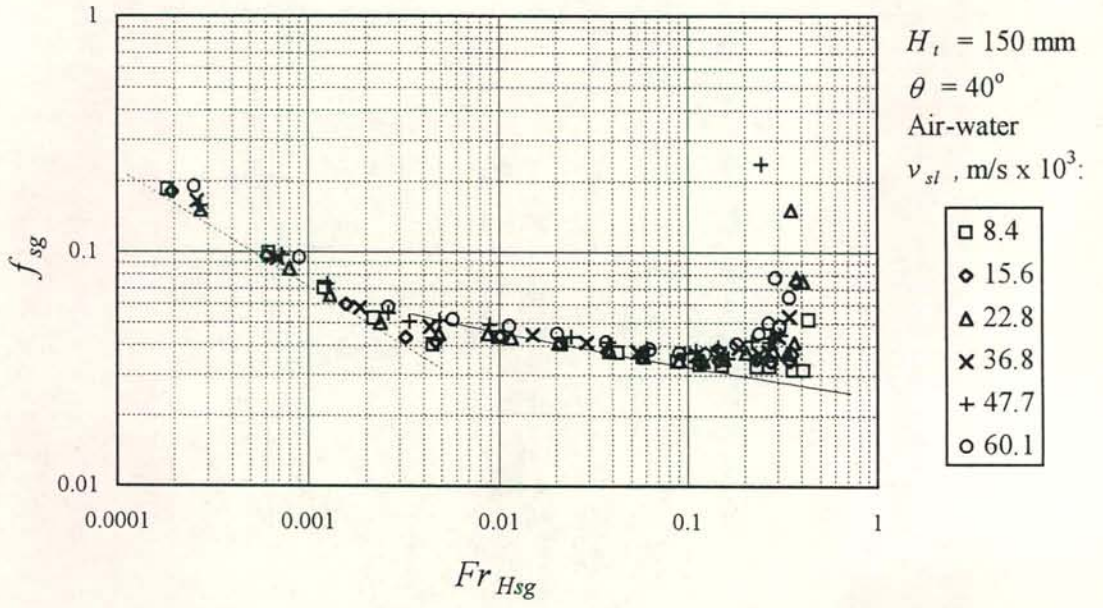

Figure E.24 (a): Friction factor for air-water flow at 40° inclination plotted against the superficial gas densimetric Froude number. Broken and solid line: Single-phase laminar and turbulent friction factor.

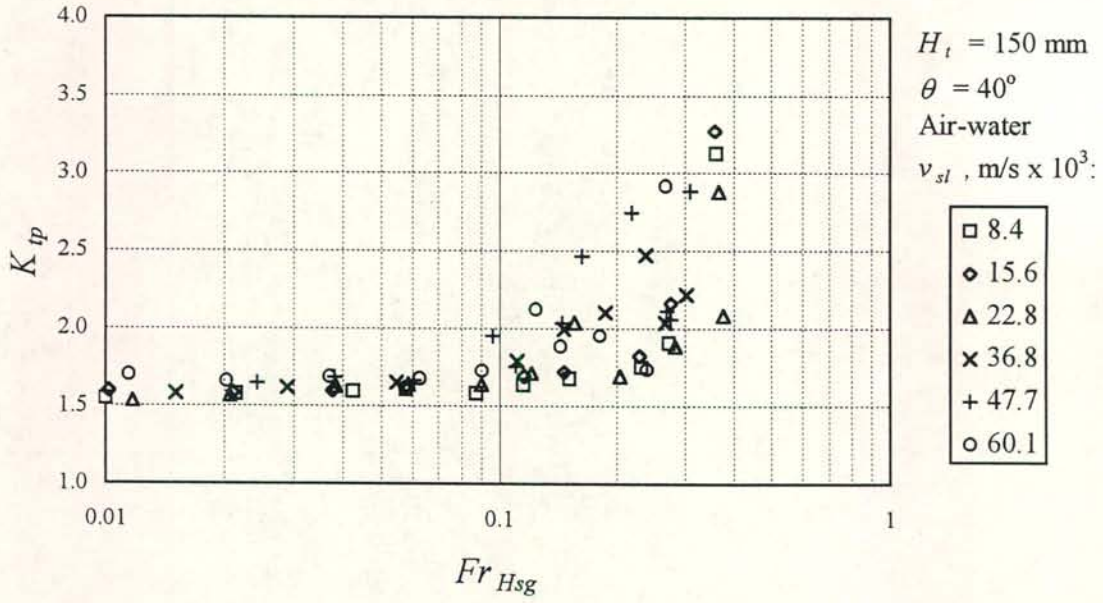

Figure E.24 (b): Two-phase entrance pressure drop coefficient for air-water flow at 40° inclination plotted against the superficial gas densimetric Froude number. The gas flow is fully turbulent.

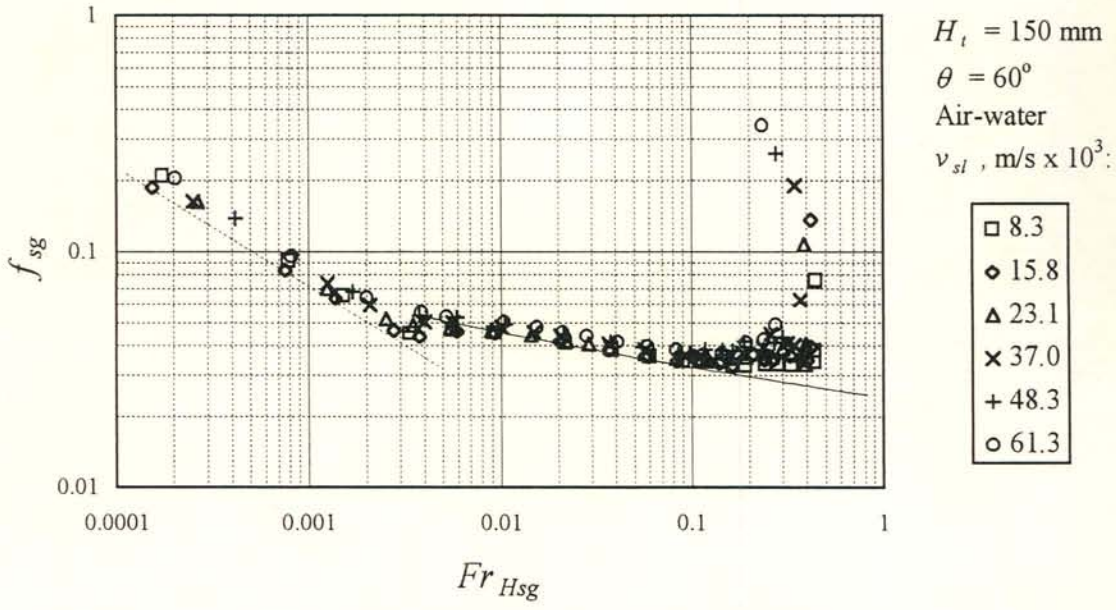

Figure E.25 (a): Friction factor for air-water flow at 60° inclination plotted against the superficial gas densimetric Froude number. Broken and solid line: Single-phase laminar and turbulent friction factor.

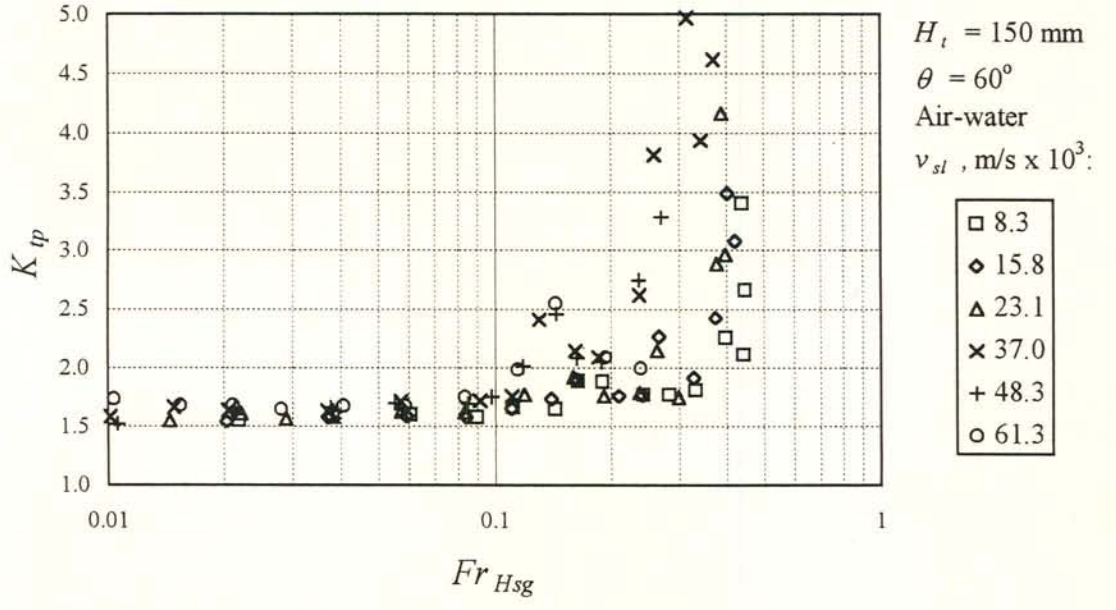

Figure E.25 (b): Two-phase entrance pressure drop coefficient for air-water flow at 60° inclination plotted against the superficial gas densimetric Froude number. The gas flow is fully turbulent.

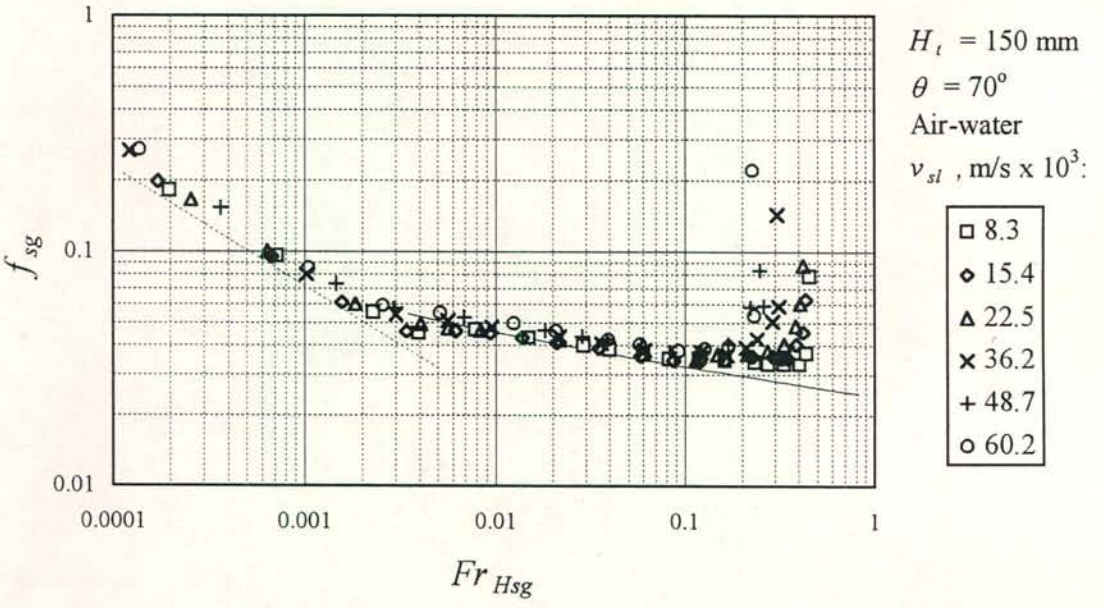

Figure E.26 (a): Friction factor for air-water flow at 70° inclination plotted against the superficial gas densimetric Froude number. Broken and solid line: Single-phase laminar and turbulent friction factor.

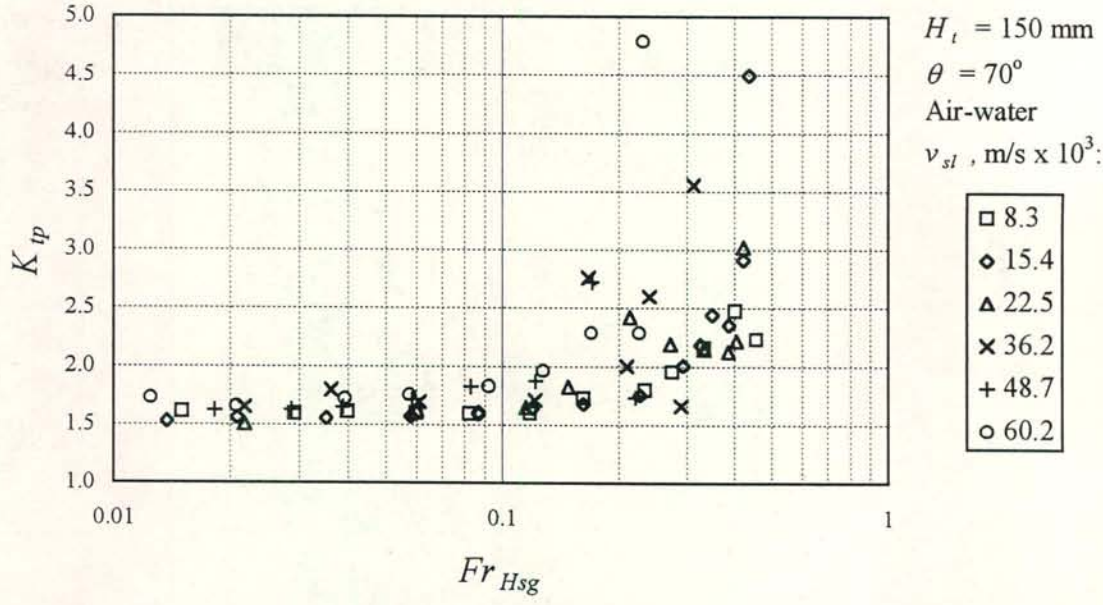

Figure E.26 (b): Two-phase entrance pressure drop coefficient for air-water flow at 70° inclination plotted against the superficial gas densimetric Froude number. The gas flow is fully turbulent.

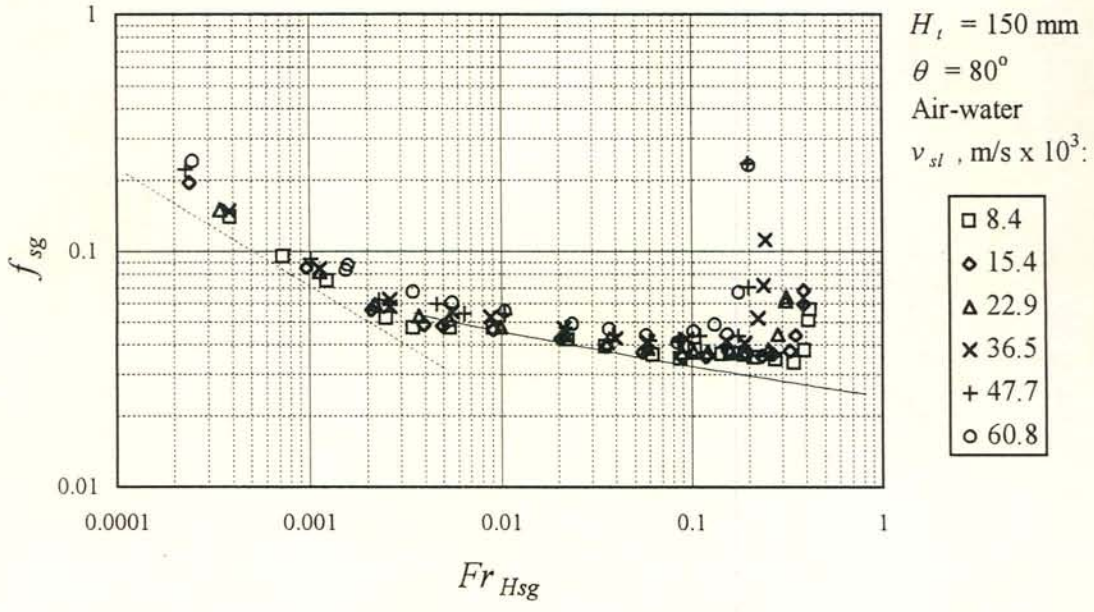

Figure E.27 (a): Friction factor for air-water flow at 80° inclination plotted against the superficial gas densimetric Froude number. Broken and solid line: Single-phase laminar and turbulent friction factor.

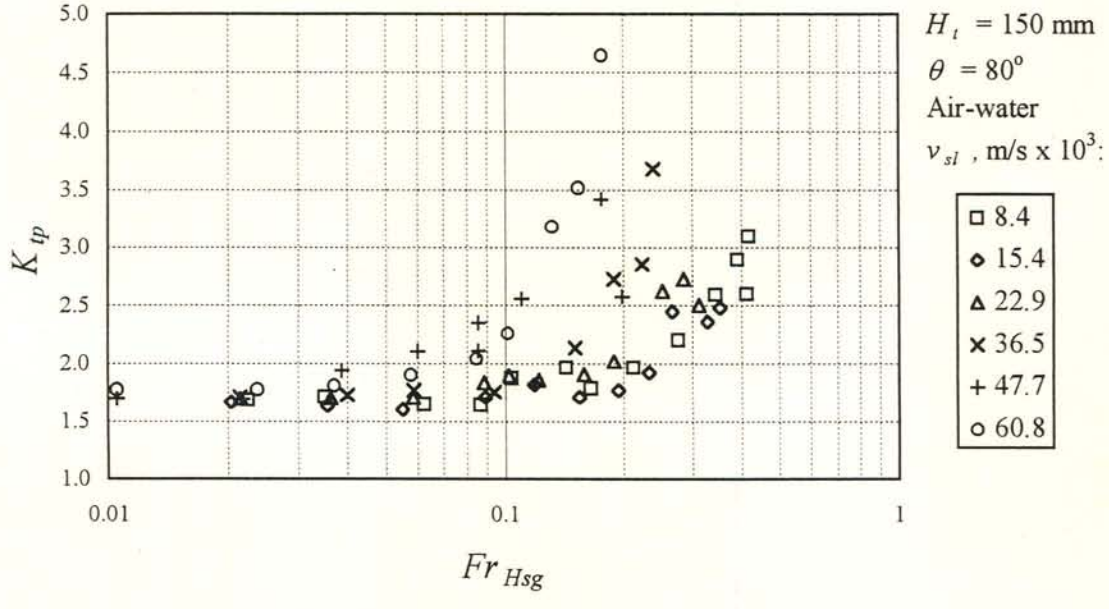

Figure E.27 (b): Two-phase entrance pressure drop coefficient for air-water flow at 80° inclination plotted against the superficial gas densimetric Froude number. The gas flow is fully turbulent.

E.6 Air-water pressure gradient and entrance pressure drop for the 50 mm duct (W_t = 20 mm)

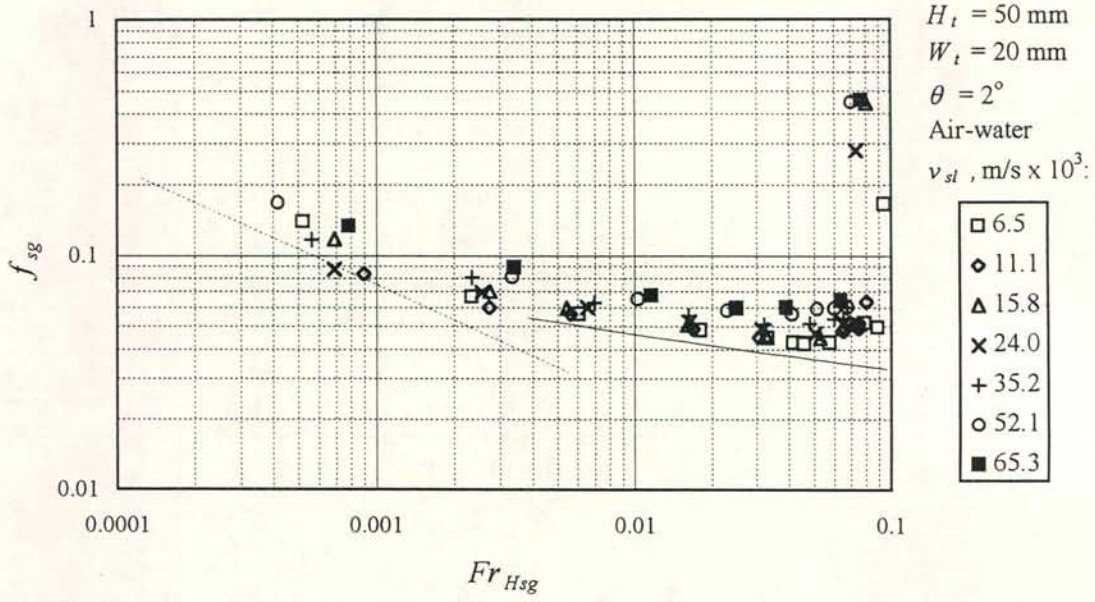

Figure E.28 (a): Friction factor for air-water flow at 2° inclination plotted against the superficial gas densimetric Froude number. Broken and solid line: Single-phase laminar and turbulent friction factor.

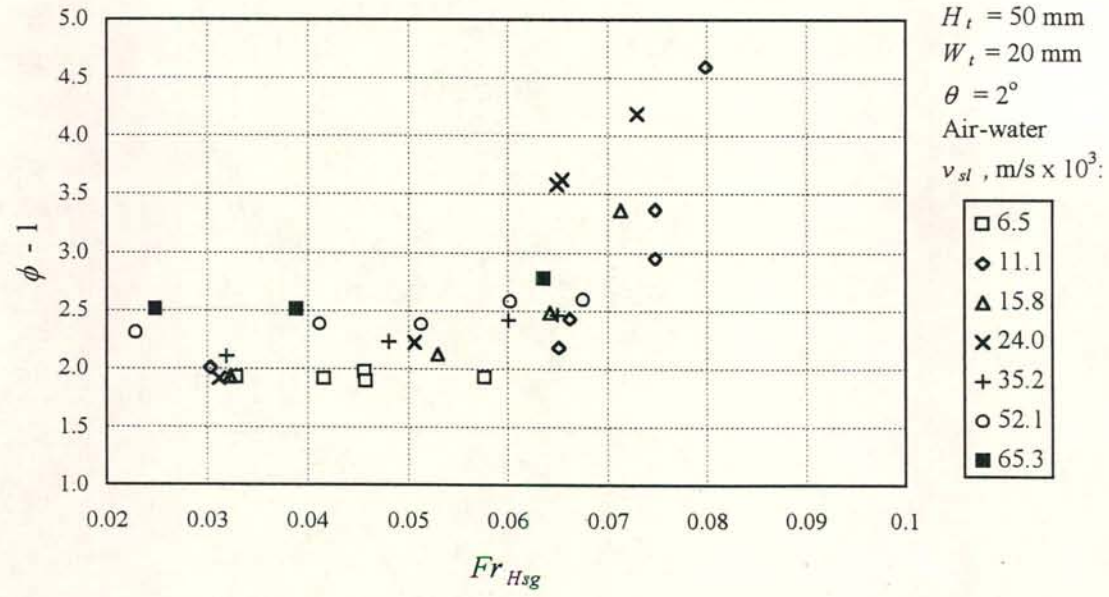

Figure E.28 (b): Two-phase entrance pressure drop coefficient for air-water flow at 2° inclination plotted against the superficial gas densimetric Froude number. The gas flow is fully turbulent.

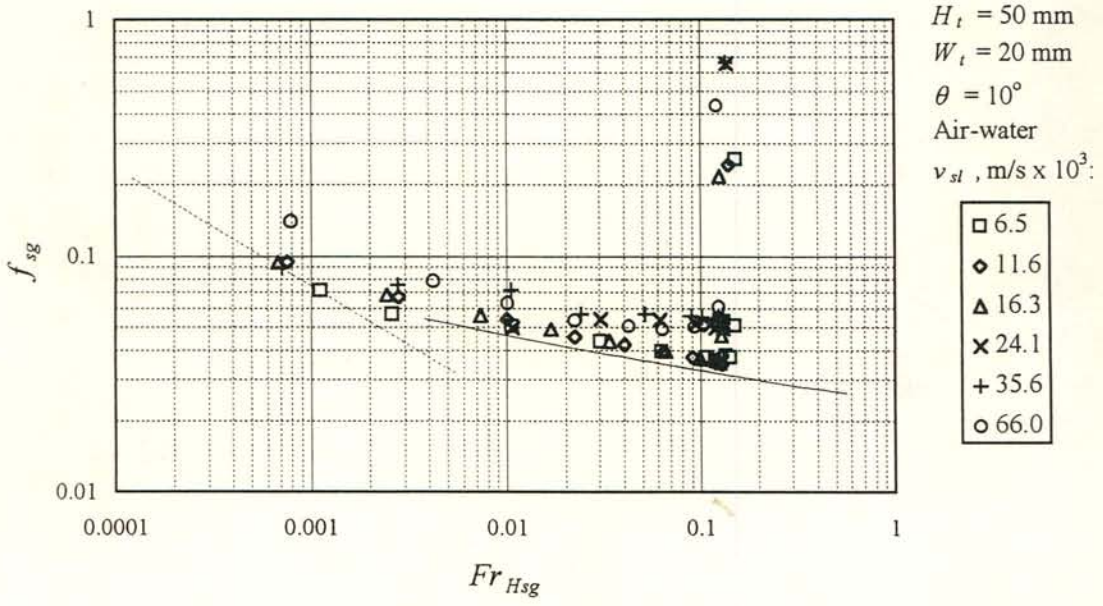

Figure E.29 (a): Friction factor for air-water flow at 10° inclination plotted against the superficial gas densimetric Froude number. Broken and solid line: Single-phase laminar and turbulent friction factor.

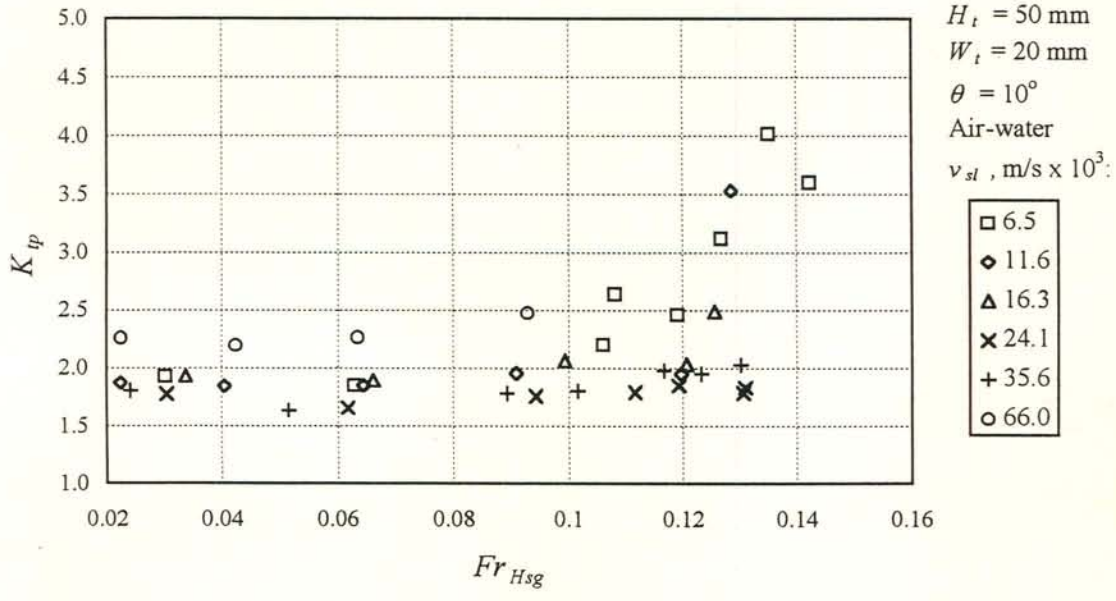

Figure E.29 (b): Two-phase entrance pressure drop coefficient for air-water flow at 10° inclination plotted against the superficial gas densimetric Froude number. The gas flow is fully turbulent.

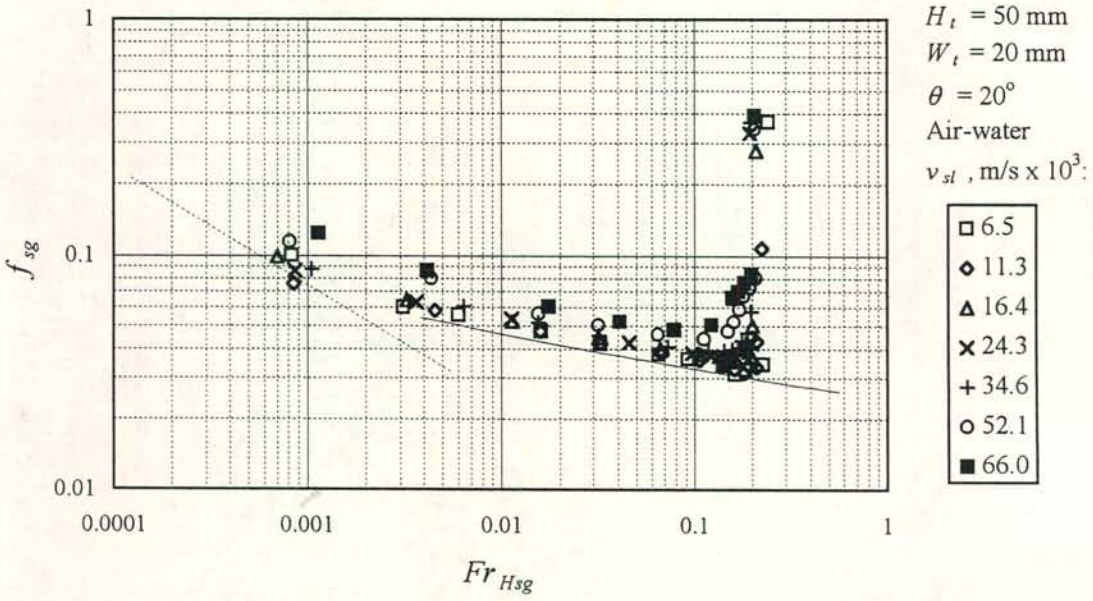

Figure E.30 (a): Friction factor for air-water flow at 20° inclination plotted against the superficial gas densimetric Froude number. Broken and solid line: Single-phase laminar and turbulent friction factor.

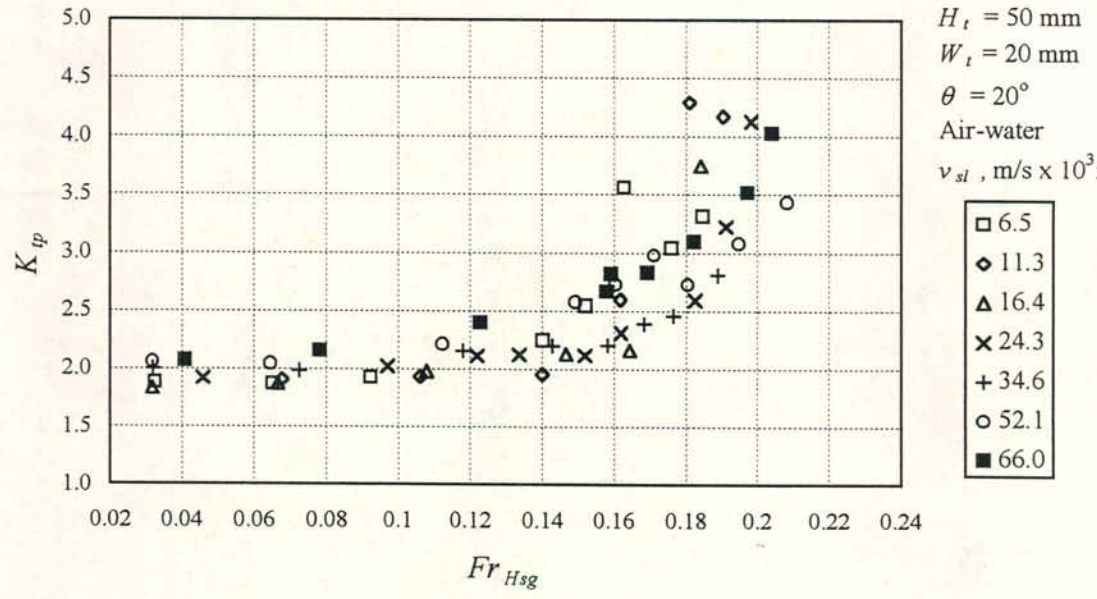

Figure E.30 (b): Two-phase entrance pressure drop coefficient for air-water flow at 20° inclination plotted against the superficial gas densimetric Froude number. The gas flow is fully turbulent.

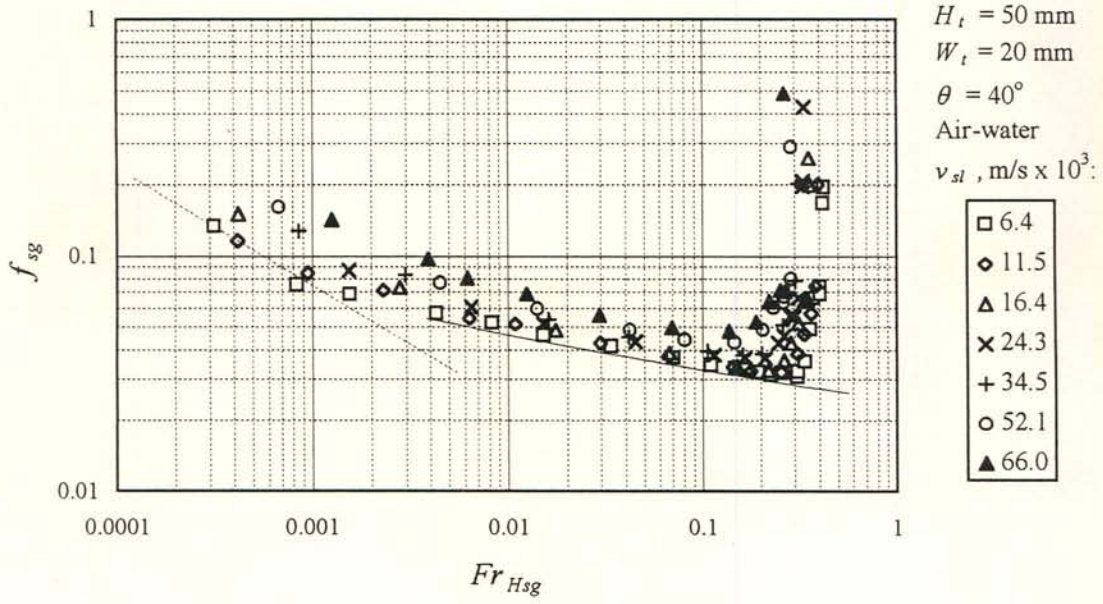

Figure E.31 (a): Friction factor for air-water flow at 40° inclination plotted against the superficial gas densimetric Froude number. Broken and solid line: Single-phase laminar and turbulent friction factor.

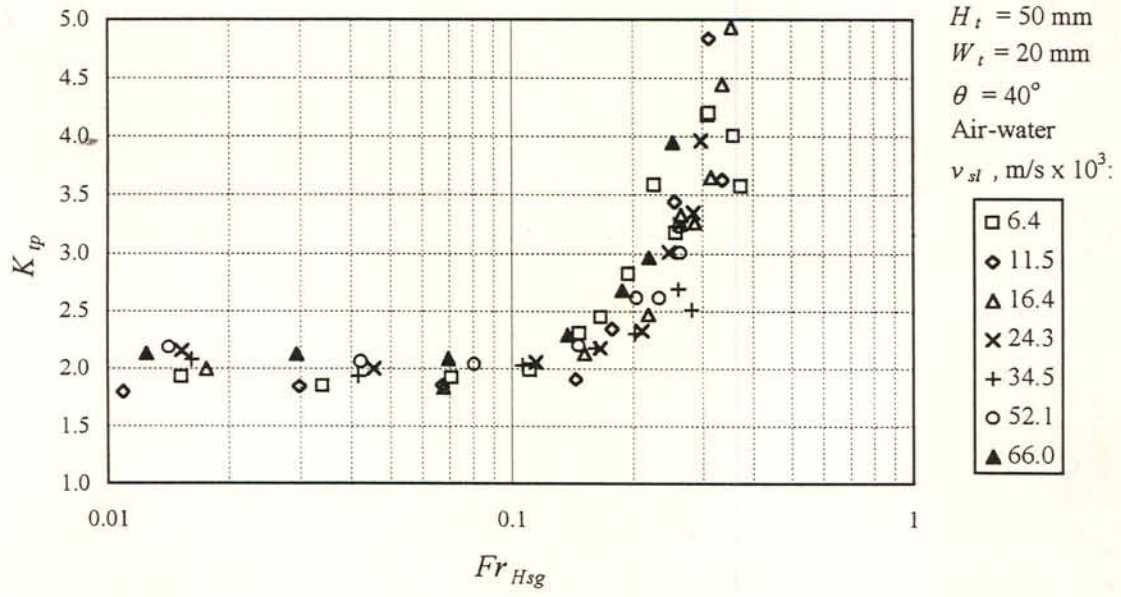

Figure E.31 (b): Two-phase entrance pressure drop coefficient for air-water flow at 40° inclination plotted against the superficial gas densimetric Froude number. The gas flow is fully turbulent.

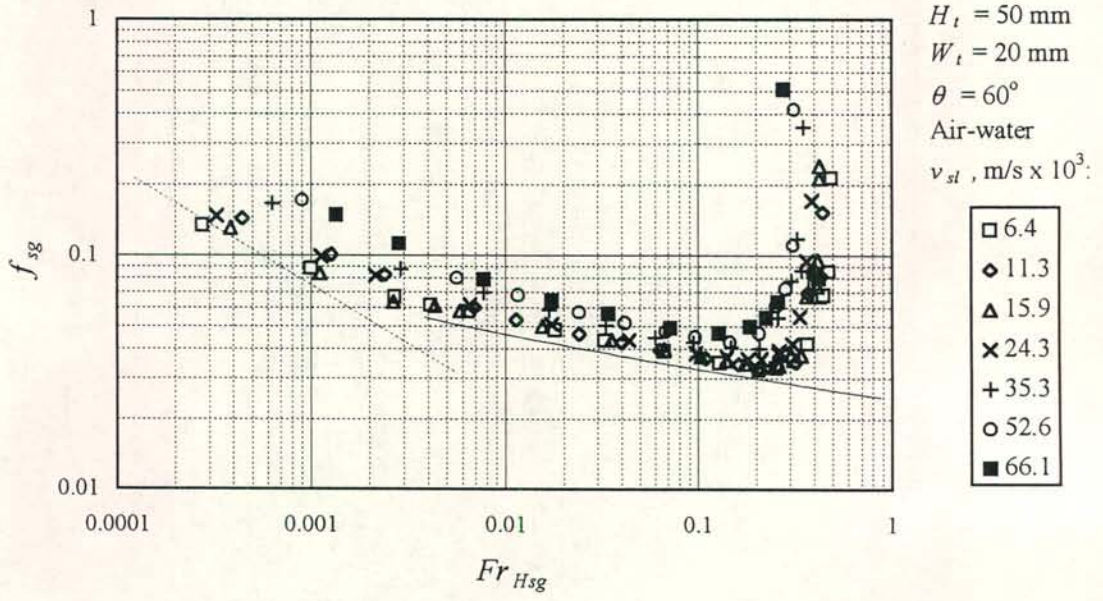

Figure E.32 (a): Friction factor for air-water flow at 60° inclination plotted against the superficial gas densimetric Froude number. Broken and solid line: Single-phase laminar and turbulent friction factor.

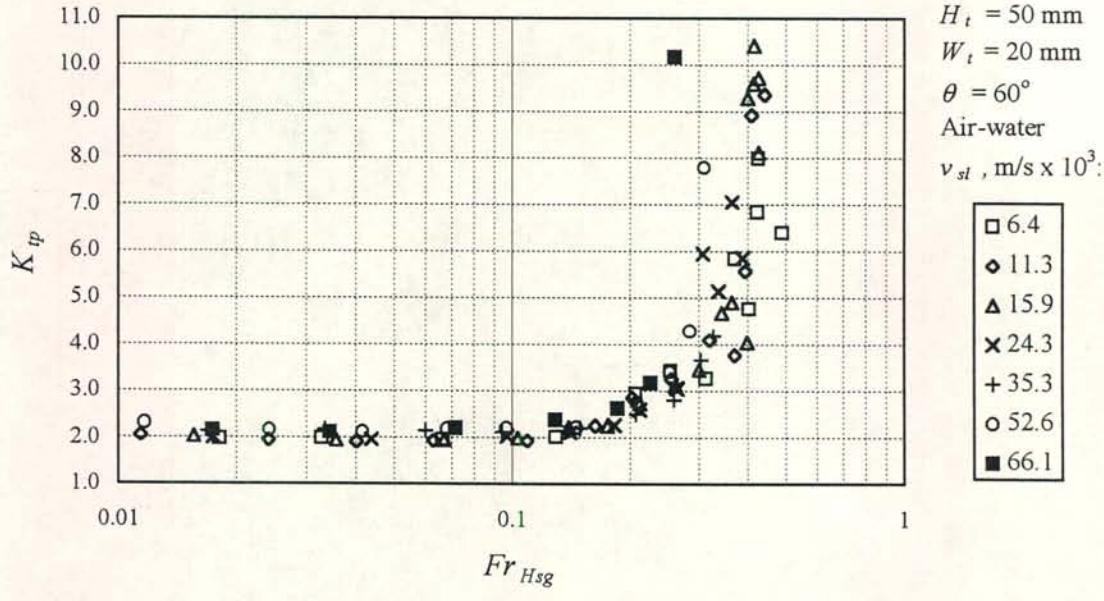

Figure E.32 (b): Two-phase entrance pressure drop coefficient for air-water flow at 60° inclination plotted against the superficial gas densimetric Froude number. The gas flow is fully turbulent.

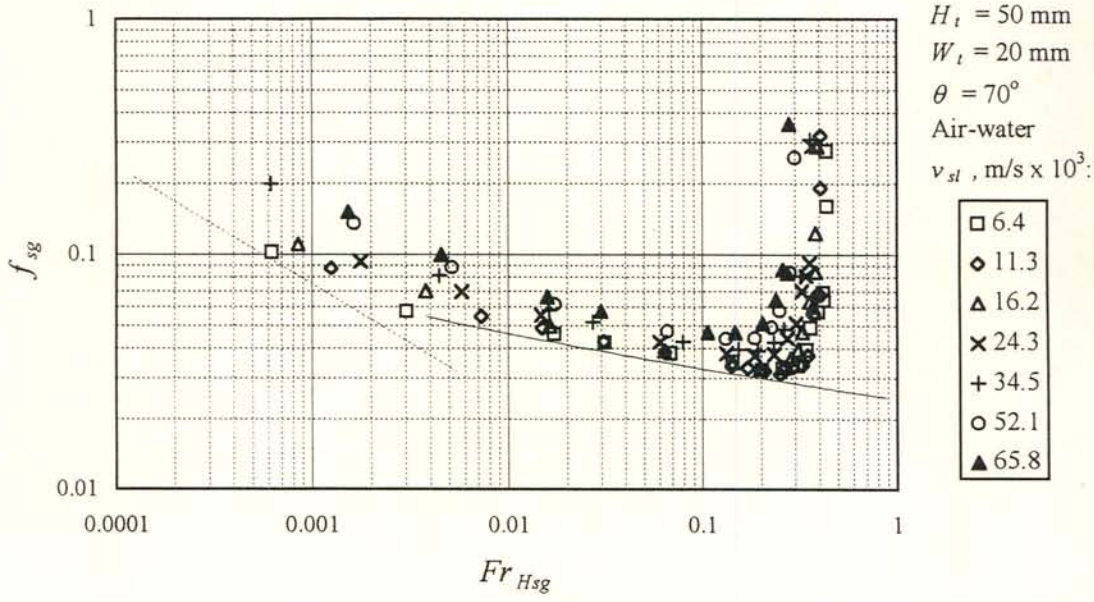

Figure E.33 (a): Friction factor for air-water flow at 70° inclination plotted against the superficial gas densimetric Froude number. Broken and solid line: Single-phase laminar and turbulent friction factor.

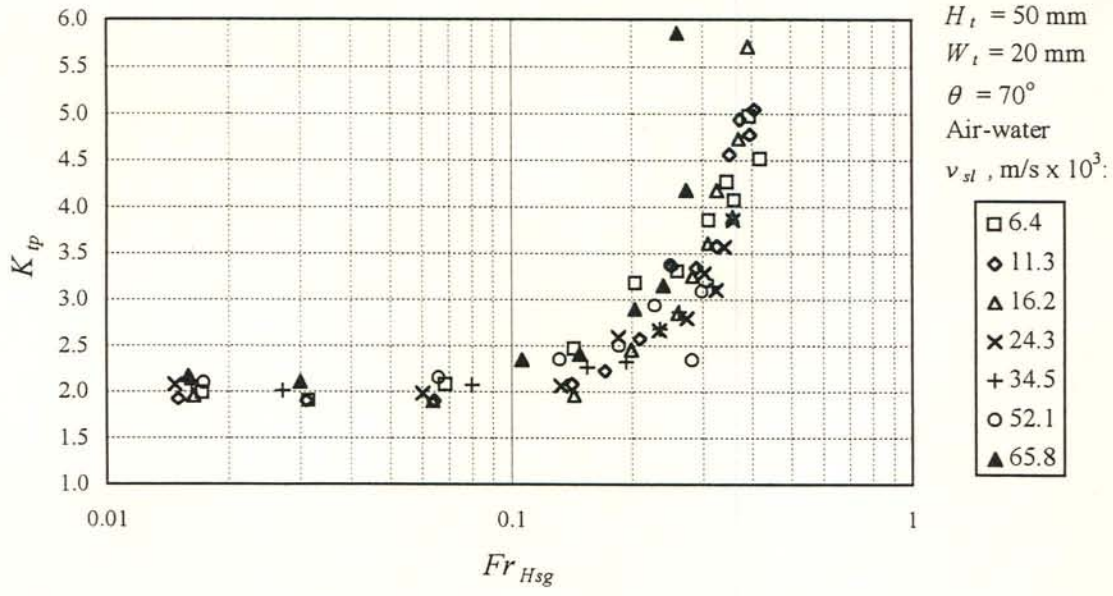

Figure E.33 (b): Two-phase entrance pressure drop coefficient for air-water flow at 70° inclination plotted against the superficial gas densimetric Froude number. The gas flow is fully turbulent.

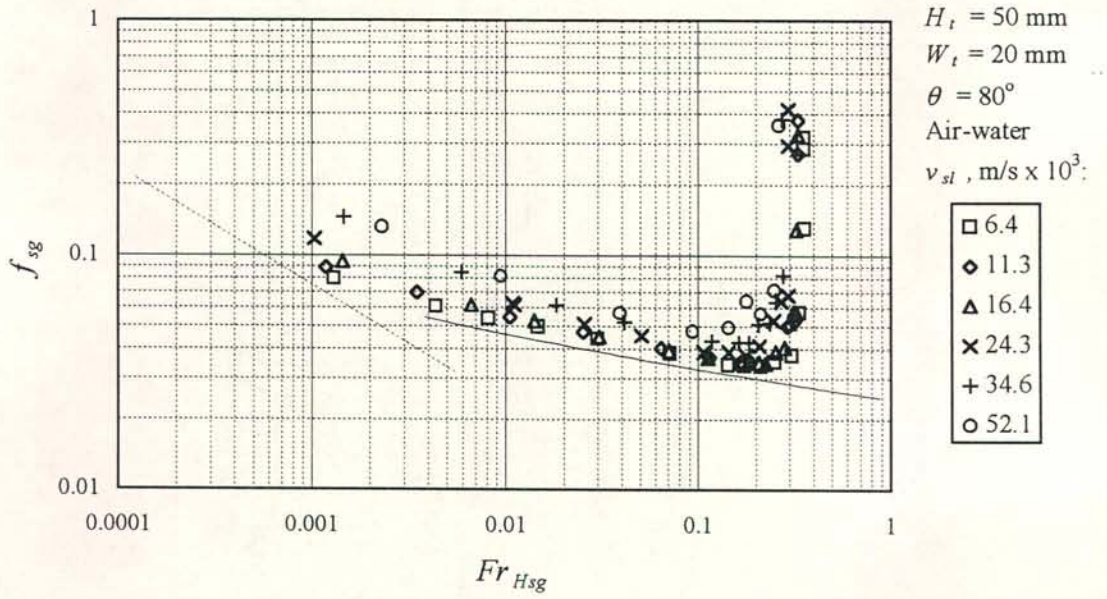

Figure E.34 (a): Friction factor for air-water flow at 80° inclination plotted against the superficial gas densimetric Froude number. Broken and solid line: Single-phase laminar and turbulent friction factor.

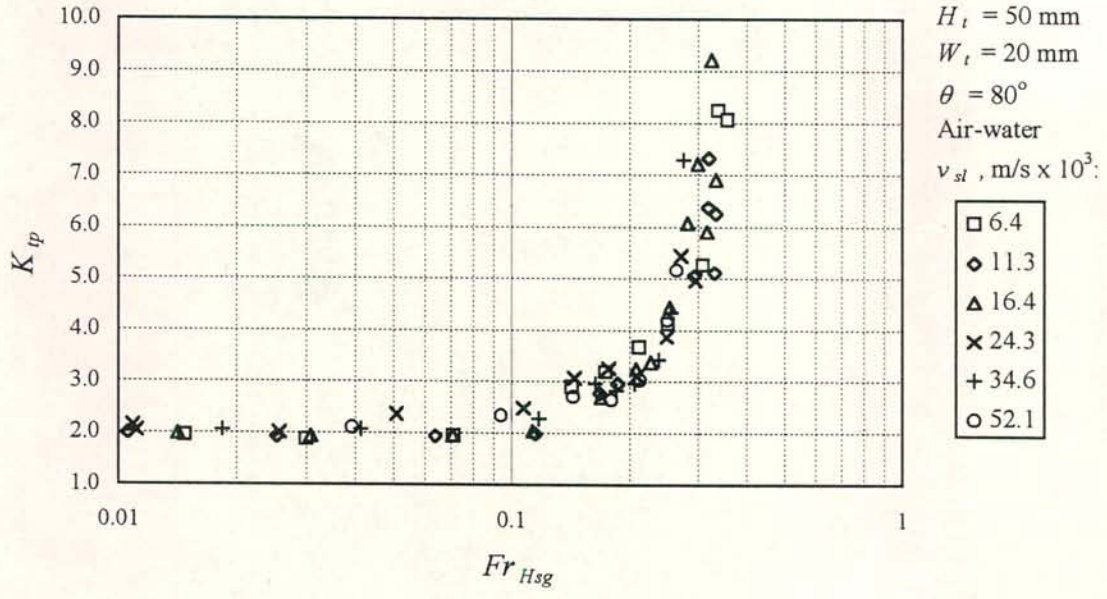

Figure E.34 (b): Two-phase entrance pressure drop coefficient for air-water flow at 80° inclination plotted against the superficial gas densimetric Froude number. The gas flow is fully turbulent.

APPENDIX F

FLOODING DATA

F.1 Flooding data for the long configuration inclined at 60 ° to the horizontal

Table F.1: Flooding data for the 50 mm duct (W_t = 10 mm).

Gas	Liquid	p_2 [N/m^2]	T_g [°C]	T_l [°C]	v_{sg} [m/s]	v_{sl} [m/s x 10^3]
Air	Water	101926	18.53	18.92	13.551	9.448
Air	Water	102375	20.04	22.63	12.568	15.405
Air	Water	102544	18.19	17.99	13.892	4.915
Air	Water	102019	18.36	17.83	12.166	30.369
Air	Water	102045	18.05	18.83	14.924	1.978
Air	Water	102639	18.71	18.28	10.793	46.721
Air	Water	101657	18.80	18.91	9.217	61.618
Air	Methanol	101799	20.35	21.57	11.692	15.517
Air	Methanol	102039	20.15	21.53	12.861	5.889
Air	Methanol	101287	19.90	20.83	12.474	12.884
Air	Methanol	102001	18.71	18.26	10.627	46.721
Air	Methanol	101772	17.47	17.22	7.586	70.861
Air	Methanol	102256	17.33	17.73	12.754	8.991
Air	Propanol	101607	19.39	20.58	11.067	6.643
Air	Propanol	101883	19.63	22.05	10.572	14.078
Air	Propanol	101883	19.63	22.05	10.572	14.078
Air	Propanol	101827	19.90	21.98	10.153	29.525
Air	Propanol	101389	19.24	19.85	8.630	46.214
Air	Propanol	101855	19.19	19.55	7.462	69.699
Argon	Water	102806	18.47	19.36	12.464	4.973
Argon	Water	101826	18.60	19.96	11.499	9.406
Argon	Water	102462	18.56	17.62	10.959	15.006
Argon	Water	102199	18.51	18.16	10.475	28.727
Argon	Water	102441	18.70	18.30	9.758	45.230
Argon	Water	101053	19.49	21.29	8.015	62.524
Helium	Water	102122	19.05	20.27	36.617	9.293
Helium	Water	101722	19.16	20.45	33.592	30.369
Helium	Water	102341	19.16	20.41	27.151	61.618
Helium	Water	103148	18.15	18.91	40.385	5.002
Helium	Water	102922	18.40	18.97	30.024	47.241
Helium	Methanol	101804	18.71	19.74	33.342	3.621
Helium	Methanol	102177	18.82	22.58	34.586	12.287
Helium	Methanol	102145	18.82	21.33	32.493	18.814
Helium	Methanol	101967	18.64	19.28	31.614	18.814

Table F.1: Continued.

Gas	Liquid	p_2 [N/m^2]	T_g [°C]	T_l [°C]	v_{sg} [m/s]	v_{sl} [m/s x 10^3]
Helium	Methanol	102347	18.80	21.34	30.977	36.653
Helium	Methanol	101873	18.88	20.75	23.501	53.819
Hydrogen	Methanol	103283	17.76	18.75	43.354	19.150
Hydrogen	Methanol	102451	17.57	18.57	42.737	19.150
Hydrogen	Methanol	102434	17.82	18.97	45.831	9.662
Hydrogen	Methanol	102505	17.73	18.90	37.114	35.430
Hydrogen	Methanol	101164	17.93	19.09	28.741	57.454
Hydrogen	Methanol	102639	18.12	19.15	22.195	74.592

Table F.2: Flooding data for the 100 mm duct.

Gas	Liquid	p_2 [N/m^2]	T_g [°C]	T_l [°C]	v_{sg} [m/s]	v_{sl} [m/s x 10^3]
Air	Water	102040	16.22	17.63	19.639	1.417
Air	Water	102286	15.58	16.46	18.561	7.827
Air	Water	102124	15.80	16.15	18.052	15.655
Air	Water	102883	17.49	18.02	20.934	0.671
Air	Water	103205	15.86	16.58	18.416	15.655
Air	Water	102751	17.57	17.59	16.834	30.849
Air	Water	102131	18.30	18.36	12.509	63.568
Air	Methanol	101824	18.53	18.97	17.579	3.085
Air	Methanol	102187	18.23	18.70	16.429	18.401
Air	Methanol	101223	18.29	17.37	10.419	74.919
Air	Methanol	102562	14.85	16.31	19.866	0.902
Air	Methanol	101316	16.12	16.84	13.593	34.962
Air	Propanol	101788	12.32	14.66	16.909	0.463
Air	Propanol	101733	13.97	14.81	13.766	13.801
Air	Propanol	102357	18.33	19.47	13.522	31.784
Air	Propanol	101979	17.44	18.49	10.930	56.696

Table F.3: Flooding data for the 150 mm duct.

Gas	Liquid	p_2 [N/m^2]	T_g [°C]	T_l [°C]	v_{sg} [m/s]	v_{sl} [m/s x 10^3]
Air	Water	107410	20.16	19.70	25.298	0.648
Air	Water	107083	27.55	24.36	24.595	1.502
Air	Water	107083	27.55	24.36	24.595	1.502
Air	Water	106640	20.66	20.86	22.735	5.254
Air	Water	107356	24.28	23.18	21.994	10.508
Air	Water	106728	13.39	14.82	20.801	20.244
Air	Water	105569	22.26	22.01	17.816	49.164

Table F.3: Continued.

Gas	Liquid	p_2 [N/m^2]	T_g [°C]	T_l [°C]	v_{sg} [m/s]	v_{sl} [m/s x 10^3]
Air	Water	105494	22.10	21.38	16.815	59.852
Air	Water	106221	24.56	23.92	19.333	36.226
Air	Methanol	102515	18.73	21.04	23.134	1.670
Air	Methanol	102667	16.88	19.26	22.705	5.892
Air	Methanol	101786	23.43	24.24	20.924	10.802
Air	Methanol	102410	16.26	16.47	19.877	22.350
Air	Methanol	102691	17.91	17.87	16.741	46.296
Air	Propanol	102033	20.64	22.41	19.743	1.296
Air	Propanol	101799	25.63	26.64	19.781	5.540
Air	Propanol	102776	21.87	22.59	18.350	9.393
Air	Propanol	101744	28.72	28.76	17.876	24.585
Air	Propanol	101265	26.38	27.02	14.141	49.857

F.2 Flooding data for the short configuration

F.2.1 Flooding data for 50 mm duct (W_t = 10 mm)

Table F.4: Flooding data for air-water flow in the 50 mm duct (W_t = 10 mm) at various inclinations.

Inclination [°]	p_2 [N/m^2]	T_g [°C]	T_l [°C]	v_{sg} [m/s]	v_{sl} [m/s x 10^3]
2	100289	15.01	14.61	5.634	8.797
2	101531	14.84	13.67	5.252	18.485
2	101281	15.23	15.38	5.010	31.079
2	101265	15.29	15.95	5.005	47.241
2	101566	15.42	16.16	4.562	54.508
2	101119	15.83	16.23	4.121	68.135
10	101882	14.62	14.23	7.266	9.163
10	102080	14.78	14.99	6.880	18.358
10	101661	15.19	15.36	6.624	31.634
10	101685	15.27	15.73	6.934	37.295
10	102080	15.77	17.08	7.221	46.619
10	101726	15.88	17.69	7.362	62.709
20	101232	15.33	15.58	9.385	7.459
20	102163	15.56	16.18	9.091	18.846
20	101052	15.79	16.78	8.486	31.354
20	101437	15.95	17.01	9.492	46.928
20	101729	16.15	17.51	8.504	62.987
40	101534	14.90	14.47	12.091	9.499

Table F.4: Continued.

Inclination [°]	p_2 [N/m^2]	T_g [°C]	T_l [°C]	v_{sg} [m/s]	v_{sl} [m/s x 10^3]
40	101160	15.12	15.01	11.410	18.550
40	101481	15.56	15.63	11.101	30.809
40	101725	15.50	15.57	10.853	39.367
40	101932	15.73	15.88	9.744	46.014
40	102085	15.86	16.10	9.772	62.709
60	103489	14.41	14.34	14.119	4.921
60	103733	14.74	14.24	13.055	12.092
60	103103	15.03	14.67	12.309	31.079
60	103483	15.03	14.99	12.088	38.935
60	101829	15.50	15.70	11.524	46.928
60	103832	15.48	15.66	9.581	68.797
60	101476	15.91	15.98	14.351	4.962
60	101593	16.39	16.56	13.756	7.245
60	101846	16.58	16.92	12.606	18.746
60	102501	16.90	18.39	12.574	31.354
60	102873	16.99	18.08	10.371	59.360
70	101628	15.91	15.57	13.119	9.273
70	101110	15.78	15.75	12.885	18.405
70	101171	15.90	16.11	12.874	30.026
70	103605	16.23	16.42	11.141	47.241
70	101209	16.30	16.77	10.547	56.689
70	100996	16.41	16.79	9.646	68.797
80	103917	15.46	14.93	13.177	9.183
80	102974	15.62	16.02	12.742	18.453
80	102960	16.08	16.56	12.442	31.634
80	103643	16.06	16.26	11.228	43.208
80	101832	16.12	16.46	10.102	56.239
80	101570	16.18	16.58	9.508	69.471
90	106141	14.00	14.76	10.032	6.491
90	106230	14.58	15.35	9.666	9.490
90	105108	13.81	14.60	9.037	17.715
90	106294	14.89	16.15	7.955	28.727
90	105580	12.24	11.05	7.371	46.214
90	106861	12.05	11.26	7.062	60.738

Table F.5: Flooding data for air-methanol flow in the 50 mm duct (W_t = 10 mm) at a 90° inclination.

Inclination [°]	p_2 [N/m^2]	T_g [°C]	T_l [°C]	v_{sg} [m/s]	v_{sl} [m/s x 10^3]
90	104448	13.85	15.14	8.471	5.824
90	104662	14.22	15.99	7.969	11.072
90	104156	14.64	16.80	7.312	18.485
90	103664	14.70	16.71	6.251	44.288
90	103865	14.78	16.38	5.581	54.508
90	103627	14.85	16.32	4.832	70.861

Table F.6: Flooding data for air-propanol flow in the 50 mm duct (W_t = 10 mm) at various inclinations.

Inclination [°]	p_2 [N/m^2]	T_g [°C]	T_l [°C]	v_{sg} [m/s]	v_{sl} [m/s x 10^3]
2	100162	16.32	17.60	5.580	7.086
2	99566	15.60	15.23	5.111	15.517
2	99490	15.76	15.71	4.479	28.727
2	99622	15.74	15.67	4.353	35.430
2	99844	15.60	15.44	4.683	44.288
2	99877	15.56	15.28	4.378	52.061
2	99794	15.53	15.32	4.324	60.738
5	99072	15.39	15.51	6.284	5.967
5	100408	15.15	15.13	5.698	15.294
5	100434	15.16	15.41	5.521	28.344
5	100342	15.35	16.41	5.306	37.295
5	100691	15.57	16.63	5.277	45.230
5	101187	15.72	16.80	5.033	68.575
10	100611	15.51	15.58	7.031	6.052
10	100652	15.76	16.03	6.529	15.184
10	100955	15.78	16.08	6.371	29.121
10	100794	15.86	16.05	6.237	46.214
10	100811	15.95	16.27	6.519	62.524
15	101386	16.00	16.36	8.257	6.377
15	100934	15.06	14.44	7.569	15.405
15	100448	15.04	14.28	7.569	27.254
15	100395	15.20	14.49	7.396	35.430
15	100541	15.20	14.78	7.747	43.384
15	101427	15.31	14.97	7.214	51.849
15	101360	15.30	14.94	7.637	67.487
20	102215	15.94	16.79	8.933	4.596
20	102114	15.82	16.46	9.181	6.609
20	101666	15.54	15.71	8.755	15.367
20	101952	16.32	17.23	8.470	30.369
20	101950	15.66	15.86	8.191	36.743
20	101893	16.28	16.85	8.466	45.787
20	102411	16.17	16.53	7.802	63.458
80	100027	15.64	15.83	10.449	4.868
80	100891	16.39	17.33	10.007	6.377
80	101895	16.25	18.41	9.531	16.228
80	102592	16.37	18.26	10.142	30.369
80	102416	16.33	18.07	9.514	38.651
80	102492	16.13	17.38	8.954	46.214
80	102349	16.12	17.01	7.538	63.458
80	101852	15.06	17.18	10.002	29.941
80	102879	15.31	17.24	8.361	55.216
90	104248	15.07	15.62	6.931	4.724
90	104017	9.87	9.92	6.060	10.629
90	103592	13.80	16.48	5.704	20.639
90	103366	13.94	16.47	5.772	29.941
90	102213	14.00	16.53	4.855	49.438
90	101693	14.03	16.49	4.354	70.861

F.2.2 Flooding data for the 100 mm duct

Table F.7: Flooding data for air-water flow in the 100 mm duct at various inclinations.

Inclination [°]	p_2 [N/m^2]	T_g [°C]	T_l [°C]	v_{sg} [m/s]	v_{sl} [m/s x 10^3]
2	100827	18.32	19.76	8.710	6.091
2	100842	18.42	19.25	8.268	15.539
2	100636	18.31	19.01	7.925	23.308
2	100632	18.26	19.02	7.839	31.216
2	100643	18.32	18.80	7.326	46.003
2	100657	18.38	18.69	6.901	63.568
20	101482	14.42	14.56	13.058	7.296
20	101474	16.26	16.71	12.606	14.984
20	101150	17.24	17.46	12.319	23.138
20	101584	17.81	17.93	12.671	50.101
20	102166	18.04	18.15	12.873	63.433
20	101219	17.62	17.64	12.366	31.156
40	103957	18.70	19.25	17.718	7.752
40	101764	18.94	19.75	16.706	15.749
40	101673	19.20	20.00	15.876	23.308
40	101795	19.26	19.97	15.503	31.309
40	104128	19.48	19.99	14.423	51.164
40	103954	19.54	19.70	14.541	65.554
60	101323	20.73	20.75	19.845	6.328
60	103833	21.62	21.75	18.655	12.747
60	102525	21.32	21.64	18.497	23.308
60	102030	21.55	21.59	17.624	34.277
60	101279	21.18	21.86	15.405	50.670
60	102926	21.04	21.17	14.235	64.745
70	101333	20.89	22.00	19.913	8.007
70	101701	21.22	22.82	19.744	15.955
70	100987	21.42	22.76	19.339	23.544
70	100803	21.52	22.48	16.411	34.076
70	100863	21.62	23.02	14.637	51.478
70	101019	21.77	22.90	13.753	64.965
80	102879	17.95	18.64	19.338	8.697
80	102686	20.80	21.95	18.839	16.038
80	102514	20.86	21.65	17.463	23.250
80	102142	20.66	21.40	15.233	34.277
80	102230	20.56	21.31	12.972	49.946
80	105281	20.52	20.94	11.771	64.745

Table F.7: Continued.

Inclination [°]	p_2 [N/m^2]	T_g [°C]	T_l [°C]	v_{sg} [m/s]	v_{sl} [m/s x 10^3]
90	103766	21.57	21.90	12.484	6.196
90	103934	18.61	18.73	12.014	9.365
90	104593	19.34	19.78	11.468	15.655
90	104120	20.33	20.76	10.976	23.308
90	104486	21.79	24.55	10.310	30.849
90	103415	22.02	24.47	9.585	45.603
90	102025	20.10	20.20	8.866	55.204
90	104076	20.15	20.71	7.825	69.925

Table F.8: Flooding data for air-methanol flow in the 100 mm duct at a 90° inclination.

Inclination [°]	p_2 [N/m^2]	T_g [°C]	T_l [°C]	v_{sg} [m/s]	v_{sl} [m/s x 10^3]
90	102887	15.56	15.95	9.700	7.234
90	102750	20.33	21.86	9.525	10.595
90	103067	21.49	22.69	9.189	17.481
90	101319	17.75	16.38	7.477	34.962
90	101183	18.30	16.85	7.385	41.132
90	101832	18.15	16.65	7.185	51.164
90	102640	18.20	16.52	6.825	58.270
90	102926	16.08	15.78	8.054	26.222
90	103410	16.36	15.28	7.093	51.164

Table F.9: Flooding data for air-propanol flow in the 100 mm duct at various inclinations.

Inclination [°]	p_2 [N/m^2]	T_g [°C]	T_l [°C]	v_{sg} [m/s]	v_{sl} [m/s x 10^3]
2	100458	20.41	21.45	7.988	5.142
2	100387	20.06	21.21	7.414	8.169
2	100392	20.28	21.02	7.239	15.470
2	100376	20.58	21.70	6.735	22.873
2	100545	20.62	21.62	6.530	31.498
2	100412	20.65	21.76	5.704	52.182
2	100292	20.72	21.81	5.717	65.967
40	101097	16.04	17.57	15.673	4.883
40	101113	16.29	16.85	14.351	14.447
40	101309	16.80	16.86	13.729	30.140
40	103396	17.73	18.05	13.291	47.246
40	102732	17.71	17.89	12.815	64.745
90	102378	17.60	16.90	7.047	34.962
90	102793	20.45	22.08	8.332	5.019

Table F.9: Continued.

Inclination [°]	p_2 [N/m^2]	T_g [°C]	T_l [°C]	v_{sg} [m/s]	v_{sl} [m/s x 10^3]
90	102900	19.17	20.18	8.280	8.162
90	102841	18.59	19.64	7.799	14.815
90	103662	18.45	19.75	7.572	22.249
90	101034	20.43	21.78	5.792	46.616
90	100985	20.58	21.60	5.110	56.696
90	101014	20.53	21.48	4.835	67.669

F.2.3 Flooding data for the 150 mm duct

Table F.10: Flooding data for air-water flow in the 150 mm duct at various inclinations.

Inclination [°]	p_2 [N/m^2]	T_g [°C]	T_l [°C]	v_{sg} [m/s]	v_{sl} [m/s x 10^3]
2	100454	24.47	25.64	9.581	8.381
2	100446	24.10	25.13	9.081	15.643
2	100455	23.43	24.25	9.133	20.589
2	100425	23.66	24.72	8.466	36.866
2	100386	23.85	24.79	7.954	48.557
2	100364	23.95	24.80	7.619	61.182
20	101608	26.00	26.36	17.829	8.391
20	101488	25.70	26.26	17.970	15.611
20	101678	25.61	25.81	17.256	22.776
20	102282	25.54	25.45	17.248	36.768
20	102192	24.01	24.23	17.402	47.682
20	102074	23.81	24.10	17.390	60.087
40	102011	24.83	25.20	22.369	8.313
40	101982	26.16	26.07	20.979	15.715
40	105272	26.31	25.68	20.484	22.943
40	101893	25.90	25.42	19.302	34.244
40	102050	24.84	24.97	18.405	49.111
40	102067	24.80	24.55	18.862	59.652
60	103239	26.07	26.39	23.175	8.312
60	102077	27.30	27.87	22.799	15.776
60	102055	27.25	27.55	22.136	23.066
60	101830	26.92	27.42	20.615	36.985
60	101785	27.22	27.13	19.281	48.302
60	101574	26.75	26.60	18.476	61.264
70	101908	22.26	22.79	23.105	8.260
70	102854	23.56	24.05	22.979	15.447
70	103255	23.95	24.34	22.575	22.549
70	102105	23.98	24.33	19.558	36.198

Table F.10: Continued.

Inclination [°]	p_2 [N/m^2]	T_g [°C]	T_l [°C]	v_{sg} [m/s]	v_{sl} [m/s x 10^3]
70	101575	24.07	24.29	17.944	48.729
70	101420	24.30	24.37	16.882	60.192
80	102557	22.16	22.65	22.321	8.382
80	102616	22.79	23.43	21.687	15.436
80	102246	23.24	24.29	19.443	22.943
80	102652	23.67	24.56	17.227	36.534
80	103613	24.94	25.91	15.425	47.732
80	101556	24.89	25.38	14.748	60.830
90	102199	24.34	25.72	10.237	8.452
90	101906	24.40	25.91	9.026	15.565
90	101996	24.26	25.37	9.158	20.946
90	102162	24.33	25.42	8.587	36.466
90	102283	24.34	25.22	8.004	48.989
90	102472	24.23	24.91	7.893	60.166

F.2.4 Flooding data for 50 mm duct (W_t = 20 mm)

Table F.11: Flooding data for air-water flow in the 50 mm duct (W_t = 20 mm) at various inclinations.

Inclination [°]	p_2 [N/m^2]	T_g [°C]	T_l [°C]	v_{sg} [m/s]	v_{sl} [m/s x 10^3]
2	99362	13.87	13.44	6.183	6.483
2	99314	13.82	13.26	5.691	11.088
2	99359	13.86	13.46	5.688	15.826
2	99436	13.97	13.49	5.439	24.039
2	99400	13.99	13.51	5.237	35.178
2	99618	14.13	13.52	5.321	52.134
2	99532	14.15	13.47	5.559	65.257
10	101008	14.11	15.01	7.789	6.463
10	100762	14.35	15.80	7.496	11.561
10	101042	14.42	15.52	7.082	16.320
10	100814	14.47	15.36	7.399	24.103
10	100868	14.53	15.56	7.380	35.626
10	100944	14.61	15.43	7.322	51.923
10	101185	14.67	14.97	6.967	65.965
20	101410	13.65	13.88	9.792	6.577
20	100378	13.61	13.88	9.462	11.305
20	100733	13.59	13.90	9.144	16.410
20	100260	13.77	13.95	8.922	24.251
20	100228	13.86	13.93	8.914	34.644
20	100343	14.24	13.95	9.149	52.097

Table F.11: Continued.

Inclination [°]	p_2 [N/m^2]	T_g [°C]	T_l [°C]	v_{sg} [m/s]	v_{sl} [m/s x 10^3]
20	101442	14.02	13.82	9.004	66.006
40	101192	13.58	13.97	12.926	6.382
40	101235	13.68	13.98	12.534	11.487
40	101110	13.69	13.89	11.935	16.410
40	102019	13.84	13.93	11.494	24.251
40	100988	13.96	13.91	11.155	34.462
40	100452	14.08	13.87	10.713	52.149
40	100515	14.09	13.83	10.378	66.006
60	101890	13.97	14.44	13.915	6.353
60	101312	14.00	14.89	13.245	11.332
60	101792	14.52	15.81	12.980	15.895
60	101250	14.74	15.69	12.437	24.296
60	102132	14.91	15.84	11.800	35.263
60	102232	14.97	15.12	11.176	52.648
60	102178	14.98	14.98	10.466	66.144
70	101800	13.61	13.76	13.097	6.382
70	101204	13.57	13.60	12.720	11.305
70	101682	13.54	13.60	12.438	16.228
70	101653	13.67	13.65	12.090	24.251
70	101748	13.85	13.70	11.941	34.462
70	101314	13.90	13.68	10.914	52.149
70	101549	13.99	13.72	10.522	65.824
80	101775	14.11	13.78	11.878	6.382
80	101820	13.67	13.47	11.440	11.305
80	101692	13.46	13.36	11.467	16.410
80	101997	14.00	13.70	10.775	24.251
80	101538	13.83	13.61	10.438	34.644
80	101594	14.02	13.74	10.236	52.149
80	102246	14.06	13.76	9.418	66.189
90	103405	14.61	15.56	7.925	6.370
90	103913	14.91	16.52	7.582	11.575
90	104594	15.21	16.60	7.296	16.215
90	101863	15.25	16.61	6.682	24.382
90	103054	14.82	14.84	5.738	35.054
90	101968	15.29	16.50	5.769	35.480
90	103596	14.95	14.87	5.330	46.924
90	101179	15.05	14.88	4.610	56.466
90	102029	15.35	16.19	4.452	66.224

F.3 Flooding data plotted against the proposed correlation given by equation (5.4)

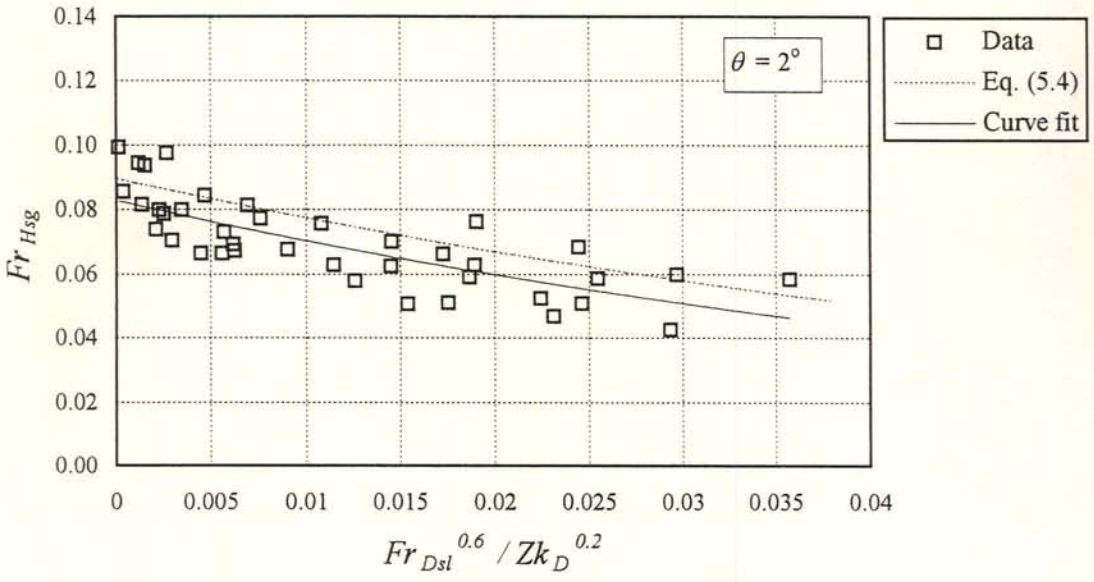

Figure F.1: Flooding data for ducts inclined at 2° to the horizontal. The solid line represents the best fit according to which $K_o = 0.082$ and $n = 16.3$.

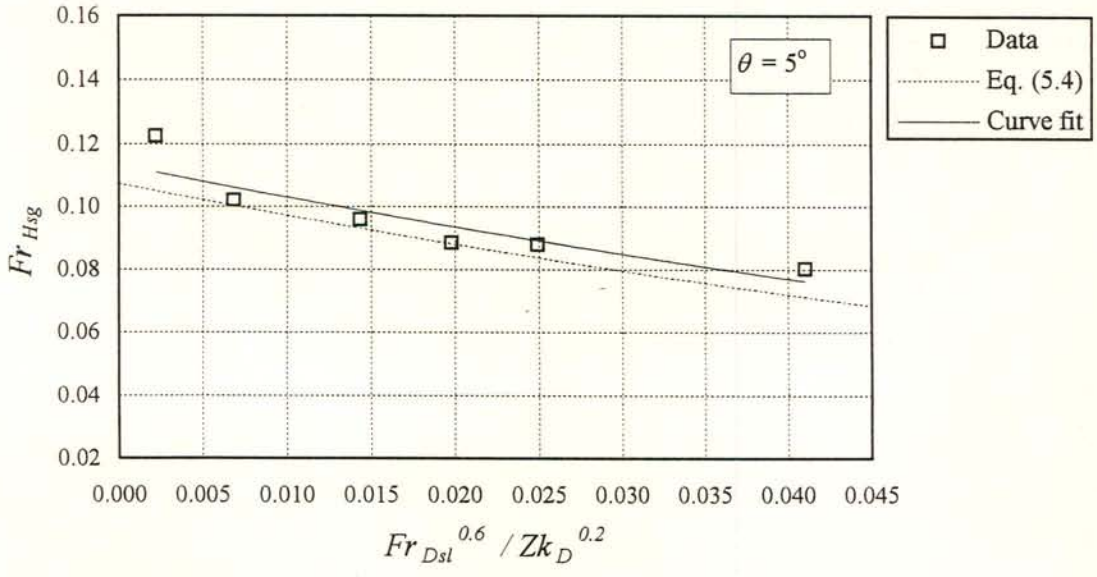

Figure F.2: Flooding data for ducts inclined at 5° to the horizontal. The solid line represents the best fit according to which $K_o = 0.114$ and $n = 9.7$.

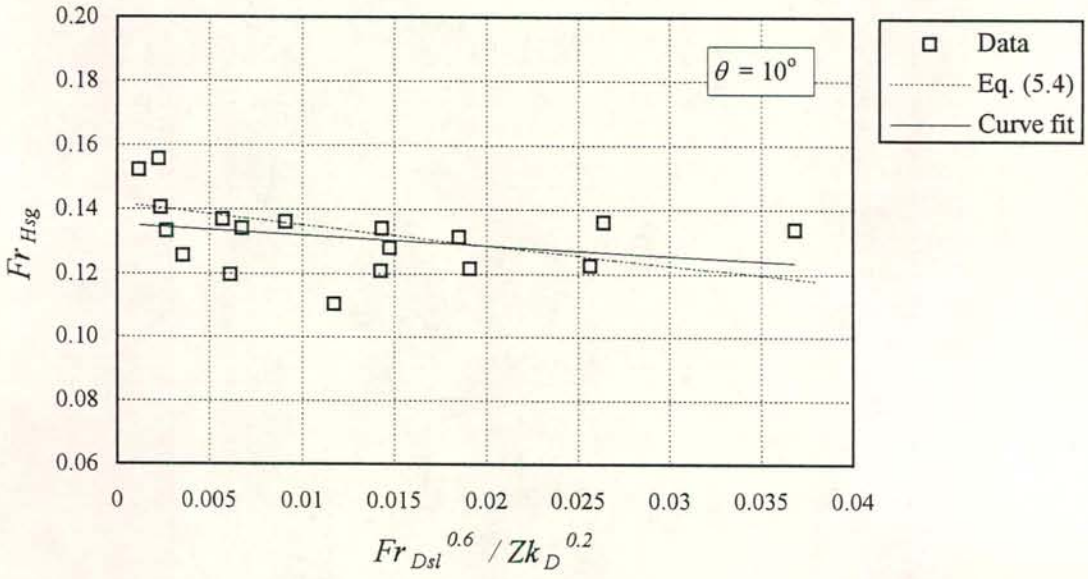

Figure F.3: Flooding data for ducts inclined at 10° to the horizontal. The solid line represents the best fit according to which $K_o = 0.131$ and $n = 0.8$.

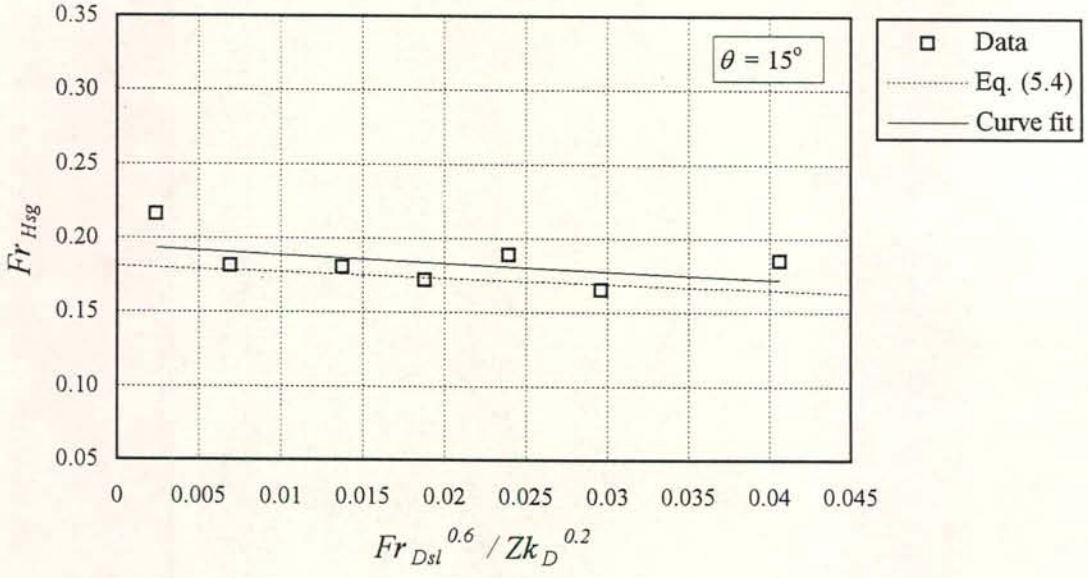

Figure F.4: Flooding data for ducts inclined at 15° to the horizontal. The solid line represents the best fit according to which $K_o = 0.195$ and $n = 3.1$.

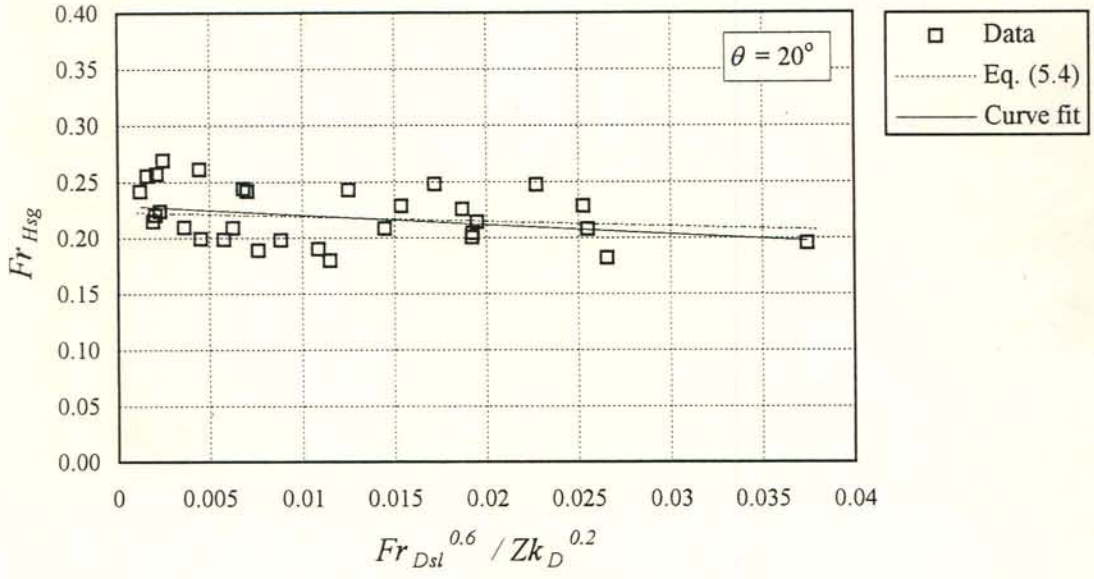

Figure F.5: Flooding data for ducts inclined at 20° to the horizontal. The solid line represents the best fit according to which $K_o = 0.234$ and $n = 4.5$.

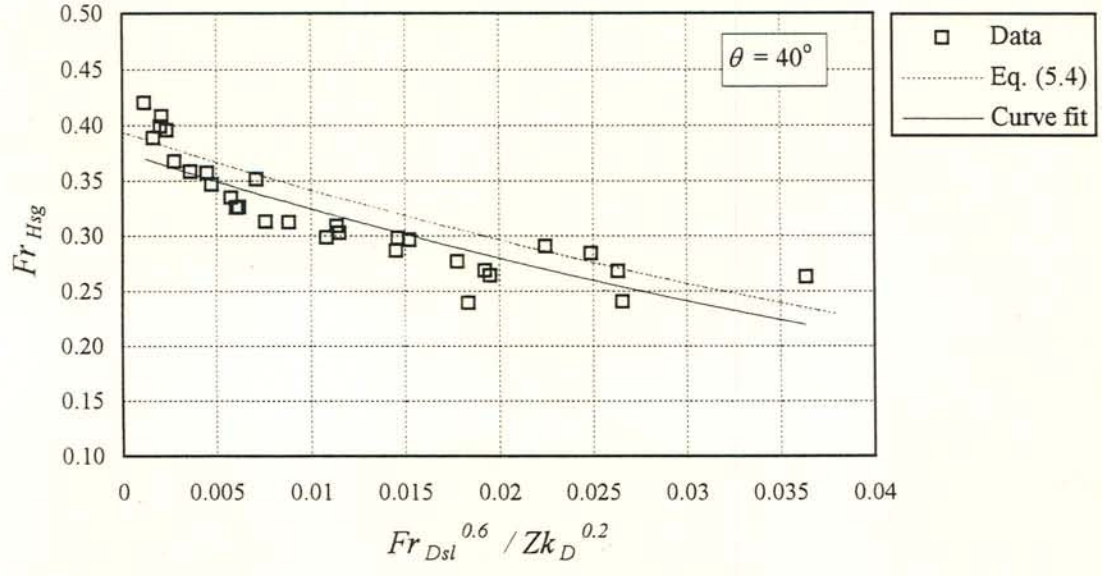

Figure F.6: Flooding data for ducts inclined at 40° to the horizontal. The solid line represents the best fit according to which $K_o = 0.371$ and $n = 13.1$.

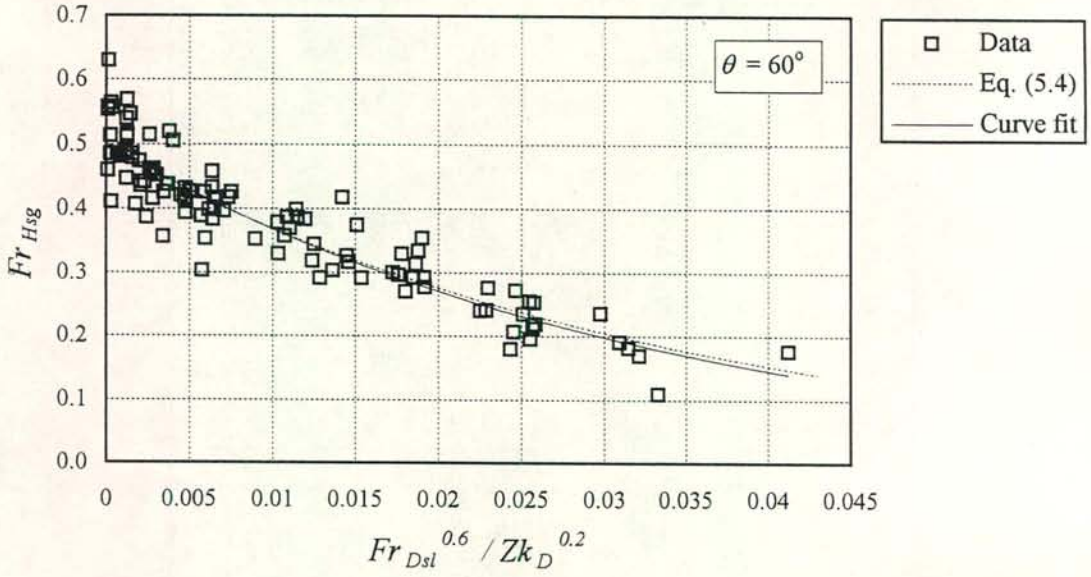

Figure F.7: Flooding data for ducts inclined at 60° to the horizontal. The solid line represents the best fit according to which $K_o = 0.504$ and $n = 31.1$.

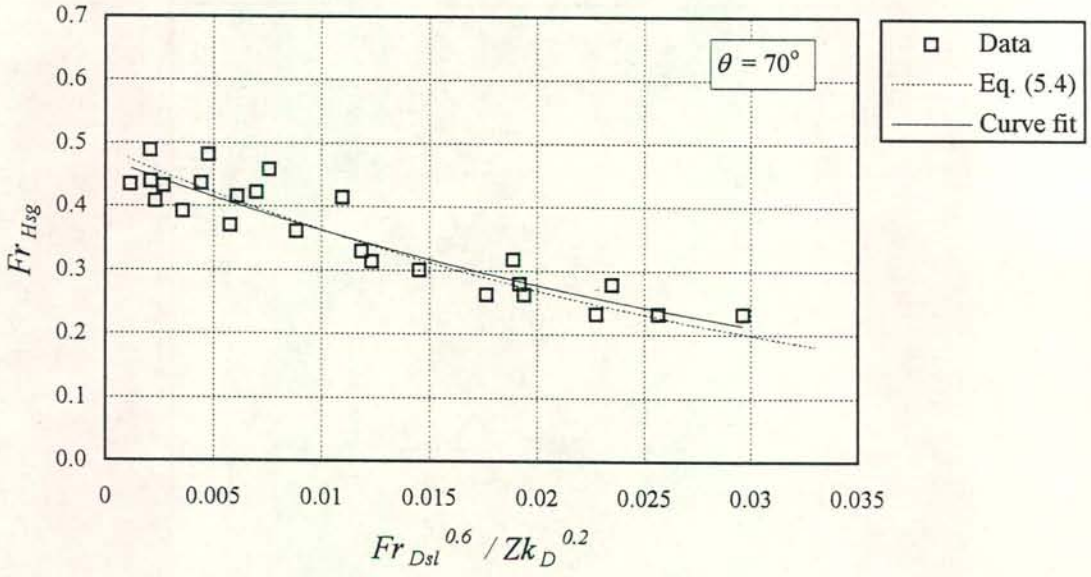

Figure F.8: Flooding data for ducts inclined at 70° to the horizontal. The solid line represents the best fit according to which $K_o = 0.499$ and $n = 28.1$.

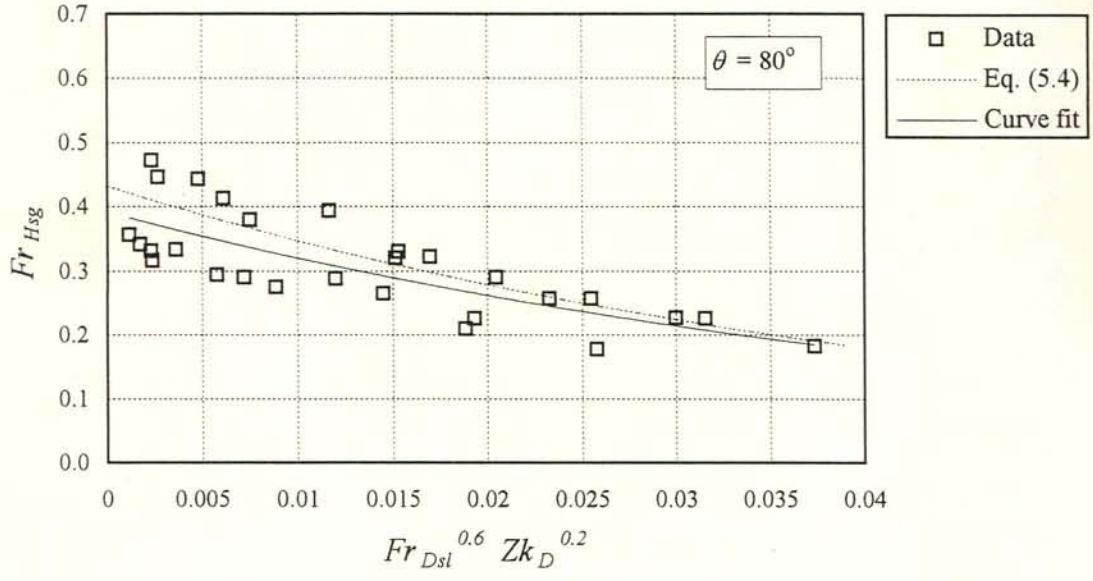

Figure F.9: Flooding data for ducts inclined at 80° to the horizontal. The solid line represents the best fit according to which K_o = 0.425 and n = 22.6.

APPENDIX G

DRAFT EQUATION FOR FORCED DRAFT INCLINED HEAT EXCHANGERS

G.1 Conservation laws and thermodynamic relations

The relevant conservation laws and thermodynamic relations for a perfect gas are briefly summarised in sections G.1.1 to G.1.4. The conservation equations are presented in their one-dimensional form.

G.1.1 Conservation of mass

When applying the law of conservation of mass to a control volume, the resultant equation, called the continuity equation, is

$$\frac{\partial}{\partial t}\left(M_{C.V.}\right) = m_i - m_o \tag{G.1}$$

or

$$m_i = m_o \tag{G.2}$$

in the case of steady flow, where

$$m = \rho v A \tag{G.3}$$

G.1.2 The momentum theorem

The momentum theorem for fluid flow through a control volume is based on Newton's second law of motion for a system of fixed identity

$$\sum \overline{F} = M \frac{D}{Dt}\left(\bar{v}\right) \tag{G.4}$$

In the case of flow through a control volume, equation (G.4) becomes

$$\sum F = \frac{\partial}{\partial t}\left(M v\right)_{C.V.} + \left(m v\right)_o - \left(m v\right)_i \tag{G.5}$$

$\sum F$ is the resultant force acting on the fluid inside the control volume including gravity, pressure and shear forces and the reaction of drag forces exerted by the fluid on flow obstacles. For steady flow equation (G.5) reduces to

$$\sum F = m\left(v_o - v_i\right) \tag{G.6}$$

G.1.3 The first law of thermodynamics

The first law of thermodynamics for a system undergoing a change from state 1 to state 2 is based on the definition

$$\Omega_{12} = E_2 - E_1 + W_{12} \tag{G.7}$$

It can be written in a differential form for a small change in state:

$$\delta \Omega = dE + \delta W \tag{G.8}$$

$\delta\Omega$ is the heat added to the system, dE is the change in energy of the system and δW is the work done by the system on its surroundings. A distinction is made by using the differential notations δ and d because E is a system property whereas Ω and W are not. When a system of fixed identity undergoes a change in state while moving through space with time, the first law can be written as a rate equation

$$\frac{D\Omega}{Dt} = \frac{DE}{Dt} + \frac{DW}{Dt} \tag{G.9}$$

The corresponding relation applicable to a control volume is

$$Q = \left(\frac{\partial E}{\partial t}\right)_{C.V.} + m_o\left(e + \frac{p}{\rho}\right)_o - m_i\left(e + \frac{p}{\rho}\right)_i + P \tag{G.10}$$

where e is the energy per unit mass of fluid passing through the control volume. It consists of internal energy u, kinetic energy $1/2\ v^2$ and potential energy gz:

$$e = u + 1/2\, v^2 + gz \tag{G.11}$$

Q is the time rate of heat added to the control volume (heat transfer rate) and P is the rate at which work is done by the fluid on its surrounding as it passes through the control volume, such as shaft work and shear work. p/ρ represents the work done by the pressure forces acting on the fluid at the control volume surface.

The terms u and p/ρ often appear as a sum, which is called the enthalpy i:

$$i = u + p/\rho \tag{G.12}$$

Substitute equations (G.11) and (G.12) in equation (G.10) to obtain the following relationship for steady flow:

$$Q = m\left\{\left(i + 1/2\, v^2 + gz\right)_o - \left(i + 1/2\, v^2 + gz\right)_i\right\} + P \tag{G.13}$$

G.1.4 Perfect gas relations

The well-known thermal equation of state for a perfect gas is

$$p/\rho = R\, T \tag{G.14}$$

The internal energy u of a thermally perfect gas is a function of its temperature and can be expressed as

$$d\, u = c_v\, d\, T \tag{G.15}$$

where c_v is the specific heat at constant-volume heating and is defined as

$$c_v = \left(\frac{\partial u}{\partial T}\right)_v \tag{G.16}$$

When a perfect gas undergoes a change of state and c_v is constant, equation (G.15) can be integrated to yield

$$u_2 - u_1 = c_v\left(T_2 - T_1\right) \tag{G.17}$$

Similarly a relationship for a change in enthalpy in terms of a change in temperature can be obtained:

$$di = c_p \, dT \tag{G.18}$$

and upon integration

$$i_2 - i_1 = c_p \left(T_2 - T_1 \right) \tag{G.19}$$

c_p is the specific heat at constant pressure and is defined as

$$c_p = \left(\frac{\partial i}{\partial T} \right)_p \tag{G.20}$$

When a perfect gas undergoes an isentropic change of state, the following relationship holds:

$$p / \rho^{\gamma} = constant \tag{G.21}$$

It can further be shown that the relationship between the specific heats and the gas constant R is

$$c_p = c_v + R \tag{G.22}$$

Equation (G.22) is not an additional independent equation because it follows directly from the equation of state and the definitions of c_v, c_p and the enthalpy i.

G.2 Solution procedure for the draft equation

The following five equations form the basic system of equations to solve for the air flow through the condenser and the resultant heat transfer.

$$m_{ai} = m_{ao} \tag{G.2}$$

$$m_a = \rho_a v_a A \tag{G.3}$$

$$\sum F = m_a\left(v_{ao} - v_{ai}\right) \tag{G.6}$$

$$Q = m_a\left\{\left(c_p\, T_a + 1/2\, v_a^2 + gz\right)_o - \left(c_p\, T_a + 1/2\, v_a^2 + gz\right)_i\right\} + P \tag{G.23}$$

$$p_a/\rho_a = R_a\, T_a \tag{G.14}$$

The enthalpy i has been replaced in equation (G.13) with the relation given by equation (G.19) to obtain equation (G.23).

The above-listed equations contain eight variables, namely m_a, ρ_a, v_a, F, Q, T_a, P and p_a. With three additional equations for F, Q and P respectively the system of equations can, in principle, be solved. The complex geometry of a typical cooling tower and the non-linear nature of the equations require however a solution procedure where components of the equations are solved individually instead of simultaneously, to eventually arrive at the draft equation.

The analysis of the air flow through the system is based on one-dimensional flow. Because the flow is not one-dimensional, correction factors, defined in section G.3, are applied to account for two- and three-dimensional effects.

The air experiences a change in static pressure as it passes through the system due to:

1) flow obstacles such as tower supports, safety grids etc. ,
2) changes in velocity as a result of changes in flow area and/or density,
3) gravity and
4) the fan performance.

Instead of solving simultaneously for these four components, equations (G.2), (G.3), (G.6), (G.23) and (G.14) are selectively applied to each of the four components in sections G.4 to G.7 respectively. The relations obtained for each component are then added to yield an expression for the resultant change in static pressure, which in turn leads to the draft equation.

G.3 Momentum and energy correction factors

In one-dimensional flow modelling the velocity distribution at a cross-section along the flow domain is assumed to be uniform and any velocity related terms such as the momentum are expressed in terms of the actual velocity at the section. If the velocity varies across a section, such terms can be expressed in terms of the mean velocity v_m

$$v_m = \frac{1}{A}\int_A v\,dA \tag{G.24}$$

together with a correction factor α. For the one-dimensional approach to be valid the corrected and actual velocity terms must be equal. In the case of momentum we have

$$\alpha_m \rho v_m^2 A = \int_A \rho v^2 dA \tag{G.25}$$

and it follows that the momentum velocity distribution or correction factor is

$$\alpha_m = \frac{1}{A v_m^2}\int_A v^2 dA \tag{G.26}$$

Similarly an energy velocity distribution factor α_e can be obtained, i.e.

$$\alpha_e = \frac{1}{A v_m^3}\int_A v^3 dA \tag{G.27}$$

G.4 Irreversible change in total pressure due to flow obstacles

Boundary layer separation usually occurs at abrupt changes in flow area where the fluid flows past an obstacle. Figure G.1 illustrates such a case. The only work done on the fluid as it passes through the control volume is by the pressure forces. P (equation G.13)) is therefore zero. If the flow is adiabatic and there is no change in elevation equation (G.13) reduces to

$$i_2 + \alpha_{e2}\, 1/2\, v_2^2 = i_1 + \alpha_{e1}\, 1/2\, v_1^2 \tag{G.28}$$

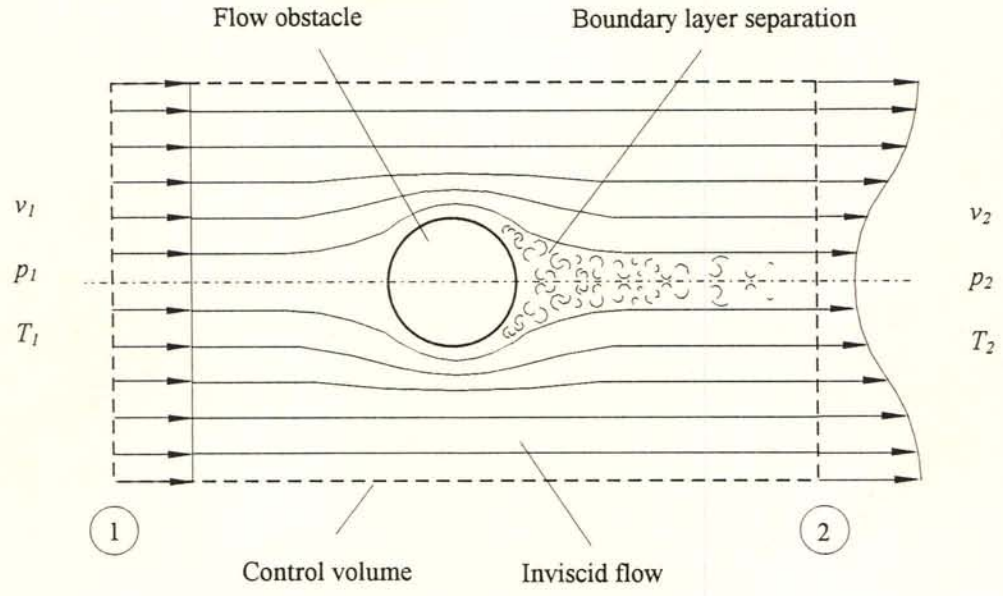

Figure G.1: Flow past an obstacle such as a tower support.

Note that the correction factors α have been introduced to account for the variation in velocity as depicted in figure G.1. Substitute equation (G.12) in equation (G.28) and replace u with the expression given by equation (G.17) to obtain:

$$p_2/\rho_2 + c_v T_2 + \alpha_{e2}\, 1/2\, v_2^2 = p_1/\rho_1 + c_v T_1 + \alpha_{e1}\, 1/2\, v_1^2 \qquad \text{(G.29)}$$

In the case of incompressible flow equation (G.29) can be rearranged as follows

$$\left(p_1 + \alpha_{e1}\, 1/2\, \rho v_1^2\right) - \left(p_2 + \alpha_{e2}\, 1/2\, \rho v_2^2\right) = \rho\, c_v \left(T_2 - T_1\right) \qquad \text{(G.30)}$$

The left-hand side of equation (G.30) is what is referred to as the change in total pressure. The equation illustrates that a conversion from mechanical energy (left-hand side) into thermal energy (right-hand side) occurs. Because there is boundary layer flow present, the flow is not isentropic. If the gain in thermal energy is of no practical use, the decrease in total pressure can be regarded as an irreversible loss. This irreversible loss in total pressure is usually expressed in terms of a coefficient K_{loss}, (the so-called loss coefficient) and the fluid kinetic energy:

$$\textit{Loss in total pressure} = K_{loss}\, 1/2\, \rho v^2 \qquad \text{(G.31)}$$

It follows that the corresponding change in static pressure due to a flow obstacle is

$$p_1 - p_2 = \alpha_{e2}\, 1/2\, \rho v_2^2 - \alpha_{e1}\, 1/2\, \rho v_1^2 + K_{loss}\, 1/2\, \rho v^2 \qquad \text{(G.32)}$$

This derivation does not restrict the loss coefficient principle to incompressible flow. Loss coefficients are usually determined by means of experiment and the equation (G.32) can be applied to quantify the irreversible pressure loss in terms of K_{loss} for compressible flow as well, where K_{loss} is defined as:

$$K_{loss} = \frac{\left(p_1 + \alpha_{e1}\, 1/2\, \rho_1 v_1^2\right) - \left(p_2 + \alpha_{e2}\, 1/2\, \rho_2 v_2^2\right)}{1/2\, \rho v^2} \qquad \text{(G.33)}$$

The term below the line is an arbitrarily selected reference kinetic energy of the fluid. Equation (G.33) should be regarded as a definition rather than a law of conservation of energy. When making use of equation (G.33) for design purposes, care must be taken to identify the correct kinetic energy term $1/2\, \rho v^2$ the loss coefficient has been referred to.

G.5 Static pressure change during isentropic compressible flow

In many flow passages the flow is adiabatic and no external work is done by the working fluid. For such conditions the energy equation (G.13) reduces to

$$i_1 + 1/2\, v_1^2 = i_2 + 1/2\, v_2^2 \qquad \text{(G.34)}$$

The gravity terms have been omitted because they will be dealt with separately. Equation (G.34) applies to flow with or without friction. Introducing equation (G.19), equation (G.34) becomes

$$T_1 + \frac{v_1^2}{2c_p} = T_2 + \frac{v_2^2}{2c_p} \qquad \text{(G.35)}$$

The ratio of the specific heats $\gamma = c_p/c_v$ and equation (G.22) yield the following expression for c_p:

$$c_p = \frac{\gamma R}{\gamma - 1} \qquad \text{(G.36)}$$

$$c_p = \frac{\gamma R}{\gamma - 1} \tag{G.36}$$

Substituting for c_p in equation (G.35) yields

$$T_1\left(1+\frac{\gamma-1}{2}\left(\frac{v_1}{\sqrt{\gamma R T_1}}\right)^2\right) = T_2\left(1+\frac{\gamma-1}{2}\left(\frac{v_2}{\sqrt{\gamma R T_2}}\right)^2\right) \tag{G.37}$$

If the flow is frictionless it may be regarded as isentropic, in which case equation (G.21) is applicable. By making use of equation (G.21) and the equation of state the following relation can be derived:

$$p_1/p_2 = \left(T_1/T_2\right)^{\frac{\lambda}{\lambda-1}} \tag{G.38}$$

Substitute equation (G.38) into equation (G.37) to eliminate T and introduce the Mach number M to obtain:

$$p_1\left(1+\frac{\lambda-1}{2}M_1^2\right)^{\frac{\lambda}{\lambda-1}} = p_2\left(1+\frac{\lambda-1}{2}M_2^2\right)^{\frac{\lambda}{\lambda-1}} \tag{G.39}$$

Add and subtract p_1 and p_2 on the left- and right-hand side of equation (G.39) respectively and rearrange:

$$p_1 + p_1\left[\left(1+\frac{\lambda-1}{2}M_1^2\right)^{\frac{\lambda}{\lambda-1}} - 1\right] = p_2 + p_2\left[\left(1+\frac{\lambda-1}{2}M_2^2\right)^{\frac{\lambda}{\lambda-1}} - 1\right] \tag{G.40}$$

The expressions in the parenthesis may be expanded by the binomial theorem for small values of the Mach number [76ZU1]:

$$p_1 + p_1\left(1+\frac{\lambda M_1^2}{2}+\frac{\lambda M_1^4}{8}+\ldots-1\right) = p_2 + p_2\left(1+\frac{\lambda M_2^2}{2}+\frac{\lambda M_2^4}{8}+\ldots-1\right) \tag{G.41}$$

$\gamma M^2/2$ can be taken out of the brackets and replaced with $\rho v^2/2$. Thus

$$p_1 + \frac{\rho_1 v_1^2}{2}\left(1+\frac{M_1^2}{4}+\ldots\right) = p_2 + \frac{\rho v_2^2}{2}\left(1+\frac{M_2^2}{4}+\ldots\right) \tag{G.42}$$

In the case of low Mach number flow the higher order terms of M may be ignored resulting in

$$p_1 + \alpha_{e1}\, 1/2\, \rho_1\, v_1^2 = p_2 + \alpha_{e2}\, 1/2\, \rho_2\, v_2^2 \tag{G.43}$$

where α_{e1} and α_{e2} have been introduced to account for any non-uniform velocity distributions that may be present.

G.6 Change in static pressure of a perfect gas rising in a gravity field

Consider air rising in the atmosphere as shown in figure G.2. Apply the conservation equations (G.2), (G.6) and (G.13). The equations for this control volume are

Conservation of mass:

$$\frac{\partial}{\partial z}(\rho v) = 0 \tag{G.44}$$

Momentum theorem:

$$\frac{\partial p}{\partial z} + \rho g + \frac{\partial}{\partial z}(\rho v^2) = 0 \tag{G.45}$$

First law of thermodynamics:

$$\frac{\partial}{\partial z}\left(i + \frac{v^2}{2} + gz\right) = 0 \tag{G.46}$$

Equations (G.44) to (G.46) together with the enthalpy and temperature relation (equation (G.18)) and the equation of state (equation (G.14)) form a set of five equations to solve for the five variables ρ, v, p, i, and T. Substitute equation (G.19) in equation (G.45) to eliminate i and find

$$\frac{\partial T}{\partial z} = -\frac{1}{c_p}\left(\frac{\partial}{\partial z}(v^2/2) + g\right) \tag{G.47}$$

Note that the aim is to derive an expression for the change in static pressure due to a change in elevation. A relation for a change in static pressure due to a change in velocity

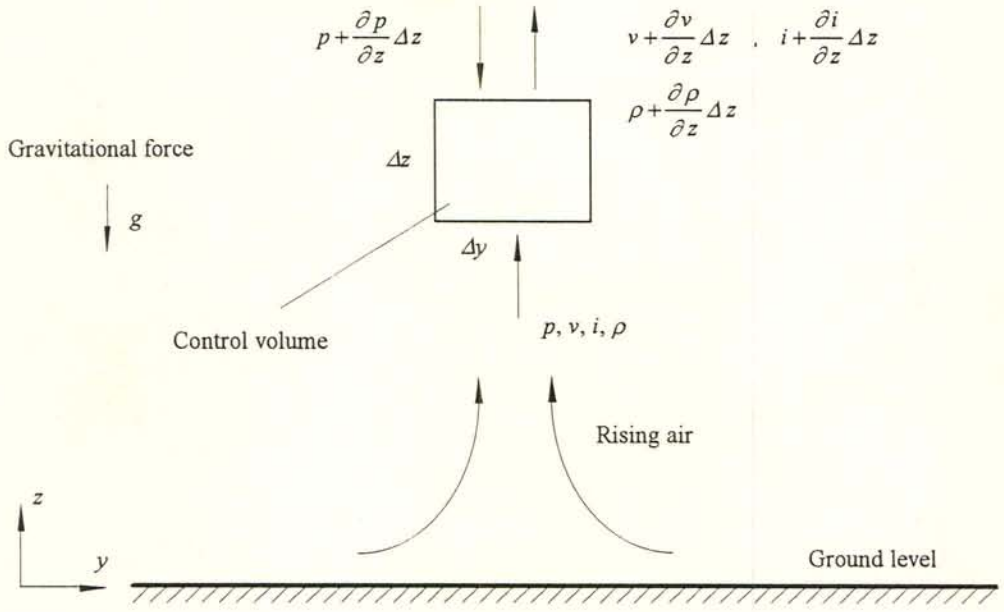

Figure G.2: Control volume for air rising in the atmosphere.

has already been obtained (equation (G.42)). We therefore proceed without the velocity terms. Equation (G.47) then becomes

$$\frac{\partial T}{\partial z} = -\frac{g}{c_p} \tag{G.48}$$

and equation (G.45) reduces to

$$\frac{\partial p}{\partial z} = -\rho g \tag{G.49}$$

Integrate equation (G.48) with respect to z. The resulting equation

$$T_2 = T_1 - g/c_p\left(z_2 - z_1\right) \tag{G.50}$$

is the dry adiabatic lapse rate (*DALR*). T_1 is the temperature at the reference elevation z_1. Eliminate ρ by substituting the equation of state into equation (G.49) and replace the temperature T by the expression given by equation (G.50). The resulting relation can be integrated by separation of variables, resulting in a expression for the static pressure as a function of the elevation z:

$$p_1 - p_2 = \Delta p_{12g} = p_1 \left\{ 1 - \left[1 - \frac{g\left(z_2 - z_1\right)/c_p}{T_1} \right]^{\frac{c_p}{R}} \right\} \tag{G.51}$$

With g = 9.81 m/s^2, c_p = 1006 J/kg K and R = 287.8 J/kg K for air in equation (G.51), the change in static pressure can be expressed as

$$\Delta p_{12g} = p_1 \left\{ 1 - \left[1 - 0.00975\left(z_2 - z_1\right)/T_1 \right]^{3.5} \right\} \tag{G.52}$$

G.7 Change in static pressure across a fan

The rise in total pressure across an axial flow fan can be expressed as

$$\left(p_o + \alpha_{eo}\, 1/2\, \rho_o v_o^2\right) - \left(p_i + \alpha_{ei}\, 1/2\, \rho_i v_i^2\right) = \Delta p_{Fs} + \alpha_{eo}\, 1/2\, \rho_o v_o^2 \tag{G.53}$$

Δp_{Fs} is the fan static pressure rise and is defined as

$$\Delta p_{Fs} = p_o - \left(p_i + \alpha_{ei}\, 1/2\, \rho_i v_i^2\right) \tag{G.54}$$

The corresponding fan static efficiency is defined as

$$\eta_{Fs} = \frac{\Delta p_{Fs} V_F}{P_F} \tag{G.55}$$

where P_F is the fan shaft power. Note that the fan static pressure rise Δp_{Fs} and the change in static pressure across a fan $\left(p_i - p_o\right)$ are not the same. Δp_{Fs} is a definition while $\left(p_i - p_o\right)$ is related to Δp_{Fs} by equation (G.53).

The fan static pressure and corresponding shaft or fan power are usually determined experimentally according to standard fan test codes. When model tests are conducted and/or the performance characteristics of the prototype-fan are generated at ambient conditions (pressure and temperature) differing from the operating conditions of the actual installation, the performance results may be scaled according to the fan laws [80BS1]:

1) Volume flow rate: $$\frac{V_F}{V_{Fm}} = \left(\frac{N_F}{N_{Fm}}\right)\left(\frac{D_F}{D_{Fm}}\right)^3 \quad \text{(G.56)}$$

2) Fan static pressure: $$\frac{\Delta p_{Fs}}{\Delta p_{Fsm}} = \left(\frac{N_F}{N_{Fm}}\right)^2\left(\frac{D_F}{D_{Fm}}\right)^2\left(\frac{\rho_F}{\rho_{Fm}}\right) \quad \text{(G.57)}$$

3) Fan shaft power consumption: $$\frac{P_s}{P_{Fm}} = \left(\frac{N_F}{N_{Fm}}\right)^3\left(\frac{D_F}{D_{Fm}}\right)^5\left(\frac{\rho_F}{\rho_{Fm}}\right) \quad \text{(G.58)}$$

According to the VDI fan test code [66VD1] the tip clearance of the prototype-fan and the model which result in the same static efficiency, are related as follows:

4) Tip clearance: $$\frac{s_F}{s_{Fm}} = \left(\frac{\Delta p_{Fm}}{\Delta p_F}\right)^{0.1}\left(\frac{D_F}{D_{Fm}}\right)^{0.8} \quad \text{(G.59)}$$

G.8 The draft equation

A schematic of an air-cooled condenser/dephlegmator unit is shown in figure 9.5. Stagnant air accelerates from 1 to 2. Equations (G.43) and (G.52) apply and the resulting change in static pressure is:

$$p_{a1} - p_{a2} = \alpha_{ea2}\, 1/2\, \rho_{a2} v_{a2}^2 + \Delta p_{12g} \quad \text{(G.60)}$$

From 2 to 3 the air flows past the tower supports and other flow obstacles such as a safety grid upstream of the fan. According to equations (G.33) and (G.52) we have

$$p_{a3} - p_{a2} = \alpha_{e2}\, 1/2\, \rho_{a2} v_{a2}^2 - \alpha_{e3}\, 1/2\, \rho_{a3} v_{a3}^2 + K_{ts}\, 1/2\, \rho_{a2} v_{a2}^2 + K_{up}\, 1/2\, \rho_{a3} v_{a3}^2 + \Delta p_{23g} \quad \text{(G.61)}$$

K_{ts} and K_{up} account for losses experienced across the tower supports and flow resistances upstream of the fan respectively. The change in static pressure across the fan is obtained from equation (G.53), i.e.

$$p_{a3} - p_{a4} = -\Delta p_{Fs} + \alpha_{e3} \frac{1}{2} \rho_{a3} v_{a3}^2 + \Delta p_{34g} \quad \text{(G.62)}$$

where the gravity component has been added. Between 4 and 5 losses occur due to flow resistances downstream of the fan (K_{do}) where the support bridge of the fan drive and the walkway are located. A further decrease in total pressure is experienced due to plenum losses (K_{pl}) and gravity:

$$p_{a4} - p_{a5} = \alpha_{e5}\, 1/2\, \rho_{a5} v_{a5}^2 - \alpha\, 1/2\, \rho_{a4} v_{a4}^2 + K_{do}\, 1/2\, \rho_{a4} v_{a4}^2 + K_{pl}\, 1/2\, \rho_{a4} v_{a4}^2 + \Delta p_{45g} \quad \text{(G.63)}$$

From 5 to 6 the air is heated as it passes through the finned tube bundles. The pressure drop across the bundles is expressed in terms of a heat exchanger loss coefficient K_{he} and the kinetic energy based on the harmonic mean density

$$p_{a5} - p_{a6} = \alpha_{e6}\, 1/2\, \rho v_{a6}^2 - \alpha_{e5}\, 1/2\, \rho_{a5}^2 + K_{he}\, 1/2 \rho_{a56} v_{a56}^2 \quad \text{(G.64)}$$

where the harmonic mean density through the heat exchanger is

$$\rho_{a56} \approx 2 p_{a1} \Big/ \left[R_a \left(T_{a5} + T_{a6} \right) \right] \quad \text{(G.65)}$$

and the approach velocity is based on the heat exchanger frontal area

$$v_{a56} = m_a \Big/ \left(\rho_{a56} A_{fr} \right) \quad \text{(G.66)}$$

The change in static pressure due gravity is negligible across the finned tube bundles. Above the heat exchanger bundles (6) the air turns upwards and enters the atmosphere (7). The change in static pressure between (6) and (7) is according equations (G.43) and (G.52)

$$p_{a6} - p_{a7} = \alpha_{e7}\, 1/2\, \rho_{a7} v_{a7}^2 - \alpha_{e6}\, 1/2\, \rho_{a6} v_{a6}^2 + K\, 1/2\, \rho_{a6} v_{a6}^2 + \Delta p_{67g} \quad \text{(G.67)}$$

The loss coefficient K includes the turning and jetting losses between (6) and (7).

Upon addition of equations (G.60) to (G.64) and equation (G.67) we obtain

$$\begin{aligned} p_{a1} - p_{a7} = {} & K_{ts}\, 1/2\, \rho_{a2} v_{a2}^2 + K_{up}\, 1/2\, \rho_{a3} v_{a3}^2 - \Delta p_{Fs} - \alpha_{e4}\, 1/2\, \rho_{a4} v_{a4}^2 \\ & + \left(\Delta p_{12} + \Delta p_{23} + \Delta p_{34} + \Delta p_{45} \right)_g + K_{he}\, 1/2\, \rho_{a56} v_{a56}^2 + \Delta p_{67g} \\ & + K\, 1/2\, \rho_{a6} v_{a6}^2 + \alpha_{e7}\, 1/2\, \rho_{a7} v_{a7}^2 \end{aligned} \quad \text{(G.68)}$$

According to Venter [90VE1] the fan exit kinetic energy is dissipated in the plenum in the case of such A-frame configurations and hence it may be assumed that $K_{pl} \approx \alpha_{e4}$.

A total heat exchanger loss coefficient $K_{\theta t}$ is defined which includes the loss in pressure across the finned tube bundles, the turning and jetting losses and the kinetic energy at (7).

The gravitational change in static pressure from (1) to (5) is approximated by equation (G.52) where the rise in air temperature due to energy input by the fan is neglected. Equation (G.52) can further be substituted for the gravitational pressure change between (6) and (7).

We further define a fan static pressure rise coefficient as

$$K_{Fs} = 2\,\Delta p_{Fs}\,\rho_{a3} \Big/ \left(m_a / A_{Fc}\right)^2 \tag{G.69}$$

Introduce the above-stated assumptions and definitions and substitute equations (G.3), (G.52) and (G.69) into equation (G.68) to arrive at an expression for the change in static pressure across the cooling tower.

$$\begin{aligned} p_{a1} - p_{a7} = {} & K_{ts}\left(m_a / A_2\right)^2 \Big/ \left(2\rho_{a2}\right) + K_{up}\left(m_a / A_{Fe}\right)^2 \Big/ \left(2\rho_{a3}\right) - K_{Fs}\left(m_a / A_{Fc}\right)^2 \Big/ \left(2\rho_{a3}\right) \\ & + K_{do}\left(m_a / A_{Fe}\right)^2 \Big/ \left(2\rho_{a4}\right) + p_{a1}\left[1 - \left\{1 - 0.00975 H_5 / T_{a1}\right\}^{3.5}\right] \\ & + K_{\theta t}\left(m_a / A_{fr}\right) \Big/ \left(2\rho_{a56}\right) + p_{a6}\left[1 - \left\{1 - 0.00975\left(H_7 - H_6\right) / T_{a6}\right\}^{3.5}\right] \end{aligned} \tag{G.70}$$

Far away from the tower the static pressure difference between elevations (1) and (8) can be expressed by equation (G.52) if the ambient air temperature varies according to the *DALR*.

$$\begin{aligned} p_{a1} - p_{a8} = {} & \left(p_{a1} - p_{a7}\right) = \left(p_{a1} - p_{a6}\right) + \left(p_{a6} - p_{a7}\right) \\ \approx {} & p_{a1}\left[1 - \left\{1 - 0.00975\, H_6 / T_{a1}\right\}^{3.5}\right] \\ & + p_{a6}\left[1 - \left\{1 - 0.00975\left(H_7 - H_6\right) / T_{a1}\right\}^{3.5}\right] \end{aligned} \tag{G.71}$$

where the ambient temperature at elevation (6) is approximated by T_{a1}. Set equation (G.70) equal equation (G.71) and by assuming $H_5 \approx H_6$, $p_{a1} \approx p_{a6}$, $\rho_{a2} \approx \rho_{a1}$ and $\rho_{a4} \approx \rho_{a3}$ the final draft equation is obtained:

$$p_{a1}\left[\left\{1-0.00975\left(H_7-H_6\right)/T_{a6}\right\}^{3.5}-\left\{1-0.00975\left(H_7-H_6\right)/T_{a1}\right\}^{3.5}\right]= K_{ts}\left(m_a/A_2\right)^2/\left(2\rho_{a1}\right)+K_{up}\left(m_a/A_{Fe}\right)^2/\left(2\rho_{a3}\right)-K_{Fs}\left(m_a/A_{Fc}\right)^2/\left(2\rho_{a3}\right) + K_{do}\left(m_a/A_{Fe}\right)/\left(2\rho_{a3}\right)+K_{\theta t}\left(m_a/A_{fr}\right)/\left(2\rho_{a56}\right) \quad \text{(G.72)}$$

The air densities at elevation (3) and after the heat exchanger (6) are approximated by

$$\rho_{a3} \approx p_{a1}/\left(R_a T_{a3}\right) \quad \text{(G.72)}$$

and

$$\rho_{a6} \approx p_{a1}/\left(R_a T_{a6}\right) \quad \text{(G.73)}$$

respectively. The temperature at elevation (3) is calculated according to the *DALR*, i.e.

$$T_{a3} = T_{a1} - 0.00975 H_3 \quad \text{(G.74)}$$

and the inlet temperature to the finned tube bundles is

$$T_{a5} = T_{a1} - 0.00975 H_5 + P_F/\left(m_a c_{pa1}\right) \quad \text{(G.75)}$$

Equation (G.75) expresses the resultant change in temperature experienced between elevations (1) (ground elevation) and (5) (average heat exchanger height) due to the *DALR* and the rise in temperature across the fan. According to the energy equation the temperature rise across the fan is

$$\left(T_{a4}-T_{a3}\right)_F = \left(i_{a4}-i_{a5}\right)/c_{pa1} = P_F/\left(m_a c_{pa1}\right) \quad \text{(G.76)}$$

where the change in elevation across the fan is ignored, the inlet and the outlet kinetic energy are assumed to be equal and $c_{pa3} \approx c_{pa1}$.

G.9 Draft equation loss coefficients

Consider a column supporting the heat exchanger. The drag force exerted by the moving air on such a column is

$$F_{Dts} = C_{Dts}\, 1/2\, \rho_{a1} v_{a2}^2 A_{ts} \tag{G.77}$$

A_{ts} is the projected area of the column in the flow direction, i.e.

$$A_{ts} = L_{ts} D_{ts} \tag{G.78}$$

The corresponding pressure drop experienced by the flow is

$$\Delta p_{ts} = F_{Dts} / \left(A_2 / n_{ts} \right) \tag{G.79}$$

where A_2 is the flow area of the air approaching the tower just outside the support structure and n_{ts} is the number of support columns. Substitute equation (G.77) into (G.79) and rearrange to solve for K_{ts}:

$$K_{ts} = \Delta p_{ts} / \left(1/2\, \rho_{a2} v_{a2}^2 \right) = C_{Dts} L_{ts} D_{ts} n_{ts} / A_2 \tag{G.80}$$

For the present system a value of 1.6 is assumed.

The upstream and downstream loss coefficients

$$K_{up} = \Delta p_{up} / \left(1/2\, \rho_{a3} v_{a3}^2 \right) = 2 \Delta p_{up} \rho_{a3} / \left(m_a / A_{Fe} \right)^2 \tag{G.81a}$$

$$K_{do} = \Delta p_{do} / \left(1/2\, \rho_{a4} v_{a4}^2 \right) = 2 \Delta p_{do} \rho_{a4} / \left(m_a / A_{Fe} \right)^2 \tag{G.81b}$$

are determined according to the bulk method [85VE1] which relates the loss coefficients to the distance between the fan rotor and the flow obstacle and its projected blockage area.

Van Aarde and Kröger [93VA1] derived an expression for the total loss coefficient K_{tot}, i.e

$$K_{\theta t} = 2\rho_{a56}\Delta p_{\theta t}\Big/\left(m_a/A_{fr}\right)^2$$
$$= K_{heiso} + \frac{2}{\sigma_{min}^2}\left(\frac{\rho_{a5}-\rho_{a6}}{\rho_{a5}+\rho_{a6}}\right) + \left(\frac{2\rho_{a6}}{\rho_{a5}+\rho_{a6}}\right)\left(\frac{1}{\sin\theta_m}\right)\left(\frac{1}{\sin\theta_m} - 1 + 2K_c^{0.5}\right)$$
$$+ K_d\left(\frac{2\rho_{a5}}{\rho_{a5}+\rho_{a6}}\right) \qquad \text{(G.82)}$$

σ_{min} is the ratio of the minimum free flow area through the heat exchanger bundle to the bundle frontal area.

The coefficient K_{heiso} describes the loss across the heat exchanger bundle for isothermal conditions and a normal approach velocity, including inlet, frictional and exit losses. K_{heiso} was determined in a standard wind-tunnel (see Appendix J) and is expressed as a function of the heat exchanger flow parameter Ry [m^{-1}]

$$K_{heiso} = 4464.4\, Ry^{-0.4393} \qquad \text{(G.83)}$$

where

$$Ry = m_a\Big/\left(\mu_a\, A_{fr}\right) \qquad \text{(G.84)}$$

The second term on the right-hand side of equation (G.82) accounts for acceleration effects due to heating and the subsequent decrease in the density of the air. Together the first and the second term represent the heat exchanger loss for a normal approach velocity during non-isothermal operation.

The third term represents the additional loss incurred due to oblique flow at the inlet to the bundle. K_c is a contraction loss coefficient for normal flow and is determined according to an expression by Kays [50KA1]

$$K_c = \left[\left(1/\sigma_c - 1\right)/\sigma_{in}\right]^2 \qquad \text{(G.85)}$$

where σ_{in} is the ratio of the flow area between the fins to the free stream (frontal) area, i.e.

$$\sigma_{in} = \left(P_{f(1)} - t_f\right)\Big/P_{f(1)} \qquad \text{(G.86)}$$

The contraction coefficient σ_c at the leading edge of rectangular fins may be approximated by the jet contraction ratio for parallel plates [00WE1]

$$\sigma_c = 0.614 + 0.0457\,\sigma_{21} - 0.337\,\sigma_{21}^2 + 0.408\,\sigma_{21}^3 + 2.672\,\sigma_{21}^4 - 5.963\,\sigma_{21}^5 + 3.559\,\sigma_{21}^6 \tag{G.87}$$

During oblique flow through finned tube bundles as encountered in A-frame type condensers, the curvature of the downstream flow pattern causes the actual mean incidence angle θ_m to differ from the bundle semi-apex angle θ_b . The actual mean incidence angle is, according to Kotzé *et al.* [86KO2],

$$\theta_m = 0.0019\,\theta_b^2 + 0.91330\,\theta_b - 3.1558 \tag{G.88}$$

The bundle downstream loss coefficient K_d in the fourth term on the right-hand side of equation (G.82) consists of turning and jetting losses (K_{dj}) in the V-region of the A-frame arrangement and the loss of the kinetic energy into the atmosphere (K_o):

$$K_d = K_{dj} + K_o \tag{G.89}$$

Expressions for K_{dj} and K_o have been presented by Van Aarde and Kröger [93VA1] in terms of the heat exchanger layout and geometry where

$$K_{dj} = \left\{\left[-2.8919\frac{L_w}{L_t} + 2.9329\left(\frac{L_w}{L_t}\right)^2\right]\left[\sin\theta_b - \frac{D_{vh}}{2L_t} + \frac{L_w}{L_t}\right]^{-1}\left[1 - \frac{0.5\,D_{vh}/L_t}{\sin\theta_b + L_w/L_t}\right]^{-1}\right.$$
$$x\left[\frac{28}{\theta_b}\right]^{0.4} + \left(exp\left(2.36987 + 5.8601x10^{-2}\,\theta_b - 3.3797\,x\,10^{-3}\,\theta_b^2\right)\right)^{0.5}$$
$$\left. x\left[1 - \frac{0.5\,D_{vh}/L_t}{\sin\theta_b + L_t/L_w}\right]^{0.5}\left[1 + \frac{L_w}{L_t\sin\theta_b}\right]^{-1}\right\}^2 \tag{G.90}$$

and

$$K_o = \left\{\left[-2.8919\frac{L_w}{L_t} + 2.9329\left(\frac{L_w}{L_t}\right)^2\right]\left[1 - \frac{0.5\,D_{vh}/L_t}{\sin\theta_b + L_w/L_t}\right]^3 + 1.9874\right.$$
$$\left. - 3.02783\left[\frac{0.5\,D_{vh}/L_t}{\sin\theta_b + L_w/L_t}\right] + 2.0817\left[\frac{0.5\,D_{vh}/L_t}{\sin\theta_b + L_w/L_t}\right]^2\right\}$$
$$x\left[\sin\theta_b - D_{vh}/2\,L_t + L_w/L_t\right]^{-2} \tag{G.91}$$

L_w is the half-width of the walkway between the A-frames, L_t is the tube length of a condenser/dephlegmator unit and D_{vh} is the diameter of the steam duct on top of the cooling units. Equations (G.88) and (G.89) are valid inside the following ranges:

$$20° \le \theta_b \le 35°$$

$$0 \le \frac{0.5 D_{vh}/L_t}{\sin\theta_b + L_w/L_t} \le 0.17886$$

$$0 \le L_w/L_t \; 0.09033$$

$$0 \le D_{vh}/L_t \le 0.303 \quad \text{for } L_w = 0$$

$$K_{he} \ge 30$$

APPENDIX H

FIELD TEST DATA AND SAMPLE CALCULATION

H.1 Performance evaluation of a single condenser unit

Table H.1(a): Air outlet temperature distribution $T_{ao(2)}$ [°C] of bundles 1 and 2.

51.54	51.20	51.34	50.84	49.91	49.62	49.27	47.18	48.10	48.42
52.38	50.52	49.58	49.67	48.86	49.69	48.96	47.44	47.55	48.09
51.00	50.03	49.02	49.92	48.79	49.39	49.24	47.74	48.21	47.76
50.74	49.03	48.65	50.17	49.67	49.18	48.95	47.66	47.23	46.52
50.61	49.58	49.38	50.71	48.56	49.39	49.43	48.27	48.24	47.76
50.42	50.18	50.57	52.47	51.20	51.44	49.97	48.34	48.39	46.86
49.75	49.31	49.55	50.45	48.91	52.36	49.63	49.29	49.57	48.38
48.13	48.98	48.32	49.41	45.76	50.06	48.35	48.05	47.73	47.05

Table H.1(b): Air outlet velocity distribution $v_{ao(2)}$ [m/s] of bundles 1 and 2.

2.711	2.684	2.508	2.836	3.442	3.728	3.164	3.914	3.784	2.811
2.658	2.889	3.177	3.208	3.758	3.434	3.368	3.747	3.824	3.427
2.982	2.901	3.359	2.974	3.914	3.680	3.301	3.704	3.826	3.738
2.730	3.340	3.632	3.109	3.717	3.435	3.640	4.089	4.245	4.405
2.763	3.084	3.209	2.648	4.016	3.386	3.149	3.422	3.717	3.896
2.289	3.295	3.374	2.397	3.043	2.252	3.156	3.376	3.680	4.231
3.384	3.016	3.183	2.946	4.361	2.240	2.955	2.673	2.709	3.198
3.503	2.951	2.876	2.785	4.000	1.712	1.554	1.770	1.924	1.950

Table H.1(c): Time of airside measurements and ambient temperature: Bundle 1 and 2.

Set no.	Time period	T_a at 10 m elevation [°C]	T_a at 40 m elevation [°C]
1	11h20 - 11h23	17.33	16.74
2	11h23 - 11h25	17.23	16.59
3	11h25 - 11h27	17.23	16.59
4	11h27 - 11h30	17.43	16.59
5	11h30 - 11h32	17.43	16.79
6	11h32 - 11h34	17.57	16.79
7	11h34 - 11h36	17.57	17.08
8	11h36 - 11h38	18.23	17.08

Table H.2(a): Air outlet temperature distribution $T_{ao(2)}$ [°C] of bundles 3 and 4.

48.90	49.89	50.65	49.31	50.39	52.55	52.36	52.31	50.50	52.84
50.49	49.53	49.47	47.96	50.38	52.32	51.57	51.52	50.40	51.30
50.05	49.26	49.38	48.82	49.82	51.70	52.11	52.20	51.51	50.92
51.17	49.58	49.14	49.67	50.79	51.46	51.56	51.30	51.34	50.11
51.06	49.88	49.27	49.03	49.11	51.45	50.53	50.54	50.24	49.87
51.30	50.09	49.70	48.23	48.16	50.85	51.25	51.46	52.80	52.81
51.62	50.32	50.20	49.19	48.47	50.69	51.73	51.23	51.76	50.51
51.76	51.70	50.95	49.12	47.60	50.08	50.12	50.58	51.05	48.97

Table H.2(b): Air outlet velocity distribution $v_{ao(2)}$ [m/s] of bundles 3 and 4.

3.978	3.440	3.413	3.685	3.354	2.879	3.037	2.673	3.529	2.544
3.116	3.657	3.724	3.947	3.805	3.021	3.090	2.821	3.361	2.971
3.366	3.498	3.540	3.497	3.427	3.156	2.461	2.278	2.269	3.198
2.505	3.229	3.511	3.223	3.261	3.254	3.013	2.820	2.944	3.607
2.394	2.914	3.271	3.212	3.632	3.145	3.274	3.059	3.058	3.404
2.357	2.775	3.265	3.632	3.929	3.378	3.271	3.109	2.723	2.358
2.389	2.811	3.102	3.391	3.855	3.972	2.622	2.777	2.630	3.501
2.026	2.128	2.275	2.508	3.247	3.814	2.519	2.553	2.396	3.482

Table H.2(c): Time of airside measurements and ambient temperature: Bundle 3 and 4.

Set no.	Time period	T_a at 10 m elevation [°C]	T_a at 40 m elevation [°C]
1	13h43 - 13h45	20.39	19.48
2	13h45 - 13h50	20.07	19.48
3	13h50 - 13h52	20.07	19.43
4	13h52 - 13h54	20.31	19.43
5	13h54 - 13h56	20.31	19.48
6	13h56 - 13h58	20.31	19.48
7	13h58 - 14h00	20.46	19.58
8	14h00 - 14h02	20.46	19.58

Table H.3(a): Air outlet temperature distribution $T_{ao(2)}$ [°C] of bundles 5 and 6.

52.24	51.06	51.74	50.65	52.78	49.72	49.19	48.80	48.58	50.93
51.33	50.78	51.75	51.05	52.31	50.47	49.14	48.87	47.89	50.40
50.46	50.43	50.89	51.02	51.63	50.54	49.17	49.69	48.77	49.18
49.58	49.99	50.33	50.45	51.25	50.22	48.86	50.21	48.98	49.27
49.20	50.09	49.71	49.77	50.40	48.95	48.51	48.32	48.33	48.87
49.33	49.66	48.95	49.12	49.49	48.91	47.88	48.34	48.75	48.82
49.79	50.59	49.73	48.69	49.53	48.43	48.00	48.64	48.70	49.19
48.43	49.25	48.27	45.93	48.30	47.28	48.09	49.12	47.89	48.62

Table H.3(b): Air outlet velocity distribution $v_{ao(2)}$ [m/s] of bundles 5 and 6.

2.272	2.507	2.473	3.064	2.609	4.144	3.772	3.635	3.838	3.221
2.937	2.886	2.713	2.927	2.805	3.206	3.139	3.233	3.979	3.434
3.064	3.055	2.997	2.995	3.290	3.298	3.118	2.530	3.445	3.605
3.617	3.065	3.134	3.102	3.322	3.469	3.181	2.229	3.403	3.637
3.240	2.989	2.920	3.085	3.432	3.607	3.045	2.625	3.153	3.679
3.284	3.271	3.323	3.267	3.665	3.483	3.490	2.791	2.930	3.369
3.689	2.704	2.818	2.815	3.640	4.084	3.246	2.535	3.148	3.167
4.579	3.124	3.036	3.716	3.513	3.552	2.456	1.975	2.767	3.166

Table H.3(c): Time of airside measurements and ambient temperature: Bundle 5 and 6.

Set no.	Time period	T_a at 10 m elevation [°C]	T_a at 40 m elevation [°C]
1	14h54 - 14h56	21.09	20.70
2	14h56 - 14h57	21.09	20.70
3	14h57 - 14h59	21.04	20.70
4	14h59 - 15h01	21.04	20.55
5	15h01 - 15h02	21.04	20.55
6	15h02 - 15h04	21.21	20.55
7	15h04 - 15h05	21.21	20.55
8	15h05 - 15h07	21.21	20.55

Table H.4(a): Air outlet temperature distribution $T_{ao(2)}$ [°C] of bundles 7 and 8.

45.36	44.45	45.31	46.89	47.31	46.28	46.05	46.07	48.42	49.11
44.56	43.00	45.17	46.47	47.09	46.32	46.24	46.00	47.85	48.53
45.44	45.00	45.01	46.08	46.42	45.58	45.83	46.42	46.81	47.41
45.30	44.33	44.52	45.78	47.46	45.01	45.89	45.88	46.57	48.01
44.62	43.46	44.44	45.00	46.01	44.94	45.89	46.03	46.37	47.23
44.94	44.35	44.70	44.67	48.06	44.92	45.55	45.76	45.70	46.26
46.20	46.39	45.38	45.04	48.60	43.90	44.91	44.83	45.17	44.92
47.55	46.54	46.85	47.73	48.70	42.82	43.94	43.90	45.30	43.66

Table H.4(b): Air outlet velocity distribution $v_{ao(2)}$ [m/s] of bundles 7 and 8.

4.167	3.750	3.608	3.330	3.448	2.660	3.521	3.078	3.065	2.880
4.607	4.212	3.788	3.328	3.348	2.261	3.300	3.013	2.750	2.955
3.408	3.621	3.550	3.348	3.610	2.498	3.441	2.867	3.045	3.262
4.083	3.693	3.686	3.432	2.891	3.311	3.650	3.247	3.277	2.938
4.189	3.868	3.523	3.725	3.492	3.050	3.330	2.727	3.100	3.116
3.648	3.371	3.398	3.569	2.496	3.337	3.535	3.254	3.464	3.150
2.920	2.534	2.794	3.222	2.015	4.061	3.403	3.317	3.179	3.776
2.332	2.295	2.152	2.004	1.778	4.500	3.293	3.572	3.521	4.073

Table H.4(c): Time of airside measurements and ambient temperature: Bundle 7 and 8.

Set no.	Time period	T_a at 10 m elevation [°C]	T_a at 40 m elevation [°C]
1	15h38 - 15h40	21.04	20.55
2	15h40 - 15h42	21.04	20.55
3	15h42 - 15h44	21.53	20.55
4	15h44 - 15h46	21.53	21.23
5	15h46 - 15h49	21.52	21.23
6	15h49 - 15h51	21.52	21.04
7	15h51 - 15h54	21.23	21.04
8	15h54 - 15h56	21.23	20.50

H.2 Performance evaluation of a single dephlegmator unit

H.2.1 Case 1

Table H.5(a):Case 1: Bundle 1 and 2 air outlet temperature distribution $T_{ao(2)}$ [°C]; α = -2°.

41.35	44.10	44.05	45.98	46.58	47.52	46.11	44.74	45.32	43.51
43.85	46.05	45.06	48.97	49.41	49.74	47.22	45.87	48.54	46.24
45.83	47.45	46.62	49.43	49.93	50.26	48.23	47.14	48.99	47.37
47.82	48.86	48.17	49.90	50.45	50.78	49.24	48.40	49.45	48.50
49.77	50.31	50.27	50.85	51.36	51.15	50.24	49.98	50.48	50.01
51.13	51.78	51.84	51.86	52.11	51.53	51.21	50.86	51.15	50.86
51.99	50.70	51.91	53.02	53.52	52.59	52.37	51.75	52.64	51.79
51.48	50.11	52.30	53.28	53.68	53.02	52.59	51.93	53.12	51.98
50.42	50.36	52.27	53.14	52.88	51.19	49.61	52.11	51.88	52.00

Table H.5(b):Case 1: Bundle 1 and 2 air outlet velocity distribution $v_{ao(2)}$ [m/s]; α = -2°.

2.081	1.853	1.919	1.873	2.135	1.748	1.764	2.075	1.892	2.146
2.171	1.923	1.923	1.788	1.853	1.758	1.746	2.014	1.710	1.919
2.039	1.822	1.789	1.761	1.709	1.722	1.789	1.924	1.698	1.815
1.906	1.721	1.656	1.734	1.565	1.686	1.833	1.835	1.686	1.711
1.830	1.648	1.440	1.707	1.646	1.983	1.857	1.583	1.593	1.624
1.574	1.154	1.087	1.287	1.388	1.667	1.471	1.537	1.532	1.633
1.355	0.659	0.912	0.936	0.784	1.352	1.167	1.174	1.357	1.384
1.011	0.322	0.823	0.724	0.971	0.977	0.867	0.884	0.977	1.334
0.311	0.663	0.558	0.743	0.876	0.547	0.196	0.667	0.479	0.872

Table H.5(c): Case 1: Bundle 1and 2 time of testing, steamside data and air inlet temperature; α = -2°.

Time	$T_{ai(1)}$, °C	$T_{ai(1)}$, °C	T_{v1}, °C	T_{v1}, °C	T_{v4}, °C	T_{v4}, °C	$T_{ejector}$, °C	$T_{ejector}$, °C	p_{v1}, N/m^2	p_{v4}, N/m^2	Δp_{14}, N/m^2
15h10	18.99	19.00	54.32	54.59	54.72	54.30	54.54	54.31	16492	15729	547
15h13	19.03	19.10	54.50	54.75	54.78	54.39	54.63	54.41	16628	15870	559
15h16	19.04	19.12	54.82	55.06	54.99	54.55	54.97	54.76	16958	16208	554
15h17	18.89	19.05	55.11	55.34	55.31	54.88	55.27	55.06	17174	16427	556
15h18	19.38	19.40	54.93	55.18	55.17	54.77	55.05	54.84	16997	16260	558
15h23	19.60	19.66	55.07	55.30	55.27	54.84	55.21	55.01	17108	16384	542
15h25	19.63	19.72	55.33	55.60	55.48	54.99	55.49	55.30	17407	16669	566
15h27	19.16	19.13	55.78	56.04	55.95	55.45	55.90	55.72	17743	16998	583

Table H.6(a):Case 2(a): Bundle 1 and 2 air outlet temperature distribution $T_{ao(2)}$ [°C]; $\alpha = 2°$.

47.01	46.17	46.92	47.75	47.32	49.89	46.06	47.13	46.40	47.82
51.29	49.96	50.61	51.81	51.92	52.78	51.31	49.52	49.10	51.26
52.18	51.04	50.65	51.20	51.26	52.39	51.11	49.77	49.89	50.91
50.03	49.06	50.06	50.75	51.38	51.28	50.65	50.16	50.28	51.54
49.78	48.55	49.72	50.64	51.14	50.82	50.38	50.28	50.47	51.21
50.19	48.13	49.60	50.38	50.72	50.26	50.26	50.26	50.81	51.49
50.80	49.31	50.53	51.06	51.27	51.62	51.14	50.98	51.16	51.73
51.02	51.13	51.99	52.57	52.24	51.90	52.02	51.85	51.80	52.10
51.75	51.75	51.20	52.74	50.22	51.87	52.16	51.90	51.55	51.68

Table H.6(b):Case 2(a): Bundle 1 and 2 air outlet velocity distribution $v_{ao(2)}$ [m/s]; $\alpha = 2°$.

2.052	2.111	2.103	2.102	2.460	2.410	2.447	2.411	2.065	2.554
1.950	2.095	1.769	1.898	2.155	1.636	1.948	2.338	2.248	2.213
2.192	2.331	1.888	1.817	2.174	1.311	1.713	1.968	2.064	1.716
2.473	2.606	2.229	2.134	2.056	1.953	1.834	1.866	2.047	1.720
2.401	2.490	2.320	2.072	2.253	2.158	2.059	1.781	1.900	1.959
2.184	2.549	2.316	2.078	2.106	2.177	2.002	1.822	1.641	1.495
2.098	2.114	1.659	1.763	1.808	1.617	1.575	1.298	1.651	1.653
1.799	1.362	1.020	0.949	1.146	1.151	1.135	1.278	1.301	1.327
1.502	1.182	0.922	0.941	0.802	1.827	1.176	1.179	1.382	1.274

Table H.6(c): Case 2(a): Bundle 1 and 2 time of testing, steamside data and air inlet temperature; $\alpha = 2°$.

Time	$T_{ai(1)}$, °C	$T_{ai(1)}$, °C	T_{v1}, °C	T_{v1}, °C	T_{v4}, °C	T_{v4}, °C	$T_{ejector}$, °C	$T_{ejector}$, °C	p_{v1}, N/m^2	p_{v4}, N/m^2	Δp_{14}, N/m^2
14h32	19.04	19.20	55.13	55.47	57.23	57.02	56.90	56.76	18175	17273	696
14h33	18.71	18.78	55.07	55.38	57.02	56.85	56.87	56.69	18116	17204	711
14h36	19.22	19.38	55.07	55.34	56.96	56.78	56.83	56.64	18132	17232	692
14h37	18.86	18.81	55.06	55.35	56.83	56.66	56.79	56.55	18127	17204	699
14h38	18.78	18.72	55.00	55.29	56.71	56.57	56.74	56.49	18092	17165	704
14h40	18.71	18.75	55.04	55.32	56.58	56.46	56.69	56.42	18132	17197	710
14h42	19.28	19.37	55.23	55.48	56.57	56.46	56.69	56.41	18277	17358	693
14h44	18.72	18.79	55.19	55.43	56.60	56.48	56.70	56.42	18206	17275	703
14h45	19.30	19.32	55.22	55.47	56.56	56.42	56.69	56.40	18294	17369	703

Table H.7(a):Case 2(a): Bundle 3 and 4 air outlet temperature distribution $T_{ao(2)}$ [°C]; $\alpha = 2°$.

41.78	44.18	44.37	44.80	47.78	47.70	47.26	46.17	46.37	46.84
46.34	47.38	46.69	48.12	49.93	49.76	49.16	47.58	48.96	48.75
48.26	48.85	48.33	49.30	50.62	50.46	49.67	48.90	49.76	49.82
49.13	49.33	49.70	49.89	50.77	50.48	49.83	49.64	50.12	50.29
49.19	50.24	50.44	50.27	50.72	50.66	50.16	49.97	50.40	50.21
49.90	51.04	51.04	50.73	51.09	50.66	50.45	50.18	50.46	50.36
50.84	51.61	51.43	51.42	52.00	51.30	51.27	50.79	51.16	50.78
51.78	52.05	51.92	52.23	52.36	51.97	51.71	51.53	52.16	50.48
52.03	52.35	52.26	52.66	52.63	52.11	52.30	52.16	52.58	51.00

Table H.7(b):Case 2(a): Bundle 3 and 4 air outlet velocity distribution $v_{ao(2)}$ [m/s]; $\alpha = 2°$.

2.608	2.368	2.437	2.326	2.543	2.084	2.115	2.452	2.279	2.567
2.506	2.215	2.299	2.153	2.233	2.032	2.050	2.290	2.013	2.218
2.537	2.422	2.425	2.356	2.077	2.216	2.272	2.266	2.076	2.038
2.311	2.184	1.949	2.144	2.015	2.455	2.251	1.952	1.952	1.942
2.692	1.956	1.665	2.012	2.156	2.295	1.991	1.946	1.988	2.062
2.004	1.779	1.593	1.869	1.817	2.203	1.970	2.005	2.087	2.084
1.731	1.475	1.295	1.491	1.379	1.718	1.540	1.587	1.816	1.826
1.348	1.164	1.121	1.284	1.327	1.393	1.382	1.354	1.436	2.042
1.311	1.151	1.181	1.209	1.481	1.260	0.999	1.124	1.203	1.765

Table H.7(c): Case 2(a): Bundle 3 and 4 time of testing, steamside data and air inlet temperature; $\alpha = 2°$.

Time	$T_{ai(1)}$, °C	$T_{ai(1)}$, °C	T_{v1}, °C	T_{v1}, °C	T_{v4}, °C	T_{v4}, °C	$T_{ejector}$, °C	$T_{ejector}$, °C	p_{v1}, N/m^2	p_{v4}, N/m^2	Δp_{14}, N/m^2
15h02	19.14	19.12	54.99	55.25	56.33	56.07	56.40	56.14	18030	17070	698
15h04	19.45	19.58	55.04	55.28	56.24	56.00	56.35	56.10	18119	17179	701
15h06	19.47	19.62	55.25	55.47	56.32	56.06	56.39	56.17	18263	17322	697
15h07	18.99	19.12	55.11	55.35	56.38	56.04	56.39	56.17	18184	17223	716
15h08	19.33	19.40	55.18	55.45	56.31	56.00	56.36	56.14	18274	17313	716
15h10	19.39	19.44	55.46	55.72	56.30	56.07	56.44	56.21	18488	17538	702
15h11	18.78	18.81	55.28	55.54	56.33	56.10	56.48	56.24	18275	17306	738
15h12	18.74	18.86	55.24	55.52	56.31	55.95	56.42	56.22	18277	17295	751
15h13	18.81	18.89	55.33	55.62	56.33	55.81	56.44	56.26	18370	17387	745

Table H.8(a):Case 2(b): Bundle 1 and 2 air outlet temperature distribution $T_{ao(2)}$ [°C]; $\alpha = 2°$.

35.68	32.77	33.10	34.87	35.74	35.19	30.62	31.17	33.98	34.89
35.45	31.69	33.24	34.95	35.95	34.81	30.94	31.64	34.05	35.17
35.45	33.20	33.85	35.11	36.09	35.01	31.91	32.23	34.22	35.41
35.56	33.95	34.72	35.34	35.80	34.87	32.67	33.05	34.54	35.46
35.02	34.91	35.21	35.25	35.25	34.87	33.47	33.45	34.62	35.02
35.19	35.65	35.73	35.49	35.44	34.66	33.94	33.91	34.60	34.70
36.00	36.47	36.25	36.46	37.01	35.55	35.09	34.90	35.65	35.23
40.62	39.97	40.06	40.06	41.12	39.06	38.76	39.19	39.69	37.01
41.89	41.89	42.24	41.52	41.42	40.74	41.05	41.14	41.55	39.22

Table H.8(b):Case 2(b): Bundle 1 and 2 air outlet velocity distribution $v_{ao(2)}$ [m/s]; $\alpha = 2°$.

2.444	2.189	2.260	2.293	2.467	2.007	2.056	2.351	2.082	2.435
2.368	2.175	2.235	2.188	2.286	2.056	1.989	2.246	2.025	2.296
2.279	2.122	2.141	2.259	2.076	2.211	2.323	2.299	2.151	2.169
2.032	2.018	1.861	2.192	2.253	2.578	2.345	1.999	1.997	2.043
2.495	1.770	1.559	2.045	2.279	2.312	2.026	1.938	1.977	2.045
1.830	1.609	1.492	1.866	1.925	2.379	2.099	2.065	2.137	2.185
1.649	1.387	1.256	1.560	1.150	1.947	1.583	1.647	1.858	1.915
1.312	1.166	1.184	1.396	1.168	1.485	1.377	1.479	1.448	2.297
1.056	1.002	1.177	0.972	1.049	1.665	1.277	1.330	1.433	1.891

Table H.8(c): Case 2(b): Bundle 1 and 2 time of testing, steamside data and air inlet temperature; $\alpha = 2°$.

Time	$T_{ai(1)}$, °C	$T_{ai(1)}$, °C	T_{v1}, °C	T_{v1}, °C	T_{v4}, °C	T_{v4}, °C	$T_{ejector}$, °C	$T_{ejector}$, °C	p_{v1}, N/m^2	p_{v4}, N/m^2	Δp_{14}, N/m^2
8h01	10.84	10.92	44.72	44.96	38.74	38.56	38.77	38.59	12530	8363	4474
8h03	10.89	10.91	45.20	45.45	38.82	38.64	38.82	38.64	12910	8415	4816
8h05	10.97	10.95	45.83	46.01	38.85	38.69	38.88	38.67	13200	8429	5115
8h06	11.10	11.04	46.16	46.39	38.94	38.83	39.00	38.75	13529	8471	5403
8h08	11.03	10.96	46.61	46.70	39.05	38.88	39.21	38.92	13769	8532	5598
8h10	11.04	10.97	46.92	46.97	39.23	39.13	39.40	39.07	13999	8614	5761
8h11	11.10	10.97	47.39	47.46	39.54	39.47	39.75	39.39	14336	8748	5982
8h16	11.67	11.54	48.98	48.97	40.74	40.67	41.04	40.66	15397	9229	6596
8h18	11.53	11.39	49.08	49.09	40.85	40.75	41.11	40.72	15422	9254	6604

Table H.9(a):Case 2(b): Bundle 3 and 4 air outlet temperature distribution $T_{ao(2)}$ [°C]; $\alpha = 2°$.

39.85	37.95	37.45	37.77	39.52	39.15	38.80	39.42	39.65	38.46
39.70	36.54	37.68	36.44	38.43	39.71	39.21	39.00	38.44	37.75
39.32	35.98	37.90	36.94	38.43	40.33	39.47	39.20	37.54	38.74
38.86	35.93	37.47	37.63	39.25	39.89	39.40	39.42	37.82	39.87
38.58	36.06	37.01	37.99	39.11	39.17	38.70	39.15	38.30	39.45
38.51	35.99	36.76	37.67	38.33	38.03	37.95	38.45	38.48	39.43
38.58	36.86	37.70	38.26	38.77	39.58	38.79	38.75	38.63	39.36
39.10	38.65	39.41	40.29	39.80	40.32	39.56	39.79	39.56	39.94
41.33	41.73	41.51	42.72	41.06	42.16	42.60	42.27	42.17	41.44

Table H.9(b):Case 2(b): Bundle 3 and 4 air outlet velocity distribution $v_{ao(2)}$ [m/s]; $\alpha = 2°$.

1.997	1.982	1.945	1.984	2.254	2.296	2.405	2.541	2.197	2.521
2.023	2.028	1.712	1.825	2.026	1.527	1.786	2.220	2.263	2.284
2.288	2.397	1.952	1.948	2.161	1.345	1.798	1.996	2.040	1.572
2.434	2.476	2.169	2.144	1.818	1.919	1.681	1.816	2.185	1.652
2.343	2.394	2.225	2.035	2.190	2.050	1.988	1.817	1.958	2.014
2.141	2.526	2.417	2.214	2.237	2.397	2.233	2.068	1.806	1.513
2.177	2.146	1.668	1.847	1.842	1.605	1.629	1.434	1.790	1.765
1.877	1.557	1.252	1.272	1.631	1.494	1.367	1.417	1.407	1.418
1.810	1.401	1.156	1.114	1.224	2.096	1.205	1.209	1.413	1.334

Table H.9(c): Case 2(b): Bundle 3 and 4 time of testing, steamside data and air inlet temperature; $\alpha = 2°$.

Time	$T_{ai(1)}$, °C	$T_{ai(1)}$, °C	T_{v1}, °C	T_{v1}, °C	T_{v4}, °C	T_{v4}, °C	$T_{ejector}$, °C	$T_{ejector}$, °C	p_{v1}, N/m^2	p_{v4}, N/m^2	Δp_{14}, N/m^2
8h31	11.72	11.58	50.42	50.57	42.10	42.02	42.33	42.00	16376	9686	7309
8h33	11.81	11.68	50.48	50.63	42.18	42.10	42.37	42.05	16263	9708	7175
8h34	11.83	11.76	50.24	50.46	42.19	42.15	42.35	42.03	16127	9674	7066
8h36	11.83	11.73	50.51	50.64	42.34	42.27	42.52	42.22	16233	9741	7097
8h37	11.96	11.87	50.50	50.64	42.40	42.33	42.60	42.31	16227	9766	7070
8h39	12.12	12.07	50.30	50.51	42.49	42.48	42.62	42.34	16053	9768	6883
8h41	12.13	12.07	50.14	50.30	42.50	42.51	42.61	42.34	15914	9746	6748
8h43	12.17	12.13	50.20	50.37	42.50	42.46	42.64	42.38	15910	9743	6738
8h44	12.25	12.19	50.27	50.39	42.59	42.52	42.72	42.47	15955	9775	6761

Table H.10(a):Case 3: Bundle 1 and 2 air outlet temperature distribution $T_{ao(2)}$ [°C]; $\alpha = 10°$.

23.91	22.66	25.26	21.64	19.84	32.42	27.30	23.91	20.73	22.30
27.60	25.84	29.02	27.35	21.20	33.60	31.26	29.16	26.18	26.71
32.47	31.44	33.94	33.56	28.96	37.55	34.77	33.07	31.58	32.26
34.55	33.22	35.17	35.79	30.55	37.78	35.79	35.28	33.92	34.94
36.11	34.61	35.94	37.34	34.76	37.92	36.67	36.86	36.02	37.28
37.37	35.23	36.00	36.46	36.01	36.62	36.08	35.84	36.64	37.95
37.28	36.03	36.96	37.24	37.14	37.89	37.14	36.68	37.13	37.98
38.14	37.54	38.34	38.69	38.06	38.70	38.06	37.79	37.79	38.27
39.89	39.82	40.71	40.46	40.36	39.94	40.09	39.57	39.93	39.96

Table H.10(b):Case 3: Bundle 1 and 2 air outlet velocity distribution $v_{ao(2)}$ [m/s]; $\alpha = 10°$.

2.557	2.459	2.668	2.595	2.907	3.092	3.218	3.288	2.896	3.439
2.527	2.570	2.347	2.379	2.740	2.140	2.491	2.894	2.894	2.925
2.999	3.089	2.626	2.559	2.867	1.867	2.404	2.710	2.913	2.200
3.222	3.293	2.994	2.937	2.839	2.796	2.522	2.704	3.260	2.762
3.086	3.150	3.083	2.787	2.978	3.074	2.868	2.572	3.052	2.812
2.391	2.846	3.026	2.921	3.127	3.479	3.220	2.969	2.655	2.189
2.885	2.901	2.446	2.541	2.804	2.576	2.646	2.243	2.666	2.345
3.133	2.256	2.011	1.828	2.608	2.287	2.176	2.223	2.237	2.605
2.782	2.327	1.971	1.943	2.625	3.048	2.174	2.182	2.265	2.349

Table H.10(c): Case 3: Bundle 1 and 2 time of testing, steamside data and air inlet temperature; $\alpha = 10°$.

Time	$T_{ai(1)}$, °C	$T_{ai(1)}$, °C	T_{v1}, °C	T_{v1}, °C	T_{v4}, °C	T_{v4}, °C	$T_{ejector}$, °C	$T_{ejector}$, °C	p_{v1}, N/m^2	p_{v4}, N/m^2	Δp_{14}, N/m^2
10h08	14.25	14.35	47.99	48.10	36.07	33.47	40.96	40.69	14316	10071	4169
10h13	14.37	14.45	48.12	48.35	36.27	34.39	40.33	40.06	14331	10139	4125
10h14	14.31	14.43	48.11	48.43	36.03	33.97	40.39	40.10	14415	10177	4188
10h16	14.80	14.87	47.84	48.19	34.93	32.42	40.16	39.88	14175	10131	3988
10h17	14.63	14.71	47.71	47.99	36.50	34.46	40.03	39.77	14110	10126	3920
10h19	14.46	14.58	47.70	47.96	37.27	34.96	39.92	39.69	14082	10103	3900
10h21	14.71	14.79	47.81	48.15	38.72	36.80	40.95	40.66	14178	10140	3968
10h23	14.85	14.95	48.02	48.31	38.48	36.04	41.27	41.06	14285	10267	3946
10h25	14.86	14.90	48.24	48.68	39.05	36.61	42.48	42.32	14483	10338	4043

Table H.11(a):Case 3: Bundle 3 and 4 air outlet temperature distribution $T_{ao(2)}$ [°C]; $\alpha = 10°$.

24.95	23.31	25.79	25.14	25.54	27.71	24.56	29.01	30.91	27.18
26.71	24.30	31.12	29.99	31.89	31.52	30.62	33.05	34.06	27.68
34.70	32.73	36.13	36.66	37.00	35.94	35.11	36.86	38.70	34.77
38.57	37.19	39.49	40.10	40.67	38.45	38.42	39.15	40.81	38.94
40.32	40.56	41.44	41.35	41.91	41.12	40.85	40.75	42.16	40.74
39.09	39.81	40.42	40.19	40.52	40.41	40.26	39.90	40.29	40.35
39.53	40.11	40.27	40.33	40.87	40.57	40.54	39.89	40.31	39.95
40.41	40.92	40.64	40.94	41.45	40.73	40.81	40.81	41.34	39.68
41.40	42.11	42.09	42.59	42.89	41.82	41.62	41.75	42.07	40.21

Table H.11(b):Case 3: Bundle 3 and 4 air outlet velocity distribution $v_{ao(2)}$ [m/s]; $\alpha = 10°$.

3.405	2.989	3.056	2.868	3.272	2.528	2.580	2.929	2.836	3.300
3.386	3.018	3.132	2.806	3.038	2.727	2.696	2.908	2.630	2.941
3.393	3.161	3.201	3.052	2.794	3.000	3.063	3.009	2.797	2.714
3.228	3.068	2.816	2.939	2.942	3.396	3.138	2.666	2.617	2.645
3.878	2.869	2.530	2.784	2.968	3.113	2.683	2.647	2.588	2.704
3.122	2.787	2.627	2.859	2.971	2.937	2.535	2.610	2.849	2.909
2.677	2.354	2.316	2.455	2.348	2.740	2.251	2.305	2.592	2.637
2.522	2.124	2.234	2.486	2.234	2.648	2.188	1.998	2.281	3.066
2.146	1.804	1.938	1.865	2.234	2.513	1.994	1.985	2.130	3.146

Table H.11(c): Case 3: Bundle 3 and 4 time of testing, steamside data and air inlet temperature; $\alpha = 10°$.

Time	$T_{ai(1)}$, °C	$T_{ai(1)}$, °C	T_{v1}, °C	T_{v1}, °C	T_{v4}, °C	T_{v4}, °C	$T_{ejector}$, °C	$T_{ejector}$, °C	p_{v1}, N/m^2	p_{v4}, N/m^2	Δp_{14}, N/m^2
11h05	15.76	15.91	49.39	49.74	35.97	33.29	42.95	42.84	15208	11286	3900
11h09	15.60	15.65	49.73	50.05	37.16	33.87	43.24	43.18	15488	11409	4061
11h11	15.66	15.71	49.74	50.17	36.33	33.23	43.49	43.43	15525	11458	4037
11h13	16.05	16.06	49.74	50.14	36.87	33.66	43.46	43.41	15446	11532	3889
11h15	15.78	15.83	49.64	50.02	36.73	33.13	43.66	43.65	15364	11523	3811
11h17	16.06	16.08	49.33	49.78	34.76	31.68	43.60	43.57	15124	11484	3607
11h19	16.55	16.57	49.20	49.64	33.16	30.29	43.43	43.36	15066	11550	3478
11h21	15.90	15.99	49.76	50.17	33.69	30.26	43.33	43.25	15405	11634	3750
11h23	16.44	16.48	49.84	50.21	35.68	32.06	43.39	43.35	15406	11726	3643

Table H.12(a):Case 4(a): Bundle 1 and 2 air outlet temperature distribution $T_{ao(2)}$ [°C]; $\alpha = 13°$.

44.06	33.91	34.45	23.46	24.09	24.51	24.15	24.39	22.16	24.49
43.53	39.90	39.51	32.18	29.32	30.29	30.63	33.26	26.73	31.33
44.17	42.13	41.20	37.68	31.14	34.55	36.54	38.15	36.24	38.42
42.13	42.16	41.55	39.83	35.08	41.58	39.99	39.87	40.61	40.82
42.50	41.95	41.49	40.50	40.25	41.38	41.15	41.36	41.66	41.37
44.70	44.93	43.34	42.29	41.85	41.35	41.24	41.48	42.47	42.27
43.56	43.57	43.74	43.27	42.89	42.35	42.38	42.38	43.41	42.23
43.97	45.15	45.43	43.87	43.97	43.49	44.03	43.44	44.48	43.37
46.54	47.51	46.30	45.91	45.36	45.13	45.84	45.38	46.13	44.55

Table H.12(b):Case 4(a): Bundle 1 and 2 air outlet velocity distribution $v_{ao(2)}$ [m/s]; $\alpha = 13°$.

2.315	2.587	2.626	2.664	2.977	3.868	3.420	3.271	3.042	3.820
2.105	2.662	2.564	2.466	2.668	3.287	3.345	3.002	3.282	4.072
2.040	2.557	2.606	2.655	2.512	2.583	2.685	2.753	2.758	3.232
2.918	2.833	2.947	3.061	2.886	2.708	2.576	3.050	2.862	3.674
3.208	2.921	3.214	3.506	3.405	3.534	2.714	2.838	2.683	3.604
2.735	2.675	3.147	3.619	3.746	3.881	3.164	3.071	2.851	3.476
1.206	2.798	2.729	2.659	3.394	3.455	3.162	2.938	2.648	3.582
2.707	2.499	2.475	2.450	2.870	3.253	2.577	2.752	2.535	3.195
2.530	2.024	2.129	2.234	3.041	3.164	2.067	2.356	2.151	2.926

Table H.12(c): Case 4(a): Bundle 1 and 2 time of testing, steamside data and air inlet temperature; $\alpha = 13°$.

Time	$T_{ai(1)}$, °C	$T_{ai(1)}$, °C	T_{v1}, °C	T_{v1}, °C	T_{v4}, °C	T_{v4}, °C	$T_{ejector}$, °C	$T_{ejector}$, °C	p_{v1}, N/m^2	p_{v4}, N/m^2	Δp_{14}, N/m^2
6h28	20.06	19.81	56.81	56.82	25.98	27.48	32.54	37.44	16898	13118	4456
6h30	19.80	19.54	56.88	56.87	26.17	27.36	33.02	37.64	16950	13138	4484
6h32	19.46	19.38	56.64	56.68	25.91	27.15	33.15	37.33	16749	13117	4282
6h33	19.45	19.34	56.51	56.58	25.49	26.67	33.10	37.23	16679	13136	4226
6h35	19.57	19.45	56.45	56.49	25.08	26.09	32.95	36.91	16621	13156	4167
6h36	19.67	19.54	56.45	56.46	24.72	25.82	32.74	36.70	16618	13212	4098
6h38	19.71	19.60	56.52	56.50	24.41	25.68	32.61	36.77	16648	13278	4087
6h39	19.71	19.52	56.67	56.68	24.41	25.56	32.49	36.55	16773	13524	3935
6h41	19.68	19.58	56.60	56.59	24.27	25.22	32.33	36.31	16699	13577	3827

Table H.13(a):Case 4(b): Bundle 1 and 2 air outlet temperature distribution $T_{ao(2)}$ [°C]; $\alpha = 13°$.

58.26	55.61	56.12	54.76	55.74	52.76	52.91	54.04	52.72	51.79
59.62	57.77	58.02	57.62	58.69	56.01	55.50	56.29	55.39	54.75
60.00	57.99	58.08	57.99	59.08	56.72	55.99	56.54	55.94	55.48
57.69	57.54	57.65	57.60	59.29	58.22	57.85	57.19	57.34	57.72
57.79	57.44	57.30	57.26	58.48	57.22	57.78	57.58	57.58	57.31
59.53	59.92	58.51	57.68	57.92	56.67	57.52	57.59	58.16	57.70
58.55	58.86	58.99	59.14	58.50	57.90	58.04	58.21	58.86	57.55
58.74	59.77	60.44	59.45	59.36	58.78	59.05	58.75	59.59	58.43
59.56	60.83	60.12	59.94	58.98	58.37	59.59	59.17	59.79	58.23

Table H.13(b):Case 4(b): Bundle 1 and 2 air outlet velocity distribution $v_{ao(2)}$ [m/s]; $\alpha = 13°$.

2.223	2.691	2.732	2.773	3.109	3.837	3.418	3.235	3.083	3.962
1.848	2.623	2.585	2.546	2.629	3.178	3.177	3.020	3.365	3.970
1.897	2.555	2.572	2.588	2.592	2.878	2.958	2.902	3.139	3.605
2.724	2.727	2.896	3.064	2.714	2.562	2.538	2.878	2.821	3.413
3.010	2.821	3.023	3.225	3.113	3.263	2.567	2.621	2.544	3.418
2.594	2.719	3.143	3.567	3.538	3.520	2.937	2.877	2.713	3.376
2.947	2.768	2.670	2.572	3.236	3.205	3.005	2.722	2.510	3.349
3.069	2.417	2.412	2.407	2.914	3.043	2.775	2.882	2.546	2.940
2.509	1.885	2.073	2.260	2.940	2.993	2.123	2.323	2.183	2.724

Table H.13(c): Case 4(b): Bundle 1 and 2 time of testing, steamside data and air inlet temperature; $\alpha = 13°$.

Time	$T_{ai(1)}$, °C	$T_{ai(1)}$, °C	T_{v1}, °C	T_{v1}, °C	T_{v4}, °C	T_{v4}, °C	$T_{ejector}$, °C	$T_{ejector}$, °C	p_{v1}, N/m^2	p_{v4}, N/m^2	Δp_{14}, N/m^2
17h09	27.26	27.12	65.22	65.26	64.30	64.59	64.40	64.75	25757	25680	629
17h10	27.21	27.05	65.97	66.00	65.22	65.42	65.35	65.58	26599	26566	582
17h11	27.24	27.07	66.12	66.15	65.40	65.44	65.48	65.69	26749	26713	580
17h13	27.18	27.06	66.49	66.52	65.84	65.69	65.83	66.02	27138	27072	592
17h14	27.23	27.09	66.67	66.70	66.04	65.93	66.03	66.23	27355	27311	581
17h15	27.22	27.08	66.92	66.94	66.21	66.15	66.28	66.47	27607	27547	597
17h16	27.21	27.01	67.00	67.03	66.28	66.16	66.34	66.53	27708	27639	588
17h17	27.24	27.03	67.14	67.18	66.40	66.29	66.50	66.69	27904	27848	575
17h18	27.23	27.08	67.26	67.29	66.57	66.34	66.63	66.82	28035	28002	565

Table H.14(a):Case 5: Bundle 1 and 2 air outlet temperature distribution $T_{ao(2)}$ [°C]; $\alpha = 16°$.

20.33	18.00	18.59	18.13	18.07	20.73	17.97	19.67	19.51	21.42
22.56	19.08	22.87	22.73	24.30	24.23	21.74	24.50	25.77	25.23
26.72	24.74	27.49	28.17	30.73	29.76	26.96	29.19	30.82	31.79
31.16	30.34	32.69	33.56	35.13	32.60	32.08	33.38	34.75	37.04
34.03	34.38	35.52	36.17	37.13	35.74	35.21	35.86	37.08	39.36
35.03	35.48	36.15	36.21	38.10	38.01	37.65	36.75	37.19	38.73
35.95	36.38	36.53	36.82	38.87	38.12	38.06	37.16	37.66	38.02
36.86	37.37	36.96	37.22	39.14	37.98	38.03	38.02	38.67	36.98
38.60	39.66	39.44	39.54	40.65	39.44	39.21	39.31	39.61	37.88

Table H.14(b):Case 5: Bundle 1 and 2 air outlet velocity distribution $v_{ao(2)}$ [m/s]; $\alpha = 16°$.

3.771	3.433	3.499	3.237	3.605	2.888	2.902	3.290	3.216	3.618
3.731	3.307	3.408	3.156	3.287	3.168	2.978	3.152	2.892	3.167
3.795	3.612	3.588	3.420	3.147	3.460	3.402	3.310	3.119	3.036
3.633	3.406	3.207	3.354	3.251	3.708	3.410	2.971	2.893	2.734
4.290	3.302	2.962	3.258	3.054	3.535	2.927	2.921	2.858	2.699
3.809	3.499	3.339	3.566	2.923	2.358	1.981	2.304	2.888	2.509
3.429	2.987	2.977	3.033	2.597	3.160	2.491	2.533	2.869	2.673
3.236	2.700	2.868	3.190	2.548	3.223	2.630	2.411	2.724	3.476
2.696	2.197	2.370	2.481	2.434	3.313	2.604	2.576	2.907	3.431

Table H.14(c): Case 5: Bundle 1 and 2 time of testing, steamside data and air inlet temperature; $\alpha = 16°$.

Time	$T_{ai(1)}$, °C	$T_{ai(1)}$, °C	T_{v1}, °C	T_{v1}, °C	T_{v4}, °C	T_{v4}, °C	$T_{ejector}$, °C	$T_{ejector}$, °C	p_{v1}, N/m^2	p_{v4}, N/m^2	Δp_{14}, N/m^2
10h10	14.11	14.12	48.09	48.38	27.14	26.28	42.34	41.61	14377	9755	4731
10h12	14.01	14.01	48.55	48.77	27.83	26.68	42.01	41.27	14664	9901	4888
10h14	14.14	14.13	48.51	48.81	27.42	26.67	41.70	40.96	14678	10045	4754
10h16	14.33	14.34	48.60	48.85	27.04	26.52	41.46	40.72	14654	10177	4597
10h18	14.44	14.49	48.78	49.03	27.02	26.38	41.28	40.56	14848	10352	4618
10h20	14.47	14.49	48.80	49.05	26.83	26.32	41.14	40.40	14797	10462	4452
10h22	14.49	14.55	48.90	49.18	26.81	26.19	41.05	40.32	14825	10596	4335
10h24	14.69	14.74	49.09	49.39	26.60	26.03	40.90	40.21	14889	10666	4340
10h26	14.60	14.68	49.23	49.62	26.55	25.93	40.81	40.15	15009	10786	4351

Table H.15(a):Case 5: Bundle 3 and 4 air outlet temperature distribution $T_{ao(2)}$ [°C]; $\alpha = 16°$.

24.24	23.55	26.37	23.96	22.61	28.87	25.29	27.31	25.24	23.69
24.98	25.45	27.68	24.17	20.88	31.31	30.00	27.92	23.58	23.45
32.43	31.81	33.53	31.10	24.58	36.18	35.06	32.88	29.85	28.21
36.12	35.30	36.97	36.51	28.13	38.25	37.48	36.85	34.87	31.57
38.28	36.91	38.01	38.85	35.11	38.59	38.61	38.60	37.81	36.15
39.21	37.62	37.81	38.22	37.16	38.26	37.75	37.48	37.88	37.44
38.72	37.32	38.24	38.20	38.16	38.32	37.71	38.13	38.22	38.62
39.16	38.54	39.13	39.75	39.03	39.27	38.51	38.56	38.69	39.50
40.46	40.26	41.17	40.58	40.84	39.72	40.13	39.84	40.24	40.58

Table H.15(b):Case 5: Bundle 3 and 4 air outlet velocity distribution $v_{ao(2)}$ [m/s]; $\alpha = 16°$.

2.922	2.869	3.064	2.946	3.332	3.538	3.650	3.724	3.254	3.935
2.909	2.921	2.765	2.732	3.197	2.585	2.923	3.473	3.252	3.342
3.201	3.402	2.952	2.720	3.147	2.066	2.473	3.003	3.102	2.734
3.668	3.680	3.335	3.134	3.054	3.076	2.833	2.905	3.388	3.034
3.576	3.532	3.405	3.066	3.314	3.492	3.233	2.928	3.383	3.025
2.223	2.597	3.127	3.244	3.552	3.845	3.621	3.501	2.895	2.827
3.490	3.424	2.967	3.000	3.434	3.528	3.459	2.754	3.052	3.432
3.558	2.787	2.500	2.071	3.147	2.781	2.719	2.714	2.781	2.927
3.421	2.948	2.600	2.628	3.233	3.571	2.376	2.373	2.669	2.700

Table H.15(c): Case 5: Bundle 3 and 4 time of testing, steamside data and air inlet temperature; $\alpha = 16°$.

Time	$T_{ai(1)}$, °C	$T_{ai(1)}$, °C	T_{v1}, °C	T_{v1}, °C	T_{v4}, °C	T_{v4}, °C	$T_{ejector}$, °C	$T_{ejector}$, °C	p_{v1}, N/m^2	p_{v4}, N/m^2	Δp_{14}, N/m^2
10h39	14.72	14.82	49.48	49.84	27.96	27.44	40.73	39.94	15151	10911	4396
10h41	14.89	14.94	49.32	49.70	27.66	27.20	40.78	40.04	15053	10940	4273
10h43	15.26	15.35	49.25	49.62	27.44	26.93	40.80	40.10	15002	11040	4106
10h45	14.95	15.05	49.33	49.70	27.70	27.00	40.80	40.13	15049	11047	4158
10h47	14.84	14.91	49.33	49.74	27.78	27.12	40.82	40.17	14984	10960	4185
10h48	15.46	15.51	49.60	50.00	27.30	26.85	40.84	40.21	15158	11126	4201
10h50	14.99	15.13	49.86	50.21	27.73	27.15	40.96	40.30	15261	11183	4247
10h52	14.88	14.96	49.81	50.16	27.34	26.96	41.01	40.36	15248	11185	4231
10h54	15.10	15.15	49.91	50.26	26.79	26.47	41.03	40.39	15387	11247	4321

10.3 Air flow rate and heat transfer sample calculation

The sample calculation illustrates how the air mass flow rate passing through and the heat rejected by a unit is determined. The data of case 4(b) are used for this purpose. Consider the air outlet temperature and velocity at the top left area increment of the grid in tables H.13(a) and (b):

$$T_{ao(2)} = 58.26\ °C = 331.4\ K$$
$$v_{ao(2)} = 2.223\ m/s$$

The average air inlet temperature at the time of recording the outlet temperature and velocity is, according to the first row of table H.13(c) at 17h09,

$$T_{ai(1)} = 27.19\ °C = 300.3\ K$$

Ambient pressure : $p_{a1} = 91330\ N/m^2$

Incremental area: $\Delta A_{fr(2)} = 0.512\ m^2$

The air density on the outlet side is

$$\rho_{ao(2)} = \frac{p_{a1}}{R_a T_{ao(2)}} = \frac{91330}{287.08\,x\,331.4} = 0.960\ kg/m^3 \qquad (C.1.1)$$

Let the area increment under consideration be the j'th area. The air mass flow rate through the j'th increment is

$$\Delta m_{a_j} = \rho_{ao(2)j} v_{ao(2)j} \Delta A_{fr(2)j} = 0.960\,x\,2.223\,x\,0.512 = 1.093\ kg/s \qquad (8.2)$$

Summation of the incremental flow yields the total mass flow rate passing through bundle 1

$$m_{ab1} = \sum_{j=1}^{45} \rho_{ao(2)j} v_{ao(2)j} \Delta A_{fr(2)j} = 59.9\ kg/s \qquad (8.3)$$

and similarly through bundle 2

$$m_{ab2} = \sum_{j=46}^{90} \rho_{ao(2)j} v_{ao(2)j} \Delta A_{fr(2)j} = 66.6 \text{ kg/s} \quad (8.3)$$

Assuming symmetric performance, the air mass flow rate passing through the entire unit can be estimated by

$$m_a = 4\left(m_{ab1} + m_{ab2}\right) = 4\,x\,(59.9 + 66.6) = 506.1 \text{ kg/s}$$

The heat rejection rate by the j'th increment to the air is

$$\Delta Q_{aj} = \Delta m_{aj} c_{pamj} \left(T_{ao(2)j} - T_{ai(1)}\right) \quad (F.1)$$

The specific heat c_{pamj} is evaluated at the arithmetic mean air temperature:

$$T_{amj} = \left(T_{ao(2)j} + T_{ai(1)j}\right)/2 = (331.4 + 300.3)/2 = 315.8 \text{ K}$$

$$\begin{aligned} c_{pamj} &= 1.045356\,x\,10^{3} - 3.161783\,x\,10^{-1}\,x\,T_{amj} \\ &\quad + 7.083814\,x\,10^{-4}\,x\,T_{amj}^{2} - 2.705209\,x\,10^{-7}\,x\,T_{amj}^{3} \\ &= 1.045356\,x\,10^{3} - 3.161783\,x\,10^{-1}\,x\,315.8 \\ &\quad + 7.083814\,x\,10^{-4}\,x\,315.8^{2} - 2.705209\,x\,10^{-7}\,x\,315.8^{3} = 1007.6 \text{ J/kg K} \end{aligned} \quad (C.1.3)$$

Evaluate the incremental heat transfer rate with equation (F.1)

$$\Delta Q_{aj} = 1007.6\,x\,1.093\,x\,(331.4 - 300.3) = 34251 \text{ W}$$

The heat transfer to the air by bundles 1 is

$$Q_{ab1} = \sum_{j=1}^{45} \Delta m_{aj} c_{pamj} \left(T_{ao2(2)j} - T_{ai(1)j}\right) = 1882177 \text{ W} \quad (8.4)$$

and similarly for bundle 2 we have

$$Q_{ab2} = \sum_{j=46}^{90} \Delta m_{aj} c_{pamj} \left(T_{ao2(2)j} - T_{ai(1)j}\right) = 1995428 \text{ W} \quad (8.4)$$

As for the air mass flow rate, the total heat rejected by the dephlegmator is estimated as

$$Q_a = 4\left(Q_{ab1} + Q_{ab2}\right) = 4\,x\,(1.882 + 1.995) = 15.92 \text{ MW}$$

APPENDIX I

PRESSURE DROP AND FLOODING DURING REFLUX CONDENSATION IN AN INCLINED AIR-COOLED FINNED TUBE

I.1 Introduction

In chapter 10 the dephlegmator performance results originating from the field tests are compared to the analysis presented in section 9.2.2. Conclusions based on this comparison are of little meaning unless the validity of the model is confirmed by experiment. The actual dephlegmator performance may not serve as a reference for this purpose due to the existence of the cold zones. Furthermore, a full scale plant is not always conducive to the generation of reliable experimental results because conditions are sometimes not controllable and data acquisition is difficult in the harsh environment.

To evaluate the validity of the model, Schoenfeld [97SC1] investigated reflux condensation under laboratory conditions in a concurrent study. Steam at sub-atmospheric pressures representative of the operating conditions in the full scale plant was condensed in an air-cooled elliptical finned tube, identical to the type employed in the second row of the condenser and dephlegmator bundles.

A schematic of the experimental apparatus constructed by Schoenfeld [97SC1] is shown in figure I.1. Air is drawn from the surroundings through the finned tube by a centrifugal fan via a manifold containing four ducts. The ducts lead to four separate air boxes joined to the wooden casing which encloses the finned tube. Six thermocouples equally spaced along the bell-mouth inlet to the finned tube measure the air inlet temperature while the air outlet temperature is monitored by four thermocouples, i.e. one per outlet duct. The air flow rate is measured by propeller-type anemometers located inside each air duct.

A water-heated shell-and-tube boiler generates steam. The boiler is linked to the bottom header of the finned tube by a flexible stainless steel pipe. During reflux condensation the condensate drains back to the boiler via a measuring flask. The condensation rate is determined by the calibrated flask and a stop watch.

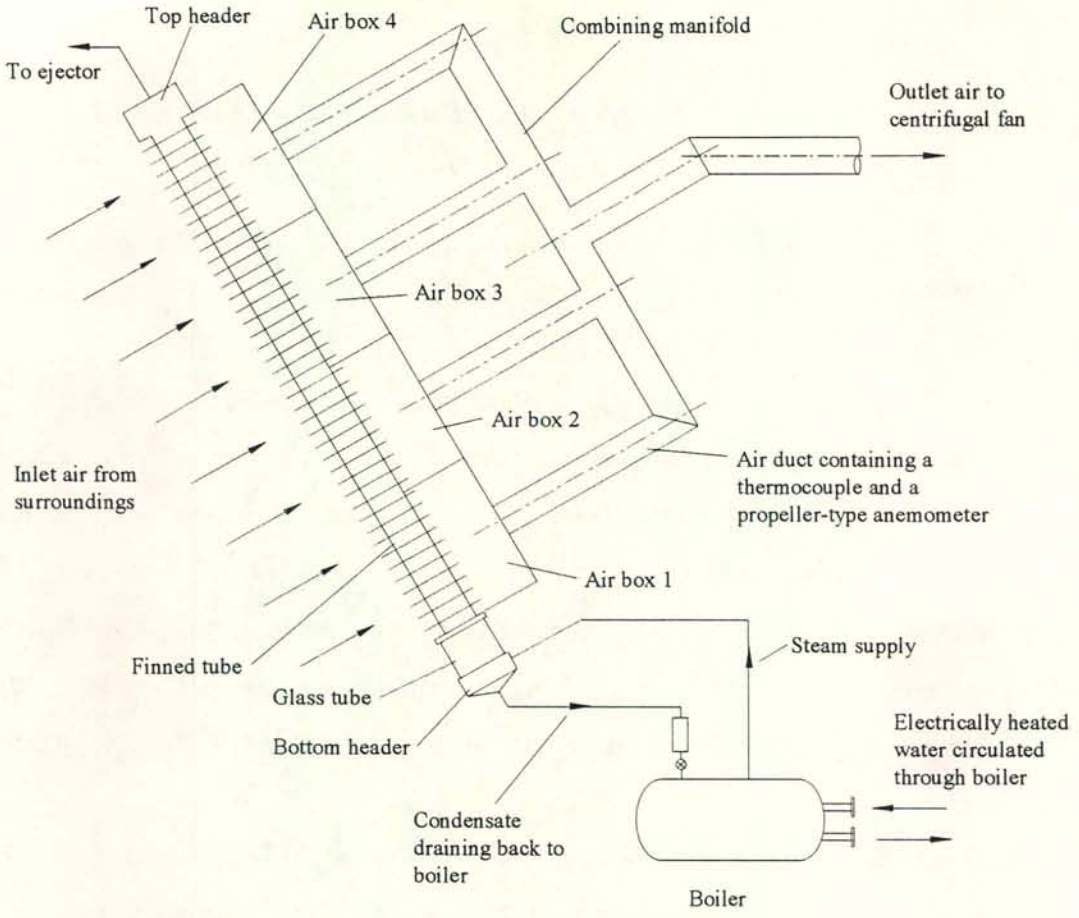

Figure I.1: Schematic of the apparatus constructed by Schoenfeld [97SC1] to study reflux condensation in an inclined air-cooled finned tube.

Additional instrumentation includes thermocouples to measure the steam temperature inside the bottom and top header and a pressure transducer which measures the pressure drop across the headers.

A 126 mm i.d. 150 mm long glass tube is located between the stainless steel header and the sharp-edged flange welded to the bottom end of the finned tube. The condensate flow can be observed through the glass section as it drains into the header.

A water driven ejector connected to the top header evacuates the system before start-up and prevents accumulation of leakage air during the course of an experiment.

During a typical test run the air flow rate and the power input to the electrically heated water circulated through the boiler are adjusted such that the system stabilises at a predetermined temperature. Once equilibrium conditions have been reached, the temperatures, pressure drop, air flow rate and condensation rates are recorded. The air flow rate is increased to a new value and the routine is repeated. In the process a pressure drop curve is generated as a function of the vapour flow rate entering the finned tube for a specific system temperature. Such a curve is analogous to figure 4.1 for example. Note however that in figure 4.1 the pressure gradient inside the ducts is presented while in the case of the experiments by Schoenfeld [97SC1] the pressure drop across the entire duct length, including the entrance pressure drop at the sharp-edged flange, was measured.

I.2 Theory

I.2.1 Conservation of mass

Consider total reflux condensation in a single-tube as shown in figure I.2. The suction rate of the ejector connected to the top header is negligible and hence the condensate drains at the same as rate at which vapour enters the bottom the tube:

$$m_{v2} = m_c \tag{I.1}$$

I.2.2 Pressure drop

To evaluate the pressure drop across the headers, equation (9.44) can be applied by setting the outlet vapour velocity v_{sv3} equal to zero, i.e.

$$\begin{aligned}\Delta p_{14} = & \frac{1}{2}\rho_v v_{sv2}^2\left(K_{tp} - \sigma_{21}^2\right) \\ & + \frac{1}{2}\rho_v v_{sv2}^2\left[\frac{L_t}{D_e} K Re_{sv2}^n\left(\frac{a_1}{n+3} + \frac{a_2}{(n+2)Re_{sv2}}\right)\right] \\ & + \rho_v g L_t \sin\theta_t - \rho_v v_{sv2}^2\end{aligned} \tag{I.2}$$

where v_{sv2} is the superficial vapour velocity at the duct inlet and Re_{sv2} is the Reynolds number.

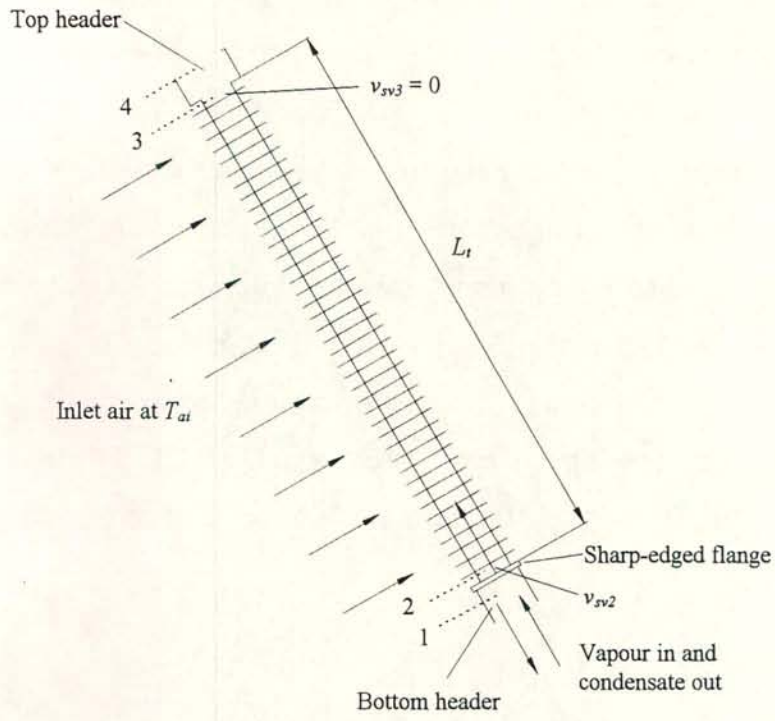

Figure I.2: Total reflux condensation in an inclined air-cooled finned tube.

The corresponding mean vapour pressure inside the elliptical duct is obtained from equation (9.31)

$$p_{vm} = p_{v1} - \Delta p_{12} - \frac{1}{2}\rho_v v_{sv2}^2 \frac{L}{D_e} K Re_{sv2}^n \left[\frac{a_1}{n+3} \left\{ 1 - \frac{1}{(n+4)} \right\} + \frac{a_2}{(n+2)Re_{sv2}} \left\{ 1 - \frac{1}{(n+4)} \right\} \right] + 1/2\,\rho_v g\, L_t \sin\theta_t + 2/3\,\rho_v v_{sv2}^2 \qquad \text{(I.3)}$$

The change in static pressure experienced by the vapour as it enters the condenser tube through the sharp-edged flange is represented by the first term on the right-hand side of equation (I.2). K_{tp} includes part of the acceleration effect and the drop in pressure as mechanical energy is dissipated while work is done on the draining condensate. See section 4.1.2 for the definition of K_{tp}.

The second term is the integrated frictional pressure drop experienced by the vapour during turbulent flow. The coefficients a_1 and a_2 account for the enhanced shear at the vapour condensate interface due to the distortion of the vapour velocity profile during

condensation [95GR1]. a_1 and a_2 are functions of the suction Reynolds number Re_{vn}, as given by equations (9.11a) and (9.11b). Re_{vn} is defined as

$$Re_{vn} = m_c D_e / (\mu_v L_t A_{ti}) \tag{I.4}$$

The third and fourth term on the right-hand side of equation (I.2) represent the gravitational pressure drop and pressure gain due to the decrease in momentum respectively.

There is no exit pressure drop Δp_{34} at the top header where the outlet velocity is zero.

The four components of equation (I.2) are plotted separately against the inlet velocity for saturated steam at 50 °C. The gravity component is very small compared to the remaining three terms. The pressure gain due the change in momentum is of the same order as the entrance pressure drop. At low vapour flow rates they are practically equal and cancel each other. Consequently the total pressure drop is almost equal to the frictional pressure drop for the current tube configuration and steam flow conditions.

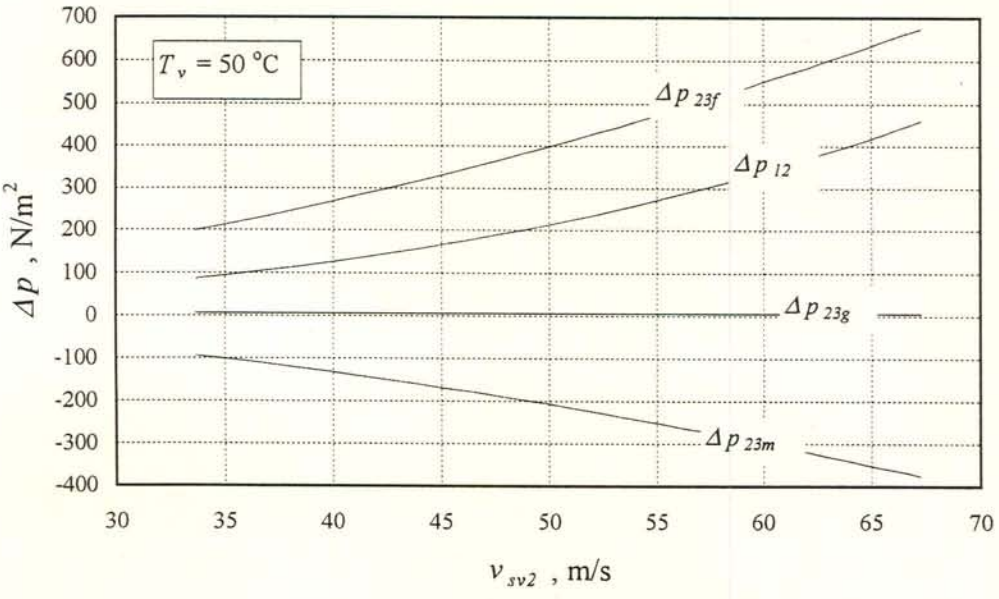

Figure I.3: Inlet pressure drop Δp_{12}, frictional pressure drop Δp_{23f}, gravitational pressure drop Δp_{23g} and the momentum component Δp_{23m} plotted against the inlet vapour velocity for saturated steam at 50 °C.

Equation (I.2) can be presented in a non-dimensional form by dividing each term by the inlet kinetic energy or dynamic head:

$$\Delta p_{14} / \left(1/2\, \rho_v\, v_{sv}^2\right) = \Delta p_{14}^* = \Delta p_{12}^* + \Delta p_{23f}^* + \Delta p_{23g}^* + \Delta p_{23m}^* \tag{I.5}$$

where

$$\Delta p_{12}^* = K_{tp} - \sigma_{21}^2 \tag{I.6a}$$

$$\Delta p_{23f}^* = \left(L_t / D_e\right) K\, Re_{sv2}^n \left(\frac{a_1}{(n+3)} + \frac{a_2}{(n+2)\, Re_{sv2}} \right) \tag{I.6b}$$

$$\Delta p_{23g}^* = \left(\rho_v g\, L_t\, \sin\theta\right) / \left(1/2\, \rho_v v_{sv2}^2\right) \tag{I.6c}$$

$$\Delta p_{23m}^* = -2 \tag{I.6c}$$

K_{tp} is a directly related to the densimetric vapour Froude number based on the duct height as outlined in Part A. The dimensionless inlet pressure is thus Froude number dependent, the functional relationship being given by equation (9.37). The dimensionless frictional pressure drop is a function of the vapour Reynolds number analogous to the well known friction factor-Reynolds number relation, while the dimensionless pressure gain Δp^*_{23m} is a constant.

The combination yielding the total pressure drop across the headers is both Froude and Reynolds number related. The upper boundary of the model is, however, determined by the Froude number which determines the conditions where the frictional pressure drop starts to deviate from the Reynolds number relation for single-phase flow and when the strong rise in pressure occurs as flooding is approached.

The operating range of an inclined reflux condenser should therefore be specified in terms of the vapour Froude number but the Reynolds number forms an integral part when modelling the flow below the upper performance limit.

Because the total pressure drop is Froude and Reynolds number dependent, a dimensionless plot against either of these groups cannot fully correlate the temperature

effect. This is illustrated in figures I.4 (a) and (b) where Δp_{14}^* is plotted against the inlet Froude and Reynolds number respectively. The curves are plotted inside the range of the model which is valid up to $Fr_{Hsv} = 0.4$. At low vapour flow rates where the inlet and the momentum components cancel each other the predictions for the different temperatures converge on the Reynolds graph. This trend is fortuitous and is not necessarily valid in general.

At higher vapour flows where the inlet pressure drop rises (see figure I.3) the Froude number effect becomes stronger and the lines on the Reynolds number graph diverge.

On the Froude number graph the predictions for the three saturation temperatures differ across the entire domain, which is not surprising as the model and thus the plot are limited to the Reynolds number region. The conditions where the pressure drop becomes Froude number related just before flooding are not accounted for by the model and are hence excluded from the plot.

I.2.3 Heat transfer

The heat transfer analysis presented in section 9.2.1 for an entire fan unit applies directly. The simplified equations valid for single-tube condensation are summarised as follows.

The heat transfer to the air and the condensation rate are

$$\begin{aligned} Q_a &= m_a c_{pam}\left(T_{ao} - T_{ai}\right) \\ &= m_c i_{lg} = m_a c_{pam}\left(T_{vm} - T_{ai}\right) e \end{aligned} \tag{I.7}$$

The condenser effectiveness is [86HO1]

$$e = 1 - exp\left[-(UA)/\left(m_a c_{pam}\right)\right] \tag{I.8}$$

where the overall thermal conductance is defined as

$$(UA) = \left[1/h_{ae}A_a + 1/h_c A_c\right]^{-1} \tag{I.9}$$

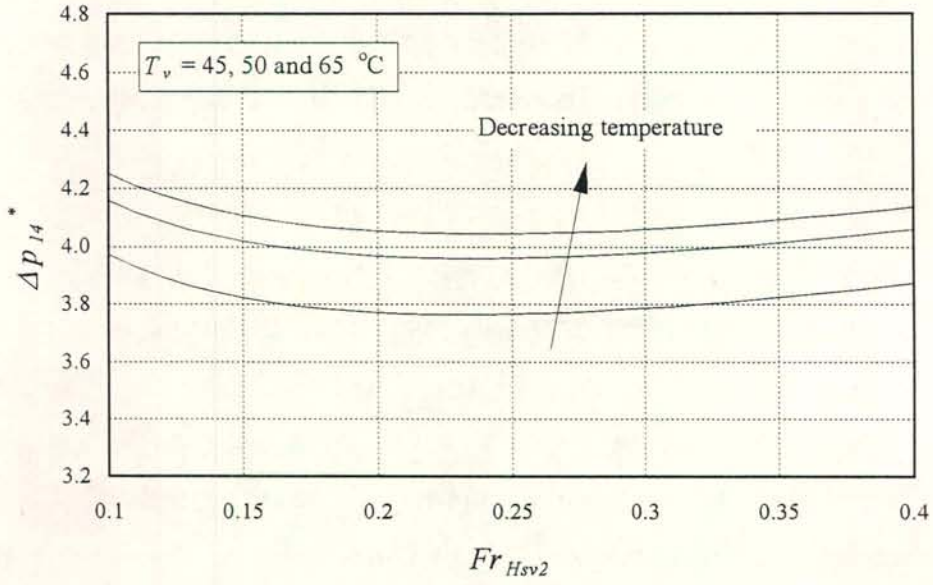

Figure I.4 (a): Total pressure drop across a reflux condenser plotted in a dimensionless form against the inlet densimetric vapour Froude number.

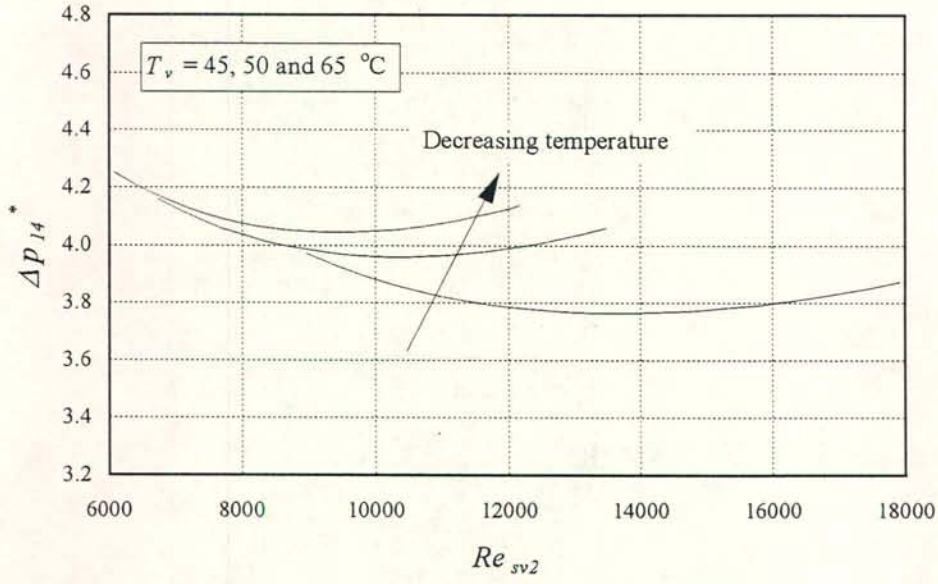

Figure I.4 (b): Total pressure drop across a reflux condenser plotted in a dimensionless form against the inlet vapour Reynolds number.

Effective airside thermal conductance:

$$h_{ae}A_a = \left[1/h_a e_f A_a + \sum_n \frac{R_n}{A_n}\right]^{-1} \tag{I.10}$$

Inside duct surface area exposed to steam:

$$A_c = A_{ti} L_t \tag{I.11}$$

Condensation heat transfer coefficient:

$$h_c = 0.9245\left[\frac{L_t\, k_c^3\, \rho_c^2\, g\cos(\theta_t)\, i_{lg}}{\mu_c\, m_{a1}\, c_{pam}(T_v - T_{ai})\left[1-exp\left\{-(U_c H_t\, L_t)/(m_{a1}\, c_{pam})\right\}\right]}\right]^{0.333} \tag{I.12}$$

Air mass flow rate flowing on one side of the duct:

$$m_{a1} = m_a/2 \tag{I.13}$$

Overall heat transfer coefficient based on the condensation surface area required for equation (I.12):

$$U_c H_t\, L_t = h_{ae} A_a/2 \tag{I.14}$$

The heat transfer performance characteristic for the finned tube was obtained in a standard wind-tunnel (see Appendix J), i.e.

$$h_{ae}A_a = Ny\, k_{am}\, Pr_{am}^{1/3}\, A_{fr} \tag{I.15}$$

where the characteristic heat transfer parameter Ny [m^{-1}] is expressed as

$$Ny = 2594.951\, Ry^{0.3184} \tag{I.16}$$

Heat exchanger flow parameter:

$$Ry = \frac{m_a}{\mu_{am} A_{fr}} \tag{I.17}$$

I.3 Experimental results

Three complete sets of reflux condensation data for steam saturation temperatures of ≈45, ≈50 and ≈65 °C respectively are quoted from Schoenfeld [97SC1] and compared to the analysis.

The ranges of flow rates and dimensionless groups covered by the data are:

T_v = 45 °C:	31.4	<	v_{sv2}	<	82.3 m/s
	1.890	<	v_{sc2}	<	5.578 m/s x 10^3
	0.070	<	Fr_{Hsv2}	<	0.482
	5169	<	Re_{sv2}	<	13514
T_v = 50 °C:	30.1	<	v_{sv2}	<	72.1 m/s
	2.238	<	v_{sc2}	<	6.172 m/s x 10^3
	0.081	<	Fr_{Hsv2}	<	0.468
	6063	<	Re_{sv2}	<	14710
T_v = 65 °C:	20.9	<	v_{sv2}	<	57.6 m/s
	2.829	<	v_{sc2}	<	9.574 m/s x 10^3
	0.073	<	Fr_{Hsv2}	<	0.580
	7596	<	Re_{sv2}	<	21691

The measured pressure drop characteristics for a system temperature of 45 °C are shown in figure I.5 in a dimensionless form. Below Froude numbers of 0.4 the pressure drop exhibits the trend depicted in figure I.4 (a). The condensate drains continuously into the bottom header and there is no accumulation inside the finned tube.

Above $Fr_{Hsv2} \approx 0.4$ the pressure drop starts to rise. This marks the onset of vapour-condensate interaction at the sharp-edged inlet flange. The condensate is sporadically sucked into the finned tube and the entrance pressure drop starts to rise.

Upon a further increase in the vapour flow rate flooding occurs and the subsequent accumulation of condensate inside the finned tube causes the pressure drop to rise sharply.

A fundamental difference between adiabatic counterflow and reflux condensation was observed in the region above $Fr_{Hsv2} \approx 0.4$ up to flooding. While in both cases the pressure drop begins to rise, the adiabatic flow exhibits a strong transient nature (see figures 4.26g and 4.26h) while such pressure oscillations were not recorded during reflux condensation.

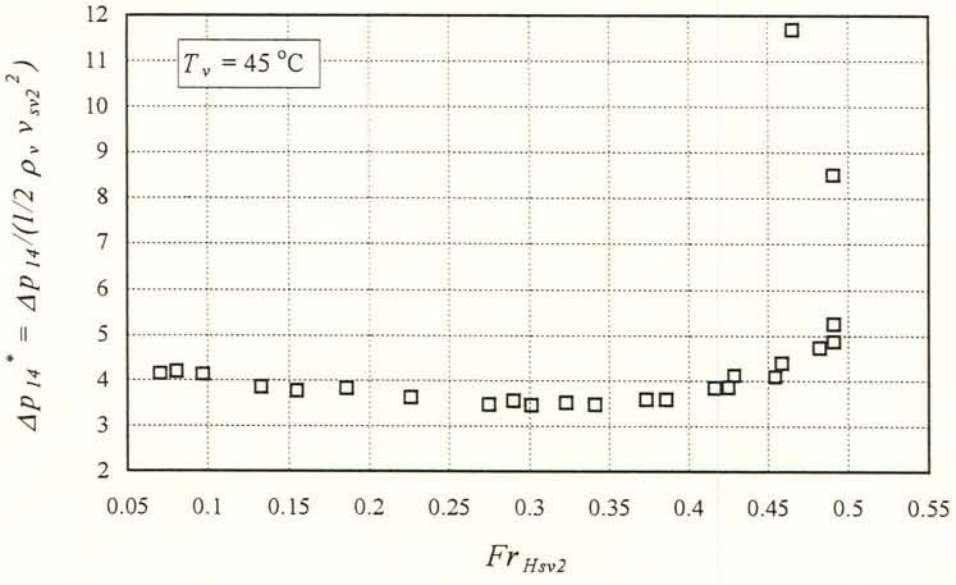

Figure I.5: Typical pressure drop characteristics for reflux condensation in an air-cooled finned tube inclined at 60° to the horizontal. Data taken from Schoenfeld [97SC1].

I.3.1 Pressure drop

The pressure drop model is employed to predict the experimental results in the region below vapour flow rates of $Fr_{Hsv2} \approx 0.4$ where the adiabatic flow is steady and the nature of the flow at the sharp-edged flange corresponds to the observations for reflux condensation.

Because the non-dimensional plots shown in figures I.4 (a) and (b) can only partially account for the temperature effect on the pressure drop, the comparison between experiment and theory is presented in a dimensional form as shown in figure I.6. The advantage of a dimensional plot is that it exposes the measured temperature effect and the trend followed by the model.

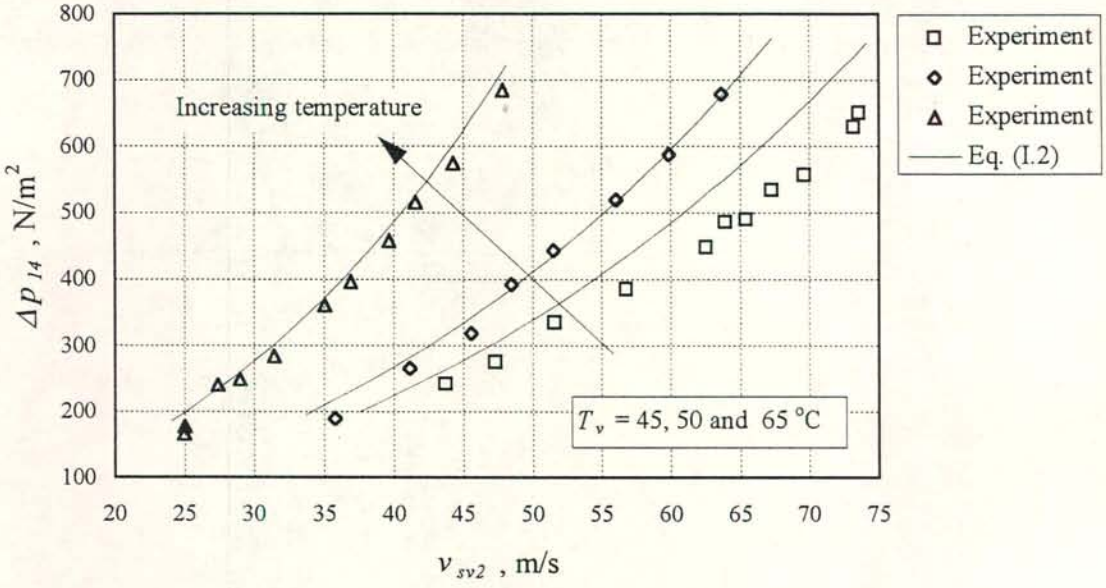

Figure I.6: Comparison between the pressure drop model given by equation (I.2) and the experimental results by Schoenfeld [97SC1].

I.3.2 Flooding

In section 2.6 (page 2.52) it is explained that the flooding definition for adiabatic flow in terms of a liquid inlet sinter cannot be applied to reflux condensation. It is furthermore stated that the vapour flow rate at the onset of the strong rise in pressure at sufficiently high heat transfer rates can be regarded as equivalent to the gas flow rate at which liquid is driven up past the point of injection in an adiabatic system. The flooding correlation developed in part A should therefore be able to predict the vapour velocity at the onset of the strong rise in pressure during reflux condensation.

In figures I.7(a) to (c) the three reflux condensation pressure drop characteristics by Schoenfeld [97SC1] are shown together with the flooding prediction according to

equation (5.4), which is depicted as a vertical line. The pressure drop prediction according to equation (I.2) is also shown.

The highest attainable vapour flow rates before the sharp increase in the pressure drop, as indicted on figures I.7 (a) to (c), are taken as the experimental flooding flow rates and are compared to equation (5.4) in figure I.8 (a) in terms of the vapour Froude numbers.

During total reflux condensation the superficial condensate velocity at station 2 can be expressed in terms of the vapour superficial velocity at 2 through the mass balance given by equation (I.1). The resulting expression for v_{sv2} can be substituted into the correlation for flooding given by equation (5.3). This yields an implicit relationship for the flooding superficial velocity at the condenser duct inlet as function of the fluid properties and the duct geometry. The fluid properties are temperature dependent and therefore an expression for the flooding vapour velocity in terms of the system temperature can be obtained. The flooding data shown in figure I.8 (a) is replotted in figure I.8 (b) against the saturation temperature of the system. The flooding superficial velocities decreases strongly as the system temperature rises mainly as a result of an increase in the vapour density.

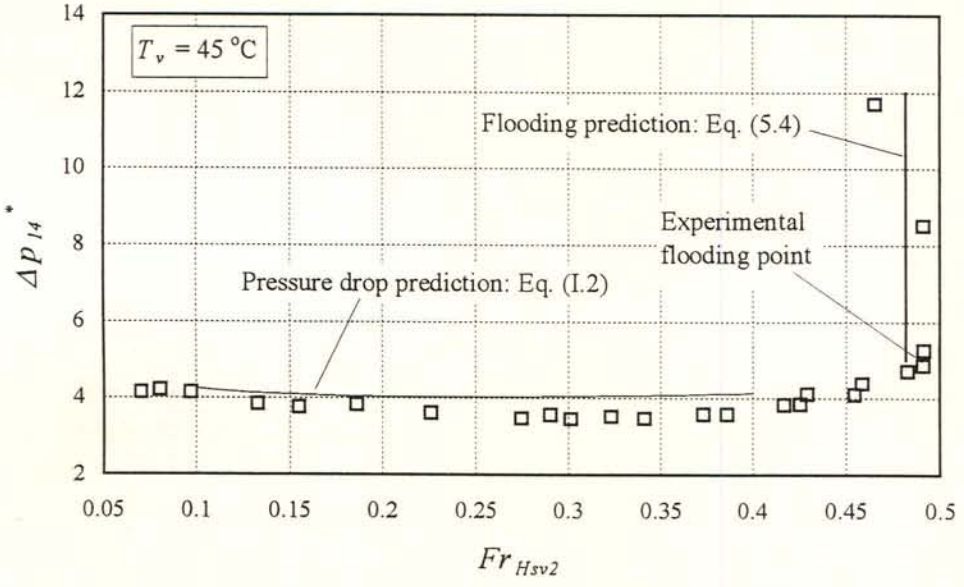

Figure I.7 (a): Pressure drop and flooding characteristics for reflux condensation at a saturation temperature of 45 °C. Data taken from Schoenfeld [97SC1].

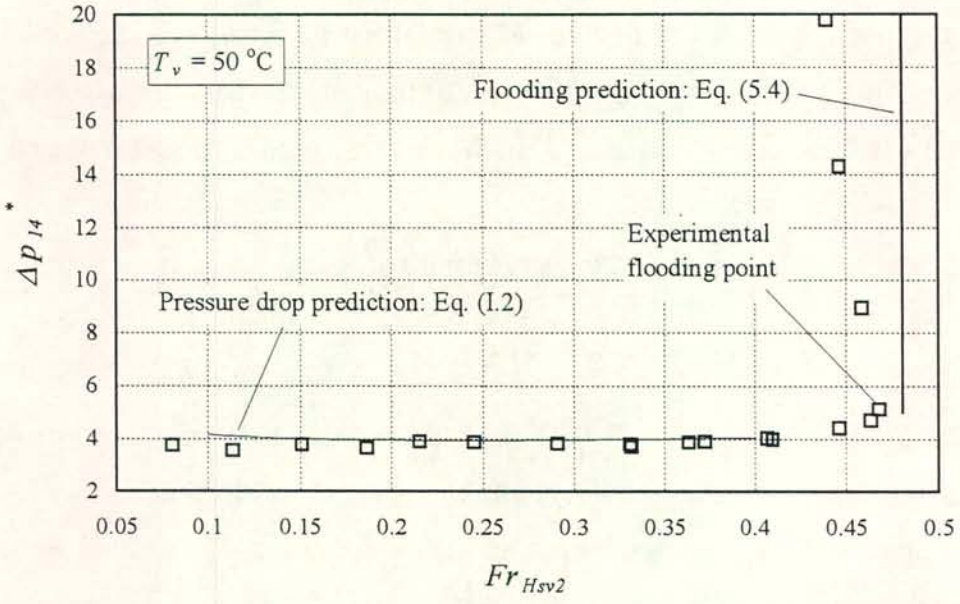

Figure I.7 (b): Pressure drop and flooding characteristics for reflux condensation at a saturation temperature of 50 °C. Data taken from Schoenfeld [97SC1].

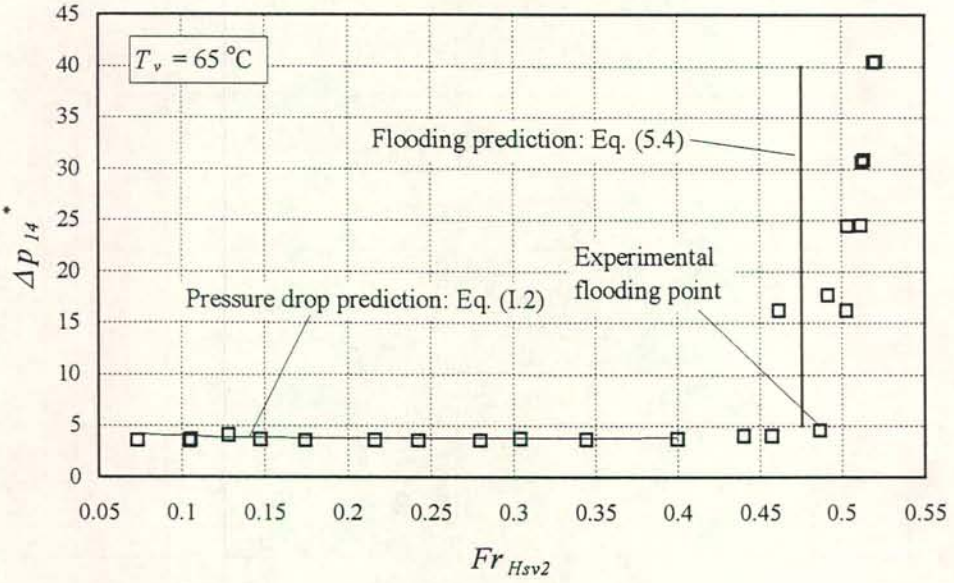

Figure I.7 (c): Pressure drop and flooding characteristics for reflux condensation at a saturation temperature of 65 °C. Data taken from Schoenfeld [97SC1].

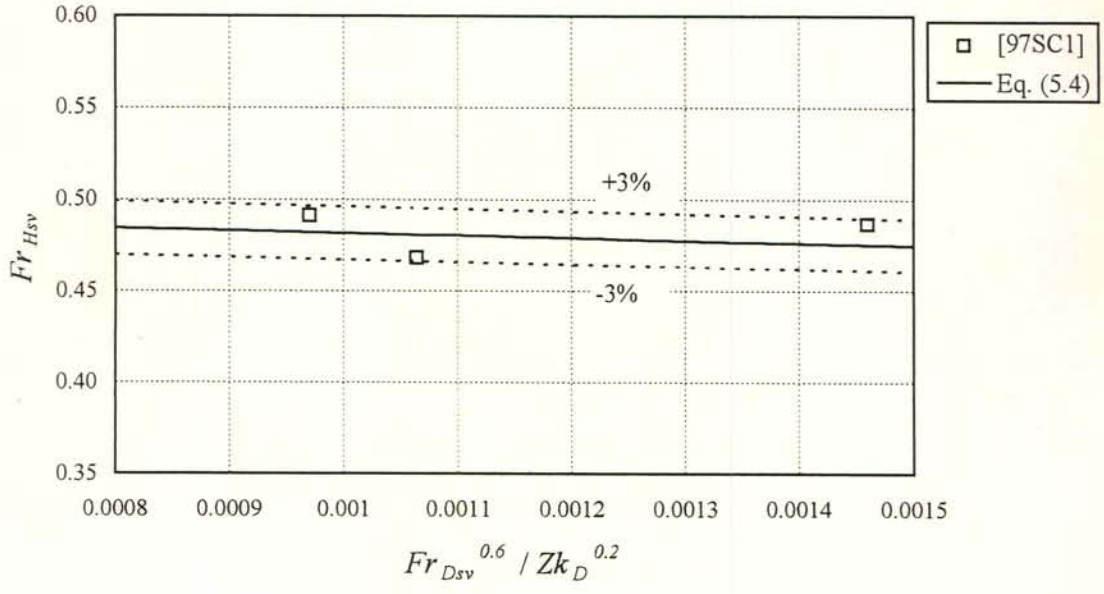

Figure I.8 (a): The flooding data for reflux condensation by Schoenfeld [97SC1] compared to the prediction according to equation (5.4) which has been developed under adiabatic conditions.

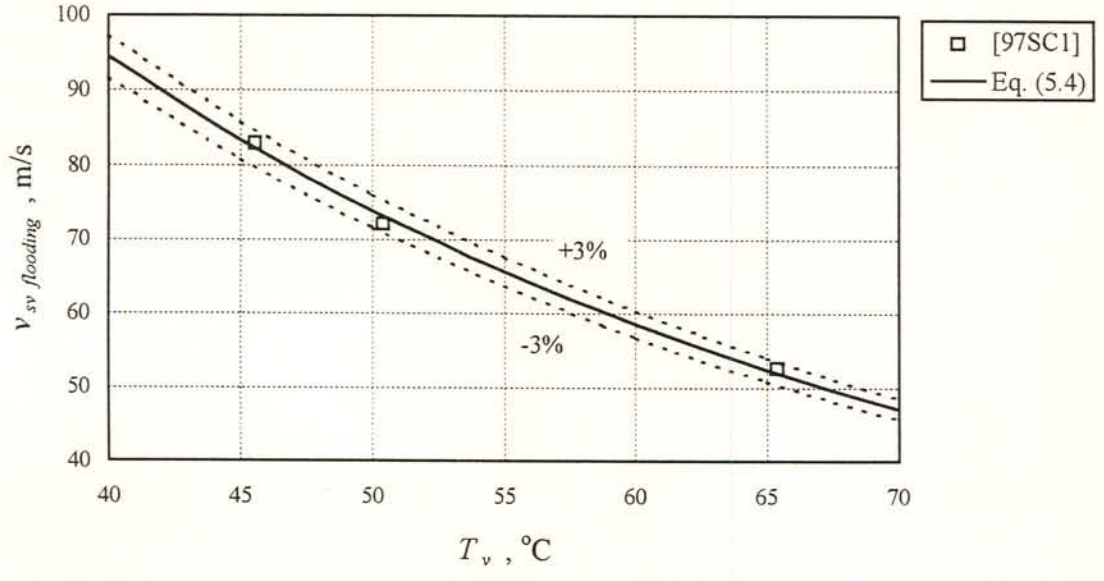

Figure I.8 (b): A replot of figure I.8 (a) for total reflux condensation, in terms of the flooding superficial velocity and the saturation temperature of the system.

I.3.3 Heat transfer

The heat transfer rate achieved during reflux condensation can be obtained from the experiments by Schoenfeld [97SC1] by either making use of the condensate flow measurements or the airside data, i.e. air mass flow rate and change in temperature. Under ideal experimental conditions these two heat transfer rates should be equal. The best energy balances were achieved in the mid range of air flow rates tested (see table I.1). At the lower end of the test range the condensate measurements yielded higher heat transfer rates than the airside data while the opposite was found for high air flow rates.

Comparison of the data with the predictions according to the heat transfer characteristics of the finned tube revealed that good agreement is achieved between theory and experiment for the condensate measurements at low heat transfer rates and for the airside data at high heat transfer rates, i.e. high air flow rates.

Accurate determination of the heat transfer should be possible for low air flow rates by measuring the condensate flow rate. At low air flow rates the condensation rate is small which allows a relatively long time period over which the volume flow rate of the condensate can be determined in the measuring flask. As the vapour flow into the finned tube increases at higher air flow rates, the condensate does not drain continuously anymore. This makes it difficult to measure condensation rates representative of steady-state conditions, which, however, can be achieved by recording and averaging the airside data over a sufficiently long period.

For the purpose of the present comparison between the experimental heat transfer data and theory the measured condensation rate is used for vapour flows below $Fr_{Hsv2} = 0.2$ while the airside data is taken for vapour flows above $Fr_{Hsv2} = 0.2$.

A mean steamside temperature is required for the theoretical prediction of the heat transfer in equation (I.7). The present pressure drop model is only valid up to $Fr_{Hsv2} = 0.4$ and the mean vapour temperature can therefore not be calculated above vapour flow rates of $Fr_{Hsv2} = 0.4$. Thus, the average of the measured bottom and top header

temperature must be taken for T_{vm} in equation (I.7). For the purpose of consistency the measured mean vapour temperature was employed across the entire range of data.

The heat transfer according to experiment and theory are compared in figures I.9 (a) to (c) for the three steam temperatures tested. The heat transfer is plotted against the densimetric vapour Froude number at the inlet of the finned tube that should ideally have been achieved if the inflow of vapour had not been limited by flooding. This enables direct interpretation of the limiting conditions due to flooding. The flooding prediction according to equation (5.4) is depicted as a vertical line. It is evident from the figures that at flooding the measured heat transfer drops below the predicted values.

I.4 Discussion and conclusion

In general good agreement is achieved between theory and experiment. The pressure drop model succeeds in predicting the observed temperature effect as shown in figure I.5. The measured pressure drop is plotted against the predicted pressure drop in figure I.10. In the case of the 50 and 65 °C degree data the deviation is approximately ±5%.

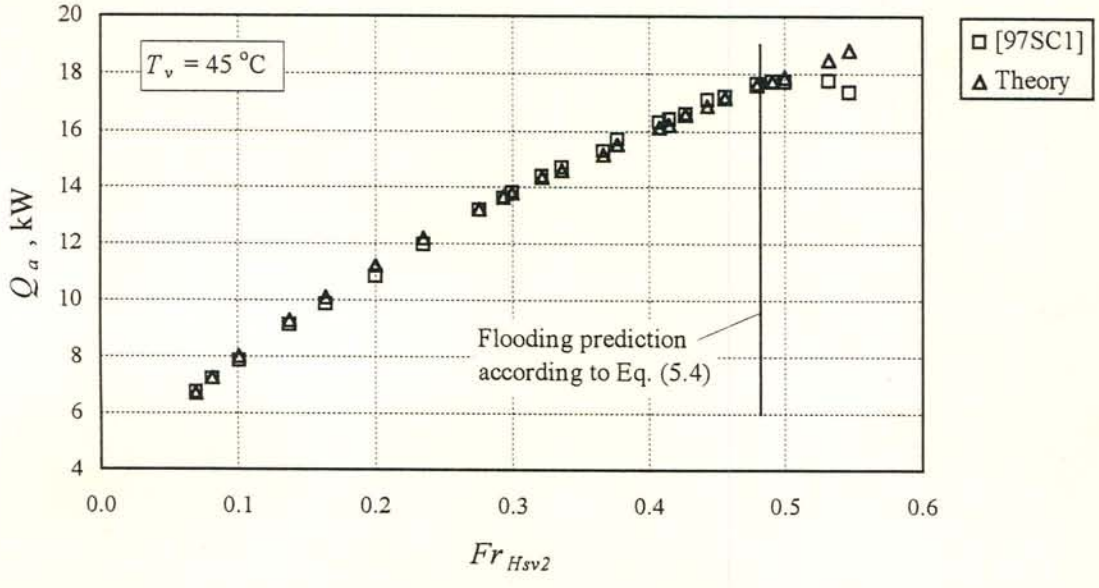

Figure I.9 (a): Predicted and measured heat transfer rate for a steam temperature of 45 °C during reflux condensation in an air-cooled finned tube inclined at 60 ° to the horizontal. Data taken from Schoenfeld [97SC1].

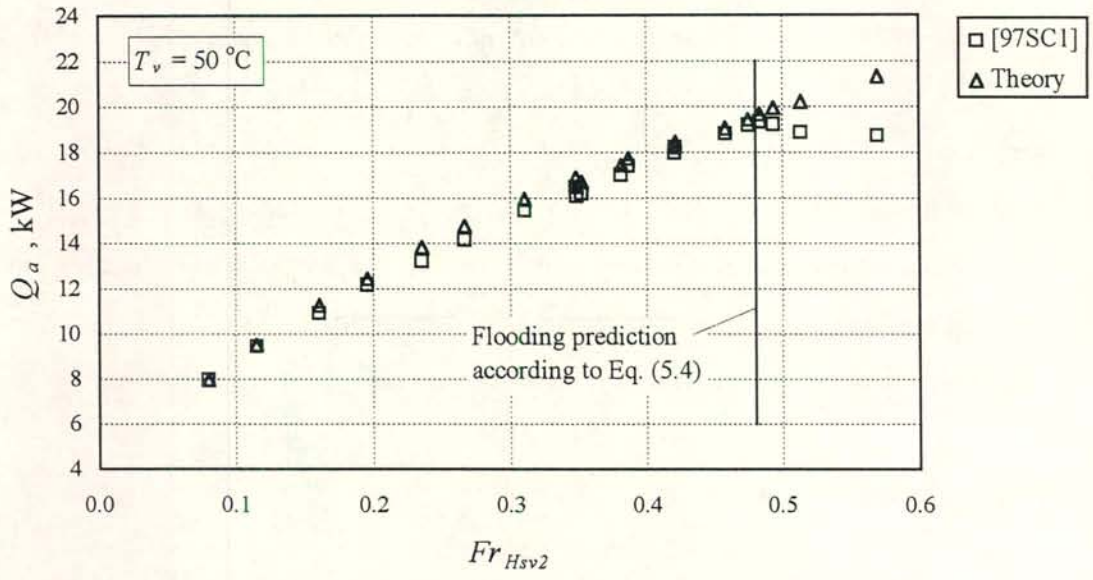

Figure I.9 (b): Predicted and measured heat transfer rate for a steam temperature of 50 °C during reflux condensation in an air-cooled finned tube inclined at 60 ° to the horizontal. Data taken from Schoenfeld [97SC1].

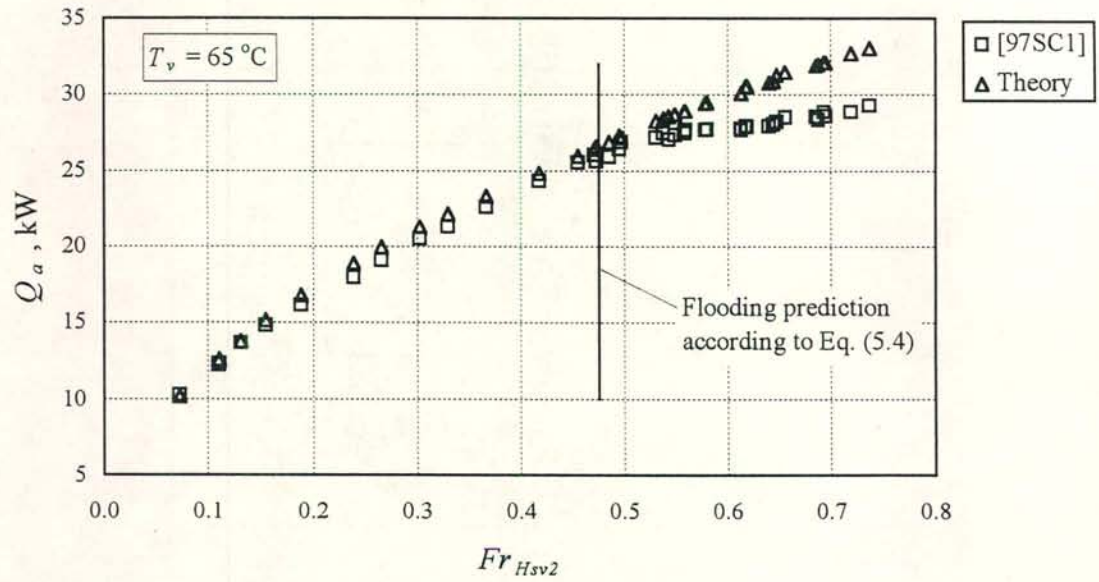

Figure I.9 (b): Predicted and measured heat transfer rate for a steam temperature of 50 °C during reflux condensation in an air-cooled finned tube inclined at 60 ° to the horizontal. Data taken from Schoenfeld [97SC1].

The 45 °C data are, however, over predicted by up to 15%. Possible reasons may be the inlet vapour momentum in equation (I.2) which does not include a momentum correction factor for the velocity profile at the inlet and the assumption of turbulent flow along the entire duct length.

The effect of the uncorrected inlet momentum should be reflected by the data of all three temperatures tested, which is not the case. Furthermore, the comprehensive study on pressure drop during condensation by Groenewald [93GR1] revealed that the assumption of turbulent flow in the laminar region introduces errors of less than 1%. Thus both these simplifications do not explain the overprediction by 15% in the case of $T_v = 45$ °C.

At conditions below flooding the experimental heat transfer is in agreement with the theory. The deviation is approximately ±5% as shown in figure I.11. Once flooding has occurred the accumulation of condensate has an adverse effect on the condensation heat transfer coefficient and the condensation rate starts to deviate from the prediction. The condensation heat transfer coefficient by Groenewald [93GR1] is based on stratified flow and the model employed is therefore not valid for vapour flow rates at and above flooding.

The flooding correlation developed for adiabatic flow successfully predicts the inlet vapour velocity at flooding during reflux condensation in a single-tube. This substantiates the observation by other researches [83BA1, 92GI1] that the inception of flooding is located at the tube inlet where the flow rates are at their maximum.

The sub-cooling observed by Banerjee *et al.* [83BA1] at flooding in vertical tubes was not encountered by Schoenfeld [97SC1]. Sub-cooling occurs in the single-phase column formed upon flooding according to Banerjee *et al.* It thus appears that the vortex-type flow encountered in inclined ducts of high aspect ratio prevents the formation of such a single-phase region. During the intense interaction in the inclined elliptical duct the condensate is continuously heated by the incoming vapour.

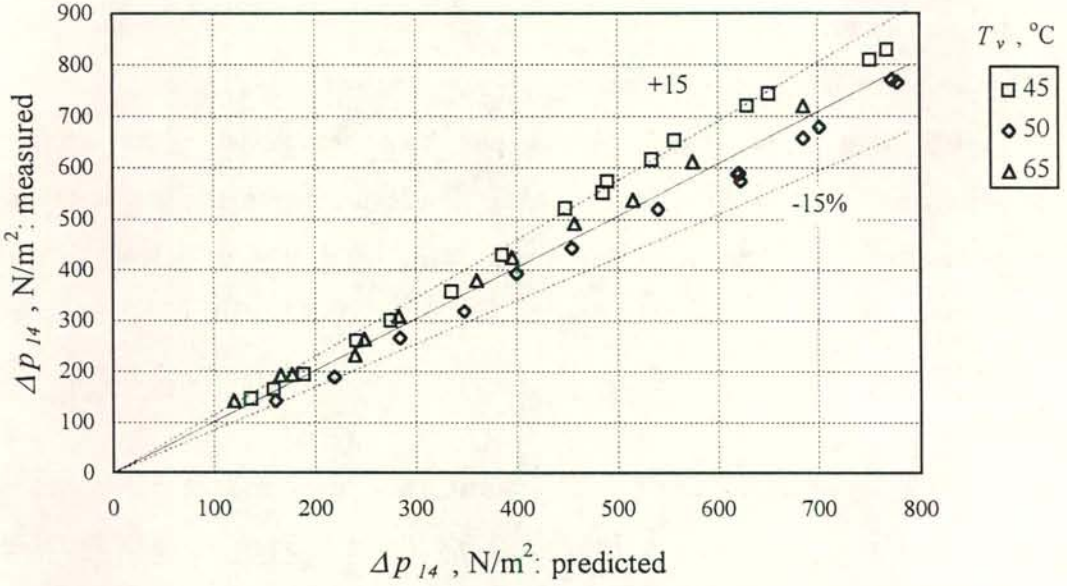

Figure I.10: Measured versus predicted pressure drop across the headers of the inclined reflux condenser duct.

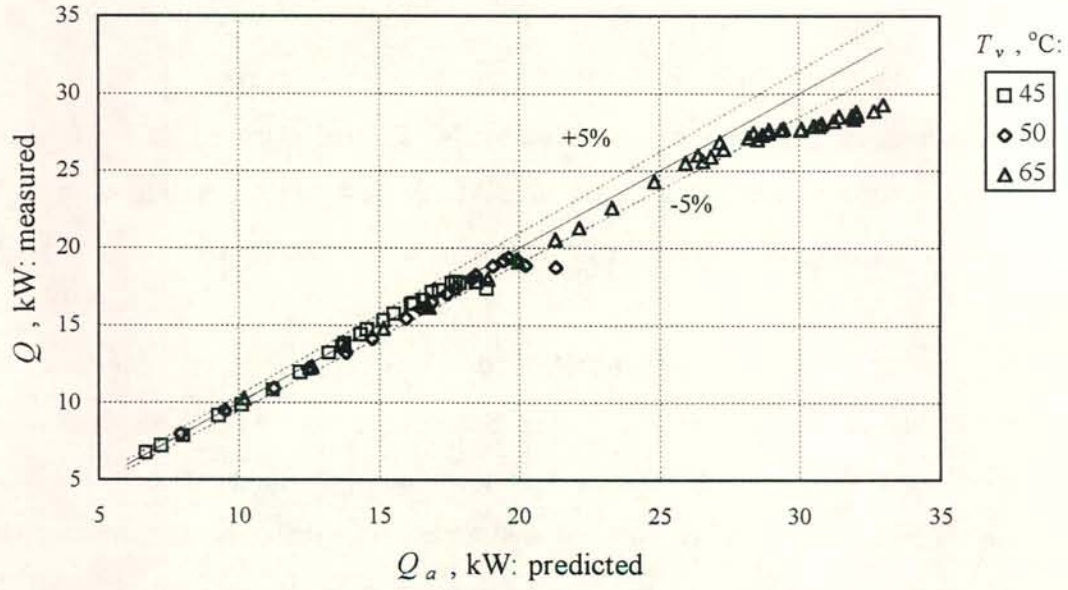

Figure I.11: Measured versus predicted heat transfer achieved by the inclined reflux condenser duct.

I.5 Sample calculation

Consider the 9th data set in table I.2 for steam at a saturation temperature of approximately 50 °C. The data were recorded below flooding and hence the pressure drop and heat transfer model apply. The geometry of the elliptical duct is:

Hydraulic diameter	D_e	=	0.02593 m
Inside area of duct per unit length	A_{ti}	=	0.20524 m^2/m
Inside cross-sectional duct flow area	A_{tc}	=	0.00133 m^2
Inside height of duct	H_t	=	0.097 m
Effective finned length of duct	L_t	=	6.982 m
Frontal area	A_{fr}	=	0.3491 m^2
Duct inclination to the horizontal	θ_t	=	60 °

I.5.1 Experimental heat transfer

Separate data were recorded for each air box. The sample calculation below is carried out for the readings of air box 1. The total heat transfer is obtained by summation of heat transfer in each box.

The measured steamside temperatures and condensate flow rate are:

Bottom header temperature	T_{v1}	=	50.81 °C = 323.99 K
Top header temperature	T_{v4}	=	49.67 °C = 322.82 K
Condensate mass flow rate	m_c	=	7.09 x 10^{-3} kg/s

The corresponding mean vapour temperature is

$$T_{vm} = 1/2\left(T_{v1} + T_{v4}\right) = 1/2\,(50.81 + 49.67) = 50.255\ °C$$

The steamside properties evaluated at the bottom header temperature are:

Vapour density	ρ_v	=	0.08632 kg/m^3
Vapour viscosity	μ_v	=	1.0796 x 10^{-5} kg/m s

Condensate density	ρ_c	=	987.76 kg/m^3
Condensate viscosity	μ_c	=	5.3648 x 10^{-4} kg/m s
Condensate conductivity	k_c	=	0.6438 W/m K
Latent heat of vaporisation	i_{lg}	=	2380872 J/kg

The measured airside temperatures and air mass flow rate at box 1 are:

Air inlet temperature	T_{ai1}	=	21.10 °C	= 294.25 K
Air outlet temperature	T_{ao1}	=	39.04 °C	= 312.19 K
Air mass flow rate	m_a	=	0.238 kg/s	

The arithmetic mean air temperature is

$$T_{am1} = 1/2\left(T_{ao1} + T_{ao2}\right) = 1/2\,(21.10 + 39.04) = 30.07 \ ^\circ\text{C}$$

and the specific heat c_{pam1} evaluated at the mean temperature is according to equation (C.1.2) 1007.072 J/kg K.

The heat transferred to the air in box 1 is obtained from equation (I.7)

$$\begin{aligned} Q_{a1} &= m_{a1}\, c_{pam1}\left(T_{ao1} - T_{ai1}\right) \\ &= 0.238\, x\, 1007.072\, x\,(39.04 - 21.10) = 4299.92 \ \text{W} \end{aligned}$$

Summation of the heat transfer in each of the four sections yields the total, i.e. Q_a = 17390 W.

The heat transfer obtained from the condensate mass flow rate is

$$Q_c = m_c\, i_{lg} = 7.09\, x\, 10^{-3}\, x\, 2380872 = 16880 \ \text{W}$$

The energy balance or percentage deviation is defined as

$$EB = \left(Q_c - Q_a\right)/Q_c \ x\, 100\% = (16880 - 17390)/16880 \ x\, 100\% = -3.0\%$$

I.5.2 Predicted heat transfer

Evaluation of the air properties at the mean temperature requires the air outlet temperature, which is an unknown in the set of heat transfer equations. The equations are therefore solved by an iterative procedure. The solution for air box 1 converges at an outlet temperature of T_{ao1} = 38.90 °C (312.05 K).

The arithmetic mean air temperature is

$$T_{am1} = 1/2\left(T_{ao1} + T_{ao2}\right) = 1/2\,(21.10 + 38.90) = 30.00\ °C = 303.15\ K$$

The ambient pressure at the time of testing was 101032 N/m^2.

The air properties evaluated at the mean temperature are:

Density	ρ_{am1}	=	1.1609 kg/m^3
Specific heat	c_{pam1}	=	1007.07 J/kg
Viscosity	μ_{am1}	=	1.8613 x 10^{-5} kg/m s
Conductivity	k_{am1}	=	0.02646 W/m K
Prandtl number	Pr_{am1}	=	0.7083

The finned tube length in air box 1 is

$$L_{t1} = L_t/4 = 6.982/4 = 1.7455\ \text{m}$$

The corresponding finned tube frontal area is

$$A_{fr1} = L_{t1}\,x\,Fin\ width = 6.982\,x\,0.05 = 0.08728\ \text{m}^2$$

The characteristic flow parameter for air box 1 is obtained from equation (I.7)

$$Ry_1 = 0.238/\left(1.8613\,x\,10^{-5}\,x\,0.08728\right) = 146511\ \text{m}^{-1}$$

Substitute Ry_1 into equation to find the characteristic heat transfer parameter

$$Ny_1 = 2594.951\,x\,146511^{0.3184} = 114536\ \text{m}^{-1}$$

The effective airside thermal conductance can be found from equation (I.15)

$$\left(h_{ae} A_a\right)_1 = 114536\, x\, 0.02646\, x\, 0.7083^{0.333}\ x\ 0.08728 = 235.79\ \text{W/K}$$

The air flow rate passing on one side of the duct required for the condensation heat transfer correlation is half the flow rate of air box 1, i.e. 0.119 kg/s. The overall heat transfer coefficient based on one side of the condensation surface area is obtained from equation (I.14)

$$U_c\, H_t\, L_{t1} = 235.79/2 = 117.895\ \text{W/K}$$

The condensation heat transfer coefficient can now be obtained from equation (I.12)

$$h_{c1} = 0.9245\, x \left[\frac{1.7455\, x\, 0.6438^3\ x\, 987.8^2\ x\ 9.81\, x\, cos\, 60^o\ x\, 2380872}{5.3648\, x\, 10^{-4}\ x\, 0.119\, x\, 1007.07\, x\, (323.405 - 294.25)\, x \left[exp\left\{ -117.895/\left(0.119\, x\, 1007.07\right)\right\}\right]} \right]^{0.333}$$

$$= 15288.5\ \text{W/m}^2\,\text{K}$$

The steamside area of section 1of the finned tube is

$$A_{c1} = A_{ti}\, L_{t1} = 0.20524\, x\, 1.7455 = 0.3582\ \text{m}^2$$

The overall thermal conduction is obtained from equation (I.9)

$$(UA)_1 = \left[1/235.79 + 1/\left(15288.5\, x\, 0.3582\right)\right]^{-1} = 226.058\ \text{W/K}$$

and the corresponding condenser effectiveness is according to equation (I.8)

$$e_1 = 1 - exp\left[-226.058/\left(0.238\, x\, 1007.07\right)\right] = 0.6106$$

The airside heat transfer can now be obtained from equation (I.7)

$$Q_a = m_{a1} c_{pam1} \left(T_{vm} - T_{ai1}\right) e_1 = 0.238\, x\, 1007.07\, x\, (323.405 - 294.25)\, x\, 0.6106$$
$$= 4266.86\ \text{W}$$

The percentage deviation from the experimental value for air box 1 is

$$\%\,deviation = (4299.92 - 4266.86)\,x\,/4299.92 = 0.8\ \%$$

Summation of the heat transfer predicted for the four air boxes yields a total of 17.731 kW which is 2.0 % above the experimental value of 17.390 kW.

I.5.3 Predicted pressure drop across the headers

The vapour and condensate flow rates in this section are based on the airside heat transfer. The superficial vapour velocity at the duct inlet is

$$v_{sv2} = Q_a / \left(\rho_v\, A_{tc}\, i_{lg}\right)$$
$$= 17390 / \left(0.08632\,x\,1330\,x\,10^{-6}\,x\,2380872\right) = 63.621\ \text{m/s}$$

The corresponding densimetric Froude number is obtained from equation (4.6)

$$Fr_{Hsv2} = 0.08632\,x\,63.621^2 / \left[9.81x\,0.097\,x\,(987.76 - 0.08632)\right] = 0.372$$

The inlet loss coefficient is obtained from equation (9.38)

$$K_{tp} = 1.622 + 2.078\,x\,0.0372 = 2.395$$

and the corresponding pressure drop is (1st term on the right-hand side of equation (I.2))

$$\Delta p_{12} = 0.5\,x\,0.08632\,x\,63.621^2\left(2.395 - 0.107^2\right) = 416.4\ \text{N/m}^2$$

The vapour Reynolds number at the inlet is according to equation (4.3)

$$Re_{sv2} = 0.08632\,x\,63.621x\,25.93\,x\,10^{-3} / 1.0792\,x\,10^{-5} = 13194$$

The condensate flow rate based on the airside heat transfer is

$$m_c = Q_a / i_{lg} = 17390/2380872 = 7.304\,x\,10^{-3}\ \text{kg/s}$$

Substitute the condensate mass flow rate into equation (I.4) to obtain the suction Reynolds number required for the frictional pressure

$$Re_{vn} = 7.304\,x\,10^{-3}\,x\,25.93\,x\,25.93\,x\,10^{-3} / \left(1.0793\,x\,10^{-5}\,x\,6.982\,x\,0.20524\right) = 12.245$$

The coefficients a_1 and a_2 are obtained from equation (9.11)

$$a_1 = 1.0649 + 1.041x10^{-3}\ x12.245 - 2.011x10^{-7}\ x12.245^3 = 1.0772$$
$$a_2 = 290.1479 + 59.3153x12.245 - 1.5995x10^{-2}\ x12.245^3 = 1045.8$$

The frictional pressure drop inside the duct can now be obtained by employing the second term on the right-hand side of equation (I.2), i.e.

$$\Delta p_{23f} = 0.5x0.08632x63.621^2\left[\frac{6.982}{25.93x10^{-3}}x0.2259x13194^{-0.2088}\right.$$
$$\left.x\left\{\frac{1.0772}{(-0.2088+3)} + \frac{1045.8}{(-0.2088+2)\,Re_{sv2}}\right\}\right] = 360.5\ \text{N/m}^2$$

The gravitational pressure drop is

$$\Delta p_{23g} = \rho_v\, g\, L_t\, sin\,\theta_t = 0.08632x9.81x6.892x\,sin\,60^o = 5.120\ \text{N/m}^2$$

The gain in pressure due the decrease in the vapour momentum is

$$\Delta p_{23m} = -\rho_v\, v_{sv2}^2 = -0.08632x63.621^2 = -349.4\ \text{N/m}^2$$

The resulting pressure drop across the headers can now be obtained from equation (I.2)

$$\Delta p_{14} = 416.4 + 630.5 + 5.120 - 349.4 = 702.62\ \text{N/m}^2$$

The measured pressure drop for this data point is 678.9 N/m^2 which represents a deviation of 3.5%.

The vapour pressure corresponding to the saturation temperature T_{vl} inside the bottom header is 12760.5 N/m^2. The mean vapour pressure inside the duct can be obtained from equation (I.3) upon substitution of the appropriate values, i.e.

$$\Delta p_{vm} = 12760.5 - 416.4 - 0.5x0.08632x63.621^2\ x\frac{6.982}{25.93x10^{-3}}x0.2259x13194^{-0.2088}$$
$$x\left[\frac{1.0772}{(-0.2088+3)}\left\{1-\frac{1}{(-0.2088+4)}\right\}\right.$$
$$\left.+\frac{1045.8}{(-0.2088+2)\,x13194}\left\{1-\frac{1}{(-0.2088+4)}\right\}\right]$$

$$+ 0.5\,x\,0.08632\,x\,9.81\,x\,6.982\,x\,sin\,60^{o} + 2/3\,0.08632\,x\,63.621^{2}$$

$$= 12760.5 - 416.4 - 464.2 - 2.560 + 232.9 = 12115.4 \ \text{N/m}^2$$

The corresponding mean vapour temperature is 49.79 °C which deviates by 0.9 % from the measured arithmetic mean of 50.26 °C.

I.5.4 Flooding

The fourth last data point in table I.2 is defined as flooding The data point is marked in figure I.7(b). It represents the vapour flow rate at the onset of the strong pressure rise across the headers. The conditions at the flooding are:

Bottom header temperature	T_{vl}	=	50.41 °C
Vapour density	ρ_v	=	0.0846 kg/m^3
Condensate density	ρ_c	=	987.96 kg/m^3
Condensate viscosity	μ_c	=	5.4039 x 10^{-4} kg/m s
Latent heat of vaporisation	i_{lg}	=	2381910 J/kg
Airside heat transfer	Q_a	=	19319 W
Inlet vapour Froude number	Fr_{Hsv2}	=	0.4682
Inlet superficial vapour velocity	v_{sv2}	=	72.1 m/s

The flooding correlation given by equation (5.4) requires the condensate superficial velocity at the bottom of the finned tube where flooding is expected to commence, which can be obtained from the heat transfer. The condensate mass flow rate corresponding the heat transfer rate Q_a at flooding is

$$m_c = Q_a / i_{lg} = 19318/2381910 = 8.110\,x\,10^{-3} \ \text{kg/s}$$

The corresponding condensate superficial velocity at the inlet is

$$v_{sc2} = m_c / \left(\rho_c\, A_{tc}\right) = 8.110\,x\,10^{-3} / \left(987.96\,x\,1330\,x\,10^{-6}\right) = 6.172\,x\,10^{-3} \ \text{m/s}$$

The superficial condensate Froude number is obtained from equation (5.1)

$$Fr_{Dsv2} = 987.96\,x\left(6.172\,x\,10^{-3}\right)^2 / \left[9.81x\,25.93\,x\,10^{-3}\,x\left(987.96 - 0.0846\right)\right]$$
$$= 1.498\,x\,10^{-3}$$

The *Zk* number is

$$Zk_D = \left(\rho_c\, D_e \sigma\right)^{0.5} / \mu_c = \left(987.96\,x\,25.93\,x\,10^{-3}\,x\,0.0679\right)^{0.5} / 5.4039\,x\,10^{-4} = 2439.6$$

Find the empirical flooding parameters K_o and n from equations (5.5) and (5.6) for 60° to be 0.4952 and 27.761 respectively. Upon substitution of the appropriate values into equation (5.4) find the flooding vapour Froude number:

$$Fr_{Hsv\,flooding} = 0.4952\,x\,exp\left(-27.761x\left(1.498\,x\,10^{-3}\right)^{0.6} / 2439.6^{0.2}\right) = 0.4808$$

The vapour Froude number at the finned tube inlet corresponding to the airside heat transfer Q_a of 19130 W measured at flooding is 0.4682. It differs by 2.7 % from the prediction according to equation (5.4).

Solve for the predicted flooding superficial vapour

$$v_{sv\,flooding} = \left[\left\{g\,H_t\left(\rho_c - \rho_v\right)/\rho_v\right\} Fr_{Hsv\,flooding}\right]^{0.5}$$
$$= \left[\left\{9.81\,x\,0.097\,x\left(9.87.96 - 0.0846\right)/0.0846\right\} x\,0.4808\right]^{0.5} = 73.1 \text{ m/s}$$

which represents a deviation of 1.4 % from the experimental value of 72.1 m/s.

I.6 Tabulated reflux condensation data by Schoenfeld [97SC1]

In the following tables p_a is the ambient pressure while T_{v1} and T_{v4} are the bottom and top header steamside temperatures respectively.

Each data point comprises four sets of airside measurements (a set consists of the inlet temperature T_{ai}, the outlet temperature T_{ao} and the mass flow rate m_a) denoted by the subscripts 1 to 4 which refer to the four air boxes depicted in figure I.1. For example, T_{ai1} is the average of the readings by the three thermocouples placed along the inlet to air box 1 while T_{ao1} is the temperature measured by the thermocouple located inside the duct of air box 1 after the finned tube. m_{a1} is the corresponding air mass flow rate as measured by the anemometer inside the duct of air box 1.

m_c is the condensate mass flow rate measured in the calibrated flask with a stop watch. Q_c is the heat transfer rate corresponding to the condensate mass flow rate m_c while Q_a is the heat transfer rate calculated according to the airside data. *EB* denotes the energy balance, i.e. the percentage deviation between Q_c and Q_a , which should ideally be zero.

Fr_{Hsv2} is the superficial densimetric vapour Froude number at the inlet to the finned tube corresponding to Q_c for $Fr_{Hsv2} < 0.2$ and Q_a for $Fr_{Hsv2} > 0.2$ respectively. The steamside pressure drop measured across the headers is given in the column denoted by Δp_{14}.

Table I.1 (a): Ambient pressure, airside and steamside temperatures for the system temperature of 45 °C.

p_a , N/m^2	T_{v1} , °C	T_{v4} , °C	T_{ai1} , °C	T_{ai2} , °C	T_{ai3} , °C	T_{ai4} , °C	T_{ao1} , °C	T_{ao2} , °C	T_{ao3} , °C	T_{ao4} , °C
100358	45.60	45.10	22.49	21.53	21.09	20.84	40.29	40.55	40.24	39.92
100796	45.61	45.06	21.81	21.40	21.04	20.61	40.08	40.30	40.09	39.72
100358	45.33	44.74	22.83	21.97	21.29	21.08	39.32	39.95	39.52	39.13
100358	45.01	44.28	23.08	22.14	21.59	21.34	38.12	38.97	38.48	38.01
100358	44.96	44.17	23.00	22.04	21.74	21.51	37.63	38.40	37.88	37.44
100358	45.14	44.22	23.09	22.36	22.12	21.89	37.00	37.65	37.23	36.81
100358	45.20	44.18	22.89	22.34	22.09	21.92	36.24	36.98	36.51	36.10
100358	45.24	44.09	22.70	22.11	21.83	21.49	35.57	36.47	35.92	35.49

Table I.1 (a): Continued.

p_a, N/m^2	T_{v1}, °C	T_{v4}, °C	T_{ai1}, °C	T_{ai2}, °C	T_{ai3}, °C	T_{ai4}, °C	T_{ao1}, °C	T_{ao2}, °C	T_{ao3}, °C	T_{ao4}, °C
100796	45.43	44.24	21.39	21.19	20.85	20.60	35.47	36.14	35.75	35.33
100358	45.26	44.02	22.64	22.34	21.81	21.61	35.32	35.93	35.49	35.11
100358	45.54	44.22	22.66	22.27	21.90	21.78	35.15	35.74	35.30	34.94
100796	45.26	43.88	21.40	20.73	20.42	20.20	34.58	35.50	34.94	34.48
100358	45.52	43.93	22.68	22.08	21.66	21.48	34.13	34.95	34.46	34.00
100796	45.03	43.48	21.41	20.84	20.25	19.99	33.76	34.83	34.25	33.68
100358	45.46	43.64	21.98	21.94	21.60	21.46	33.70	34.04	33.78	33.56
100796	45.30	43.47	21.06	20.30	19.83	19.52	33.06	34.31	33.69	33.06
100796	45.63	43.62	21.21	20.54	19.67	19.19	32.92	34.02	33.44	32.89
100763	45.61	43.71	20.89	20.22	19.90	19.71	33.26	33.93	33.44	33.12
100763	45.69	43.55	21.62	20.89	20.20	20.02	32.68	33.67	33.08	32.63
100763	45.71	43.26	21.80	20.86	20.32	20.30	32.27	33.24	32.67	32.22
100763	45.55	42.89	21.90	21.14	20.56	20.46	31.88	32.88	32.33	31.83
100763	45.48	42.51	21.66	21.01	20.57	20.32	31.45	32.39	31.91	31.49
100763	45.57	40.94	21.34	20.64	20.31	20.13	30.14	31.01	30.50	29.98
100763	45.76	39.68	21.26	20.70	20.14	19.73	28.95	30.11	29.50	28.86

Table I.1 (b): Air mass flow rate and steamside data for the system temperature of 45 °C.

m_{a1}, kg/s	m_{a2}, kg/s	m_{a3}, kg/s	m_{a4}, kg/s	m_c, g/s	Q_a, kW	Q_c, kW	EB, %	Fr_{Hsv2}, ---	Δp_{14}, N/m^2
0.079	0.081	0.080	0.080	2.81	6.05	6.73	10.1	0.070	137
0.087	0.088	0.087	0.088	3.01	6.64	7.20	7.9	0.081	159
0.104	0.106	0.106	0.105	3.28	7.50	7.85	4.5	0.097	189
0.132	0.135	0.136	0.136	3.81	8.88	9.12	2.6	0.133	241
0.152	0.154	0.155	0.157	4.11	9.81	9.84	0.3	0.155	275
0.180	0.181	0.187	0.188	4.52	10.98	10.82	-1.4	0.186	335
0.199	0.201	0.218	0.220	4.93	11.95	11.80	-1.2	0.226	385
0.230	0.230	0.241	0.245	5.27	13.18	12.62	-4.5	0.275	448
0.223	0.224	0.233	0.241	5.45	13.60	13.05	-4.3	0.290	486
0.255	0.257	0.257	0.257	5.49	13.81	13.14	-5.0	0.301	490
0.268	0.271	0.274	0.275	5.66	14.39	13.55	-6.2	0.323	534
0.249	0.253	0.259	0.267	5.79	14.69	13.86	-6.0	0.341	558
0.307	0.312	0.318	0.320	6.09	15.72	14.58	-7.8	0.386	651
0.272	0.274	0.283	0.294	6.01	15.29	14.39	-6.2	0.373	630
0.339	0.337	0.332	0.339	6.33	16.31	15.15	-7.6	0.417	751
0.293	0.295	0.309	0.323	6.39	16.42	15.30	-7.3	0.425	768
0.323	0.323	0.320	0.324	6.63	17.10	15.87	-7.8	0.455	872
0.313	0.310	0.308	0.313	6.49	16.60	15.53	-6.9	0.429	828
0.351	0.344	0.342	0.349	6.71	17.20	16.06	-7.1	0.459	945
0.375	0.370	0.369	0.375	6.81	17.66	16.30	-8.3	0.483	1070
0.397	0.386	0.390	0.399	6.82	17.74	16.32	-8.7	0.491	1122
0.405	0.396	0.401	0.410	6.85	17.72	16.40	-8.1	0.492	1214
0.452	0.437	0.451	0.459	6.73	17.75	16.11	-10.2	0.491	1965
0.491	0.463	0.489	0.496	6.74	17.36	16.13	-7.6	0.466	2558

Table I.2 (a): Ambient pressure, airside and steamside temperatures for the system temperature of 50 °C.

p_a, N/m^2	T_{v1}, °C	T_{v4}, °C	T_{ai1}, °C	T_{ai2}, °C	T_{ai3}, °C	T_{ai4}, °C	T_{ao1}, °C	T_{ao2}, °C	T_{ao3}, °C	T_{ao4}, °C
101032	50.09	49.77	22.69	20.42	19.40	19.23	44.32	43.74	43.20	42.24
101032	50.12	49.67	22.64	20.16	19.41	19.22	44.00	43.25	42.59	41.64
101032	50.17	49.60	22.09	20.67	19.89	19.63	43.15	42.39	41.65	40.80
101032	50.32	49.70	21.67	20.87	20.13	19.86	42.47	41.73	40.99	40.25
101032	50.78	50.05	21.73	20.73	20.15	19.93	41.74	41.04	40.60	40.00
101032	50.96	50.17	21.41	20.86	20.30	19.91	41.15	40.51	40.09	39.45
101032	51.02	50.08	21.06	20.78	20.26	20.04	40.28	39.70	39.33	38.71
101032	50.98	49.94	20.95	20.55	20.09	19.86	39.64	39.06	38.64	38.04
101032	50.84	49.67	21.10	20.24	19.74	19.58	39.04	38.24	37.80	37.18
101032	50.70	49.32	21.00	19.95	19.39	19.07	38.44	37.57	37.04	36.35
100728	49.88	48.90	19.94	18.91	18.23	17.66	38.96	38.28	37.79	37.10
100728	50.20	49.16	20.03	18.71	18.22	17.87	39.05	38.23	37.80	37.16
100728	50.36	49.20	20.45	19.03	18.28	18.01	38.82	37.94	37.39	36.77
100728	50.35	49.02	20.86	19.29	18.66	18.38	38.22	37.20	36.75	36.10
100728	50.28	48.65	20.43	19.36	18.78	18.36	37.36	36.53	36.08	35.44
100728	50.33	48.50	20.50	19.53	19.06	18.70	36.97	36.25	35.81	35.15
100728	50.41	48.43	20.00	19.60	19.13	18.93	36.56	36.04	35.64	35.06
100728	50.60	47.19	19.68	19.23	18.91	18.62	35.49	34.98	34.51	34.09
100728	50.36	44.67	19.39	18.91	18.56	18.15	33.56	32.86	32.27	32.20
100728	50.40	42.37	19.05	18.66	18.34	18.24	30.90	30.27	29.56	30.33

Table I.2 (b): Air mass flow rate and steamside data for the system temperature of 50 °C.

m_{a1}, kg/s	m_{a2}, kg/s	m_{a3}, kg/s	m_{a4}, kg/s	m_c, g/s	Q_a, kW	Q_c, kW	EB, %	Fr_{Hsv2}, ---	Δp_{14}, N/m^2
0.071	0.075	0.079	0.078	3.34	7.16	7.96	10.0	0.081	142
0.090	0.095	0.099	0.099	3.97	8.87	9.46	6.3	0.114	189
0.117	0.119	0.127	0.126	4.58	10.75	10.91	1.5	0.151	266
0.135	0.136	0.148	0.147	5.11	12.03	12.17	1.2	0.187	319
0.162	0.161	0.163	0.163	5.65	13.45	13.45	0.0	0.223	392
0.178	0.174	0.181	0.181	6.04	14.41	14.38	-0.2	0.254	443
0.195	0.206	0.203	0.204	6.47	15.72	15.40	-2.0	0.302	519
0.219	0.220	0.221	0.225	6.77	16.77	16.12	-4.0	0.344	588
0.238	0.241	0.241	0.245	7.09	17.71	16.88	-4.9	0.386	679
0.253	0.257	0.259	0.263	7.37	18.51	17.55	-5.5	0.424	766
0.206	0.209	0.206	0.204	6.61	16.33	15.75	-3.6	0.342	574
0.209	0.209	0.208	0.204	6.73	16.45	16.03	-2.6	0.343	590
0.229	0.225	0.224	0.221	6.93	17.30	16.51	-4.8	0.376	657
0.254	0.252	0.251	0.248	7.17	18.28	17.08	-7.0	0.420	770
0.276	0.273	0.271	0.271	7.46	19.12	17.77	-7.6	0.461	922
0.289	0.286	0.286	0.287	7.59	19.49	18.08	-7.8	0.478	1022
0.295	0.290	0.292	0.292	7.66	19.63	18.25	-7.6	0.484	1125
0.307	0.302	0.304	0.305	7.71	19.54	18.36	-6.4	0.475	1927
0.337	0.333	0.335	0.335	7.55	19.14	17.98	-6.4	0.461	2996
0.400	0.389	0.401	0.400	7.32	18.97	17.44	-8.8	0.452	4078

Table I.3 (a): Ambient pressure, airside and steamside temperatures for the system temperature of 65 °C.

p_a , N/m^2	T_{v1} , °C	T_{v4} , °C	T_{ai1} , °C	T_{ai2} , °C	T_{ai3} , °C	T_{ai4} , °C	T_{ao1} , °C	T_{ao2} , °C	T_{ao3} , °C	T_{ao4} , °C
100520	64.35	64.24	22.53	20.84	19.64	19.17	55.26	55.04	54.29	53.53
100520	64.29	64.17	22.44	20.59	19.73	19.20	55.34	54.79	53.97	53.19
100520	64.43	64.32	22.35	20.54	19.65	19.25	55.44	54.85	54.03	53.30
100520	64.73	64.60	22.15	20.48	19.57	19.33	55.38	54.75	53.88	53.17
100520	65.34	65.16	21.95	20.38	19.77	19.40	55.42	54.71	53.85	53.19
100520	65.48	65.28	21.77	20.55	19.94	19.52	54.90	54.08	53.21	52.54
100520	65.45	65.17	21.64	20.48	19.85	19.63	53.84	52.87	52.00	51.35
100520	65.69	65.37	21.51	20.39	20.02	19.67	53.27	52.30	51.50	50.90
100520	65.64	65.27	21.38	20.49	20.17	19.72	52.36	51.32	50.55	49.91
100520	65.43	65.00	21.34	20.30	19.99	19.65	51.44	50.30	49.54	48.90
100520	65.33	64.84	21.19	20.27	19.93	19.59	50.64	49.52	48.71	48.03
100520	65.26	64.68	21.05	19.89	19.67	19.29	49.72	48.49	47.64	46.90
100520	65.26	64.55	20.98	19.67	19.23	18.86	49.04	47.70	46.77	45.98
100520	65.30	64.54	20.99	19.65	19.13	18.75	48.81	47.49	46.46	45.64
100520	65.39	64.49	21.00	19.74	18.99	18.76	48.38	47.04	45.96	45.11
100520	65.77	62.64	20.88	19.59	18.79	18.46	46.88	45.43	44.21	43.99
100520	65.64	62.13	20.80	19.64	18.63	18.33	45.80	44.29	42.92	43.03
100520	65.66	61.80	20.83	19.78	18.70	18.43	45.62	44.16	42.79	42.93
100520	65.57	59.80	20.90	19.85	18.61	18.32	43.86	42.32	40.84	41.71
100520	65.58	59.95	20.99	19.96	18.62	18.45	43.75	42.24	40.74	41.69
100520	65.58	58.07	21.01	20.02	18.90	18.50	41.94	40.52	39.09	40.86
100520	65.53	58.12	20.97	20.06	18.75	18.61	42.06	40.64	39.16	40.85
100520	65.25	54.49	20.23	19.20	18.46	18.24	38.44	37.07	36.53	39.58
100520	65.18	54.51	20.22	19.02	18.39	18.19	38.40	37.02	36.53	39.47
100520	65.21	53.11	20.07	19.08	18.43	18.11	36.78	35.41	35.35	38.69
100520	65.24	52.83	20.11	19.19	18.36	18.13	36.61	35.24	35.24	38.70
100520	65.31	50.18	20.12	19.26	18.32	18.07	33.91	32.53	33.49	37.11
100520	65.40	49.69	20.11	19.26	18.28	17.97	33.72	32.29	33.28	37.02
100520	65.26	48.88	20.23	19.79	18.79	18.09	32.55	31.60	32.70	36.09
100520	65.38	47.83	20.19	19.78	18.50	17.88	32.23	31.23	32.35	35.92
101004	65.43	62.89	22.09	21.02	19.26	18.66	46.85	45.79	44.63	44.17
101004	65.50	62.55	22.34	21.09	19.62	19.01	46.94	45.82	44.65	44.29
101004	65.58	59.30	20.74	19.75	19.12	18.81	43.05	41.94	41.01	42.12
101004	65.63	60.07	20.91	19.74	19.24	18.91	43.55	42.31	41.41	42.36
101004	65.79	54.39	21.05	19.80	19.24	19.10	38.15	36.78	36.43	39.59
101004	65.78	54.58	21.04	19.96	19.41	19.14	38.27	36.93	36.65	39.73
101004	65.76	52.87	21.37	20.08	19.46	19.16	36.71	35.21	35.28	38.66
101004	65.79	52.76	21.45	20.31	19.57	19.42	36.72	35.23	35.31	38.70
101004	65.35	51.34	21.44	20.64	19.85	19.63	35.08	33.76	34.40	37.75
101004	65.35	50.79	21.35	20.99	19.66	19.35	34.97	33.68	34.05	37.47

Table I.3 (b): Air mass flow rate and steamside data for the system temperature of 65 °C.

m_{a1}, kg/s	m_{a2}, kg/s	m_{a3}, kg/s	m_{a4}, kg/s	m_c, g/s	Q_a, kW	Q_c, kW	EB, %	Fr_{Hsv2}, ---	Δp_{14}, N/m^2
0.061	0.065	0.064	0.063	4.36	8.67	10.24	15.35	0.074	120
0.079	0.084	0.083	0.081	5.2	11.15	12.21	8.69	0.105	166
0.080	0.083	0.084	0.081	5.24	11.22	12.30	8.77	0.106	177
0.090	0.093	0.093	0.089	5.81	12.47	13.64	8.54	0.128	240
0.100	0.103	0.103	0.101	6.31	13.91	14.80	6.03	0.148	249
0.115	0.119	0.119	0.115	6.88	15.67	16.13	2.87	0.175	283
0.136	0.139	0.142	0.138	7.6	17.95	17.82	-0.74	0.217	360
0.147	0.151	0.152	0.150	8.15	19.10	19.11	0.07	0.243	396
0.163	0.164	0.171	0.167	8.75	20.49	20.52	0.12	0.280	457
0.169	0.173	0.187	0.182	9.2	21.28	21.58	1.37	0.304	515
0.184	0.191	0.203	0.196	9.54	22.58	22.38	-0.93	0.344	575
0.207	0.212	0.221	0.216	10.08	24.32	23.64	-2.85	0.400	685
0.221	0.227	0.236	0.231	10.48	25.51	24.58	-3.77	0.440	815
0.228	0.231	0.243	0.239	10.71	26.03	25.12	-3.61	0.458	842
0.238	0.243	0.255	0.253	10.93	26.89	25.64	-4.88	0.487	1026
0.247	0.248	0.264	0.261	10.76	26.39	25.23	-4.62	0.462	3493
0.268	0.271	0.285	0.282	10.89	27.46	25.53	-7.55	0.503	3792
0.266	0.271	0.285	0.282	10.64	27.17	24.95	-8.90	0.492	4055
0.290	0.294	0.313	0.310	10.99	27.67	25.77	-7.36	0.512	5828
0.289	0.294	0.314	0.309	10.97	27.45	25.72	-6.70	0.503	5724
0.311	0.319	0.343	0.338	11.07	27.73	25.96	-6.81	0.514	7384
0.311	0.315	0.341	0.336	10.94	27.67	25.65	-7.85	0.513	7315
0.367	0.365	0.367	0.361	11.22	27.73	26.32	-5.38	0.521	9807
0.364	0.364	0.365	0.361	11.11	27.67	26.06	-6.15	0.520	9765
0.395	0.394	0.397	0.394	10.9	28.05	25.57	-9.72	0.534	10703
0.395	0.394	0.399	0.395	10.82	27.89	25.38	-9.90	0.527	11026
0.463	0.451	0.470	0.466	10.89	28.57	25.54	-11.85	0.551	12745
0.465	0.450	0.470	0.467	11.15	28.33	26.15	-8.35	0.540	13215
0.512	0.514	0.524	0.523	11.43	29.28	26.81	-9.22	0.580	13506
0.511	0.513	0.524	0.520	11.27	28.86	26.43	-9.19	0.561	14183
0.260	0.257	0.254	0.254	10.53	25.91	24.70	-4.92	0.451	2797
0.257	0.256	0.254	0.254	10.61	25.61	24.88	-2.95	0.440	3275
0.303	0.300	0.298	0.297	10.72	27.05	25.14	-7.62	0.489	6270
0.300	0.298	0.298	0.299	10.78	27.33	25.28	-8.12	0.498	5714
0.387	0.383	0.389	0.385	11.12	27.89	26.07	-6.99	0.516	10539
0.387	0.381	0.386	0.385	11.03	27.91	25.86	-7.93	0.517	10355
0.433	0.421	0.433	0.433	11.16	28.50	26.16	-8.94	0.539	11575
0.427	0.421	0.435	0.434	11.09	28.21	26.00	-8.51	0.528	11721
0.476	0.481	0.486	0.484	11.32	28.84	26.55	-8.64	0.561	12180
0.482	0.481	0.484	0.481	11.17	28.55	26.20	-8.96	0.550	12482

APPENDIX J

PERFORMANCE CHARACTERISTICS OF FINNED TUBE BUNDLES

J.1 Test facility

The heat transfer and pressure drop characteristics of the finned tube bundles employed in the air-cooled condenser were obtained in a test facility comprising a standard wind-tunnel [47WI1] and a warm water circulation system. A test bundle made up of two staggered rows or a single-row of finned tubes can be mounted onto the wind-tunnel while warm water is circulated through the bundle.

A radial fan draws air uniformly from the surroundings through a rounded inlet section located upstream of the test bundle where its wet- and dry-bulb temperature is measured. The cooling air passes across the heated finned tubes and through an insulated connecting section before entering a mixer. The mixer divides the air flow into small streams which are diverted across each other. A set of thermocouples measure the dry-bulb temperature behind the mixer where an accurate mean temperature can be obtained.

The air flow is determined by measuring the pressure drop across one or more elliptical nozzles mounted in a plate located between two perforated plates behind the mixer.

The water is heated by a set of electrical elements. During testing the power input to the elements is adjusted such that the water stabilises at a temperature representative of the condenser operating conditions, typically 60 °C. The water inlet and outlet temperature at the bundles is measured by two sets of thermocouples respectively. The thermocouples are calibrated by running the facility under isothermal conditions at the operating temperature to account for heat losses to the environment.

The water flow rate is determined by timing the rise in the water level in a calibrated tank.

J.2 Theory

Conservation of energy requires that the heat transferred from the water is equal to the heat transferred to the air stream:

$$Q_a = m_a c_{pa}\left(T_{ao} - T_{ai}\right) = Q_w = m_w c_{pw}\left(T_{wo} - T_{wi}\right) \tag{J.1}$$

Since the change in water temperature is very small compared to the change in temperature experienced by the air stream, the heat transferred to the air is determined with a greater accuracy and is hence employed in the analysis that follows. The quality of the data can however be determined by comparison of Q_a and Q_w, which should ideally be equal if calibration successfully accounts for losses to the environment.

The heat transfer can be expressed in terms of an overall heat transfer coefficient [86HO1]

$$Q_a = U_a\, A_a F_T\, \Delta T_{lm} \tag{J.2}$$

where U_a is the overall heat transfer coefficient based on the airside area A_a

$$U_a = \left(\frac{1}{h_a e_f} + \frac{A_a}{h_w A_w} + \sum_n \frac{A_n}{A_n} R_n \right)^{-1} \tag{J.3}$$

e_f is the effectiveness of the finned surface. The summation term includes all the thermal resistances other than those owing to the airside and waterside convection, such as the conduction resistance in the duct walls.

F_t is a correction factor for a crossflow heat exchanger and ΔT_{lm} is the logarithmic mean temperature difference given by

$$\Delta T_{lm} = \frac{\left(T_{wi} - T_{ao}\right) - \left(T_{wo} - T_{ai}\right)}{ln\left[\left(T_{wi} - T_{ao}\right)/\left(T_{wo} - T_{ai}\right)\right]} \tag{J.4}$$

Substitute equation (J.2) into equation (J.3) and rearrange to find a new effective heat transfer coefficient h_{ae} based on the airside surface defined as

$$h_{ae} A_a = \left(\frac{1}{h_a \, e_f \, A_a} + \sum_n \frac{R_n}{A_n} \right)^{-1} = \left(\frac{F_t \, \Delta T_{lm}}{Q_a} - \frac{1}{h_w \, A_w} \right)^{-1} \tag{J.5}$$

Kröger [86KR1] outlines a modified form of the method by Kern [80KE1] to present experimentally obtained performance data of finned tubes, such as in equation (J.5), in a dimensional form. It can be summarised as follows:

Based on a method originally proposed by Colburn [33CO1], the heat transfer coefficient under conditions of forced convection through finned surfaces may be expressed as

$$Nu_a / \left(Re_a \, Pr_a^{0.333} \right) = f\left(Re_a \right) \tag{J.6}$$

or

$$Nu_a = a_{Nu} \, Re_a^{b_{Nu}} \, Pr_a^{0.333} \tag{J.7}$$

where an exponential relationship has been assumed for *f(Re)*. Both the Nusselt number *Nu* and the Reynolds number *Re* contain equivalent or hydraulic diameters which can be left out of equation (J.7) because of their relatively arbitrary nature. In the absence of the equivalent diameter, equation (J.7) can be written as

$$h_a / k_a = a_h Ry^{b_h} \, Pr_a^{0.333} \tag{J.8}$$

where *Ry* is the characteristic flow parameter

$$Ry = m_a / \left(\mu_a A_{fr} \right) \tag{J.9}$$

The effective finned surface area A_a and the frontal area A_{fr} play an important role in the performance of finned tube bundles and may be introduced into equation (J.8) as follows:

$$h_a \, e_f \, A / k_a = A_{fr} \, Pr_a^{0.333}$$

which yields a relationship for the characteristic heat transfer parameter *Ny* upon rearranging, i.e.

$$Ny = h_{ea} \, A_a / \left(k_a \, A_{fr} \, Pr_a^{0.333} \right) = a_{Ny} Ry^{b_{Ny}} \tag{J.10}$$

Equation (J.10) sums up two advantages of this data presentation method. i) The product of the effective airside heat transfer coefficient and the surface area $h_{ea}A_a$ is kept in a combined form as it was obtained by experiment according to equation (J.5) and ii) the actual heat transfer achieved by a bundle is expressed per unit frontal area. In the process the need for determining the surface area of the finned surface, often made up of complex sophisticated fins, is eliminated and only the frontal area of the full scale heat exchanger is required for the performance prediction.

The change in total pressure across the bundle experienced by the air stream during isothermal flow conditions may also be expressed in a dimensionless form analogous to equation (J.7) as

$$K_{heiso} = \Delta p_{iso} / \left(1/2\, \rho_a\, v_a^{\,2}\right) = a\, Re_a^{\,b} \tag{J.11}$$

where K_{heiso} is a heat exchanger loss coefficient based on the free steam conditions and Δp_{iso} is the change in total pressure. Similar to the heat transfer equations the heat exchanger loss coefficient can be expressed in terms of the characteristic flow parameter by not including the equivalent diameter in the Reynolds number *Re*, i.e.

$$K_{heiso} = a_{K_{he}}\, Ry^{\,b_{K_{he}}} \tag{J.12}$$

J.3 Experimental performance data

The performance characteristics of the bundles employed in the air-cooled condenser were determined at the University of Stellenbosch before commencement of this dissertation and were therefore available in the form of equations (J.10) and (J.12). The present author did however conduct the performance testing of the finned tube used in the experiments by Schoenfeld [97SC1]. The tests are briefly discussed to illustrate the data processing and the accuracy achieved by the test facility.

The test bundle was made up of ten 0.47 m long finned tube sections constituting a single-row one-pass cross-flow heat exchanger. It is shown schematically in figure J.1. The bundle specifications are:

Frontal area	A_{fr}	=	0.235 m^2
Number of finned tubes	n_t	=	10
Total length of finned tubes	L_t	=	4.7 m
Inside area of duct per unit length	A_{ti}	=	0.20524 m^2/m
Inside cross-sectional duct flow area	A_{tc}	=	0.00133 m^2
Hydraulic diameter	D_e	=	0.02592 m

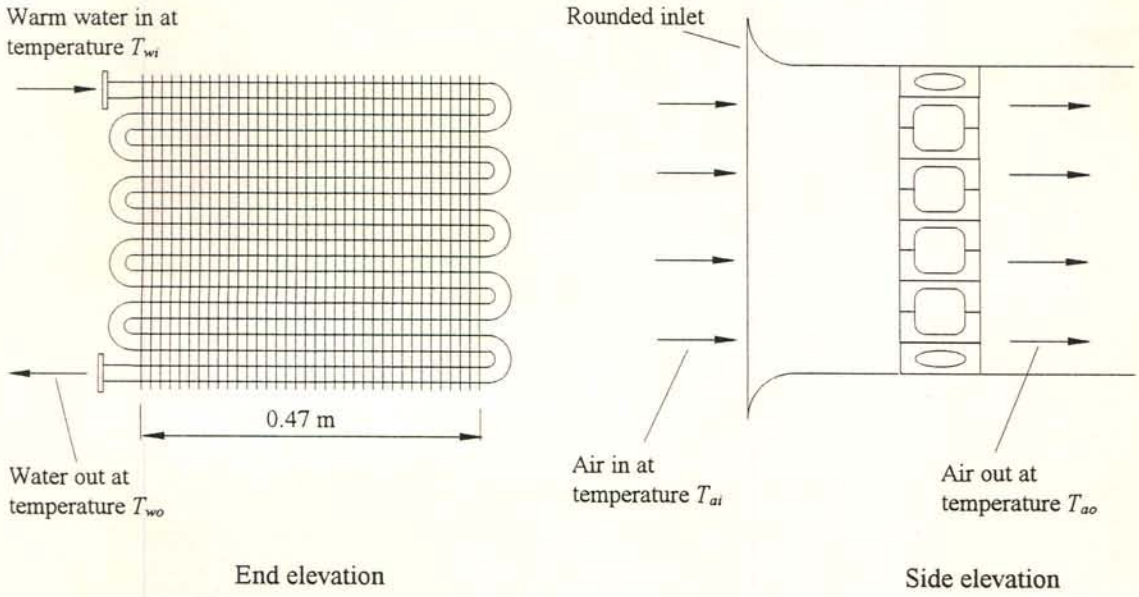

Figure J.1: Test bundle for performance characteristics.

The measured airside and waterside temperatures and flow rates are given in table J.1 Consider the first data point. The fluid properties at the arithmetic mean temperatures are respectively:

Air:

Mean temperature	T_{am}	=	32.7182 °C
Density	ρ_a	=	1.13064 kg/m^3
Viscosity	μ_a	=	1.8544×10^{-5} kg/m s
Specific heat	c_{pa}	=	1018.413 J/kg K
Conductivity	k_a	=	0.026544 W/m K
Prandtl number	Pr_a	=	0.7115

The effect of the humidity of 0.01287 kg/kg dry air on the properties is incorporated in the above-listed values.

Water:

Mean temperature	T_{wm}	=	67.3241 °C
Viscosity	μ_w	=	0.4160 x 10^{-3} kg/m s
Specific heat	c_{pw}	=	4189.35 J/kg K
Conductivity	k_w	=	0.65988 W/m K
Prandtl number	Pr_w	=	2.6393

Table J.1: Airside and waterside temperatures, mass flow rates and energy balance.

No. 1	p_{ai}, N/m^2	T_{ai}, °C	T_{ao}, °C	T_{wi}, °C	T_{wo}, °C	m_a, k/s	m_w, k/s	Energy balance, %
1	100047	26.6303	38.8061	68.6461	66.0020	2.5079	2.8404	1.2
2	100048	26.5303	40.6297	68.7470	66.3490	1.9880	2.8403	0.0
3	100050	26.3976	42.6235	68.2759	66.1685	1.5275	2.8410	-0.6
4	100053	26.2468	45.2917	68.2824	66.4191	1.1424	2.8410	0.1
5	100055	26.1210	48.7009	68.5361	66.9352	0.8218	2.8406	0.8
6	100061	25.7250	51.4949	67.9582	66.6309	0.6054	2.8416	-0.6

The airside heat transfer is according to equation (J.1)

$$Q_a = 2.5079\,x\,1018.413\,x\,(38.8061 - 26.6303) = 31097.8 \text{ W}$$

and similarly find the waterside heat transfer to be

$$Q_w = 2.8404\,x\,4189.35\,x\,(68.6461 - 66.0020) = 31463.3 \text{ W}$$

The percentage difference or measure of the energy balance is

$$EB = \left(Q_w - Q_a\right) x\,100 / Q_a = (31463.3 - 31097.8)\,x\,100/31097.8 = 1.0 \text{ \%!}$$

The log mean temperature difference is obtained from equation (J.4)

$$\Delta T_{lm} = \frac{(68.6461 - 38.8061) - (66.0020 - 26.6303)}{ln\left[(68.6461 - 38.8061)/(66.0020 - 26.6303)\right]} = 34.3860 \ ^{\circ}C$$

According to Roetzel [84RO1] the temperature correction factor can be expressed as

$$F_t = 1 - \sum_{i=1}^{4} \sum_{k=1}^{4} a_{i,k} \left(1 - \phi_{cf}\right)^k \sin\left(2i \arctan \frac{\phi_h}{\phi_c}\right) \tag{J.12}$$

where the dimensionless temperature changes of the hot and the cold stream are respectively defined as

$$\phi_h = \frac{T_{hi} - T_{ho}}{T_{hi} - T_{ci}} \tag{J.13}$$

and

$$\phi_h = \frac{T_{hi} - T_{ho}}{T_{hi} - T_{ci}} \tag{J.14}$$

The values of the empirical constant $a_{i,k}$ are given in table J.2 for a single-row one-pass cross-flow heat exchanger. Evaluation of equation (J.12) for data point 1 yields a temperature correction factor of $F_t = 0.9966$.

Table J.2: Empirical values for equation (J.12)

$a_{i,k}$	$i = 1$	2	3	4
$k = 1$	-4.62×10^{-1}	-3.13×10^{-2}	-1.74×10^{-1}	-4.20×10^{-2}
2	5.08×10^{0}	5.29×10^{-1}	1.32×10^{0}	3.47×10^{-1}
3	-1.57×10^{1}	-2.37×10^{0}	-2.39×10^{0}	-8.53×10^{-1}
4	1.72×10^{1}	3.18×10^{0}	1.99×10^{0}	6.49×10^{-1}

The waterside convection coefficient h_w required in equation (J.5) is obtained from a correlation by Gnielinski [75GN1]

$$Nu_w = \frac{(f/8)(Re_w - 1000)\, Pr_w \left[1 + (D_e/L_t)^{0.67}\right]}{1 + 12.7(f/8)^{0.5}\left(Pr_w^{0.67} - 1\right)} \tag{J.15}$$

where Nu_w is the waterside Nusselt number. The Reynolds number is

$$Re_w = m_w D_e / (A_{tc} \mu_w) = 2.8404 x 25.92 x 10^{-3} / (1330 x 10^{-6} x 0.416 x 10^{-3})$$
$$= 133132.8$$

The Darcy friction factor f is obtained from a correlation by Filonenko [54FI1]

$$f = (1.82 log_{10} Re_w - 1.64)^{-2} = (1.82 x log_{10}(133132.8) - 1.64)^{-2} = 0.016927$$

Substitute the values of f and Re_w into equation (J.15) to find the Nusselt number

$$Nu_w = \frac{(0.016927/8)(133132.8 - 1000)\ x 2.6393\ x 10 x \left[1 + (25.92 x 10^{-3}/4.7)^{0.67}\right]}{1 + 12.7(0.016927/8)^{0.5}(2.6393^{0.67} - 1)}$$
$$= 495.4161$$

and the corresponding convection coefficient

$$h_w = k_w Nu_w / D_e = 0.65988 x 495.4161/25.92\ x 10^{-3} = 12611.4\ \text{W/m}^2\text{K}$$

The waterside surface area is

$$A_w = A_{ti} L_t = 0.20524 x 4.7 = 0.9646\ \text{m}^2$$

The product of the effective airside convection coefficient and the surface area in equation (J.5) can now be found upon substitution of the appropriate values, i.e.

$$h_{ae} A_a = \left(\frac{F_t \Delta T_{lm}}{Q_a} - \frac{1}{h_w A_w}\right)^{-1} = \left(\frac{0.9966 x\ 34.3860}{31097.8} - \frac{1}{12611.4 x\ 0.9646}\right)^{-1}$$
$$= 980.609\ \text{W/K}$$

The corresponding characteristic heat transfer parameter is found from equation (J.10)

$$Ny = 980.608/(0.026544 x 0.235 x\ 0.7115^{0.333}) = 1760101\ \text{m}^{-1}$$

and the characteristic flow parameter is according equation (J.9)

$$Ry = 2.5079/(1.8544 x 10^{-5}\ x 0.235) = 575492\ \text{m}^{-1}$$

The tabulated *Ry-Ny* values are presented in table J.3. By making use of a least squares fit a correlation for the data is obtained in the form of equation (J.10) where a_{Ny} =

2594.95 and $b_{Ny} = 0.3184$. The data and the correlation are shown in figure J.2 while the percentage deviation of the experimental data points from the correlation is listed in table J.3. A very good curve fit is achieved by the exponential form inside the range tested. The biggest deviation is 0.5%!

Table J.3: Test bundle *Ry-Ny* values.

No. 1	*Ry*, m^{-1}	*Ny*, m^{-1} experimental	*Ny*, m^{-1} correlation	Percentage deviation, %
1	575492	176101	177074	0.5
2	455239	164712	164339	-0.2
3	349015	151415	151008	-0.3
4	260224	138131	137532	-0.4
5	186476	123658	123687	0.0
6	136974	111723	112114	0.3

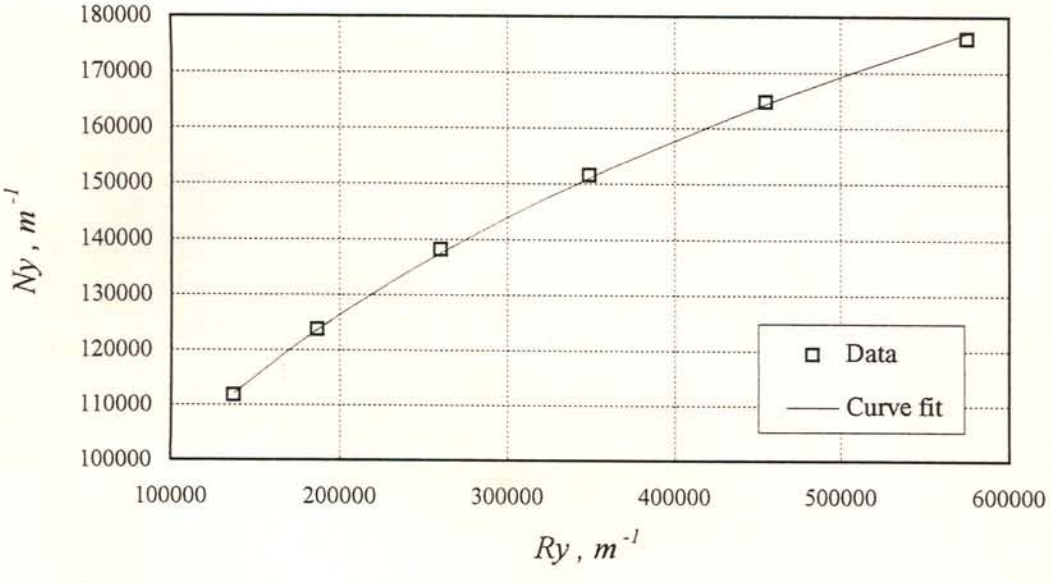

Figure J.2: Heat transfer performance characteristic of test bundle.

J.4 Performance characteristics of the full scale condenser under investigation

A double row test bundle was constructed to obtain the heat transfer characteristics for the finned tube bundles employed in the condenser and dephlegmator units. The heat transfer characteristic were determined for each row individually. By testing row (2) in

the presence of row (1) in a double row prototype bundle, the turbulence induced by row (1) is effectively accounted for by the *Ny-Ry* characteristics of row (2).

The heat transfer characteristics of row (1) and (2) are

Row (1): $Ny_{(1)} = 583.830\, Ry_{(1)}^{0.4031}$ (J.16a)

Row (2): $Ny_{(2)} = 1277.7255\, Ry_{(2)}^{0.3806}$ (J.16b)

Equation (G.82) (derivation of the draft equation) requires a loss coefficient K_{heiso} which accounts for the loss in total pressure for normal flow under isothermal conditions. The loss coefficient was determined in the wind-tunnel for the double row bundle and is expressed as a function of the characteristic flow parameter, i.e.

$$K_{heiso} = 4464.4\, Ry^{-0.4393} \quad \text{(J.17)}$$